

REPORT DOCUMENTATION PAGE				Form Approved OMB No. 0704-0188	
a. REPORT SECURITY CLASSIFICATION UNCLASSIFIED			1b. RESTRICTIVE MARKINGS		
a. SECURITY CLASSIFICATION AUTHORITY			3. DISTRIBUTION/AVAILABILITY OF REPORT Approved for public release; distribution unlimited.		
b. DECLASSIFICATION/DOWNGRADING SCHEDULE					
PERFORMING ORGANIZATION REPORT NUMBER(S)			5. MONITORING ORGANIZATION REPORT NUMBER(S) AFOSR-EX-85-0702		
a. NAME OF PERFORMING ORGANIZATION UNIVERSAL ENERGY SYSTEMS INC.		6b. OFFICE SYMBOL (if applicable)	7a. NAME OF MONITORING ORGANIZATION Air Force Office of Scientific Research/XOT		
c. ADDRESS (City, State, and ZIP Code) 4401 Dayton Xenia Rd Dayton OH 45432			7b. ADDRESS (City, State, and ZIP Code) Building 410 Bolling AFB DC 20332		
a. NAME OF FUNDING/SPONSORING ORGANIZATION AFOSR		8b. OFFICE SYMBOL (if applicable) XOT	9. PROCUREMENT INSTRUMENT IDENTIFICATION NUMBER F49620-85-C-0013		
c. ADDRESS (City, State, and ZIP Code) Building 410 Bolling AFB DC 20332			10. SOURCE OF FUNDING NUMBERS		
			PROGRAM ELEMENT NO. 61102F	PROJECT NO. 3396	TASK NO. D5
1. TITLE (Include Security Classification) USAF Research Initiation Program Volume 3					
2. PERSONAL AUTHOR(S) Program Director Rodney C. Darrah					
13a. TYPE OF REPORT Interim		13b. TIME COVERED FROM _____ TO _____	14. DATE OF REPORT (Year, Month, Day) April 1988		15. PAGE COUNT
6. SUPPLEMENTARY NOTATION					
7. COSATI CODES			18. SUBJECT TERMS (Continue on reverse if necessary and identify by block number)		
FIELD	GROUP	SUB-GROUP			
9. ABSTRACT (Continue on reverse if necessary and identify by block number) (SEE REVERSE)					
20. DISTRIBUTION/AVAILABILITY OF ABSTRACT <input checked="" type="checkbox"/> UNCLASSIFIED/UNLIMITED <input type="checkbox"/> SAME AS RPT. <input type="checkbox"/> DTIC USERS			21. ABSTRACT SECURITY CLASSIFICATION Unclassified		
22a. NAME OF RESPONSIBLE INDIVIDUAL Lt. Col Claude Cavender, Program Manager			22b. TELEPHONE (Include Area Code) (202) 767-4970		22c. OFFICE SYMBOL XOT

INTRODUCTION

Research Initiation Program - 1985

AFOSR has provided funding for follow-on research efforts for the participants in the Summer Faculty Research Program. Initially this program was conducted by AFOSR and popularly known as the Mini-Grant Program. Since 1983 the program has been conducted by the Summer Faculty Research Program (SFRP) contractor and is now called the Research Initiation Program (RIP). Funding is provided to establish RIP awards to about half the number of participants in the SFRP.

Participants in the 1985 SFRP competed for funding under the 1985 RIP. Participants submitted cost and technical proposals to the contractor by 1 November 1985, following their participation in the 1985 SFRP.

Evaluation of these proposals was made by the contractor. Evaluation criteria consisted of:

1. Technical Excellence of the proposal
2. Continuation of the SFRP effort
3. Cost sharing by the University

The list of proposals selected for award was forwarded to AFOSR for approval of funding. Those approved by AFOSR were funded for research efforts to be completed by 31 December 1986.

The following summarizes the events for the evaluation of proposals and award of funding under the RIP.

- A. Rip proposals were submitted to the contractor by 1 November 1985. The proposals were limited to \$20,000 plus cost sharing by the universities. The universities were encouraged to cost share since this is an effort to establish a long term effort between the Air Force and the university.
- B. Proposals were evaluated on the criteria listed above and the final award approval was given by AFOSR after consultation with the Air Force Laboratories.
- C. Subcontracts were negotiated with the universities. The period of performance of the subcontract was between October 1985 and December 1986.

Copies of the Final Reports are presented in Volumes I through III of the 1985 Research Initiation Program Report. There were a total of 82 RIP awards made under the 1985 program.

UNITED STATES AIR FORCE
1986 RESEARCH INITIATION PROGRAM

Conducted by
UNIVERSAL ENERGY SYSTEMS, INC.

under
USAF Contract Number F49620-85-C-0013

RESEARCH REPORTS
VOLUME III OF III

Submitted to
Air Force Office of Scientific Research
Bolling Air Force Base
Washington, DC

By
Universal Energy Systems, Inc.
April 1988



Accession	
NTIS	CHAS <input checked="" type="checkbox"/>
DTIC	TAB <input type="checkbox"/>
Unannounced	<input type="checkbox"/>
Justification	
By	
Distribution	
Availability Codes	
Dist	Avail and/or Special
A-1	

TABLE OF CONTENTS

<u>SECTION</u>	<u>PAGE</u>
INTRODUCTION	i
STATISTICS	ii
PARTICIPANT LABORATORY ASSIGNMENT	vii
RESEARCH REPORTS	xv

INTRODUCTION

Research Initiation Program - 1986

AFOSR has provided funding for follow-on research efforts for the participants in the Summer Faculty Research Program. Initially this program was conducted by AFOSR and popularly known as the Mini-Grant Program. Since 1983 the program has been conducted by the Summer Faculty Research Program (SFRP) contractor and is now called the Research Initiation Program (RIP). Funding is provided to establish RIP awards to about half the number of participants in the SFRP.

Participants in the 1986 SFRP competed for funding under the 1986 RIP. Participants submitted cost and technical proposals to the contractor by 1 November 1986, following their participation in the 1986 SFRP.

Evaluation of these proposals was made by the contractor. Evaluation criteria consisted of:

1. Technical Excellence of the proposal
2. Continuation of the SFRP effort
3. Cost sharing by the University

The list of proposals selected for award was forwarded to AFOSR for approval of funding. Those approved by AFOSR were funded for research efforts to be completed by 31 December 1987.

The following summarizes the events for the evaluation of proposals and award of funding under the RIP.

- A. Rip proposals were submitted to the contractor by 1 November 1986. The proposals were limited to \$20,000 plus cost sharing by the universities. The universities were encouraged to cost share since this is an effort to establish a long term effort between the Air Force and the university.
- B. Proposals were evaluated on the criteria listed above and the final award approval was given by AFOSR after consultation with the Air Force Laboratories.
- C. Subcontracts were negotiated with the universities. The period of performance of the subcontract was between October 1986 and December 1987.

Copies of the Final Reports are presented in Volumes I through III of the 1986 Research Initiation Program Report. There were a total of 98 RIP awards made under the 1986 program.

STATISTICS

Total SFRP Participants	158
Total RIP Proposals submitted by SFRP	134
Total RIP Proposals submitted by GSSSP	7
Total RIP Proposals submitted	141

Total RIP's funded to SFRP	94
Total RIP's funded to GSSSP	4
Total RIP's funded	98

Total RIP's Proposals submitted by HBCU's	14
Total RIP's Proposals funded to HBCU's	9

<u>Laboratory</u>	<u>SFRP Participants</u>	<u>RIP's Submitted</u>	<u>RIP's Funded</u>
AAMRL	9	11 (3 GSSSP)	5 (1 GSSSP)
APL	8	7	6
-AD	11	12 (3 GSSSP)	9 (3 GSSSP)
AEDC	6	6	3
-AL	7	6	5
BRMC	2	2	0
LC	1	1	1
ESMC	0	0	0
ESD	2	1	1
ESC	7	6	5
FDL	13	13 (1 GSSSP)	9
FJSRL	8	8	4
GL	13	9	7
HRL/OT	4	4	2
HRL/LR	4	4	2
HRL/MO	3	2	2
HRL/ID	4	4	3
LMC	2	1	1
-ML	11	8	6
OEHL	4	4	3
RPL	5	4	4
RADC	9	8	7
SAM	17	13	8
WHMC	1	1	1
WL	7	6	4
Total	158	141	98

LIST OF UNIVERSITY THAT PARTICIPATED

Adelphi University	1	Meharry Medical College	2
Alabama A&M University	2	Miami University of Ohio	1
Alabama, University of	5	Miami, University of	1
Alaska, University of	1	Mississippi State University	1
Alfred University	2	Mississippi, University of	1
Auburn University	1	Missouri, University of	2
Boise State University	1	Morehouse College	2
Bradley University	1	Motlow State College	1
Brown University	1	Nebraska, University of	1
Carleton College	1	New Mexico, University of	1
Catholic University of America	1	New Orleans, University of	1
Cedarville College	1	New York University	1
Cincinnati, University of	3	Norfolk State University	1
Colorado, University of	1	North Carolina A&T University	1
Dartmouth College	1	North Carolina, University of	1
Davidson College	1	North Texas State University	1
Dayton, University of	5	Northern Arizona Univeristy	1
Drexel University	1	Northwestern University	1
Duke University	1	Oakwood College	1
Eastern Kentucky University	1	Ohio State University	4
Eastern Montana College	1	Ohio University	3
Edinboro University	1	Oklahoma State University	2
Florida Atlantic University	1	Oklahoma, University of	1
Florida International University	1	Oregon State University	1
Florida State University	2	Pacific University	1
Florida University	3	Paine College	1
Florida, University of	3	Pennsylvania State University	1
Franklin and Marshall College	1	Portland, University of	1
Georgia Institute of Technology	1	Purdue University	2
Georgia, University of	2	Scanton, University of	1
Grambling State University	1	South Carolina, University of	1
Houghton College	1	Southern Illinois University	1
Indiana University	2	Southern Michigan, University of	1
Iowa State University	1	Southern University	1
Iowa, University of	1	Stetson University	1
Jackson State University	4	Stevens Institute of Technology	1
Jefferson State	1	Syracuse, University of	1
Jesm Baromedical Research	1	Tennessee, University of	1
Kansas State Unviersity	1	Texas A&I University	1
Kennesaw University	1	Texas A&M University	2
Lehigh University	1	Texas Southern University	2
Louisiana State University	5	Texas, University of	2
Lowell, University of	2	The Citadel	2
Lyndon State College	1	Toledo, University of	1

(Continued)

LIST OF UNIVERSITY THAT PARTICIPATED

MIT	1	Touglao College	1
Maine, University of	1	Trinity University	1
Marquette University	1	Tulsa, University of	2
Mary Washington College	1	U.S. Naval Academy	1
Massachusetts, University of	1	Valparaiso University	1
Vanderbilt University	1	West Virginia University	1
Warren Wilson College	1	Wichita State University	1
Washington State University	2	Wisconsin-Eau Claire	1
Wayne State University	1	Worcester Polytechnic	1
West Florida, University of	1	Wright State University	4
West Georgia College	1	Wyoming, University of	2
		Xavier University	1

PARTICIPANTS LABORATORY ASSIGNMENT

PARTICIPANT LABORATORY ASSIGNMENT (Page 1)

ARMAMENT LABORATORY

(Eglin Air Force Base)

Dr. Prabhat Hajela
University of Florida
Specialty: Aeronautics & Astronautics

Dr. Boghos D. Sivazlian
The University of Florida
Specialty: Operations Research

Dr. David I. Lawson
Stetson University
Specialty: Mathematics

Mr. Chris Reed (GSRP)
Florida University
Specialty: Aerodynamics

Dr. Barbara Rice
Alabama A&M University
Specialty: Mathematics

Mr. Jim Sirkis (GSRP)
Florida University
Specialty: Engineering Mechanics

Dr. Sally A. Sage
West Georgia College
Specialty: Computer Science

Ms. Jennifer Davidson (GSRP)
Florida University
Specialty: Mathematics

Dr. Meckinley Scott
University of Alabama
Specialty: Statistics

ARNOLD ENGINEERING DEVELOPMENT CENTER

(Arnold Air Force Systems)

Dr. Glen Johnson
Vanderbilt University
Specialty: Mechanical Eng.

Dr. Arthur A. Mason
The University of Tennessee
Specialty: Physics

ELECTRONIC SYSTEMS DIVISION

(Hanscom Air Force Base)

Dr. Stephan E. Kolitz
University of Massachusetts
Specialty: Operations Research

PARTICIPANT LABORATORY ASSIGNMENT (Page 2)

ENGINEERING AND SERVICES CENTER
(Tyndall Air Force Base)

Dr. Thomas A. Carney
Florida State University
Specialty: Meteorology

Dr. William T. Cooper
Florida State University
Specialty: Chemistry

Dr. Yong S. Kim
The Catholic Univ. of America
Specialty: Civil Engineering

Dr. Cheng Liu
University of North Carolina
Specialty: Civil Engineering

Dr. Roy M. Ventullo
University of Dayton
Specialty: Microbiology

FRANK J. SEILER RESEARCH RESEARCH LABORATORY
(United State Air Force Academy)

Dr. David R. Anderson
University of Colorado
Specialty: Organic Chemistry

Dr. Bernard J. Piersma
Houghton College
Specialty: Physical Chemistry

Dr. William D. Siuru, Jr.
University of Colorado
Specialty: Mechanical Eng.

Dr. Timothy R. Troutt
Washington State University
Specialty: Mechanical Eng.

GEOPHYSICS LABORATORY
(Hanscom Air Force Base)

Dr. John E. Ahlquist
Florida State University
Specialty: Meteorology

Dr. Frank P. Battles
Mass. Maritime Academy
Specialty: Physics

Dr. Wolfgang Christian
Davidson College
Specialty: Physics

Dr. Donald F. Collins
Warren Wilson College
Specialty: Physics

Dr. Patrick T. Gannon, Sr.
Lyndon State College
Specialty: Atmospheric Science

Dr. C. Randal Lishawa
Jefferson State University
Specialty: Physical Chemistry

Dr. Robert M. Nehs
Texas Southern University
Specialty: Mathematics

PARTICIPANT LABORATORY ASSIGNMENT (Page 3)

LOGISTICS COMMAND

(Wright-Patterson Air Force Base)

Dr. Ming-Shing Hung
Kent State University
Specialty: Business Administration
Management Science

LOGISTICS MANAGEMENT CENTER

(Gunter Air Force System)

Dr. Dan B. Rinks
Louisiana State University
Specialty: Quantitative Mgmt. Science

ASTRONAUTICS LABORATORY

(Edwards Air Force Base)

Dr. William M. Grissom
Morehouse College
Specialty: Mechanical Engineering

Dr. Joel R. Klink
Univ. of Wisconsin-Eau Claire
Specialty: Organic Chemistry

Dr. Siavash H. Sohrab
Northwestern University
Specialty: Engineering Physics

Dr. Nicholas E. Takach
University of Tulsa
Specialty: Chemistry

ROME AIR DEVELOPMENT CENTER

(Griffis Air Force Base)

Dr. Donald F. Hanson
University of Mississippi
Specialty: Electrical Engineering

Dr. John M. Jobe
Miami University of Ohio
Specialty: Statistics

Dr. Philipp G. Kornreich
Syracuse University
Specialty: Electrical Engineering

Dr. Mou-Liang Kung
Norfolk State University
Specialty: Mathematics

Dr. Craig G. Prohazka
University of Lowell
Specialty: Electrical Engineering

Dr. Richard S. Quimby
Worcester Polytechnic Institute
Specialty: Physics

Dr. Stephen T. Welstead
University of Alabama
Specialty: Applied Mathematics

PARTICIPANT LABORATORY ASSIGNMENT (Page 4)

WEAPONS LABORATORY

(Kirtland Air Force Base)

Dr. Albert W. Biggs
University of Alabama
Specialty: Electrical Eng.

Dr. Fabian C. Hadipriono
The Ohio State University
Specialty: Engineering, Civil

Dr. Alexandru A. Pelin
Florida International Univ.
Specialty: Computer Science

Dr. Martin A. Shadday, Jr.
University of South Carolina
Specialty: Mechanical Engineering

AERO PROPULSION LABORATORY

(Wright-Patterson Air Force Base)

Dr. Lea D. Chen
The University of Iowa
Specialty: Organic Chemistry

Dr. Jacob N. Chung
Washington State University
Specialty: Mechanical Engineering

Dr. Shirshak K. Dhali
Southern Illinois University
Specialty: Electrical Engineering

Dr. James C. Ilo
Wichita State University
Specialty: Chemistry

Dr. Mo Samimy
Ohio State University
Specialty: Mechanical Engineering

Dr. Robert P. Taylor
Mississippi State University
Specialty: Mechanical Engineering

AVIONICS LABORATORY

(Wright-Patterson Air Force Base)

Dr. John Y. Cheung
University of Oklahoma
Specialty: Electrical Engineering

Dr. William A. Grosky
Wayne State University
Specialty: Eng. & Applied Science

Dr. Ken Tomiyama
Pennsylvania State University
Specialty: System Science

Dr. Dennis W. Whitson
Indiana Univ. of Pennsylvania
Specialty: Physics

Dr. George W. Zobrist
University of Missouri-Rolla
Specialty: Electrical Engineering

PARTICIPANT LABORATORY ASSIGNMENT (Page 5)

FLIGHT DYNAMICS LABORATORY

(Wright-Patterson Air Force Base)

Dr. Bor-Chin Chang
Bradley University
Specialty: Electrical Eng.

Dr. George R. Doyle, Jr.
University of Dayton
Specialty: Mechanical Eng.

Dr. Paul S.T. Lee
N.C. A&T State University
Specialty: Quantitative Methods

Dr. V. Dakshina Murty
University of Portland
Specialty: Engineering Mechanics

Dr. Singiresu S. Rao
Purdue University
Specialty: Engineering Design

Dr. Tsun-wai G. Yip
Ohio State University
Specialty: Aeronautics

Dr. Ajmal Yousuff
Drexel University
Specialty: Aeronautics

Dr. Richard W. Young
University of Cincinnati
Specialty: Applied Mechanics

Dr. Peter J. Disimile
University of Cincinnati
Specialty: Fluid Mechanics

MATERIALS LABORATORY

(Wright-Patterson Air Force Base)

Dr. Lokesh R. Dharani
University of Missouri-Rolla
Specialty: Engineering Mechanics

Dr. Gerald R. Graves
Louisiana State University
Specialty: Industrial Engineering

Dr. Gopal M. Mehrotra
Wright State University
Specialty: Metallurgy

Dr. Robert A. Patsiga
Indiana Univ. of Pennsylvania
Specialty: Organic Polymer Chem.

Dr. Nisar Shaikh
University of Nebraska-Lincoln
Specialty: Applied Mathematics

Dr. Stuart R. Stock
Georgia Institute of Technology
Specialty: Metallurgy

PARTICIPANT LABORATORY ASSIGNMENT (Page 6)

HARRY G. ARMSTRONG AEROSPACE MEDICAL RESEARCH LABORATORY
(Wright-Patterson Air Force Base)

Ms. Beverly Girten
Ohio University
Specialty: Physiology

Dr. Albert R. Wellens
University of Miami
Specialty: Experimental Social

Dr. Jacqueline G. Paver
Duke University
Specialty: Biomechanical Eng.

Dr. Robert L. Yolton
Pacific University
Specialty: Psychology, Optometry

Dr. Kuldip S. Rattan
Wright State University
Specialty: Electrical Engineering

HUMAN RESOURCES LABORATORY - LOGISTICS AND HUMAN FACTORS DIVISION
(Wright-Patterson Air Force Base)

Dr. Patricia T. Boggs
Wright State University
Specialty: Decision Science

Dr. Stephen L. Loy
Iowa State University
Specialty: Management Information

HUMAN RESOURCES LABORATORY - OPERATIONS TRAINING DIVISION
(Williams Air Force Base)

Dr. Billy R. Wooten
Brown University
Specialty: Philosophy, Psychology

HUMAN RESOURCES LABORATORY - MANPOWER AND PERSONNEL DIVISION
(Brooks Air Force Base)

Dr. Richard H. Cox
Kansas State University
Specialty: Motor Learning & Control

Dr. Jorge L. Mendoza
Texas A&M University
Specialty: Psychology

USAF OCCUPATIONAL AND ENVIRONMENT HEALTH LABORATORY
(Brooks Air Force Base)

Dr. Clifford C. Houk
Ohio University
Specialty: Inorganic Chemistry

Dr. Shirley A. Williams
Jackson State University
Specialty: Physiology

Dr. Ralph J. Rascati
Kennesaw College
Specialty: Biochemistry

HUMAN RESOURCES LABORATORY - TRAINING SYSTEMS
(Brooks Air Force Base)

Dr. Charles E. Lance
University of Georgia
Specialty: Psychology

Dr. Doris J. Walker-Dalhouse
Jackson State University
Specialty: Reading Education

Dr. Philip D. Olivier
University of Texas
Specialty: Electrical Engineering

SCHOOL OF AEROSPACE MEDICINE
(Brooks Air Force Base)

Dr. Hoffman H. Chen
Grambling State University
Specialty: Mechanical Engineering

Dr. Frank O. Hadlock
Florida Atlantic University
Specialty: Mathematics

Dr. Brenda J. Claiborne
University of Texas
Specialty: Biology

Dr. Parsottam J. Patel
Meharry Medical College
Specialty: Microbiology

Dr. Vito G. DelVecchio
University of Scranton
Specialty: Biochemistry, Genetics

Dr. Richard M. Schori
Oregon State University
Specialty: Mathematics

Dr. Ramesh C. Gupta
University of Maine at Orono
Specialty: Mathematical Statistics

Dr. Shih-sung Wen
Jackson State University
Specialty: Educational Psychology

WILFORD HALL MEDICAL CENTER
(Lackland Air Force Base)

Dr. Donald W. Welch
Texas A&M University
Specialty: Microbiology

RESEARCH REPORTS

MINI-GRANT RESEARCH REPORTS
1986 RESEARCH INITIATION PROGRAM

<u>Technical Report Number</u> Volume I	<u>Title and Mini-Grant No.</u>	<u>Professor</u>
1	Weather Forecast Evaluation be Decomposition of the Wind Field into Barotropic and Baroclinic Components 760-6MG-041	Dr. Jon Ahlquist
2	An EPR Study of the Role of Catalysts in the Thermal Decom- position of Nitroaromatic Compounds 760-6MG-044	Dr. David Anderson
3	Stellar Scintillometer Based Studies of Optical Turbulence 760-6MG-058	Dr. Frank Battles
4	Requested A No-Cost Time Extention. To Be Submitted In 1987 Mini-Grant Final Report. 760-6MG-072	Dr. Albert Biggs
5	Basic Research on the Impact of Cognitive Styles on Decision Making 760-6MG-127	Dr. Patricia Boggs
6	A Feasibility Study and Test Appli- cation of Uncertainty Estimates to an Atmospheric Dispersion Model with Potential Utility in Air Force Operations 760-6MG-050	Dr. Thomas Carney
7	Design of H Multivariable Optimal Control Systems 760-6MG-013	Dr. Bor-Chin Chang
8	Visualization of Hydrocarbon Jet Diffusion Flames 760-6MG-113	Dr. Lea Chen

- | | | |
|----|--|------------------------|
| 9 | Requested A No-Cost Time Extension.
To Be Submitted In 1987 Mini-Grant
Final Report.
760-6MG-118 | Dr. Hoffman Chen |
| 10 | Report Not Received In Time.
Will Be Provided When Available.
760-6MG-135 | Dr. John Cheung |
| 11 | Infrared Fluorescence and Photo-
acoustic Measurements of NO ($v=2$)
Relaxation as a Function of Temp-
erature
760-6MG-030 | Dr. Wolfgang Christian |
| 12 | Heat and Mass Transfer in a Dual-
Latent Heat Packed Bed Thermal
Storage System
760-6MG-067 | Dr. Jacob Chung |
| 13 | Long-term Potentiation in Inter-
neurons in the Mammalian Brain
760-6MG-101 | Dr. Brenda Claiborne |
| 14 | The Development of Image Processing
Algorithms for AFGL Ultraviolet
Camera and Other Imaging Systems
760-6MG-028 | Dr. Donald Collins |
| 15 | Report Not Received In Time.
Will Be Provided When Available.
760-6MG-081 | Dr. William Cooper |
| 16 | Relationship Between Stages of
Motor Learning and Kinesthetic
Sensitivity
760-6MG-069 | Dr. Richard Cox |
| 17 | Received A No-Cost Time Extension.
To Be Submitted In 1987 Mini-Grant
Final Report.
760-6MG-024 | Ms. Jennifer Davidson |
| 18 | Report Not Received In Time.
Will Be Provided When Available.
760-6MG-076 | Dr. Vito DelVecchio |

- | | | |
|----|---|--------------------|
| 19 | Investigation of Pulsed Discharges
in Nitrogen for Plasma Processing
760-6MG-046 | Dr. Shirshak Dhali |
| 20 | Modeling of Failure Mechanisms in
Ceramic Composites Under Flexural
Loading
760-6MG-115 | Dr. Lokesh Dharani |
| 21 | Requested A No-Cost Time Extention.
To Be Submitted In 1987 Mini-Grant
Final Report.
760-6MG-075 | Dr. Peter Disimile |
| 22 | Requested A No-Cost Time Extention.
To Be Submitted In 1987 Mini-Grant
Final Report.
760-6MG-006 | Dr. George Doyle |
| 23 | Sensitivity of Mesoscale Wind to
Variations in Vegetation Canopy
Parameters and Surface Properties
760-6MG-100 | Dr. Patrick Gannon |
| 24 | Effects of Exercise and Dobutamine
on Suspension Hypokinesia/
Hypodunamia Deconditioning in Rats
760-6MG-139 | Ms. Beverly Girten |
| 25 | An Investigation of Computer
Communications Using Knowledge-
Based Systems
760-6MG-015 | Dr. Gerald Graves |

Volume II

- | | | |
|----|--|-----------------------|
| 26 | Droplet Size Distribution Measure-Dr. William Grissom
ment In A Single Element Liquid
Rocket Injector
760-6MG-040 | |
| 27 | A Unified Approach of the Linear
Camera Calibration Problem
760-6MG-070 | Dr. William Grosky |
| 28 | Survival Anaysis of Radiated
Animals for Small Sample Sizes
760-6MG-053 | Dr. Ramesh Gupta |
| 29 | Report Not Received In Time.
Will Be Provided When Available.
760-6MG-054 | Dr. Fabian Hadipriono |

- | | | |
|----|---|--------------------|
| 30 | Requested A No-Cost Time Extention.
To Be Submitted In 1987 Mini-Grant
Final Report.
760-6MG-073 | Dr. Frank Hadlock |
| 31 | Studies in Optimum Shape Synthesis
for Structures Undergoing Plastic
Deformation
760-6MG-002 | Dr. Prabhat Hajela |
| 32 | Report Not Received In Time.
Will Be Provided When Available.
760-6MG-092 | Dr. Donald Hanson |
| 33 | Pulsed Power Conductors
760-6MG-005 | Dr. James Ho |
| 34 | The Locally Implicit Method for
Computational Aerodynamics
760-6MG-111 | Dr. Peter Hoffman |
| 35 | Fluorescent Dye Binding Identifi-
cation of Asbestos on Membrane
Filters and in Bulk Materials
760-6MG-066 | Dr. Clifford Houk |
| 36 | Requested A No-Cost Time Extention.
To Be Submitted In 1987 Mini-Grant
Final Report.
760-6MG-105 | Dr. Ming S. Hung |
| 37 | Report Not Received In Time.
Will Be Provided When Available.
760-6MG-019 | Dr. John Jobe |
| 38 | Expert System for Optimal Design
760-6MG-016 | Dr. Glen Johnson |
| 39 | Report Not Received In Time.
Will Be Provided When Available.
760-6MG-004 | Dr. Yong Kim |
| 40 | The Synthesis of Some New Energetic
Materials
760-6MG-056 | Dr. Joel Klink |

- | | | |
|----|--|-----------------------|
| 41 | Report Not Received In Time.
Will Be Provided When Available.
760-6MG-094 | Dr. Steve Kolitz |
| 42 | MBE Grown Al-Cu Alloy Films
760-6MG-090 | Dr. Philipp Kornreich |
| 43 | Simulation for Priority Handling
Algorithms
760-6MG-011 | Dr. Mou-Liang Kung |
| 44 | Received A No-Cost Time Extention.
To Be Submitted In 1987 Mini-Grant
Final Report.
760-6MG-031 | Dr. Charles Lance |
| 45 | A Neural Network Simulation
Generator, Simualtions of Learned
Serial Behavior, and a Neural
Explanation of Emergent Communi-
cation
760-6MG-001 | Dr. David Lawson |
| 46 | Data Processing and Statistical
Analysis of In-Service Aircraft
Transparency Failures
760-6MG-023 | Dr. Paul Lee |
| 47 | Trajectory Studies of the
Bimolecular Reaction of
H2Ov/H2O
760-6MG-107 | Dr. C. Lishawa |
| 48 | Comparison of Field Rut Depth
Measurements and Rutting Pre-
dictions of Asphalt Pavement
Under High Tire Pressure and
Temperature
760-6MG-009
NOT PUBLISHABLE AT THIS TIME | Dr. Cheng Liu |
| 49 | Report Not Received In Time.
Will Be Provided When Available.
760-6MG-134 | Dr. Stephen Loy |
| 50 | Received A No-Cost Time Extention.
To Be Submitted In 1987 Mini-Grant
Final Report.
760-6MG-099 | Dr. Arthur Mason |

51	Report Not Received In Time. Will Be Provided When Available. 760-6MG-121	Dr. Gopal Mehrotra
52	Report Not Received In Time. Will Be Provided When Available. 760-6MG-136	Dr. Jorge Mendoza
53	Report Not Received In Time. Will Be Provided When Available. 760-6MG-079	Dr. Dakshina Murty
54	Development of a New Finite Element Grid for Limited Area Weather Models 760-6MG-120	Dr. Robert Nehs
55	Report Not Received In Time. Will Be Provided When Available. 760-6MG-032	Dr. Philip Olivier
56	Report Not Received In Time. Will Be Provided When Available. 760-6MG-131	Dr. Parsottam Patel
57	Report Not Received In Time. Will Be Provided When Available. 760-6MG-065	Dr. Robert Patsiga
58	Report Not Received In Time. Will Be Provided When Available. 760-6MG-020	Dr. Jacqueline Paver
59	Automatic Program Generation from Specifications Using Prolong 760-6MG-117	Dr. Alexandru Pelin
60	Some Novel Aspects of Organic Electrochemistry in Room Temp- erature Molten Salts 760-6MG-038	Dr. Bernard Piersma
61	Improved Distributed Operating System Communication Protocols 760-6MG-061	Dr. Craig Prohazka

- 62 Turnable Infrared to Visible Light Conversion in Rare Earth and Transition Metal Doped Fluoride Glasses
760-6MG-042 Dr. Richard Quimby
- 63 Optimal Structural Modifications to Enhance the Robustness of Actively Controlled Large Flexible Structures
760-6MG-036 Dr. Singiresu Rao
- 64 Report Not Received In Time. Will Be Provided When Available.
760-6MG-062 Dr. Ralph Rascati
- 65 MATRIXs-Based Computer Simulation of the Cardiovascular System Under +Gz Stress
760-6MG-104 Dr. Kuldip Rattan
- 66 Adaptive Grid Generation Techniques for Transonic Projectile Base Flow Problems
760-6MG-034 Mr. Chris Reed

Volume III

- 67 Utilization of the Image Algebra
760-6MG-106 Dr. Barbara Rice
- 68 Simulation Studies of MICAP Allocation Systems for EOQ Items
760-6MG-084 Dr. Dan Rinks
- 69 Computer Modeling of Infrared Signatures
760-6MG-017 Dr. Sally Sage
- 70 Received A No-Cost Time Extension. To Be Submitted In 1987 Mini-Grant Final Report.
760-6MG-059 Dr. Mo Samimy
- 71 An Intentional Tutor
760-6MG-052 Dr. Richard Schori
- 72 Report Not Received In Time. Will Be Provided When Available.
760-6MG-025 Dr. Meckinley Scott

- | | | |
|----|---|----------------------|
| 73 | Report Not Received In Time.
Will Be Provided When Available.
760-6MG-089 | Dr. Martin Shadday |
| 74 | Report Not Received In Time.
Will Be Provided When Available.
760-6MG-007 | Dr. Nisar Shaikh |
| 75 | Report Not Received In Time.
Will Be Provided When Available.
760-6MG-142 | Mr. Jim Sirkis |
| 76 | Two-Dimensional Flight Simulation
Model for an Aircraft with a
Rapidly Rotating Airfoil;
760-6MG-071 | Dr. William Siuru |
| 77 | Mission Effectiveness Analysis of
an Aircraft Attacking Passive
Targets;
760-6MG-018 | Dr. Boghos Sivazlian |
| 78 | Requested A No-Cost Time Extention.
To Be Submitted In 1987 Mini-Grant
Final Report.
760-6MG-110 | Dr. Siavash Sohrab |
| 79 | Synchrotron White Beam Topography
of Striations and Interface Break-
down in GaAs and of Strain Fields
in Si;
760-6MG-103 | Dr. Stuart Stock |
| 80 | Received A No-Cost Time Extention.
To Be Submitted In 1987 Mini-Grant
Final Report.
760-6MG-130 | Dr. Nicholas Takach |
| 81 | Complete Statistical Classification
of Natural Surface Roughness on
Gas Turbine Blades;
760-6MG-064 | Dr. Robert Taylor |
| 82 | Evaluation of Atmospheric Effects
for Operational Tactical Decision
Aid
760-6MG-047 | Dr. Ken Tomiyama |

- | | | |
|----|--|---------------------------|
| 83 | An Investigation Concerning the Formation of a Dynamic Stall Vortex on a Pitching Airfoil
760-6MG-087 | Dr. Timothy Troutt |
| 84 | Biodegradation of Aqueous Film Forming Foam Components in Laboratory Scale Microcosms
760-6MG-124 | Dr. Roy Ventullo |
| 85 | Requested A No-Cost Time Extension. To Be Submitted In 1987 Mini-Grant Final Report.
760-6MG-080 | Dr. Doris Walker-Dalhouse |
| 86 | Received A No-Cost Time Extension. To Be Submitted In 1987 Mini-Grant Final Report.
760-6MG-091 | Dr. Donald Welch |
| 87 | Effects of Telecommunication Media upon Group Decision Making Processes within a Multi-Team Situation Assessment Task
760-6MG-085 | Dr. Albert Wellens |
| 88 | Report Not Received In Time. Will Be Provided When Available.
760-6MG-063 | Dr. Steve Welstead |
| 89 | Can a supervisory Control Simulation System Assess Cognitive Abilities?
760-6MG-049 | Dr. Shih-sung Wen |
| 90 | Effects on the BICFET of the Fermi Distribution Factor and the ATA Mole Fraction
760-6MG-088 | Dr. Dennis Whitson |
| 91 | The Warehouse Layout Program
760-OMG-038 | Dr. Jesse Williams |
| 92 | Received A No-Cost Time Extension. To Be Submitted In 1987 Mini-Grant Final Report.
760-6MG-078 | Dr. Shirley Williams |

- 93 Report Not Received In Time. Dr. Billy Wooten
Will Be Provided When Available.
760-6MG-051
- 94 Report Not Received In Time. Dr. Tsun-wai Yip
Will Be Provided When Available.
760-6MG-109
- 95 Changes in Perceived Workload and Dr. Robert Yolton
Physiological Responses Associated
with Monocular Versus Binocular
Viewing Conditions
760-6MG-037
- 96 Finite Element Analysis of Thermo- Dr. Richard Young
mechanically Coupled Stress and
Temperature Fields
760-6MG-129
- 97 Simplification of H₂ Compensators Dr. Ajmal Yousuff
760-6MG-098
- 98 Late Appointment. Dr. George Zobrist
Final Report Will Be Provided
When Available.
760-6MG-055

1655s

USAF - LES SUMMER FACULTY RESEARCH PROGRAM/
MINI GRANT PROGRAM

Sponsored by the
AIR FORCE OFFICE OF SCIENTIFIC SERVICES
BOLLING AFB, DC

conducted by the
Universal Energy Systems, Inc.

FINAL REPORT

UTILIZATION OF THE IMAGE ALGEBRA

Prepared by:	Barbara S. Rice
Academic Rank:	Associate Professor
Department and	Department of Mathematics
University:	Alabama A&M University
Research Location:	Air Force Armament Laboratory, Advanced Seeker Division, Electro-Optical Terminal Guidance Branch
USAF Researcher:	Neal Urquhart
Date:	February 27, 1988
Contract No.	F49620-85-C-0013/SB5851-0360

ACKNOWLEDGEMENTS

I would like to express my appreciation to the Air Force Office of Scientific Services, Bolling AFB, DC, for sponsorship of this effort. I appreciate very greatly this opportunity to continue my participation in the Image Algebra Project. This document represents a continuation of the work I performed as a 1986 Summer Faculty Research Program Fellow at the Air Force Armament Laboratory, Eglin AFB, Florida.

Special thanks are due to Dr. Sam Lambert (AFATL) for his enthusiastic interest in the Summer Faculty Research Program and the Mini Grant Program; and to Mr. Neal Urquhart (ASE) for his unfailing interest and support, and for his guidance of the Image Algebra Program.

I am also appreciative of the encouragement I received from my home institution, Alabama A&M University.

PREFACE

The Image Algebra Project is based on a plan to consider image transformations as operations on images. The image algebra provides an algebraic formulation to specify the images, templates, and operations of transformations, thus replacing lengthy pixel-by-pixel computational programs. The goal of the image algebra is to describe the precise form of images, templates, and the several kinds of operations; to develop the theory of computation within the image algebra; to identify known image transformations with their specification in the image algebra; and to provide machine implementation of the image algebra.

This problem has been addressed in the Image Algebra Project, 1985-8; the Final Report of Phase I of this project is available as a Defense Technical Information Center Technical Report [4]. Phase II of this project is described in Program Review reports [6], with a final report scheduled at the completion of the project. Certain topics of the image algebra have also been described in technical journals [5, 9]. These reports cover a vast area of theoretical and technical work, and consequently it is difficult for the novice user to grasp the form and mechanics of the image algebra, and acquire insight for its structure, from primary sources alone. A need was identified for the development of a more expository approach to the image algebra.

This document, Utilization of the Image Algebra, has been prepared to assist prospective users in learning the techniques of the image algebra. The emphasis of this manual is the demonstration of the usage of images, templates, and the several operations in the setting of the image algebra, together with the interpretation of image processing techniques in the image algebra.

I. IMAGES AND IMAGE TRANSFORMATIONS

We first consider a precise definition for an image. In this document we will consider images formed in the following way: pixels (picture elements) correspond to locations in an $m \times n$ rectangular array X , with (i,j) denoting the pixel in row i and column j of the array. At each pixel, a sensor provides a numerical value, the gray level; $a(i,j)$ indicates the gray level value at pixel (i,j) . Gray values indicate measurements made by the sensor of the appropriate phenomenon (e.g. heat, intensity of radiation). The array $A = \{a(i,j)\}$ is an image. For purposes of illustration, in this document we will suppose that all values $a(i,j)$ are real; more generally, gray values may be complex valued.

Definition I-1:

If X is an $m \times n$ rectangular space, and $A = \{A(x) : x \text{ is in } X\}$ is a real valued function on X , then A is an image.

We next give consideration to the role of image transformations. We realize that gray level values are subject to numerous kinds of errors, and that data recorded as an image may require some interpretation. Consequently, recognition of the characteristics of the image may depend on some processing of the raw gray level data to minimize the effects of such errors.

Intensity enhancement and image smoothing provide two examples of image transformations:

INTENSITY ENHANCEMENT - Multiply each gray level value by a fixed constant k ; thus for each x in X , the transformed image value $B(x)$ is given by $k A(x)$.

IMAGE SMOOTHING - For each x in X , replace each value $A(x)$ by the average of the gray level values at x and its immediate neighbors to obtain the transformed image value $B(x)$.

In these examples we note that a process has been prescribed to transform an image on X into another image on X : we could write $T(A) = B$ where for each x in X , $T(A)(x) = B(x)$; for the transformation replaces the gray value of the image A at x by a new gray value at x .

It may be desirable to consider processes which transform an image on X into an image on another space Y . We may, for example, consider performing image magnification and rotation. Part of the image would be lost in a rotation of the image at 45 degrees unless an appropriately larger space Y is used for the transformed image. The idea in each of these situations is that a process is defined which associates a gray value function A on a space X with another gray value function B on a space Y ;

we say that the original image A on X is transformed into a new image B on Y , and we write $B = T(A)$.

In many image processing transformations, the transformed value at each pixel depends only on the gray level values at certain pixels adjacent to x . For this reason, it is appropriate to consider some concept of neighborhoods of a pixel.

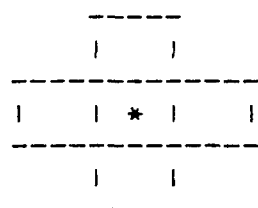
Definition I-2:

The Von Neumann neighborhood of x is formed by the pixel x , together with the pixels at the immediate north, south, east, and west of x . It is usual to denote this neighborhood by the diagram of Figure I-1(a) at the left below, with the location of the pixel x denoted by the symbol $*$.

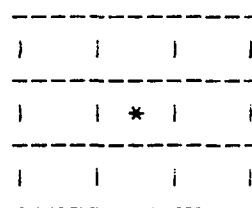
Definition I-3:

The Moore neighborhood of x is formed by pixel x together with the eight pixels having vertices or edges which touch x . This neighborhood is denoted by the diagram of Figure I-1(b) at the right below; the location of x is again denoted by the symbol $*$.

Figure I-1:



(a) Von Neumann Neighborhood



(b) Moore neighborhood

Some image transformations have been described by the use of a mask. A mask is an identification of a geometrical configuration of pixels about a center pixel, with numerical values assigned as weights at each pixel of the configuration. The mask is represented by a diagram of the pixels of the configuration, with the center indicated by the symbol $*$; the assigned weights are indicated at each pixel of the configuration. In practice, the mask is considered to be centered, in turn, at each pixel of the space.

We illustrate with three examples of masks which are used in detecting features of an image. In Figure I-2, mask (a) is used to detect horizontal line segments; mask (b) is used to detect isolated points; and mask (c) is used in detection of a horizontal edge.

Figure I-2:

```

-----
| -1| -1| -1|
-----
|  2| *2|  2|
-----
| -1| -1| -1|
-----
(a)

```

```

-----
| -1| -1| -1|
-----
| -1| * 8| -1|
-----
| -1| -1| -1|
-----
(b)

```

```

-----
| -1| -2| -1|
-----
|  0| * 0|  0|
-----
|  1|  2|  1|
-----
(c)

```

We now consider a slight modification of this process: at each point x of X , we will specify a neighborhood of x , $N(x)$; then at each pixel y of this neighborhood $N(x)$ we will specify a weight $w_x(y)$. In this way we associate with each x of X , first a set in X , $N(x)$; and second a weight function w_x defined on X , which may be nonzero only on $N(x)$. A mask can be described in this way, for appropriate choices of the neighborhood system and of the weight functions, as we can see in the examples below.

Example I-1:

For x in X , $N(x) = x$; and $w_x(x) = 1$.

This corresponds to the mask

```

-----
| * 1|
-----

```

Example I-2:

For x in X , $N(x)$ is the Moore neighborhood of x ;
for y in $N(x)$, $w_x(y) = 1$.

This corresponds to the mask

```

-----
|  1|  1|  1|
-----
|  1| * 1|  1|
-----
|  1|  1|  1|
-----

```

Example I-3:

For x in X , $N(x)$ is the von Neumann neighborhood of x ;
for y in $N(x)$, $w_x(y) = 1$.

This corresponds to the mask

```

-----
|  1|
-----
|  1| * 1|  1|
-----
|  1|
-----

```

Example I-4:

For x in X , $N(x)$ is the Moore neighborhood of x ; at the center x , $w_x(x) = 8$; and for y in $N(x)$, but distinct from x , $w_x(y) = -1$.

This corresponds to mask (b) of Figure I-2 above.

Although this matching of a neighborhood and a weight function for every point of x in X can be used to describe a mask which is centered at each point of X in turn, the process is more general than designating masks. There is no requirement that the same kind of neighborhood $N(x)$ be used for all x of X ; nor is there any requirement that the weights agree at corresponding pixels of all neighborhoods. We will develop this process of assigning a neighborhood and a weight function to each pixel x of X in later sections of this manual; it is central to the image algebra.

Definition I-2 (Preliminary):

A template T on X is a collection $\{t_x: x \text{ is in } X\}$ of functions on X ; corresponding to the function t_x there is a set $N(x)$ in X , with $t_x(y) = 0$ if y is not in $N(x)$. To denote a template, we write $T = \{(N(x), t_x) : x \text{ is in } X\}$, or $T = (N(x), t_x)$.

We return now to the traditional idea of the mask and consider its use in performing image transformations. Masks are often used in this way:

Consider the mask centered at x . Multiply each weight of the mask by the gray level value at corresponding pixel of the image; the transformed gray level value at x is the sum of all products so formed. This process is repeated for every point of X . (Note that some modification of this process is needed for points which are on the boundary of X , since the mask centered at a boundary point is not entirely contained in X .)

We have just described the operation of a mask on an image. In the image algebra, many image transformations will be described by the operation of a template on an image. In the image algebra we will see that there are several kinds of operations:

IMAGE - IMAGE operations, in which a resultant IMAGE is assigned to each ordered pair of images, under the operation;

IMAGE - TEMPLATE operations, in which a resultant IMAGE is assigned to each ordered pair consisting of one image and one template;

TEMPLATE - TEMPLATE operations, in which a resultant TEMPLATE is assigned to each ordered pair of templates.

These operations will be described fully in the following sections of this document. The precise definition of these operations, and the development of the mathematical structure resulting from these definitions, is the goal of the image algebra.

II. IMAGE - IMAGE OPERATIONS

Since each image on X is a real valued function on X , we can define certain image operations by employing the corresponding pointwise operations at each point of X . Binary operations assign, to each ordered pair of images, a unique resultant image; unary operations assign a unique resultant image for a single image. Since the points of X are pixels, we define the following operations for images, by using the pixel by pixel computation of the corresponding operation for real numbers.

Definition II-1:

If A and B are images on a space X , then C is the sum of A and B , written $A + B = C$, if $C(x) = A(x) + B(x)$, for each x in X .

Definition II-2:

If A and B are images on a space X , then C is the product of A and B , written $A * B = C$, if $C(x) = A(x) * B(x)$, for each x in X .

Definition II-3:

If A and B are images on a space X , then C is the maximum of A and B , written $A \vee B = C$, if $C(x) = A(x) \vee B(x)$, for each x in X .

In the following examples, for convenience of demonstration, we will use a 2×3 space X , although, in practice, the space X on which images are defined is much larger. Since each of these operations is defined in a pointwise manner, the process is unchanged, regardless of the size of X .

Example II-1:

If $A = \begin{matrix} 1 & 2 & 0 \\ -1 & 2 & 1 \end{matrix}$ and $B = \begin{matrix} 2 & 3 & 1 \\ 0 & -1 & 4 \end{matrix}$, then

$A + B = \begin{matrix} 3 & 5 & 1 \\ -1 & 1 & 5 \end{matrix}$;

$A * B = \begin{matrix} 2 & 6 & 0 \\ 0 & -2 & 4 \end{matrix}$; and

$A \vee B = \begin{matrix} 2 & 3 & 1 \\ 0 & 2 & 4 \end{matrix}$.

Definition II-4:

An image K is said to be a constant image, if for each x in X , $K(x) = k$, for some constant k .

We note that the identity image under addition, 0 , and the identity image, 1 , under multiplication, are constant images, with

$$0(x) = 0 \quad \text{and} \quad 1(x) = 1, \quad \text{for all } x \text{ in } X,$$

for $A + 0 = A$, and $A * 1 = A$.

Example II-2:

Using image A as in Example II-1,

$$K + A = \begin{matrix} & k+1 & k+2 & k+0 \\ k+1 & k-1 & k+2 & k+1 \end{matrix} \quad K * A = \begin{matrix} & k & 2k & 0 \\ k & -k & 2k & k \end{matrix}.$$

Just as the additive and multiplicative inverses are defined for real numbers, we can define the corresponding unary operations for images:

Definition II-5:

If A is an image on X , then $-A$, the additive inverse image of A , is given by $-A = \{-A(x), \text{ for } x \text{ in } X\}$.

Definition II-6:

If A is an image on X , then A^{-1} , is given by $A^{-1}(x) = 1/A(x)$, if $A(x)$ is non zero; otherwise $A^{-1}(x) = 0$.

We note that $-A$ has the character of an additive inverse, for $A + (-A) = 0$, for any image A . By contrast, A^{-1} does not have the multiplicative inverse property $A * A^{-1} = 1$, since for any x with $A(x) = 0$, then $A(x) * A^{-1}(x) = 0$, also. On the other hand, it is always true that $(A * A^{-1}) * A = A$.

Example II-3:

Using image B as given in Example II-1,

$$-B = \begin{matrix} & -2 & -3 & -1 \\ 0 & 0 & 3 & -4 \end{matrix} \quad \text{and} \quad B^{-1} = \begin{matrix} & 1/2 & 1/3 & 1 \\ 0 & 0 & -1 & 1/4 \end{matrix}$$

In a very natural way, the operations of additive and multiplicative inversion can be used to define the binary operations of subtraction, division, and minimization. We have the following definitions which can be expressed within the image algebra:

Definition II-7:

If A and B are images on X , then the difference $A - B$ is given by $A - B = A + (-B)$.

Definition II-8:

If A and B are images on X , then the quotient A / B is given by $A / B = A * (B^{-1})$.

We observe that since B^{-1} is not a true inverse, then A and $B * (A / B)$ are not necessarily identical, as we can note, by direct computation, at pixels x with $B(x) = 0$, but $A(x)$ nonzero.

Definition II-9:

If A and B are images on X , then the minimum $A \wedge B$ is given by $A \wedge B = - ((-A) \vee (-B))$.

Example II-4:

Using A and B as in Example II-1, we have

$$A - B = \begin{matrix} & -1 & -1 & -1 \\ -1 & -1 & 1 & -3 \end{matrix} ; \quad A / B = \begin{matrix} & 1/2 & 2/3 & 0 \\ & 0 & -2 & 1/4 \end{matrix} ; \text{ and}$$

$$A \wedge B = \begin{matrix} & 1 & 2 & 0 \\ -1 & -1 & -1 & 1 \end{matrix} .$$

The process of complementing a set is often useful, and consequently it is helpful to have an operation of this kind in the image algebra. If A is an image on X , and if X' is the set in X for which $A(x)$ is non zero, then the complementation operation on A will define an image A^{\sim} which has value 0 on X' , and value 1 on the complement of X' in X . We have the following definition in the image algebra:

Definition II-10

If A is an image on X , then A^{\sim} , the complementation of A , is the image $A^{\sim} = I - (A * A^{-1})$, where I is the multiplicative identity image on X .

Example II-5:

Using A as in Example II-1, since $A(x) * A^{-1}(x) = 1$, if $A(x)$ is non zero, and since $A(x) * A^{-1}(x) = 0$, if $A(x) = 0$, then

$$A * A^{-1} = \begin{matrix} & 1 & 1 & 0 \\ 1 & 1 & 1 & 1 \end{matrix} \quad \text{and} \quad A^{\sim} = \begin{matrix} & 0 & 0 & 1 \\ 0 & 0 & 0 & 0 \end{matrix} .$$

Functions can be defined on images, by computing the functional value of the gray value for each pixel of the space X , provided that the domain of the function includes the set of all gray values of the image.

Definition II-11:

If A is an image on X , and if f is a real valued function which is defined for every value $A(x)$, for x in X , then $f(A)$ is the image on X given by

$$f(A) = \{f(A(x)) , \text{ for } x \text{ in } X\}.$$

Example II-6:

Using A as in example II-1,

$$\sin A = \begin{matrix} \sin(1) & \sin(2) & \sin(3) \\ \sin(-1) & \sin(2) & \sin(1) \end{matrix} , \text{ and}$$

$$\exp A = \begin{matrix} \exp(1) & \exp(2) & \exp(3) \\ \exp(-1) & \exp(2) & \exp(1) \end{matrix} .$$

Definition II-12:

If A and B are images on X , exponentiation of images $C = A^B$ is defined in this way:

$$C(x) = A(x)^{B(x)} \text{ where defined; otherwise } C(x) = 0.$$

Example II-7 :

Using A and B as in Example II-1,

$$A^B = \begin{matrix} 1 & 8 & 0 \\ 1 & 1/2 & 1 \end{matrix} .$$

The companion logarithmic expression for images is defined in the usual way, through the equivalent exponential expression.

Definition II-13:

If A and B are images on X , then $C = \log_A(B)$, provided $A^C = B$.

The operations defined above, unary and binary, assign to each image or pair of images, a resultant image. In contrast with these, we now consider a very familiar and useful kind of operator, the dot product, which will assign a numerical value to each pair of images.

Definition II-14:

If A and B are images on X , the dot product of A and B , written $A \cdot B$ is the real number given by

$$\sum A(x) * B(x) , \text{ where the sum is over all } x \text{ in } X.$$

Example II-7:

Using A and B as given in Example II-1 above, $A \cdot B = 10$.

Definition II-15:

If A is an image on X, the sum of A on X, written $\sum A$, is $A \cdot I$, where I is the multiplicative identity image on I.

Example II-8:

Using A as given in Example II-1, $\sum A = 5$.

III. THE TEMPLATE

The use of a mask in performing image transformations was described in Section I of this manual. To perform operations with a given mask, we think of this mask shifted, in turn, to each point of X . With the mask centered at a point x of the space, we then multiply each weight of the mask by the gray value of the image at the corresponding pixel; we consider all such products formed in accordance with the configuration of the mask. The sum of all such products is the transformed image gray value at x . We now turn to the development of the structure of the template as a generalization of the concept of the mask. We wish to preserve the notion of a configuration or neighborhood of a point; we also wish to preserve a definition of weights for each pixel of the neighborhood; but we do not wish to preserve the requirement that a single configuration and weight assignment is shifted to each pixel of the space in turn.

Definition III-1

Let X be an $m \times n$ rectangular space. If for each x in X , there is a pair $(N(x), t_x)$, where

1. $N(x)$ is a set in X , and
2. t_x is a function on X , with $t_x(y) = 0$ if y is not in $N(x)$;

then the collection of pairs $\{(N(x), t_x) : x \text{ is in } X\}$, is a template T on X , and we write $T = (N(x), t_x)$.

In Definition III-1, the set $N(x)$ is known as the configuration or neighborhood of x ; the functions t_x are known as weight functions.

As indicated in Section I, it is sometimes desirable to consider transformations of images on X into images on a space Y . In this case, for each x in X , the neighborhood $N(x)$ is a set in Y and the function t_x is a weight function on Y ; the template is said to be a template from X to Y . In this document for purposes of illustration we will consider only templates on X , of Definition III-1; however the extensions needed for the more general setting should become apparent.

We see that a template T on the space X consists of a collection of neighborhoods and a set of weight functions; for each x , the support of each weight function t_x must be contained in the neighborhood $N(x)$. We can consider this definition in slightly different characterizations:

1. If X is a space, and if for each x in X , t_x is a function on X , then the collection of these functions $\{t_x(y)\}$ for x and y in X , can be regarded as a template on X . For each x , the neighborhood $N(x)$ is a set for which $t_x(y) = 0$, for all y which

are not in $N(x)$; that is, the neighborhood $N(x)$ is a set in X which contains the support of the function t_x .

2. A template is formed if, for each x in X , a set $N(x)$ is specified as neighborhood of x , and if a function t_x is defined on the neighborhood $N(x)$. (For points y of X which fail to be in the set $N(x)$, let $t_x(y) = 0$).

3. If T is a template on X , for each x , each weight function t_x is an image on X ; each image can have nonzero gray values $t_x(y)$ only for y in $N(x)$. Consequently, a template is a collection of images on X , with one image for each x in X .

In this section we will consider a variety of situations in which we identify the template structure. Since the use of masks in image processing was one motivation for the development of the template, we will begin with templates that result from the use of a mask. We now consider the process of translating the use of a mask into the template structure.

Suppose that X is an $m \times n$ space; we consider a mask on the space X . There are mn points of X , so we need to find the mn neighborhoods in X and the mn functions on X formed by considering the mask centered at each of the mn pixels of X , in turn. For each x in X , the configuration of the mask centered at x is superimposed on X ; the set of pixels of X in this intersection is the neighborhood $N(x)$. For y in $N(x)$, the function value $t_x(y)$ is the weight at the corresponding location of the centered mask, if any; for pixels y in X which fail to be in $N(x)$, $t_x(y)$ is 0.

Example III-1:

If X is a 2×3 space, and M is the mask

 | 1 | * | 1 | 1 | ,

we can form its corresponding template. We list the weight functions t_x below; for each x we take $N(x)$ to be the support of t_x .

$$t_{(1,1)} = \begin{matrix} 1 & 1 & 0 \\ 0 & 0 & 0 \end{matrix}$$

$$t_{(1,2)} = \begin{matrix} 1 & 1 & 1 \\ 0 & 0 & 0 \end{matrix}$$

$$t_{(1,3)} = \begin{matrix} 0 & 1 & 1 \\ 0 & 0 & 0 \end{matrix}$$

$$t_{(2,1)} = \begin{matrix} 0 & 0 & 0 \\ 1 & 1 & 0 \end{matrix}$$

$$\begin{array}{rcl}
 t(2,2) & = & \begin{array}{ccc} 0 & 0 & 0 \\ & 1 & 1 & 1 \end{array} \\
 t(2,3) & = & \begin{array}{ccc} 0 & 0 & 0 \\ & 0 & 1 & 1 \end{array}
 \end{array}$$

This is the process by which a mask for images on a space X can be used to define a corresponding template on X .

In Example III-1 we notice that for some x in X , the configuration of the mask centered at x is not entirely contained in X . Weights corresponding to locations of the centered mask which were not in X were simply omitted in defining the function t_x . This corresponds to losing some of the weights of the mask for points which are close to the boundary of the space. It also presents a numerical complication in some computations: the number of pixels in the mask configuration at x is not constant for all x in X .

As a variant of the above formulation of the template on X corresponding to a mask on X , we consider an alternate method in which we think of the space as "wrapped around", so that first the horizontal edges form adjacent rows, and then the vertical edges form adjacent columns. In this idealization, a mask centered at a point x will lie entirely within the wrapped space, so that each point of the configuration of the mask centered at x will identify a pixel of X .

We will now describe this idea more precisely. We have considered a mask by indicating the geometrical arrangement of pixels with respect to the center pixel, and the specified weight at each pixel. We now look at an alternative definition of a mask. Given the $m \times n$ space X , suppose a mask is given in this way: if $(0,0)$ denotes the center of the mask, each location of the configuration can be indexed (r,s) to denote that the location is r units below and s units to the right of the center (negative r indicates above the center, and negative s to the left of the center, accordingly). Let I be the set of indices (r,s) corresponding to pixels of the the configuration. If the weight of the mask at location (r,s) is $a_{r,s}$, then the template has the following form:

For $x = (k,l)$ of X , the neighborhood of x , $N(x)$, is the set of all pixels $(k+r \bmod m, l+s \bmod n)$, where (r,s) is in I ; and $t_x(k+r \bmod m, l+s \bmod n) = a_{r,s}$.

Example III-2:

X is the 3×3 rectangular space; the mask is

```

-----
|  1 |
-----
|* 1|  1|.
-----

```

The mask of Example III-2 has configuration which can be indexed by $I = (0,0), (-1,0), (0,1)$; the weights are $a_{0,0} = 1$, $a_{-1,0} = 1$, and $a_{0,1} = 1$.

The template resulting from the wrapping of the space X has the weight functions listed below. For each x we take $N(x)$ to be the support of t_x .

$$t_{(1,1)} = \begin{matrix} 1 & 1 & 0 \\ 0 & 0 & 0 \\ 1 & 0 & 0 \end{matrix}$$

$$t_{(1,2)} = \begin{matrix} 0 & 1 & 1 \\ 0 & 0 & 0 \\ 0 & 1 & 0 \end{matrix}$$

$$t_{(1,3)} = \begin{matrix} 1 & 0 & 1 \\ 0 & 0 & 0 \\ 0 & 0 & 1 \end{matrix}$$

$$t_{(2,1)} = \begin{matrix} 1 & 0 & 0 \\ 1 & 1 & 0 \\ 0 & 0 & 0 \end{matrix}$$

$$t_{(2,2)} = \begin{matrix} 0 & 1 & 0 \\ 0 & 1 & 1 \\ 0 & 0 & 0 \end{matrix}$$

$$t_{(2,3)} = \begin{matrix} 0 & 0 & 1 \\ 1 & 0 & 1 \\ 0 & 0 & 0 \end{matrix}$$

$$t_{(3,1)} = \begin{matrix} 0 & 0 & 0 \\ 1 & 0 & 0 \\ 1 & 1 & 0 \end{matrix}$$

$$t_{(3,2)} = \begin{matrix} 0 & 0 & 0 \\ 0 & 1 & 0 \\ 0 & 1 & 1 \end{matrix}$$

$$t_{(3,3)} = \begin{matrix} 0 & 0 & 0 \\ 0 & 0 & 1 \\ 1 & 0 & 1 \end{matrix}$$

It may seem artificial to force this wrapping of the space, for in centering the mask at a point x , mask locations which extend beyond a boundary of the space X reappear at the opposite boundary of the space. On the other hand, this process provides a uniform specification of the configuration for every point x of the space; and for spaces of large dimension, proportionately few pixels are affected.

The procedure just defined provides an example of a translation invariant template; with these templates, knowing the neighborhood $N(x)$ at a point x of X , and knowing the weights $t_x(y)$ at each pixel y of the neighborhood $N(x)$, we find the configuration $N(v)$ and weight function t_v for every v in X , by the equations

$$N(v) = \{z + v - x : z \text{ is in } N(x)\} \quad \text{and}$$

$$f_v(w) = f_x(w - v + x) \text{ for } w \text{ in } X.$$

We turn to one more representation of a template - as a matrix. The space X is an $m \times n$ rectangular array. We can consider X as a linear array of length mn by using the lexicographic ordering of the elements of X . To do this we proceed by listing in a single row the n elements of row 1, followed in order by the n elements of row 2, row 3, . . . , until we reach the elements of row m .

Example III-3:

X is a 3×3 space; the ordered pair (i,j) , denotes the pixel of row i and column j . We can write X as a 1×9 horizontal array X' by listing the pixels of X in this order:

$(1,1), (1,2), (1,3), (2,1), (2,2), (2,3), (3,1), (3,2), (3,3).$

Furthermore, each weight function is indexed by a pixel of X ; the pixels of X can be listed in an $m \times 1$ vertical array X'' with the k th element of the vertical array corresponding to the k th element of the horizontal array X' .

We are now in a position to write the template as a matrix, M^T . The element a_{kl} is the value $t_x(y)$, where x is the element in row k of the vertical listing of X'' of X , and y is the element in column l of the horizontal listing X' of X .

Example III-4:

T is the template of Example III-1; T can be represented by the matrix M^T given below:

$$M^T = \begin{matrix} & \begin{matrix} 1 & 1 & 0 & 0 & 0 & 0 \end{matrix} \\ \begin{matrix} 1 & 1 & 0 & 0 & 0 & 0 \\ 0 & 1 & 1 & 0 & 0 & 0 \\ 0 & 0 & 0 & 1 & 1 & 0 \\ 0 & 0 & 0 & 1 & 1 & 1 \\ 0 & 0 & 0 & 0 & 1 & 1 \end{matrix} & \end{matrix}$$

Example III-5:

T is the template of Example III-2; T can be represented by the matrix M^T given below:

$$M^T = \begin{pmatrix} 1 & 1 & 0 & 0 & 0 & 0 & 1 & 0 & 0 \\ 0 & 1 & 1 & 0 & 0 & 0 & 0 & 1 & 0 \\ 1 & 0 & 1 & 0 & 0 & 0 & 0 & 0 & 1 \\ 1 & 0 & 0 & 1 & 1 & 0 & 0 & 0 & 0 \\ 0 & 1 & 0 & 0 & 1 & 1 & 0 & 0 & 0 \\ 0 & 0 & 1 & 1 & 0 & 1 & 0 & 0 & 0 \\ 0 & 0 & 0 & 1 & 0 & 0 & 1 & 1 & 0 \\ 0 & 0 & 0 & 0 & 1 & 0 & 0 & 1 & 1 \\ 0 & 0 & 0 & 0 & 0 & 1 & 1 & 0 & 1 \end{pmatrix} .$$

In these examples we become aware of two facts:

1. If the space X is $m \times n$, the matrix A of a template on X results in an $mn \times mn$ matrix.
2. When subdivided into blocks of size $m \times n$, the block structure of the matrix A of a template on an $m \times n$ space X has properties worthy of investigation through the algebra of matrices.

We have defined the template to provide a generalization of the mask, yet all the examples above have provided a translation of a mask into a template. It is actually very easy to specify a template which does not correspond to an underlying mask; the mask places a requirement on the neighborhood structure at each pixel and on the weights defined at each pixel of a neighborhood. With a mask, for interior points x and y , the neighborhood at a pixel y must be a translation of the neighborhood at x , in the sense that $N(y) = N(x) + (y-x)$, and for z in $N(y)$, $t_y(z) = t_x(z-y+x)$. There are no requirements of these kinds for templates.

Example III-6:

A template is defined on a 3×3 space X to have the weight functions t_x listed below; for each x , $N(x)$ is the support of t_x .

$$\begin{aligned} t_{(1,1)} &= \begin{pmatrix} 1 & 1 & 0 \\ 1 & 0 & 0 \\ 1 & 0 & 0 \end{pmatrix} \\ t_{(1,2)} &= \begin{pmatrix} 0 & 2 & 1 \\ 0 & 0 & 0 \\ 0 & 0 & 0 \end{pmatrix} \\ t_{(1,3)} &= \begin{pmatrix} 0 & 0 & 3 \\ 0 & 0 & 0 \\ 0 & 0 & 1 \end{pmatrix} \\ t_{(2,1)} &= \begin{pmatrix} 1 & 0 & 0 \\ 4 & 1 & 0 \\ 0 & 0 & 0 \end{pmatrix} \end{aligned}$$

$$t(2,2) = \begin{matrix} 0 & 0 & 0 \\ 0 & 5 & 1 \\ 0 & 0 & 0 \end{matrix}$$

$$t(2,3) = \begin{matrix} 0 & 0 & 1 \\ 2 & 0 & 6 \\ 0 & 0 & 0 \end{matrix}$$

$$t(3,1) = \begin{matrix} 0 & 0 & 0 \\ 1 & 0 & 0 \\ 7 & 0 & 0 \end{matrix}$$

$$t(3,2) = \begin{matrix} 0 & 0 & 0 \\ 0 & 0 & 0 \\ 0 & 8 & 1 \end{matrix}$$

$$t(3,3) = \begin{matrix} 0 & 0 & 0 \\ 0 & 0 & 1 \\ 0 & 0 & 9 \end{matrix}$$

Example III-7:

T is the template of Example III-6; by lexicographic ordering T can be identified with the following matrix:

$$M^T = \begin{matrix} & \begin{matrix} 1 & 1 & 0 & 1 & 0 & 0 & 1 & 0 & 0 \end{matrix} \\ \begin{matrix} 0 & 2 & 1 & 0 & 0 & 0 & 0 & 0 & 0 \end{matrix} & \\ \begin{matrix} 0 & 0 & 3 & 0 & 0 & 0 & 0 & 0 & 1 \end{matrix} & \\ \begin{matrix} 1 & 0 & 0 & 4 & 1 & 0 & 0 & 0 & 0 \end{matrix} & \\ \begin{matrix} 0 & 0 & 0 & 0 & 5 & 1 & 0 & 0 & 0 \end{matrix} & \\ \begin{matrix} 0 & 0 & 1 & 2 & 0 & 6 & 0 & 0 & 0 \end{matrix} & \\ \begin{matrix} 0 & 0 & 0 & 1 & 0 & 0 & 7 & 0 & 0 \end{matrix} & \\ \begin{matrix} 0 & 0 & 0 & 0 & 0 & 0 & 0 & 8 & 1 \end{matrix} & \\ \begin{matrix} 0 & 0 & 0 & 0 & 0 & 1 & 0 & 0 & 9 \end{matrix} & \end{matrix}$$

Since the elements of the diagonal list the function values $t_x(x)$, it is clear that we do not have identical weights assigned at the center of each neighborhood. This template does not result from a mask.

IV. IMAGE TEMPLATE OPERATIONS

In previous sections we have considered the image and the template. We have noted that an image is a real valued function on a set X . We have noted that a template $T = (N(x), t_x)$ on X can be regarded as a collection of functions $\{t_x\}$ indexed by x in X , where each of the functions t_x is defined on the set X and has nonzero function values only on its neighborhood $N(x)$. To summarize these ideas, if X is a set, a real valued function on X is an image A ; an image valued function on X is a template.

One motivation for the development of a template for image processing is suggested by the use of a mask which is centered, successively, at each pixel. With the mask centered at pixel x , the weights of the mask are multiplied by the gray values at the corresponding pixels of the image; these products are summed and the result is recorded as the transformed image value at x . The centering of the mask at each point x of the space X can be accomplished by the definition of an appropriate template: at each point x , the function $t_x(y)$ assigned to x indicates the weights of the mask centered at x for pixels y of $N(x)$, and has value 2 otherwise. The collection of all these functions t_x forms a template.

We now have an image and a template. We have seen that this definition of a template seems to support the traditional use of a mask. We are not yet finished. We still need to define the interaction of the image with the template. This should include the transformations of images through traditional masking operations, in which the resultant gray level value of the transformed image is obtained through the interaction of the image with the mask at x . In traditional masking transformations we multiply corresponding image values and mask values; we then sum these products so formed, according to the configuration of the mask. Consequently it is not surprising that the first image - template operation has a form to reflect this procedure.

Preliminary Definition IV-1:

If A is an image on X , and T is a template on X , then the operation \oplus assigns to the pair (A, T) an image $A \oplus T$ on X ; for each x in X ,

$$A \oplus T (x) = \sum A(y) * t_x(y) , \text{ where the sum is over all } y \text{ in } X.$$

For each x in the space X , this definition requires a multiplication and a summation at every y in X . But considering our experience with masks, we expect many of the values $t_x(y)$ to be zero, for any x , since weights at pixels not on the configuration of the mask are zero.

We recall that for template T on X , for every x in X , t_x is an image on X , and $t_x(y) = 0$ for y not in $N(x)$, the neighborhood of x . This idea of the neighborhood means that the operation \oplus can be defined with the summation over $N(x)$, rather than over the whole set X . Consequently, we write

Definition IV-1:

If A is an image on X , and $T = (N(x), t_x)$ is a template on X , then the operation \oplus assigns to the pair (A, T) an image $A \oplus T$ on X ; for each x in X ,

$$A \oplus T(x) = \sum A(y) * t_x(y), \text{ where the sum is for all } y \text{ in } N(x).$$

As we have seen, the definitions of the template and of the image - template operation \oplus reflect the usual masking computations for an image A on a space X . In the following examples we will use the symbol $*$ to indicate the center of the neighborhood, as before; the symbol $[*]$ will indicate a pixel which is the center of a neighborhood but which is not itself in that neighborhood.

Example IV-1:

Let X be a 2×3 space, and consider the mask $\begin{array}{c} \text{-----} \\ 1 \ 1[*] \ 1 \\ \text{-----} \end{array}$.

Let T be the corresponding template (Example III-1), where $t_x(y)$ is the weight at the corresponding location of the mask centered at x , if any; otherwise it is zero. Weights of the superimposed mask at locations not in X are simply deleted. Template T has this structure, as we saw in Section III:

$$\begin{array}{lcl} t(1,1) & = & \begin{array}{ccc} 1 & 1 & 0 \\ 0 & 0 & 0 \end{array} \\ t(1,2) & = & \begin{array}{ccc} 1 & 1 & 1 \\ 0 & 0 & 0 \end{array} \\ t(1,3) & = & \begin{array}{ccc} 0 & 1 & 1 \\ 0 & 0 & 0 \end{array} \\ t(2,1) & = & \begin{array}{ccc} 0 & 0 & 0 \\ 1 & 1 & 0 \end{array} \\ t(2,2) & = & \begin{array}{ccc} 0 & 0 & 0 \\ 1 & 1 & 1 \end{array} \\ t(2,3) & = & \begin{array}{ccc} 0 & 0 & 0 \\ 0 & 1 & 1 \end{array} \end{array}$$

$$\text{If } A = \begin{array}{ccc} 3 & 4 & 1 \\ 2 & 5 & 3 \end{array}, \text{ then } A \oplus T = \begin{array}{ccc} 7 & 8 & 5 \\ 7 & 10 & 8 \end{array}.$$

We will use this conversion of masks to corresponding templates to provide examples of the image-template operation \oplus .

Example IV-2:

Let X be a 4×4 rectangular array.

A is an image on X , with

$A =$	0	0	0	0	;
	0	1	2	0	
	0	1	3	0	
	0	0	0	0	

T is the template on X formed from the mask

1 * 1 1 ;

T' is the template on X formed from the mask

1 * 1 1 ;

T'' is the template on X formed from the mask

1 * 2 1 .

Then $A \oplus T =$

0	0	0	0	;
1	3	3	2	
1	4	4	3	
0	0	0	0	

$A \oplus T' =$

0	1	2	0	;
1	4	6	2	
1	5	6	3	
0	1	3	0	

; and

$A \oplus T'' =$

0	0	0	0	.
1	4	5	2	
1	5	7	3	
0	0	0	0	

We now consider some elementary image transformations which can be represented by using the operation \oplus with an appropriately chosen template. We will provide examples of a translation, a magnification, and a rotation of an image on a 4×4 space X . Though the space X is very small, these examples should provide insight and methods of approach for further applications.

Translations of the image can be accomplished through the choice of the appropriate mask, conversion to the corresponding template, and the use of the operation \oplus .

Example IV-3:

Suppose that A is an image on a 4×4 space X , and that we wish to move the image one pixel to the right and one pixel down, so that the gray value $A(i,j)$ will appear, after translation, in location $(i+1,j+1)$ of X .

We will use the mask

$$\begin{array}{c} \text{-----} \\ | \ 1 \ 1 \ | \ ; \\ \text{-----} \\ | \ 1 \ 1 \ | \\ \text{-----} \end{array}$$

this mask, centered at any pixel x of X , will "pick up" the value of the image A at the pixel diagonally one unit to the left and one unit above x , and record it as the transformed image value at x . This verbal description has precise formulation in the image algebra:

For the template, we have $T = (N(x), t_x)$,

where for each $x = (i,j)$ in X ,

$N(x) = (i-1,j-1)$ if $i > 1$ and $j > 1$;
otherwise $N(x)$ is the empty set; and

$t_x(y) = 1$ for y in $N(x)$, otherwise
 $t_x(y) = 0$.

Then $A \oplus T$ is the translation of A which moves this image one unit down and one unit to the right.

In Example IV-3, the template which was used corresponded to a predetermined mask. In the following examples the template of the transformation $A \oplus T$ does not result from a predetermined mask.

Example IV-4:

For an image A on a 4×4 space X , the transformed image B will be a twofold magnification of the portion of the image not on the boundary. To express this in the image algebra, we need to find the template T such that $B = A \oplus T$. As before, we could write, for each x in X , the weight function t_x of the template. Instead we will specify the neighborhood $N(x)$ for each point x of X , and define each image t_x to have value 1 on the neighborhood $N(x)$, and value 0 elsewhere. We take

$$N((1,1)) = N((1,2)) = N((2,1)) = N((2,2)) = (2,2)$$

$$N((1,3)) = N((1,4)) = N((2,3)) = N((2,4)) = (2,3)$$

$$N((3,1)) = N((3,2)) = N((4,1)) = N((4,2)) = (3,2)$$

$$N((3,3)) = N((3,4)) = N((4,3)) = N((4,4)) = (3,3).$$

For y in the space X , we define $t_x(y) = 1$, for y in $N(x)$; otherwise $t_x(y) = 0$.

To aid in verification of the process, we indicate some of the weight functions; the others can be obtained in a similar manner from the template definition:

$$t_{(1,1)} = \begin{matrix} 0 & 0 & 0 & 0 \\ 0 & 1 & 0 & 0 \\ 0 & 0 & 0 & 0 \\ 0 & 0 & 0 & 0 \end{matrix}; \text{ and}$$

$$t_{(1,1)} = t_{(1,2)} = t_{(2,1)} = t_{(2,2)}.$$

Then for $A = \begin{matrix} 0 & 0 & 0 & 0 \\ 0 & 1 & 2 & 0 \\ 0 & 3 & 4 & 0 \\ 0 & 0 & 0 & 0 \end{matrix}$, $A \oplus T = \begin{matrix} 1 & 1 & 2 & 2 \\ 1 & 1 & 2 & 2 \\ 3 & 3 & 4 & 4 \\ 3 & 3 & 4 & 4 \end{matrix}$.

We note that the template used in this example does not correspond to a mask, because the neighborhood $N(x)$ is not in the same geometrical configuration with respect to the center x , for all x in X .

Rotations of an image can also be accomplished through the definition of an appropriate template and the use of the image - template operation \oplus . In the most simple form of rotation, a template will be defined at x to have as neighborhood $N(x)$ the single pixel which would coincide with x after the rotation; the weight function $t_x(y)$ will have value 1 for y in the neighborhood $N(x)$, and value 0 otherwise.

Example IV-5:

We consider the rotation of an image A defined on a 3×3 space X ; in this example the rotation will be 90 degrees counterclockwise about the $(2,2)$ pixel.

Let $A = \begin{matrix} a & b & c \\ d & e & f \\ g & h & i \end{matrix}$; the rotated image $B = \begin{matrix} c & f & i \\ b & e & h \\ a & d & g \end{matrix}$

For the template T , we define a single pixel as the neighborhood $N(x)$ for each x of X in this way:

$$\begin{array}{lll} N((1,1)) = (1,3) & N((1,2)) = (2,3) & N((1,3)) = (3,3) \\ N((2,1)) = (1,2) & N((2,2)) = (2,2) & N((2,3)) = (3,2) \\ N((3,1)) = (1,1) & N((3,2)) = (2,1) & N((3,3)) = (3,1); \end{array}$$

For each x in X , $t_x(y) = 1$ for y in $N(x)$, and is 0 otherwise.

$$\begin{array}{lll}
 t(1,1) = \begin{pmatrix} 0 & 0 & 1 \\ 0 & 0 & 0 \\ 0 & 0 & 0 \end{pmatrix} & t(1,2) = \begin{pmatrix} 0 & 0 & 0 \\ 0 & 0 & 1 \\ 0 & 0 & 0 \end{pmatrix} & t(1,3) = \begin{pmatrix} 0 & 0 & 0 \\ 0 & 0 & 0 \\ 0 & 0 & 1 \end{pmatrix} \\
 t(2,1) = \begin{pmatrix} 0 & 1 & 0 \\ 0 & 0 & 0 \\ 0 & 0 & 0 \end{pmatrix} & t(2,2) = \begin{pmatrix} 0 & 0 & 0 \\ 0 & 1 & 0 \\ 0 & 0 & 0 \end{pmatrix} & t(2,3) = \begin{pmatrix} 0 & 0 & 0 \\ 0 & 0 & 0 \\ 0 & 1 & 0 \end{pmatrix} \\
 t(3,1) = \begin{pmatrix} 1 & 0 & 0 \\ 0 & 0 & 0 \\ 0 & 0 & 0 \end{pmatrix} & t(3,2) = \begin{pmatrix} 0 & 0 & 0 \\ 1 & 0 & 0 \\ 0 & 0 & 0 \end{pmatrix} & t(3,3) = \begin{pmatrix} 0 & 0 & 0 \\ 0 & 0 & 0 \\ 1 & 0 & 0 \end{pmatrix}
 \end{array}$$

It can be verified that $B = A + T$ in the image algebra.

In these examples we computed images $B = A \oplus T$ for templates to produce traditional masking transformations, a translation, a magnification, and a rotation of the image A . Though these templates were defined in a very tedious manner, and the practicality of these examples is very slight, we make these observations:

1. The image - template operation \oplus can be employed in performing a variety of image transformations, including the traditional masking operations, translations, rotations, and magnifications.
2. The templates, once defined, can be stored for future use. It is possible to envision a library of templates available for usage.
3. With the development of machine computation of the operation \oplus , given the input of image A and template T , the problem of writing a program to compute the transformed image $A \oplus T$, pixel by pixel, no longer exists.

The operation \oplus has a connection with the linear algebra, which we now observe. Through lexicographic ordering on the $m \times n$ rectangular space X , described in Section III, X and any image on X can be represented by mn dimensional vectors. We have seen the matrix M^T formed for the template T on X , by using the lexicographic ordering for x in X to provide the row index, and for y in X to provide the column index, for the gray level functions $t_x(y)$. It can be shown that if $B = A \oplus T$ in the image algebra, and if the symbol $*$ denotes the operation of matrix multiplication then $BV = M^T * AV$, where BV and AV are the mn dimensional column vectors corresponding to images B and A , respectively.

Example IV-6:

We use the template T of Example IV-1 and let $A = \begin{matrix} a & b & c \\ c & e & f \end{matrix}$.

In the image algebra $E = A \oplus T = \begin{matrix} a+b & a+b+c & b+c \\ c+e & d+e+f & e+f \end{matrix}$.

We write the matrix $MT = \begin{matrix} 1 & 1 & 0 & 0 & 0 & 0 \\ 1 & 1 & 1 & 0 & 0 & 0 \\ 0 & 1 & 1 & 0 & 0 & 0 \\ 0 & 0 & 0 & 1 & 1 & 0 \\ 0 & 0 & 0 & 1 & 1 & 1 \\ 0 & 0 & 0 & 0 & 1 & 1 \end{matrix}$ and $AV = \begin{matrix} a \\ b \\ c \\ c \\ e \\ f \end{matrix}$;

then in matrix multiplication,

$$MT * AV = \begin{matrix} a+b \\ a+b+c \\ b+c \\ c+e \\ d+e+f \\ e+f \end{matrix} = EV.$$

With this identification, we see that many results of linear algebra have a direct restatement in the image algebra.

Though we have seen some of the uses of the image - template operation \oplus , other operations are needed to perform binary and gray level morphological transformations. We consider these definitions of the operation \odot and \boxplus :

Definition IV-2:

If X is a space, A is an image on X , and $T = (N(x), t_x)$ is a template on X , then $C = A \odot T$ is an image on X , if for each x in X

$$A \odot T(x) = \bigvee (a(y) * t_x(y)),$$

where this maximum is taken over all y of X which are in $N(x)$.

Definition IV-3:

If X is a space, A is an image on X , and $T = (N(x), t_x)$ is a template on X , then $C = A \boxplus T$ is an image on X , if for each x in X

$$A \boxplus T(x) = \bigvee (a(y) + t_x(y)),$$

where this maximum is taken over all y of X which are in $N(x)$.

From these definitions we form a verbal description of the indicated computations:

To form the gray value of the image $A \odot T$ at pixel x , consider the neighborhood $N(x)$ and the function t_x of the template T . At each pixel y of the neighborhood, multiply the

image gray value $a(y)$ and the value $t_x(y)$. Then compute the maximum of the products so formed, for all y in $N(x)$. This maximum value is the gray value at x of the image $A \odot T$.

To form the gray value of the image $A \boxtimes T$ at pixel x , consider the neighborhood $N(x)$ and the function t_x of the template T . At each pixel y of this neighborhood, add the image gray value $a(y)$ and the value $t_x(y)$. Then compute the maximum of the sums so formed, for all y in $N(x)$. This maximum value is the gray value at x of the image $A \boxtimes T$.

Example IV-7:

Using templates T , T' , and T'' of Example IV-1, and

$$A = \begin{matrix} & 0 & 1 & 1 & 0 \\ & 1 & 2 & 2 & 1 \\ & 1 & 2 & 3 & 1 \\ & 0 & 1 & 1 & 0 \end{matrix}, \text{ then}$$

$$A \odot T = \begin{matrix} 1 & 1 & 1 & 1 \\ 2 & 2 & 2 & 2 \\ 2 & 3 & 3 & 3 \\ 1 & 1 & 1 & 1 \end{matrix} \quad A \boxtimes T = \begin{matrix} 2 & 2 & 2 & 2 \\ 3 & 3 & 3 & 3 \\ 3 & 4 & 4 & 4 \\ 2 & 2 & 2 & 2 \end{matrix}$$

$$A \odot T' = \begin{matrix} 1 & 2 & 2 & 1 \\ 2 & 2 & 3 & 2 \\ 2 & 3 & 3 & 3 \\ 1 & 2 & 3 & 1 \end{matrix} \quad A \boxtimes T' = \begin{matrix} 2 & 3 & 3 & 2 \\ 3 & 3 & 4 & 3 \\ 3 & 4 & 4 & 4 \\ 2 & 3 & 4 & 2 \end{matrix}$$

$$A \odot T'' = \begin{matrix} 1 & 2 & 2 & 1 \\ 2 & 4 & 4 & 2 \\ 2 & 4 & 6 & 3 \\ 1 & 2 & 2 & 1 \end{matrix} \quad A \boxtimes T'' = \begin{matrix} 2 & 3 & 3 & 2 \\ 3 & 4 & 4 & 3 \\ 3 & 4 & 5 & 4 \\ 2 & 3 & 3 & 2 \end{matrix}$$

Corresponding to these operations there are the following complementary operations \ominus and \boxminus :

Definition IV-4:

If A is an image on X , and if T is a template on X , then

$$A \ominus T = - (A \odot -T), \text{ and}$$

$$A \boxminus T = - (-A \boxtimes -T).$$

Example IV-8:

Using the 4×4 image A and the templates T , T' , and T'' of Example IV-7,

$$A \ominus T = \begin{matrix} 0 & 0 & 0 & 0 \\ 1 & 1 & 1 & 1 \\ 1 & 1 & 1 & 1 \\ 0 & 0 & 0 & 0 \end{matrix} \quad A \boxminus T = \begin{matrix} 1 & 1 & 1 & 1 \\ 2 & 2 & 2 & 2 \\ 2 & 2 & 2 & 2 \\ 1 & 1 & 1 & 1 \end{matrix}$$

$$A \odot T' = \begin{matrix} 0 & 0 & 0 & 0 \\ 0 & 1 & 1 & 0 \\ 0 & 1 & 1 & 0 \\ 0 & 0 & 0 & 0 \end{matrix}$$

$$A \odot T'' = \begin{matrix} 0 & 0 & 0 & 0 \\ 2 & 1 & 1 & 2 \\ 2 & 1 & 1 & 2 \\ 0 & 0 & 0 & 0 \end{matrix}$$

$$A \boxtimes T' = \begin{matrix} 1 & 1 & 1 & 1 \\ 1 & 2 & 2 & 1 \\ 1 & 2 & 2 & 1 \\ 1 & 1 & 1 & 1 \end{matrix}$$

$$A \boxtimes T'' = \begin{matrix} 2 & 1 & 1 & 2 \\ 3 & 2 & 2 & 3 \\ 3 & 2 & 2 & 3 \\ 2 & 1 & 1 & 2 \end{matrix}$$

V. TEMPLATE - TEMPLATE OPERATIONS

In Sections I and II of this document we considered images, operations on images, and image - image operations; in Section III we considered templates; and in Section IV we considered image - template operations. We now consider certain operations which are defined for pairs of templates, in which the result of the operation is a template. Since a template is defined by its neighborhood structure and by its collection of gray level functions, then in any template - template operation we need to describe the neighborhood system and the gray level functions resulting from that operation.

In the following definitions we assume that S and T are templates on X ; with $S = (M(x), s_x)$ and $T = (N(x), t_x)$. We first consider the template - template operations which correspond most nearly to the addition (+), multiplication (*), and maximum (\vee) of the gray level functions of the templates.

Definition V-1:

The operation of template addition + assigns to the pair (S, T) of templates a resultant template R on X . We write

$$R = S + T, \text{ where } R = (K(x), r_x).$$

$$K(x) = M(x) \cup N(x).$$

For y in $K(x)$, $r_x(y) = s_x(y) + t_x(y)$; otherwise, $r_x(y) = 0$.

Definition V-2:

The operation of template multiplication * assigns to the pair (S, T) of templates a resultant template R on X . We write

$$R = S * T, \text{ where } R = (K(x), r_x).$$

$$K(x) = M(x) \cup N(x).$$

For y in $K(x)$, $r_x(y) = s_x(y) * t_x(y)$; otherwise, $r_x(y) = 0$.

Definition V-3:

The operation of template maximization \vee assigns to the pair (S, T) of templates a resultant template R on X . We write

$$R = S \vee T \text{ where } R = (K(x), r_x).$$

$$K(x) = M(x) \cup N(x).$$

For y in $K(x)$, $r_x(y) = s_x(y) \vee t_x(y)$; otherwise, $r_x(y) = 0$.

We illustrate by using templates which are defined by a mask diagram indicating the geometrical neighborhood of x , with the center pixel x denoted by the symbol $*$ and the weight function values denoted at each pixel of the neighborhood.

Example V-1:

$$\begin{array}{rcl}
 \text{For} & T = \begin{array}{|c|} \hline 1 \ 2 \\ \hline 1 * 1 \\ \hline 1 \ 1 \\ \hline \end{array} & \text{and} \quad S = \begin{array}{|c|} \hline 1 \ 1 * 3 \ 2 \\ \hline \end{array} \\
 & & \\
 & \text{then } T + S = \begin{array}{|c|} \hline 1 \ 2 \\ \hline 1 \ 1 * 4 \ 2 \\ \hline 1 \ 1 \\ \hline \end{array} ; \\
 & & \\
 & T * S = \begin{array}{|c|} \hline 1 * 3 \\ \hline \end{array} ; \text{ and} \\
 & & \\
 & T \vee S = \begin{array}{|c|} \hline 1 \ 2 \\ \hline 1 \ 1 * 3 \ 2 \\ \hline 1 \ 1 \\ \hline \end{array} .
 \end{array}$$

Example V-2:

$$\begin{array}{rcl}
 \text{For} & T = \begin{array}{|c|} \hline 1 \ 1 \ 1 \ 1 \\ \hline 1 \ 1 * 1 \ 1 \\ \hline 1 \ 1 \ 1 \ 1 \\ \hline \end{array} & \text{and} \quad S = \begin{array}{|c|} \hline 1 - 1 \\ \hline 1 \ 0 \ 1 * 2 \ 1 \ 1 \\ \hline 1 \ 1 \\ \hline \end{array} , \\
 & & \\
 T + S = \begin{array}{|c|} \hline 1 \ 1 \ 0 \ 1 \ 1 \\ \hline 1 \ 1 * 3 \ 2 \ 1 \\ \hline 1 \ 1 \ 2 \ 1 \ 1 \\ \hline \end{array} ; & T * S = \begin{array}{|c|} \hline 1 \ 0 \ -1 \ 0 \\ \hline 1 \ 0 \ 1 * 2 \ 1 \ 1 \\ \hline 1 \ 0 \ 1 \ 1 \ 0 \\ \hline \end{array} ; & \text{and } T \vee S = \begin{array}{|c|} \hline 1 \ 1 \ 1 \ 1 \ 1 \\ \hline 1 \ 1 * 2 \ 1 \ 1 \ 1 \\ \hline 1 \ 1 \ 1 \ 1 \ 1 \\ \hline \end{array} .
 \end{array}$$

We next consider the template - template operations which correspond to the image - template operations \oplus , \odot , and \boxtimes . We take, as before, templates S and T on X .

Definition V-4:

The operation \oplus assigns to the pair $S = (M(x), s_x)$ and $T = (N(x), t_x)$ of templates on X a resultant template R on X . We write

$$R = S \oplus T, \text{ where } R = (K(x), r_x).$$

$K(x) = \bigcup M(v)$, where the union is taken for all v in $N(x)$.

For z in $K(x)$, $r_x(z) = \sum s_v(z) + t_x(v)$, with the sum taken for all v in $N(x)$ with z in $M(v)$;
otherwise, $r_x(z) = 0$.

Definition V-5:

The operation \odot assigns to the pair $S = (M(x), s_x)$ and $T = (N(x), t_x)$ of templates on X a resultant template R on X . We write

$$R = S \odot T, \text{ where } R = (K(x), r_x).$$

$K(x) = \bigcup M(v)$, where the union is taken for all v in $N(x)$.

For z in $K(x)$, $r_x(z) = \bigvee (s_v(z) + t_x(v))$, with the maximum taken for all v in $N(x)$ with z in $M(v)$;
otherwise, $r_x(z) = 0$.

Definition V-6:

The operation \boxtimes assigns to the pair $S = (M(x), s_x)$ and $T = (N(x), t_x)$ of templates on X a resultant template R on X . We write

$$R = S \boxtimes T, \text{ where } R = (K(x), r_x), \text{ and}$$

$K(x) = \bigcup M(v)$, where the union is taken for all v in $N(x)$.

For z in $K(x)$, $r_x(z) = \bigvee (s_v(z) + t_x(v))$, with the maximum taken for all v in $N(x)$ with z in $M(v)$;
otherwise, $r_x(z) = 0$.

We will illustrate by using templates which are specified by a mask to indicate the geometrical configuration or neighborhood of x , with the center pixel denoted by the symbol $*$, and the weight function values denoted at each pixel of the neighborhood. In these cases the resultant templates $S \oplus T$, $S \odot T$, and $S \boxtimes T$ can be specified by a mask.

For each of the operations $S \oplus T$, $S \odot T$, and $S \boxtimes T$, at each x , the neighborhood $K(x)$ of the resultant template R is found by the same process, which we now describe:

1. Indicate the neighborhood $N(x)$ of the template T .
2. At pixel v of $N(x)$, note the neighborhood $M(v)$ of S .
3. Form the union of all pixels which are in a neighborhood

$M(v)$, for some v in $N(x)$; this union is the neighborhood $K(x)$ of R .

We note that if z is in $K(x)$, then z is in some neighborhood $M(v')$ for which v' is in $N(x)$.

Example V-3:

$M(v)$	$N(x)$	$K(x)$
----- ----- * -----	----- ----- * ----- -----	----- ----- ----- * ----- -----

Example V-4:

$M(v)$	$N(x)$	$K(x)$
----- * -----	----- ----- * ----- -----	----- ----- * ----- -----

Example V-5

$M(v)$	$N(x)$	$K(x)$
----- ----- * ----- -----	----- * -----	----- ----- * ----- -----

Example V-6:

$M(v)$	$N(x)$	$K(x)$
----- ----- * -----	----- * -----	----- ----- * -----

Example V-7:

M(v)	N(x)	K(x)
----- * ----- -----	----- * -----	----- * ----- -----

In some cases, we need to indicate that a pixel is not in a neighborhood. We use the symbol [] to indicate a pixel which is not in that neighborhood; while the symbol [*] will denote a pixel which is the center of a given neighborhood, but which is not in that neighborhood. The procedure indicated above is valid in these cases.

Example V-8:

M(v)	N(x)	K(x)
----- [>] -----	----- * -----	----- [>] -----

Example V-9:

M(v)	N(x)	K(x)
----- [>] -----	----- ----- * ----- -----	----- ----- * ----- -----

Example V-10:

M(v)	N(x)	K(x)
----- [>] -----	----- [>] -----	----- [>] [] -----

We recall that for given templates S and T, the neighborhood systems for the operations $S \oplus T$, $S \odot T$, and $S \boxtimes T$ are identical. We now consider a computational description of the determination of the weight functions for these templates.

The weight function r_x for $R = S \oplus T$, is found in this way:

1. Indicate the neighborhood $K(x)$ for the template $S + T$.

2. For v in the neighborhood $N(x)$ of template T ,
 - a. Find the weight $t_x(v)$ of template T .
 - b. Find the neighborhood $M(v)$ and weight function s_v of template S .
 - c. Multiply the weight $s_v(z)$, for z in $M(v)$, by $t_x(v)$; record the product at pixel z of $K(x)$.
3. Repeat step 2 for every v in $N(x)$.
4. For every pixel in $K(x)$, sum all products obtained for that pixel by steps 2 and 3. This sum is $r_x(z)$ for z in $K(x)$.
5. Set $r_x(z) = 0$ for z not in $K(x)$.

To determine the weight $r_x(z)$, we must determine all pairs (v, z) for which z is in $M(v)$ and v is in $N(x)$. Consequently it is difficult to envision the computation of a single weight value. On the other hand, the process indicated here provides the determination of all weight values for pixels of the neighborhood $K(x)$; from this the weight at each pixel can be identified.

Example V-11:

$$\begin{array}{c} \text{S} \\ \hline 1 * 1 \mid 3 \mid \\ \hline \end{array} + \begin{array}{c} \text{T} \\ \hline 1 * 2 \mid \\ \hline 1 \mid 1 \mid \\ \hline \end{array} = \begin{array}{c} \text{S} \oplus \text{T} \\ \hline 1 * 2 \mid 6 \mid \\ \hline 1 \mid 1 \mid 3 \mid \\ \hline \end{array} ; \quad \text{using}$$

$$\begin{array}{c} \hline 1 * 2 \mid 6 \mid \\ \hline 1 \mid 1 \mid 1 \mid \\ \hline \end{array} \quad \text{and} \quad \begin{array}{c} \hline 1 * \mid \mid \\ \hline 1 \mid 1 \mid 3 \mid \\ \hline \end{array} \quad \text{from intermediate steps 2 and 3.}$$

Example V-12:

$$\begin{array}{c} \text{S} \\ \hline 1 * 1 \mid 3 \mid \\ \hline \end{array} + \begin{array}{c} \text{T} \\ \hline 1 * 2 \mid 1 \mid \\ \hline \end{array} = \begin{array}{c} \text{S} \oplus \text{T} \\ \hline 1 * 2 \mid 7 \mid 3 \mid \\ \hline \end{array} ;$$

since by intermediate steps 2 and 3 we have

$$\begin{array}{c} \hline 1 * 2 \mid 6 \mid \mid \\ \hline \end{array} \quad \text{and} \quad \begin{array}{c} \hline 1 * \mid 1 \mid 3 \mid \\ \hline \end{array}$$

Example V-13:

S		T		$S \oplus T$
1* 1 3		1* 4 5		1* 4 17 15
+ =		1 3 7		1 19 44 31
1 4 2				1 12 34 14

since as intermediate steps 2 and 3 we have

1* 4 12		1* 1 5 15		1* 1		1* 1
1 16 8	,	1 20 10	,	1 3 9	,	and 1 7 21
1		1		1 12 6		1 28 14

Once this process is visualized, it is straightforward to proceed to the computation $R = S \oplus T$ in this way:

1. For x in X , indicate the configuration or neighborhood $K(x)$ of the pixel x for the template R .
2. For v in $N(x)$, the neighborhood of x for the template T , multiply the weight $t_x(v)$ with each weight $s_v(z)$ in turn,, for z in $M(v)$, the neighborhood of v of template S . Record each product in the corresponding pixel z . Note that z is a pixel of $K(x)$.
3. At each pixel z of $K(x)$, find the sum of all products formed in this manner. This sum is the weight $r_x(z)$ of the template R at pixel z .

Example V-14:

S		T		$S \oplus T$		$S \oplus T$
1* 1 3		1* 4 5		1* 4 17 15		1* 4 12
+ =		1 3 7		1 19 44 31	, using	1 5 15
1 4 2				1 12 34 14		1 16 8
						1 20 10
						1 3 9
						1 7 21
						1 12 6
						1 28 14

If S and T are templates which can be represented by 3×3 masks, then $S \oplus T$ is a template which can be represented by a 5×5 mask. We can write the resultant mask very specifically:

$$S \oplus T = R, \quad \text{where}$$

$$S = \begin{array}{|c|c|c|} \hline s_1 & s_2 & s_3 \\ \hline s_4 & s_5 & s_6 \\ \hline s_7 & s_8 & s_9 \\ \hline \end{array} \quad T = \begin{array}{|c|c|c|} \hline t_1 & t_2 & t_3 \\ \hline t_4 & t_5 & t_6 \\ \hline t_7 & t_8 & t_9 \\ \hline \end{array}, \text{ and}$$

$$R = \begin{array}{|c|c|c|c|c|} \hline r_1 & r_2 & r_3 & r_4 & r_5 \\ \hline r_6 & r_7 & r_8 & r_9 & r_{10} \\ \hline r_{11} & r_{12} & r_{13} & r_{14} & r_{15} \\ \hline r_{16} & r_{17} & r_{18} & r_{19} & r_{20} \\ \hline r_{21} & r_{22} & r_{23} & r_{24} & r_{25} \\ \hline \end{array}$$

Furthermore, the entries r_i are specified in this way:

$$\begin{aligned} r_1 &= s_1 * t_1 \\ r_2 &= s_2 * t_1 + s_2 * t_1 \\ r_3 &= s_3 * t_1 + s_2 * t_2 + s_1 * t_3 \\ r_4 &= s_3 * t_2 + s_2 * t_3 \\ r_5 &= s_3 * t_3 \\ r_6 &= s_4 * t_1 + s_1 * t_4 \\ r_7 &= s_5 * t_1 + s_4 * t_2 + s_2 * t_4 + s_1 * t_5 \\ r_8 &= s_6 * t_1 + s_5 * t_2 + s_4 * t_3 + s_3 * t_4 + s_2 * t_5 + s_1 * t_6 \\ r_9 &= s_6 * t_2 + s_5 * t_3 + s_3 * t_5 + s_2 * t_6 \\ r_{10} &= s_6 * t_3 + s_3 * t_6 \\ r_{11} &= s_7 * t_1 + s_4 * t_4 + s_1 * t_7 \\ r_{12} &= s_8 * t_1 + s_7 * t_2 + s_5 * t_4 + s_4 * t_5 + s_2 * t_7 + s_1 * t_8 \\ r_{13} &= s_9 * t_1 + s_8 * t_2 + s_7 * t_3 + s_6 * t_4 + s_5 * t_5 + s_4 * t_6 + s_3 * t_7 + \\ &\quad s_2 * t_8 + s_1 * t_9 \\ r_{14} &= s_9 * t_2 + s_8 * t_3 + s_6 * t_5 + s_5 * t_6 + s_3 * t_8 + s_2 * t_9 \\ r_{15} &= s_9 * t_3 + s_6 * t_6 + s_3 * t_9 \\ r_{16} &= s_7 * t_4 + s_4 * t_7 \\ r_{17} &= s_8 * t_4 + s_7 * t_5 + s_5 * t_7 + s_4 * t_8 \\ r_{18} &= s_9 * t_4 + s_8 * t_5 + s_7 * t_6 + s_6 * t_7 + s_5 * t_8 + s_4 * t_9 \\ r_{19} &= s_9 * t_5 + s_8 * t_6 + s_6 * t_8 + s_5 * t_9 \\ r_{20} &= s_9 * t_6 + s_6 * t_9 \\ r_{21} &= s_7 * t_7 \\ r_{22} &= s_8 * t_7 + s_7 * t_8 \end{aligned}$$

$r_{23} = s_9 * t_7 + s_8 * t_8 + s_7 * t_9$
 $r_{24} = s_9 * t_8 + s_8 * t_9$
 $r_{25} = s_9 * t_9$

From this representation it can be seen that for templates S and T represented by 3×3 masks, we have $S \oplus T = T \oplus S$. We note that $T \oplus S$ can be computed by interchanging the symbols s_i and t_i , for all i , in the representation of $S \oplus T$. Due to the appearance of single terms $s_i * t_i$ and pairings $s_i * t_k + s_k * t_i$ in each summation, the gray level values of $S \oplus T$ and $T \oplus S$ agree at each pixel of $K(x)$, for each x in X .

We now consider the computation of the operation \odot for pairs of templates. The distinction between the operation $S \odot T$ and $S \oplus T$, which we have described above, lies in the calculation of the gray level function. For $S \odot T$, a maximization of specified products of weights replaces the summation of those products in computing $S \oplus T$. The neighborhood system of $S \odot T$ is identical to that of $S \oplus T$. We let $R = S \odot T$, where $R = (K(x), r_x)$. Since that neighborhood system $K(x)$ is described above, we turn to the computation of each gray level function r_x on $K(x)$.

The weight function r_x for $S \odot T$ is found in this way :

1. Indicate the neighborhood $K(x)$ for the template $S \vee T$.
2. For v in the neighborhood $N(x)$ of template T ,
 - a. Find the weight $t_x(v)$ of template T ;
 - b. Find the neighborhood $M(v)$ and weight function s_v of the template S ; and
 - c. Multiply each weight $s_v(z)$, for z in $M(v)$, by $t_x(v)$; record each product at pixel z of $K(x)$.
3. Repeat step 2 for every v in $N(x)$.
4. For every pixel in $K(x)$, compute the maximum of all products obtained for that pixel by steps 2 and 3. This maximum is $r_x(z)$ for z in $K(x)$.
5. Set $r_x(z) = 0$ for z not in $K(x)$.

Example V-15:

S	T	Intermediate steps 2 and 3		$S \odot T$
-----	-----	-----	-----	-----
1* 1 1 3 1	1* 2 1	1* 2 1 6 1	1* 1 1	1* 2 1 6 1
-----	-----	-----	-----	-----
	1 1 1	1 1 1	1 1 1 3 1	1 1 1 3 1
	-----	-----	-----	-----

Example V-1E

By comparison with Example V-12, we see that $S \oplus T$ is not $S \oplus T$, in this case.

Example V-17:

since from intermediate steps 2 and 3 we have

As before with $S \oplus T$ it is convenient to proceed in the following way:

- 67-46

formed in this manner. This maximum value is the weight $r_x(z)$ of template $S \odot T$ at pixel z .

Example V-16:

$$\begin{array}{c}
 \begin{array}{|c|c|c|} \hline S \\ \hline 1 & 1 & 3 \\ \hline 4 & 1 & 2 \\ \hline \end{array}
 \quad
 \begin{array}{|c|c|c|} \hline T \\ \hline 1 & 4 & 5 \\ \hline 3 & 1 & 7 \\ \hline \end{array}
 \quad
 = \quad
 \begin{array}{|c|c|c|} \hline S \odot T \\ \hline 1 & 4 & 12 \\ \hline 12 & 20 & 21 \\ \hline 12 & 28 & 14 \\ \hline \end{array}
 \quad
 \text{using} \quad
 \begin{array}{|c|c|c|} \hline \\ \hline 1 & 4 & 12 \\ \hline 1 & 5 & 15 \\ \hline 1 & 16 & 8 \\ \hline 1 & 20 & 10 \\ \hline 1 & 3 & 9 \\ \hline 1 & 7 & 21 \\ \hline 1 & 12 & 6 \\ \hline 1 & 28 & 14 \\ \hline \end{array}
 \end{array}$$

If S and T are templates which can be represented by 3×3 masks, and if all weights of the masks are non-negative, then the template $S \odot T$ can be represented by a 5×5 mask. We write

$$S \odot T = R, \text{ where}$$

$$\begin{array}{c}
 \begin{array}{|c|c|c|} \hline S \\ \hline s_1 & s_2 & s_3 \\ \hline s_4 & s_5 & s_6 \\ \hline s_7 & s_8 & s_9 \\ \hline \end{array}
 \quad
 \begin{array}{|c|c|c|} \hline T \\ \hline t_1 & t_2 & t_3 \\ \hline t_4 & t_5 & t_6 \\ \hline t_7 & t_8 & t_9 \\ \hline \end{array}
 \quad
 \text{and}
 \end{array}$$

$$\begin{array}{c}
 \begin{array}{|c|c|c|c|c|} \hline R \\ \hline r_1 & r_2 & r_3 & r_4 & r_5 \\ \hline r_6 & r_7 & r_8 & r_9 & r_{10} \\ \hline r_{11} & r_{12} & r_{13} & r_{14} & r_{15} \\ \hline r_{16} & r_{17} & r_{18} & r_{19} & r_{20} \\ \hline r_{21} & r_{22} & r_{23} & r_{24} & r_{25} \\ \hline \end{array}
 \end{array}$$

Furthermore, the entries r_i are specified in this way:

$$\begin{aligned}
 r_1 &= s_1 t_1 \\
 r_2 &= s_2 t_1 \vee s_2 t_2 \\
 r_3 &= s_3 t_1 \vee s_2 t_2 \vee s_1 t_3 \\
 r_4 &= s_3 t_2 \vee s_2 t_3 \\
 r_5 &= s_3 t_3
 \end{aligned}$$

$r_6 = s_4 * t_1 \vee s_1 * t_4$
 $r_7 = s_5 * t_1 \vee s_4 * t_2 \vee s_2 * t_4 \vee s_1 * t_5$
 $r_8 = s_6 * t_1 \vee s_5 * t_2 \vee s_4 * t_3 \vee s_3 * t_4 \vee s_2 * t_5 \vee s_1 * t_6$
 $r_9 = s_6 * t_2 \vee s_5 * t_3 \vee s_3 * t_5 \vee s_2 * t_6$
 $r_{10} = s_6 * t_3 \vee s_3 * t_6$
 $r_{11} = s_7 * t_1 \vee s_4 * t_4 \vee s_1 * t_7$
 $r_{12} = s_8 * t_1 \vee s_7 * t_2 \vee s_5 * t_4 \vee s_4 * t_5 \vee s_2 * t_7 \vee s_1 * t_8$
 $r_{13} = s_9 * t_1 \vee s_8 * t_2 \vee s_7 * t_3 \vee s_6 * t_4 \vee s_5 * t_5 \vee s_4 * t_6 \vee s_3 * t_7 \vee$
 $s_2 * t_8 \vee s_1 * t_9$
 $r_{14} = s_9 * t_2 \vee s_8 * t_3 \vee s_6 * t_5 \vee s_5 * t_6 \vee s_3 * t_8 \vee s_2 * t_9$
 $r_{15} = s_9 * t_3 \vee s_6 * t_6 \vee s_3 * t_9$
 $r_{16} = s_7 * t_4 \vee s_4 * t_7$
 $r_{17} = s_8 * t_4 \vee s_7 * t_5 \vee s_5 * t_7 \vee s_4 * t_8$
 $r_{18} = s_9 * t_4 \vee s_8 * t_5 \vee s_7 * t_6 \vee s_6 * t_7 \vee s_5 * t_8 \vee s_4 * t_9$
 $r_{19} = s_9 * t_5 \vee s_8 * t_6 \vee s_6 * t_8 \vee s_5 * t_9$
 $r_{20} = s_9 * t_6 \vee s_6 * t_9$
 $r_{21} = s_7 * t_7$
 $r_{22} = s_8 * t_7 \vee s_7 * t_8$
 $r_{23} = s_9 * t_7 \vee s_8 * t_8 \vee s_7 * t_9$
 $r_{24} = s_9 * t_8 \vee s_8 * t_9$
 $r_{25} = s_9 * t_9$

From this representation it can be seen that for templates S and T represented by 3×3 masks, we have $S \odot T = T \odot S$. We note that $T \odot S$ can be computed by interchanging the symbols s_i and t_i for all i , in the representation of $S \vee T$. Due to the appearance of single terms $s_i * t_i$ and pairings $(s_i * t_k) \vee (s_k * t_i)$ in each computation, the gray level values of $S \odot T$ and $T \odot S$ agree at each pixel of $K(x)$, for each x in X .

If all weights of template T are non-negative, it may be advantageous to compute $R = S \odot T$ by an iterative scheme of matching the largest weights of T with the largest weights of S , in turn, to obtain certain weights r_x for x in the neighborhood $K(x)$. We begin with the largest weight of T in the intermediate computations and continue using weights of T in order of decreasing size.

Example V-19:

S	T	$S \odot T$
-----	-----	-----
1 * 1 0	1 5 3 7	1 5 3 7 0
-----	-----	-----
1 1 -1	1 1 * 4 1	1 5 * 4 7 0
-----	-----	-----
	1 3 8 5	1 3 8 5 0
	-----	-----
		1 3 8 5 -5

Intermediate steps are as follows:

-----	-----	-----	-----	-----
1 1 1 1 1	1 1 171 1	151 171 1	151 171 1	1513171 1
-----	-----	-----	-----	-----
1 1 171 1	1 1 171 1	151 171 1	151 4171 1	151 4171 1
-----	-----	-----	-----	-----
1 181 1 1	1 181 1 1	1 18151 1	1 18151 1	1318151 1
-----	-----	-----	-----	-----
1 181 1 1	1 181 1 1	1 18151 1	1 18151 1	1318151 1
-----	-----	-----	-----	-----

with computation at the remaining pixels of $K(x)$ by direct calculation.

The procedure of computing $R = S \boxdot T$, where S and T are templates defined by masks, differs from the operations \oplus and \odot in the calculation of the weight functions, for the neighborhood system of $S \boxdot T$ is identical to that of $S \oplus T$ and $S \odot T$. For $S \boxdot T$, a maximization of specified sums of weights replaces the maximization of the corresponding products used in computing $S \odot T$. We now turn to the computation of each gray level function r_x on $K(x)$.

The weight function r_x for $S \boxdot T$ is found in this way:

1. Indicate the neighborhood $K(x)$ for the template $S \boxdot T$.
2. For v in the neighborhood $N(x)$ of template T ,
 - a. Find the weight $t_x(v)$ of template T ,
 - b. Find the neighborhood $M(v)$ and weight function s_v of the template S , and
 - c. For z in $M(v)$, sum the weights $s_v(z)$ and $t_x(v)$; record each sum at pixel z , which is also a pixel of $K(x)$.
3. Repeat step 2 for every v in $N(x)$.
4. For every pixel in $K(x)$, compute the maximum of all sums obtained at that pixel by steps 2 and 3. This maximum is $r_x(z)$ for z in $K(x)$.
5. Set $r_x(z) = 0$ for z not in $K(x)$.

Example V-20:

S	T	Intermediate steps 2 and 3		$S \boxdot T$
-----	-----	-----	-----	-----
1* 11 3 1	1* 21	1* 31 5 1	1* 1 1	1* 31 5 1
-----	-----	-----	-----	-----
	1 1 1	1 1 1	1 2 1 4 1	1 2 1 4 1
-----	-----	-----	-----	-----

Example V-21:

S	T	Intermediate steps 2 and 3	
----- 1* 1 3 -----	----- 1* 2 1 -----	----- 1* 3 5 -----	----- 1* 1 2 4 -----
		S \boxtimes T	
		----- 1* 3 5 4 -----	

Example V-22:

S	T	S \boxtimes T
----- 1* 1 3 -----	----- 1* 4 5 -----	----- 1* 5 7 8 -----
----- 1 4 2 -----	----- 1 3 7 -----	----- 1 8 9 10 -----
		----- 1 7 11 9 -----

from intermediate steps 2 and 3 we have

----- 1* 5 7 -----	----- 1* 6 8 -----	----- 1* 1 -----	----- 1* 1 -----
----- 1 8 6 -----	----- 1 9 7 -----	----- 1 4 6 -----	----- 1 8 10 -----
----- 1 1 -----	----- 1 1 -----	----- 1 7 5 -----	----- 1 11 9 -----

For the operation \boxtimes , zero weight values on the neighborhood or configuration are very important, due to the summation of weights used, in place of the multiplication of + and v. This can be seen by comparison of the following examples:

Example V-23:

S = ----- 1* 1 3 -----	T = ----- 1* 2 -----	S v T = ----- 1* 3 5 -----
S = ----- 1* 1 3 -----	T = ----- 1* 2 0 -----	S v T = ----- 1* 3 5 3 -----
S = ----- 1* 1 3 -----	T = ----- 1* 2 0 0 -----	S v T = ----- 1* 3 5 3 3 -----
S = ----- 1* 1 3 -----	T = ----- 1 0 1* 2 0 -----	S v T = ----- 1 1 1* 3 5 3 -----

we also note the following examples, in which the center pixel x is not in the neighborhood $N(x)$.

Example V-24:

$$\begin{array}{lll}
 \begin{array}{c} \text{-----} \\ S = \begin{bmatrix} 1 & 1 & 3 \end{bmatrix} \\ \text{-----} \end{array} & \begin{array}{c} \text{-----} \\ T = \begin{bmatrix} 1 & 1 & 2 \end{bmatrix} \\ \text{-----} \end{array} & \begin{array}{c} \text{-----} \\ S \boxtimes T = \begin{bmatrix} 1 & 1 & 5 \end{bmatrix} \\ \text{-----} \end{array} \\
 \begin{array}{c} \text{-----} \\ S = \begin{bmatrix} 1 & 1 & 3 \end{bmatrix} \\ \text{-----} \end{array} & \begin{array}{c} \text{-----} \\ T = \begin{bmatrix} 1 & 1 & 2 & 0 \end{bmatrix} \\ \text{-----} \end{array} & \begin{array}{c} \text{-----} \\ S \boxtimes T = \begin{bmatrix} 1 & 1 & 5 & 3 \end{bmatrix} \\ \text{-----} \end{array}
 \end{array}$$

As before with \oplus and $S \odot T$, it is convenient to proceed in the following way:

1. For each x in X , indicate the configuration or neighborhood $K(x)$ of the pixel x for $S \boxtimes T$.
2. For v in $N(x)$, the neighborhood of x for the template T , sum the weight $t_x(v)$ and the weight $s_v(z)$, for each z in $M(v)$, the neighborhood of v of template S . Record each sum in the corresponding pixel z . Note that z is a pixel of $K(x)$.
3. At each pixel z of $K(x)$, find the maximum of all sums formed in this manner. This maximum value is the weight $r_x(z)$ of template $S \boxtimes T$ at pixel z .

Example 25:

$$\begin{array}{llll}
 \begin{array}{c} \text{-----} \\ S = \begin{bmatrix} 1 & 1 & 3 \end{bmatrix} \\ \text{-----} \end{array} & \begin{array}{c} \text{-----} \\ T = \begin{bmatrix} 1 & 4 & 5 \end{bmatrix} \\ \text{-----} \end{array} & = & \begin{array}{c} \text{-----} \\ S \boxtimes T = \begin{bmatrix} 1 & 5 & 7 & 8 \end{bmatrix} \\ \text{-----} \end{array} \\
 \begin{array}{c} \text{-----} \\ S = \begin{bmatrix} 1 & 4 & 2 \end{bmatrix} \\ \text{-----} \end{array} & \begin{array}{c} \text{-----} \\ T = \begin{bmatrix} 1 & 3 & 7 \end{bmatrix} \\ \text{-----} \end{array} & = & \begin{array}{c} \text{-----} \\ S \boxtimes T = \begin{bmatrix} 1 & 8 & 9 & 10 \end{bmatrix} \\ \text{-----} \end{array}
 \end{array}$$

using

$$\begin{array}{c} \text{-----} \\ \begin{bmatrix} 1 & 5 & 7 & 8 \end{bmatrix} \\ \text{-----} \\ \begin{bmatrix} 1 & 6 & 9 \end{bmatrix} \\ \text{-----} \\ \begin{bmatrix} 1 & 8 & 6 \end{bmatrix} \\ \text{-----} \\ \begin{bmatrix} 1 & 9 & 7 \end{bmatrix} \\ \text{-----} \\ \begin{bmatrix} 1 & 4 & 6 \end{bmatrix} \\ \text{-----} \\ \begin{bmatrix} 1 & 8 & 10 \end{bmatrix} \\ \text{-----} \\ \begin{bmatrix} 1 & 7 & 5 \end{bmatrix} \\ \text{-----} \\ \begin{bmatrix} 1 & 11 & 9 \end{bmatrix} \\ \text{-----} \end{array}$$

If S and T are templates which can be represented by 3×3 masks, and if all weights of the masks are non-negative, then the template $S \boxtimes T$ can be represented by a 5×5 mask. We write

$$S \boxtimes T = R, \text{ where}$$

$$S = \begin{array}{|c|c|c|} \hline s_1 & s_2 & s_3 \\ \hline s_4 & *s_5 & s_6 \\ \hline s_7 & s_8 & s_9 \\ \hline \end{array}, \quad T = \begin{array}{|c|c|c|} \hline t_1 & t_2 & t_3 \\ \hline t_4 & *t_5 & t_6 \\ \hline t_7 & t_8 & t_9 \\ \hline \end{array}, \quad \text{and}$$

$$R = \begin{array}{|c|c|c|c|c|} \hline r_1 & r_2 & r_3 & r_4 & r_5 \\ \hline r_6 & r_7 & r_8 & r_9 & r_{10} \\ \hline r_{11} & r_{12} & *r_{13} & r_{14} & r_{15} \\ \hline r_{16} & r_{17} & r_{18} & r_{19} & r_{20} \\ \hline r_{21} & r_{22} & r_{23} & r_{24} & r_{25} \\ \hline \end{array}$$

Furthermore, the entries r_i are specified in the following way, with all summations computed before the maximizations:

$$\begin{aligned} r_1 &= s_1 + t_1 \\ r_2 &= s_2 + t_1 \vee s_2 + t_1 \\ r_3 &= s_3 + t_1 \vee s_2 + t_2 \vee s_1 + t_3 \\ r_4 &= s_3 + t_2 \vee s_2 + t_3 \\ r_5 &= s_3 + t_3 \\ r_6 &= s_4 + t_1 \vee s_1 + t_4 \\ r_7 &= s_5 + t_1 \vee s_4 + t_2 \vee s_2 + t_4 \vee s_1 + t_5 \\ r_8 &= s_6 + t_1 \vee s_5 + t_2 \vee s_4 + t_3 \vee s_3 + t_4 \vee s_2 + t_5 \vee s_1 + t_6 \\ r_9 &= s_6 + t_2 \vee s_5 + t_3 \vee s_3 + t_5 \vee s_2 + t_6 \\ r_{10} &= s_6 + t_3 \vee s_3 + t_6 \\ r_{11} &= s_7 + t_1 \vee s_4 + t_4 \vee s_1 + t_7 \\ r_{12} &= s_8 + t_1 \vee s_7 + t_2 \vee s_5 + t_4 \vee s_4 + t_5 \vee s_2 + t_7 \vee s_1 + t_8 \\ r_{13} &= s_9 + t_1 \vee s_8 + t_2 \vee s_7 + t_3 \vee s_6 + t_4 \vee s_5 + t_5 \vee s_4 + t_6 \vee s_3 + t_7 \vee \\ &\quad s_2 + t_8 \vee s_1 + t_9 \\ r_{14} &= s_9 + t_2 \vee s_8 + t_3 \vee s_6 + t_5 \vee s_5 + t_6 \vee s_3 + t_8 \vee s_2 + t_9 \\ r_{15} &= s_9 + t_3 \vee s_6 + t_6 \vee s_3 + t_9 \\ r_{16} &= s_7 + t_4 \vee s_4 + t_7 \\ r_{17} &= s_8 + t_4 \vee s_7 + t_5 \vee s_5 + t_7 \vee s_4 + t_8 \\ r_{18} &= s_9 + t_4 \vee s_8 + t_5 \vee s_7 + t_6 \vee s_6 + t_7 \vee s_5 + t_8 \vee s_4 + t_9 \\ r_{19} &= s_9 + t_5 \vee s_8 + t_6 \vee s_6 + t_8 \vee s_5 + t_9 \\ r_{20} &= s_9 + t_6 \vee s_6 + t_9 \\ r_{21} &= s_7 + t_7 \\ r_{22} &= s_8 + t_7 \vee s_7 + t_8 \\ r_{23} &= s_9 + t_7 \vee s_8 + t_8 \vee s_7 + t_9 \\ r_{24} &= s_9 + t_8 \vee s_8 + t_9 \\ r_{25} &= s_9 + t_9 \end{aligned}$$

From this representation it can be seen that for templates S and T represented by 3×3 masks, we have $S \boxdot T = T \boxdot S$. We note that $T \boxdot S$ can be computed by interchanging the symbols s_i and t_i , for all i , in the representation of $S \boxdot T$. Due to the appearance of single terms $s_i \vee t_i$ and pairings $(s_i + t_k) \vee (s_k + t_i)$ in each computation, the gray level values of $S \boxdot T$ and $T \boxdot S$ agree at each pixel of $K(x)$, for each x in X .

Finally, we have the complementary template - template operations of \odot and \boxminus which can be defined within the image algebra.

Definition V-7:

If S and T are templates on X ,

$$S \odot T = - (S \vee -T) \quad \text{and}$$

$$S \boxminus T = - (-S \vee -T) .$$

VI. TEMPLATE DECOMPOSITION

In the previous section we considered templates formed using the template - template operations: $S \oplus T$, $S \odot T$, and $S \boxdot T$. We now turn to a related problem, the decomposition of a template R. Given R on X, is it possible to find templates S and T on R with $R = S \oplus T$, or $R = S \odot T$, or $R = S \boxdot T$?

In some cases, the decomposition may become apparent by inspection; it is then a matter of checking to determine that the proposed decomposition is valid.

Example VI-1:

We consider templates on X defined by the following masks:

R	S	T
----- -1 -2 -1 ----- 2 * 2 0 ----- 1 2 1 -----	----- 1 * 2 1 -----	----- -1 ----- * 0 ----- 1 -----

We note that $R = S \oplus T$ is a decomposition of the template R.

The above decomposition was obtained by inspection. We now consider a method of obtaining template decompositions for the template operation $+$ in the case of templates which can be represented by a mask. We first note a correspondence between templates defined by masks and polynomial-like representations.

We will indicate a neighborhood of x by assigning each pixel of the neighborhood indices (i,j), with (0,0) denoting the center pixel, to denote that the pixel is at the location i rows and j columns from the center pixel. Positive i denotes below the center, while positive j denotes right of center.

Figure VI-1 Indexing of pixels of a neighborhood

...	
...		(-1,-1)		(-1,0)		(-1,1)		...
...		(0,-1)		* (0,0)		(0,1)		...
...		(+1,-1)		(+1,0)		(+1,1)		...
...	

We now identify an algebraic expression with a template defined by a mask. Since a mask specifies a neighborhood and all weight values for pixels of the neighborhood, we let I denote the set of all indices (i,j) corresponding to the pixels of the neighborhood. If the weight at the (i,j) pixel of the neighborhood is given by $c(i,j)$, then the mask can be identified by the expression

$$\sum c(i,j) x^i y^j, \quad \text{for } (i,j) \text{ in } I.$$

The exponent of x indicates the row location, and the exponent of y indicates the column location, with respect to the center pixel, of the weight $c(i,j)$.

Example VI-2:

In each case below, the template given by the mask at the left corresponds to the expression listed at the right.

----- 1 *1 3 -----	$2y^{-1} + 1 + 3y$
----------------------------------	--------------------

----- 2 ----- *1 ----- 3 -----	$2x^{-1} + 1 + 3x$
--	--------------------

----- *2 1 ----- 3 -----	$2 + y + 3x$
--	--------------

----- [] *1 3 2 -----	$y + 3y^2 + 2y^3$
--------------------------------------	-------------------

----- *1 2 ----- 3 4 -----	$1 + 2y + 3x + 4xy$
--	---------------------

----- 1 2 ----- 3 *4 -----	$x^{-1}y^{-1} + 2x^{-1} + 3y^{-1} + 4$
--	--

Suppose S and T are templates on a space X and that for each of these templates a mask indicates the neighborhood and the weights at every pixel of the neighborhood. We write the expression which can be associated with each of these masks, by the process described above:

$$\begin{aligned} \text{Template } S \text{ and } P(x,y) &= \sum b(k,l) x^k y^l, \text{ for } (k,l) \text{ in } J \\ \text{Template } T \text{ and } Q(x,y) &= \sum c(i,j) x^i y^j, \text{ for } (i,j) \text{ in } I. \end{aligned}$$

In multiplying $P(x,y)$ and $Q(x,y)$, each term of the expression

$$\sum_j b(k,l) x^k y^l \text{ is multiplied by each term of } \sum_i c(i,j) x^i y^j.$$

The coefficient of $x^p y^q$ in this product is

$$a(p,q) = \sum c(i,j) b(k,l) \quad \text{where } (i,j) \text{ is in } I, (k,l) \text{ is in } J, \\ \text{and } p = i + k, \text{ and } q = j + l.$$

Let K denote the set of all pairs (p,q) formed in this way. Then the template $S + T$ corresponds to the expression

$$\sum a(p,q) x^p y^q, \text{ for } (p,q) \text{ in } K$$

This is a rephrasing, in the language of polynomials, of the computation of $S \oplus T$. The addition of exponents corresponds to the representation of a pixel z in a neighborhood (from $S \oplus T$) of x , given z in the neighborhood (from S) of y , and y in a neighborhood (from T) of x . The weight of $S \oplus T$ at location (p,q) with respect to the center of its neighborhood is the sum of products of weights of S and of T given by the coefficient $a(p,q)$ of $x^p y^q$ in the product of the expressions

$$\sum_K a(p,q) x^p y^q = \sum_I c(i,j) x^i y^j * \sum_J b(k,l) x^k y^l.$$

We now have a representation for template decomposition using the operation \oplus . To the template R form the expression $P(x,y)$ which is obtained from its mask, by the process described above. We then have the following result:

If $P(x,y)$ has a factorization over the reals, with

$$P(x,y) = P_1(x,y) * P_2(x,y)$$

then R has the decomposition

$$R = S + T, \text{ where}$$

S is the template corresponding to $P_1(x,y)$ and
 T is the template corresponding to $P_2(x,y)$.

Example VI-3:

R is the template with mask

1	*	2	1

1		4	1

The polynomial corresponding to R is

$$z + 7y + 3yz + 4x + 2xy = (z + y) * (1 + 2x + 3y); \text{ thus}$$

$$R = \begin{array}{|c|c|c|} \hline 1 & 1 & 3 \\ \hline 1 & 2 & \\ \hline \end{array} \oplus \begin{array}{|c|c|c|} \hline 1 & 2 & 1 \\ \hline \end{array}.$$

REFERENCES

1. R.C. Gonzalez and P. Wintz: Digital Image Processing, Second Edition, Addison Wesley, Reading, MA, 1987
2. P.E. Miller and A. Corneil: Development of Mathematical Structures for Image Processing, Technical Report AFATL-TR-83-61
3. W.K. Pratt: Digital Image Processing, John Wiley, New York, 1978
4. G.X. Ritter, M. Schrader-Frechette and P. Gader: Image Algebra, Defense Technical Information Center Technical Report AFATL-TR-86-79
5. G.X. Ritter, M. Schrader-Frechette and J. Wilson: "Image Algebra: A Rigorous and Translucent Way of Expressing All Image Processing Operations", in Proceedings of the 1987 Technical Symposium Southeast on Optics, Electro-Optics, and Sensors, Orlando, FL (May 1987)
6. G.X. Ritter et al: Image Algebra Project, Phase II Program Review, FO 8635-84-0295, 1986
7. A. Rosenfeld and A. Kak: Digital Picture Processing, vol. 1 and 2, Second Edition, Academic Press, 1982
8. J. Serra: Image Analysis and Mathematical Morphology, Academic Press, 1982
9. J.N. Wilson and G.X. Ritter: "Functional Specification of Neighborhoods in an Image Processing Language", in Proceedings of the Fourth International Symposium on Optical and Optoelectronic Applied Science and Engineering, Society of Photo-Optical Instrumentation Engineers, The Hague, The Netherlands (March, 1987)

Simulation Studies of MICAP Allocation
Systems for EOQ Items

Dan B. Rinks
Department of Quantitative Business Analysis
Louisiana State University
Baton Rouge, Louisiana, USA 70803

Abstract

The United States Air Force operates one of the largest multi-echelon inventory systems in the world. Individual bases hold inventory to meet the demands of their customers at the base. These bases are re-supplied by central depots that are, in turn, re-supplied by vendors. This study examines the efficacy of rationing assets at the depot whenever the on-hand level gets low as a means of improving weapon system availabilities. A large scale simulation model of the USAF's multi-echelon inventory system is used to study the effects of such a rationing procedure.

BACKGROUND

The United States Air Force operates one of the largest multi-echelon inventory systems in the world. Individual bases hold inventory to meet the demands of their customers at the base. These bases are re-supplied by central depots that are, in turn, re-supplied by vendors.

It is important to note that there are essentially two separate inventory systems that are used to support Air Force operations. The first system is for investment items that are recoverable when they fail; that is, these items are repaired. Recoverable items typically have high cost and low demand. Consequently, a (s-l,s) policy of one-for-one replenishment at the base level is optimal. This system has received a considerable amount of attention by the Air Force for two reasons. First, as previously stated, the cost of the items is high; total investment for recoverables is in excess of \$10 billion. Secondly, a demand at the base level for a recoverable item is commonly associated with a weapon-system being taken out of service.

There is a significant body of research on the problem of the base-depot supply system for recoverable items. Foremost, are the METRIC models developed by Sherbrooke [10], [11], and [12] and the models of Muckstadt [6], [7], and [8]. These models determine "optimal" base and depot stock levels for each item subject to a constraint on system investment or system performance.

The second supply system is for consumable or EOQ items. In comparison to recoverable items, consumable items have lower cost and higher demand. In the scheme of the Air Force inventory, EOQ items can generally be classified into Group C of an ABC inventory classification. As the name implies, consumable items are "used up" and are not repaired. Both the bases and the depots use economic order quantity - reorder point stockage

policies for EOQ items. Most demands for items in the EOQ system are not related to a weapon system being taken out of service. However, in some instances EOQ items can result in a weapon system being grounded.

By and large the EOQ supply system has not received nearly as much attention as the recoverable spares supply system as the Air Force has attempted to improve weapon system availabilities through better logistics support. Recently, however, the Air Force community has come to realize that the EOQ supply system may offer a cost effective means of reducing the down time of weapon systems.

One way the Air Force has attempted to deal with this problem is by establishing a priority classification scheme for demands. In essence, by assigning a priority to a demand there is a recognition that EOQ items are used for a variety of purposes that have significantly different consequences in supporting the mission readiness whenever a demand must be backordered. To date, demand priorities have only been used to determine the sequence that backordered demands will be filled when assets become available after a resupply. Thus, a low priority demand is always filled if there are serviceable assets on-hand.

This study examines the efficacy of a method the Air Force Logistics Command (AFLC) has proposed for rationing assets at the depot as a means of improving weapon system availabilities. Rationing of assets in this context involves not meeting low priority, non-essential demands from the bases even though assets are available in order to hold those assets for anticipated higher priority demands. A large scale simulation model of the USAF's multi-echelon inventory system is used to assess the effects of the proposed rationing procedure.

The remainder of the paper is organized in the following fashion. In the next section, the system being modelled is described. Then the protocol for the proposed rationing procedure is given. Following this, the results of the simulation study are presented. The paper concludes with a discussion of why the proposed rationing procedure does not accomplish its desired result.

THE MULTI-ECHELON INVENTORY SYSTEM FOR EOQ ITEMS

The basic flows in the multi-echelon system for EOQ items is depicted in Figure 1 and described below.

1. Customers demand items at the retail (base) level. A demand for an item can be distinguished by the intended use for the item. In doing so a priority code is assigned to the demand. A demand that effects the mission capability of an Air Force entity is labelled MICAP and given a numeric from 1 to 8 (the lower the numeric the more severe the impact on performance). Demands which do not effect mission capabilities are labelled Non-MICAP and assigned numerics from 1 to 15.
2. If the base has positive on-hand inventory of the item, then the customer's request is satisfied from stock. If not, the demand is backordered until the base receives a replenishment from the depot, and a priority (rush) replenishment order for the backordered amount is placed to the depot. If the depot has positive on-hand inventory for the item, then the base's request is shipped from stock. If not, the request is backordered until the depot receives a replenishment from the vendor.
3. Bases follow Standard Base Supply System (SBSS) stockage policy. This policy is basically a reorder point (ROP), reorder quantity (EOQ) procedure. Safety levels for items are set at one standard deviation of

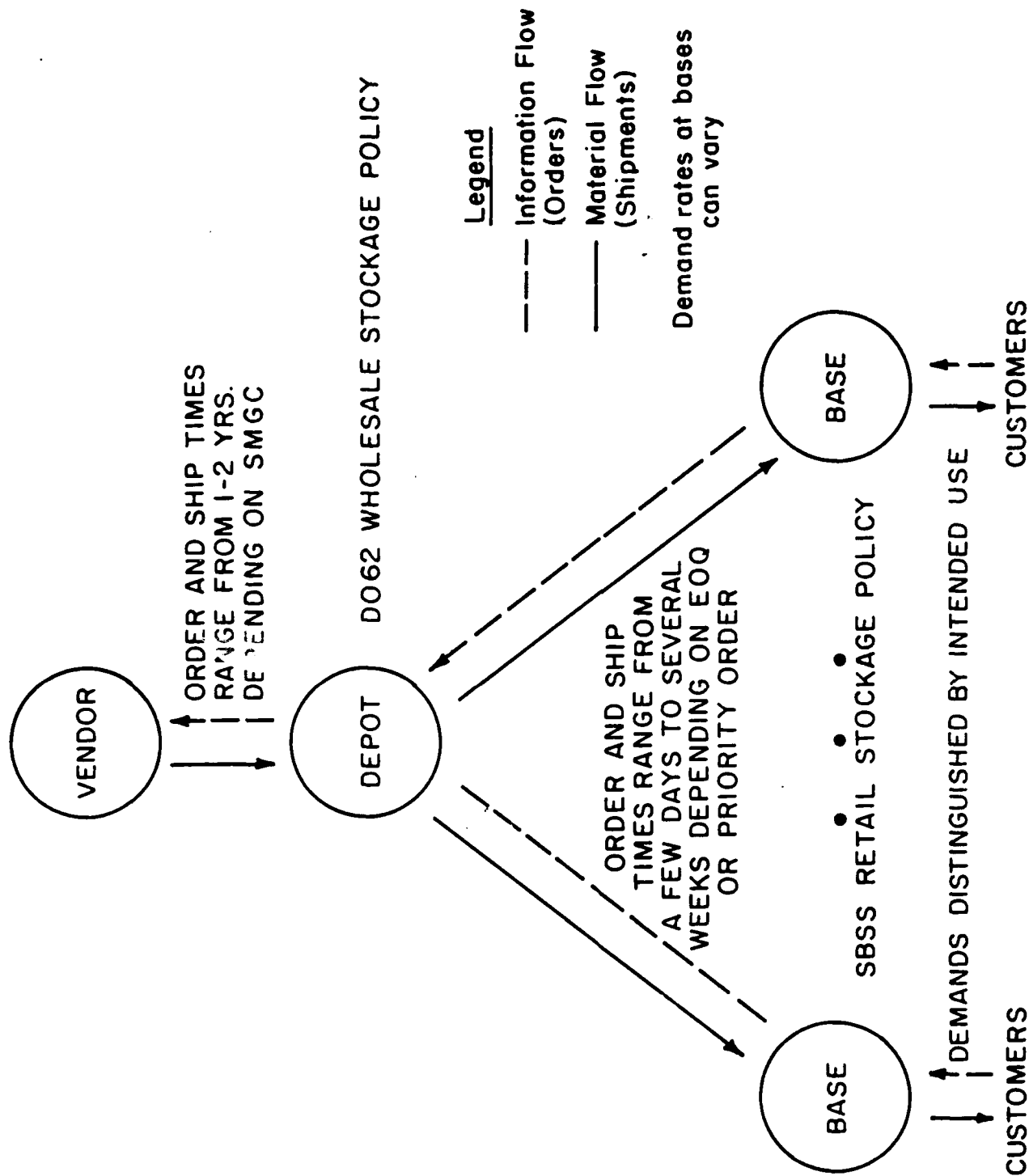


Figure 1. Basic flows in the multi-echelon system for EOQ items

leadtime demand for bases in the continental United States and two standard deviations of leadtime demand otherwise.

4. Whenever a base reorder point is breached, an EOQ order to the wholesale (depot) level is placed. EOQ orders are assigned a priority code in the lowest category (Non-MICAP priority 9-15). Under current policy, if the depot has positive on-hand inventory for the item, then the base's EOQ request is shipped from stock. If not, the base's demand is backordered until the depot receives a replenishment from the vendor. Note that under the current policy, the depot fills orders strictly on a first come-first served basis as long as it has positive on-hand inventory; demand priorities are used only to determine the sequence that backordered demands will be filled when assets become available after a resupply.

5. Order and ship times (OST) from Base-Depot-Base are stochastic. Base leadtimes range from a few days to several weeks with the distributions depending on the type of order (EOQ or rush) and base location. Backordered requests receive priority (rush) treatment.

6. Stockage policy at the depot follows the procedures set forth in [1] and specific instructions from computing wholesale requirements are documented in [4]. This latter system is known as the EOQ Requirements System (DO62). This policy is also a ROP-EOQ type procedure. Further details of the depot stockage policy, as well as the proposed rationing procedure, are given the next section.

7. Whenever the depot reorder point is breached, an order to the vendor is placed. Order and ship times from Depot-Vendor-Depot are stochastic. Depot leadtimes have a range from about six months to three years with the distributions depending on the supply management grouping code (SMGC).

Several features of the Air Force inventory management system for EOQ items make the problem at hand interesting. First of all is the sheer size of the system. There are over 500,000 line items with an investment value of over \$2 billion. Because of this size, it is imperative that the management system be highly automated, and it is. A consequence of the size is that drastic changes in operating policies are very difficult to implement. Changes tend to be incremental, building upon the existing system, rather than a re-design of the system.

It must also be recognized that parts of the existing system, such as the organizational and physical structures, that define the differing roles of the depot and base levels, are "frozen." In the logistics organizational chain of command, the depot is above the base. Changes in operating policies that seek to improve system performance are much more likely to be directed toward the depot. Part of this bias is due to the belief that the depots have a world-wide perspective whereas the bases are local-oriented. However, the purpose of the depot is to support the bases. Backorders at the depot are only of consequence when they cause shortages at the bases, whereas shortages at the bases directly effect weapon system availabilities. In spite of this, single-echelon stockage policies that "optimize" performance at the depot and single-echelon stockage policies that "optimize" performance at the base level are the basis for much of the existing inventory management system.

In addition to the pragmatic issues just discussed, there are also the usual host of challenges associated with modeling multi-echelon inventory problems. Predominant among these are the complex nature of the stochastic elements.

The demand process. Although the simplifying assumption of Poisson arrivals of customers at the base level is supported by the data, the differentiation of demand into priority categories quickly complicates the analysis. Furthermore, demand rates among bases differ significantly for an item because bases have different primary missions assigned to them.

Because the demand rates vary at the base level, the EOQs the bases place to the depot are not for the same amount. Backorders at the bases generate priority (rush) orders to the depot. Thus, the depot has two classes of demand: EOQs and priority (rush) orders, both being distinguished by the priority codes used for rationing assets.

Order and ship times. Leadtime distributions at the base level depend on whether the order to the depot is an EOQ or rush order. Leadtime distributions at the depot level depend on the supply management grouping code (SMGC). The SMGC for an item is a function of its dollar value of annual demand and determines the level of management attention paid to the item. Low management-intensity items are classified as SMGC 'T' items, while medium-intensity items and high-intensity items are labelled as 'P' and 'M' items, respectively.

THE D062 DEPOT REQUIREMENTS SYSTEM AND PROTOCOL FOR RATIONING ASSETS

The D062 System

The actual policies and procedures of the D062 Wholesale Requirements System are quite convoluted. In order to construct an accurate model of the D062 system, the latest revision of the D062 documentation was acquired from the contractor (BDM Corporation) responsible for running and maintaining D062. Numerous checks were made to insure that our model does, in fact, emulate the actual D062 system. The primary calculations in D062 involve

the manner in which the depot reorder point and depot reorder quantity are computed. These are described below.

The methodology for computing safety levels at the wholesale level in D062 is based on Presutti and Trepp [9]. In practice, unit fill rates at the depot, and subsequently at the bases, have been consistently lower than that predicted by theory. Because of this, and other reasons, the method for computing safety levels has been changed several times by the Air Force Logistics Command (AFLC) as they attempted to "fine tune" D062.

The Presutti and Trepp model minimizes the total of variable ordering and holding cost subject to a constraint on time-weighted, essentiality-weighted, backorders.

$$\text{Minimize} \quad \sum_{i=1}^n \frac{A_i D_i}{Q_i} + \sum_{i=1}^n a_i c_i \left(\mu_i + k_i \sigma_i + \frac{Q_i}{2} \right) \quad (1)$$

$$\text{subject to} \quad \sum_{i=1}^n \frac{0.5}{2} \frac{Z_i \sigma_i^2}{Q_i} (1 - \exp(-\sqrt{2} \frac{Q_i}{\sigma_i})) \exp(-\sqrt{2} k_i) \leq \beta \quad (2)$$

The following definitions apply; the subscript i refers to the i th item, where $i=1, \dots, n$.

- Q_i = order quantity (units)
- RQP_i = reorder level (units)
- k_i = safety factor
- σ_i = standard deviation of demand during a leadtime
- a_i = holding cost fraction
- A_i = ordering cost (dollars per order)
- c_i = item cost (dollars per unit)
- μ_i = mean demand during a leadtime
- Z_i = item essentiality

ISF = implied shortage factor

β = expected number of essentiality-weighted units in a backordered status at any point in time

The method of Lagrange yields Equation (3) as the solution for the safety factor for the items:

$$k_i = -0.707 \ln \left[\frac{\sqrt{2} Q_i c_i a_i}{0.5 \text{ ISF } Z_i \sigma_i (1 - \exp^{-\sqrt{2} Q_i / \sigma_i})} \right] \quad (3)$$

where

$$\text{ISF} = \sum_{i=1}^n \frac{\sigma_i a_i c_i}{\sqrt{2} \beta} \quad (4)$$

and all other variables except Q_i are known or estimated quantities. Order quantities, Q_i , are also found as part of the solution methodology. However, DO62 uses the simple Wilson lot size formula with certain constraints.

Having found the safety factor, the reorder point is computed in the usual manner.

$$\text{ROP}_i = \mu_i + k_i \sigma_i \quad (5)$$

In practice the implied shortage factor ISF is specified in such a manner that the aggregate safety levels are approximately equal to 55 days of demand [3]. Consequently, the problem is not really solved as a constrained optimization problem. Rather ISF is used as a "control knob." Larger values of ISF result in larger values of k_i , which, in turn, result in fewer backorders: smaller values for ISF have the opposite effect.

The average number of units in backorder status at a random point in time, B_T , for an item with stockage policy Q_i and k_i is

$$B_T = \frac{0.5}{2} \frac{\sigma_i^2}{Q_i} (1 - \exp(-\sqrt{2}Q_i/\sigma_i)) \exp(-\sqrt{2}k_i) \quad (6)$$

This expression assumes that demands during a leadtime are Laplace distributed.

The method that is currently used for computing safety levels at the depot incorporates two modifications from the original Presutti and Trepp procedure and some additional constraints. First, the square root of unit cost instead of using cost is used in the formula for computing the safety factor. The origin for this change is unclear, but is consistent with the observation by Frazza and Kaplan: "If a single-echelon model is run at the upper echelon, then in safety-level calculations the square root of unit price is a more appropriate input than unit price." [2, pg. 185].

$$k_i = -0.707 \ln \left[\frac{\sqrt{2} Q_i \sqrt{c_i} a_i}{0.5 \text{ ISF } \sigma_i (1 - e^{-\sqrt{2}Q_i/\sigma_i})} \right] \quad (7)$$

The safety factor is constrained such that $0 \leq k_i \leq 3$. If the computed k_i is less than zero, it is set equal to zero; and, if the computed k_i is greater than three, it is set equal to three.

The second modification involved the manner in which the item essentiality is treated. Previously, Z_i appeared in the functional for computing the safety factor. In the present procedure, this is no longer the case; rather Z_i is used in the calculation of the safety level/reorder point

$$ROP_i = \mu_i + \frac{1}{Z_i} k_i \sigma_i \quad (8)$$

where $Z_i = 1, 2, \dots, 72$ depending on the mission item essentiality code assigned (MIEC).

In addition, the safety level (SL)

$$SL = \frac{1}{Z_i} k_i \sigma_i \quad (9)$$

cannot exceed the total leadtime demand quantity. If SL is computed to be greater than the leadtime quantity, it is adjusted to equal the leadtime quantity.

Although there are several minor modifications, the computation for the amount that the depot orders from the vendor begins by calculating Wilson's lot size. The simple Wilson lot size is then constrained to be at least a year's supply but not more than three years' supply. Next, the order quantity is adjusted upward to account for any overshooting of the reorder level. Thus, the system operates like an order-up-to-level system. Finally, if the buy quantity is less than \$1000 worth of assets, the buy quantity is recomputed to buy 15 years of support or an amount that has a dollar value equal to the depot ordering cost.

The computation of both the reorder point and the reorder quantity is dynamic in the sense that estimates of demand used in the calculations are based upon a moving average of historical demand. Specifically, the most recent eight quarters plus the current quarter of demands are used in the demand leveling calculations.

Protocol For Rationing Assets

Specific instructions for the proposed rationing procedure are detailed in [5]. As described in this document, the aim of the rationing procedure is to improve mission capability. The MICAP Allocation System, as it is referred to by the Air Force:

- a. Provides an automated method to project stock shortages for items;
- b. Initiates world-wide asset reporting when a stock shortage has been projected for an item; and
- c. Implements automated rationing of available assets on those items where stock shortages have been projected.

At the first of each month, D062 will make a projection of whether or not an item will stockout in the next six months. Basically what happens is that serviceable on-hand assets plus assets that are "due-in to the depot" are balanced against backorders plus projected monthly demands for each month in the next six months. In order for an item to be in a projected stockout position for a given month, it will have more backorders and projected demands than it has serviceable on-hand assets plus due-ins for that month. If there is a projected stockout during any month of the six-month period, the rationing process will be in effect.

In addition, D062 will identify items previously in a projected stockout position which have not been changed to a non-stockout position. Rationing will cease on items changed to a non-stockout position.

For use in the rationing process, D062 will compute an upper asset preservation level and a lower asset preservation level. The upper asset preservation level is defined to be three times the 30-day world-wide demand level and the lower asset preservation level will be one-half the upper level rounded up to the next whole number.

Items subjected to rationing will have orders to the depot filled in the following manner:

1. MICAP priority 1-8 requisitions will ship to zero.
2. Non-MICAP priority 1-3 requisitions will ship to zero.
3. Non-MICAP priority 4-8 requisitions will ship down to the lower asset preservation level.

4. Non-MICAP priority 9-15 requisitions will ship only if the number of assets is above the upper asset preservation level. Note this category include EOQ orders.

THE SIMULATION STUDY

A simulation study was deemed an appropriate methodology to assess the proposed rationing procedure. Two factors influenced this decision. First, analytical models that closely replicate the Air Force EOQ inventory system do not exist. Neither the stockage policies of the depot or base levels nor the stochastic elements of the system can be well approximated by simplifying assumptions that lead to a tractable, closed form model. Furthermore, we were convinced that models that did not capture important nuances of the existing system would not be judged adequate by the Air Force. Second, an ongoing program of incremental changes in operating policies made the construction of a simulation model of the existing system a worthwhile project in itself.

A simulation model encompassing detailed depot and base level stockage policies was constructed using SIMSCRIPT, a versatile simulation modelling language. While it is extremely difficult to completely validate a model as large and as complex as MECH: A SIMULATION PROGRAM OF A MULTI-ECHELON EOQ SYSTEM FOR CONSUMABLES, the model has been exercised extensively. The model gives results that are consistent with intuitive logic and observed behavior of the actual system. All tests suggest that MECH closely replicates the Air Force EOQ inventory system.

Data

In order to test the the efficacy of the proposed rationing procedure, a data base of EOQ items was collected. Specifically, the population of

items used in the analysis consisted of C-130E data from Little Rock AFB (Ark.), Clark AB (Pa.), Pope AFB (North Carolina), and Little Rock ANGB (Ark.). There were 189 EOQ items that were matched as common to all four bases and Air Logistic Center sources.

Transaction data were used to estimate the daily demand rate and the daily demand frequency rate at each of the four bases. With the assumptions that each customer at the retail level orders the same amount and customer arrivals are Poisson distributed, this information is sufficient to calculate the parameters necessary to generate demand at the bases. Previous empirical studies conducted by the Air Force Logistics Management Center (AFLMC) have shown that a constant Poisson process (Poisson arrivals, constant transaction sizes) models the demand process at the base level adequately.

In order to estimate the proportion of demands that occur in the four priority groups, worldwide EOQ demand data from July 1987 was examined. This data, grouped into the categories delineated in the proposed rationing procedure, revealed the following priority codes distribution.

MICAP Demands	3%
Non-MICAP Priority 1-3 Demands	18%
Non-MICAP Priority 4-8 Demands	19%
Non-MICAP Priority 9-15 Demands	60%

This distribution was used for all items in the analysis.

To complete the item characteristics portion of the data base, transaction data were used to determine unit prices, supply management grouping codes (SMGCs), and mission essentiality codes (MIECs) for each item.

Analysts at AFLMC familiar with depot and base level operations

provided the inputs for estimating order and ship times. Both Base-Depot-Base and Depot-Vendor-Depot OSTs were assumed lognormal distributed, consistent with observations that the distributions should be skewed to the right. Table 1 gives the parameters used in the simulations for Base-Depot-Base leadtimes.

The parameters for Depot-Vendor-Depot OSTs are listed in Table 2. Means for the Depot-Vendor-Depot distributions are those cited by Hanks [3]; standard deviations were specified as one-half the mean values. In addition, leadtimes for Depot-Vendor-Depot variates were restricted in the simulations to be greater than or equal to one-half the mean OST and less than or equal to twice the mean OST. These restrictions were consistent with AFLMC analysts' knowledge of actual order and ship times.

To complete the parameterization, the following Air Force cost values were used in the simulations. The implied shortage factor (ISF) was set at \$70/unit/year and the holding cost fraction at 15%. The depot ordering cost was \$620 if the annual dollar usage for an item was less than \$25000; otherwise, the depot ordering cost was \$970. For purposes of computing EOQs at the base level, the inventory holding cost fraction was 15% and the cost to place an order was \$5.25.

Simulation Protocol and Performance Statistics

For each item, the simulation consisted of a 5-year initialization period, followed by a 50-year period in which statistics were collected. Note that the fixed simulation period for every item results in differing number of replenishment cycles at the depot for the items.

In order to evaluate the proposed rationing scheme, measurements at both the depot and base levels are necessary. At the base level, the following statistics were collected for use in assessing performance: units

Table 1

Parameters For Base-Depot-Base Order and Ship Times

Lognormal Distribution		
Order Type	Mean (Days)	Std. Dev. (Days)
EOQ	17	10
Priority (Rush)	10	7

Table 2

Parameter For Depot-Vendor-Depot Order And Ship Times

"Censored" Lognormal Distribution				
SMGC	Mean (Days)	Std. Dev. (Days)	Minimum (Days)	Maximum (Days)
T	323	162	162	646
P	449	225	225	900
M	559	280	280	1120

demand, units backordered, unit fill rate, backorder days (all priorities), time-weighted backorders (all priorities), and MICAP backorder days. At the depot level, the following statistics (undifferentiated by priority codes), were collected: units demanded, units backordered, aggregate fill rate, backorder days, and time-weighted backorders. In addition demands, backorders, and fill rates for each demand priority code category were accumulated. MICAP backorder days at the base level is a direct measure for evaluating the impact on mission capability. The remainder of the statistics, such as fill rates and backorder days for all priorities, are useful for assessing the overall effects of rationing on providing service for both non-MICAP and MICAP demands.

SIMULATION RESULTS AND CONCLUSIONS

To provide a base case for comparison, fifty years of activity for the population of items were simulated using the existing depot stockage policy, e.g. with the MICAP rationing procedure not in use. Then, with all other simulated conditions the same as the base case, fifty years of activity were simulated with the depot rationing scheme in effect. Performance statistics for individual items were aggregated to develop performance statistics for the population.

Table 3 reports the aggregate statistics for the four bases individually for the fifty years in which statistics were collected. Although there are variations from base to base, all performance measures are worse for the case when MICAP rationing was implemented. There were more backorders; fill rates were lower; backorder days and time-weighted backorders (all priorities) both increased; and most telling, MICAP backorder days increased dramatically.

Table 3.

Aggregate Statistics For The Four Bases

	Base Case		
	No MICAP Rationing	MICAP Rationing	
Aggregate Statistics for Base 1			
Units Demanded	508,344	508,272	
Units Backordered	23,406	46,934	
Unit Fill Rate	0.954	0.908	
Backorder Days (All Priorities)	829,016	1,241,225	
Time Weighted Backorders (All Priorities)	45.43	122.81	
MICAP Backorder Days	16,531	66,583	
Aggregate Statistics for Base 2			
Units Demanded	166,039	165,891	
Units Backordered	4,860	8,985	
Unit Fill Rate	0.971	0.946	
Backorder Days (All Priorities)	157,814	423,746	
Time Weighted Backorders (All Priorities)	8.65	23.22	
MICAP Backorder Days	2,537	8,272	
Aggregate Statistics for Base 3			
Units Demanded	1,555,790	1,555,949	
Units Backordered	119,602	208,991	
Unit Fill Rate	0.923	0.866	
Backorder Days (All Priorities)	5,273,586	10,457,212	
Time Weighted Backorders (All Priorities)	288.96	572.99	
MICAP Backorder Days	142,090	284,154	
Aggregate Statistics for Base 4			
Units Demanded	727,461	727,511	
Units Backordered	46,511	76,035	
Unit Fill Rate	0.936	0.895	
Backorder Days (All Priorities)	1,897,724	3,608,995	
Time Weighted Backorders (All Priorities)	103.99	197.75	
MICAP Backorder Days	83,756	111,845	

Table 4.

Annual Aggregate Statistics For The Four Bases As A Group

Aggregate Annual Statistics for the 4 Bases	Base Case	
	No MICAP Rationing	MICAP Rationing
Average Annual Demand	59,152	59,152
Average Annual Backorders	3,888	6,819
Aggregate Base Fill Rate	0.934	0.885
Aggregate Average Annual Backorder Days	163,160	334,622
Aggregate Time Weighted Backorders	447.01	916.77
Aggregate Average Annual MICAP Backorder Days	4,898	9,417

Table 5.

Aggregate Annual Statistics For The Depot

	Base Case		
	No MICAP Rationing	MICAP Rationing	
Aggregate Annual Statistics for the Depot			
Average Demand	59,174	59,152	
Average Backorders	4,100	6,560	
Fill Rate	0.931	0.889	
Average Backorder Days	68,792	52,962	
Time Weighted Backorders	1,872	2,935	
MICAP Analysis from the Perspective of the Depot			
Average Demand with MICAP Priority	121.96	231.16	
Average Backorders with MICAP Priority	55.68	9.60	
Fill Rate for MICAP Priority Demands	0.544	0.958	
Average Demand with Non-MICAP Priority 1-3	718.30	1,256.86	
Average Backorders with Non-MICAP Priority 1-3	376.65	45.00	
Fill Rate for Non-MICAP Priority 1-3 Demands	0.477	0.965	
Average Demand with Non-MICAP Priority 4-8	747.40	1,323.66	
Average Backorders with Non-MICAP Priority 4-8	397.85	402.29	
Fill Rate for Non-MICAP Priority 4-8 Demands	0.468	0.696	
Average Demand with Non-MICAP Priority 9-15	57,586.12	56,340.50	
Average Backorders with Non-MICAP Priority 9-15	3,269.60	6,103.10	
Fill Rate for Non-MICAP Priority 9-15 Demands	0.943	0.892	

The results are more parsimonious and somewhat easier to interpret if all four bases are grouped together and the results are annualized. Base level results organized in this fashion are presented in Table 4. Consider the following comparisons.

- o Average annual backorders increased by 75% (from 3888 to 6819) when MICAP rationing was implemented.
- o The aggregate fill rate at the bases declined by 4.9%.
- o Both average annual backorder days and time-weighted backorders (all priority codes) more than doubled.
- o Average annual MICAP backorder days--the most direct measure of shortages that affect mission capability--increased by 92% (from 4898 to 9417).

These measure provide clear and convincing evidence that the MICAP rationing scheme without lateral resupply does not work. The tradeoff implied in the design of the rationing scheme was that MICAP service would improve at the expense of low priority, non-essential demands. The simulation results show that not only would there not be any improvement in MICAPs, the MICAP rationing scheme would seriously degrade service for all priority codes at the bases.

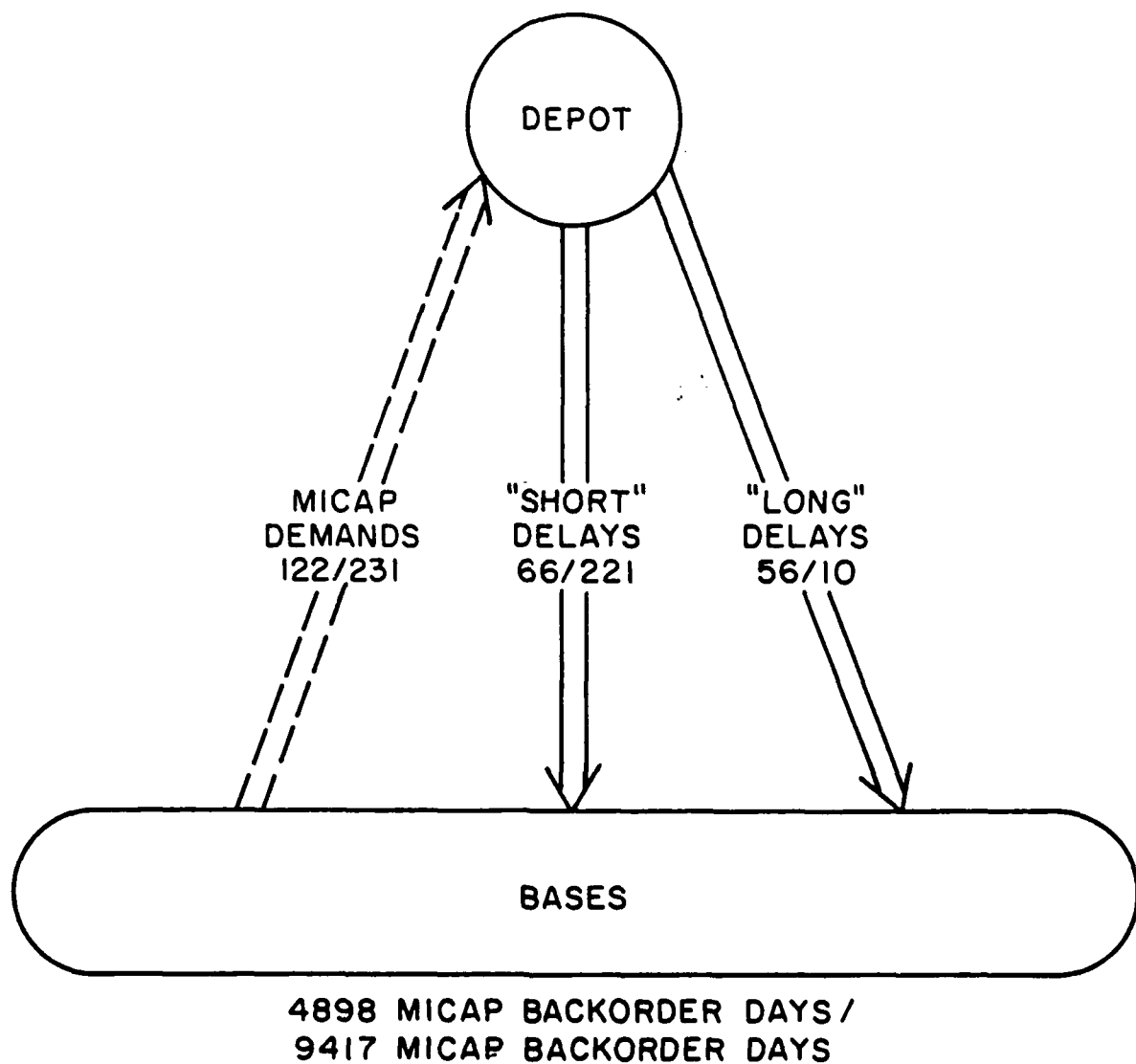
Insights into the reasons for the failure of the proposed MICAP rationing scheme are gained by examining the average annual depot performance measures in Table 5. To begin, we note that overall (all priority codes) performance at the depot declined. There were more backorders; the fill rate decreased; and time-weighted backorders increased. Given the nature of the rationing scheme, not all of these effects at the depot were unexpected.

However, if we look at what is happening by priority code category, the picture starts to come into focus. Basically, what happens is that the depot does not routinely fill base EOQ orders during the time periods when

rationing is in effect because EOQ orders are classified in the lowest priority category (non-MICAP priority 9-15). The consequence of this is that more MICAPs are generated at the base level because the bases stock out more often. To illustrate, the average annual demand with MICAP priority at the depot was 121.96 without the rationing procedure and was 231.16 with the rationing procedure (an 89.5% increase). Although the rationing procedure was successful at reducing the backordering of MICAP demands at the depot (from 55.68 per year to 9.60 per year), MICAP backorder days at the bases nevertheless dramatically increased.

Figure 2 depicts the situation for MICAP demands. A rush order to the depot is generated by a base for a MICAP demand if the item is out of stock at the base. A "short" delay in filling the demand at the base occurs when the depot is able to fill a MICAP priority demand from stock. Thus, the delay is the priority (rush) order and ship time. On the other hand, a "long" delay occurs when the depot is unable to fill a MICAP priority demand because the depot is stocked out. In this case, the MICAP priority demand is backordered at the depot until the depot is replenished; the depot priority ships to the base as soon as it has been replenished. As Figure 2 illustrates, there were fewer "long" MICAP backorders with the rationing scheme, but a lot more "short" backorders delays at the bases. Without the performance statistics at the bases, it would have been very easy to interpret the depot performance statistics as evidence that the rationing procedure was working as anticipated.

In summary, the proposed MICAP rationing is counter-productive and should not be implemented. An ancillary to the MICAP rationing scheme is a proposal for lateral resupply between the bases. There is reason to believe that this idea has merit, and an analysis is in progress to evaluate lateral



Legend

XXX/YYY - No MICAP Rationing / MICAP Rationing

Figure 2. Delays for MICAP demands

resupply. However, the consequences of the basic rationing scheme are so negative, it is unlikely that lateral resupply would reverse the recommendation against implementation of rationing¹.

¹Support for this research was provided by the United States Air Force Office of Scientific Research under grant number F49620-85-C-0013. The views and conclusions expressed are those of the author and should not necessarily be taken as those of the United States Air Force.

REFERENCES

- [1] Department of Defense, "Procurement Cycles and Safety Levels of Supply for Secondary Items," DOB Instruction 4140.39, Washington, D.C.: Department of Defense, July 1970.
- [2] Frazza, S. and Kaplan, A.J., "Decentralized Stockage Policies in a Multiechelon Environment," Naval Research Logistics Quarterly, 33 (1986), pp. 179-189.
- [3] Hanks, C.H., The Influence of Systems Support Division Funding and Safety Levels on Aircraft Availability, Final Report, HQ USAF/LEXY, Logisitcs Management Institute, Bethesda, Maryland, October 1985.
- [4] Headquarters, Air Force Logistics Command, "Requirements Procedures for Economic Order Quantity Items," (EOQ Buy Budget Computation System - D062), AFLC Regulation 57-6, Wright-Patterson Air Force Base, Ohio: Headquarters, Air Force Logistics Command, 22 August 1984.
- [5] Headquarters, Air Force Logistics Command, "MICAP Allocation," DAR NO: LOG-LOL-D78-124-B, Wright-Patterson Air Force Base, Ohio: Headquarters, Air Force Logistics Command, 15 March 1984.
- [6] Muckstadt, J., "A Model for a Multi-Item, Multi-Echelon, Multi-Identure Inventory System," Management Science, 20 (1973), pp. 472-481.
- [7] Muckstadt, J., "Some Approximations in Multi-Item, Multi-Echelon Inventory Systems for Recoverable Items," Naval Research Logistics Quarterly, 25 (1978), pp. 377-394.
- [8] Muckstadt, J., "A Three-Echelon, Multi-Item Models for Recoverable Items," Naval Research Logistics Quarterly, 26 (1979), pp. 199-221.
- [9] Presutti, V.J. and Trepp, R.C., "More Ado About Economic Order Quantity (EOQ)," Naval Research Logistics Quarterly, June 1970, pp. 243-251.
- [10] Sheerbrooke, C.C., "METRIC: A Multi-Echelon Technique for Recoverable Item Control," Operations Reserach, 16 (1986), pp. 122-141.

- [11] Sheerbrooke, C.C., "Improved Approximations for Multi-Identure, Multi-Echelon Availability Models." Logistics Management Institute, Washington, D.C., February 19, 1985.
- [12] Sheerbrooke, C.C., "VARI-METRIC: A Multi-Identure, Multi-Echelon Inventory Model with EOQ Items." Sheerbrooke & Associates, Potomac, Maryland, June 12, 1985.

1987 USAF-UES RESEARCH INITIATION PROGRAM

Sponsored by the

AIR FORCE OFFICE OF SCIENTIFIC RESEARCH

Conducted by the

Universal Energy Systems, Inc.

Final Report

COMPUTER MODELING OF INFRARED SIGNATURES

Prepared by:	Sally A. Sage
Academic Rank:	Assistant Professor
Department and University:	Department of Applied Computer Science Southern College of Technology
Research Sponsor:	Air Force Armament Laboratory, Eglin AFB Division: AS Branch: Advanced Guidance, Air to Air
USAF Research Contact:	Dr. Steve Butler
Date:	December 15, 1987
Contract No:	F49620-85-C-0013/SB5851-0360
Purchase Order No:	S-760-6MG-017

COMPUTER MODELING OF INFRARED SIGNATURES

by

Sally A. Sage

ABSTRACT

This report describes a computer model of infrared radiation (IR) signatures for aircraft. The goal of the system is to use a data file describing an air target to produce a computer-generated IR image that corresponds closely to an actual IR photograph of that target. The IR image provides information which can be used to calculate the IR signature of the target. The aircraft is modeled by a set of three-dimensional triangular facets which covers its outer surface. The aircraft's plume is also based on a facet model, but the plume is generated interactively so that a user can control the details of the plume's construction. The three-dimensional coordinates of the target and plume are rotated using user-specified sensor angles. The coordinates are then projected into the YZ plane to produce a two-dimensional image. The image is composed of facets in the sensor's line-of-sight. These facets are assigned temperatures and the area of each set of facets which corresponds to a particular temperature is calculated. The IR target signature can then be computed by the integration of the radiance over the projected area of the target along the line-of-sight of the sensor.

Acknowledgments

I would like to express my appreciation to the Air Force Systems Command, the Air Force Office of Scientific Research, and the Air Force Armament Laboratory, Eglin AFB for the opportunity to work in the Research Initiation Program. I am especially grateful to Dr. Steve Butler and Captain Lawrence Jones for giving me the opportunity and the guidance necessary for my research. I am also grateful to John Morgan and Stephanie Linz for their valuable contributions to the project.

I. Introduction

An important concern presently facing the aerospace industry is the design of aircraft which can avoid detection. Considerable effort has been directed to radar and visible signatures, but accurate models of infrared radiation (IR) signatures are still needed to provide a detailed analysis to aid designers in minimizing IR emissions. This research effort was conducted for two summers at Eglin AFB Armament Laboratory (1985 and 1986) and was continued this past summer at Southern College of Technology in Marietta, Georgia. The work has focused on the development of a computer model for aircraft IR signatures.

The goal of the IR modeling system is to use a data file describing an air target to produce a computer-generated IR image which corresponds closely to an actual IR photograph of that target. The computer-generated IR image provides information which can be used by the system to calculate the IR signature of the target. The target is modeled by a set of three-dimensional triangular facets which covers the outer surface of the target. The target's plume is also based on a facet model, but the plume is generated interactively so the user can control the details of the plume's construction. The three-dimensional facets of the target and plume are rotated with user-specified sensor angles (azimuth and elevation). The facet coordinates are then projected into the YZ plane to produce a two-dimensional image. The facets are sorted from "back to front" with respect to the sensor; thus, the final image is composed of facets in the sensor's line-of-sight. The viewable facets are assigned

temperatures and the area of each set of facets which corresponds to a particular temperature is calculated. The IR target signature can then be computed by the integration of the radiance over the projected area of the target along the line-of-sight of the sensor.

II. Objectives of the Research Effort

The most significant IR emission of an aircraft is the plume, which is formed behind the aircraft by the hot exhaust of the engines. Thus, a considerable amount of effort has been devoted to improving the plume model. During the summer of 1986 the system was integrated into a complete, interactive package with menu options that included the ability to assign temperatures to facets as well as the ability to generate a plume interactively. The goals for this research effort included the following objectives:

- (1) The most important, time-consuming problem with the system concerns the hidden-line algorithm used to sort the facets from back to front. The current algorithm is not sufficiently accurate and occasionally sorts facets incorrectly. It appears that a more sophisticated algorithm, based on the concepts of partial ordering and topological sorting, could be implemented.
- (2) The current routines used to assign temperatures to components are sufficient, but could be improved.
- (3) Additional shape choices, such as ovals, squares and rectangles should be added to the plume creation menu.
- (4) The ability of the user to edit the plume interactively should be improved:
 - (a) use former values as default values
 - (b) allow the user to specify individual offsets of each sub-component, including the front and back of a single, three-dimensional sub-component.
- (5) Other interactive aspects of the system could also be improved:

- (a) use default file names
- (b) allow new data files to be read during program execution

III. Overview of the Target Modeling System

The input is stored externally in four files: the target data file, the target temperature file, the plume data file, and the plume temperature file. The original data files contained a list of facets and coordinates, but no information that related a particular facet to a target component (i.e. wing, nose, engine, etc.). This component information is available through other sources and has been added to the data files. In general, the component ID codes are used to determine the corresponding surface temperatures. Each entry in the temperature file corresponds to a facet number in the data file. Thus, the facets are conveniently assigned temperatures, and the temperatures are accessible for later calculations.

The major data structures of the IR system include several arrays:

ICOMP -- A list of component identification codes and the corresponding facet indices which point into LLIST. The facet indices indicate the group of facets which correspond to each component.

LLIST -- A list of triangular facets describing the target. Each column corresponds to the three vertices of a facet and contains indices into array PNT. Note: a group of sequential columns describe a particular component.

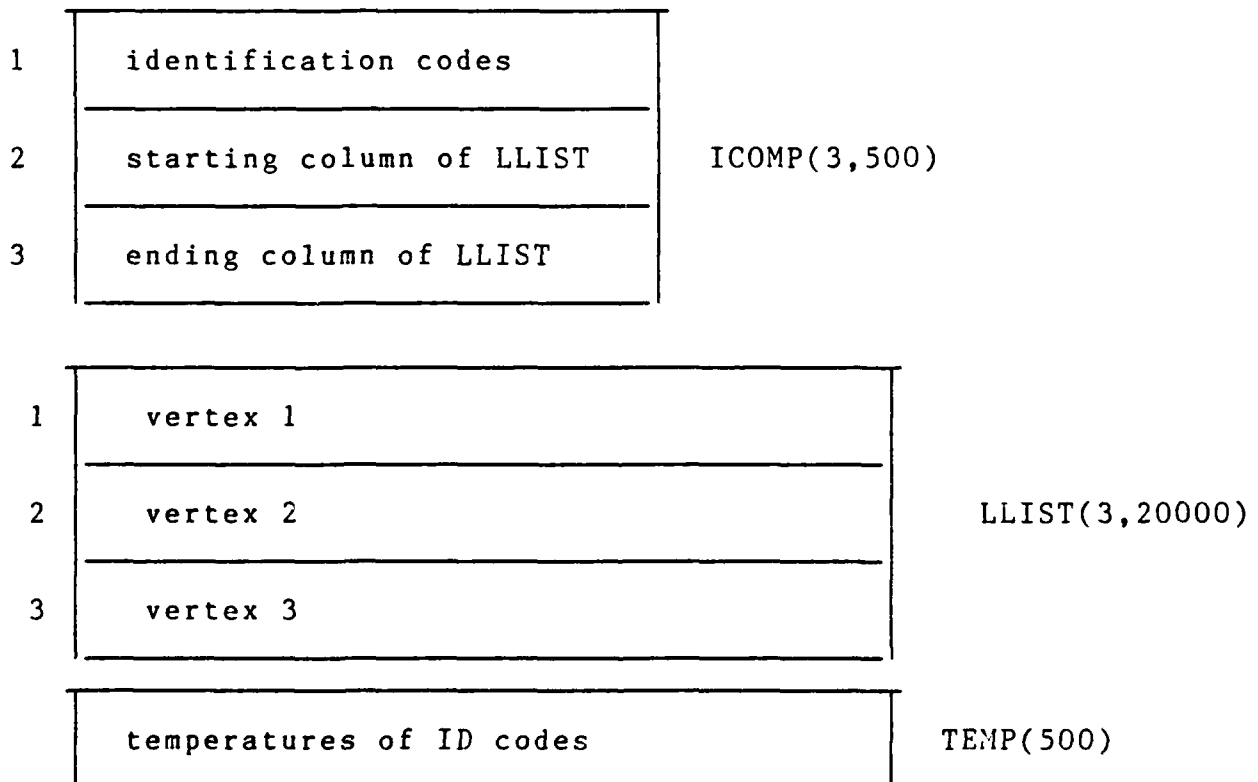
TEMP -- A list of temperatures. TEMP is parallel to LLIST; each facet number of LLIST has a corresponding temperature in TEMP(i).

PNT -- A list of three-dimensional coordinates. Each column contains the X,Y,Z coordinates of a facet vertex.

AREA -- A list of the areas corresponding to temperatures. The subscript corresponds to the temperature and the contents correspond to the calculated area.

FDIS -- A three-dimensional array that contains the generated image. Dimensions one and two correspond to the YZ plane. Dimension three corresponds to the transparent layers of the plume.

Figure 1 show a diagram of the arrays into which the input data is read. The arrays contain both the target data and the plume data, but these data sets are kept separate (the target data is stored first, followed by the plume data). The data sets are stored externally in four files: the target data file, the target temperature file, the plume data file, and the plume temperature file. By convention, each data file has the extension ".TRG" and each temperature file has the same name as its corresponding data file but uses ".TMP" as a file extension.



1	X coordinate	PNT(3,10000)
2	Y coordinate	
3	Z coordinate	

Figure 1. Data structures corresponding to data files

The plume was originally implemented as a single cone-like shape which was constructed geometrically by a sequence of circles and cones. The IR model, however, requires a plume model which is more sophisticated. A more accurate plume model consists of concentric layers of varying shapes; this corresponds more closely to the gaseous properties of the exhaust. The inner plume layers have hotter temperatures, while the outer layers have cooler temperatures. Thus, the plume facets require an implementation which can simulate a "transparent" property. The image generated by the original IR system displays only those facets in the direct line-of-sight of the sensor. In other words, only the outermost layer of the plume is visible; covered facets are not visible. These visible facets have cooler temperatures and do not contribute much to the plume signature. The hotter facets, which are hidden, make a significant contribution to the signature. To keep a record of the hidden layers of the plume, the display image array (FDIS) has been changed from a two-dimensional array to a three-dimensional array. As the plume is generated from back to front, the visible facets which are about to be covered, are saved. Later, when the IR signature is calculated, these transparent layers can be used

to calculate areas which contribute to the overall radiance.

The plume is composed of composite shapes referred to as components. Each component consists of a group of sub-components which can be two-dimensional or three-dimensional. The two-dimensional shapes are used to cover the ends of the three-dimensional shapes to produce a solid three-dimensional model. The identification codes for the plume components range from 6000 to 6999. Each component is assigned to a unique 100's group and individual sub-components are numbered sequentially within their 100's group. For example, suppose a plume is composed of an inner plume and an outer plume. The inner plume is assigned the component group 6000 and the outer plume is assigned the component group 6100. Further, if the inner plume is constructed from two disks and one cone, then inner plume will have three sub-components: 6000, 6001, and 6002.

The components of the plume consist of shapes which are generated geometrically. Originally, the only shapes available were a circle (two-dimensional) and a cone (three-dimensional with circular front and back). Additional two-dimensional shapes have been added, including ovals, squares, and rectangles. These two-dimensional shapes are also available in any combination to construct three-dimensional shapes. For example, it is possible to have a three-dimensional shape that has a square front and oval back. The plume generation routines make extensive use of a menu system so that plumes can be created and edited in an interactive environment. The routines include features such as adding, deleting and changing the sub-components. The X, Y, Z

coordinates of the sub-components are generated geometrically. To manipulate a two-dimensional shape the user must know the X coordinate of the shape and the radii (horizontal and vertical). To manipulate a three-dimensional shape, the user must know the starting X coordinate, the starting radii, the ending X coordinate and the ending radii.

The X, Y, Z coordinates of the plume are projected into the YZ plane to create a display image. Thus, the X coordinate is used for front to back positioning, while the Y and Z coordinates are related to the radii of the shape. The points generated to describe the shapes are centered around the Y and Z axes unless otherwise specified. If the user wishes to shift either the Y or Z coordinates, it is possible to enter the Y and Z offsets for individual components.

Further, the entire plume may be shifted along either the X, Y, or Z axis. This feature is currently used to attach the plume to the target. The plume can be generated generically to fit several aircraft. By convention, the front X coordinate of the plume is zero and the X coordinates range from zero to some negative value. In most of the aircraft data files, the nose of the aircraft also has an X coordinate equal to zero and the tail is positioned at some negative value. When the generic plume is attached to a particular aircraft, it must be shifted so that it is positioned behind the engine.

IV. The Hidden Surface Algorithm

In general, the hidden-surface problem can be defined in the following way: the pixels that compose an image should be

arranged so that any pixel displayed belongs to a surface that is in the direct line-of-sight of the viewer. To accomplish this, the facets which are projected onto the YZ plane must be compared to each other to determine which ones can be seen. The previous hidden line algorithm used a depth-sort algorithm to seed each facet with a single point. The seed points were then sorted into a order of increasing distance from the sensor. This method is not very satisfactory because it gives incorrect displays due to a wide variety of facet sizes.

The new hidden surface method compares each facet with every other facet to determine whether the facets overlap on the view plane. If the facets do overlap then it is determined which facet lies in front and which behind. This information for all comparisons of pairs of facets in the scene is used to set up a network. If facet I is in front of facet J then an edge is added to the network leading from node J to node I. Once the network has been constructed, a routine executes a topological sort on this network to output the facets in order from back to front.

Further details of the algorithm can be found in [Angell].

V. Conclusions and Recommendations

The goals of the project were reached. Many small features have been added to the system to improve the "user-friendliness" of the system. The new hidden surface algorithm is more accurate than the previous algorithm.

The IR system has the potential to become an important part of IR signature analysis. As this project continues to develop successfully, more and more features are desired. Future

research efforts should include the following recommendations:

(1) A routine should be added to automatically scan the target data and determine the X,Y,Z offsets required to attach the plume behind the engine.

(2) Additional geometric shapes may be useful in the plume construction.

(3) A version of the system that runs in batch mode would be useful for processing several viewing aspects during a single execution phase.

(4) Additional parameters which can affect the IR sensor, such as speed and atmospheric conditions, should be added to the system.

Bibliography

Angell, I. and G. Griffith [1987]. High Resolution Graphics
Using FORTRAN 77, Halsted Press, Great Britain.

FINAL REPORT NUMBER 70
RECEIVED A NO-COST TIME EXTENSION
TO BE SUBMITTED IN 1987 MINI-GRANT FINAL REPORT
Dr. Mo Samimy
760-6MG-059

1986-87 USAF-UES MINI GRANT PROGRAM

Sponsored by the
AIR FORCE OFFICE OF SCIENTIFIC RESEARCH
Conducted by the
Universal Energy Systems, Inc.

FINAL REPORT
An Intentional Tutor

Principal Investigator:	Richard M. Schori
PI Academic Rank:	Professor
PI SSN:	334-30-5333
PI Telephone No.:	(503) 754-4686
PI Department:	Mathematics
Co-Investigator:	Edward M. Gellenbeck
Academic Rank:	Ph.D. Candidate
Department:	Computer Science
University:	Oregon State University Corvallis, Oregon 97331
Sponsoring Laboratory:	USAFSAM, Brooks Air Force Base San Antonio, Texas
Focal Point:	Dr. Bryce Hartman
Total Effort:	\$25,893
Dates:	12/15/86-12/15/87
Date:	December 15, 1987
Contract Number:	F49620-85-C-0013/SB5851-0360

PROJECT ABSTRACT

AN INTENTIONAL TUTOR

by

Richard M. Schori and Edward M. Gellenbeck

The Air Force is interested in the development of a tutor to assist in the ground-based training of tactical fighter pilots. Such a training device would have applications in any educational environment. In this paper we concentrate on the high-level design of a tutoring system for implementation on a microcomputer. This system or "shell" should consist of software and procedures for inserting any subject material into the system and result in an effective tutor on that subject. With that goal, we review hypertext and hypermedia and information presentation techniques, and incorporate these concepts into our notion of a "graph of content", which is a graphical method of relating concepts. We review various teaching strategies as they are related to computerized tutors and concentrate on the four learning styles described by Kolb. We discuss how this theory can be implemented by presenting each concept in the context of each of the four learning styles. We report on our development of an expert system for determining the favored learning style of a student. We discuss the theory that very large software systems need to evolve from smaller systems and relate that theory to the Intentional Tutor project. Finally, we give a high-level design for a tutoring system which we believe could evolve into an Intentional Tutor.

ACKNOWLEDGMENTS

We thank the Air Force Systems Command and the Air Force Office of Scientific Research for sponsoring this research. We give special thanks to Dr. Bryce Hartman of the School of Aerospace Medicine, Brooks Air Force Base, Texas, for originally introducing us to the Intentional Tutor project. We also thank Southwest Research Institute for hosting us during the summer and in particular we thank Glenn Humphress for his congenial, imaginative, and tireless input into the Intentional Tutor project. We also thank the Department of Mathematics at Oregon State University for cost sharing on this project.

I. INTRODUCTION

In this introduction we include background information, objectives, and a statement on the scope of our effort.

A. BACKGROUND INFORMATION

Dr. Bryce Hartman of the USAF School of Aerospace Medicine in San Antonio, Texas is interested in developing computer-based training facilities for fighter pilots. Together with the Human Performance Engineering Department at Southwest Research Institute and several small research and development companies in San Antonio, Texas, he has been working on what is called an Intentional Tutor. This project is to develop a training device that could be deployed with tactical fighter squadrons and used by pilots for ground-based training in tactics, aircraft systems, etc. Such a training device would have applications in any teaching environment.

One of the most important components of this training facility is a human-computer interface that is able to establish a relationship with the trainee that is intentional in a compelling way, as well as being interactive and adaptive. Dr. Hartman recruited Professor Richard M. Schori to work on the Intentional Tutor through the Air Force Summer Faculty Research Program.

Richard M. Schori received his Ph.D. in mathematics from the University of Iowa in 1964 and has actively published in topology since that time. One of his specialties is infinite-dimensional topology and through this he has gained considerable experience in abstract geometric thinking and reasoning. On the other hand he has had a considerable

practical experience in applied research, administration, teaching and pedagogy, athletics and coaching, psychology, and computers. He had his own research projects for four summers during college in a research department at Bell and Howell Company, he has held full time academic positions at major universities continually since his Ph.D., was promoted to (full) professor in 1973, and during the five year period 1978-83 he was Chairman of the Department of Mathematics at Oregon State University. He has had an interest in the various psychological and learning types of people and the corresponding pedagogical implications. He has been using microcomputers extensively for the past five years and owns two of them. He is interested in the topics of artificial intelligence (AI) and neural networks, and attended graduate level courses in AI during the academic year 1986-87.

The Intentional Tutor project is ambitious, long term, and highly interdisciplinary. Dr. Schori's versatile background, which includes working well with other people, was a deciding factor for being recruited to work on this project. Additionally, the existing research group is predominantly from the areas of psychology and biology and whereas he can productively interact with them, he can also provide a bridge from them to the mathematical modeling, computer science, and AI communities.

In the fall of 1986, prior to but anticipating the Mini Grant, Dr. Schori advertized for and then ran a graduate student seminar entitled "Intelligent Tutors". Six students attended including Edward Gellenbeck. The material covered was an introduction to the Intentional Tutor Project in San Antonio as well as the research area in artificial intelligence known as "intelligent tutors". Mr. Gellenbeck showed great interest and insight into these subjects and

when the Mini Grant was awarded he was successfully recruited to work with Dr. Schori. Since that time Dr. Schori and Mr. Gellenbeck have worked as co-investigators on the project.

Edward M. Gellenbeck is a Ph.D. student in Computer Science at Oregon State University. He has a strong background in system level programming which he gained through formal education (M.S. in computer science from California State University, Chico 1986) and professional work (system programmer, IBM 1984). His doctoral concentration at Oregon State University is artificial intelligence and he also is very interested in cognitive science.

B. OBJECTIVES OF THIS GRANT

The objectives for this grant were to accomplish as many aspects of the following three items as possible:

1. Continue the work started by Dr. Schori under the Summer Faculty Research Program (1986) on the Intentional Tutor project with particular emphasis on the "graph of content" idea. Included in this would be the recruitment of an graduate student in artificial intelligence from the Department of Computer Science at Oregon State University.
2. Investigate the various software tools for the efficient presentation of information on a computer and investigate the various pedagogical theories as they relate to a tutoring system based on a microcomputer.
3. Make a selection of information presentation techniques and teaching strategies and incorporate them into a high-level design of a tutor in the environment of a microcomputer.

C. SCOPE OF THE EFFORT

We decided to concentrate our efforts on a high level design of a tutor that could be implemented on a microcomputer with today's software technology. This represented a significant scaling-down of the concept and direction of the Intentional Tutor Project being carried out in San Antonio. Our decision was based on the fact that we had limited resources, coordination with the project in San Antonio would be difficult since we were working in Oregon, and our belief that tutors need to be available on machines that are readily accessible.

II. OVERVIEW.

This short overview contains our major conclusions, a summary of our grant related activities, and a brief description of the content of this report.

A. MAJOR CONCLUSIONS

We start this report by giving our three main conclusions.

1. Information presentation is both a strength and weakness of computer-based tutoring. A strength is that hypertext methods allow for efficient and versatile access to large amounts of material. A weakness is that it is preferable to read large amounts of information from a printed page than from a computer screen.

2. Building an Intelligent Teaching System (ITS) is hard, still very much of a research area. We recommend that a scaled down version be designed and built for a microcomputer. We believe that large, complicated systems need to evolve from smaller systems.

3. We believe that each person, in a formal learning environment, has a preferred learning style. This preferred learning style can be identified and effectively used by a computer-based tutor.

B. GRANT RELATED ACTIVITIES

Our research direction was a consequence of our background and the following grant related activities. (1) We ran an "Intelligent Tutors" seminar during which the second author was recruited for this project. (2) We purchased a PC and some relevant software to gain hands-on experience in understanding and developing ideas and software for the project. (3) We attended the Annual Meeting of the AAAI during July 13-17, 1987, in Seattle. (4) The second author did a major study of and wrote a report to the Air Force on "Human-computer Interfaces." (5) We read a great deal on the topic and consulted with many people.

C. REPORT ORGANIZATION

This report contains three main sections which represent the focus of our research.

Section III is on our idea of a graph of content and how it relates to and naturally ties in with the notions of

hypertext and hypermedia that are currently very much in the news.

Section IV reports on our study of pedagogical theories and how they are relevant to a tutor. We concentrate on learning styles and on our development of an expert system for diagnosing the favored learning style of a student.

Section V contains a high-level design of what we call an Evolving Tutor. It is a scaled down version of an Intentional Tutor but it provides the architecture for a tutor based on current software implemented on a microcomputer that can evolve into an Intentional Tutor.

Section VI contains our recommendations for further work on the Intentional Tutor project.

III. "GRAPH OF CONTENT" FOR INFORMATION PRESENTATION

This is a long section that discusses the concept of graph of content and the associated ideas of hypertext and hypermedia that are currently very much in the news. We discuss existing hypertext software, implementations of hypertext, and uses of the graph of content in a computer-based tutoring environment.

The term "graph of content" was coined in Schori (1986). Many of the ideas were motivated by Goldstein (1982) and his notion of a "genetic graph". Conceptually it is a graphical method of illustrating how concepts are related as well as a computerized method for quickly jumping to an actual presentation of that material. The nodes or vertices of the graph represent ideas, concepts, or topics on which the subject will be tutored. The links or edges between the nodes repre-

sent relationships between the nodes such as prerequisite, generalization, special case, or analogy.

In displaying a graph of content, generally on a computer screen, we represent a node as an ellipse or rectangle with a word or two inside indicating the concept, idea, or topic. The links are represented by arcs between the ellipses. We may place an arrow on an arc if the corresponding link is a directional relationship such as prerequisite. When the nodes are activated with the click of a mouse, more details appear. There are two possibilities. Either 1) a description of the concept appears, or 2) another graph of content appears, at a lower hierarchical level, which gives more details of the given concept. In the latter case, the resulting nodes may be activated with the same results. Eventually, however, the process will result in a presentation of information.

The graph of content takes the place of a table of contents as normally seen in a book. The advantage of presenting material utilizing a graph of content is that the interconnection of topics or concepts is much clearer than with a normal listing of topics in a table of contents.

In January, 1987, when we started this project, we had not heard of hypertext and were on our way to reinventing it. A graph of content, as discussed above, contains active nodes. We had started programming a prototype version of our system in Smalltalk/V when we read about Guide (1986) developed by Owl International for a Macintosh computer. We were personally committed to MS-DOS based machines and purchased one of the first copies of Guide (1987) for IBM compatibles. This version was released in June, 1987, and runs under Microsoft Windows.

A. HYPERTEXT AND HYPERMEDIA

Hypertext has been called "nonsequential writing" by Ted Nelson, the man who coined the term in 1965. It is an associative, electronic presentation of information. Instead of the linear way that information is presented in a book, hypertext connotes a nonlinear body of information with "links" between documents that guide readers from one to another. It is not a traditional data base with a hierarchical structure. Rather, it allows you to organize text, pictures, and sound by association--by context, the way the human mind does. Hypermedia is the logical extension of hypertext, encompassing graphics, animation, video, sound, and so on.

As a data retrieval method, the concept of hypertext was first discussed in "As We May Think," a prophetic July, 1945 Atlantic Monthly article by Vannevar Bush. Bush was Franklin D. Roosevelt's science adviser and held many distinguished positions. He had several inventions in the 1930s that foreshadowed the electronic computers developed after World War II. One was the Rapid Selector, a device using a code and microfilm to facilitate information retrieval.

Bush became acutely aware of the problems associated with the growing mountain of research data, in particular the data generated by the Manhattan Project. As Bush saw it, storage and retrieval problems stemmed from the fact that documents are filed alphabetically by page number in a rigidly structured hierarchy of classes and subclasses modeled after library systems. Such a filing structure breaks down if you have to locate something within a particular document. Bush imagined a text storage system in which the documents and their content were indexed by association--the way we think.

Each time a new document was stored, logical links would be forged that would connect it to other documents already in storage.

To illustrate these links, imagine an introduction to a scientific article which contains several technical terms. These terms are highlighted on the computer screen as an indication that there are links to further information concerning the terms. A pointing device such as a mouse can be used to activate a highlighted term. Activation opens another window which defines the technical term and in that explanation there may be other highlighted terms which may be activated and so on. This leaves the reader with the option of going deeper into the technicalities of the paper or off on side trips by picking topics at will for further exploration.

1. Software for Creating Hypertext

We were already acquainted with Guide by Owl International. While attending the AAAI meeting in Seattle, July, 1987, we saw demonstrations of Notecards from Xerox and KnowledgePro (1987) by Knowledge Garden. In August, 1987, Apple Company announced their product Hypercard. We will briefly describe these commercial products for creating hypertext documents.

a. Guide by Owl International.

Guide was the first hypertext product for microcomputers. The product was initially introduced for the Macintosh in September, 1986, with a nearly identical version for MS-DOS based machines in June, 1987. As you type a document into a Guide file, you can highlight a word or phrase or a

portion of a graph and create a "button". Subsequently, when activated by a mouse, the button is replaced by passages of text, graphics, or more buttons. These buttons are the links that connect associated ideas and which enable the user to bypass pages of irrelevant material in the typical printed page metaphor. These replacements may be separate files, or other parts of the same Guide file you are creating, or another Guide file that has already been created.

We found two limitations to Guide, Version 1.00, for IBM compatibles. First, we could not utilize specialized technical word processors that were not supported under Microsoft Windows. This prevented us from developing a prototype tutor in calculus using Guide as a shell. The other limitation is that we could not from within Guide access other programs. For example, we would want to have interactive subprograms for testing students. We understand that Version 2.00 of Guide will have the capacity to control applications. (As of early December, 1987, this version has not been released.) However, in the PC product, this capability is limited to those programs running under Microsoft Windows.

b. KnowledgePro by Knowledge Garden.

This is a product that is not as well known as Guide or Hypercard but which has considerable capabilities. It combines hypertext with rule-based and frame-based expert system shells and direct procedural control that includes access to external files. We have a demo of KnowledgePro and feel that it is potentially a powerful tool for creating educational/tutoring software. As was the case with Guide, this product is unable to utilize a technical word processor

with the capacity to handle mathematical symbols. This would prevent us from creating a prototype calculus tutor.

c. HyperCard by Apple Company.

This is the product that came out in August, 1987, with a great deal of media coverage and descriptions with many superlatives. It has the hypertext features of being able to organize information by association instead of only a strict hierarchical manner as in traditional data base technology. HyperCard uses the concept of a card which is restricted to the size of your screen. One, in effect, create stacks of cards containing different types of data and you create links between these stacks so that related information can be quickly accessed. It also can access other programs and other media such as automatic telephone dialing.

d. Notecards by Xerox.

Xerox's Notecards is the oldest of these products. It is not designed for micros but is implemented on UNIX-based Xerox LISP machines. It is very powerful hypertext-based software package implemented in LISP. We saw a demonstration of Notecards and felt that the screen seemed too cluttered with its assortment of features.

2. Implementations of Hypertext

In the previous section we discussed hypertext authoring tools. Here we talk about hypertext/hypermedia systems that are already implemented or are in the process thereof. An example is the Grolier Electronic Encyclopedia which comes with built-in data and links. It is an example of static

hypertext, that is, hypertext where the text and links are set and cannot be changed.

We will describe two hypertext systems that are being implemented at universities. We believe that even though they may represent state of the art methods of presenting information, we do not believe they have sound pedagogical principles built into their systems. We have a recent verbal from an employee at Owl International that the Veterinary School at the University of Mississippi is doing an excellent job of building a hypermedia system.

a. Intermedia at Brown University

Brown University is developing and using a large scale, object-oriented hypertext/hypermedia system (Byte, Feb. 1987). They use the Sun workstation and IBM RT PC for hardware. Their software is Macintosh-like having been especially built on top of CadMac and MacApp that had been ported to the RT PC. Intermedia currently uses text and 2-D and 3-D graphics. They plan to add sound and video and access to CD-ROM data. Documents are stored and then instructors or users mark blocks within a document that serve as anchor points. Then links are created from point to point to form webs. The webs do not become part of the document but are stored separately. Several webs may overlies one set of material. Thus, users following one set of links through a body of information need not see the links other people are using.

b. Cornell University Medical College

Cornell University Medical College has chosen a hypertext network as a solution to the problem of information overload. They are using a network of Mac IIs with WORM video disk players and Guide software. Currently, the entire

second-year curriculum is on line and they are working to put the first year on the network as well.

B. MORE ON THE GRAPH OF CONTENT

In this section we discuss the pedagogical advantages of the graph of content, report on our development of what we call a "generic graph of content" for information presentation, and discuss potential uses of a graph of content in a computerized tutor.

1. Pedagogical Advantages of Graph of Content

There is evidence that people can better remember ideas, facts, and concepts if they can graphically see how these ideas are related to each other. Anderson (1985 p. 183-186) claims that subjects' memories can be significantly improved when material is presented in the form of a hierarchical tree as compared to a random presentation. He also claims that studies have shown that the benefits can be obtained with a tree organization involving a loose associative structure. An explanation he claims for the improvement when the information is presented in an organized way is that the subjects form a memory network during the study phase similar to the tree structures they were studying. This has a similarity to the ideas of Grossberg (1982 p. 296) who claims that work on associative learning shows that long term memory is effected by spatial patterns.

2. A Generic Graph of Content for Information Presentation

By a generic graph of content we mean software and a procedure whereby tutoring software can be created without the aid of an expert programmer, by selecting a subject, like calculus, an F-16 hydraulics manual, or mountaineering, and tapping the knowledge of a few experts in the field. Our idea is to emphasize the presentation of the material in an attractive, pedagogically sound, convenient to use package that could be utilized as a study aid for someone taking a conventional lecture course on the subject. We feel this would be a useful contribution to the development of an intentional tutor. Our approach was to take a subject we knew, like calculus, and build a graph of content for it and see if some general patterns or concepts emerged. We hoped this would allow us to then strip away the specific content of the calculus and have an underlying structure that would be a generic graph of content.

When the first author was teaching calculus (Math 305, Sequences and Series) in the Winter Term of 1986 at Oregon State University, he constructed on paper a graph of content of the course. The active nodes that would be in a computerized version were left to the imagination. Even though the graph contained only the main topic headings such as "sequences" and "series" and subtopics such as "definition" and "examples", the graph, with all of its interconnections, became quite large with something on the order of 40 nodes. This seemed impractical for one computer screen and modified examples were investigated.

The result was a graph which has, at the first stage, just three nodes standing for concept, prerequisites, and

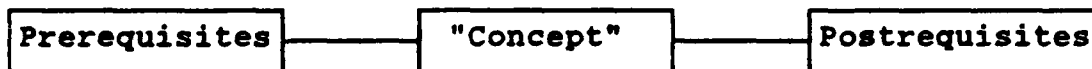


Fig. 1

postrequisites (see Fig. 1). In the figure, "concept" is in quotes since in its place would be an actual concept, like "derivative" from the calculus. All of these boxes will be active. If either "Prerequisites" or "Postrequisites" is activated, then a menu of terms appears right below the activated box. See Fig. 2 which illustrates the case when "Prerequisites" was activated for the concept "derivative". The items, like "limit", in this menu are active. If "limit"

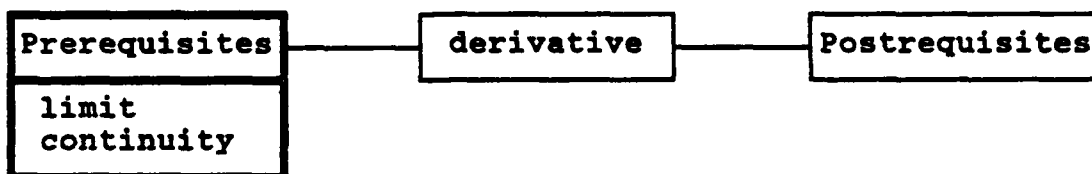


Fig. 2

is activated, then another graph of the form of Fig. 1 appears with "limit" in the middle box. If "Postrequisites" of that graph is activated, then Fig. 3 appears. Note that derivative is a postrequisite of limit, maintaining the relationship that was established if Fig. 2.

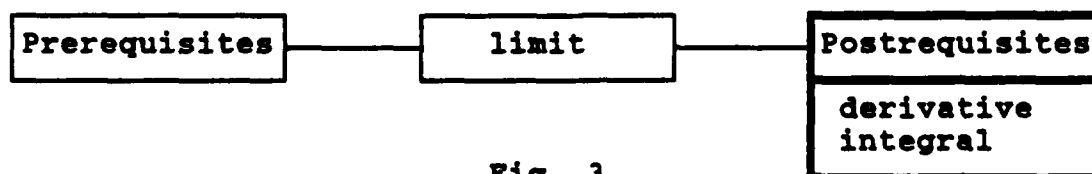


Fig. 3

Alternately, if the middle or concept node is activated, then a more detailed graph appears as, in Fig. 4, where the concept was assumed to be derivative.

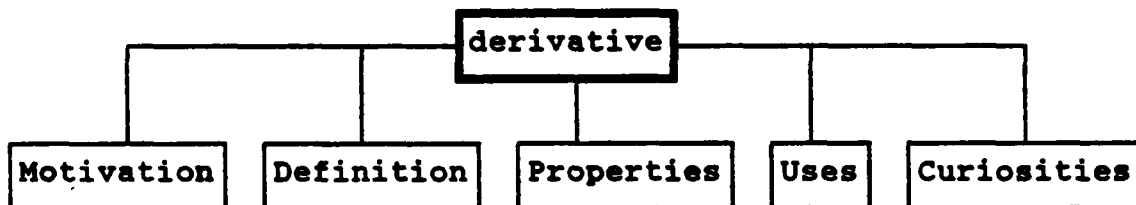


Fig. 4

If one of these nodes is activated, then either another menu appears or text (and graphics) appears that gives a detailed discussion of the topic. Such a discussion would be in the hypertext format where technical words within a sentence would be active and would provide links to a detailed discussion of the concepts. The idea is that the top level descriptions are general in nature and by going deeper and deeper into the file by successive activations of words the descriptions get progressively more detailed.

In a subject like calculus which keeps building upon itself with many prerequisite relationships, the prerequisite/postrequisite format is well suited. In a subject like "mountaineering" where the syllabus consists largely of facts and descriptions, then the format illustrated in Fig. 5 works well. In this case, examples of "Components" are



Fig. 5

1) general preparation, 2) climbing fundamentals, 3) rock

climbing, and 4) snow and ice climbing. An example of "Is part of", in this case, is "sports".

With available software for creating hypertext and the above formats we have the basis for a "generic graph of content" into which one could insert essentially any topic. We do not claim that such a product would constitute a tutor, but it would represent a technologically advanced, convenient presentation of material.

3. Other Uses of Graphs

We list here several potential uses of a graph of content other than presentation of information in a computerized tutor. At this stage we are not presenting a high level design for a tutor incorporating all of the following possibilities. We are just listing potential uses of a graph of content.

a. Modeling the student

The component of an Intelligent Teaching System (ITS) that represents the student's current state of knowledge is called the student model (VanLehn, 1987). We will not restrict ourselves to just modeling the student's knowledge of a given topic but will consider modeling other attributes of a student relative to a given topic such as interest level and efficacy (see section IV.C.2 for definition). Any model of the student is used to adapt the instruction to the particular student's needs. We conceive of using shades of a color, say blue, as the background color of the ellipse (node of graph) to indicate the level of an attribute for a given student relative to a topic. For example, if we are modeling the student's knowledge of the various topics and

concepts, white would correspond to no knowledge and a bright blue would correspond to mastery of the topic. Shades in between would correspond to intermediate levels of knowledge.

When modeling more than one attribute of a student relative to a given topic, we can split the ellipse into regions, say left, middle, and right reserved for different shades of the colors, blue, red, and green corresponding to knowledge, interest level, and efficacy, respectively. There are alternate methods of representing the levels of an attribute, say with bar graphs in an ellipse or simply as an integer from 1 to 10 where 1 would correspond to essentially no knowledge and 10 corresponds to mastery of the topic. The determination of the student's level of knowledge, interest in, or efficacy for any given topic will be obtained through a testing process.

b. Modeling the ideal, or goal state, of the student

VanLehn (1987) discusses that an ITS usually employs an expert model as well as a student model. We prefer to think of modeling a "goal state" instead of an expert's knowledge where the goal state defines the level of understanding that the student is expected to attain. We could include along with each concept or topic a percentage of the goal state knowledge that is currently understood by the student.

c. Recommendations on choice of topics

In his article on the genetic graph, Goldstein (1982) discusses the "choice of topic" problem. In older forms of computer-aided instruction (CAI), the order in which topics are introduced is predefined. In expert-based ITSs the student is often given the ability to explore a subject in

his own way and the role of the tutor is to analyze his responses in terms of an underlying skill set. We believe that our graph of content, similar to the genetic graph, is useful in this choice of topics problem because we believe in the educational heuristic that learning is facilitated by being able to explain new concepts in terms of those already acquired.

The graph of content makes available the relationships between the various topics and concepts in the syllabus. The modeling of the student's knowledge can then be used to give those topics the highest priority that are on the edge or "frontier" of the student's knowledge model. There are many pedagogical theories and teaching heuristics that may be employed. We feel that the graph of content with a model of the student's knowledge, interest level, and efficacy (see V.A.3 of this paper) relative to the different concepts can effectively be used to guide the student efficiently through a complicated syllabus.

There are two methods for using the genetic graph for topic selection: the frontier and the web methods. The first refers to picking topics, concepts, facts, or rules that are on the frontier of a student's genetic graph. The web method is where the teacher seeks to explain the syllabus as a whole to give the student perspective and later the teacher returns to various subtopics and presents those at deeper levels of understanding. The web method is preferred for a syllabus of facts and the frontier method preferred for procedural skills that have prerequisite relations.

Second, once a topic, or more particularly a concept, is selected the genetic graph supplies guidance for explaining the concept in more than one way to the student by means of relating it to its evolutionary predecessors. For example,

students will have their choice of seeing a analogous concept, or a special case, or a generalization of the concept. The ability to explain a concept in more than one way is an important tutoring technique.

IV. APPLYING PEDAGOGICAL PRINCIPLES TO COMPUTER-BASED TUTORING

The pedagogical strategy pursued by a computer-based tutor is crucial to its effectiveness. While a wide range of pedagogical strategies has been identified for teaching, few studies exist of effective tutoring strategies for computer-based tutoring (Soloway, et al 1987).

As part of this grant effort, we studied various pedagogical strategies that might be used for computer-based tutoring. This section concludes with a brief description of the pedagogical strategies examined and their applicability to computer-based tutoring.

We selected learning styles (Kolb, 1984) as the pedagogical strategy for detailed study. A computer program was developed under this grant which identifies the preferred learning style of a student. The discussion of learning styles as a pedagogical strategy and the software developed comprise the bulk of this section.

A. LEARNING STYLE

As a pedagogical theory, learning style relates to a typology that divides students into four categories. Each category contains a consistent set of characteristics of learning strategies, motivations, and rewards. As such,

knowledge of the particular typology allows the manipulation of the teaching methods to match the students' preferences. It is the inherent assumption that such matching increases learning speed, retention, and satisfaction.

Learning style theory was developed by David Kolb (1984) from empirical observations of MIT civil engineering students. The typology creates four quadrants based on the interaction of two axes as shown in Fig. 6. One axis represents an indicator of the method of interaction with the environment by a continuum between Reflective Observation (RO) and Active Experimentation (AE). The alternate axis represents an indicator of the method of information processing that is received from the environment by a continuum between Abstract Conceptualization (AC) and Concrete Experience (CE). The four typologies are divergent, assimilative, convergent, and accommodative. Persons may be assigned to a particular typology based upon a series of ranking questions contained in the Learning Style Inventory (LSI) (Kolb, 1984).

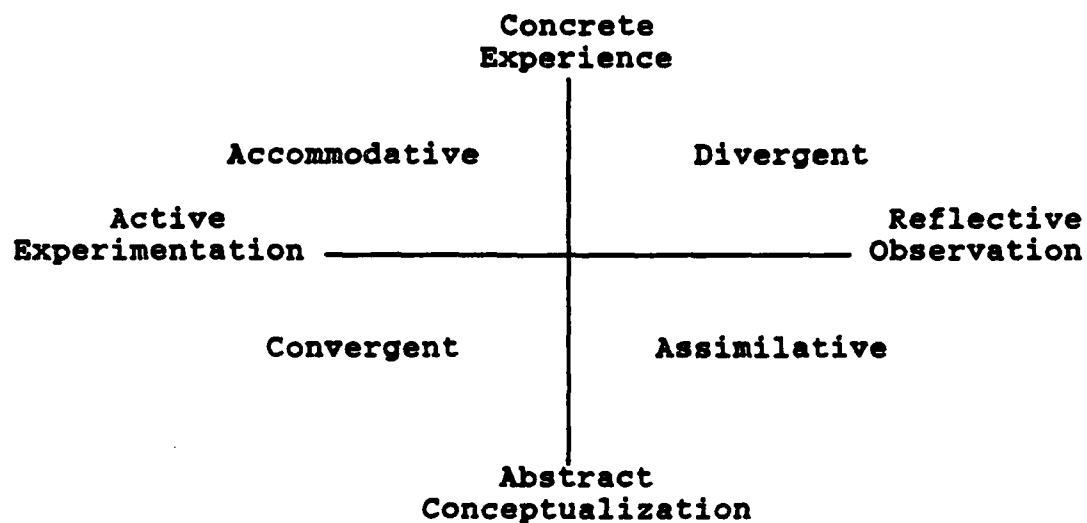


Fig. 6

Kolb (1984) describes the characteristics of the four learning styles as follows:

The convergent learning style relies primarily on the dominant learning abilities of abstract conceptualization and active experimentation. The greatest strength of this approach lies in problem solving, decision making, and the practical application of ideas. This learning style is called the converger because a person with this style seems to do best in situations like conventional intelligence tests, where there is a single correct answer or solution to a question or problem. In this learning style, knowledge is organized in such a way that through hypothetical-deductive reasoning, it can be focused on specific problems. Convergent people are controlled in their expression of emotion. They prefer dealing with technical tasks and problems rather than social and interpersonal issues.

The divergent learning style has the opposite learning strengths from convergence, emphasizing concrete experience and reflective observation. The greatest strength of this orientation lies in imaginative ability and awareness of meaning and values. The primary adaptive ability of divergence is to view concrete situations from many perspectives and to organize many relationships into a meaningful "gestalt." The emphasis in this orientation is on adaptation by observation rather than action. This style is called diverger because a person of this type performs better in situations that call for generation of alternative ideas and implications, such as a "brainstorming" idea session. Those oriented toward divergence are interested in people and tend to be imaginative and feeling-oriented.

In assimilation, the dominant learning abilities are abstract conceptualization and reflective observation. The greatest strength of this orientation lies in inductive reasoning and the ability to create theoretical models, in assimilating disparate observations into an integrated explanation. As in convergence, this orientation is less focused on people and more concerned with ideas and abstract concepts. Ideas, however, are judged less in this orientation by their practical value. Here, it is more important that the theory be logically sound and precise.

The accommodative learning style has the opposite strengths from assimilation, emphasizing concrete experience and active experimentation. The greatest strength of this orientation lies in doing things, in carrying out plans and tasks and getting involved in new experiences. The adaptive emphasis of this orientation is on opportunity seeking, risk taking, and action. This style is called accommodation because it is best suited for those situations where one must adapt oneself to changing immediate circumstances. In situations where the theory or plans do not fit the facts, those with an accommodative style will most likely discard the plan or theory. (With the opposite learning style, assimilation, one would be more likely to disregard or reexamine the facts.) People with an accommodative orientation tend to solve problems in an intuitive trial-and-error manner, relying heavily on other people for information rather than on their own analytic ability. Those with accommodative learning styles are at ease with people but are sometimes seen as impatient and "pushy."

These four learning styles form the basis for a pedagogical strategy which states that optimum learning conditions are created by dealing sequentially with the following questions which are matched to the four learning style (McCarthy and Leflar, 1983). This involves what is termed the 4-MAT strategy which sequentially addresses the questions:

- * Why does the student need and/or want to learn this material (related to divergent knowledge)?
- * What new information needs to be didactically transferred to the student and how does it relate to information already known (related to assimilative knowledge)?
- * What experiences or applications can be used to reinforce the information didactically given (related to convergent knowledge)?

* What new or unknown connections or intuitions are stimulated in the student as a result of the new information (related to accommodative knowledge)?

By the teacher successfully addressing these four questions, a student operates in each of the learning style quadrants for a portion of the learning experience. This increases retention by stimulating both short and long term memory. The 4-MAT strategy for teaching promotes attention, involvement, and group interaction.

The 4-MAT strategy may be extended to computer-based tutors. The tutor should also operate in each of the learning style quadrants for a portion of the tutoring experience. In addition, knowledge of the preferred learning style of the student could help individualize the tutoring session by varying the emphasis and order of operation for each of the learning style quadrants. By presenting material from the student's preferred learning style quadrant initially, we feel the student's interest and self-efficacy would be beneficially increased throughout the tutoring session.

B. SOFTWARE FOR IDENTIFYING PREFERRED LEARNING STYLE

An expert system was developed under this grant which identifies a student's preferred learning style. It was felt that this expert system could be used in conjunction with a computer-based tutoring system. The preferred learning style identified by the expert system could be used by the tutoring system to aid the tutor in three key decisions: (1) when to interrupt the student, (2) what to say to the student, and (3) what to do next.

Dr. Kenneth Williamson of Oregon State University served as the expert. Dr. Williamson has been involved in experiential learning for over six years as a consultant and leader of workshops on the use of learning styles as a pedagogical strategy.

A forward-chaining rule based expert system was developed using the expert system development package EXSYS. The expert system presents a series of questions to the student user and the student types in his or her responses. After sufficient questions have been posed (usually about five) the expert system presents the identified preferred learning style to the student. In addition, a list of study suggestions appropriate to the student's identified learning style is provided to the student.

The expert system was tested informally on several graduate students at Oregon State University and its identification of the preferred learning style was determined to be correct when compared with the results of a standard test. More testing and refinement of the system would be needed before we would feel comfortable in utilizing this expert system in tutoring software.

C. OTHER PEDAGOGICAL STRATEGIES FOR COMPUTER-BASED TUTORING

This section on applying pedagogical principles to computer-based tutoring concludes with a brief discussion of six possible pedagogical strategies we examined for computer-based tutoring.

1. Create a Flow State in the Learning Process

A flow state is a hyperattentive state where the

person is so intent on the task at hand that he naturally disregards irrelevant stimuli such as hunger or the passage of time. For example, chess players in a flow state will not notice that they are stiff from bending over the board or that they are hungry. There is no awareness of time passing. Actions are not performed for some external reward, but are instead done because the flow state is rewarding in and of itself for the individual. Csikszentmihalyi (1975) listed several factors that must be present in a task itself to induce a flow state in a person. Included among the factors are:

- a. The task must be challenging.
- b. The task must match the skills of the performer.
- c. There must be clear rules and clear goals.

Tutoring heuristics would have to be developed to help induce a flow state in the learning process. A first approximation might be: a moderate level of knowledge of the topic and a high interest level in and efficacy for the topic.

2. Utilize the Concept of Self-Efficacy

This theory deals with how people judge their personal capability for achieving a positive outcome on a given task. A student with a high sense of efficacy towards a task believes that he/she can accomplish the task. People avoid activities (including learning) that they believe exceed their coping capabilities, but they undertake and perform assuredly those that they judge themselves capable of managing (Bandera, 1977). Self-efficacy is positively correlated with performance (Bandera, 1982).

In utilizing self-efficacy in a tutoring situation, a tutor's first goal would be to evaluate the self-efficacy of the student relative to the various topics. This can be done by asking the student. Relative self-efficacy evaluations can be used in the choice of topic problem. A second goal of a tutor is to attempt to raise the student's sense of self-efficacy towards a given topic. This can be aided by presenting the material at an appropriate level at which the student can achieve some initial success.

3. Utilize the Primacy and Recency Effects

Primacy and recency refer to the importance of the first and last parts of serial presentation. During a given lecture or session at a tutoring device it is known that the first and last parts of the session have the most influence on the subject (Ellis, 1978).

4. Use of the Premack Principle

The Premack Principle (Ellis, 1978) in the choice of topics is good pedagogy. That is, the scheduling of topics of high interest to the subject immediately after topics of low interest is an example of the Premack Principle.

5. Utilize the Interest Level of the Student

A high level of interest by the student in a given topic is important for achieving a flow state. We will equate, for this discussion, interest with intrinsic motivation. We know that, in general, motivation includes extrinsic

motivation which includes incentives such as fame and money. Motivation can be too high for efficient learning. There appears to be an optimal level of motivation for learning of any task, the optimum depending on the difficulty of the task. In general, the more difficult the task, the lower the level of motivation that will promote efficient learning (Logan, 1976).

6. Pay Attention to Irrelevant Drive

The notion of irrelevant drive plays a role in learning theory. Typical irrelevant drives are fear and anxiety. It is known that the right amount of irrelevant drive increases performance but that too much reduces performance (Logan, 1976).

V. CONCEPTUAL DESIGN FOR AN EVOLVING TUTOR

The implementation of an intelligent tutoring system (ITS) is a very difficult undertaking. This section presents an alternative design and implementation strategy for an ITS referred to as the Evolving Tutor. The Evolving Tutor credits its inspiration to the Intentional Tutor Project of the USAF. It differs from the Intentional Tutor by lowering its initial objectives to remain implementable on IBM-AT or Apple MacIntosh computer systems. While some preliminary efforts have been taken towards the implementation of the Evolving Tutor, a functioning version has not been implemented.

This section will proceed as follows: first, the complexity of traditional intelligent tutoring systems is discussed. Second, the philosophy motivating an evolving tutoring system is presented. Third, the modules comprising the Evolving Tutor are detailed. Fourth, a prototype tutoring session on the Evolving Tutor is described. Finally, future possibilities of expanding the Evolving Tutor will be suggested.

A. COMPLEXITY OF INTELLIGENT TUTORING SYSTEMS

While the basic architecture for ITSs has been around for years, few successful implementations exist. Soloway and VanLehn (1987) discuss the difficulties inherent in the implementation of an ITS in terms of its four modules: the environment module, the expert module, the student modeling module, and the tutoring module. A discussion of the complexity of each of these modules follows. Obviously, the integration of the four modules into a functioning ITS is in itself a substantial challenge.

1. Environment Module

The module receiving the most attention right now from the AI community seems to be the environment module. The environment module is the interface between the ITS and the student. It may take the form of natural language, menus, or object-oriented simulations.

Despite the attention focused on the environment module, successful implementations have been largely restricted to research settings. Natural language interfaces, one of the most active AI research areas, is still one of the least

implemented of all AI technologies (Newquist, 1987). Menus have proved very useful in computer-aided instruction since the 1960's, but their use is restricted to certain types of queries. Examples of good object-oriented simulations include an ITS for interpreting ground tracks (Swigger, et al. 1987) and one which simulates the functional components of a naval steam plant (Hollan, et al. 1984).

2. Expert Module

The most recognized success of the AI community is the emergence of expert systems in a variety of domains. The distinguishing feature of expert systems is a formal representation of the domain knowledge which allows reasoning within the domain. The expert module of an ITS is based on a formal representation of the domain knowledge and a reasoning system which can solve domain problems, even ones posed by the student. The hope among ITS researchers was to apply the results and knowledge bases derived from expert system research directly towards the implementation of domain modules in ITS's.

Unfortunately, going from successful domain knowledge representations in expert systems to successful expert modules in ITSs remains an elusive task. Clancy (1982) discusses the difficulties in going from the domain knowledge contained in the rule-based expert system MYCIN to an expert module in an ITS. Robust representation of domain knowledge remains an open and active AI research area.

3. Student Modeling Module

The most troublesome module to implement in a traditional ITS is the student modeling module. The student modeling module's function is to create and update an accurate model of the student's knowledge based on the student's behavior. It is used by the ITS to aid the tutoring module in decisions about which curriculum to present next, when to offer advice, and how to formulate explanations.

Implementation of the student modeling module addresses many open research areas in AI including goal induction from behavior, assignment of blame, and creation of bug libraries for procedural skills. These are very hard problems and will not be solved in the near future.

4. Tutoring Module

The tutoring module implements the pedagogical strategy for the tutoring session. While quite a range of pedagogical strategies is available from the education research community, which of these strategies will prove successful for computer-based tutoring of specific domains remains an open research question.

The difficulty of implementing an ITS has resulted in prototype systems being built for tutoring micro-domains on very expensive computer hardware. Very little progress has been made in the development of ITSs which deal with more complex domains of interest to the Air Force and are realizable on microcomputers.

B. PHILOSOPHY FOR THE EVOLVING DEVELOPMENT OF AN ITS

The complexity of ITS's requires a different approach to their design and implementation. In order to deal with the complexity, we advocate an incremental development strategy which encourages experimentation on a base tutoring system. The base tutoring system will provide a flexible architecture to allow experimentation while delivering a tutoring session sufficiently complex and complete to be useful in its own right.

Historically, software systems were created by developing a complete set of specifications, coding the components independently, and integrating these components to produce the system.

In 1987, Frederick Brooks suggested that the software systems we build today are too complicated to be fully detailed in advance and implemented correctly. Rather, these systems should be grown by incremental development. This involves getting a scaled-down version running as soon as possible and then adding incrementally the features which complete the system.

Since much of the software required for intelligent tutors is currently an open AI research area, an extension to Brooks' growing system is proposed. An evolving system is suggested in which a scaled-down version of the system is constructed and serves as a base system for extensions. The base system must have a flexible architecture which allows experimentation without requiring significant changes to the existing base system software. In addition, the base system must be capable of providing a tutoring session which is sufficiently complex and complete to be useful in its own right.

The advantages of the evolving approach are many. First, since a functioning tutoring system is available, feedback from students will be available during the entire evolutionary sequence. Second, incremental features can be tested more easily by their incorporation into an existing system than by construction of a test system. Third, morale and productivity of the system developers has been shown to be higher with growing systems. Last, management and funding sources respond more favorably to working systems than to more elaborate but opaque specifications.

C. MODULES IN THE EVOLVING TUTOR

The modules in the proposed tutor are based on the three recognized methods of instruction: didactic, coaching, and socratic (Adler 1984). The following sections discuss these three modules in detail. We feel all three methods of instruction can contribute to the effectiveness of a tutoring session. Furthermore, if the tutor is to serve as a structure for experimentation, the capability to address each of these three methods of instruction seems essential.

1. The Didactic Module

The first module is the didactic module. The goal of the didactic module is to aid the student in the acquisition of domain knowledge. This is accomplished by providing immediate, flexible, and user-directed access to an organized body of textual and graphical information.

The computer is a good candidate for providing didactic tutoring. Textual and graphical information can be economically stored on disks, CD-ROM, and video to be displayed on

a computer monitor. Links within the information provide quick, user-directed access to the relevant information.

A hypertext information system would serve as the software for the didactic module in the Evolving Tutor. Good hypertext systems are commercially available (see Section III.A.1.) for both IBM-AT class and Apple MacIntosh hardware.

2. The Coaching Module

The second module is the coaching module. The goal of the coaching module is the development of the student's intellectual skills. This may be accomplished by challenging the student to manipulate simulations, solve problems, or play intellectual games.

Since coaching implies a one-to-one interaction, the computer may be the only feasible way of providing coaching in a number of situations. Either the number or availability of tutors for coaching may be insufficient for the number of students or the cost of providing the coaching may be prohibitive.

The computer has at least four inherent advantages over a human coach. First, a computer program can have endless patience with the student's mistakes. Second, some students will practice with fewer inhibitions under a computer coach, less afraid of exposing their 'inadequacies' to an impersonal computer. Third, immediacy is crucial with coaching. The computer can oftentimes better provide this immediacy in complex, computational domains than human coaches. Fourth, the computer can effectively be used to off-load distractions inherent to the problem being solved but irrelevant to the intellectual skill being learned.

The interface to the coaching module in the Evolving Tutor will be graphically oriented and directly manipulable by the student. Schneiderman (1982) suggests the key virtues of a directly manipulable interface include:

- a. Novices can learn the basic functions quickly.
- b. Knowledgeable intermittent users retain the operational concepts.
- c. Error messages are rarely needed.
- d. Users can see immediately if their actions are furthering their goals, and if not, can simply change the directions of their activities.
- e. Users have reduced anxiety because the system is comprehensible and because actions are so easily reversible.

The superiority of direct manipulation interfaces is becoming more widely recognized by computer users. MacIntosh interface standards enforce a graphical and directly manipulable interface on its software developers. Microsoft Windows, together with a mouse, is bringing direct manipulation interfaces to IBM-AT class computers. Computer games, which provide immediate graphical feedback to their users, have demonstrated how engaging and satisfying good direct manipulation interfaces can be.

The coaching module corresponds to object-oriented simulations in traditional ITS's. While implementations of object-oriented simulations for ITS's have generally been done on high-end LISP machines, impressive simulations are possible on both MacIntosh and IBM-AT class computers. MacIntosh programmers, using the Mac Toolbox routines and graphic software, have produced object-oriented simulations

designed to tutor such diverse domains as neural activity, transient and steady-state behavior of transmission lines, and social mobility in the France of King Louis XIV (Kinko, 1987). IBM-AT programmers are able to use Digitalk's Small-talk/V or Whitewater Group's Actor software to create comparable object-oriented simulations for the IBM-AT class computers.

3. Socratic Module

The third module is the socratic module. The goal of the socratic module is to integrate the student's existing knowledge. This is accomplished by asking questions which require the student to relate the subject material just learned to common sense and/or previously learned material.

Ideally, a conversation between the computer and the student using natural language would be used (see section V.F), but this is still a research topic. However, a computer can easily pose true/false, multiple choice, and fill-in-the-blank type questions to the student and provide immediate feedback to the student regarding his or her responses. The correctness of the student's responses can also be used to judge the student's proficiency with the domain subject.

A student's sense of involvement will generally be increased by using the quality of the student's responses as the basis for advancement, grades, or other tangible replies. Graphical feedback to the student based on the quality of his or her aggregate responses should also prove to be an effective motivator.

D. PROTOTYPE TUTORING LESSON

All three modules are integrated and play an important role in the prototype tutoring lesson. The student is allowed to switch freely among the modules according to his or her need. Mastery of the module is determined by the quality of the student's responses to the socratic module.

The coaching module serves as the basis to the lesson and presents an engaging challenge for the student to solve. During the challenge the student will probably encounter tasks which he is not able to perform correctly. The knowledge required for the task is available to the student through the didactic module. After some searching by the student, the knowledge will be acquired and the challenge can be resumed.

Once the challenge is successfully solved, the socratic module presents a series of questions to the student designed to integrate the concepts used during the challenge with the student's general knowledge. Students would be allowed to gather new information during the socratic module via both the didactic and coaching module.

E. COMPUTER IMPLEMENTATIONS

A multi-tasking operating system environment will allow the student to switch quickly and easily from one module to another. On an IBM-AT class computer, Microsoft Windows or any other multi-tasking operating system could be employed. Apple's new MultiFinder operating system provides quick context switching to MacIntosh implementations.

Apple's MacIntosh II supports up to four computer monitors concurrently. It would be possible to use a separate

monitor for the coaching, socratic, and didactic modules. The student could switch from one module to the other by moving the mouse from one monitor to the other.

F. POSSIBILITIES FOR EXPANSION OF THE EVOLVING TUTOR

The Evolving Tutor will serve as a structure for experimenting with the open AI research areas in ITS's. This section mentions a few possible experimentations without getting into details or specific recommendations.

A natural language interface to the socratic module in which a more natural dialog takes place between the student and computer is an obvious enhancement. A student model could guide the socratic module in focusing on questions which stretch the student's understanding to the fullest without confusing the student entirely.

The coaching module could adjust the type and amount of feedback to the student based on a model of the student's knowledge. The didactic model could change or restrict the presentation of certain kinds of information based on the model of the student's knowledge.

Hypermedia, the presentation of a variety of media via the computer, could improve the didactic model. Information presented to the student could take the form of interactive video disks, audio recordings, or interactive graphics. It is felt that more engaging and stimulating presentations improve the effectiveness of the tutoring session.

Better representations of the domain knowledge could help both the coaching and socratic module. More realistic object-oriented simulations will be possible with the better representations. The socratic module would be able to engage

the student in more of a two-way dialogue, each questioning the other, with better domain representations.

The Evolving Tutor could be useful for trying different mixes of coaching, didactic, and socratic methods in tutoring sessions. Do students learn best when coaching is emphasized? Or are socratic methods more effective in improving the student's understanding? Controlled studies could be done by both varying the emphasis of the tutoring session and testing and comparing student's understanding. The results collected could provide insight into pedagogical strategies for tutoring and teaching in general.

VI. RECOMMENDATIONS

We have discussed many ideas in this paper, provided new ideas and concepts, and have asked many questions. Here we will make some recommendations.

A. We recommend that the Intentional Tutor project in San Antonio investigate the use the Macintosh II with multiple screens as the basis for a hypermedia work station. The Mac has sufficiently many developmental tools and hypertext creating software such as Guide or Hypercard to make it a relatively inexpensive yet powerful work station.

B. We recommend that the Intentional Tutor project adopt the incremental development strategy that we refer to as the evolving tutor. This means that a scaled-down version of the Intentional Tutor should be constructed and serve as a base for later extensions.

C. We recommend that the Intentional Tutor project be used as a test-bed for comparative studies of different pedagogical strategies applied to computer-based tutors.

VII. REFERENCES

Adler, M. J. (1984). The Paideia Program, An Educational Syllabus. New York: Macmillan Publishing Co.

Anderson, J.R. (1980). Cognitive Psychology and its Implications. New York: W.H. Freeman.

Bandera, A. (1977). Social Learning Theory, Englewood Cliffs, New Jersey: Prentice Hall.

Bandera, A. (1982). The self-efficacy mechanism in human agency. American Psychologist, 37(2), 122-147.

Brooks, F. P. (1987). No silver bullet: essence and accidents of software engineering. IEEE Computer, Vol. 20, No. 4: 10-19.

Bush, Vannevar (1945). As we may think, Atlantic Monthly, July.

Clancy, W. J. (1982). Tutoring rules for guiding a case method dialogue. In Sleeman, D. H. and Brown, J. S. (Eds.), Intelligent Tutoring Systems. London: Academic Press.

Ellis, H.C. (1978). Fundamentals of Human Learning, Memory, and Cognition, Dubuque, Iowa: Wm. C. Brown Co.

Goldstein, I. (1982). The Genetic Graph: a representation for the evolution of procedural knowledge. D. Sleeman and J.S. Brown (Eds.), Intelligent Tutoring Systems. London: Academic Press.

Grossberg, S. (1982). Studies of Mind and Brain. Boston: Reidel Press.

Hollan, J. D., Hutchins, E. L. and Weitzman, L. (1984). Steamer: An interactive inspectable simulation-based training system. The AI Magazine, summer: 15-27.

Kinko's Service Corp. (1987). Kinko's Academic Courseware Exchange, Fall 1987 Catalog. Santa Barbara, CA.

Kolb, D.A. (1984). Experiential Learning. New Jersey: Prentice-Hall.

Logan, F.S. (1976). Fundamentals of Learning and Motivation, Dubuque, Iowa: Wm. C. Brown Co.

McCarthy, B. and S. Leflar (1983). 4 MAT in Action. Oak Brook, Illinois: Excel, Inc.

Miller, J. R. and Neches, R. (1987). Intelligent Interfaces. Conference Tutorial Program, Sixth National Conference on Artificial Intelligence. AAAI-87, Seattle, WA.

Newquist, H. P. (1987). AI technology we haven't heard much of lately. AI Expert, Vol. 2, No. 10: 69-73.

Schneiderman, B. (1982). The future of interactive systems and the emergence of direct manipulation. Behavior and Information Technology, Vol. 1: 237-256.

Schori, R.M. (1986). Final Report: An Intentional Tutor. 1986 USAF-UES Summer Faculty Research Program. Dayton, Ohio: Universal Energy Systems, Inc.

Soloway, E. and VanLehn, D. (1987). AI and Education. Conference Tutorial Program, Sixth National Conference on Artificial Intelligence. AAAI-87, Seattle, WA.

Swigger, K., Burns, H., Loveland, H., and Jackson, T. (1987). An intelligent tutoring system for interpreting ground tracks. Proceedings from the Sixth National Conference on Artificial Intelligence. AAAI-87, Seattle, WA.

VanLehn, K. (1988). Student Modelling. In M. Polson and J. Richardson (Eds.), Foundations of Intelligent Tutoring Systems. Hillsdale, New York: Erlbaum.

FINAL REPORT NUMBER 72
REPORT NOT RECEIVED IN TIME
WILL BE PROVIDED WHEN AVAILABLE
Dr. Meckinley Scott
760-6MG-025

FINAL REPORT NUMBER 73
REPORT NOT RECEIVED IN TIME
WILL BE PROVIDED WHEN AVAILABLE
Dr. Martin Shadday
760-6MG-089

FINAL REPORT NUMBER 74
REPORT NOT RECEIVED IN TIME
WILL BE PROVIDED WHEN AVAILABLE
Dr. Nisar Shaikh
760-6MG-007

FINAL REPORT NUMBER 75
REPORT NOT RECEIVED IN TIME
WILL BE PROVIDED WHEN AVAILABLE
Mr. Jim Sirkis (GSSSP)
760-6MG-142

TWO-DIMENSIONAL FLIGHT
SIMULATION MODEL FOR AN AIRCRAFT
WITH A RAPIDLY ROTATING AIRFOIL

FINAL REPORT

June 1987

Submitted to: Universal Energy Systems, Inc.
4401 Dayton-Xenia Road
Dayton, OH 45432

Space And Flight Systems Laboratory
University of Colorado at Colorado Springs
1867 Austin Bluffs Parkway, Suite 202
Colorado Springs, CO 80907

Principle Investigator
William D. Siuru, Jr., PhD, PE

Associate Investigator
Craig Barber

ACKNOWLEDGEMENTS

This research was performed under a Minigrant from the Air Force Office of Scientific Research (AFOSR) and was administered by the Universal Energy Systems, Inc. of Dayton, Ohio.

We would like to thank Dr. Charles E. Fosha, Director SFSL, for his support and helpful suggestions during the course of this research project.

Special thanks are given to Brian Siuru who provided much support by running computer simulations, reducing experimental data, and proofreading this final report.

TABLE OF CONTENTS

ACKNOWLEDGEMENTS

I.	INTRODUCTION	I-1
II.	THEORY	II-1
III.	AERODYNAMIC PARAMETERS	III-1
IV.	SIMULATION MODEL DEVELOPMENT	IV-1
V.	DYNAMIC ANALYSIS	V-1
VI.	SIMULATION RESULTS	VI-1
VII.	CONCLUSIONS AND RECOMMENDATIONS	VII-1

REFERENCES

APPENDICES

A	TWO-DIMENSIONAL MODEL DEVELOPED IN BASIC	A-1
B	TWO-DIMENSIONAL MODEL DEVELOPED IN FORTRAN	B-1
C	SIZING PROGRAM	C-1

SECTION I

INTRODUCTION

While extensive experimental and computational investigations have been conducted with respect to the dynamic lift enhancement achieved through the use of rapidly pitching, oscillating, and plunging airfoils, very little research has been done to understand how such unconventional aerodynamics would affect the flight mechanics of an aircraft using these concepts. A comprehensive understanding of these flight mechanics is needed before these concepts can be evaluated as viable candidates for future supermaneuverable aerospace vehicles.

The basic objective of this investigation was to develop a simulation model that can be used to gain an insight into how the incorporation of rapidly pitching, oscillating, and plunging airfoils affects aircraft flight mechanics. Because of the complexity of the problem, this initial model was limited to two-dimensions. This simpler approach allows a better understanding of the underlining mathematics involved and provides an excellent method to identify the features that should be incorporated in more sophisticated and realistic three-dimensional simulation models.

An important part of this investigation was to identify gaps in experimental or computation data needed as input to

simulation models. While the data base on these airfoil motions is rather extensive, they are still substantial areas of the total phenomena where data is still needed for realistic simulations. The identification of these gaps can be used to focus future experimental and computation efforts.

Figure I-1 shows a schematic of the simulation model developed here. The basic model is the two-dimensional form of the equations of motions. The aircraft parameters needed as input are such aircraft characteristics as dimensions, propulsive thrust, airspeed and altitude, and steady state lift, drag, and moment coefficients. The unsteady aerodynamics that drive the model come from the available experimental and computational data in the form of lift, drag and moment coefficients normally expressed as functions of time. An important ingredient of this model is the non-dimensional similarity parameter

$$\alpha^+ = \dot{\alpha} c / U \quad (I-1)$$

where

$\dot{\alpha}$ = the rate at which the airfoil pitches, oscillates or plunges

c = airfoil chord

U_{∞} = freestream velocity

This parameter allows the model to account for changes in the unsteady parameters due to varying flight conditions namely the airspeed and the rate at which the airfoil revolves. Another important part of the model is the interaction between the

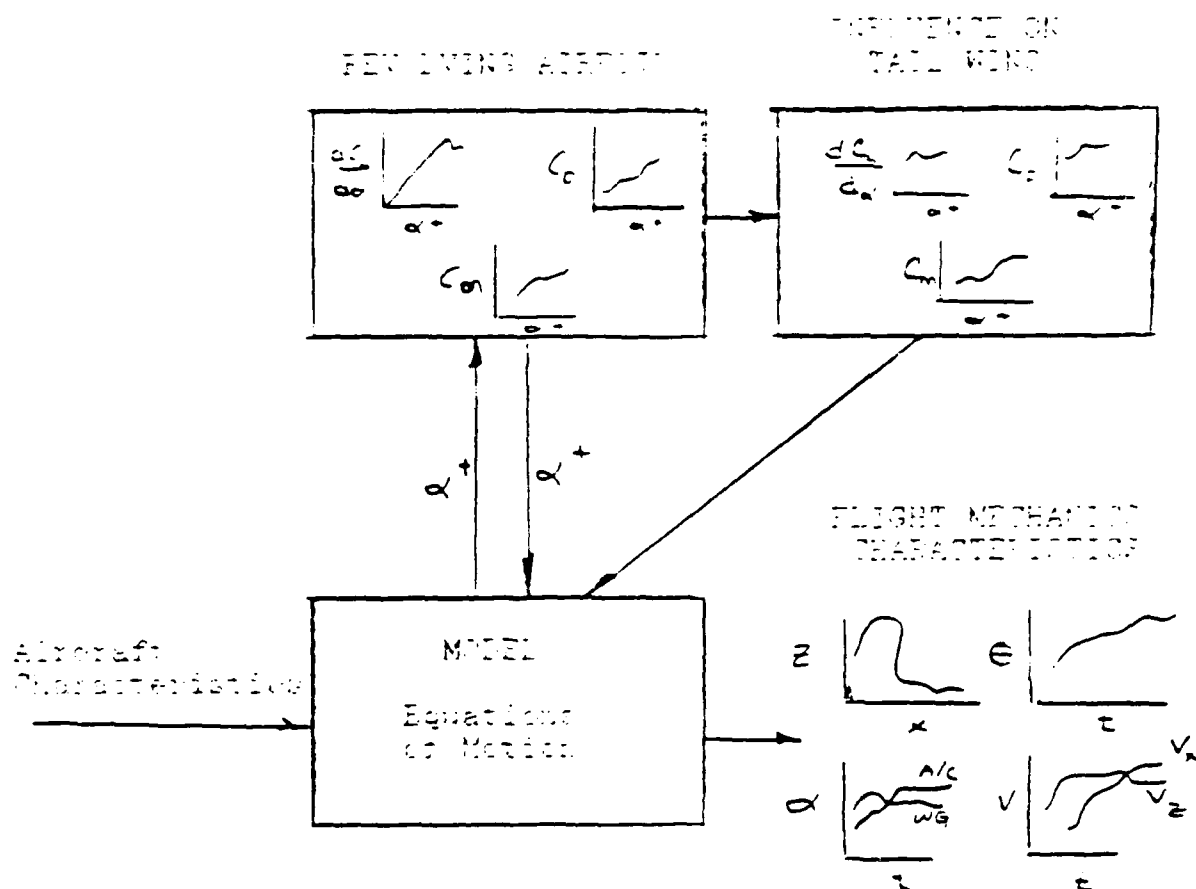


Figure I - 1
Schematic of Simulation Model

rotating airfoil and tail surface. The model is also amenable to the case where a rotating canard is used and this motion affects the lift, drag and moment of the main wing.

The output of the model includes the important flight mechanics characteristics including the flight path, the aircraft and wing angles-of-attack, horizontal and vertical velocities and accelerations, and the aircraft pitch angle.

SECTION II

THEORY

The equations of motion in three-dimensional form, as shown for example in Table II-1, reduce to the following for the two-dimensional problem. The coordinate system used is shown in Figure II-1.

Angular EOM

$$\ddot{Q} = \frac{M_A + M_T}{I_{yy}} \quad (\text{II-1})$$

where \ddot{Q} = angular acceleration around pitch axis

M_A = moment around the pitch axis due to aerodynamic forces

M_T = moment around the pitch axis due to propulsive thrust forces

I_{yy} = moment of inertia about the pitch axis

EOM Along Flight Path

$$\dot{V} = \{F_T + F_{gf} - D\}/m \quad (\text{II-2})$$

TABLE II - 1

THREE-DIMENSIONAL EQUATIONS OF MOTION

$$\begin{aligned}
X - mg \sin \theta &= m(\dot{U} + QW - RV) & \frac{dx'}{dt} &= U \cos \theta \cos \psi + V(\sin \phi \sin \theta \cos \psi - \cos \phi \sin \psi) \\
& & & + W(\cos \phi \sin \theta \cos \psi + \sin \phi \sin \psi) \\
Y + mg \cos \theta \sin \phi &= m(\dot{V} + RU - PW) \\
Z + mg \cos \theta \cos \phi &= m(\dot{W} + PV - QU) & \frac{dy'}{dt} &= U \cos \theta \sin \psi + V(\sin \phi \sin \theta \sin \psi + \cos \phi \cos \psi) \\
& & & - W(\cos \phi \sin \theta \sin \psi - \sin \phi \cos \psi) \\
L &= A\dot{P} - ER + QR(C - B) - EPQ + QH'_x - RH'_y & \frac{dz'}{dt} &= U \sin \theta + V \sin \phi \cos \theta + W \cos \phi \cos \theta \\
M &= B\dot{Q} + RP(A - C) + E(P^2 - R^2) + RH'_x - PH'_y \\
N &= -E\dot{P} + CR + PQ(E - A) + EQR + PH'_y - QH'_x \\
P &= \phi - \psi \sin \theta \\
Q &= \dot{\theta} \cos \phi + \psi \cos \theta \sin \phi \\
R &= \psi \cos \theta \cos \phi - \dot{\theta} \sin \phi \\
\dot{\theta} &= Q \cos \phi - R \sin \phi \\
\phi &= P + Q \sin \phi \tan \theta + R \cos \phi \tan \theta \\
\psi &= (Q \sin \phi + R \cos \phi) \sec \theta
\end{aligned}$$

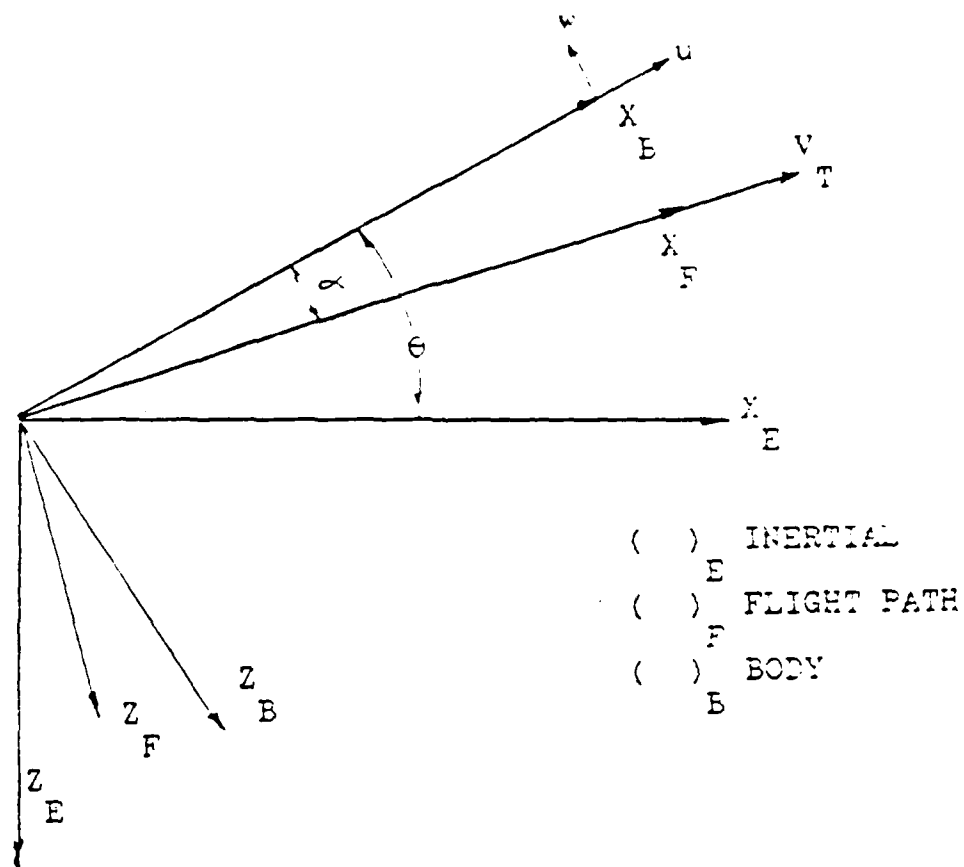


Figure II - 1
Coordinate Systems

where \dot{V}_T = acceleration along the flight path.

$F_{T_{xf}}$ = component of thrust along flight path.

$F_{E_{xf}}$ = component of aircraft weight along flight path.

D = drag force

m = aircraft mass

EOM Normal to Flight Path

$$\dot{\alpha} = Q + \{F_{T_{zf}} + F_{E_{zf}} - L\}/mV_T \quad (II-3)$$

where $\dot{\alpha}$ = rate of angle of attack change

Q = pitch rate

$F_{T_{zf}}$ = component of thrust force perpendicular to flight path

L = lift force

Thrust Force

For simplification, it is assumed that the thrust force acts through the center of gravity of the aircraft and along X_B the horizontal body axis of the aircraft. With this assumption,

$$M_T = 0; \quad F_{T_{xf}} = T; \quad F_{T_{zf}} = 0$$

Weight Forces

Referring to Figure II-2, the gravitational forces in the flight path coordinate system can be written

$$F_{xf} = mg\{\sin\theta\cos\alpha - \cos\theta\sin\alpha\} = -mg\sin(\theta - \alpha) \quad (II-4)$$

and

$$F_{zf} = mg\{\cos\theta\cos\alpha + \sin\theta\sin\alpha\} = mg\cos(\theta - \alpha) \quad (II-5)$$

Lift Forces

Referring to Figure II-3, the total lift force acting on the aircraft can be written

$$\begin{aligned} L_{total} &= L_{wing} + L_{fuse} + L_{tail} \\ &= q\{S_{wing} C_{l_{wing}} + S_{fuse} C_{l_{fuse}} + S_{tail} C_{l_{tail}}\} \end{aligned} \quad (II-6)$$

where $q = \text{dynamic pressure} = \frac{1}{2} \rho V^2$ (the dynamic pressure is assumed here to be the same over the wing, fuselage, and tail)

$S = \text{the surface area of the wings, fuselage, and tail}$
xxx

$C_l = \text{the lift coefficient of the wings, fuselage, and tail}$
xxx

If area ratios are defined thusly

$$N_{wing} = S_{wing} / S_{total}; \quad N_{fuse} = S_{fuse} / S_{total}; \quad N_{tail} = S_{tail} / S_{total}$$

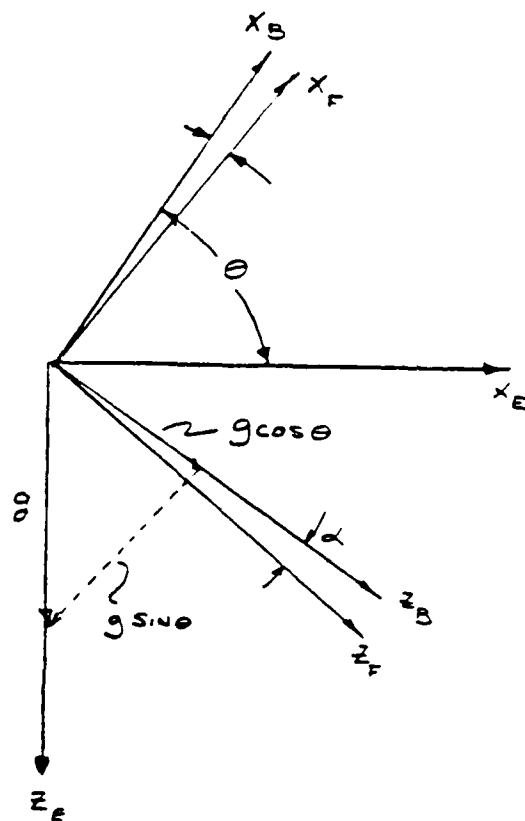


Figure II - 2
Gravitational Forces

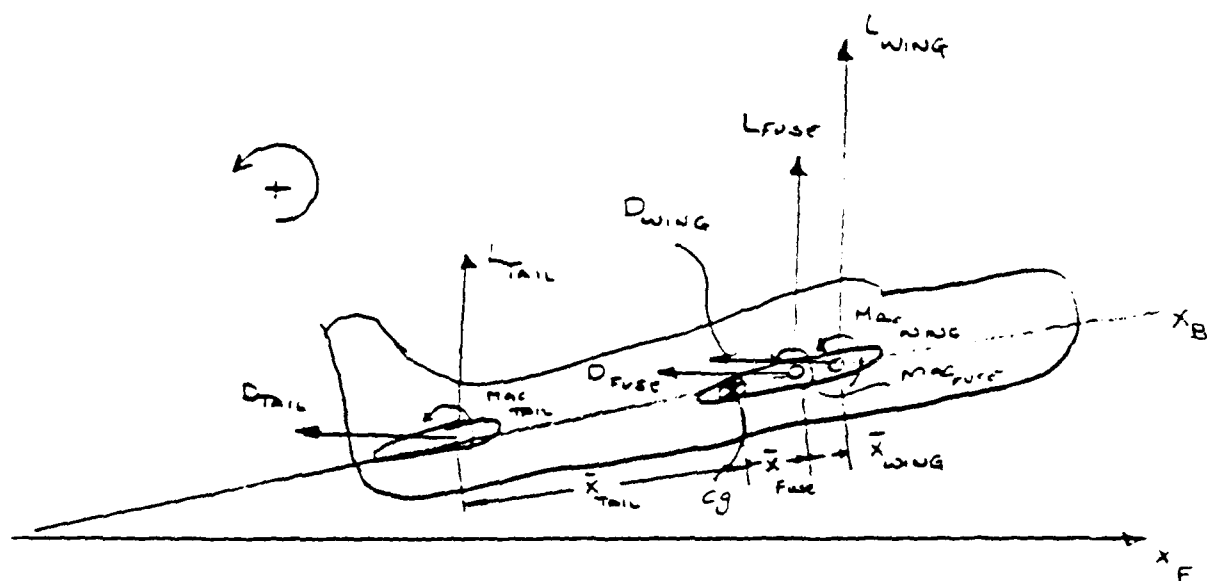


Figure II - 3
Lift, Drag, and Moments

the lift can be written as

$$L_{\text{total}} = \{qS\} \times \{N_{\text{wing}} C_{l_{\text{wing}}} + N_{\text{fuse}} C_{l_{\text{fuse}}} + N_{\text{tail}} C_{l_{\text{tail}}}\}$$

In a similar manner, the total drag force can be written

$$D_{\text{total}} = \{qS\} \times \{N_{\text{wing}} C_{d_{\text{wing}}} + N_{\text{fuse}} C_{d_{\text{fuse}}} + N_{\text{tail}} C_{d_{\text{tail}}}\}$$

Aerodynamic Moment

Referring again to Figure II-3, the moments due to the aerodynamic forces can be written.

$$M_A = \{qS\} \times \{N_{\text{wing}} C_{m_{\text{wing}}} + N_{\text{fuse}} C_{m_{\text{fuse}}} + N_{\text{tail}} C_{m_{\text{tail}}}\} +$$

$$L_{\text{total}} (N_{\text{wing}} \bar{X}_{\text{wing}} + N_{\text{fuse}} \bar{X}_{\text{fuse}} + N_{\text{tail}} \bar{X}_{\text{tail}}) \cos \alpha +$$

$$D_{\text{total}} (N_{\text{wing}} \bar{X}_{\text{wing}} + N_{\text{fuse}} \bar{X}_{\text{fuse}} + N_{\text{tail}} \bar{X}_{\text{tail}}) \sin \alpha \quad (\text{II-7})$$

where $C_{m_{\text{xxx}}}$ = moment coefficient about the component aerodynamic center for the wing, fuselage & tail
 \bar{X}_{xxx} = distance between the aircraft center of gravity and the aerodynamic center of the wing, fuselage, and tail

Tail Damping

Because of the oscillation of the tail necessary to counteract oscillations in lift and drag induced by the rapidly revolving airfoil, the tail can be expected to provide a certain amount of aerodynamic damping. For the case of a canard, the oscillating canard would provide the damping.

Figure II-4 shows the model used for the damping provided by the tail's horizontal surface. The damping moment provided by the tail can be written

$$M_{\text{tail}} = C_{d_{\text{tail}}} S_{\text{tail}} (\bar{X}_{\text{tail}} Q)^2 / 2 \quad (\text{II-8})$$

where $C_{d_{\text{tail}}}$ = flat plate drag coefficient provided by the tail's horizontal surface

S_{tail} = tail surface area

\bar{X}_{tail} = distance between tail aerodynamic center & the aircraft center of gravity

Q = pitch rate

Velocities and Flight Path

The velocities in the inertial reference frame can be determined from

$$\begin{aligned} \dot{x}_E &= V_T \cos(\theta - \alpha) \\ \dot{z}_E &= -V_T \sin(\theta - \alpha) \end{aligned} \quad (\text{II-9})$$

Finally, the flight path can be determined by integrating Equations II-9.

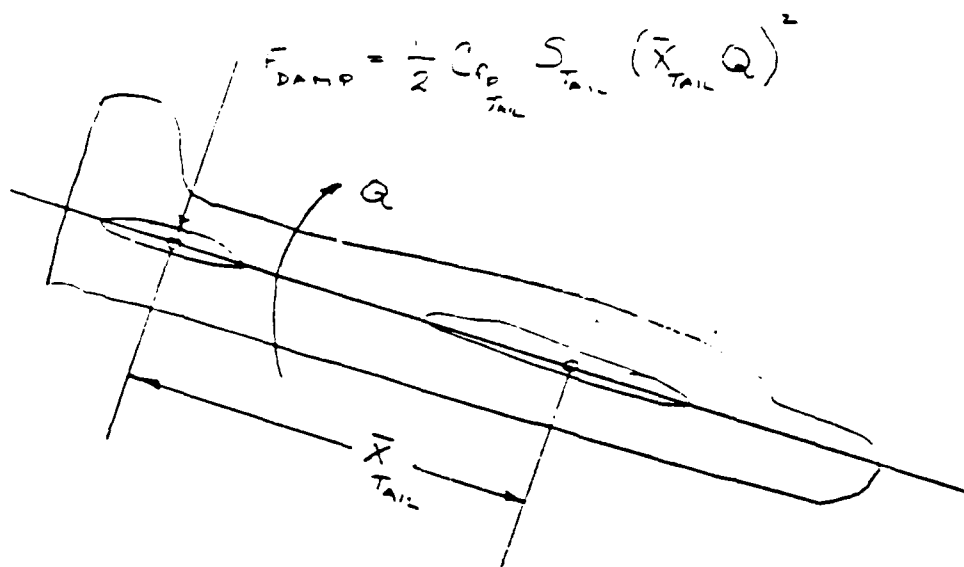


Figure II -4
Tail Damping Model

SECTION III

AERODYNAMIC PARAMETERS

Steady State

The steady state lift drag, and moment used are those found in classical aircraft design and analysis.

Lift. The lift of the main wing is expressed as

$$L_{\text{wing}} = q_{\text{wing}} S_{\text{wing}} \left\{ C_{l_o} + \frac{dC_l}{d\alpha}(\alpha) \right\} \quad (\text{III-1})$$

where q_{wing} = the dynamic pressure on the wing

S_{wing} = wing surface area

C_{l_o} = lift coefficient of the wing at zero angle-of-attack

$dC_l/d\alpha$ = slope of the lift/angle-of-attack curve

α = angle-of-attack

The lift provided by the tail or canard can be expressed in a similar fashion

$$L_{\text{tail}} = q_{\text{tail}} S_{\text{tail}} \left\{ C_{l_o} + \frac{dC_l}{d\alpha}(\alpha + \alpha' + \epsilon) \right\} \quad (\text{III-2})$$

where q_{tail} = the dynamic pressure on the horizontal tail or tail canard

S_{tail} = tail or canard surface area

C_{l_o} = lift coefficient at zero angle of attack

$dC_l/d\alpha$ = slope of the lift/angle-of-attack curve

α = angle-of-attack of aircraft

α_i = horizontal tail or canard incident angle
(usually negative for the tail and positive for the canard)

ϵ = downwash angle induced by the wing on the horizontal tail

Because of the complex interaction between the vortices shed by a oscillating wing and the tail surface the downwash angle was neglected for the steady state case. In the unsteady flight regime, this effect is assumed to be buried in the interaction between the oscillating wing and the tail surface.

Finally, the lift provided by the fuselage can be expressed as

$$L_{\text{fuse}} = q_{\text{fuse}} S_{\text{fuse}} \{C_{l_o} + \frac{dC_l}{d\alpha}(\alpha)\}_{\text{fuse}} \quad (\text{III-3})$$

where each of the terms follow the definitions given for the wing and tail. While the dynamic pressure seen by the wing, fuselage, and tail or canard can be slightly different because of the variation in the freestream velocities with respect to the surfaces, for this initial study they were assumed to be the same.

Drag. The steady state drag of the wing and tail or canard can be related to lift by the traditional relationship

$$C_d = C_{d_o} + \frac{C_l^2}{\pi AR e} \quad (III-4)$$

where C_{d_o} = drag coefficient at zero angle-of-attack

AR = aspect ratio of the wing, tail, or canard

e = Oswald efficiency factor

The drag coefficient of the fuselage takes the form

$$C_d = C_{d_o} + \frac{dC_l}{d\alpha} (\alpha) \quad (III-5)$$

To find the total drag of each component, the above coefficients were multiplied by the dynamic pressure and the appropriate surface area.

Moment. The moment about the aerodynamic center of the wing, fuselage, tail or canard, can be expressed in terms of the dynamic pressure, moment coefficient, surface area, and a mean chord distance, that is

$$M_m = C_m q S \bar{c} \quad (III-6)$$

For simplicity, the moment coefficient C_m for any of the components was assumed to be invariant with angle-of-attack.

Unsteady Aerodynamic Parameters

While the two-dimensional model developed here can be used to simulate the flight mechanics for a variety of rotating airfoil concepts, the following discussion will center around a rapidly pitching airfoil. In addition to being a concept of interest for future aerospace vehicles, there is extensive experimental data available much of which has been reduced to aerodynamic parameters namely lift, pressure drag, and moment coefficient that are directly of use in this flight mechanics simulation. See References [1] and [2] for details on the development of empirical aerodynamic parameter models.

In order to describe the relationship between the flight mechanics and the aerodynamic reactions, the similarity parameter $\alpha^+ = \dot{\alpha} c/U$ is used. This parameter allows the model to account for varying flight conditions (U_∞) and airfoil rotation rates ($\dot{\alpha}$).

While the current simulation model can use any aerodynamic parameters that can be put in analytic form, the rapidly pitching example used here employed only parameters up to the point of maximum lift. Previous investigations (Reference [1] and [2]) have shown it is possible to achieve almost the same average lift coefficient by pitching the airfoil up to the angle of attack for maximum lift as rotating through the full 60 degrees considered in these experiments. Pitching the airfoil only to the maximum lift angle-of-attack, also results in substantially

reduced average drag. Figure III-1 summarizes these conclusions. Incidentally, while not currently incorporated in the model, the model is amenable to use of "look up" tables for the aerodynamic parameters in lieu of empirical relationships.

Table III-1 describes the empirical models developed from the experimental data for a rapidly pitching airfoil. The data represents the following range of experimental conditions

Freestream Velocity	10 to 80 ft/sec
Maximum Pitch	60 deg
Pitch Rate	115 to 1150 ft/sec
Reynolds Number	25,000 to 200,000

As an example of how these empirical relationships are used in the simulation, to prevent wing stall the maximum total angle-of-attack of the wing (aircraft plus instantaneous wing value) can be limited to

$$\alpha_{Cl_{max}} = 43.5 (\alpha) + 0.14 \quad (III-7)$$

For the pitching airfoil, the lift/angle-of-attack slope can be determined from the relationship

$$\frac{dCl}{d\alpha} = \frac{3.62 \alpha + 1.86}{43.5 (\alpha) + 0.14} \quad (III-8)$$

TABLE III-I
Empirical Models

PARAMETER	MODEL
Angle Attack at Maximum Lift Coefficient	$\alpha = 43.5(\alpha')^{+0.14}$ $C_{l_{max}}$
Maximum Lift Coefficient	$C_{l_{max}} = 3.62 \alpha'^{+} + 1.98$
Maximum Drag Coefficient	$C_{d_{max}} = 6.32 \alpha'^{+} + 1.86$
Average Lift Coefficient (up to Maximum Lift)	$C_{l_{ave}} = 2.64 \alpha'^{+} + 1.05$
Average Lift Coefficient (over 60 degrees)	$C_{l_{ave}} = 2.83 \alpha'^{+} + 1.16$
Average Drag Coefficient (over 60 degrees)	$C_{d_{ave}} = 1.89 \alpha'^{+} + 0.84$

For the unsteady case, the pressure drag coefficient relationship (Equation III-4) can be replaced by

$$C_d = C_l^{2.5} / (0.8 \pi A R) \quad (\text{III-9})$$

The exponent (2.5) and the pseudo Oswald Efficiency Factor (0.8) were determined from least squares curve fits to the experimental data.

SECTION IV

SIMULATION MODEL DEVELOPMENT

The actual computer model was developed in both BASIC and FORTRAN. The actual model development was done in BASIC and the final version was converted to FORTRAN. Using these two separate programming techniques facilitated model debugging by allowing the comparison of results between the two different programs. The BASIC program is presented in Appendix A to this report and the FORTRAN version is documented in Appendix B.

Program Description

Referring back to Figure I-1, the basic model is the two-dimensional equations of motion as discussed in Section II. The aircraft parameters needed as input are the aircraft characteristics and flight conditions, as well as the steady aerodynamic parameters (detailed in Section III) are given Table IV-I. To incorporate the unsteady aerodynamic parameters for a pitching airfoil presented in Section III, the steady-state parameters were replaced by their unsteady counterparts. In each case, the switch from steady to unsteady conditions occurred from a condition of straight and level flight. The short program presented in Appendix C was used to "size" the aircraft for straight and level flight, i.e. selection of the initial angle-of-attack, location of the tail center-of-gravity, and thrust level.

TABLE IV-1
SIMULATION MODEL INPUTS

AIRCRAFT CHARACTERISTICS

- o Wing and Horizontal Tail Chord and Wingspan
- o Fuselage Length and Diameter
- o Propulsive Thrust
- o Wing, Fuselage, and Tail Center-of-Gravity Location
- o Aircraft Moment of Inertia

FLIGHT CONDITIONS

- o Initial Airspeed
- o Initial Altitude
- o Initial Pitch and Pitch Rate

STEADY STATE AERODYNAMIC PARAMETERS

- o Lift Coefficients at Zero Angle-of-Attack and Slope of the Lift/Angle-of-Attack Curve.
- o Drag Coefficients at Zero Angle-of-Attack and Efficiency Factor
- o Moment Coefficients

Table IV-II lists the output available from the model. The model has the capability to account for any effects of a forward rotating airfoil on a subsequent airfoil, for example the effects of a oscillating wing on the horizontal tail or a rotating canard on a fixed main wing. However, because experimental data on the interaction between airfoils was not available for realistic separation distances, this capability could only be tested for a hypothesized interaction model.

Model Verification

In order to test the model for the steady state case, a looping maneuver was simulated. This maneuver was chosen not only because it is a demanding one, but data was available in Reference [3] for verification, at least on a qualitative basis. Table IV-III lists the aircraft characteristics and flight conditions used in this steady state simulation. Figure IV-1 shows the key results of the simulation that agree reasonably well with the information presented in Reference [3].

TABLE IV-II

SIMULATION MODEL OUTPUTS

FLIGHT PATH - Horizontal versus Vertical Distance

INSTANTANEOUS ANGLES-OF-ATTACK - Aircraft and Wing

AIRCRAFT PITCH ANGLE

AIRCRAFT VELOCITIES - Horizontal and Vertical, plus
Airspeed

ACCELERATIONS - Horizontal, Vertical, and Total

Horizontal and Vertical Velocities, Distances, and
Accelerations are with respect to an inertial frame of
reference.

TABLE IV-III

AIRCRAFT AND FLIGHT CHARACTERISTICS

LOOPING AIRCRAFT SIMULATION

WINGSPAN AND CHORD DIMENSIONS

- Main Wing: 36.8 feet and 5.59 feet
- Horizontal Tail: 9.4 feet and 2.76 feet

WEIGHT: 1932 pounds

MOMENT OF INERTIA ABOUT YY AXIS: 1500 lbs-sec²

THRUST PROFILE:

$$T = 800 - 2.2222 (VTAS)$$

INITIAL CONDITIONS

- Airspeed: 180 ft/sec
- Altitude: Sea Level
- Pitch Rate and Angle: 0 and -20 degrees

AERODYNAMIC PARAMETERS

- Wing and Tail C_l and $dC_l/d\alpha$: 0.05 and .1
- Wing and Tail C_d^o and e : 0.042 and 1.0
- Aircraft Moment:

$$C_{mac} = -0.05 + 0.9\alpha$$

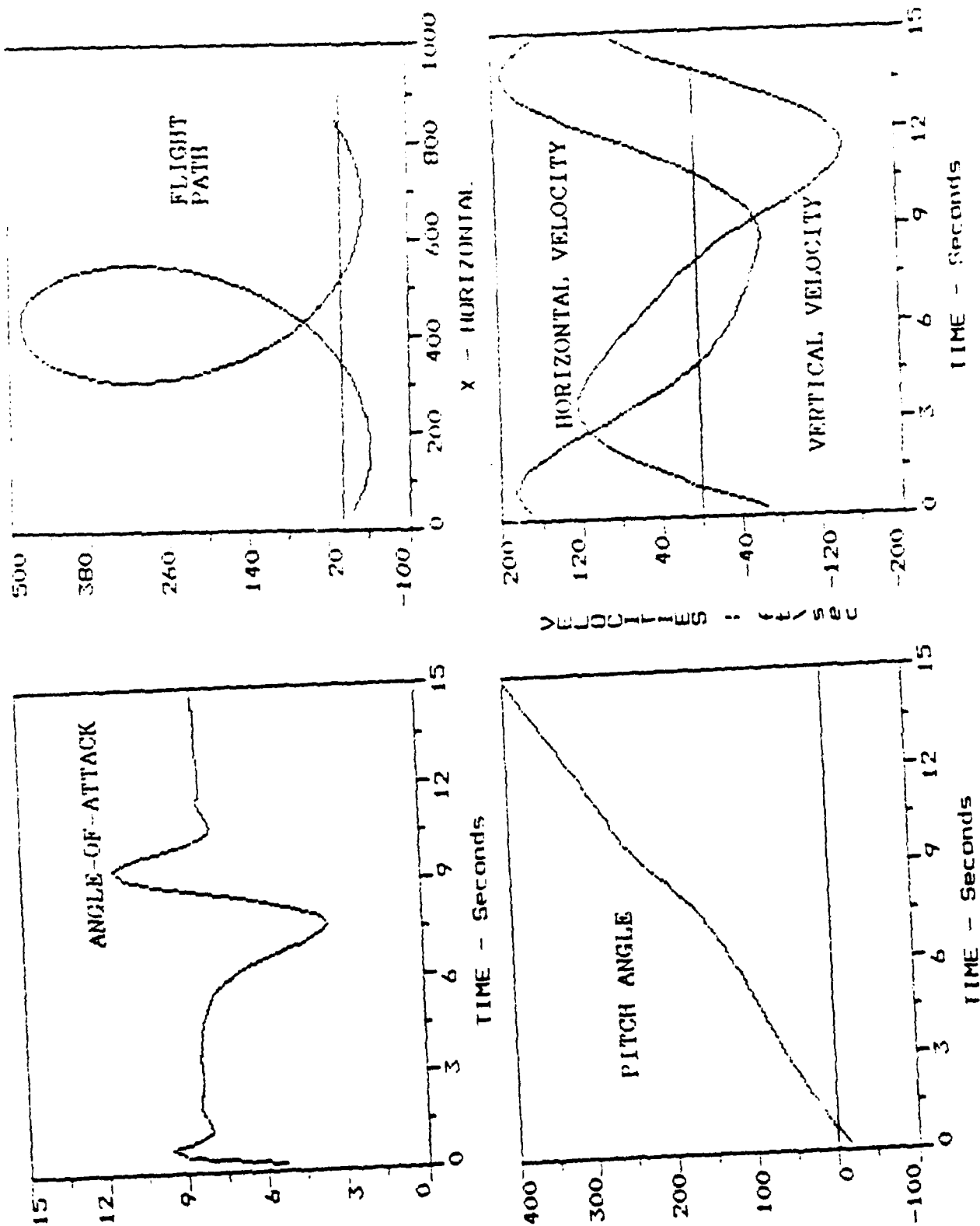


Figure IV-1
Looping Aircraft Simulation Results

SECTION V

DYNAMIC ANALYSIS

By making some assumptions to keep the model of the aircraft dynamics linear, it is possible to gain a qualitative insight into the reaction of a two-dimensional aircraft with a rotating or oscillating wing.

Using Equation II-3 and assuming the thrust force acts along the flight path of the aircraft, we can write

$$\dot{\alpha} = \dot{\theta} + \{F_{zf} - L\} / mV_T \quad (V-1)$$

In keeping with the objective of linearizing the system, by assuming that the thrust is exactly equal to the drag and gravitational force along the flight path, from Equation II-2 we find that $\dot{V}_T = 0$ and V_T is a constant.

By taking the differential of Equation V-1, using equation II-1, and assuming as before that the thrust acts through the center of gravity of the aircraft, we find that

$$\ddot{\alpha} = M_{\alpha} / I_{yy} + \frac{d}{dt} \{f_{zf} - L\} / mV_T \quad (V-2)$$

furthermore using equation II-5

$$\frac{d}{dt} \{F_{zf}\} = \frac{d}{dt} \{mg \cos(\theta - \alpha)\} = -mg \dot{\theta} \sin(\theta - \alpha)$$

By assuming small angles, this term can be considered negligible and thus Equation V-2 reduces to

$$\ddot{\alpha} = \frac{M}{A} / \frac{I}{yy} - \frac{d}{dt} \left(\frac{L}{mV} \right) \quad (V-3)$$

For the sake of keeping things linear, the effect of tail damping has also been neglected. (Actual simulations using the two-dimensional model have shown the effect of tail dampening to be a second order effect.)

By using Equation II-6 and along with equations III-1 through III-3 and representing $\alpha_f(t)$ as the variation of the main wing as a function of time we can write.

$$L = A + B\alpha + C\alpha_f(t) + D\alpha_i$$

$$\text{where } A = (qS)_{\text{total}} \times (N_{\text{wing}} + N_{\text{tail}}) C_{l_0}$$

$$B = (qS)_{\text{total}} \times (N_{\text{wing}} + N_{\text{tail}}) \frac{dC_l}{d\alpha}$$

(assuming the wing and tail have the same steady state lift/angle-of-attack slope and C_{l_0})

$$C = (qS)_{\text{total}} \times N_{\text{wing}} \frac{dC_l'}{d\alpha}$$

(here the $dC_l'/d\alpha$ denotes that the lift/angle-of-attack relationship may be different for the unsteady case)

$$D = (qS)_{\text{total}} \times N_{\text{tail}} \frac{dC_l}{d\alpha}$$

in this analysis, the lift, drag, and moment contributions of the fuselage have also been neglected.

$$\text{Thus } \frac{dL}{dt} = B\dot{\alpha} + C\alpha_f(t)$$

For further simplification, the following assumptions are made to Equation II-7.

$$(a) C_{m_{\text{wing}}} = C_{m_{\text{fuse}}} = C_{m_{\text{tail}}} = 0$$

$$(b) D_{\text{total}} \sin \alpha \ll L_{\text{total}} \cos \alpha$$

$$(c) \cos \alpha = 1$$

Then the moment equation can be written

$$M_A = F + G\alpha + H\dot{\alpha}_f(t) + J\dot{\alpha}_i$$

$$\text{where } F = (qS)_{\text{total}} \times (N_{\text{wing}} \bar{X}_{\text{wing}} + N_{\text{tail}} \bar{X}_{\text{tail}}) C_{l_o}$$

$$G = (qS)_{\text{total}} \times (N_{\text{wing}} \bar{X}_{\text{wing}} + N_{\text{tail}} \bar{X}_{\text{tail}}) \frac{dC_l}{d\alpha}$$

$$H = (qS)_{\text{total}} \times (N_{\text{wing}} \bar{X}_{\text{wing}} \frac{dC_l'}{d\alpha})$$

$$J = (qS)_{\text{total}} \times (N_{\text{tail}} \bar{X}_{\text{tail}} \frac{dC_l}{d\alpha})$$

The second-order ordinary, differential equation then can be written

$$\ddot{\alpha} + P\dot{\alpha} - R = V(t) - T\dot{\alpha}_f(t) + W\alpha_i + Y \quad (V-4)$$

Table V-I summarizes the coefficients in Equation V-4.

Equation V-4 has the following solution for the case when $\alpha_f(t)$ is simply the average input K , assuming the initial conditions for straight and level flight, $\alpha(0) = \alpha_s$ and $\dot{\alpha}(0) = 0$.

$$\alpha = \alpha_s + \frac{Z + VK}{R} \left[\left\{ \cos \Omega t + \frac{P}{2\Omega} \sin \Omega t \right\} \exp\left(-\frac{Pt}{2}\right) - 1 \right] \quad (V-5)$$

where $Z = W_i + Y$

$$\Omega = \{-R - P^2/4\}^{1/2}$$

If now an oscillating airfoil is incorporated having the following characteristics

$$\alpha_f(t) = K(1 - \cos \omega t) \text{ and } \dot{\alpha}_f(t) = K\omega \sin \omega t$$

The solution to Equation V-4 becomes

$$\alpha = \alpha_{ave} - \bar{\Phi} \exp\left(-\frac{Pt}{2}\right) \cos \Omega t - \left\{ \frac{\bar{\Phi} Pt}{2} + \Psi \omega \right\} \exp\left(-\frac{Pt}{2}\right) \sin \Omega t + \bar{\Phi} \cos \omega t + \Psi \sin \omega t \quad (V-6)$$

where α_{ave} is the solution of Equation V-4 for an average input i.e. the solution given by Equation V-5.

TABLE V-1

COEFFICIENTS IN EQUATION V-4

$$P = \frac{B}{mV_T} = \frac{(qS)_{\text{total}}}{mV_T} \left\{ N_{\text{wing}} + N_{\text{tail}} \right\} \frac{dCl}{d\alpha}$$

$$R = \frac{G}{I_{yy}} = \frac{(qS)_{\text{total}}}{I_{yy}} \left\{ N_{\text{wing}} \bar{X}_{\text{wing}} + N_{\text{tail}} \bar{X}_{\text{tail}} \right\} \frac{dCl}{d\alpha}$$

$$V = \frac{H}{I_{yy}} = \frac{(qS)_{\text{total}}}{I_{yy}} \left\{ N_{\text{wing}} \bar{X}_{\text{wing}} \right\} \frac{dCl'}{d\alpha}$$

$$T = \frac{C}{mV_T} = \frac{(qS)_{\text{total}}}{mV_T} \left\{ N_{\text{wing}} \bar{X}_{\text{wing}} \right\} \frac{dCl'}{d\alpha}$$

$$W = \frac{J}{I_{yy}} = \frac{(qS)_{\text{total}}}{I_{yy}} \left\{ N_{\text{tail}} \bar{X}_{\text{tail}} \right\} \frac{dCl}{d\alpha}$$

$$Y = \frac{F}{I_{yy}} = \frac{(qS)_{\text{total}}}{I_{yy}} \left\{ N_{\text{wing}} \bar{X}_{\text{wing}} + N_{\text{tail}} \bar{X}_{\text{tail}} \right\} Cl_o$$

$$\bar{Q} = \frac{VK(\omega^2 + R) + \omega^2 TKP}{(\omega P)^2 + (\omega^2 + R)^2}$$

$$\Psi = \frac{TK(\omega^2 + R) - VK(\omega P)^2}{(\omega P)^2 + (\omega^2 + R)^2}$$

Figure V-1 and V-2 shows the total solution of Equation V-6 plus the solution broken down into its component parts for oscillation rates of 20 and 200 deg/sec respectively. For high oscillation rates, the second part of Equation V-6 makes a negligible contribution after a second or so. And even for low oscillation rates, this portion of the solution is a sinusoidally varying function about a value of zero. Thus we would expect that when the angle-of-attack expressed as a function of time is integrated to determine the pitch, velocities, and trajectory that its effect would cancel out. Therefore for sinusoidly oscillating wings, using the average value of the oscillation in lieu of a time dependent input will give essentially the same results, at least for large rates of oscillation in comparison to the total duration of the oscillation.

Figures V-3 and V-4 show comparisons of results between the solution given by Equation V-6 and the two-dimensional simulation model for identical aircraft characteristics, flight conditions, and initial conditions. Other comparisons using oscillation rates down to about 10 degrees-per-second

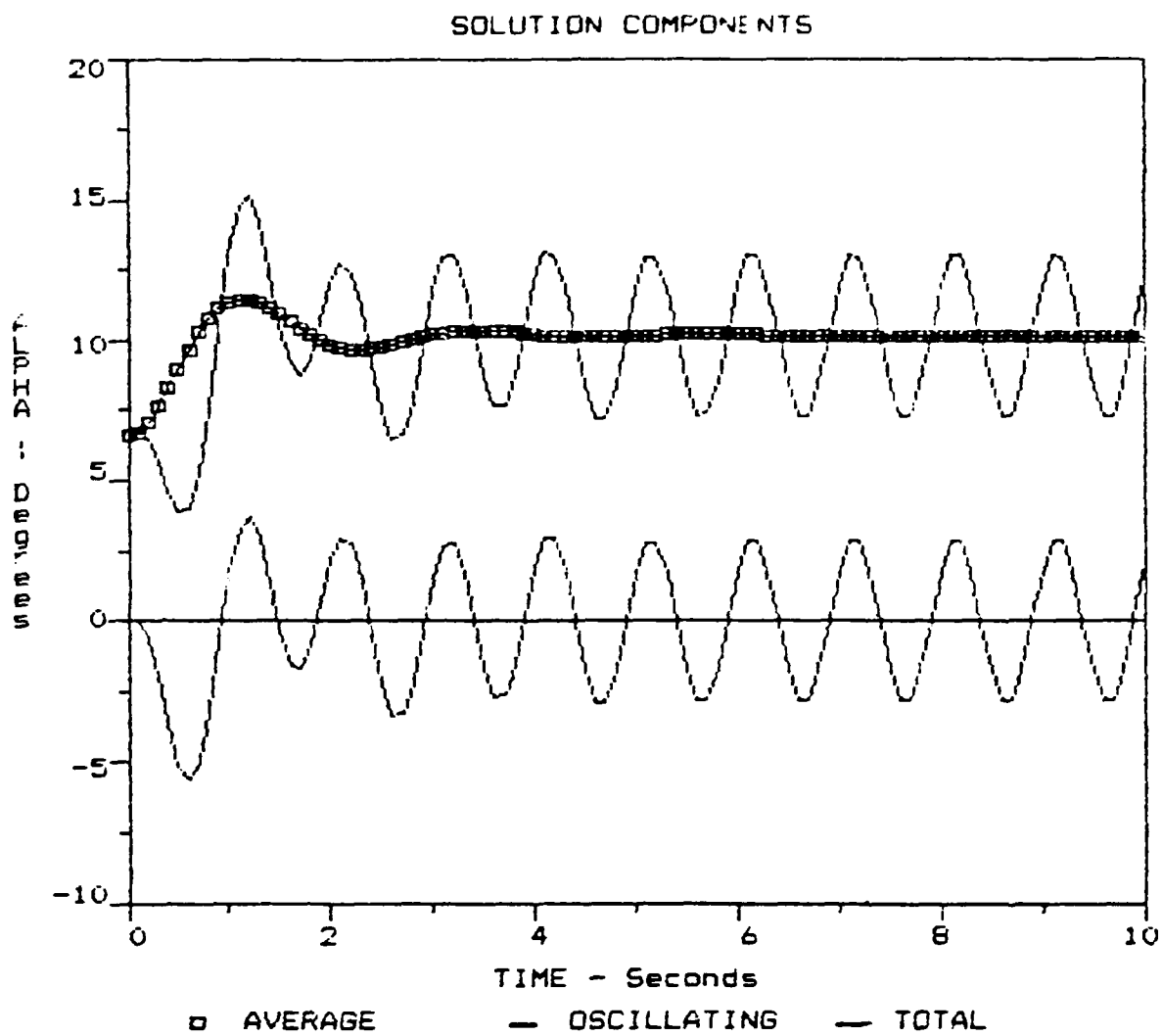


Figure V-1

Differential Equation Solution Components for
Wing Oscillation of $10(1 - \cos 2\pi t)$, 20 deg/sec

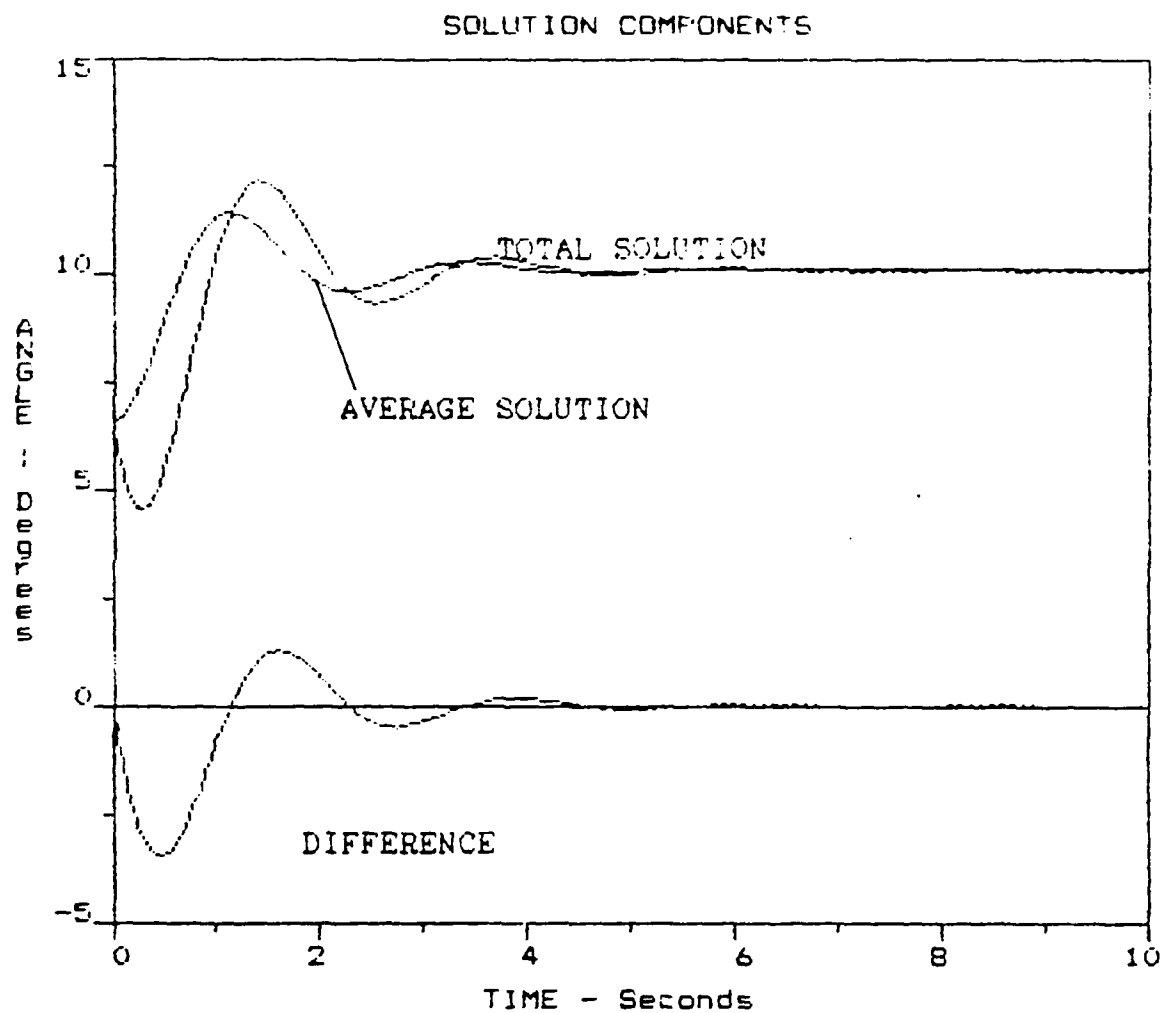


Figure V-2

Differential Equation Solution Components for
Wing Oscillation of $10(1 - \cos 20\pi t)$, 200 deg/sec

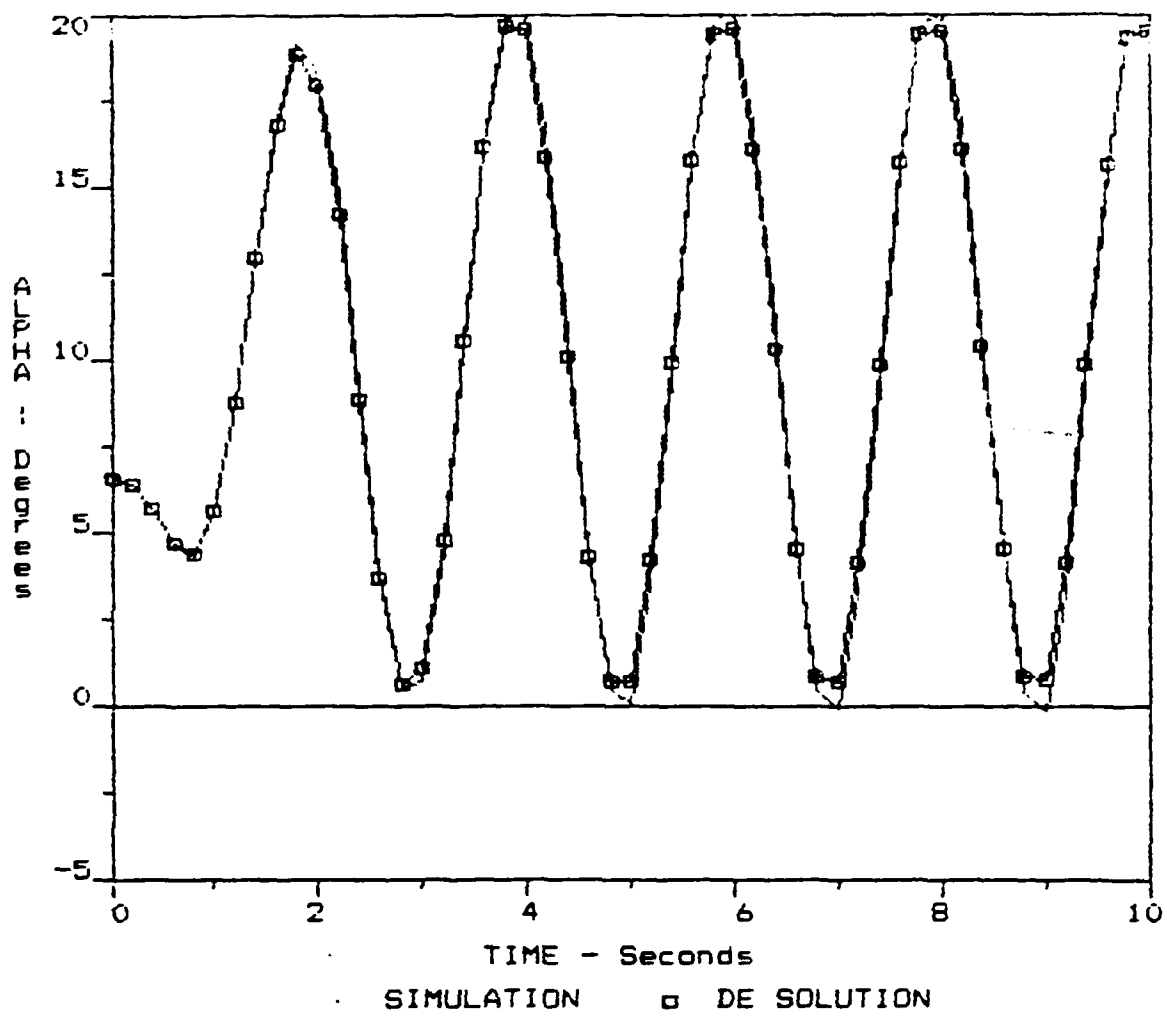


Figure V-3
Comparison of Solutions for an Oscillation
Rate of 10 deg/sec

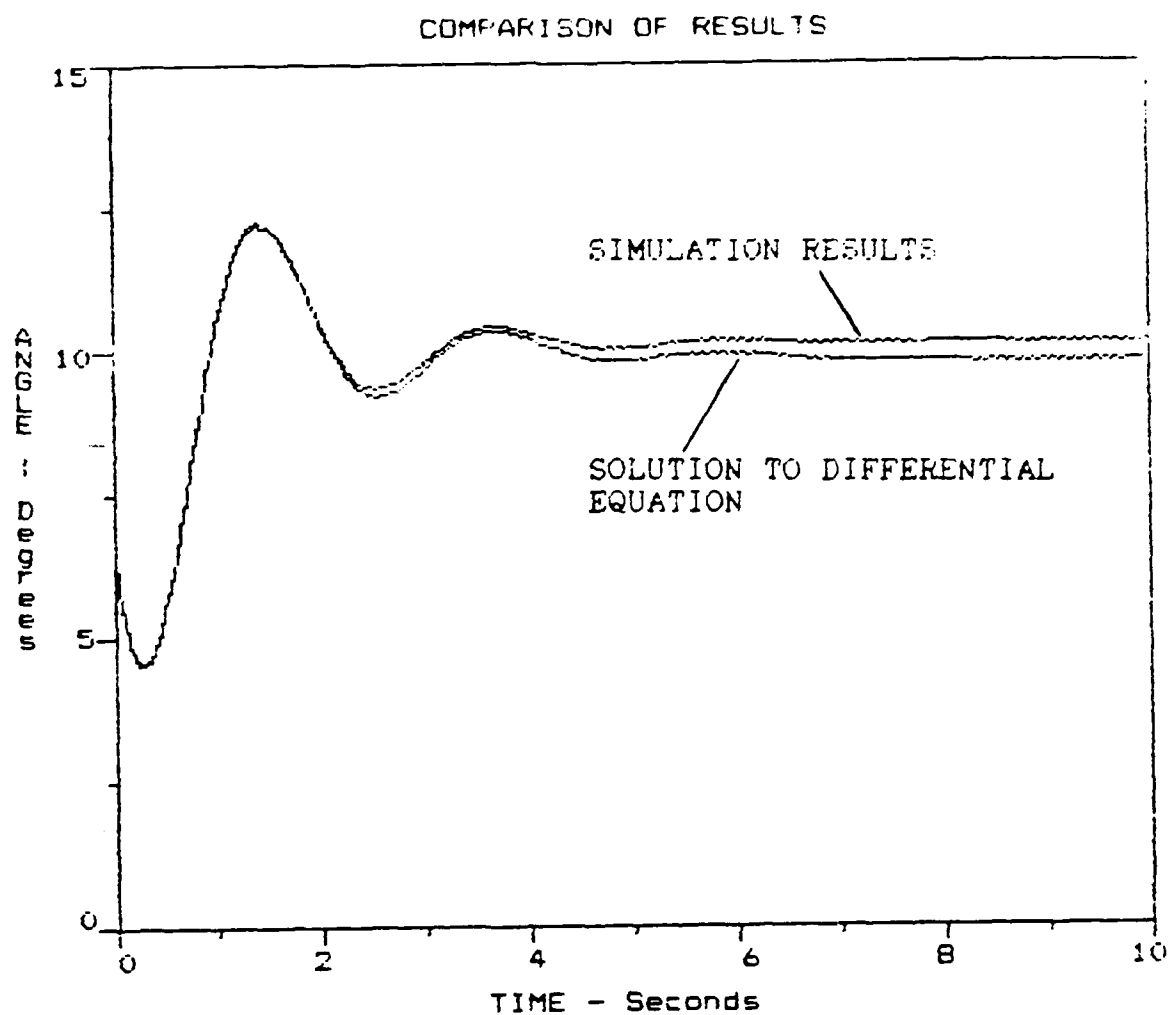


Figure V-4
Comparison of Solutions for an Oscillation
Rate of 200 deg/sec

gave similar close agreement further verifying the accuracy of the two-dimensional model.

In order to assess the effect of an airfoil pitched rapidly at a constant rate, an input such as shown in Figure V-5 was used.

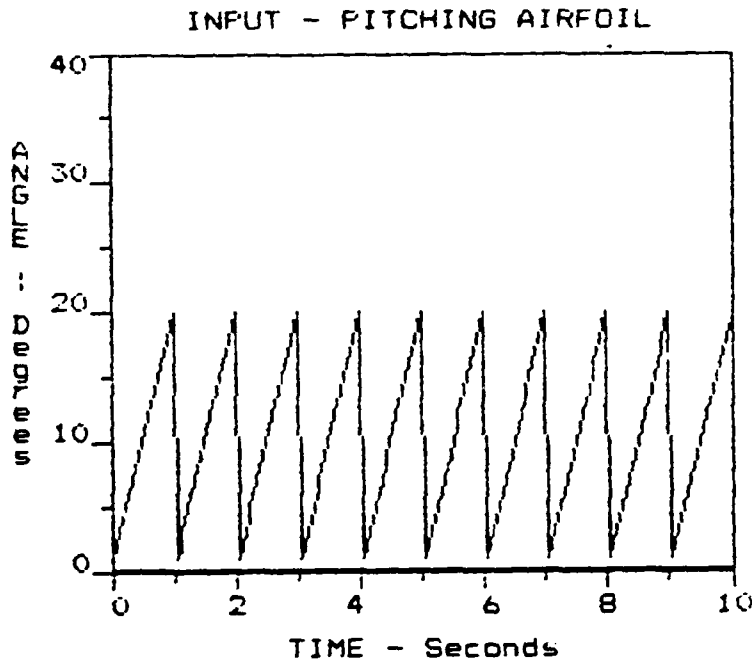


Figure V-5

Representative Pitching Airfoil

Using Laplace Transforms to solve Equation V-4 for the same initial conditions as before, but with this input, we find the solution in the Laplace domain to be

$$\begin{aligned}
 \alpha(s) = & \frac{KV + Z}{s^2(s^2 + Ps - R)} + \frac{KV - T\dot{\alpha}}{s^2(s^2 + Ps - R)} + \\
 & \frac{V\dot{\alpha}}{s^2(s^2 + Ps - R)} - \frac{Vl\dot{\alpha}}{s^2(s^2 + Ps - R)(1 - e^{-ls})}
 \end{aligned} \tag{V-7}$$

where $\dot{\alpha}$ = airfoil pitch rate

T = period of pitching motion

While the inverse of Equation V-7 could be found with some tedious effort, we can determine the character of the solution without finding the inverses of each of the terms.

First of all, the first term of Equation V-7 is identical to the "average" or first term in Equation V-6 when written in the Laplace domain. Secondly, we can use the excellent agreement previously shown between the solution of the differential equation and the two-dimensional simulation to determine the "total" solution, the left side of the Equation V-7. The difference between this "total" solution and the "average" solution is the part we are interested in analyzing. Figures V-6 and V-7 shows the results of this technique for two pitch rates, 20 and 200 degree-per-second respectively. The results are quite similar to those of the previously discussed oscillating airfoil. For high pitch rates, the contribution is very small, especially after a few seconds. For the lower pitch rates, the contribution oscillates around zero and thus will be cancelled out in subsequent integrations.

The above conclusion has important ramifications for simulating an aircraft incorporating oscillating and pitching airfoils. Because the average "input" can give essentially the same results as inputting the detailed characteristic of the pitching or oscillation, computation can be greatly simplified.

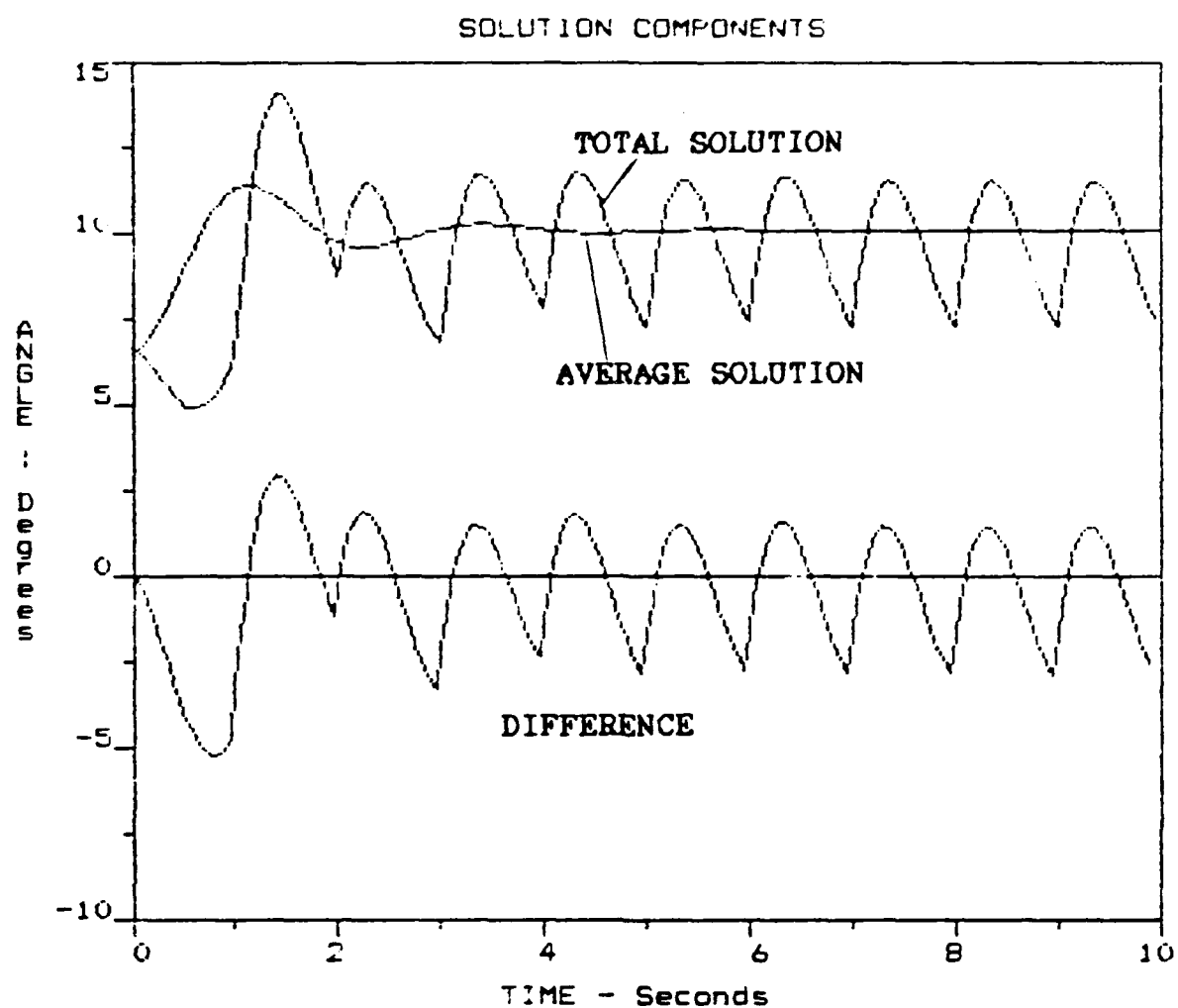


Figure V-6
Components of the Solution for an Airfoil
Pitched at a Constant rate of 20 deg/sec

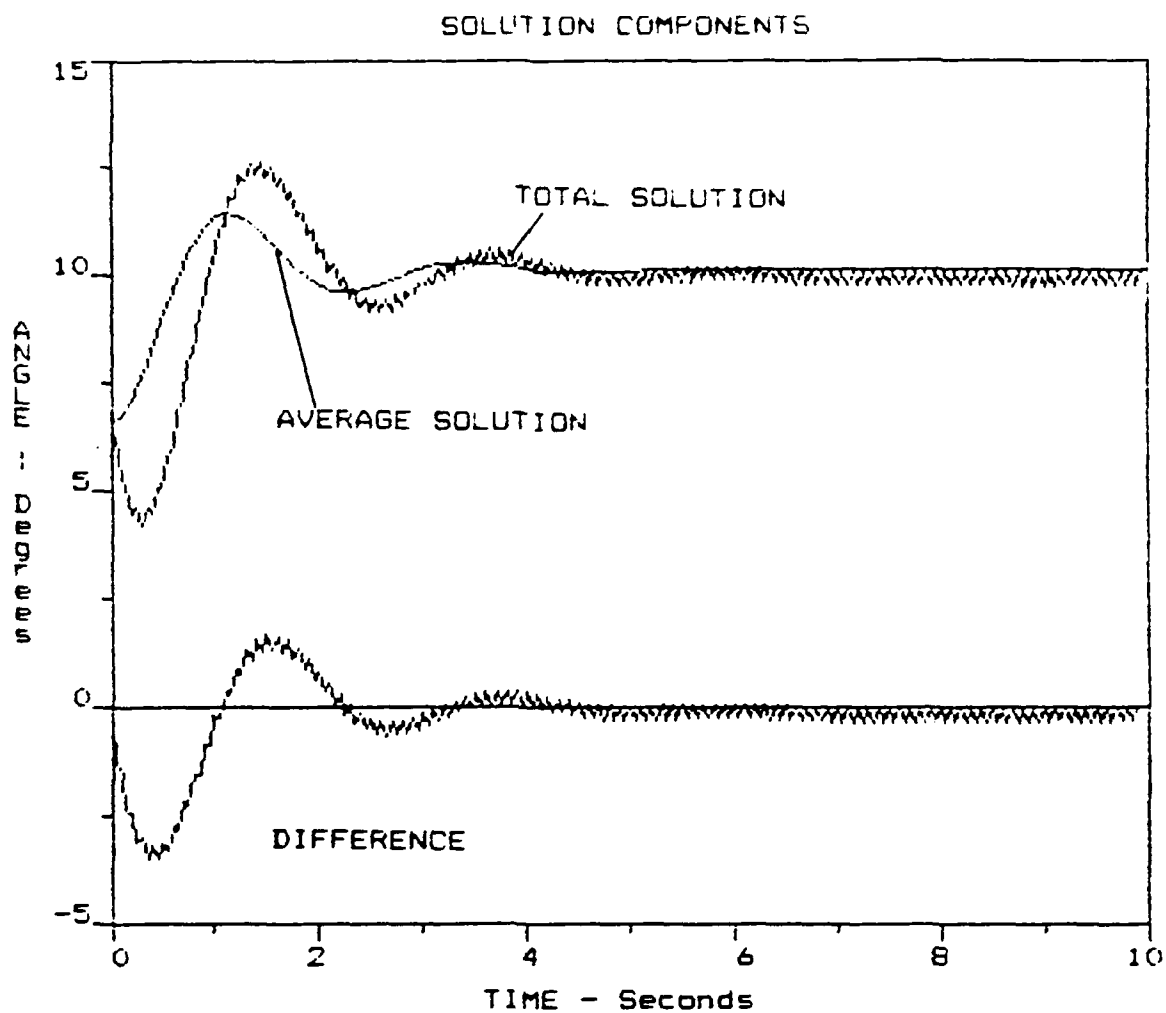


Figure V-7

Components of the Solution for an Airfoil
Pitched at a Constant Rate of 200 deg/sec

This is especially important in such cases as oscillating airfoils with their hysteresis characteristics. In essence, the effect of oscillating or pitching an airfoil can be considered the mechanism for allowing an airfoil to operate at much higher angles of attack without stalling. For flight mechanic simulations, the average value of the lift coefficient attained can be used rather than details on the lift as a function of time.

SECTION VI

SIMULATION RESULTS

The two-dimensional model previously described was used to simulate the flight mechanics of an aircraft incorporating either an oscillating or pitching airfoil. The basic aircraft used was essentially the small jet trainer described in Appendix C of Reference [4]. The aircraft characteristics are listed in Table VI-I. The program SIZING (Appendix C) was used to finalize the design for straight and level flight, the condition prior to the application of the effects of rotating the airfoil.

Oscillating Wing. A oscillating main wing was incorporated in the aircraft. The oscillation was modelled by the relationship $K(1 - \cos \omega t)$ which was added to the instantaneous angle-of-attack of the aircraft. The oscillating wing was assumed to have the same C_l and $dC_l/d\alpha$ as when the wing was operated in a fixed position, although the program can easily accomodate different values.

Figure V-1 shows simulation results when $K = 10$ degrees providing a maximum angle-of-attack of 20 degrees above the angle-of-attack of the aircraft itself and a rotation value of $\omega = 360$ deg/sec. The oscillation started 1 second into the flight and ceased after 10 seconds. This equates to a rotation rate of 20 deg/sec. For comparison, the same simulation was performed

TABLE VI-I

AIRCRAFT AND FLIGHT CHARACTERISTICS

Oscillating and Pitching Wing Simulations

WINGSPAN AND CHORD DIMENSIONS

- Main Wing: 25.19 and 5.4 feet
- Horizontal Tail: 10.08 and 2.18 feet
- Fuselage diameter and length: 6 and 24 feet

WEIGHT: 3500 pounds

MOMENT OF INERTIA ABOUT YY AXIS: 4800 lbs-sec²

DISTANCE BETWEEN CENTER-OF-GRAVITY AND COMPONENT

- Wing: 0.5 feet
- Tail: -11.9814 feet
- Fuselage: 0

THRUST: 449.885 pounds

INITIAL CONDITIONS

- Airspeed: 175 ft/sec
- Altitude: Sea Level
- Pitch Rate and Angle: 0 and 6.50659 degrees

AERODYNAMIC PARAMETERS

- Wing and Tail C_l and $dC_l/d\alpha$: 0.02 and 0.1
- Wing and Tail C_d and e : 0.04, 0.85
- Fuselage C_l , C_d , $dC_l/d\alpha$, $dC_d/d\alpha$
all = 0.005
- Moment Coefficients: all = 0

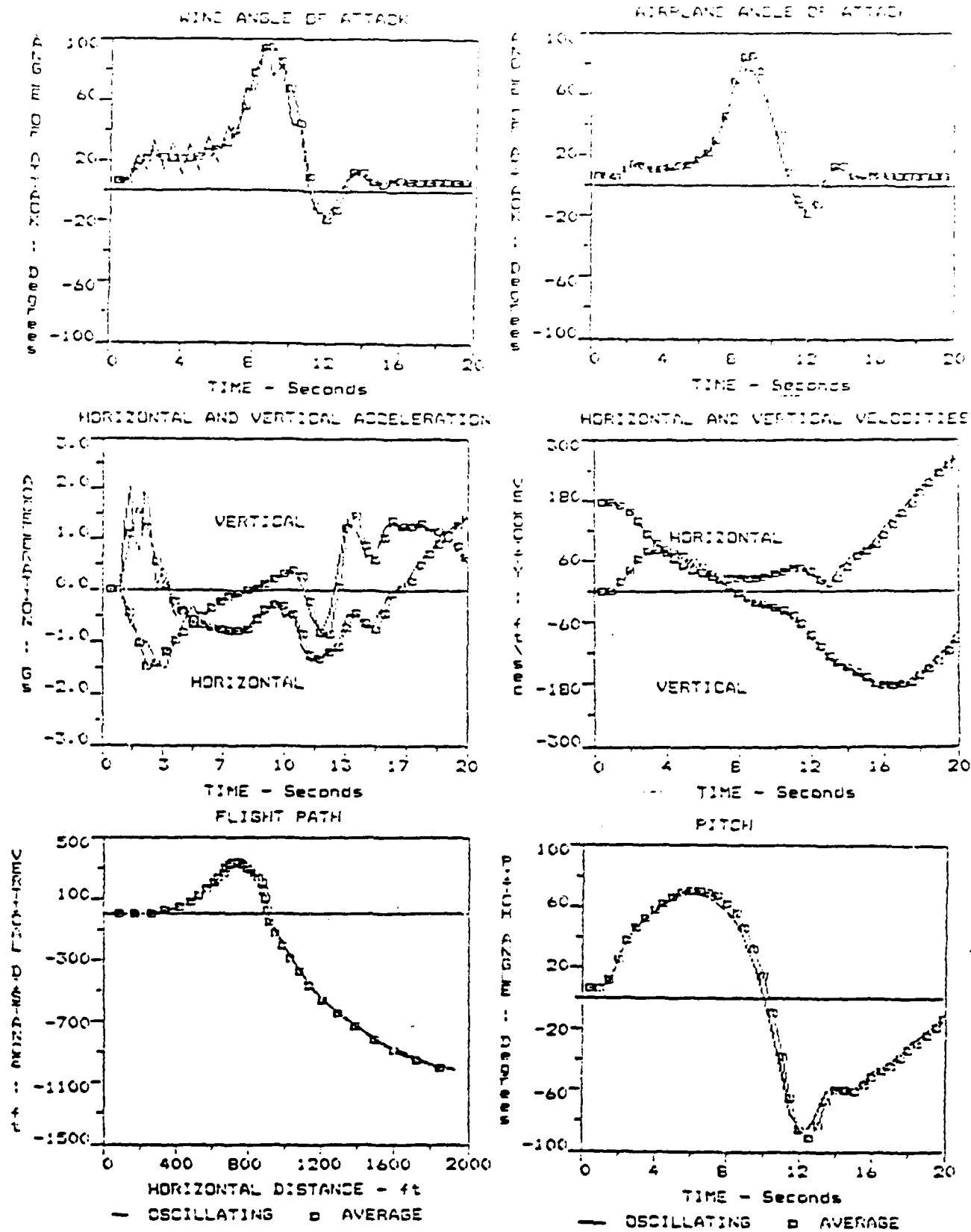


Figure VI-1

Results of Incorporating an Oscillating Airfoil
Oscillation Rate - 20 deg/sec

using an average value of 10 degrees above the instantaneous angle-of-attack of the aircraft. As can be seen, the results are very similar. The simulation was repeated using an oscillation rate of 200 deg/sec ($\omega = 3600$ deg/sec). Again as seen in Figure VI-2, the results of using detailed oscillations and only the average value of the oscillation are again very similar especially the aircraft trajectory and the velocity and acceleration profiles. It should be noted that in these simulations, the aircraft and wing angles-of-attack reach values well beyond the point of stall. Later simulations will show a more realistic case where the angle-of-attack is limited to the unstalled condition. However, the object here was to compare the results between detailed and average inputs.

Next, the capabilities of the model to handle the effects of an oscillating wing on the horizontal tail were assessed. Since no experimental data was available for reasonable wing-tail separation distances, an aerodynamic model was hypothesized. In this case, the effect was assumed to be 25 percent of the additional lift produced by the wing and lagged the wing oscillations by the time it takes for the effect to move downstream, in this case about 0.07 seconds. The results of this simulation are shown in Figure VI-3. As can be seen, the effect of oscillation on the tail are quite noticeable and thus should be considered in any realistic simulation. However, data is needed for this interaction at realistic separation distances.

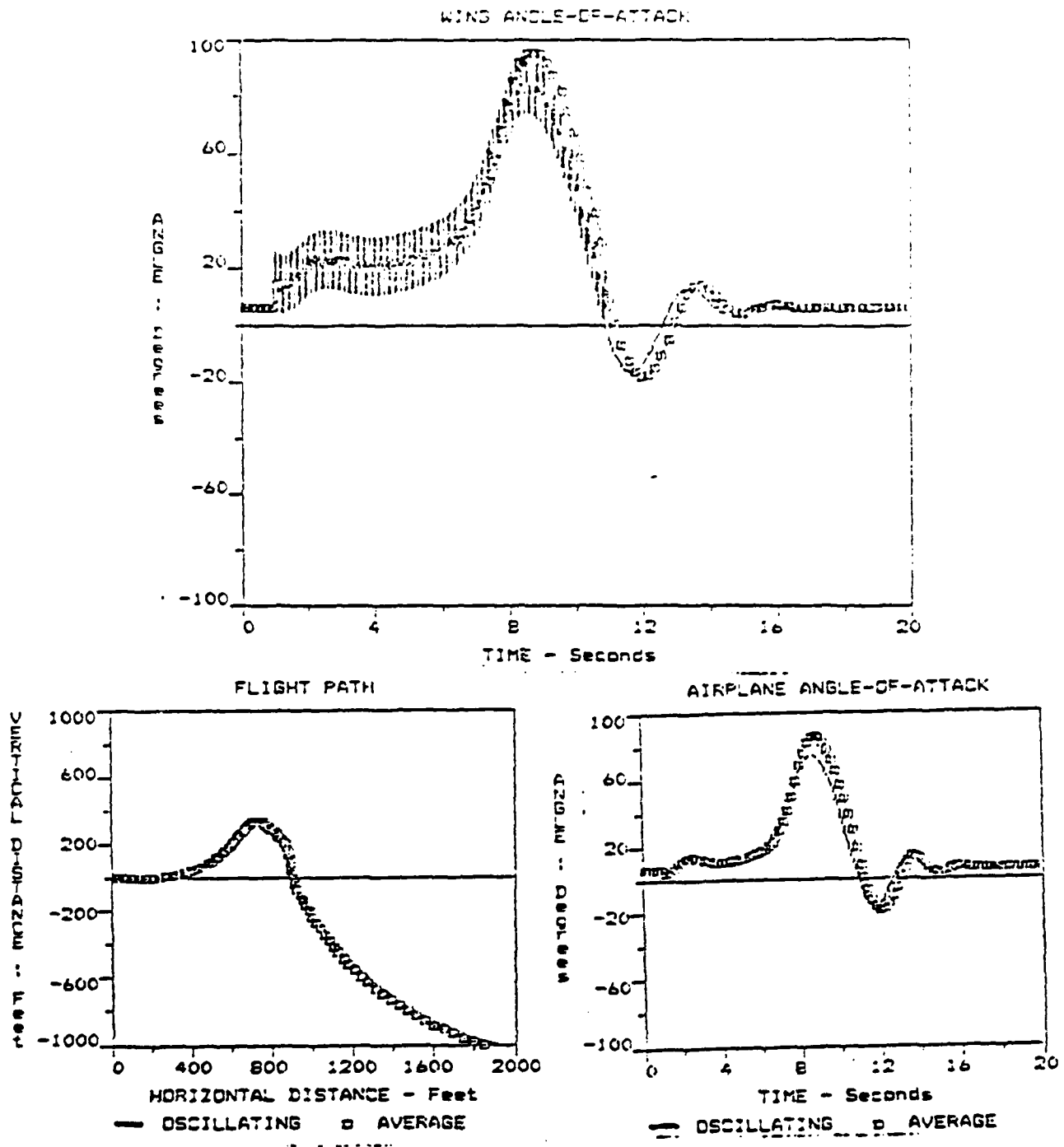


Figure VI-2
 Results of Incorporating an Oscillating Airfoil
 Oscillation Rate - 200 deg/sec

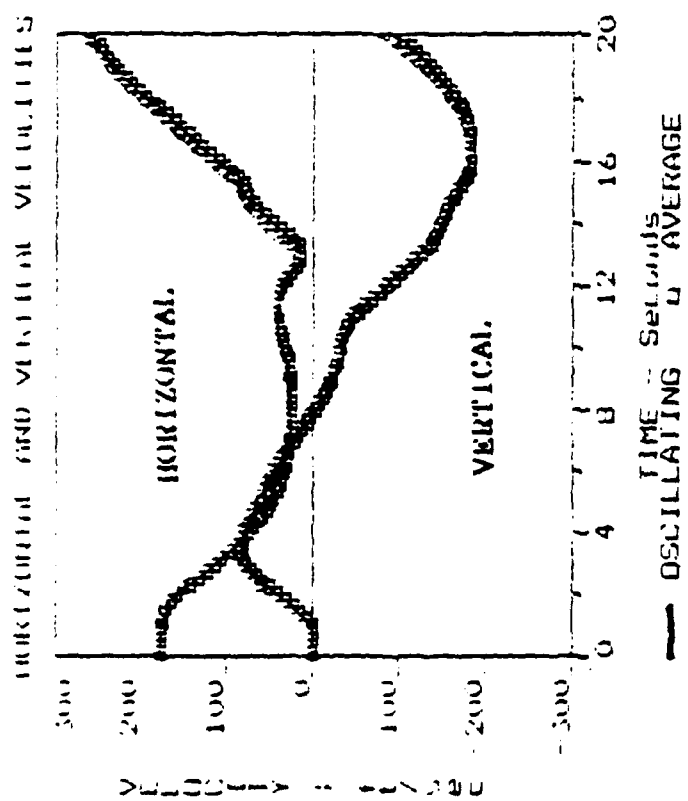
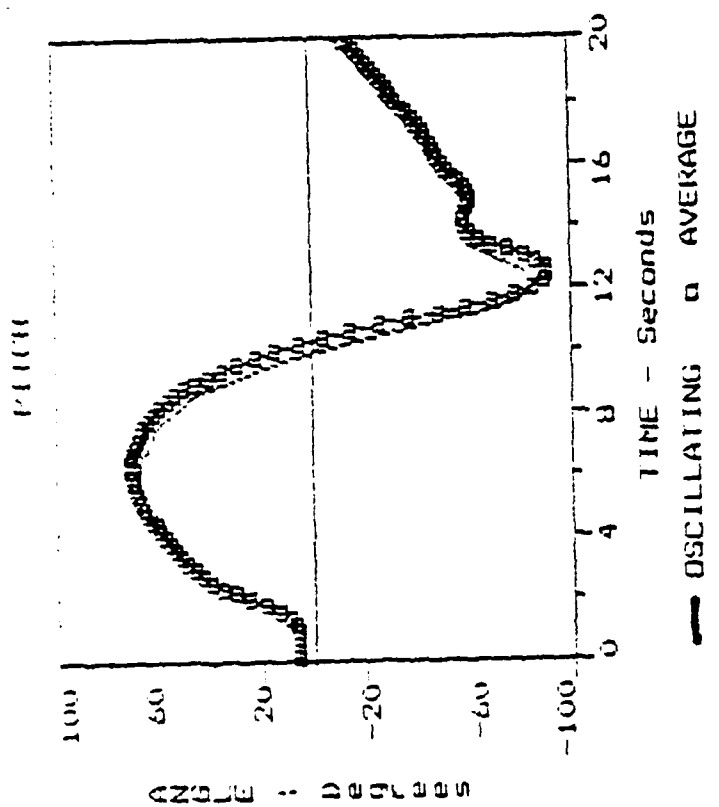


Figure VI-2 (Cont)

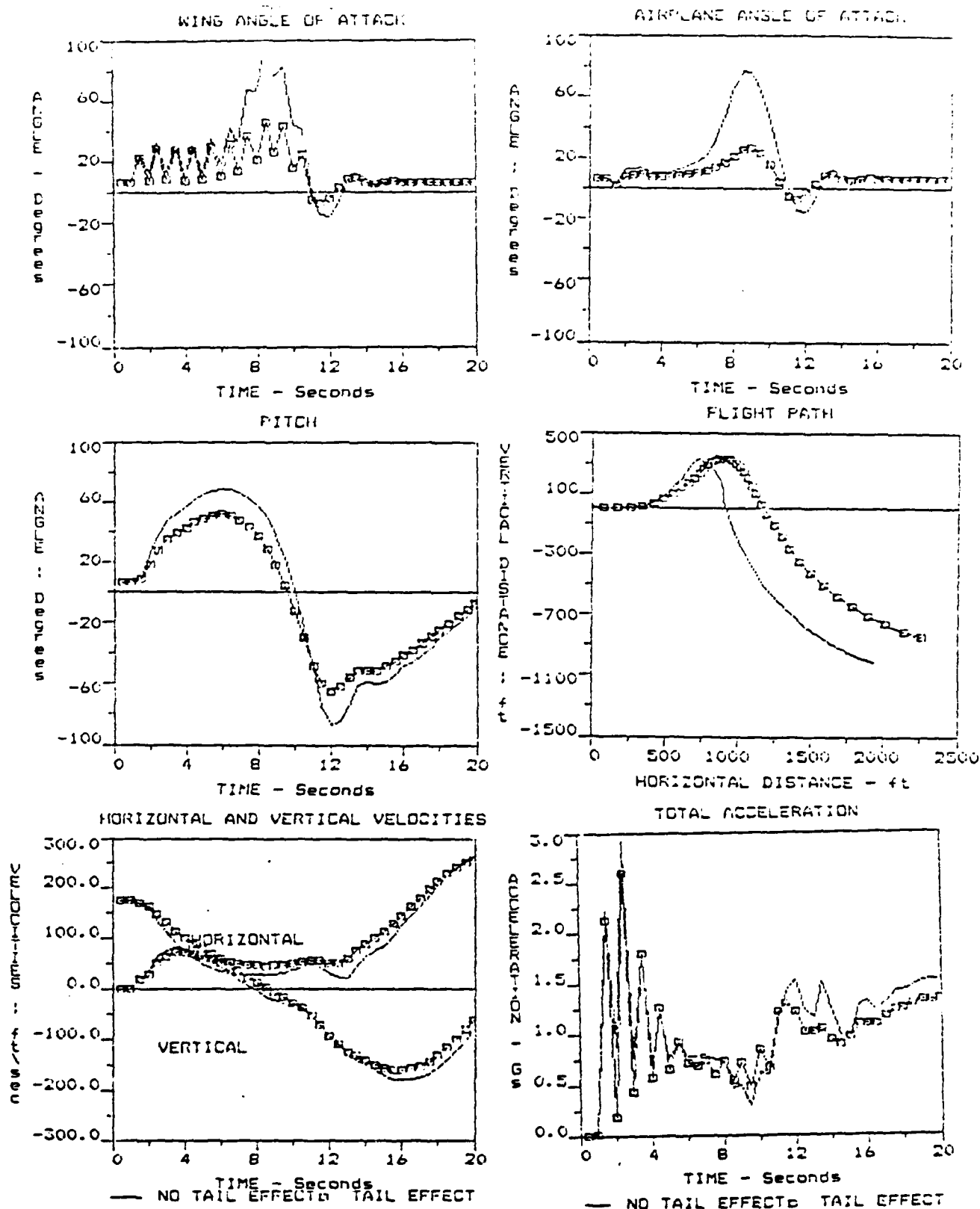


Figure VI-3

Simulation Results Showing the Effect of Rotating
on Tail Surface

A simulation was made to determine if an average tail input could be substituted for a detailed oscillating input. The results are shown in Figure VI-4, and again the results are quite similar.

Pitching Wing. To test the simulation model for a pitching airfoil pitched at a rate of 200 feet/second. In this simulation, the airfoil was assumed to return to its original angle (the angle-of-attack of the aircraft) instantaneously after reaching a maximum value of 20 degrees. The results of this simulation is shown in Figure VI-5 along with the results of only using an average lift value of 10 degrees above aircraft angle-of-attack. Again the results are almost identical.

Advantage of Pitching/Oscillating Airfoils. This simulation compared the example aircraft with and without an oscillating airfoil. In this case the wing was oscillated at a rate of 200 degrees/second. From previous discussion, we would expect that the essentially the same results if the wing was oscillated or pitched at a lower or higher rate, or if only an average value was used. $THRUST = 10500(1 - 449.885[VTAS]/175)$ and the aircraft was given a positive pitching moment coefficient of 0.3 about the aircraft center of gravity. Finally, the maximum angle of attack of the wing was limited to about 30 degrees representing the maximum angle-of-attack that can be used without stalling for a rapidly rotating wing.

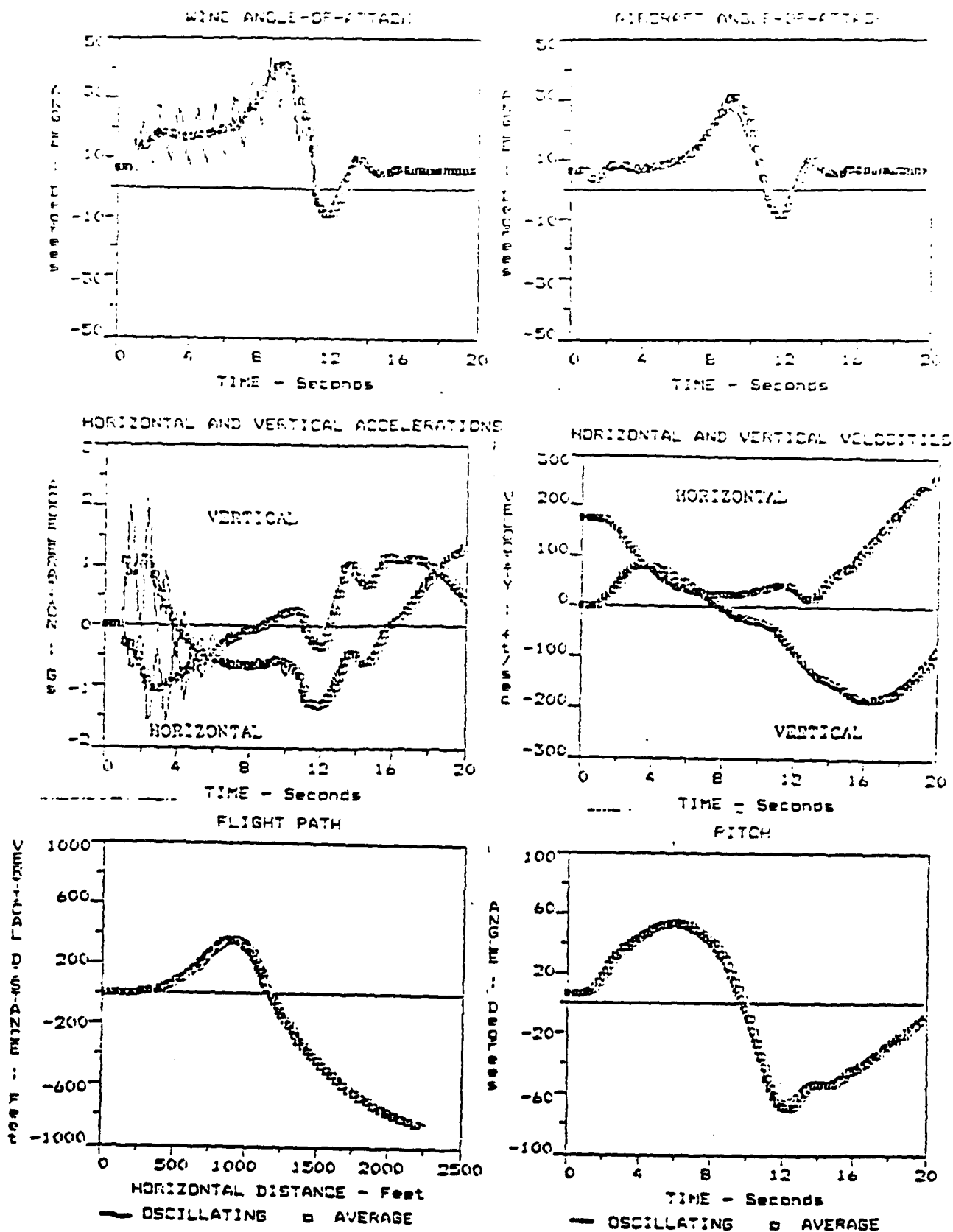


Figure VI-4

Comparison of Effect of Simulating the Wing-Tail Interaction by a Detailed and an Average Rotation

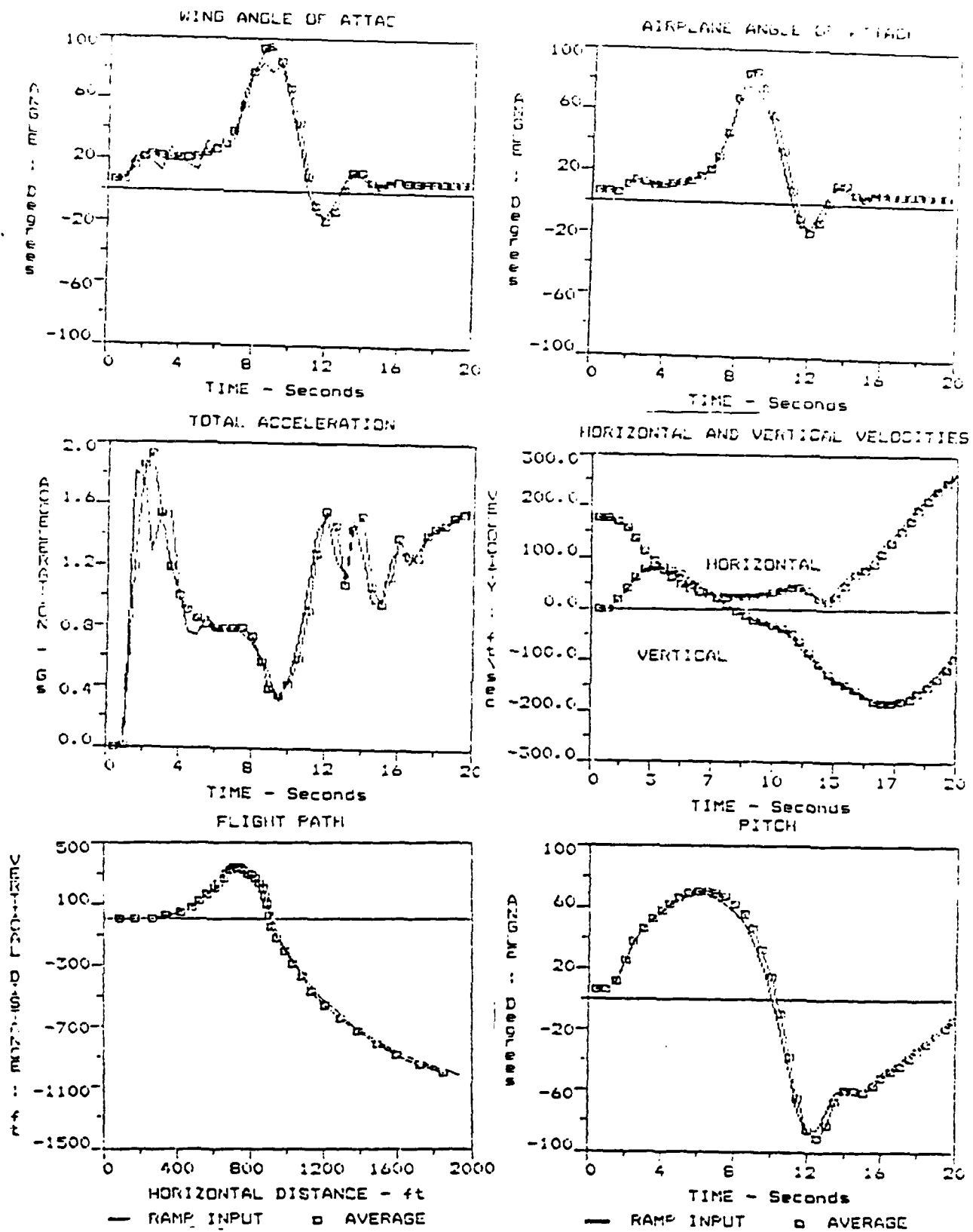


Figure VI-5

Simulation of a Aircraft with a Rapidly Pitching Wing. Pitch Rate - 200 deg/sec for 10 seconds.

The results of this simulation are shown in Figure VI-6. From the flight path, it can be seen that there is a definite advantage in incorporating a rotating airfoil, at least for this simple example.

Comparison with Differential Equation Solution. The results of the simulation using the characteristics listed in Table VI-I were compared with the solution of the linear differential equation discussed in Section V for the same conditions. In both cases drag and weight along the flight path were assumed to equal thrust. The comparison of the aircraft angle-of-attack determined by the two methods is shown in Figure VI-7. The comparison shows that factors such as the tail dampening and drag, which were neglected in deriving the differential equation, have a relatively small effect on the solution, at least for this example.

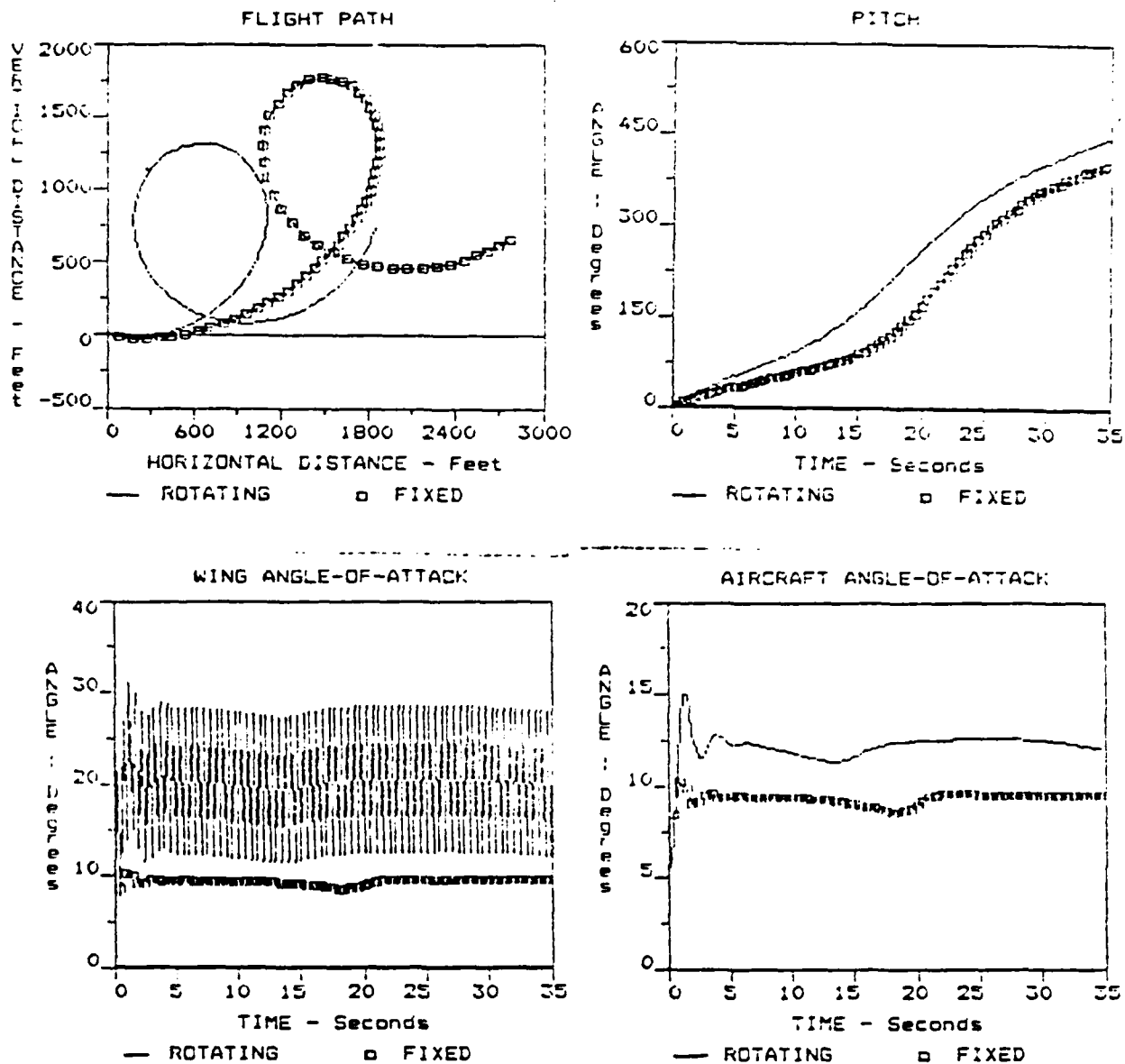


Figure VI-6

Comparison of a Light Aircraft with and without
a Rotating Airfoil - Rotation Rate = 200 deg/sec

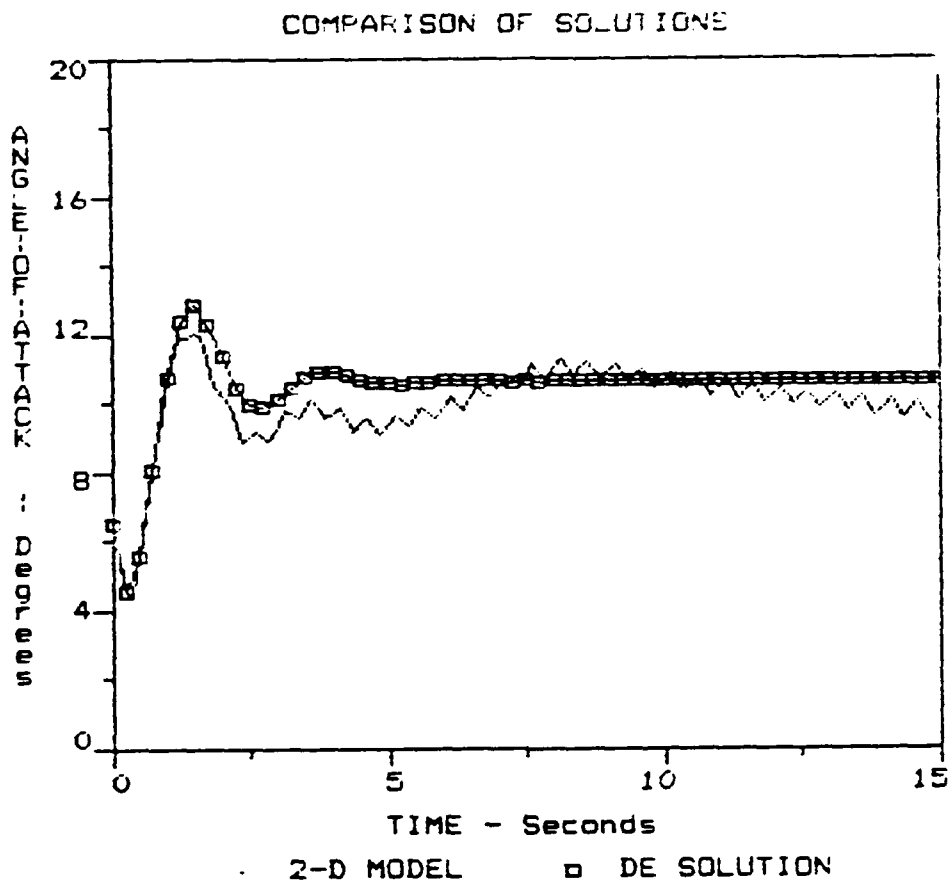


Figure VI-7

Comparison of Results - Differential Equation Solution
Versus Two-Dimensional Simulation

SECTION VII

CONCLUSIONS AND RECOMMENDATIONS

The model developed in this project can be used as a tool to qualitatively evaluate the benefits of pitching, plunging, and oscillating airfoils when incorporated in actual aircraft designs. The term qualitative is used here since to tell the complete story, a three-dimensional, six-degree of freedom, model is needed to realistically evaluate the benefits, and negative aspects, of lift enhancement through dynamic stall delay. Such a model is needed to guide the three-dimensional experiments that are underway.

Because the results of using average versus detailed, time dependent values for the wing rotation provided similar results, it appears that the effect of oscillating or pitching an airfoil can be considered as the mechanism for allowing an airfoil to operate at much higher angles-of-attack without stalling. Thus the designer has a wide choice of rotation schemes and rates to choose from to achieve the same results. Further research is still needed in more rigorous mathematical analysis to extend this conclusion to all situations that can be encountered in an actual aircraft and to include all the nonlinear effects. Techniques such as presented in References [11] and [12] would be appropriate starting points for such further mathematical refinement.

The simulations have shown that there is a very important interaction between a rotating wing and a horizontal tail. A similar key interaction probably exists between a rotating canard and a trailing main wing. Unfortunately, very little experimental data exists on this interaction for the separation distances that would be realistically found on actual aircraft designs. Thus experiments and computations are needed to fill this void.

Since other investigations, for example References [1] and [2], have shown some Reynolds Number dependency, experimental and/or computational research should be extended to the higher Reynolds Numbers found on realistic sized aircraft wings. Also in the case of pitching airfoils, experiments have been almost entirely limited to a single motion where the airfoil is pitched to a maximum value and data collection ceases. Future experiments should include more cyclic pitching motions and data collection while the airfoil is pitched down to its initial position. Finally experimental and/or computational data is needed at higher Mach Number since most of the current research has been done at speeds much lower than those that would be found on an actual highly maneuverable aircraft.

REFERENCES

- [1] "Aerodynamic Parameters for a Pitching Airfoil", William I. Siuru, Jr, John M. Walker, and David C. Chou, AIAA Paper 87-2352 (To be presented at the Applied Aerodynamics; Atmospheric Flight Mechanics; Flight Simulation; Guidance, Navigation, and Control; Lighter-than-air Systems Conferences, Monterey, CA, August 17-19, 1987)
- [2] An Investigation of the Aerodynamic Parameters for a Rapidly Pitching Airfoil, William D. Siuru, Jr. and John M. Walker. (To be published as FJSRL Technical Report)
- [3] Applied Aerodynamics, Leonard Bairstow, London: Longmass Green, & Co. 2nd ed., 1939.
- [4] Airplane Flight Dynamics and Automatic Flight Controls, Jan Roskam, Lawrence, KS: Roskam Aviation and Engineering Corporation, 1982.
- [5] Investigation of High-Angle-of-Attack Maneuvering-Limiting Factors. Donald E. Johnston, David G. Mitchell, and Thomas T. Myers, Systems Technology, Inc. AFWAL-TR-80-3141, December 1980.
- [6] "Control of Wake Structure Behind An Oscillating Airfoil", M.C. Robinson, H.E. Helin, and M.W. Luttges, University of Colorado Department of Aerospace Engineering Sciences. (AIAA proposed paper)
- [7] "Dynamic Stall Wake Interaction With a Trailing Airfoil", J. Walker, AIAA Paper 87-0239, presented at the AIAA 25th Aerospace Sciences Meeting, Reno, Nevada, January 12-15, 1987.
- [8] "Dynamic Stall of Oscillating Airfoils", J.C. Wu, C.M. Wang, Jiunn-Chi Wu, and L.N. Sankar, paper presented at the 42nd Annual Forum of the American Helicopter Society, Washington, DC, June 2-4, 1986.
- [9] Advanced Engineering Mathematics, C.R. Wylie, 2nd edition, New York: McGraw-Hill Book, Company, Inc, 1960.

REFERENCES (Continued)

- [10] Elementary Numerical Analysis. S.L. Conte, New York: McGraw-Hill Book Company, 1965.
- [11] "New Directions of Research in Nonlinear System Theory", Mathukumalli Vidyasagar, Proceedings of the IEEE, Vol. 74, No. 8, August 1986, pp 1060-1091.
- [12] Nonlinear System Analysis and Synthesis, Volume 2. Techniques and Applications. R.V. Ramnath, J.K. Hedrick, and H.M. Paynter, presented at the Winter Annual Meeting of the American Society of Mechanical Engineers, New York, NY, December 1979.

Appendices can be obtained from
Universal Energy Systems, Inc.

MISSION EFFECTIVENESS ANALYSIS OF AN
AIRCRAFT ATTACKING PASSIVE TARGETS

Research Report No. 87-20

by

Boghos D. Sivazlian
and
Hahn-Kyou Rhee

December, 1987

Department of Industrial and Systems Engineering
University of Florida
Gainesville, Florida 32611

This research was sponsored by the Air Force Office of Scientific
Research and conducted by the Universal Energy Systems, Inc. under
Contract No. F49620-85-C-0013

ABSTRACT

A sortie model involving a single aircraft attacking an arbitrary number of independent and identical passive targets is developed. Mathematical expressions for the probability of the various events associated with the sortie are obtained. Recursive relations are developed for obtaining several systems parameters. The results are used to formulate a cost related measure of effectiveness which can be used to determine the optimum sortie time of the aircraft for a given number of targets. Several numerical examples are provided.

I. INTRODUCTION

The development of a sortie model involving a single aircraft versus a single passive target was considered in [1]. The case of two targets was also studied in [2]. In this report, we extend the problem to the case of a single aircraft versus an arbitrary number of passive targets and develop appropriate measures of effectiveness.

II. OBJECTIVE OF THE RESEARCH EFFORT

The object of the studied model is to develop measures of effectiveness for a sortie through the derivation of mathematical expressions for the probabilities of the various events associated with the sortie. Given that initially there are N targets, then the probability expressions to be computed are:

1. $P_N(n,1,t)$, the probability that at time t , $(N-n)$ targets $(n=0,1,\dots,N)$ have been killed and the aircraft is not killed
2. $P_N(n,0,t)$, the probability that at time t , $(N-n)$ targets $(n=0,1,\dots,N)$ have been killed and the aircraft is killed.

The total number of probabilities to be computed is thus $2(N + 1)$. For example, if the initial number of targets to be attacked is $N=2$, then 6 probability expressions are to be derived. The sum of these probabilities must add up to 1, hence

$$\sum_{n=0}^N \left[P_N(n,1,t) + P_N(n,0,t) \right] = 1$$

Once these probabilities are obtained, they may be used to evaluate several measures of effectiveness such as mission reliability,

probability of sortie failure, expected number of targets killed, etc....

In this report, we consider the problem for the case of an arbitrary number N of targets by generalizing the results obtained for $N=1$ and $N=2$ targets.

III. AIRCRAFT SORTIE MODELING

1. Assumptions

We consider a sortie involving a single aircraft against N passive targets. We assume that the aircraft is 100% combat ready and that the time origin of the sortie is the time when the aircraft reaches enemy territory.

Once the aircraft reaches enemy territory, we assume that the time T_1 to acquire any one of the targets before attacking it has a negative exponential distribution with parameter μ . Thus $1/\mu$ is the average time it takes the aircraft to acquire a target and μdt is the probability that a target is acquired in the time interval $(t, t+dt)$. Once acquired, we assume that the target is attacked by the aircraft and that the attack time is negligible. The probability of the target being killed once attacked is p_2 ; hence $(1-p_2)$ is the probability that the target will not be killed once attacked.

Following the attack on this particular target, the aircraft goes into the process of acquiring a second target. We assume again that the time T_2 necessary to acquire a second target before attacking it, from the time the first target is attacked, has again the negative exponential distribution with parameter μ and that the same conditions

prevail as in the case of the first target. Thus μdt is the probability that a second target is acquired in the time interval $(t, t+dt)$ and p_2 is the probability that the target is killed once attacked. The same type of assumptions hold for all N targets.

From the moment the aircraft enters enemy territory, it is surrounded by a hostile environment which takes the form of enemy threats. We assume that the occurrence of enemy threats is a Poisson process with intensity λ . This asserts that the average number of enemy threat encounter per unit time, i.e. the frequency of threat encounter is λ . Equivalently, λdt is the probability that the aircraft will encounter an enemy threat in the time interval $(t, t+dt)$. Encountering more than one enemy threat over an infinitesimal time interval dt is a negligible event. Once an enemy threat is encountered, the probability that the aircraft is killed is p_1 , and the probability that the aircraft is not killed is $(1-p_1)$.

We also assume that all targets have identical characteristics, that they are all passive and that the occurrence of enemy threats is independent of target acquisition and attack. Finally the aircraft is assumed to carry an adequate supply of weapons and ammunitions to possibly destroy all targets.

2. Symbols

t = time parameter; the time origin is taken to be the instant of time the aircraft enters enemy territory

λdt = probability that in the time interval $(t, t+dt)$ the aircraft will encounter an enemy threat; λ is the frequency of occurrence of enemy threat encounters (number of threats per unit time)

μdt = probability that in the interval $(t, t+dt)$ a target is acquired and attacked; $1/\mu$ is the average time elapsed between two successive target acquisitions

p_1 = probability that the aircraft is killed once it encounters an enemy threat

p_2 = probability that the target is killed once attacked

N = number of passive targets

$\alpha = \lambda p_1$

$\beta = \mu p_2$

IV. MODEL FOR N TARGETS

We consider now the situation when during its sortie the aircraft has to deal with N targets. Our objective is to compute $P_N(i, j, t)$, the probability that at time t there are i ($i=0, 1, 2, \dots, N$) remaining targets and that the aircraft is in state j ($j=0, 1$). $j=0$ corresponds to the state "aircraft killed", and $j=1$ corresponds to the state "aircraft not killed". For example $P_N(1, 1, t)$ is the probability that at time t $(N-1)$ targets are killed and the aircraft is not killed.

The initial conditions are

$P_N(N, 1, 0) = 1$, and $P_N(i, j, 0) = 0$ for $i = 0, \dots, N-1$; $j = 0, 1$

1. Equation for $P_N(i, j, t)$

From the results of $N = 1, 2$, (see [1], [2]), we conjecture the following for $P_N(N-n, 1, t)$ and $P_N(N-n, 0, t)$ $n = 0, 1, 2, \dots, N$

$$P_N(N-n, 1, t) = \frac{(\beta t)^n}{n!} e^{-(\alpha+\beta)t}, \quad n = 0, 1, 2, \dots, N-1 \quad (1)$$

$$P_N(N-n, 0, t) = \frac{\alpha}{\alpha+\beta} \left[\frac{\beta}{\alpha+\beta} \right]^n \left[1 - e^{-(\alpha+\beta)t} \sum_{i=0}^n \frac{[(\alpha+\beta)t]^i}{i!} \right] \quad (2)$$

$$n = 0, 1, 2, \dots, N-1$$

$$P_N(0, 1, t) = e^{-\alpha t} \left[1 - e^{-\beta t} \sum_{i=0}^{N-1} \frac{(\beta t)^i}{i!} \right] \quad (3)$$

$$P_N(0, 0, t) = \alpha \int_0^t e^{-\alpha u} \left[1 - e^{-\beta u} \sum_{i=0}^{N-1} \frac{(\beta u)^i}{i!} \right] du \quad (4)$$

These conjectures may be asserted through simple inductive proofs.

To illustrate the approach, let us show that

$$P_N(1, 1, t) = P_N[N-(N-1), 1, t] = \frac{(\beta t)^{N-1}}{(N-1)!} e^{-(\alpha+\beta)t}$$

Assume

$$P_N(2, 1, t) = P_N[N-(N-2), 1, t] = \frac{(\beta t)^{N-2}}{(N-2)!} e^{-(\alpha+\beta)t}$$

Now, it may be verified that

$$P_N(1, 1, t+dt) = P_N(1, 1, t) - (\alpha+\beta) P_N(1, 1, t) dt + \beta P_N(2, 1, t) dt + o(dt)$$

So that

$$\frac{dP_N(1, 1, t)}{dt} + (\alpha+\beta) P_N(1, 1, t) = \beta P_N(2, 1, t)$$

subject to $P_N(1, 1, 0) = 0$

The solution of the differential equation subject to the initial condition is

$$P_N(1, 1, t) = \frac{(\beta t)^{N-1}}{(N-1)!} e^{-(\alpha+\beta)t}$$

But $P_N(N, 1, t) = P_1(1, 1, t) = e^{-(\alpha+\beta)t}$

Hence the conjecture is proved.

2. Expected Number of Targets Killed

Let $N(t)$ be the number of targets killed t unit times after the sortie. The expectation of $N(t)$ is

$$\begin{aligned}
 E_N[N(t)] &= \sum_{n=0}^N n[P_N(N-n,1,t) + P_N(N-n,0,t)] \\
 &= N \sum_{n=0}^N [P_N(N-n,1,t) + P_N(N-n,0,t)] \\
 &\quad - \sum_{n=0}^N (N-n) [P_N(N-n,1,t) + P_N(N-n,0,t)] \\
 &= N - \sum_{i=0}^N i[P_N(i,1,t) + P_N(i,0,t)] \\
 &= N - \sum_{i=2}^N i[P_N(0,1,t) + P_N(i,0,t)] \\
 &\quad - [P_N(1,1,t) + P_N(1,0,t)] \tag{5}
 \end{aligned}$$

$$\text{Now} \quad P_N(i,1,t) = P_{N-1}(i-1,1,t) \quad \text{for } i = 2,3,\dots, N. \tag{6}$$

$$\text{and} \quad P_N(i,0,t) = P_{N-1}(i-1,0,t) \quad \text{for } i = 2,3,\dots, N. \tag{7}$$

$$\begin{aligned}
 \text{Hence} \quad E_N[N(t)] &= N - \sum_{i=2}^N i[P_{N-1}(i-1,1,t) + P_{N-1}(i-1,0,t)] \\
 &\quad - [P_N(1,1,t) + P_N(1,0,t)] \\
 &= N - \sum_{j=1}^{N-1} (j+1) [P_{N-1}(j,1,t) + P_{N-1}(j,0,t)] \\
 &\quad - [P_N(1,1,t) + P_N(1,0,t)]
 \end{aligned}$$

$$\begin{aligned}
&= \left\{ (N-1) - \sum_{j=0}^{N-1} j [P_{N-1}(j,1,t) + P_{N-1}(j,0,t)] \right\} \\
&\quad + \left\{ 1 - \sum_{j=1}^{N-1} [P_{N-1}(j,1,t) + P_{N-1}(j,0,t)] \right\} \\
&\quad - [P_N(1,1,t) + P_N(1,0,t)] \tag{8}
\end{aligned}$$

Now the first bracketed terms on the R.H.S is $E_{N-1}[N(t)]$ while the second bracketed terms is $[P_{N-1}(0,1,t) + P_{N-1}(0,0,t)]$.

So that

$$\begin{aligned}
E_N[N(t)] &= E_{N-1}[N(t)] + [P_{N-1}(0,1,t) + P_{N-1}(0,0,t)] \\
&\quad - [P_N(1,1,t) + P_N(1,0,t)] \tag{9}
\end{aligned}$$

which establishes the recurrence relation.

Now from (3)

$$P_{N-1}(0,1,t) = e^{-\alpha t} \left[1 - e^{-\beta t} \sum_{i=0}^{N-2} \frac{(\beta t)^i}{i!} \right] \tag{10}$$

From (4)

$$P_{N-1}(0,0,t) = \alpha \int_0^t e^{-\alpha u} \left[1 - e^{-\beta u} \sum_{i=0}^{N-2} \frac{(\beta u)^i}{i!} \right] du \tag{11}$$

From (1)

$$P_N(1,1,t) = \frac{(\beta t)^{N-1}}{(N-1)!} e^{-(\alpha+\beta)t} \tag{12}$$

From (2)

$$\begin{aligned}
 P_N(1,0,t) &= \frac{\alpha}{\alpha+\beta} \left[\frac{\beta}{\alpha+\beta} \right]^{N-1} \left[1 - e^{-(\alpha+\beta)t} \sum_{i=0}^{N-1} \frac{[(\alpha+\beta)t]^i}{i!} \right] \\
 &= \frac{\alpha\beta^{N-1}}{(\alpha+\beta)^N} \int_0^t (\alpha+\beta) e^{-(\alpha+\beta)u} \frac{[(\alpha+\beta)u]^{N-1}}{(N-1)!} du \\
 &= \alpha \int_0^t e^{-(\alpha+\beta)u} \frac{(\beta u)^{N-1}}{(N-1)!} du \quad (13)
 \end{aligned}$$

So that

$$\begin{aligned}
 E_N[N(t)] &= E_{N-1}[N(t)] + e^{-\alpha t} \left[1 - e^{-\beta t} \sum_{i=0}^{N-2} \frac{(\beta t)^i}{i!} \right] \\
 &\quad + \alpha \int_0^t e^{-\alpha u} \left[1 - e^{-\beta u} \sum_{i=0}^{N-2} \frac{(\beta u)^i}{i!} \right] du \\
 &\quad - e^{-(\alpha+\beta)t} \frac{(\beta t)^{N-1}}{(N-1)!} - \alpha \int_0^t e^{-(\alpha+\beta)u} \frac{(\beta u)^{N-1}}{(N-1)!} du \\
 &= E_{N-1}[N(t)] + e^{-\alpha t} \left[1 - e^{-\beta t} \sum_{i=0}^{N-1} \frac{(\beta t)^i}{i!} \right] \\
 &\quad + \alpha \int_0^t e^{-\alpha u} \left[1 - e^{-\beta u} \sum_{i=0}^{N-1} \frac{(\beta u)^i}{i!} \right] du \\
 &= E_{N-1}[N(t)] + e^{-\alpha t} \int_0^t \frac{(\beta u)^{N-1}}{(N-1)!} \beta e^{-\beta u} du
 \end{aligned}$$

$$+ \alpha \int_0^t e^{-\alpha u} \int_0^u \frac{(\beta v)^{N-1}}{(N-1)!} \beta e^{-\beta v} dv du \quad (14)$$

The value of the double integral is

$$\alpha \int_0^t \frac{(\beta v)^{N-1}}{(N-1)!} \beta e^{-\beta v} \int_v^t e^{-\alpha u} du dv = \int_0^t \frac{(\beta v)^{N-1}}{(N-1)!} \beta e^{-\beta v} \left[-e^{-\alpha t} + e^{-\alpha v} \right] dv \quad (15)$$

So that substituting (15) in (14) yields

$$\begin{aligned} E_N[N(t)] &= E_{N-1}[N(t)] + \int_0^t \frac{(\beta v)^{N-1}}{(N-1)!} \beta e^{-(\alpha+\beta)v} dv \\ &= E_{N-1}[N(t)] + \frac{\beta^N}{(\alpha+\beta)^N} \left[1 - e^{-(\alpha+\beta)t} \sum_{i=0}^{N-1} \frac{[(\alpha+\beta)t]^i}{i!} \right] \end{aligned} \quad (16)$$

with the stipulation that

$$E_0[N(t)] = 0 \quad (17)$$

To check, let $N=1$

$$E_1[N(t)] = \frac{\beta}{\alpha+\beta} \left[1 - e^{-(\alpha+\beta)t} \right] \quad (18)$$

Integrating the integral term by parts we obtain for $N=2,3,\dots$

$$F_N(t) = \int_0^t \frac{(\beta v)^{N-1}}{(N-1)!} \beta e^{-(\alpha+\beta)v} dv$$

$$\begin{aligned}
&= -\frac{\beta}{\alpha+\beta} e^{-(\alpha+\beta)v} \frac{(\beta v)^{N-1}}{(N-1)!} \Big|_0^t + \frac{\beta}{\alpha+\beta} \int_0^t \frac{\beta^{N-1} v^{N-2}}{(N-2)!} e^{-(\alpha+\beta)v} dv \\
&= -\frac{\beta}{\alpha+\beta} e^{-(\alpha+\beta)v} \frac{(\beta t)^{N-1}}{(N-1)!} + \frac{\beta}{\alpha+\beta} \int_0^t \frac{(\beta v)^{N-2}}{(N-2)!} \beta e^{-(\alpha+\beta)v} dv \\
&= \frac{\beta}{\alpha+\beta} \left[F_{N-1}(t) - e^{-(\alpha+\beta)t} \frac{(\beta t)^{N-1}}{(N-1)!} \right]
\end{aligned}$$

where

$$F_1(t) = \frac{\beta}{\alpha+\beta} \left[1 - e^{-(\alpha+\beta)t} \right]$$

Thus we have

$$\begin{aligned}
E_N[N(t)] &= E_{N-1}[N(t)] + F_N(t) & N=1,2,3,\dots \\
E_0[N(t)] &= 0
\end{aligned} \tag{19}$$

where

$$\begin{aligned}
F_N(t) &= \frac{\beta}{\alpha+\beta} \left[F_{N-1}(t) - e^{-(\alpha+\beta)t} \frac{(\beta t)^{N-1}}{(N-1)!} \right] & N=1,2,3,\dots \\
F_0(t) &= 1
\end{aligned} \tag{20}$$

First, we derive the explicit form of $F_N(t)$ using the recursive relation in (20). Then, using the recursive relation in (19) and the results for $F_N(t)$, we compute the explicit form of $E_N[N(t)]$.

a. Derivation of $F_N(t)$

From the recursive relation (20), we obtain for $N=1$

$$F_1(t) = \frac{\beta}{\alpha+\beta} \left[F_0(t) - e^{-(\alpha+\beta)t} \frac{(\beta t)^0}{0!} \right]$$

Since $F_0(t) = 1$, we have

$$F_1(t) = \frac{\beta}{\alpha+\beta} \left[1 - e^{-(\alpha+\beta)t} \right] \quad (21)$$

For $N=2$, relation (20) becomes

$$F_2(t) = \frac{\beta}{\alpha+\beta} \left[F_1(t) - e^{-(\alpha+\beta)t} \frac{(\beta t)}{1!} \right]$$

Substitute the expression for $F_1(t)$ in (21) into the above relation, we obtain

$$\begin{aligned} F_2(t) &= \frac{\beta}{\alpha+\beta} \left[\frac{\beta}{\alpha+\beta} \left\{ 1 - e^{-(\alpha+\beta)t} \right\} - e^{-(\alpha+\beta)t} \frac{\beta t}{1!} \right] \\ &= \left[\frac{\beta}{\alpha+\beta} \right]^2 \left[1 - e^{-(\alpha+\beta)t} \right] - \left[\frac{\beta}{\alpha+\beta} \right] e^{-(\alpha+\beta)t} \frac{\beta t}{1!} \end{aligned} \quad (22)$$

For $N=3$, we have

$$F_3(t) = \frac{\beta}{\alpha+\beta} \left[F_2(t) - e^{-(\alpha+\beta)t} \frac{(\beta t)^2}{2!} \right]$$

Substituting the value of $F_2(t)$ in (22) yields

$$\begin{aligned}
 F_3(t) &= \frac{\beta}{\alpha+\beta} \left[\left(\frac{\beta}{\alpha+\beta} \right)^2 \left\{ 1 - e^{-(\alpha+\beta)t} \right\} - \left(\frac{\beta}{\alpha+\beta} \right) e^{-(\alpha+\beta)t} \frac{\beta t}{1!} - e^{-(\alpha+\beta)t} \frac{(\beta t)^2}{2!} \right] \\
 &= \left(\frac{\beta}{\alpha+\beta} \right)^3 \left[1 - e^{-(\alpha+\beta)t} \right] - \left(\frac{\beta}{\alpha+\beta} \right)^2 e^{-(\alpha+\beta)t} \frac{\beta t}{1!} \\
 &\quad - \left(\frac{\beta}{\alpha+\beta} \right) e^{-(\alpha+\beta)t} \frac{(\beta t)^2}{2!} \tag{23}
 \end{aligned}$$

Similarly for $N=4$, we have

$$F_4(t) = \frac{\beta}{\alpha+\beta} \left[F_3(t) - e^{-(\alpha+\beta)t} \frac{(\beta t)^3}{3!} \right]$$

Using the result of $F_3(t)$ in (23) yields

$$\begin{aligned}
 F_4(t) &= \frac{\beta}{\alpha+\beta} \left[\left(\frac{\beta}{\alpha+\beta} \right)^3 \left\{ 1 - e^{-(\alpha+\beta)t} \right\} - \left(\frac{\beta}{\alpha+\beta} \right)^2 e^{-(\alpha+\beta)t} \frac{\beta t}{1!} \right. \\
 &\quad \left. - \left(\frac{\beta}{\alpha+\beta} \right) e^{-(\alpha+\beta)t} \frac{(\beta t)^2}{2!} - e^{-(\alpha+\beta)t} \frac{(\beta t)^3}{3!} \right] \\
 &= \left(\frac{\beta}{\alpha+\beta} \right)^4 \left[1 - e^{-(\alpha+\beta)t} \right] - \left(\frac{\beta}{\alpha+\beta} \right)^3 e^{-(\alpha+\beta)t} \frac{\beta t}{1!} \\
 &\quad - \left(\frac{\beta}{\alpha+\beta} \right)^2 e^{-(\alpha+\beta)t} \frac{(\beta t)^2}{2!} - \left(\frac{\beta}{\alpha+\beta} \right) e^{-(\alpha+\beta)t} \frac{(\beta t)^3}{3!} \tag{24}
 \end{aligned}$$

By induction, assume that

$$\begin{aligned}
 F_{N-1}(t) = & \left(\frac{\beta}{\alpha+\beta} \right)^{N-1} \left[1 - e^{-(\alpha+\beta)t} \right] - \left(\frac{\beta}{\alpha+\beta} \right)^{N-2} e^{-(\alpha+\beta)t} \frac{\beta t}{1!} \\
 & - \left(\frac{\beta}{\alpha+\beta} \right)^{N-3} e^{-(\alpha+\beta)t} \frac{(\beta t)^2}{2!} - \left(\frac{\beta}{\alpha+\beta} \right)^{N-4} e^{-(\alpha+\beta)t} \frac{(\beta t)^3}{3!} \\
 & - \dots \dots \dots \\
 & - \left(\frac{\beta}{\alpha+\beta} \right)^2 e^{-(\alpha+\beta)t} \frac{(\beta t)^{N-3}}{(N-3)!} - \left(\frac{\beta}{\alpha+\beta} \right) e^{-(\alpha+\beta)t} \frac{(\beta t)^{N-2}}{(N-2)!} \quad (25)
 \end{aligned}$$

Substitute the value of $F_{N-1}(t)$ in (25) into relation (20); we obtain

$$\begin{aligned}
 F_N(t) = & \frac{\beta}{\alpha+\beta} \left[\left(\frac{\beta}{\alpha+\beta} \right)^{N-1} \left\{ 1 - e^{-(\alpha+\beta)t} \right\} - \left(\frac{\beta}{\alpha+\beta} \right)^{N-2} e^{-(\alpha+\beta)t} \frac{\beta t}{1!} \right. \\
 & - \left(\frac{\beta}{\alpha+\beta} \right)^{N-3} e^{-(\alpha+\beta)t} \frac{(\beta t)^2}{2!} - \left(\frac{\beta}{\alpha+\beta} \right)^{N-4} e^{-(\alpha+\beta)t} \frac{(\beta t)^3}{3!} \\
 & - \dots \dots \dots \\
 & - \left(\frac{\beta}{\alpha+\beta} \right)^2 e^{-(\alpha+\beta)t} \frac{(\beta t)^{N-3}}{(N-3)!} - \left(\frac{\beta}{\alpha+\beta} \right) e^{-(\alpha+\beta)t} \frac{(\beta t)^{N-2}}{(N-2)!} \\
 & \left. - e^{-(\alpha+\beta)t} \frac{(\beta t)^{N-1}}{(N-1)!} \right] \\
 = & \left(\frac{\beta}{\alpha+\beta} \right)^N \left[1 - e^{-(\alpha+\beta)t} \right] - \left(\frac{\beta}{\alpha+\beta} \right)^{N-1} e^{-(\alpha+\beta)t} \frac{\beta t}{1!}
 \end{aligned}$$

$$\begin{aligned}
& - \left(\frac{\beta}{\alpha+\beta} \right)^{N-2} e^{-(\alpha+\beta)t} \frac{(\beta t)^2}{2!} - \left(\frac{\beta}{\alpha+\beta} \right)^{N-3} e^{-(\alpha+\beta)t} \frac{(\beta t)^3}{3!} \\
& - \dots \\
& - \left(\frac{\beta}{\alpha+\beta} \right)^3 e^{-(\alpha+\beta)t} \frac{(\beta t)^{N-3}}{(N-3)!} - \left(\frac{\beta}{\alpha+\beta} \right)^2 e^{-(\alpha+\beta)t} \frac{(\beta t)^{N-2}}{(N-2)!} \\
& - \left(\frac{\beta}{\alpha+\beta} \right) e^{-(\alpha+\beta)t} \frac{(\beta t)^{N-1}}{(N-1)!}
\end{aligned} \tag{26}$$

Hence, for any arbitrary values of N , $F_N(t)$ can be obtained inductively from relation (20).

b. Derivation of $E_N[N(t)]$

From the recursive relation (19) we have for $N=1$

$$E_1[N(t)] = E_0[N(t)] + F_1(t)$$

Since $E_0[N(t)] = 0$, then substituting the value of $F_1(t)$ in (21) yields

$$\begin{aligned}
E_1[N(t)] &= F_1(t) \\
&= \frac{\beta}{\alpha+\beta} \left[1 - e^{-(\alpha+\beta)t} \right]
\end{aligned} \tag{27}$$

For $N=2$, relation (19) becomes

$$E_2[N(t)] = E_1[N(t)] + F_2(t)$$

Substitute the values of $E_1[N(t)]$ and $F_2(t)$ in (27) and (22) into the above relation, to obtain

$$\begin{aligned}
E_2[N(t)] &= \frac{\beta}{\alpha+\beta} \left[1 - e^{-(\alpha+\beta)t} \right] + \left[\frac{\beta}{\alpha+\beta} \right]^2 \left[1 - e^{-(\alpha+\beta)t} \right] \\
&\quad - \left[\frac{\beta}{\alpha+\beta} \right] e^{-(\alpha+\beta)t} \frac{\beta t}{1!} \\
&= \left[\frac{\beta}{\alpha+\beta} + \left[\frac{\beta}{\alpha+\beta} \right]^2 \right] \left[1 - e^{-(\alpha+\beta)t} \right] - \left[\frac{\beta}{\alpha+\beta} \right] e^{-(\alpha+\beta)t} \frac{\beta t}{1!} \quad (28)
\end{aligned}$$

For $N=3$, we have

$$E_3[N(t)] = E_2[N(t)] + F_3(t)$$

Substituting $E_2[N(t)]$ and $F_3(t)$ in (28) and (23) yields

$$\begin{aligned}
E_3[N(t)] &= \left[\frac{\beta}{\alpha+\beta} + \left[\frac{\beta}{\alpha+\beta} \right]^2 \right] \left[1 - e^{-(\alpha+\beta)t} \right] - \left[\frac{\beta}{\alpha+\beta} \right] e^{-(\alpha+\beta)t} \frac{\beta t}{1!} \\
&\quad + \left[\frac{\beta}{\alpha+\beta} \right]^3 \left[1 - e^{-(\alpha+\beta)t} \right] - \left[\frac{\beta}{\alpha+\beta} \right]^2 e^{-(\alpha+\beta)t} \frac{\beta t}{1!} \\
&\quad - \frac{\beta}{\alpha+\beta} e^{-(\alpha+\beta)t} \frac{(\beta t)^2}{2!} \\
&= \left[\frac{\beta}{\alpha+\beta} + \left[\frac{\beta}{\alpha+\beta} \right]^2 + \left[\frac{\beta}{\alpha+\beta} \right]^3 \right] \left[1 - e^{-(\alpha+\beta)t} \right] \\
&\quad - \left[\frac{\beta}{\alpha+\beta} + \left[\frac{\beta}{\alpha+\beta} \right]^2 \right] e^{-(\alpha+\beta)t} \frac{\beta t}{1!}
\end{aligned}$$

$$- \left[\frac{\beta}{\alpha+\beta} \right] e^{-(\alpha+\beta)t} \frac{(\beta t)^2}{2!} \quad (29)$$

Similarly, for $N=4$ we have

$$E_4[N(t)] = E_3[N(t)] + F_4(t)$$

Hence, substituting $E_3[N(t)]$ and $F_4(t)$ in (29) and (24), we obtain

$$\begin{aligned} E_4[N(t)] &= \left[\frac{\beta}{\alpha+\beta} + \left[\frac{\beta}{\alpha+\beta} \right]^2 + \left[\frac{\beta}{\alpha+\beta} \right]^3 \right] \left[1 - e^{-(\alpha+\beta)t} \right] \\ &\quad - \left[\frac{\beta}{\alpha+\beta} + \left[\frac{\beta}{\alpha+\beta} \right]^2 \right] e^{-(\alpha+\beta)t} \frac{\beta t}{1!} \\ &\quad - \left[\frac{\beta}{\alpha+\beta} \right] e^{-(\alpha+\beta)t} \frac{(\beta t)^2}{2!} \\ &\quad + \left[\frac{\beta}{\alpha+\beta} \right]^4 \left[1 - e^{-(\alpha+\beta)t} \right] - \left[\frac{\beta}{\alpha+\beta} \right]^3 e^{-(\alpha+\beta)t} \frac{\beta t}{1!} \\ &\quad - \left[\frac{\beta}{\alpha+\beta} \right]^2 e^{-(\alpha+\beta)t} \frac{(\beta t)^2}{2!} - \left[\frac{\beta}{\alpha+\beta} \right] e^{-(\alpha+\beta)t} \frac{(\beta t)^3}{3!} \\ E_4[N(t)] &= \left[\frac{\beta}{\alpha+\beta} + \left[\frac{\beta}{\alpha+\beta} \right]^2 + \left[\frac{\beta}{\alpha+\beta} \right]^3 + \left[\frac{\beta}{\alpha+\beta} \right]^4 \right] \left[1 - e^{-(\alpha+\beta)t} \right] \\ &\quad - \left[\frac{\beta}{\alpha+\beta} + \left[\frac{\beta}{\alpha+\beta} \right]^2 + \left[\frac{\beta}{\alpha+\beta} \right]^3 \right] e^{-(\alpha+\beta)t} \frac{\beta t}{1!} \end{aligned}$$

$$\begin{aligned}
& - \left[\frac{\beta}{\alpha+\beta} + \left(\frac{\beta}{\alpha+\beta} \right)^2 \right] e^{-(\alpha+\beta)t} \frac{(\beta t)^2}{2!} \\
& - \left(\frac{\beta}{\alpha+\beta} \right) e^{-(\alpha+\beta)t} \frac{(\beta t)^3}{3!}
\end{aligned} \tag{30}$$

By induction, assume that

$$\begin{aligned}
E_{N-1}[N(t)] &= \left[\frac{\beta}{\alpha+\beta} + \left(\frac{\beta}{\alpha+\beta} \right)^2 + \left(\frac{\beta}{\alpha+\beta} \right)^3 + \dots + \left(\frac{\beta}{\alpha+\beta} \right)^{N-1} \right] \left[1 - e^{-(\alpha+\beta)t} \right] \\
& - \left[\frac{\beta}{\alpha+\beta} + \left(\frac{\beta}{\alpha+\beta} \right)^2 + \left(\frac{\beta}{\alpha+\beta} \right)^3 + \dots + \left(\frac{\beta}{\alpha+\beta} \right)^{N-2} \right] e^{-(\alpha+\beta)t} \frac{\beta t}{1!} \\
& - \left[\frac{\beta}{\alpha+\beta} + \left(\frac{\beta}{\alpha+\beta} \right)^2 + \left(\frac{\beta}{\alpha+\beta} \right)^3 + \dots + \left(\frac{\beta}{\alpha+\beta} \right)^{N-3} \right] e^{-(\alpha+\beta)t} \frac{(\beta t)^2}{2!} \\
& - \left[\frac{\beta}{\alpha+\beta} + \left(\frac{\beta}{\alpha+\beta} \right)^2 + \left(\frac{\beta}{\alpha+\beta} \right)^3 + \dots + \left(\frac{\beta}{\alpha+\beta} \right)^{N-4} \right] e^{-(\alpha+\beta)t} \frac{(\beta t)^3}{3!} \\
& - \dots \\
& - \left[\frac{\beta}{\alpha+\beta} + \left(\frac{\beta}{\alpha+\beta} \right)^2 \right] e^{-(\alpha+\beta)t} \frac{(\beta t)^{N-3}}{(N-3)!} \\
& - \left(\frac{\beta}{\alpha+\beta} \right) e^{-(\alpha+\beta)t} \frac{(\beta t)^{N-2}}{(N-2)!}
\end{aligned} \tag{31}$$

Substituting $E_{N-1}[N(t)]$ and $F_N(t)$ obtained in (31) and (26) respectively into the recursive relation (19), we obtain

$$\begin{aligned}
E_N[N(t)] &= \left[\frac{\beta}{\alpha+\beta} + \left(\frac{\beta}{\alpha+\beta} \right)^2 + \left(\frac{\beta}{\alpha+\beta} \right)^3 + \dots + \left(\frac{\beta}{\alpha+\beta} \right)^{N-1} \right] \left[1 - e^{-(\alpha+\beta)t} \right] \\
&- \left[\frac{\beta}{\alpha+\beta} + \left(\frac{\beta}{\alpha+\beta} \right)^2 + \left(\frac{\beta}{\alpha+\beta} \right)^3 + \dots + \left(\frac{\beta}{\alpha+\beta} \right)^{N-2} \right] e^{-(\alpha+\beta)t} \frac{\beta t}{1!} \\
&- \left[\frac{\beta}{\alpha+\beta} + \left(\frac{\beta}{\alpha+\beta} \right)^2 + \left(\frac{\beta}{\alpha+\beta} \right)^3 + \dots + \left(\frac{\beta}{\alpha+\beta} \right)^{N-3} \right] e^{-(\alpha+\beta)t} \frac{(\beta t)^2}{2!} \\
&- \left[\frac{\beta}{\alpha+\beta} + \left(\frac{\beta}{\alpha+\beta} \right)^2 + \left(\frac{\beta}{\alpha+\beta} \right)^3 + \dots + \left(\frac{\beta}{\alpha+\beta} \right)^{N-4} \right] e^{-(\alpha+\beta)t} \frac{(\beta t)^3}{3!} \\
&- \dots \\
&- \left[\frac{\beta}{\alpha+\beta} + \left(\frac{\beta}{\alpha+\beta} \right)^2 \right] e^{-(\alpha+\beta)t} \frac{(\beta t)^{N-3}}{(N-3)!} \\
&- \left[\frac{\beta}{\alpha+\beta} \right] e^{-(\alpha+\beta)t} \frac{(\beta t)^{N-2}}{(N-2)!} \\
&+ \left[\frac{\beta}{\alpha+\beta} \right]^N \left[1 - e^{-(\alpha+\beta)t} \right] - \left[\frac{\beta}{\alpha+\beta} \right]^{N-1} e^{-(\alpha+\beta)t} \frac{\beta t}{1!} \\
&- \left[\frac{\beta}{\alpha+\beta} \right]^{N-2} e^{-(\alpha+\beta)t} \frac{(\beta t)^2}{2!} - \left[\frac{\beta}{\alpha+\beta} \right]^{N-3} e^{-(\alpha+\beta)t} \frac{(\beta t)^3}{3!} \\
&- \dots \\
&- \left[\frac{\beta}{\alpha+\beta} \right]^3 e^{-(\alpha+\beta)t} \frac{(\beta t)^{N-3}}{(N-3)!} - \left[\frac{\beta}{\alpha+\beta} \right]^2 e^{-(\alpha+\beta)t} \frac{(\beta t)^{N-2}}{(N-2)!}
\end{aligned}$$

$$\begin{aligned}
& - \left[\frac{\beta}{\alpha+\beta} \right] e^{-(\alpha+\beta)t} \frac{(\beta t)^{N-1}}{(N-1)!} \\
E_N[N(t)] &= \left[\frac{\beta}{\alpha+\beta} + \left[\frac{\beta}{\alpha+\beta} \right]^2 + \left[\frac{\beta}{\alpha+\beta} \right]^3 + \dots + \left[\frac{\beta}{\alpha+\beta} \right]^N \right] \left[1 - e^{-(\alpha+\beta)t} \right] \\
& - \left[\frac{\beta}{\alpha+\beta} + \left[\frac{\beta}{\alpha+\beta} \right]^2 + \left[\frac{\beta}{\alpha+\beta} \right]^3 + \dots + \left[\frac{\beta}{\alpha+\beta} \right]^{N-1} \right] e^{-(\alpha+\beta)t} \frac{\beta t}{1!} \\
& - \left[\frac{\beta}{\alpha+\beta} + \left[\frac{\beta}{\alpha+\beta} \right]^2 + \left[\frac{\beta}{\alpha+\beta} \right]^3 + \dots + \left[\frac{\beta}{\alpha+\beta} \right]^{N-2} \right] e^{-(\alpha+\beta)t} \frac{(\beta t)^2}{2!} \\
& - \left[\frac{\beta}{\alpha+\beta} + \left[\frac{\beta}{\alpha+\beta} \right]^2 + \left[\frac{\beta}{\alpha+\beta} \right]^3 + \dots + \left[\frac{\beta}{\alpha+\beta} \right]^{N-3} \right] e^{-(\alpha+\beta)t} \frac{(\beta t)^3}{3!} \\
& - \dots \\
& - \left[\frac{\beta}{\alpha+\beta} + \left[\frac{\beta}{\alpha+\beta} \right]^2 + \left[\frac{\beta}{\alpha+\beta} \right]^3 \right] e^{-(\alpha+\beta)t} \frac{(\beta t)^{N-3}}{(N-3)!} \\
& - \left[\frac{\beta}{\alpha+\beta} + \left[\frac{\beta}{\alpha+\beta} \right]^2 \right] e^{-(\alpha+\beta)t} \frac{(\beta t)^{N-2}}{(N-2)!} \\
& - \left[\frac{\beta}{\alpha+\beta} \right] e^{-(\alpha+\beta)t} \frac{(\beta t)^{N-1}}{(N-1)!} \tag{32}
\end{aligned}$$

Thus for any arbitrary values of N , $E_N[N(t)]$ can be obtained. This last relation can be rewritten as

$$\begin{aligned}
E_N[N(t)] &= \left[1 - e^{-(\alpha+\beta)t} \right] \sum_{n=1}^N \left(\frac{\beta}{\alpha+\beta} \right)^n \\
&\quad - e^{-(\alpha+\beta)t} \sum_{n=1}^{N-1} \frac{(\beta t)^n}{n!} \sum_{m=1}^{N-n} \left(\frac{\beta}{\alpha+\beta} \right)^m
\end{aligned} \tag{33}$$

Since

$$\sum_{i=1}^m \left(\frac{\beta}{\alpha+\beta} \right)^i = \frac{\beta}{\alpha} \left[1 - \left(\frac{\beta}{\alpha+\beta} \right)^m \right],$$

relation (33) becomes

$$\begin{aligned}
E_N[N(t)] &= \frac{\beta}{\alpha} \left[1 - e^{-(\alpha+\beta)t} \right] \left[1 - \left(\frac{\beta}{\alpha+\beta} \right)^N \right] \\
&\quad - \frac{\beta}{\alpha} e^{-(\alpha+\beta)t} \sum_{n=1}^{N-1} \frac{(\beta t)^n}{n!} \left[1 - \left(\frac{\beta}{\alpha+\beta} \right)^{N-n} \right]
\end{aligned} \tag{34}$$

Note that

$$\begin{aligned}
\lim_{t \rightarrow \infty} E_N[N(t)] &= \lim_{t \rightarrow \infty} \frac{\beta}{\alpha} \left[1 - e^{-(\alpha+\beta)t} \right] \left[1 - \left(\frac{\beta}{\alpha+\beta} \right)^N \right] \\
&\quad - \lim_{t \rightarrow \infty} \frac{\beta}{\alpha} e^{-(\alpha+\beta)t} \sum_{n=1}^{N-1} \frac{(\beta t)^n}{n!} \left[1 - \left(\frac{\beta}{\alpha+\beta} \right)^{N-n} \right] \\
&= \frac{\beta}{\alpha} \left[1 - \left(\frac{\beta}{\alpha+\beta} \right)^N \right] \\
&= \left[\frac{\beta}{\alpha+\beta} + \left(\frac{\beta}{\alpha+\beta} \right)^2 + \left(\frac{\beta}{\alpha+\beta} \right)^3 + \dots + \left(\frac{\beta}{\alpha+\beta} \right)^N \right]
\end{aligned} \tag{35}$$

V. MEASURES OF EFFECTIVENESS

We consider the following measures of effectiveness:

1. Probability of sortie success (mission reliability)
2. Probability of sortie failure
3. Probability that all targets are killed
4. Expected number of targets killed
5. Expected fraction of targets killed
6. Expected number of attacks on the targets
7. Expected duration of the sortie

1. Probability of Sortie Success (Mission Reliability)

This may be defined in three different ways:

- a. It is the probability that the aircraft is not killed

$$P_N(N,1,t) + P_N(N-1,1,t) + \dots + P_N(1,1,t) + P_N(0,1,t)$$

$$= \sum_{n=0}^N P_N(N-n,1,t)$$

From $P_N(N-n,1,t)$ for $n=0,1,2, \dots, N-1$, and $P_N(0,1,t)$ in (1) and (3), we have

$$\begin{aligned} \sum_{n=0}^N P_N(N-n,1,t) &= \sum_{n=0}^{N-1} P_N(N-n,1,t) + P_N(0,1,t) \\ &= e^{-(\alpha+\beta)t} \sum_{n=0}^{N-1} \frac{(\beta t)^n}{n!} + e^{-\alpha t} \left[1 - e^{-\beta t} \sum_{i=0}^{N-1} \frac{(\beta t)^i}{i!} \right] \\ &= e^{-\alpha t} \end{aligned} \tag{36}$$

- b. It is the probability that the aircraft is not killed and all targets are killed.

$$P_N(0,1,t) = e^{-\alpha t} \left[1 - e^{-\beta t} \sum_{i=0}^{N-1} \frac{(\beta t)^i}{i!} \right] \quad (37)$$

- c. It is the probability that the aircraft is not killed and at least one target is killed.

$$\begin{aligned} & P_N(N-1,1,t) + P_N(N-2,1,t) + \dots + P_N(0,1,t) \\ &= \sum_{n=1}^N P_N(N-n,1,t) \end{aligned}$$

Using $P_N(N-n,1,t)$ for $n=1,2, \dots, N-1$, and $P_N(0,1,t)$ in (1) and (3) yields

$$\begin{aligned} \sum_{n=1}^N P_N(N-n,1,t) &= \sum_{n=1}^{N-1} P_N(N-n,1,t) + P_N(0,1,t) \\ &= e^{-(\alpha+\beta)t} \sum_{n=1}^{N-1} \frac{(\beta t)^n}{n!} + e^{-\alpha t} \left[1 - e^{-\beta t} \sum_{i=0}^{N-1} \frac{(\beta t)^i}{i!} \right] \\ &= e^{-(\alpha+\beta)t} \sum_{n=1}^{N-1} \frac{(\beta t)^n}{n!} + e^{-\alpha t} - e^{-(\alpha+\beta)t} \left[\sum_{i=1}^{N-1} \frac{(\beta t)^i}{i!} + 1 \right] \\ &= e^{-\alpha t} - e^{-(\alpha+\beta)t} \\ &= e^{-\alpha t} (1 - e^{-\beta t}) \end{aligned} \quad (38)$$

2. Probability of Sortie Failure

This may be defined in three different ways

- a. It is the probability that the aircraft is killed.

$$P_N(N,0,t) + P_N(N-1,0,t) + \dots + P_N(0,0,t)$$

$$= \sum_{n=0}^N P_N(N-n,0,t)$$

Using the normalizing condition,

$$\sum_{n=0}^N P_N(N-n,0,t) + \sum_{n=0}^N P_N(N-n,1,t) = 1$$

and using relation (36),

$$\sum_{n=0}^N P_N(N-n,1,t) = e^{-\alpha t}$$

we obtain

$$\sum_{n=0}^N P_N(N-n,0,t) = 1 - e^{-\alpha t} \quad (39)$$

- b. It is the probability that none of the targets are killed and the aircraft is killed.

$$\begin{aligned} P_N(N,0,t) &= \left[\frac{\alpha}{\alpha+\beta} \right] \left[\frac{\beta}{\alpha+\beta} \right]^0 \left[1 - e^{-(\alpha+\beta)t} \sum_{i=0}^0 \frac{[(\alpha+\beta)t]^i}{i!} \right] \\ &= \frac{\alpha}{\alpha+\beta} \left[1 - e^{-(\alpha+\beta)t} \right] \end{aligned} \quad (40)$$

c. It is the probability that none of the targets are killed.

$$\begin{aligned}
 & P_N(N,1,t) + P_N(N,0,t) \\
 &= \frac{(\beta t)^0}{0!} e^{-(\alpha+\beta)t} + \frac{\alpha}{\alpha+\beta} \left[1 - e^{-(\alpha+\beta)t} \right] \\
 &= e^{-(\alpha+\beta)t} + \frac{\alpha}{\alpha+\beta} \left[1 - e^{-(\alpha+\beta)t} \right] \quad (41)
 \end{aligned}$$

3. Probability that all Targets are Killed

$$\begin{aligned}
 & P_N(0,1,t) + P_N(0,0,t) \\
 &= e^{-\alpha t} \left[1 - e^{-\beta t} \sum_{i=0}^{N-1} \frac{(\beta t)^i}{i!} \right] + \alpha \int_0^t e^{-\alpha u} \left[1 - e^{-\beta u} \sum_{i=1}^{N-1} \frac{(\beta u)^i}{i!} du \right] \quad (42)
 \end{aligned}$$

Now

$$P_N(0,0,t) = 1 - e^{-\alpha t} - \sum_{n=0}^{N-1} P_N(N-n,0,t)$$

From (2), we have

$$P_N(0,0,t) = 1 - e^{-\alpha t} - \sum_{n=0}^{N-1} \left(\frac{\alpha}{\alpha+\beta} \right) \left(\frac{\beta}{\alpha+\beta} \right)^n \left[1 - e^{-(\alpha+\beta)t} \sum_{i=0}^n \frac{[(\alpha+\beta)t]^i}{i!} \right]$$

$$\begin{aligned}
&= 1 - e^{-\alpha t} - \left(\frac{\alpha}{\alpha+\beta} \right) \sum_{n=0}^{N-1} \left(\frac{\beta}{\alpha+\beta} \right)^n \\
&\quad + \left(\frac{\alpha}{\alpha+\beta} \right) e^{-(\alpha+\beta)t} \sum_{n=0}^{N-1} \left(\frac{\beta}{\alpha+\beta} \right)^n \sum_{i=0}^n \frac{[(\alpha+\beta)t]^i}{i!} \\
&= 1 - e^{-\alpha t} - \left(\frac{\alpha}{\alpha+\beta} \right) \left[\frac{1 - \left(\frac{\beta}{\alpha+\beta} \right)^N}{1 - \frac{\beta}{\alpha+\beta}} \right] \\
&\quad + \left(\frac{\alpha}{\alpha+\beta} \right) e^{-(\alpha+\beta)t} \sum_{n=0}^{N-1} \left(\frac{\beta}{\alpha+\beta} \right)^n \sum_{i=0}^n \frac{[(\alpha+\beta)t]^i}{i!} \\
&= - e^{-\alpha t} + \left(\frac{\beta}{\alpha+\beta} \right)^N + \left(\frac{\alpha}{\alpha+\beta} \right) e^{-(\alpha+\beta)t} \sum_{n=0}^{N-1} \left(\frac{\beta}{\alpha+\beta} \right)^n \sum_{i=0}^n \frac{[(\alpha+\beta)t]^i}{i!} \quad (43)
\end{aligned}$$

Using the results of $P_N(0,1,t)$ and $P_N(0,0,t)$ in (37) and (43) yields

$$P_N(0,1,t) + P_N(0,0,t)$$

$$\begin{aligned}
&= e^{\alpha t} \left[1 - e^{-\beta t} \sum_{i=0}^{N-1} \frac{(\beta t)^i}{i!} \right] \\
&\quad - e^{-\alpha t} + \left(\frac{\beta}{\alpha+\beta} \right)^N + \left(\frac{\alpha}{\alpha+\beta} \right) e^{-(\alpha+\beta)t} \sum_{n=0}^{N-1} \left(\frac{\beta}{\alpha+\beta} \right)^n \sum_{i=0}^n \frac{[(\alpha+\beta)t]^i}{i!} \\
&= \left(\frac{\beta}{\alpha+\beta} \right)^N - e^{-(\alpha+\beta)t} \sum_{i=0}^{N-1} \frac{(\beta t)^i}{i!} + \left(\frac{\alpha}{\alpha+\beta} \right) e^{-(\alpha+\beta)t} \sum_{n=0}^{N-1} \left(\frac{\beta}{\alpha+\beta} \right)^n \sum_{i=0}^n \frac{[(\alpha+\beta)t]^i}{i!} \\
&= \left(\frac{\beta}{\alpha+\beta} \right)^N - e^{-(\alpha+\beta)t} \sum_{n=0}^{N-1} \left[\frac{(\beta t)^n}{n!} - \left(\frac{\alpha}{\alpha+\beta} \right) \left(\frac{\beta}{\alpha+\beta} \right)^n \sum_{i=0}^n \frac{[(\alpha+\beta)t]^i}{i!} \right] \quad (44)
\end{aligned}$$

4. Expected Number of Targets Killed

From (34), we have

$$E_N[N(t)] = \frac{\beta}{\alpha} \left[1 - e^{-(\alpha+\beta)t} \right] \left[1 - \left(\frac{\beta}{\alpha+\beta} \right)^N \right] - \frac{\beta}{\alpha} e^{-(\alpha+\beta)t} \sum_{n=1}^{N-1} \frac{(\beta t)^n}{n!} \left[1 - \left(\frac{\beta}{\alpha+\beta} \right)^{N-n} \right] \quad (45)$$

5. Expected Fraction of Targets Killed

$$\frac{E_N[N(t)]}{N} = \frac{\beta}{N\alpha} \left[1 - e^{-(\alpha+\beta)t} \right] \left[1 - \left(\frac{\beta}{\alpha+\beta} \right)^N \right] - \frac{\beta}{N\alpha} e^{-(\alpha+\beta)t} \sum_{n=1}^{N-1} \frac{(\beta t)^n}{n!} \left[1 - \left(\frac{\beta}{\alpha+\beta} \right)^{N-n} \right] \quad (46)$$

6. Expected Number of Targets Attacked

Let for $i=0,1,2,\dots,N$

$\hat{P}(i,1,t)$ = probability that by time t , i targets have been attacked and the airplane is not killed.

$\hat{P}(i,0,t)$ = probability that by time t , i targets have been attacked and the airplane is killed.

a. Equation for $\hat{P}(0,1,t)$

$$\begin{aligned} \hat{P}(0,1,t+dt) &= \hat{P}(0,1,t)(1-\lambda dt)(1-\mu dt) \\ &\quad + \hat{P}(0,1,t) \lambda dt (1-p_1)(1-\mu dt) + o(dt) \end{aligned}$$

$$= \hat{P}(0,1,t) - (\alpha + \mu) \hat{P}(0,1,t) + o(dt)$$

Thus

$$\frac{d\hat{P}(0,1,t)}{dt} = - (\alpha + \mu) \hat{P}(0,1,t) \quad (47)$$

$$\text{subject to } \hat{P}(0,1,0) = 1 \quad (48)$$

$$\text{Thus, } \hat{P}(0,1,t) = e^{-(\alpha + \mu)t} \quad (49)$$

b. Equation for $\hat{P}(1,1,t)$

$$\begin{aligned} \hat{P}(1,1,t+dt) &= \hat{P}(1,1,t)(1-\lambda dt)(1-\mu dt) \\ &+ \hat{P}(1,1,t) \lambda dt (1-p_1)(1-\mu dt) \\ &+ \hat{P}(0,1,t)(1-\lambda dt) \mu dt \\ &+ \hat{P}(0,1,t) \lambda dt (1-p_1) \mu dt + o(dt) \end{aligned}$$

$$\begin{aligned} \frac{d\hat{P}(1,1,t)}{dt} &= -(\alpha + \mu) \hat{P}(1,1,t) + \mu \hat{P}(0,1,t) \\ &= -(\alpha + \mu) \hat{P}(1,1,t) + \mu e^{-(\alpha + \mu)t} \end{aligned} \quad (50)$$

$$\text{subject to } \hat{P}(1,1,0) = 0 \quad (51)$$

$$\text{Thus, } \hat{P}(1,1,t) = \mu t e^{-(\alpha + \mu)t} \quad (52)$$

c. Equation for $\hat{P}(2,1,t)$

$$\hat{P}(2,1,t+dt) = \hat{P}(2,1,t) (1-\lambda dt)(1-\mu dt)$$

$$\begin{aligned}
& + \hat{P}(2,1,t) \lambda dt (1-p_1)(1-\mu dt) \\
& + \hat{P}(1,1,t) (1-\lambda dt) \mu dt \\
& + \hat{P}(1,1,t) \lambda dt (1-p_1) \mu dt + o(dt)
\end{aligned}$$

$$\begin{aligned}
\frac{d\hat{P}(2,1,t)}{dt} &= -(\alpha+\mu) \hat{P}(2,1,t) + \mu \hat{P}(1,1,t) \\
&= -(\alpha+\mu) \hat{P}(2,1,t) + \mu^2 t e^{-(\alpha+\mu)t}
\end{aligned} \tag{53}$$

$$\text{subject to } \hat{P}(2,1,0)=0 \tag{54}$$

Thus

$$\hat{P}(2,1,t) = \frac{(\mu t)^2}{2!} e^{-(\alpha+\mu)t} \tag{55}$$

d. Equation for $\hat{P}(3,1,t)$

$$\begin{aligned}
\hat{P}(3,1,t+dt) &= \hat{P}(3,1,t) (1-\lambda dt) (1-\mu dt) \\
&+ \hat{P}(3,1,t) \lambda dt (1-p_1) (1-\mu dt) \\
&+ \hat{P}(2,1,t) (1-\lambda dt) \mu dt \\
&+ \hat{P}(2,1,t) \lambda dt (1-p_1) \mu dt + o(dt)
\end{aligned}$$

$$\begin{aligned}
\frac{d\hat{P}(3,1,t)}{dt} &= -(\alpha+\mu) \hat{P}(3,1,t) + \mu \hat{P}(2,1,t) \\
&= -(\alpha+\mu) \hat{P}(3,1,t) + \frac{\mu^3 t^2}{2!} e^{-(\alpha+\mu)t}
\end{aligned} \tag{56}$$

$$\text{subject to } \hat{P}(3,1,0)=0 \tag{57}$$

Thus

$$\hat{P}(3,1,t) = \frac{(\mu t)^3}{3!} e^{-(\alpha+\mu)t} \quad (58)$$

e. Equation for $\hat{P}(i,1,t)$ for all i , $i \neq 0, N$

By induction, assume that

$$\hat{P}(i-1,1,t) = \frac{(\mu t)^{i-1}}{(i-1)!} e^{-(\alpha+\mu)t} \quad (59)$$

The equation for $\hat{P}(i,1,t)$ is

$$\begin{aligned} \hat{P}(i,1,t+dt) &= \hat{P}(i,1,t) (1-\lambda dt) (1-\mu dt) \\ &+ \hat{P}(i,1,t) \lambda dt (1-p_1) (1-\mu dt) \\ &+ \hat{P}(i-1,1,t) (1-\lambda dt) \mu dt \\ &+ \hat{P}(i-1,1,t) \lambda dt (1-p_1) \mu dt + o(dt) \end{aligned}$$

which reduces to

$$\frac{d\hat{P}(i,1,t)}{dt} = -(\alpha+\mu) \hat{P}(i,1,t) + \mu \hat{P}(i-1,1,t) \quad (60)$$

Substituting $\hat{P}(i-1,1,t)$ in (59) into (60) yields

$$\frac{d\hat{P}(i,1,t)}{dt} = -(\alpha+\mu) \hat{P}(i,1,t) + \frac{\mu^i t^{i-1}}{(i-1)!} e^{-(\alpha+\mu)t} \quad (61)$$

$$\text{subject to } \hat{P}(i,1,0)=0 \quad (62)$$

Thus

$$\hat{P}(i,1,t) = \frac{(\mu t)^i}{i!} e^{-(\alpha+\mu)t} \quad (63)$$

Hence, $\hat{P}(i,1,t)$ for $i=1,2,\dots,N-1$, can be obtained from (63).

f. Equation for $\hat{P}(N,1,t)$

$$\begin{aligned} \hat{P}(N,1,t+dt) &= \hat{P}(N,1,t) (1-\lambda dt) \\ &+ \hat{P}(N,1,t) \lambda dt (1-p_1) \\ &+ \hat{P}(N-1,1,t) (1-\lambda dt) \mu dt \\ &+ \hat{P}(N-1,1,t) \lambda dt (1-p_1) \mu dt + o(dt) \end{aligned}$$

$$\begin{aligned} \frac{d\hat{P}(N,1,t)}{dt} &= -\alpha \hat{P}(N,1,t) + \mu \hat{P}(N-1,1,t) \\ &= -\alpha \hat{P}(N,1,t) + \frac{\mu^N t^{N-1}}{(N-1)!} e^{-(\alpha+\mu)t} \end{aligned} \quad (64)$$

$$\text{subject to } \hat{P}(N,1,0)=0 \quad (65)$$

Thus

$$\hat{P}(N,1,t) = e^{-\alpha t} \left[1 - e^{-\mu t} \sum_{n=0}^{N-1} \frac{(\mu t)^n}{n!} \right] \quad (66)$$

g. Equation for $\hat{P}(0,0,t)$

$$\hat{P}(0,0,t+dt) = \hat{P}(0,0,t)$$

$$+ \hat{P}(0,1,t) \lambda dt p_1 (1-\mu dt) + o(dt)$$

$$\begin{aligned} \frac{d\hat{P}(0,0,t)}{dt} &= \alpha \hat{P}(0,1,t) \\ &= \alpha e^{-(\alpha+\mu)t} \end{aligned} \quad (67)$$

$$\text{subject to } \hat{P}(0,0,0)=0 \quad (68)$$

Thus

$$\hat{P}(0,0,t) = \frac{\alpha}{\alpha+\mu} \left[1 - e^{-(\alpha+\mu)t} \right] \quad (69)$$

h. Equation for $\hat{P}(1,0,t)$

$$\hat{P}(1,0,t+dt) = \hat{P}(1,0,t) + \hat{P}(1,1,t) \lambda dt p_1 (1-\mu dt) + o(dt)$$

$$\begin{aligned} \frac{d\hat{P}(1,0,t)}{dt} &= \alpha \hat{P}(1,1,t) \\ &= \alpha \mu t e^{-(\alpha+\mu)t} \end{aligned} \quad (70)$$

$$\text{subject to } \hat{P}(1,0,0)=0 \quad (71)$$

Thus

$$\hat{P}(1,0,t) = \left[\frac{\alpha}{\alpha+\mu} \right] \left[\frac{\mu}{\alpha+\mu} \right] \left[1 - e^{-(\alpha+\mu)t} \sum_{n=0}^{\infty} \frac{[(\alpha+\mu)t]^n}{n!} \right] \quad (72)$$

i. Equation for $\hat{P}(2,0,t)$

$$\hat{P}(2,0,t+dt) = \hat{P}(2,0,t) + \hat{P}(2,1,t) \lambda dt p_1(1-\mu dt) + o(dt)$$

$$\frac{d\hat{P}(2,0,t)}{dt} = \alpha \hat{P}(2,1,t)$$

$$= \alpha \frac{(\mu t)^2}{2!} e^{-(\alpha+\mu)t} \quad (73)$$

$$\text{subject to } \hat{P}(2,0,0) = 0 \quad (74)$$

Thus

$$\hat{P}(2,0,t) = \left[\frac{\alpha}{\alpha+\mu} \right] \left[\frac{\mu}{\alpha+\mu} \right]^2 \left[1 - e^{-(\alpha+\mu)t} \sum_{n=0}^2 \frac{[(\alpha+\mu)t]^n}{n!} \right] \quad (75)$$

j. Equation for $\hat{P}(i,0,t)$ for all $i, i \neq 0, N$

By induction, assume that

$$\hat{P}(i-1,0,t) = \left[\frac{\alpha}{\alpha+\mu} \right] \left[\frac{\mu}{\alpha+\mu} \right]^{i-1} \left[1 - e^{-(\alpha+\mu)t} \sum_{n=0}^{i-1} \frac{[(\alpha+\mu)t]^n}{n!} \right] \quad (76)$$

The equation for $\hat{P}(i,0,t)$ is

$$\hat{P}(i,0,t+dt) = \hat{P}(i,0,t) + \hat{P}(i,1,t) \lambda dt p_1(1-\mu dt) + o(dt)$$

which reduces to

$$\frac{d\hat{P}(i,0,t)}{dt} = \alpha \hat{P}(i,1,t)$$

$$= \alpha \frac{(\mu t)^i}{i!} e^{-(\alpha+\mu)t} \quad (77)$$

$$\text{subject to } \hat{P}(i,0,0)=0 \quad (78)$$

Thus

$$\hat{P}(i,0,t) = \left[\frac{\alpha}{\alpha+\mu} \right] \left[\frac{\mu}{\alpha+\mu} \right]^i \left[1 - e^{-(\alpha+\mu)t} \sum_{n=0}^i \frac{[(\alpha+\mu)t]^n}{n!} \right] \quad (79)$$

Hence, $\hat{P}(i,0,t)$ for $i=0,1,2,\dots, N-1$, can be obtained from (79).

k. Equation for $\hat{P}(N,0,t)$

$$\hat{P}(N,0,t+dt) = \hat{P}(N,0,t) + \hat{P}(N,1,t) \lambda dt p_1(1-\mu dt) + o(dt)$$

$$\begin{aligned} \frac{d\hat{P}(N,0,t)}{dt} &= \alpha \hat{P}(N,1,t) \\ &= \alpha e^{-\alpha t} \left[1 - e^{-\mu t} \sum_{n=0}^{N-1} \frac{(\mu t)^n}{n!} \right] \end{aligned} \quad (80)$$

$$\text{subject to } \hat{P}(N,0,0)=0 \quad (81)$$

Thus

$$\hat{P}(N,0,t) = \alpha \int_0^t e^{-\alpha v} \left[1 - e^{-\mu v} \sum_{n=0}^{N-1} \frac{(\mu v)^n}{n!} \right] dv \quad (82)$$

1. Summary of Results

$$\hat{P}(i,1,t) = \frac{(\mu t)^i}{i!} e^{-(\alpha+\mu)t} \quad i = 0,1,2,\dots, N-1 \quad (83)$$

$$\hat{P}(N,1,t) = e^{-\alpha t} \left[1 - e^{-\mu t} \sum_{n=0}^{N-1} \frac{(\mu t)^n}{n!} \right] \quad (84)$$

$$\hat{P}(i,0,t) = \left[\frac{\alpha}{\alpha+\mu} \right] \left[\frac{\mu}{\alpha+\mu} \right]^i \left[1 - e^{-(\alpha+\mu)t} \sum_{n=0}^i \frac{[(\alpha+\mu)t]^n}{n!} \right] \quad i=0,1,2,\dots,N-1 \quad (85)$$

$$\hat{P}(N,0,t) = \alpha \int_0^t e^{-\alpha v} \left[1 - e^{-\mu v} \sum_{n=0}^{N-1} \frac{(\mu v)^n}{n!} \right] dv \quad (86)$$

m. Expected Number of Attacks

Let $A(t)$ be the total number of attacks by time t and $E[A(t)]$ be the expected number of attacks by time t .

Then

$$E[A(t)] = \sum_{i=0}^N i [\hat{P}(i,1,t) + \hat{P}(i,0,t)]$$

Comparing the equations for $\hat{P}(i,1,t)$ and $\hat{P}(i,0,t)$ for $i=0,1,2,\dots,N$ in (83) to (86) with equations for $P_N(N-n,1,t)$ and $P_N(N-n,0,t)$ for $n=0,1,2,\dots,N$, in (1) to (4), we note that the obtained relations are the same except for the quantity β being substituted by μ . Hence the expected number of attacks is given by expression (34) with β replaced by μ .

$$E[A(t)] = \frac{\mu}{\alpha} \left[1 - e^{-(\alpha+\mu)t} \right] \left[1 - \left(\frac{\mu}{\alpha+\mu} \right)^N \right] - \frac{\mu}{\alpha} e^{-(\alpha+\mu)t} \sum_{n=1}^{N-1} \frac{(\mu t)^n}{n!} \left[1 - \left(\frac{\mu}{\alpha+\mu} \right)^{N-n} \right] \quad (87)$$

7. Expected Duration of the Sortie

If $D(t)$ is the duration of the sortie, then it may be shown (see [1]) that

$$E[D(t)] = \frac{1}{\alpha} \left[1 - e^{-\alpha t} \right] \quad (88)$$

VI. COST RELATED MEASURES OF EFFECTIVENESS

As in the cases of a single target and two targets, we consider two such measures of effectiveness (see [1], [2]).

- a. the expected cost of the sortie per expected number of targets killed.
- b. the expected gain of the sortie defined as the expected dollar benefit derived in killing the target minus the expected cost of the sortie.

The measures would include such components as

- a. initial preparation cost of the sortie
- b. expected cost associated with the duration of the sortie
- c. expected cost of aircraft loss
- d. expected cost of ammunitions used

- e. expected number of targets destroyed
- f. expected benefit derived in killing the target.

Input cost parameters would be

- a. fixed cost in preparation of the sortie, K
- b. cost per unit duration time of the sortie, C_0
- c. replacement cost of the aircraft, C_A
- d. cost of ammunition per attack on a target, C_M
- e. dollar benefit in killing a single target, B.

1. Expected Cost of the Sortie

The expected cost of the sortie is the sum of the following costs:

- a. The fixed cost in preparation of the sortie.

This is equal to K. (89)

- b. The expected cost associated with the duration of the sortie.

Using (88), this is equal to

$$C_0 E[D(t)] = C_0 \frac{1}{\alpha} \left[1 - e^{-\alpha t} \right] \quad (90)$$

- c. The expected cost associated with the probable loss of the aircraft.

Since $e^{-\alpha t}$ is the probability that the aircraft is not killed.

$1 - e^{-\alpha t}$ is the probability that the aircraft is killed, an expression which was obtained in (39). The required cost is

$$C_A (1 - e^{-\alpha t}) \quad (91)$$

d. The expected cost of ammunition used. Using (87), this is equal to

$$C_M E[A(t)] = C_M \left[\frac{\mu}{\alpha} \left\{ 1 - e^{-(\alpha+\mu)t} \right\} \left\{ 1 - \left(\frac{\mu}{\alpha+\mu} \right)^N \right\} - \frac{\mu}{\alpha} e^{-(\alpha+\mu)t} \sum_{n=1}^{N-1} \frac{(\mu t)^n}{n!} \left\{ 1 - \left(\frac{\mu}{\alpha+\mu} \right)^{N-n} \right\} \right] \quad (92)$$

Let $S(t)$ be the cost of the sortie t unit times following the start of the sortie. The total expected cost associated with a sortie is the sum of (89), (90), (91) and (92) or

$$E[S(t)] = K + C_0 \frac{1}{\alpha} \left[1 - e^{-\alpha t} \right] + C_A \left[1 - e^{-\alpha t} \right] + C_M \left[\frac{\mu}{\alpha} \left\{ 1 - e^{-(\alpha+\mu)t} \right\} \left\{ 1 - \left(\frac{\mu}{\alpha+\mu} \right)^N \right\} - \frac{\mu}{\alpha} e^{-(\alpha+\mu)t} \sum_{n=1}^{N-1} \frac{(\mu t)^n}{n!} \left\{ 1 - \left(\frac{\mu}{\alpha+\mu} \right)^{N-n} \right\} \right] \quad (93)$$

2. Expected Cost of the Sortie per Expected Number of Targets Killed

From (45), the expected number of targets killed is:

$$E_N[N(t)] = \frac{\beta}{\alpha} \left[1 - e^{-(\alpha+\beta)t} \right] \left[1 - \left(\frac{\beta}{\alpha+\beta} \right)^N \right] - \frac{\beta}{\alpha} e^{-(\alpha+\beta)t} \sum_{n=1}^{N-1} \frac{(\beta t)^n}{n!} \left[1 - \left(\frac{\beta}{\alpha+\beta} \right)^{N-n} \right] \quad (94)$$

Using (93) and (94), we obtain the following expression for the expected cost of the sortie per expected number of targets killed:

$$\begin{aligned}
\frac{E[S(t)]}{E_N[N(t)]} = & \left\{ K + C_0 \frac{1}{\alpha} \left[1 - e^{-\alpha t} \right] + C_A \left[1 - e^{-\alpha t} \right] \right. \\
& + C_M \left[\frac{\mu}{\alpha} \left\{ 1 - e^{-(\alpha+\mu)t} \right\} \left\{ 1 - \left[\frac{\mu}{\alpha+\mu} \right]^N \right\} \right. \\
& \left. \left. - \frac{\mu}{\alpha} e^{-(\alpha+\mu)t} \sum_{n=1}^{N-1} \frac{(\mu t)^n}{n!} \left\{ 1 - \left[\frac{\mu}{\alpha+\mu} \right]^{N-n} \right\} \right] \right\} \\
& \left\{ \frac{\beta}{\alpha} \left[1 - e^{-(\alpha+\beta)t} \right] \left[1 - \left[\frac{\beta}{\alpha+\beta} \right]^N \right] \right. \\
& \left. - \frac{\beta}{\alpha} e^{-(\alpha+\beta)t} \sum_{n=1}^{N-1} \frac{(\beta t)^n}{n!} \left[1 - \left[\frac{\beta}{\alpha+\beta} \right]^{N-n} \right] \right\} \quad (95)
\end{aligned}$$

3. Expected Gain of the Sortie

Let

B = dollar benefit derived in killing a single target

$E_N[N(t)]$ = expected number of targets killed

$E[S(t)]$ = expected cost of a sortie.

Then the expected gain associated with a sortie is

$$\begin{aligned}
BE_N[N(t)] - E[S(t)] = \\
B \left\{ \frac{\beta}{\alpha} \left[1 - e^{-(\alpha+\beta)t} \right] \left[1 - \left[\frac{\beta}{\alpha+\beta} \right]^N \right] - \frac{\beta}{\alpha} e^{-(\alpha+\beta)t} \sum_{n=1}^{N-1} \frac{(\beta t)^n}{n!} \left[1 - \left[\frac{\beta}{\alpha+\beta} \right]^{N-n} \right] \right\}
\end{aligned}$$

$$\begin{aligned}
& - \left\{ K + C_0 \frac{1}{\alpha} \left[1 - e^{-\alpha t} \right] + C_A \left[1 - e^{-\alpha t} \right] \right. \\
& + C_M \left[\frac{\mu}{\alpha} \left\{ 1 - e^{-(\alpha+\mu)t} \right\} \left\{ 1 - \left(\frac{\mu}{\alpha+\mu} \right)^N \right\} - \frac{\mu}{\alpha} e^{-(\alpha+\mu)t} \sum_{n=1}^{N-1} \frac{(\mu t)^n}{n!} \left\{ 1 - \left(\frac{\mu}{\alpha+\mu} \right)^{N-n} \right\} \right] \left. \right\}
\end{aligned}
\tag{96}$$

We next provide three numerical examples for which (93), (94) (95) and (96) are computed for different values of sortie time t . Appendix I provides a FORTRAN PROGRAMMING to compute the values of (93), (94), (95) and (96) given the system and cost parameters.

Example 1. (Two Targets)

$\lambda = 1.8/\text{hr}$; $p_1 = 0.08$; $\alpha = \lambda p_1 = .144/\text{hr}$

$1/\mu = 5 \text{ min}$; $p_2 = 0.50$; $\beta = \mu p_2 = 6/\text{hr}$

$k = \$2,000$; $C_0 = \$6,000/\text{hr of sortie}$; $C_A = \$30,000,000/\text{aircraft}$

At $\$20.00/\text{round of ammunition}$ and 100 rounds per attack, $C_M = \$2,000$

$B = \$2,000,000$

TABLE 1

Sortie Time $t \text{ (min)}$	$E_2[N(t)]$	$E[S(t)]$ (\\$)	$\frac{E[S(t)]}{E_2[N(t)]}$ (\\$)	$BE_2[N(t)] - E[S(t)]$ (\\$)
0.0	0.00000	2000.0	Infinity	-2000.0
1.0	0.14380	74572.0	518589.4	213023.6
2.0	0.33094	147075.1	444420.2	514799.1
4.0	0.63792	291172.0	456441.2	984663.8
5.0	0.77102	362839.8	470598.6	1179195.1
6.0	0.83561	434262.2	490755.1	1336953.0
10.0	1.23692	717827.1	580336.4	1756003.9
15.0	1.51477	1068004.1	705061.1	1961532.1
20.0	1.68125	1413800.4	840920.0	1948708.1
25.0	1.78102	1755394.8	985609.3	1806655.0
30.0	1.84082	2092887.5	1136934.0	1588746.5
999.0	1.93024	27315730.0	14151455.0	-23455246.0

The optimal sortie time is approximately 15 minutes.

Example 2 (Three Targets)

$$\lambda = 1.8/\text{hr} ; p_1 = 0.08 ; \alpha = \lambda p_1 = .144/\text{hr}$$

$$1/\mu = 5 \text{ min} ; p_2 = 0.50 ; \beta = \mu p_2 = 6/\text{hr}$$

$$k = \$2,000 ; C_0 = \$6,000/\text{hr of sortie} ; C_A = \$30,000,000/\text{aircraft}$$

$$\text{At } \$20,000/\text{round of ammunition and 100 rounds per attack, } C_M = \$2,000$$

$$B = \$2,000,000$$

TABLE 2

Time (min)	$E[N(t)]$	$E[S(t)]$ (\$)	$E[S(t)]/E[N(t)]$ (\$)	$B E[N(t)] - E[S(t)]$ (\$)
0.0	0.00000	2000.0	Infinity	-2000.0
1.0	0.18920	74749.9	395087.1	303647.3
2.0	0.47662	147624.8	309730.9	805620.6
4.0	0.94019	292212.9	310802.4	1588164.8
5.0	1.14181	364062.1	318846.0	1919561.5
6.0	1.31269	435618.1	331852.0	2189757.5
10.0	1.83368	719501.8	392380.9	2947862.3
15.0	2.24563	1069841.4	476410.9	3421413.0
20.0	2.49244	1415696.4	567995.1	3569192.8
25.0	2.64035	1757312.1	665559.3	3523396.5
30.0	2.72900	2094812.6	767613.1	3363178.0
999.0	2.86157	27317658.0	9546398.0	-21594524.0

The optimal sortie time is approximately 20 minutes.

Example 3 (Four Targets)

$\lambda = 1.8/\text{hr}$; $p_1 = 0.08$; $\alpha = \lambda p_1 = .144/\text{hr}$

$1/\mu = 5 \text{ min}$; $p_2 = 0.50$; $\beta = \mu p_2 = 6/\text{hr}$

$K = \$2,000$; $C_0 = \$6,000/\text{hr of sortie}$; $C_A = \$30,000,000/\text{aircraft}$

At $\$20.00/\text{round of ammunition}$ and $100 \text{ rounds per attack}$, $C_M = \$2,000$

$B = \$2,000,000$

TABLE 3

Time (min)	$E[N(t)]$	$E[S(t)]$ (\$)	$E[S(t)]/E[N(t)]$ (\$)	$B E[N(t)] - E[S(t)]$ (\$)
0.0	0.00000	2000.0	Infinity	-2000.0
1.0	0.23343	74924.2	320977.1	391926.3
2.0	0.61886	148167.5	239418.5	1089561.0
4.0	1.23537	293241.5	237371.0	2177503.0
5.0	1.50592	365269.8	242879.2	2642561.5
6.0	1.72976	436957.8	252612.0	3022559.3
10.0	2.41646	721156.6	298434.9	4111768.0
15.0	2.95936	1071656.4	362124.8	4847056.5
20.0	3.28462	1417570.0	431577.7	5151676.0
25.0	3.47954	1759206.9	505585.6	5199879.0
30.0	3.59636	2096715.1	583010.8	5095999.0
999.0	3.77106	27319566.0	7244524.0	-19777438.0

The optimal sortie time is approximately 25 minutes.

VII. CONCLUSIONS

A sortie model involving a single aircraft attacking an arbitrary number of independent and identical passive targets is developed by assuming the following input parameters:

- a. the frequency of occurrence of enemy threat encounter
- b. the probability that the aircraft is killed once it encounters enemy threats
- c. the average time necessary to acquire and attack a target
- d. the probability that a target is killed once attacked
- e. the sortie time

Mathematical expressions for the probability of various events associated with a sortie are derived by generalizing the results obtained for one and two targets. The results are used to formulate several measures of effectiveness.

Cost models of the sortie are also developed by considering such cost components as:

- a. initial preparation cost of the sortie
- b. expected cost associated with the duration of the sortie
- c. expected cost of aircraft loss
- d. expected cost of ammunition used
- e. expected number of targets destroyed
- f. expected benefit derived in killing a target

For, any given number of targets, the cost model provides the unique optimal sortie time which maximizes the expected gain of the sortie. The optimal sortie time could be an important criterion to use

in order to arrive at the best decision to defeat a number of potential targets during a given sortie.

A number of other sortie models can be obtained by relaxing the restrictions of our basic assumptions such as:

- a. the targets are active
- b. there are an arbitrary number of independent and identical aircraft attacks on passive targets and/or active targets
- c. the attack on each target consists of several passes

Additional methodologies may be developed by modifying existing Lanchester-type models. However, development of new sortie models will require new analytic approaches.

REFERENCES

- [1] Sivazlian, B. D., "Aircraft Sortie Effectiveness Model, Part I: Case of One Target", Research Report No. 87-6, Department of Industrial and Systems Engineering, The University of Florida, Gainesville, FL, June 1987.
- [2] Sivazlian, B. D., "Aircraft Sortie Effectiveness Model, Part II: Case of Two Targets", Research Report No. 87-7, Department of Industrial and Systems Engineering, The University of Florida, Gainesville, FL, June 1987.

APPENDIX

1. FORTRAN PROGRAMMING to compute $E_N[N(t)]$, $E[S(t)]$, $E[S(t)]/E_N[N(t)]$ and $B E_N[N(t)] - E[S(t)]$

```
*****
*  COMPUTATION OF COST RELATED MEASURES OF EFFECTIVENESS  *
*****
```

I. DESCRIPTIONS OF INPUT SYSTEM PARAMETERS

- 1). λ : mean occurence rate of enemy threats.
- 2). $1/\mu$: average time it takes the aircraft to acquire the target.
- 3). P_1 : probability that the aircraft is killed once one enemy threat is encountered.
- 4). P_2 : probability of the target being killed once attacked.
- 5). α : $\lambda \times P_1$
- 6). β : $\mu \times P_2$
- 7). N : the number of targets.
- 8). $E[N(t)]$: expected number of targets killed at time t .
- 9). $E[A(t)]$: expected number of attacks at time t .
- 10). $E[S(t)]$: expected cost of the sortie at time t .

II. DESCRIPTIONS OF INPUT COST PARAMETERS

- 1). K : fixed cost in preparation of the sortie.
- 2). C_0 : cost per unit duration time of the sortie.
- 3). CA : replacement cost of the aircraft.
- 4). C_m : cost of ammunition per attack once a target.
- 5). B : dollar benefit in killing a single target.

III. CONVERSION TABLE OF PARAMETERS AND VARIABLES

input parameter	variable	
λ	x	
μ	y	
P_1	P_1	
P_2	P_2	


```

C
C
C *** Computation of expected cost of the sortie
C   t unit times following the start of the sortie ***
C
C   Est=K+Cost1+Cost2+Cost3
C
C
C *** Computation of expected cost of the sortie
C   per expected number of targets killed ***
C
C   If(ENT.NE.0.0) RSN = Est/ENT
C
C *** Computation of expected gain of the sortie ***
C
C   BNS = BB*ENT-EST
C
C *** Characterazation of output ***
C
C   If(ENT.EQ.0.0) then
C       Write(2,17) t, ENT, EST, BNS
17   Format(F6.1,3x,F9.5,3x,F16.1,11x,'Infinity',3x,F16.1)
C   Else
C       Write(2,18) t, ENT, EST, RSN, BNS
18   Format(F6.1,3x,F9.5,3x,F16.1,3x,F16.1,3x,F16.1)
C   Endif
C
C   Write(2,19)
19   Format('-----',
C   $   '-----')
C
C   Enddo
C   Stop
C   End

```

2. Example of Input Data File

Assume that:

the number of targets $N = 5$;

$\lambda = 0.03/\text{min}$; $p_1 = 0.08$; $\mu = 0.2/\text{min}$; $p_2 = 0.5$

$K = \$2,000$; $C_0 = \$100/\text{min of sortie}$;

$C_A = \$30,000,000/\text{aircraft}$; $C_M = \$2000/\text{attack}$;

$B = \$2,000,000/\text{killing target}$.

Also assume that we compute $E_5[N(t)]$, $E[S(t)]$, $E[S(t)]/E_5[N(t)]$ and

$B E_5[N(t)] - E[S(t)]$ for twelve sortie times namely $t = 0.0, 1.0, 2.0,$

$4.0, 5.0, 6.0, 10.0, 15.0, 20.0, 25.0, 30.0, 999.0$.

Then the input data file has the following form:

5,0.03,0.2,0.08,0.5

2000.0,100.0,30000000.0,2000.0,2000000.0

12

0.0,1.0,2.0,4.0,5.0,6.0,10.0,15.0,20.0,25.0,30.0,999.0

3. Example of Output

INPUT PARAMETERS AND RESULTS OF COMPUTATION *****

I. INPUT PARAMETERS

(1) SYSTEM PARAMETERS

Number of targets (N) = 5 ;
 $\lambda = 0.030/\text{min}$; $P1 = .080$; $\alpha = 0.00240/\text{min}$
 $\mu = 0.200/\text{min}$; $P2 = .500$; $\beta = 0.10000/\text{min}$

(2) COST PARAMETERS

K = \$ 2000.0 ; $C_0 = \$ 100.0/\text{min of sortie}$;
 $CA = \$ 3000000.0/\text{aircraft}$; $CM = \$ 2000.0/\text{attack}$;
 $B = \$ 200000.0/\text{killing target}$

II. RESULTS OF COMPUTATION

Time (min)	$E[N(t)]$ (#)	$E[S(t)]$ (\$)	$E[S(t)]/E[N(t)]$ (\$)	B $E[N(t)] - E[S(t)]$ (\$)
0.0	0.00000	2000.0	Infinity	-2000.0
1.0	0.27661	75096.1	271487.7	478123.4
2.0	0.75777	148703.8	196238.5	1366838.1
4.0	1.52364	294257.9	193128.5	2753017.0
5.0	1.85753	366463.3	197285.0	3348602.3
6.0	2.13705	438281.7	205086.8	3835826.3
10.0	2.98559	722791.7	242093.9	5248375.5
15.0	3.65635	1073450.1	293584.5	6239266.0
20.0	4.05823	1419421.3	349763.2	6697048.5
25.0	4.29906	1761079.1	409642.5	6837048.0
30.0	4.44339	2098595.0	472295.9	6788186.0
999.0	4.65925	27321450.0	5863921.5	-18002960.0

FINAL REPORT NUMBER 78
REQUESTED A NO-COST TIME EXTENTSION
TO BE SUBMITTED IN 1987 MINI-GRANT FINAL REPORT
Dr. Siavash Sohrab
760-6MG-110

FINAL REPORT FOR
1986 USAF-UES SRFP/GSSP CONTINUATION GRANT

Synchrotron White Beam Topography of Striations
and Interface Breakdown in GaAs
and of Strain Fields in Si

by

Stuart R. Stock

Assistant Professor
School of Materials Engineering
Georgia Institute of Technology
Atlanta, Georgia 30332-0245

January 15, 1988

Abstract

The primary focus of this project was the characterization of striations and of interface breakdown in LEC GaAs(In) by synchrotron white beam topography. Wafers grown for the Air Force by Texas Instruments and by Rockwell and wafers provided by Hewlett-Packard OED were studied. Whenever possible wafers cut from adjacent parts of the boule were examined. Synchrotron microbeam diffraction was also applied to the study of In concentration gradients in wafers with striations.

The secondary object was to develop techniques for the mapping of long-range strain fields in silicon. Synchrotron white beam section topography was employed, and the extra Pendellosung fringes introduced by the varying strain gradients provided the data for this analysis. Strain fields around laser-drilled holes and around simulated and actual devices were studied.

Significant progress was made toward developing these new techniques and toward understanding striation formation and interface breakdown morphology. Analysis of the microbeam diffraction experiments is still underway.

I. Introduction

Characterization of growth defects in GaAs alloyed with In and with other elements and in Si containing long-range strain fields was the goal of this one-year research program. The specific areas of research were: identification of anomalous electrical regions in ion-implanted Si, elucidation of striation structure in GaAs (In) and characterization of interface breakdown morphology in GaAs (In). Little effort was devoted to studying CVD Si(Ga) layers on Si because no new specimens were available.

Synchrotron white beam x-ray diffraction topography was the technique used for studying the semiconductor crystals. Much of the research was straight-forward characterization using projection and reflection topography. In addition, section topography was used to examine strain gradients between implanted and un-implanted regions of extrinsic Si detector materials. Development of novel x-ray topographic techniques was also an important part of the program. Section topographic strain mapping was further refined. Topographic EXAFS was investigated for use in identifying changes in stoichiometry in doped and undoped GaAs. Finally, microbeam diffraction mapping was used to investigate changes in composition across striations in GaAs(In).

The importance of the materials under study and a description of synchrotron radiation and white beam topography are outlined in the proposal and will not be reiterated. Where it is necessary to the interpretation of results, additional

explanations will be furnished in the appropriate section.

II. Results

All of the synchrotron white beam topography was performed at the Stanford Synchrotron Research Laboratory (SSRL) during the following periods: December 15-23, 1986; March 27-April 8, 1987; October 30 - November 4, 1987; November '28 - December 9, 1987 and December 18-21, 1987. All of the experiments at SSRL were with white radiation and were performed in collaboration with Dr. Z.U. Rek of SSRL. Mr. Y.H. Chung (the author's student) helped during the last three periods; Mr. P.C. Huang (the author's student) and Professor T. Gross of the University of Kentucky assisted during the experiments of December 18-21, 1987. Table 1 lists the Si specimens from AFWAL/MLPO and UDRI which were studied at SSRL; Table 2 lists the GaAs samples examined.

Topographic EXAFS experiments were performed at SSRL during April 1987 in collaboration with Dr. D.K. Bowen and Ms. L. Hart of the University of Warwick, England; Dr. Bowen's group is undertaking the complex image processing required to detect contrast changes due to the topographic EXAFS effect. Some preliminary synchrotron monochromatic topographic imaging was performed at the National Synchrotron Light Source (NSLS) in collaboration with Dr. M. Kuriyama's group (National Bureau of Standards); little relevant information was obtained during the short run (February 4-6, 1987), and no further discussions is included in this report. Microbeam diffraction mapping of the spatial variation of lattice parameter in a striated GaAs(In)

wafer was performed at Line X14C, NSLS during January 5-12, 1987. This experiment by the author and Mr. Y.H. Chung was in collaboration with Drs. G.E. Ice and C.J. Sparks, Jr. of Oak Ridge National Laboratory and Dr. A. Habenschuss of Oak Ridge Associated Universities; due to a lack of manpower these results are only now being analyzed, and discussion will, therefore, be limited.

IIa. Study of anomalous electrical regions in ion-implanted Si

This portion of the project centered on identification of the mechanism(s) of performance degradation in extrinsic Si detector materials. Current fabrication requires Si amorphotization followed by Ga implantation. Certain areas of the specimens exhibited anomalous electrical behavior, and it is unclear whether impurity content or damage/strain is the primary factor in degraded performance. X-ray diffraction topography (white beam projection, section and reflection methods) was used to investigate whether damage was associated with these areas. Table 1 lists the samples studied in this part of the project.

Projection topographs of samples G0319-1416 and G0319-1438 are shown in Figure 1. The horizontal lines at top and bottom of these topographs represent the borders of different implantations. The strain gradient is quite severe in this region: diffracted intensity is much greater than background. In the topographs of the former sample there are several, somewhat irregular borders, indicating that the masking procedure probably

could be improved. Considerable damage is visible on both samples (small and large spots and lines in the center part of the specimen) and appears to be associated with surface flaws introduced during handling or testing.

Transmission projection topographs were recorded from G0343-2411-b,-c,-B and -C which had been implanted with different doses of silicon ions (Figure 2).^{*} The incident x-ray beam was normal to the surface, and symmetrical Laue patterns were obtained. Contrast at the interface between implanted and unimplanted material was clearly visible in topographs from all four samples. As different reflections are sensitive to different components of the strain gradient at the interface, one expects different contrast in different diffraction spots. This was observed: the interface had contrast above and below background and in certain hkl it was invisible. The contrast of the interface definitely was greater at larger implantation doses (for the same hkl), which is a qualitative indication of higher strain gradients (e.g. higher stress). The visibility of the border was directly related to the orientation of the diffraction vector $\underline{h} = [hkl]$ relative to the edge of the implanted region. When the projection of \underline{h} was parallel to or nearly parallel to the border, minimum contrast was observed. The converse was also true: \underline{h} perpendicular to the border gave greatest contrast. This result

^{*}The lower-case letters denote (100) wafers while the capital letters denote (111) orientations. The samples labeled by the same letter received the same implantation treatment, and the alphabetical order of samples indicated decreasing dose.

is consistent with the expected variation in strain field.

The diffracted intensity was also greater on the implanted side than on the unimplanted side of the crystal. This was most visible in section topographs (Figure 2b). With the slit oriented perpendicular to the border, a few reflections showed a change in Pendellosung fringe pattern on either side of the boundary. An extra half period was introduced on the ion implanted side, indicating significant strain was present (Figure 2c). The maximum strain from the rapidly varying strain field normal to the substrates' surface can be calculated from this result, but as it involves numerical solution of the dynamical diffraction equations for hypothetical strain distributions, the calculation of strain is beyond the scope of this project.

Section topographs recorded with the slit parallel to the implantation border were much more sensitive to the strains present (Figure 2d). A large number of extra fringes were introduced, indicating that the strain gradients extended much farther and were much more intense normal to the border than perpendicular to it. We note this result is similar to our results for devices on silicon obtained from an identical geometry (see Section II.c). Quantification of the strain is quite beyond the scope of this project as outlined above. We believe that a reasonably small effort in this area would pay enormous dividends in terms of understanding of the strains associated with implanted layers.

IIb. Striation structure and interface breakdown morphology in GaAs(In)

The structure of striations and the morphology of interface breakdown were studied for wafers and longitudinal slabs of GaAs(X), where X represents various atomic species. As In is the most commonly used isovalent dopant, the majority of samples examined were GaAs(In) and contained on the order of 1 at % In. Sets of wafers spanning the initiation and development of interface breakdown were studied with projection (transmission) and reflection settings (Table 2). Wafers from two Hewlett-Packard boules* and from two Texas Instruments boules** provided the bulk of data.

Topographs from pairs of wafers from the seed and tail ends of boules doped with different elements*** showed well-defined striations in some cases. Both tail and seed-end wafers doped with In showed striation structure as did the seed-end wafer doped with P. The striation structure was very similar in both cases (Figure 3) although there were many more dislocations visible in the P-doped material -- which may be an artefact of the growers' process. We note, however, that the tail end of the P-doped boule had a structure identical to that of undoped GaAs: cellular dislocation walls. The P in this boule was less

* Grown in a low thermal gradient, fully encapsulated, low-pressure LEC process. The nominal boule diameter was 65 mm.

** Grown by low pressure, LEC process. The diameters of the wafers examined were 3.0 in.

*** These wafers comprise the first group of Run 12/86 in Table 2.

successful than In in suppressing dislocation generation; without data on the different concentrations and growth processes, nothing further can be concluded.

Our first observation of interface breakdown was in the tail-end of the In-doped boule (G0508-2416), and the boundary of the breakdown region is shown in Figure 3c. The breakdown cells had a very uniform diameter throughout, unlike those observed in the HP and TI wafers. The cells tended to be aligned in rows, but there were numerous faults in the "stacking," and the arrays were not closed-packed. A feature common to all of the In-doped material was the presence of alternating light and dark streaks extending from the cells. This structure was evidently a precursor to cell formation.

Similar breakdown structures were observed in wafers from HP (H276, H287 and H288) and from TI (EB46). Unfortunately wafers from TI EB48 were not available from the interface breakdown region. The morphology of the breakdown zones in the other boules were very similar and only the data from H276 will be presented in detail. Figure 4 shows transmission white beam topographs from H276 which allow one to trace the spread of the cellular region*. Most of the figures are mosaics of several topographs: the areas of interest were much larger than the x-ray beam. The Burgers vectors of the dislocations observed in GaAs(In) wafers could not be identified because they were never

*The left hand edge of the topographs is the edge of the half wafer which was available to us. The topographs of Figure 4 were from the center of the boule.

out of contrast. This may be due to In decoration .

Just prior to interface breakdown, the normal concentric striation rings had given way to a very distorted pattern. (Figure 4a). The swirling pattern of striations was reminiscent of turbulence and probably reflected local instabilities in the rate of solidification. The area of the topograph labeled S showed contrast similar to the light and dark alternating streaks noted in Figure 3c, and it is believed that the two topographs showed slightly different stages in the nucleation of the cellular structure. The dislocation density was very low in this wafer.

Slice 58 was the next available wafer and the cellular structure was well-advanced and not quite circular, covering an area of about 12 mm^2 (Figure 4b). The cell size was reasonably uniform, about 0.4 mm diameter, and few dislocations were observed. Some substructure was visible, but well-defined facets (such as observed in Figure 4e or Figure 6b,c) could not be resolved.

A few dislocations were observed in slice 59, and the morphology of the breakdown zone was similar to that observed in slice 58 (Figure 4c). The zone diameter was approximately 7 mm, and the average cell diameter was somewhat larger (0.6 mm). As was seen in slice 60 which had a length of 10 mm (Figure 4d), the shape of the breakdown region was not circular, and slice 59 probably had a similar shape. Striations were faintly visible in both, and some of the cells in the lower part of the zone in

slice 60 resembled the faceted cells observed in optical micrographs. The 90° bends in the dislocations in the lower part of the slice 60 topograph were a very unusual feature in GaAs, and one could perhaps explain them by invoking dislocation motion and intersection while the temperature of the boule was near the melting point.

Figure 4e was from slice 63 and showed a wide range of cell sizes. The prism structure was very clear in the middle of the breakdown volume. The diameter was about 21 mm, and the zone was more radially symmetric. Another interesting feature was the a lobe of the interface breakdown region which almost surrounded a region of material in which constitution supercooling had not reached the initial value for interfacial instability.

Figure 5 shows topographs from wafers 32 and 42 of boule H287. Well-defined striations and interface breakdown are shown. Along the edge of the breakdown region in wafer 42, alternating light and dark streaks were observed as were jogs in the striations nearby. These features were identical to those shown above. Very few dislocations were present, indicating that the dislocations observed in wafers from boule 276 were incidental to the breakdown process.

Figure 6 shows two topographs and one optical micrograph from various cellular structures. Figure 6a was from boule H288 and was recorded in transmission. Figure 6b was recorded in reflection from TI boule EB46, wafer 66. Note that this wafer was not etched: the images exhibit diffraction contrast and not

contrast from surface topography. This wafer was not thinned so transmission topography yielded little information. The images of prismatic cells was remarkably similar to optical micrographs provided by HP (Figure 6c).

Some longitudinal slices were also studied with topography. The only well-defined interface breakdown was observed in the slab provided by Rockwell, R162 (Figure 6d). Diffraction contrast from the cell boundaries was visible. There were quite a number of breaks in the cells (horizontal boundaries) which might be related to growth interruptions.

We are currently attempting to obtain more wafers from boules exhibiting interface breakdown. A complete series of wafers, spanning the ~1cm length of the boule in which breakdown spreads, would add significantly to the understanding of the breakdown phenomena. Continued progress depends on the availability of Air Force funding, the possibility of which appears quite good.

IIC. Section Topographic Strain Mapping

In section topography a narrow, ribbon-like beam of x-rays is used to illuminate a triangular prism of material in the specimen. A parallel-sided, low absorption crystal such as Si produces section topographs containing fringes parallel to the sides of the topograph. The maxima and minima in the fringe pattern are loci of constant phase between Bloch waves at the exit surface of the crystal. Strain gradients increase the number of fringes, and spatially varying gradients are imaged in

a single section topograph as sections through hyperboloids. The approximation of geometric optics to dynamical diffraction theory allows one to relate the magnitude of the gradient to the number of addition fringes introduced in the section topograph. While this equation does not have an analytic solution, it is fairly simple to solve iteratively.

In most cases the strain gradient is not as useful as the strain itself, and Mr. Chung and the author have developed a simple method of extracting elements of the strain tensor $\epsilon_{ij}(x,y)$ from the elements of the gradient tensor as a function of position around a stress concentrator. Note that ϵ_{ij} is an average over the thickness of the specimen. The method relies on the fact that the gradient is the first derivative of strain and that the strain and strain gradient tensors are zero far from the concentrator. Strain is therefore obtained by integrating the gradient over the direction parallel to the projection of the diffraction vector.

The strain fields in silicon crystals around laser-drilled holes and around simulated and actual devices were studied using white beam section topography. Normally narrow adjustable slits are used, but only one section topograph can be recorded at any time. The large, parallel beam of synchrotron radiation made possible recording several section patterns simultaneously. A set of narrow, parallel slits were drilled in a Ta foil for this purpose and up to six section patterns could be recorded simultaneously at SSRL using the multiple slit. A set of section

topographs around a laser-drilled hole is shown in Figure 7 for this specimen. Also shown are the contours of constant dilational strain.

Simulated and actual devices have been studied with projection and section topography. Section topographs seemed to be most sensitive to strain gradients when the slit was oriented parallel to the edge of the oxide layer or device. A typical example was an (001)Si wafer with stripes of silicon nitride on a uniform oxide layer. In white beam projection topography one could always observe the location of the borders. In section topographs with the diffraction vector and slit normal to the stripe borders, however, the position of the borders were not evident. When the section patterns were recorded with the slit at 45° from the stripe border, the location of successive edges were clearly evident (Figure 8). Images of successive edges showed contrast alternating above and below the background of Pendellosung fringes. This is easily explained by noting that the strain gradients have the same magnitudes but opposite signs; channeling of x-rays is expected and will produce this type of contrast. In some section patterns, an additional half-Pendellosung period was observed indicating that there was a significant difference in strain underneath the two types of layers.

The highest sensitivity to strain appeared when the section slit was parallel to the edge of the device or layer (Figure 9). In this orientation at least nine extra fringe periods were

observed. Analysis of the local strain gradient is beyond the scope of the geometric optical approximation to the dynamical diffraction described above. Considerable numerical analysis is necessary before anything other than a qualitative understanding can be advanced. The qualitative understanding is sufficient, however, for optimizing processing conditions and will thus have a major impact.

We note that it has been a major accomplishment for the device fabricators to make samples which are perfect enough for Pendellosung fringes to be resolved. We also note that the section topograph of the extra Pendellosung fringes introduced by the devices strain field is the first ever obtained from an actual device. This major advance should lead rapidly to improved processing and to a deeper understanding of influence of layer parameters on the stress introduced.

IIId. Topographic EXAFS examination of stoichiometry variation in a longitudinal GaAs crystal*

Topographic EXAFS refers to x-ray topographic contrast due to fluctuations in absorption (e.g. EXAFS--extended x-ray absorption fine structure) of a specimen diffracting wavelengths near that of the absorption edge of an element in the sample. Even if the sample is unbent, the intrinsic divergence of the white radiation beam is sufficient for diffraction of energies spanning at least a single absorption oscillation. On bent crystals the contrast takes the form of parallel fringes.

*This research was partially supported through NSF grant INT-8513629.

Disturbances in the fringe pattern indicate anomalous regions of the sample; the strain and chemical contributions, however, must be separated. If this can be done, one will be able to simultaneously probe the spatial distribution of chemical and crystallographic defects.

Considerable effort was devoted to detecting topographic EXAFS contrast during the April 1987 run at SSRL. The facilities available at that time were not optimum for detecting this effect. The vertical beam size was limited to about 4 or 5 mm and thus the accessible energy range was less than optimum. The goniometer's angular rotation was rather coarse, given the above constraint, and thus was a great hinderance. The experiment requires locating a favorable transmission Laue spot and orienting to diffract wavelengths at the absorption edge; a real-time x-ray video camera is vital for rapid orientation. The detector available proved to be unsatisfactory, and we were forced to do the alignment using a large number of Polaroid exposures (at least 52 exposures were required).

The absorption edge for a $\langle 110 \rangle$ reflection of an undoped GaAs crystal was obtained, and numerous topographs were recorded (75 high resolution SR5 films) as the specimen was rotated across the edge. Between top and bottom of the longitudinal wafer, a 1% difference in Ga concentration was known to exist, and the absorption edge was "scanned" at either end of the crystal. The large change in contrast associated with the edge was clearly visible, but it was impossible to detect the presence of

topographic EXAFS contrast by eye. Detailed image analysis is required to determine whether topographic EXAFS was present. Our collaborators from Britain have considerable expertise in this area and are about to begin this phase of the study.

Ile. Synchrotron X-Ray microbeam diffraction mapping of lattice parameter variation in striated GaAs(In)*

The spatial variation of lattice parameter in a striated crystal of GaAs(In) (G04265-2042) was measured using monochromatic x-rays. Rocking curves from each position were recorded in reflection using the symmetric (004) planes and a fundamental wavelength of 1.786 Å. A nominal beam diameter of 10 µm was obtained using a laser-drilled Pd collimator. The collimator was positioned perpendicular to and within two centimeters of the sample using translation and rotation axes of the collimator mount. The small beam divergence led to little broadening of the beam footprint, and any small misalignment of the collimator would tend to compensate for this broadening. At diffraction angles of $\theta=39.20^\circ$ the beam irradiates an elliptical area with diameters of 10 and 15 µm.

Figure 10 shows a topograph of the area studied with microbeam diffraction and the projections of the incident beam and scan directions. The longer axis of the beam's footprint was approximately tangential to the striations, and the beam was

*This research was partially supported by the NSLS/HFBR Faculty Student Support Program of Brookhaven National Laboratory.

scanned in both X and Y directions in the specimen's surface (Figure 10). The topograph shows that the striation spacing was about 175 μm in this part of the crystal. Scan steps were 20, 40 or 80 μm , depending on the direction of the scan. Figure 11 shows a rocking curve from the specimen. The full width at half maximum (FWHM) is about 36 arc sec which is much larger than the expected width of about 15 arc sec; this is due primarily to the focusing optics used in Beam Line X14-C.

Analysis of the variation of lattice parameter with position is underway. cursory examinations of the data revealed that any variation would be subtle. Therefore, the peak positions were defined in terms of the centroid. Analysis is also complicated by the macroscopic curvature of the 250 μm thick specimen: its radius of curvature was approximately 4 m. Our preliminary conclusion is that further experiments are necessary, with double crystal contour mapping required for precise determination of the variation of lattice parameter and hence In concentration.

III. Recommendations

A great deal has been accomplished in many areas during the year of research supported by the UES-USAF SFRP/GSSP. Conclusions are included within the sections of the report (IIa-IIe) and are not repeated here.

A large amount of characterization activity can be supported at very modest annual levels on the order of \$50,000. It is the author's strong recommendation, therefore, that work of this kind be continued until such time as the Materials Laboratory can

justify internal development of x-ray diffraction topography capabilities. The specialized topography and rocking curve support for laboratories studying electronic and optoelectronic materials is absolutely essential for credibility in that community.

RUN	SAMPLE IDENTIFICATION	SAMPLE DESCRIPTION	TOPOGRAPHS RECORDED	COMMENTS
12/86	G0319-1416	(111)Si:Si	PCB = 2.3	anomalous regions
	G0319-1438	(111)Si:Si	PCA = 3	"
	G0343-2411-b	(100)Si:Si	b = 5-6	implanted/virgin areas
			[R] b = 11-13	"
	-c	(100)Si:Si	c = 2	"
	-B	(111)Si:Si	B = 4	"
	-C	(111)Si:Si	C = 2	"
			[S]C = 4	
	G0395-1931	Si:Ga(epi)/(100)Si	[S] C1 = 8-17	CVD layer
4/87	G0343-2411-b	(100)Si:Si	b = 19	implanted/virgin areas
			[S] b = 15-18, 20, 23	
	-B	(111)Si:Si	B = 12, 14-15	
			[S] B = 10-11, 16-18	
			B = 18'-26	
	-C	(111)Si:Si	C = 6-8	

Table 1: Silicon samples from AFWAL/MLPO and UDRI examined with synchrotron white beam topography at SSRL during the months indicated. Unless otherwise noted samples were examined in transmission and with projection topography. [R] denotes that the reflection setting was used instead of transmission, and [S] denotes section topography instead of projection.

RUN	SOURCE	IDENTIFICATION	DESCRIPTION	TOPOGRAPHS	COMMENTS
12 86	R	G0426-2042A	GaAs(In) c.s. free	GIN # 4-6	
	ST	G0520-2490	GaAs(P) tail	GPT # 4-6	AS
	CMC	G0519-2465*	GaAs seed	GUS # 1-3	
	ST	G0520-2478	GaAs(P) seed	GPS # 1-4	
	F	G0508-2413*	GaAs(In) seed	GIS # 1-4	
	F	G0508-2416	GaAs(In) tail	GIT # 2-5	
	HP	H276-S59	GaAs(In)	GC # 5-12	[AS]
	"	H287-S13	"	GC # 16-17	"
	"	H288-S5	"	GC # 22-26	"
	"	H288-S33	"	GC # 18-21	"
		RD2-035	GaAs(Ge)	GC # 13-15	"
		RD2-322	GaAs	GC # 27-29	"
4/87	HP	H276-S36	GaAs(In)	M # 71-2	[AS]
	"	-S46	"	M # 64-67	"
	"	-S52	"	X # 2-14	"
	"	-S54	"	X # 15-21	"
	"	-S56	"	M # 9-33	C*.15° from <001
	"	-S58	"	M # 1-8, 36-39	"
	"	-S60	"	M # 55-60	"
	"	-S63	"	X # 27, 29-31 [R]R5-7	"
				M # 41, 45-52	"
				X # 34-37	"
				[R] R # 8-10	"
	"	H378-S17	"	XX # 8	"
	"	-S26	"	XX # 3-5	"

(continued on next page)

Table 2: Gallium Arsenide samples examined with synchrotron while beam topography at SSRL during the months indicated. The samples were LEC wafers cut perpendicular to the growth direction unless otherwise indicated ([L] denotes a longitudinal slab, and [HB] denotes horizontal Bridgman crystals). Sources of the crystals are labeled when known: HP for Hewlett-Packard OED, TI for Texas Instruments, R for Rockwell, St for Spectrum Technologies CS for Crystal Specialties, MAC for M/A-Com and CMC for Cominco. Virtually all specimens were examined in transmission with the beam direction approximately along <100>. Other beam directions are noted as are topographs recorded using the reflection geometry ([R]). In many cases, multiple topographs were recorded to cover a larger area of the sample than the beam cross-sectional area ([AS]).

* indicates that these two samples may have been interchanged prior to delivery to the author.

** The USAF identification number has been deleted in order to save space.

Table 2 cont'd

Run	Source	IDENTIFICATION	DESCRIPTION	TOPOGRAPHS	COMMENTS
4/87 "	HP	H288-S30	GaAs (In)	XX # 11-13	[AS]
	"	-S35	"	XX # 15-17	"
	"	-S37	"	XX # 19-21	"
	"	H287-S22	"	XX # 52	"
	"	-S32	"	XX # 48-51	[AS]
	"	-S42	"	XX # 37,40-45	"
	"	-S48	"	XX # 23-35	"
11-12/87	TI	EB46-S15**	GaAs (In)	15#1-3	[AS]
	"	-S56	"	[R] 56 # 2-3	[AS]
	"	-S61	"	[R] GI61 # 1-6	"
	"	-S66	"	66 # 1-3	"
	"	EB48-S10**	"	[R] G810 # 1-2	"
	"	-S13	"	13 # 1-4	"
	"	-S22	"	22 # 1-4	"
	"	-S37	"	37 # 1-4	"
	"	-S49	"	49 # 1-4	"
	"	EB54#3**	" [L]	[R] GRI # 1-5	[AS]
	"	EB56#6**	GaAs (In+Si) [L]	[R] E B # 2-6	[AS]
	R	R162	GaAs (In) [L]	[R] GR # 2-12	[AS]
	CS	E021-551**	GaAs [HB] [L]	E021 # 7-10	[AS]
				[R] E021 # 1-4,6	
	MAC	B89-S187**	GaAs [HB]	MC # 1	
	CMC	C09-S54	GaAs (Cr)	MI # 2-3	[AS]

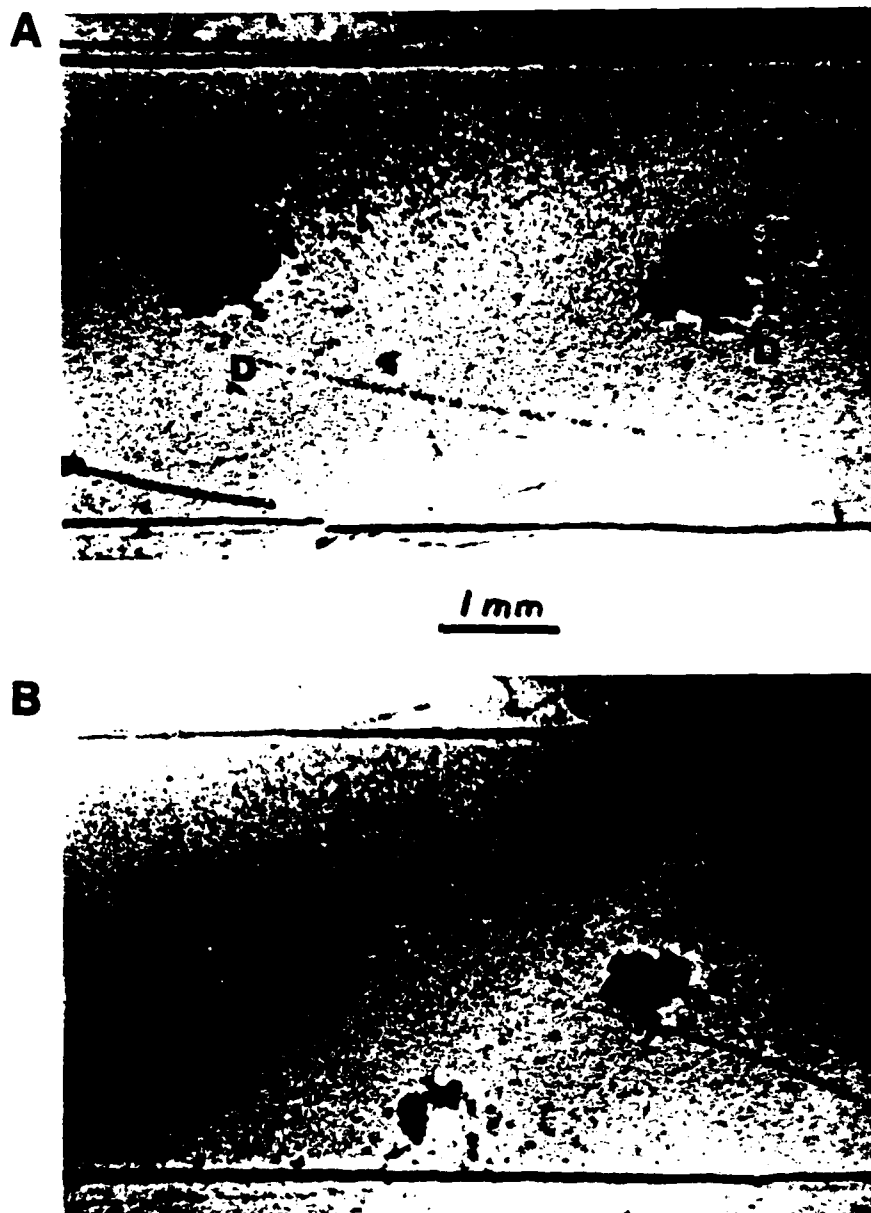


Figure 1. Projection topographs of ion-implanted Si samples G0319-1416 and G0319-1438 (a. and b., respectively). The dark lines at the top and bottom of the topographs are the borders between regions with different dosage levels. Damage is imaged as the fuzzy spots and lines, some of which is labeled by the letter D. The damage appears to be associated with surface flaws.

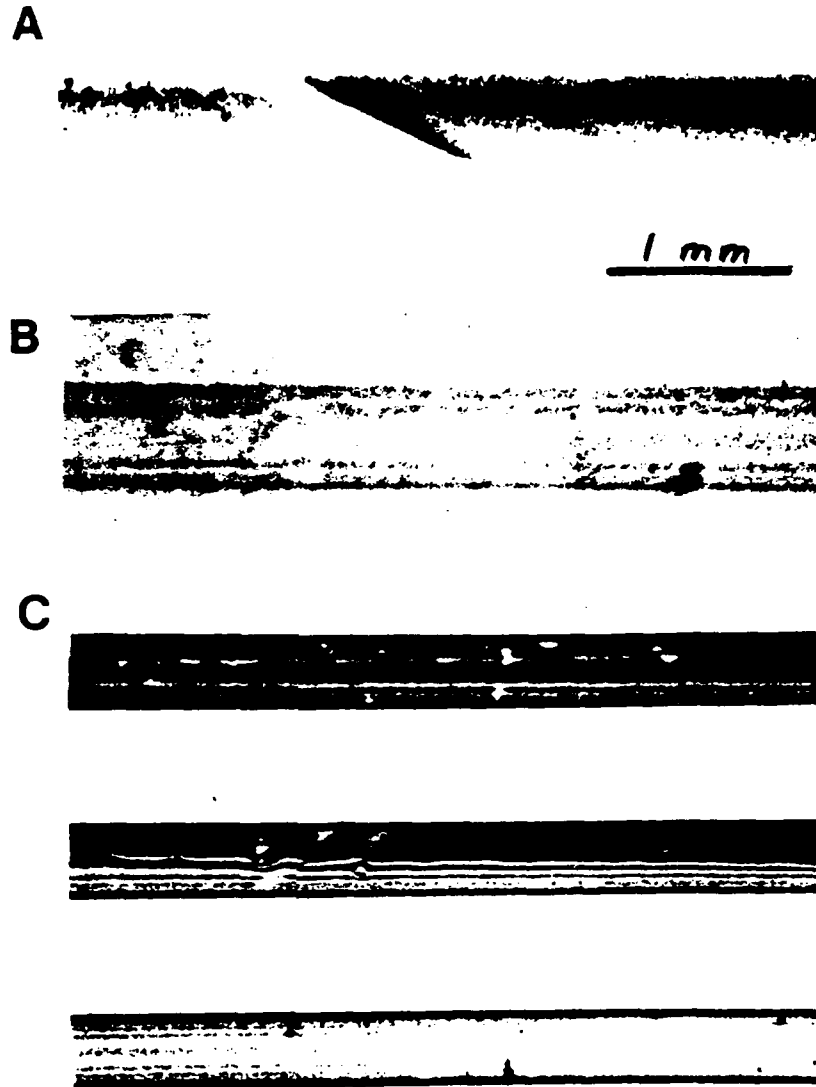


Figure 2. Section topographs from samples G0343-2411 -b, -c, -B and -C. Samples identified by lower-case letters are (001), and those given by capital letters are (111). Each letter denotes a given implantation dose, and the alphabetical order indicates decreasing dose. Part of the specimen surface was implanted, and the topographs spanned the interface between un-implanted and implanted material.

- a. Section topograph of -b with the slit normal to the implantation border. Note the change in diffracted intensity from the two sides.
- b. Section topograph of -b with the slit normal to the edge and showing the addition of an extra Pendellosung half-period on the implanted side.
- c. Section topograph of -b with the slit parallel to edge of the implanted region. Many additional fringes are introduced, and differences in diffracted intensity are clear.

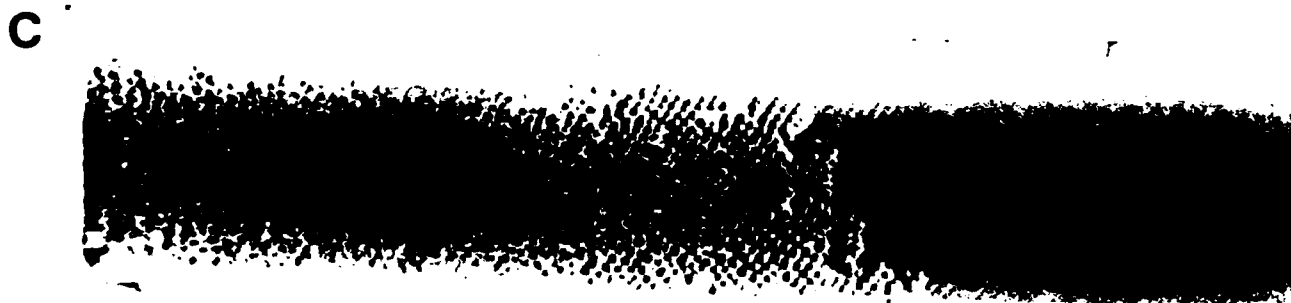
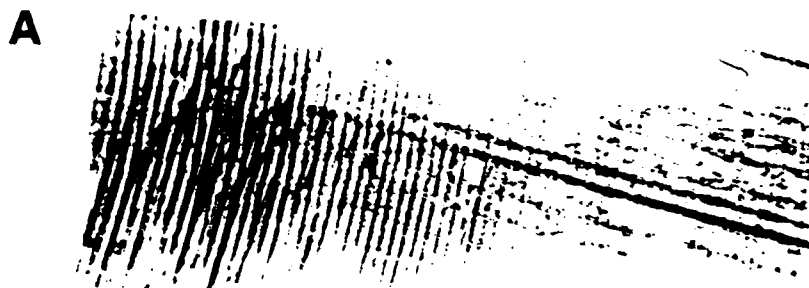


Figure 3. Topographs of wafers of GaAs doped with In and P and showing striations and interface breakdown structure.
 a. GaAs(P) wafer G0520-2478, from the seed end of the boule.
 b. GaAs(In) wafer G0508-2413, from the boule's seed end.
 c. GaAs(In) wafer G0508-2416, from the boule's tail end.
 Note the cellular zone on the left side (wafer center).

A



Figure 4. Topographs from a set of GaAs(In) wafers from boule H276 of Hewlett-Packard. These topographs illustrate the perturbation of striations just before the interface broke down and the subsequent development and spread of the cellular structure. The center of the left edge of each topograph is the center of the wafer, and topographs of wafers 56, 58, 59, 60 and 63 are shown in a.-e., respectively.

B



$\underline{h} = 511$
 $\lambda = 0.5 \text{ \AA}$
1 mm

c



$\underline{h} = 511$
 $\lambda = 0.5 \text{ \AA}$
1 mm

D

$h = 511$
 $\lambda = 0.5 \text{ \AA}$
1 mm



$h = 511$
 $\lambda = 0.5 \text{ \AA}$
Imm

E



A

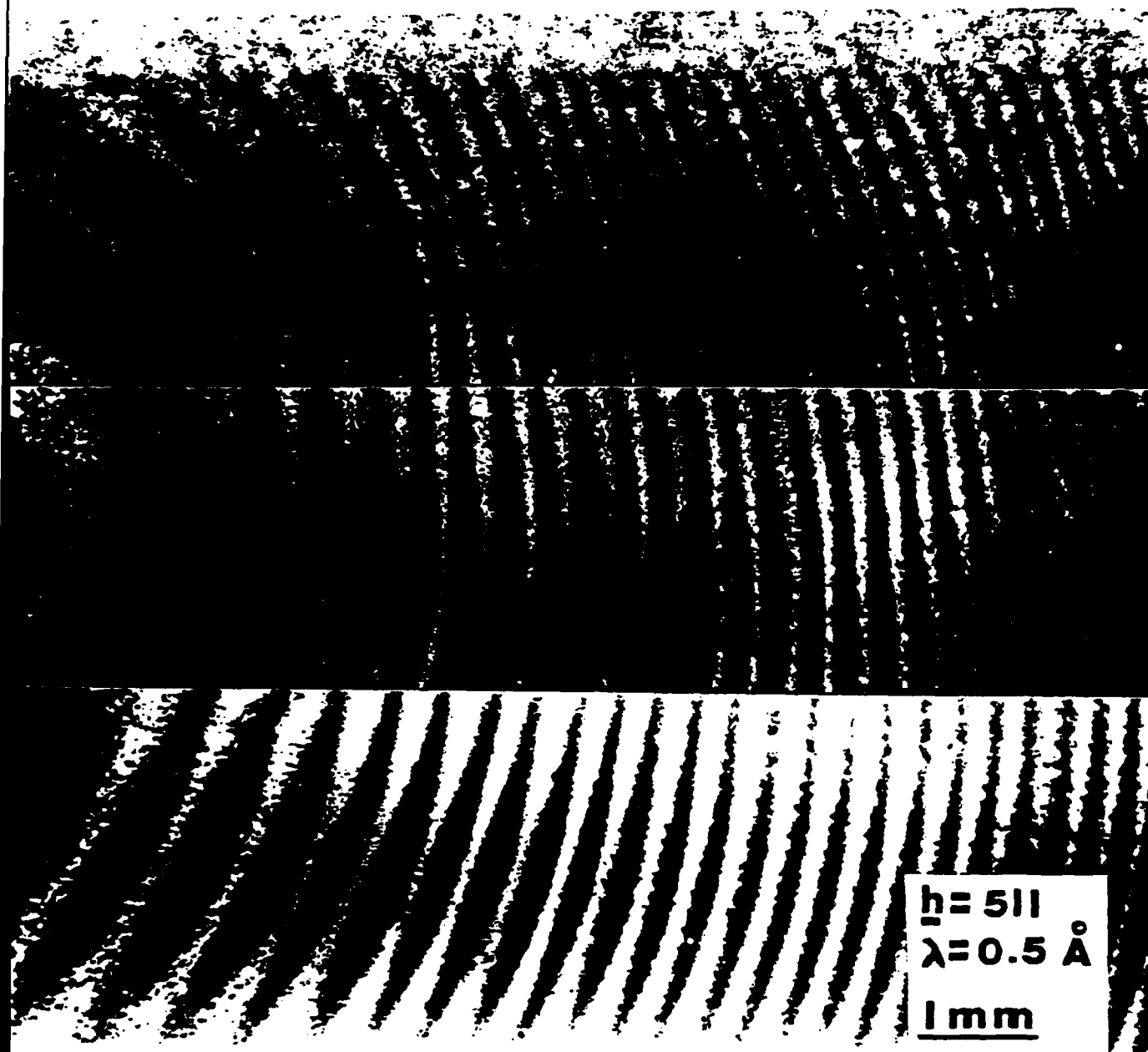
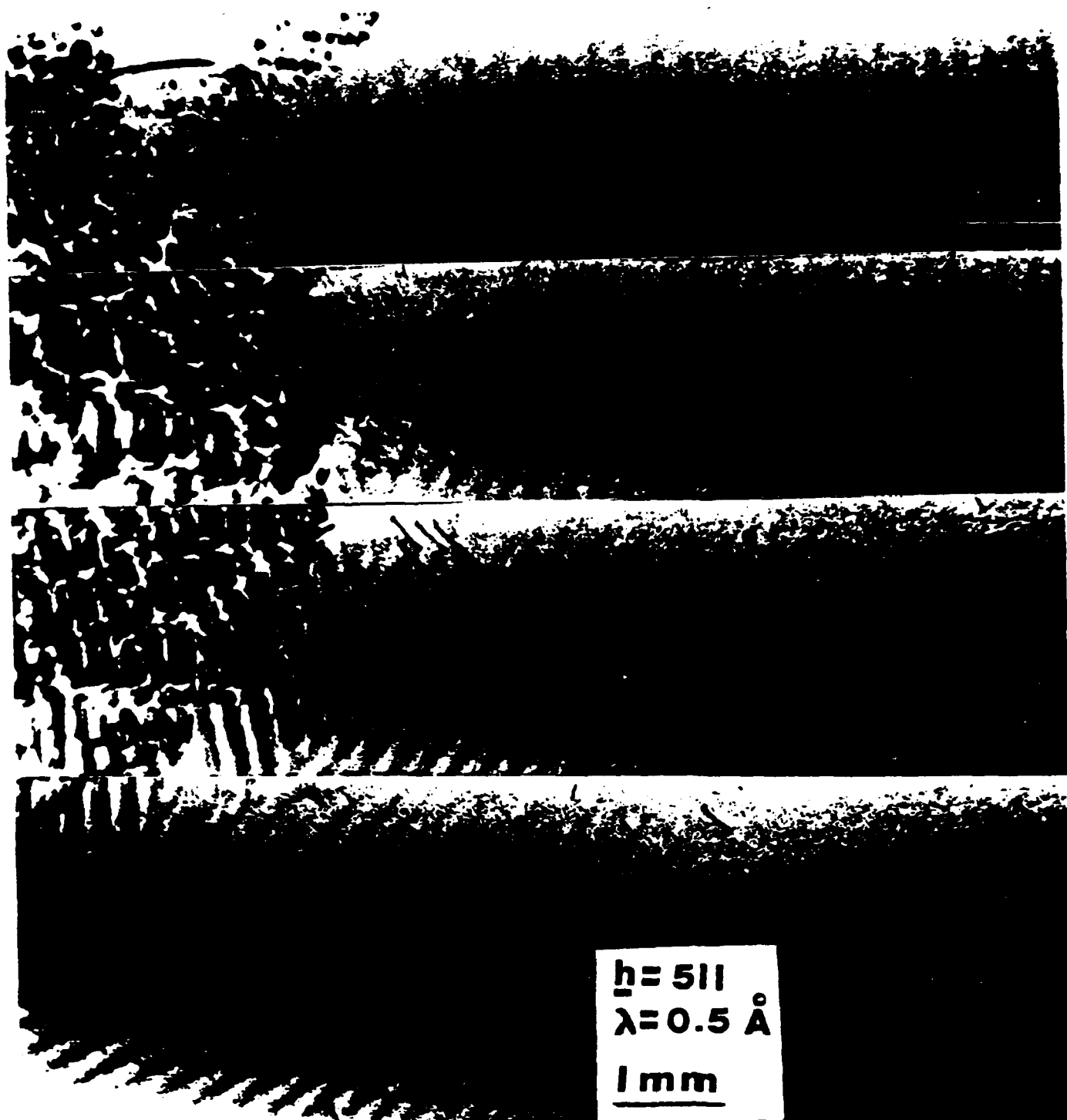
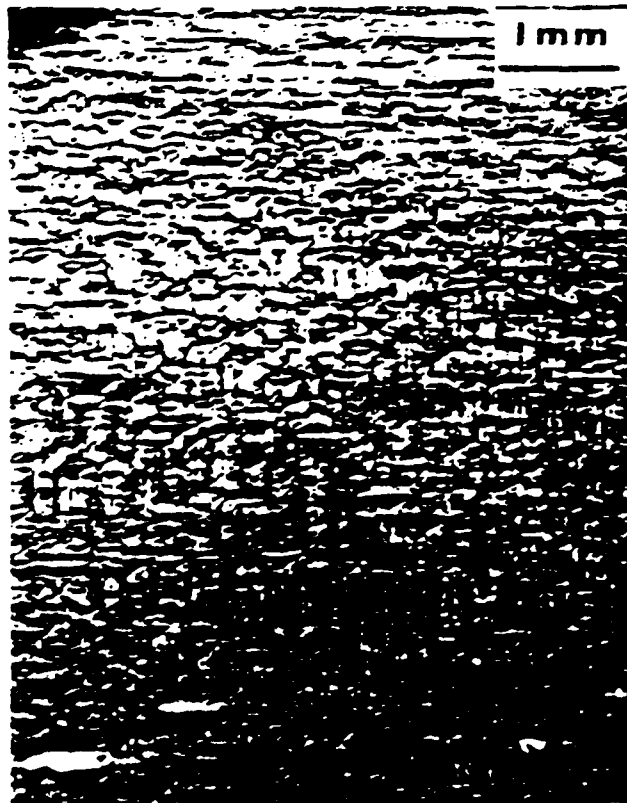


Figure 5. Topographs from Hewlett-Packard GaAs(In) boule H287 showing wafers 32 and 42 in a. and b., respectively.

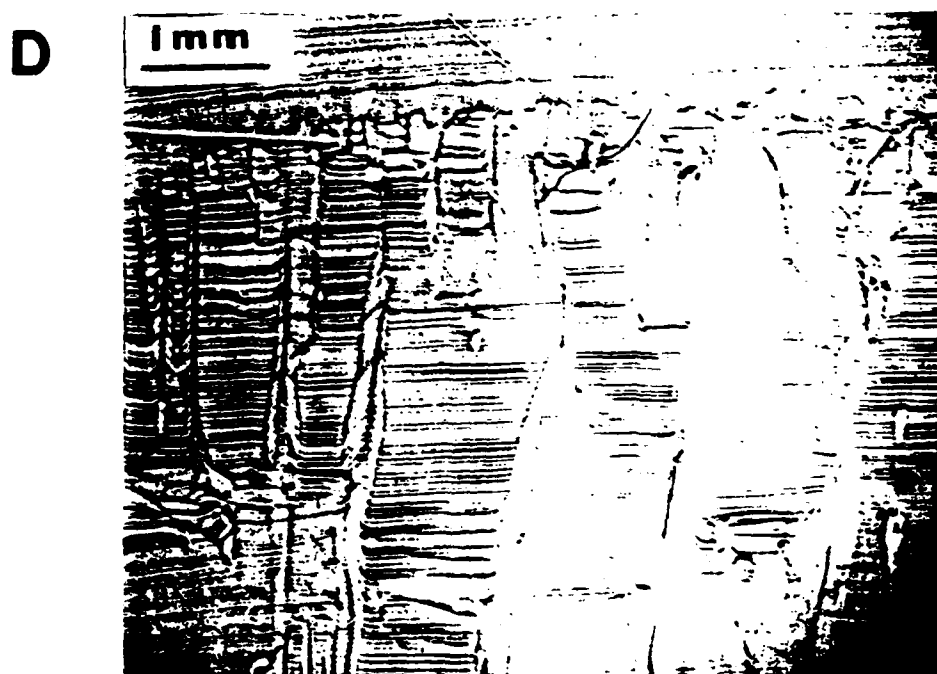
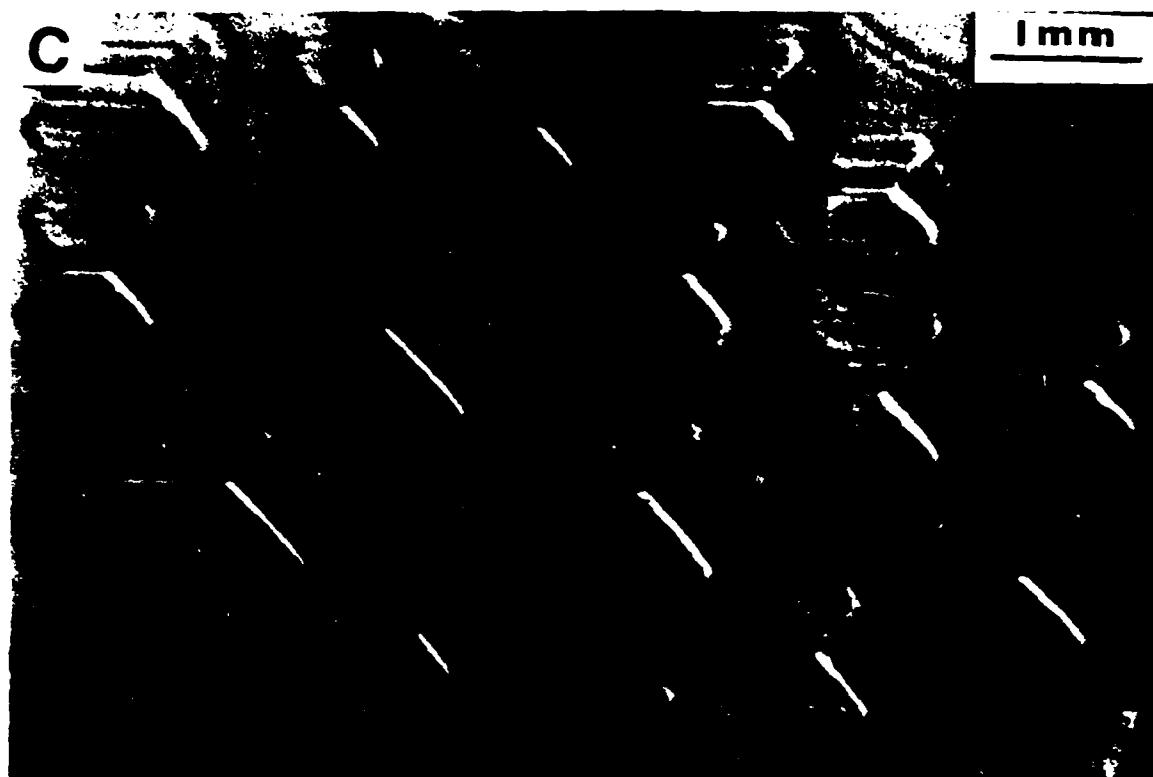
B



A**B**

$h = 511$
 $\lambda = 0.5 \text{ \AA}$
1mm

Figure 6. Comparison of cellular structures observed in a transmission topograph of a sample grown by H-P (a.), in a reflection topograph of a sample grown by T.I. (b.), in an optical micrograph of an H-P wafer (c.) and in a longitudinal slab of boule R162 provided by Rockwell (d.).



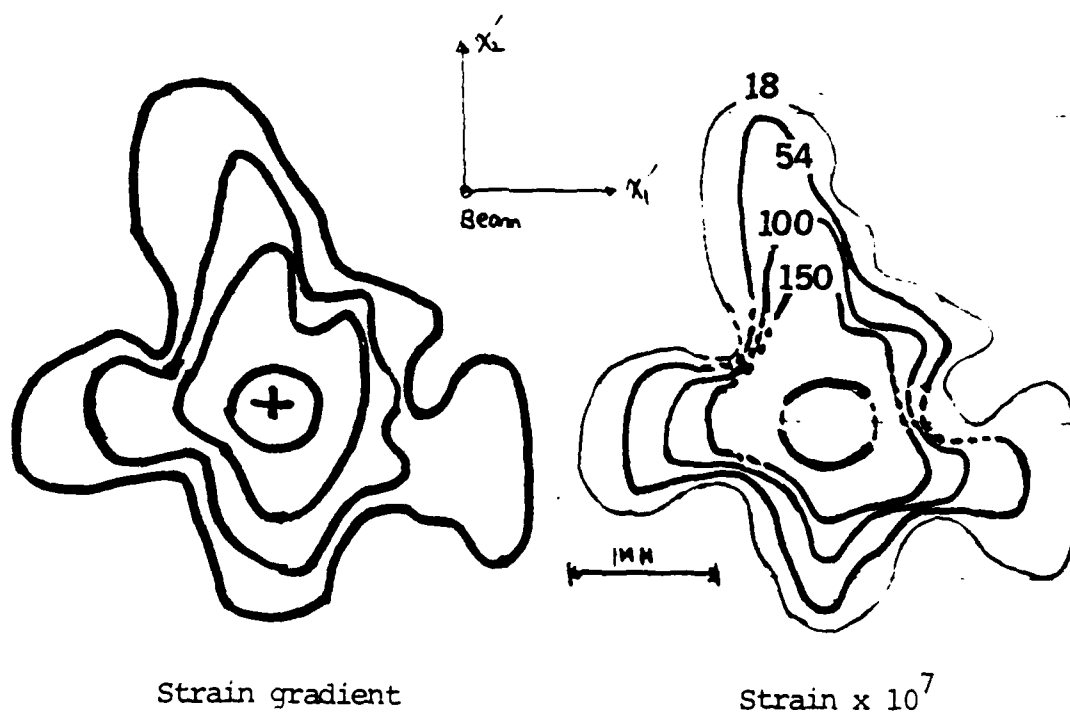
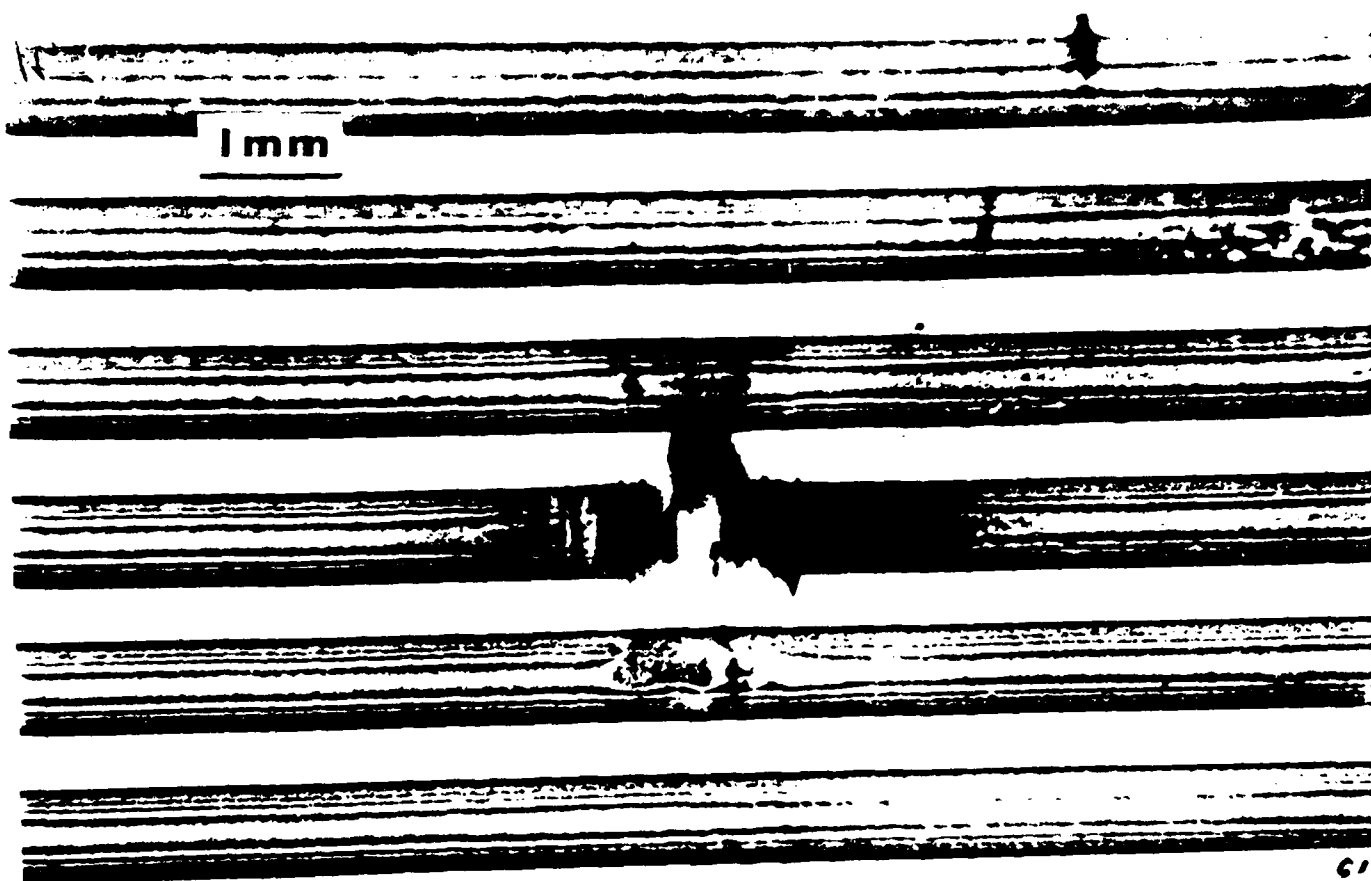


Figure 7. Section topographs and contour maps of strain gradients and of dilational strains around a laser-drilled hole in (001)Si.

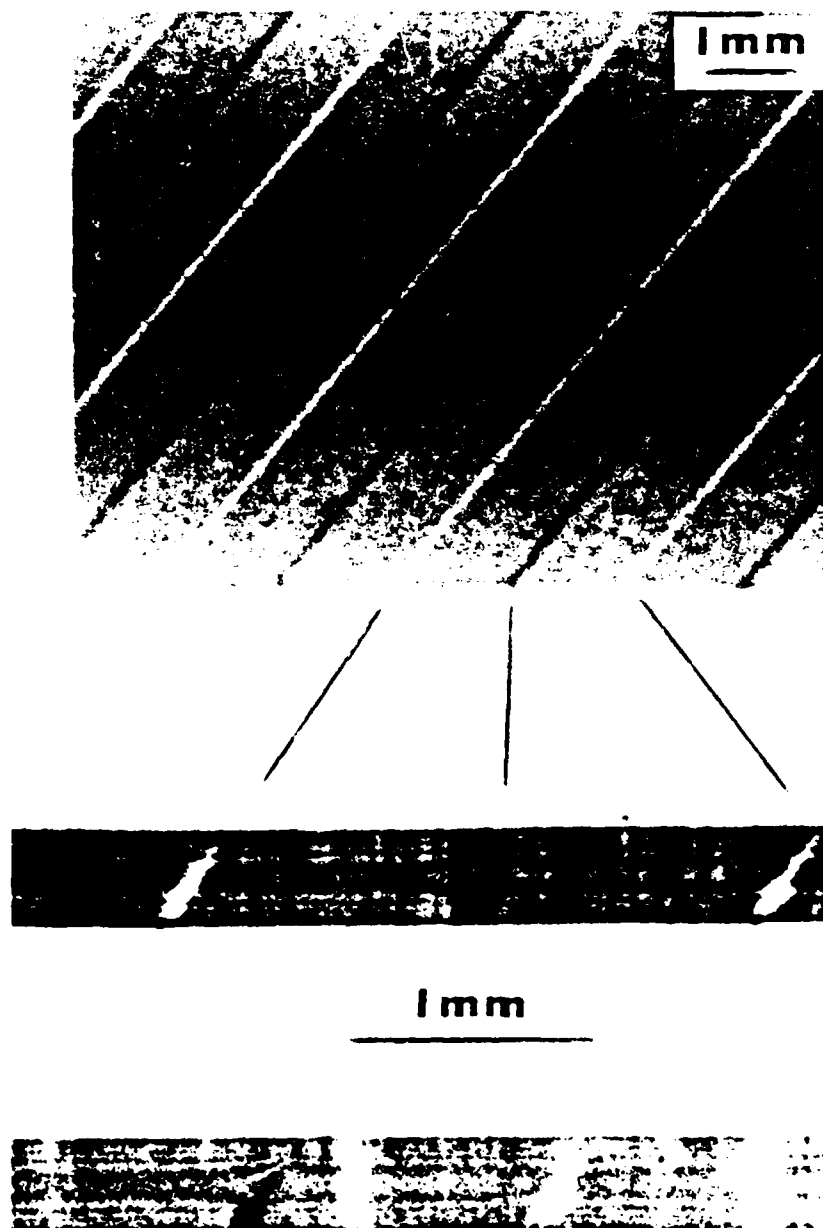


Figure 8. Section topograph of the silicon substrate when the nitride stripes were oriented at 45 deg. from the slit axis. A projection topograph recorded with the same diffraction vector is shown for reference.

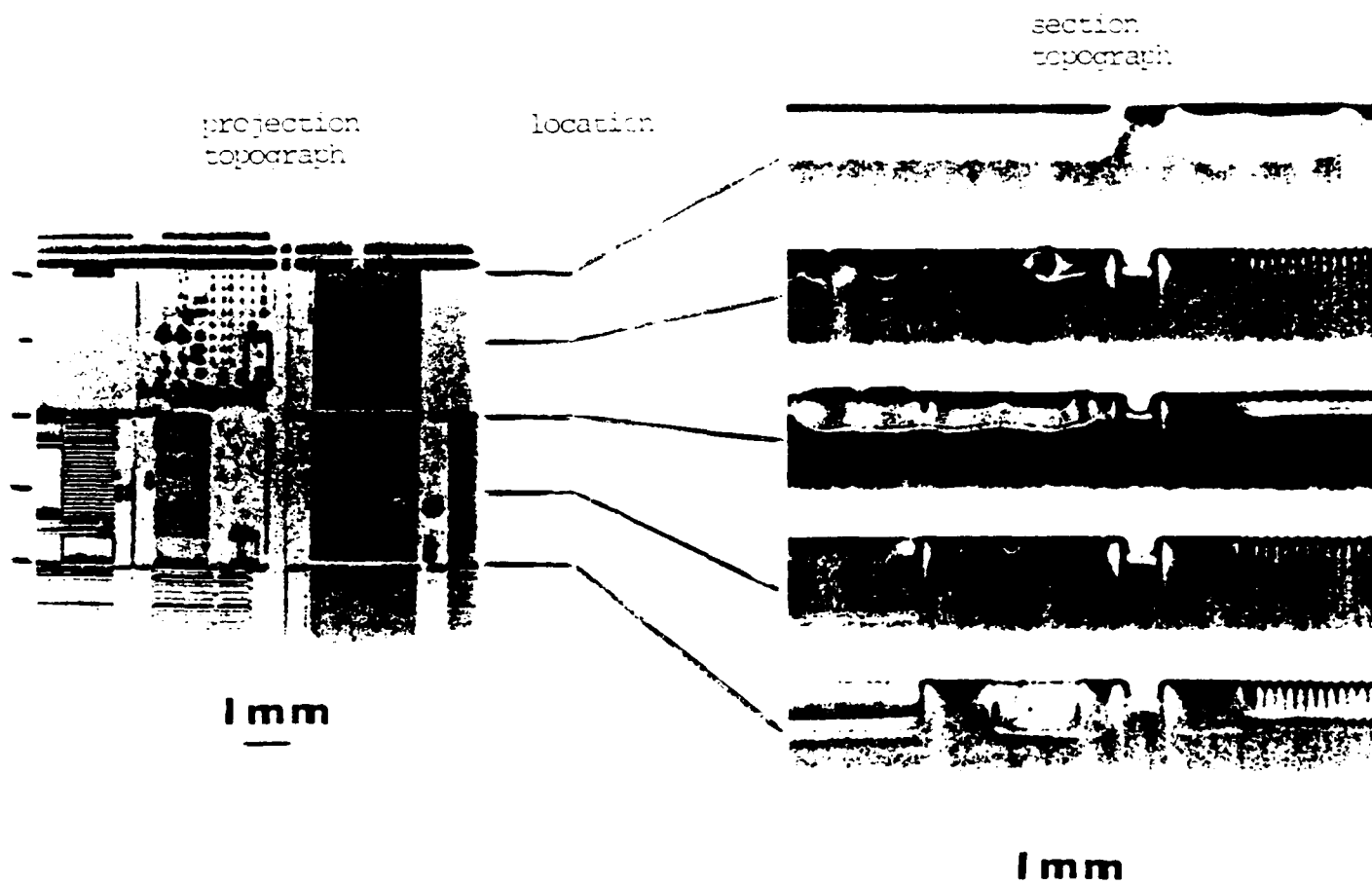
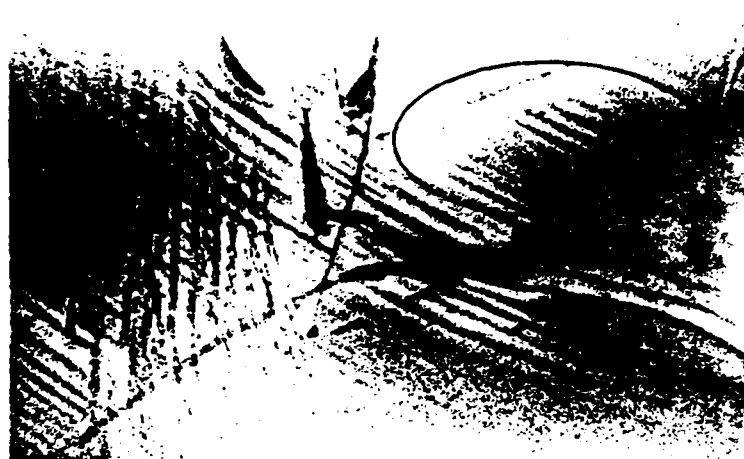


Figure 9. Section topograph of the silicon substrate with the edge of the device parallel to the slit axis and lying in the middle of the exit side of the Borrmann triangle. At least nine extra fringes have been introduced.



1 mm



Figure 10. The area of the GaAs(In) wafer studied by microbeam diffraction is indicated on the topograph as are the two scanning directions X and Y.

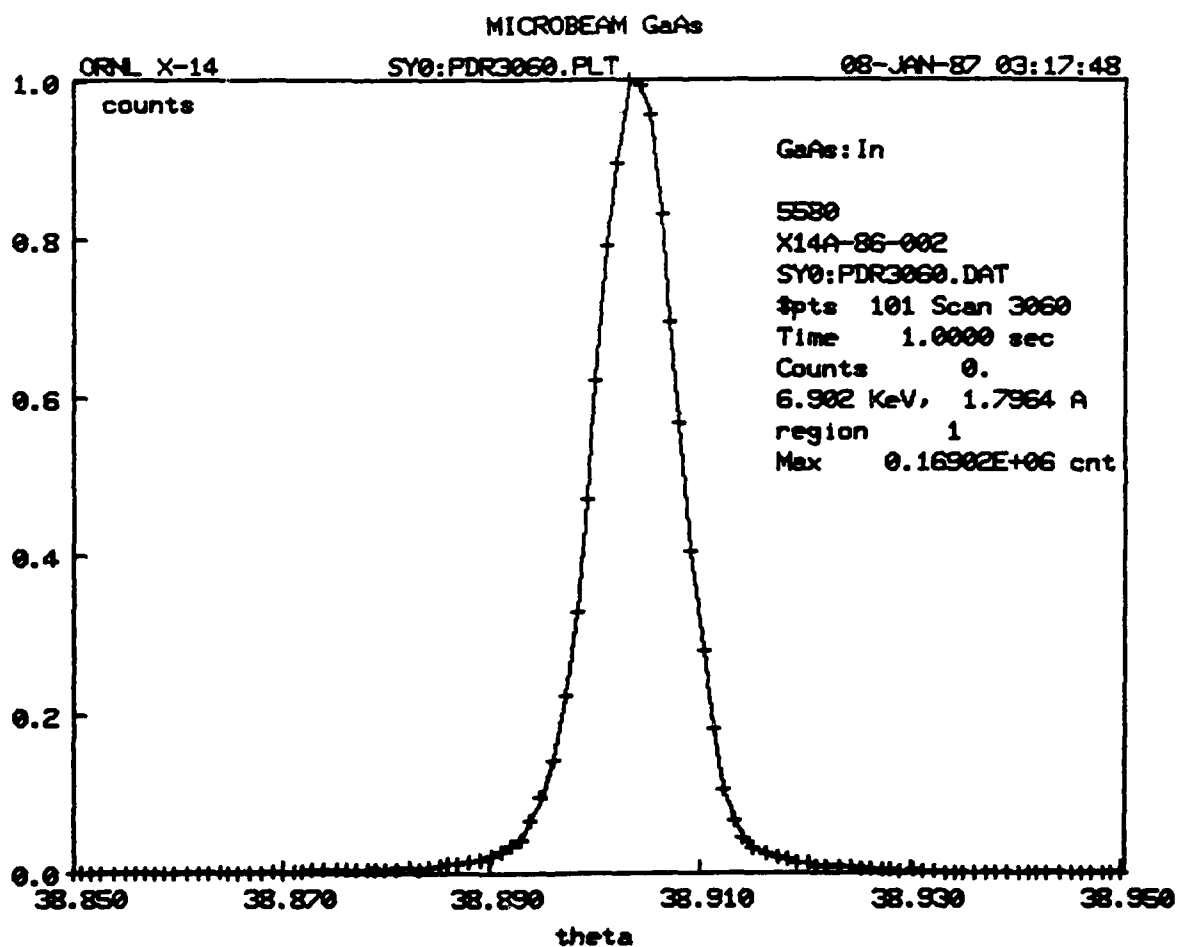


Figure 11. Rocking curve recorded with a 0.01 mm diameter beam from the sample shown in Figure 10.

FINAL REPORT NUMBER 80
RECEIVED A NO-COST TIME EXTENSION
TO BE SUBMITTED IN 1987 MINI-GRANT FINAL REPORT
Dr. Nicholas Takach
760-6MG-130

COMPLETE STATISTICAL CLASSIFICATION OF NATURAL SURFACE
ROUGHNESS ON GAS TURBINE BLADES

FINAL REPORT
for
UNIVERSAL ENERGY SYSTEMS

Contract No. F49620-85-C-0013/SB5851-0360,
Purchase Order No. S760-6MG-064

Submitted
by
Robert P. Taylor

Thermal & Fluids Dynamics Laboratory
Mechanical and Nuclear Engineering Department
Mississippi State University
Mississippi State, MS 39762

January, 1988

COMPLETE STATISTICAL CLASSIFICATION OF NATURAL SURFACE
ROUGHNESS ON GAS TURBINE BLADES

by

Robert P. Taylor
Thermal & Fluid Dynamics Laboratory
Mechanical and Nuclear Engineering Department
Mississippi State University

ABSTRACT

Results are presented from profilometer measurements of the surface roughness on inservice turbine engine blades from F-100 and TF-39 engines. Statistical computations were performed on these profiles and the important statistical parameters are reported. In addition, a procedure is outlined for the reconstitution of the rough surface using statistical parameters.

PREFACE

This program was conducted by the Mississippi State University Engineering and Industrial Research Station, P. O. Drawer ME, Mississippi State, MS 39762 under Contract F49620-85-C-0013/SB5851-0360, Purchase Order No. S-760-6MG-064. This work was sponsored by the Air Force Office of Scientific Services, Bolling AFB, DC, and was monitored by Universal Energy Systems, 4401 Dayton-Xenia Rd., Dayton, OH 45432.

This work was a cooperative effort with Dr. Richard Rivir of the Aero-Propulsion Laboratory, Wright-Patterson AFB, OH 45433. The author wishes to thank Dr. Rivir for his support and encouragement. Also, thanks go to Mr. Weslie Thomas of Kelly, AFB, TX for his assistance in obtaining engine blades for the measurements.

SECTION I

INTRODUCTION

Surface roughness can have a large effect on the skin friction and heat transfer of turbine engine blades. Some data, Rivir (1986) [1], indicate that rough blades can have heat transfer rates which are 100% greater than the rates on equivalent smooth blades. As shown in Taylor (1986) [2], turbine engine blades which have been in service for a few hundred cycles can have significant roughness. Typical average roughness heights are found to be from 1 to 12 μm (50 to 500 microinches). Unfortunately, traditional measures of surface roughness such as average roughness height and root mean square roughness height are inadequate for the determination of the effect of surface roughness on the fluid flow and heat transfer. Two surfaces with the same average roughness height can have different heat transfer rates or skin friction.

During the 1986 Summer Faculty Research Program, the author and Dr. Richard Rivir of AFWAL/POTC developed a procedure to obtain a complete statistical description of the surface roughness. The work reported herein is a continuation of that work. Surface roughness profiles have been obtained from 30 TF-39 and 30 F-100 1st stage turbine engine blades. On each blade, 6 profile traces were obtained--one each at the leading edge, the middle chord and the trailing edge on both the pressure and suction sides. This report discusses the background of research on surface roughness effects in boundary layer flow

and heat transfer, presents the procedures for measuring surface roughness profiles and for obtaining the statistical description on these profiles, and presents and discusses the results of these measurements.

SECTION II

BACKGROUND

The ultimate goal of research into the effects of surface roughness on boundary layer flow and heat transfer is the capability to predict the heat transfer rate and the skin friction when given only the flow geometry and the surface geometry. A combination of both computational model development and experimentally based empirical model development is required to meet this goal. The steps envisioned to meet these goals are listed below.

1. Development of computational boundary layer models for deterministic 3-dimensional surface roughness--cones, hemispheres, etc.
2. Experimental investigations into the effect of shape, spacing and size of deterministic roughness elements on boundary layer flow and heat transfer to calibrate the models developed in 1.
3. Expansion of the computational models for deterministic roughness to account for natural or random roughness such as that which occurs from the natural aging of a turbine blade with engine use.
4. Experimental investigations on randomly rough surfaces to calibrate the models developed in 3.
5. Expansion of the models to account for more complicated flow conditions such as 3-dimensional flows developing internal flows and separating flows.
6. Experimental investigations to calibrate the models developed in 5.

The first step in the above list is complete. A discrete element boundary layer model which compares well with the existing experimental data has been developed at Mississippi State University. The model matches the available experimental results within the stated uncertainty bands for most cases. This work is discussed in detail by Taylor, Coleman and Hodge (1984) [3].

The second step is currently underway at Mississippi State. The first stages of this work will be complete in 1988. Steps 3 through 6 are plans for future work. This report is concerned with preliminary work on the statistical classification of natural or randomly rough surfaces which is necessary for steps 3 and 4.

For deterministic roughness (cones or hemispheres in some known array), it is fairly straight forward to tell when surfaces are geometrically similar. Therefore, a few well chosen experiments can be used to calibrate the computational models for a broad range of deterministic surfaces. This is demonstrated by the broad range of applicability of the models developed in step 1 (Taylor et al, 1984, [3]). However, for randomly rough surfaces, it is not obvious (and perhaps impossible) to say when two surfaces are geometrically similar. If two surfaces are randomly rough, then the most that can be said is that they are statistically equivalent.

This idea of statistical equivalence is important for both the development of computational models and for the selection of experimental test surfaces. For computational models the averages of the predicted values for skin friction and heat transfer rates for a small sample of statistically equivalent surfaces should be essentially the same as the average values for the entire population of statistically equivalent surfaces. No two random surfaces have the exact same skin friction and heat transfer rates, but by performing computations for a small sample of statistically equivalent surfaces the mean and standard deviation of that class of surface should be obtained to a good approximation. For experimental tests, simple flows such as fully developed pipe flow or flat plate boundary layer flows will be used in the

initial experiments. For these tests artificially created randomly rough surfaces will be used as the test surfaces. If these tests are to be used to estimate the performance of real surfaces, then the test surfaces should have roughness which is statistically equivalent to the real surfaces.

SECTION III

MEASUREMENT TECHNIQUES

Surface profiles were collected using the Rank-Hobson-Taylor Surtronic III profilometer. The profilometer was set with a cut off of 0.8 and a range of 99.9. Depending on the magnitude of the roughness, the vertical magnification was set between 200 and 1000, and the horizontal magnification was set between 40 and 100. All traces were taken near the mid-span of the blade, and the direction of the traces were from the base toward the tip. All traces were approximately 1.5 cm long.

This stylus profilometer is capable, by setting the appropriate amplification ratio, of resolving surface detail between 0.1 μm and 100 μm . The major function of this instrument used in this program is the x-y recording ability. Figure 1 shows a typical section of a surface record. The instrument also has some internal computational ability and can compute the average roughness height, the maximum peak to valley height, and the number of peaks per unit profile length, and other similar parameters. The parameters which are computed directly by the instrument were developed for surface to surface contact analysis and are of limited direct use for boundary layer analysis.

Once the profile records such as Figure 1 are obtained, they are digitized and conditioned for statistical computations. The profiles were digitized with an x-y digitizing device. The record was placed on the digitizer bed, the profile was followed by hand and selected points were entered into the computer as x-y coordinates. The x-spacing of these points was at most 1/5 of the major structural scale of the

roughness. The x-y coordinates were then converted into the physical coordinate system of the record by using the proper scaling ratios. Since the turbine blades are curved, the profilometer will pickup some of the trends of the substrate. These trends must be removed for proper statistical analysis of the roughness. This trend removal is easily accomplished by least squares fitting of a polynomial to the x-y data. This trend curve is then used as the new origin of the y-coordinate. This trend removal procedure results in a mean surface height $\bar{y} \approx 0$.

SECTION IV

STATISTICAL COMPUTATIONS

Once the surface profile has been digitized and conditioned as discussed above, the following statistical functions are computed: 1. height distribution density, 2. autocorrelation function and correlation length, and 3. the root mean square height, the skewness and kurtosis of the height distribution.

The height distribution is computed by dividing the range of surface heights into regions or bins and counting the number of occurrences in each bin. The number of bins is set based on the total number of points, N , in the record by $N_{bin} = N/20$. To decide in which bin a given point belongs the following algorithm is followed

$$\text{Compute: } C = \frac{y_{max} - y_{min}}{N_{bin}} \quad (1a)$$

$$\text{Compute: } J = \frac{y_i - y_{min}}{C} \quad (1b)$$

The bin, index j , in which y_i falls is the integer $j = \max \text{ integer} < J$. The number of points, n_j , in each bin is determined by adding 1 to n_j each time j is encountered. The probability density histogram is then computed by $p_j = n_j/N$ for $j = 0, 1, \dots, N_{bin} - 1$.

The autocorrelation function is computed by evaluating the integral

$$R_x(\tau) = \lim_{L \rightarrow \infty} \frac{1}{L} \int_{-L/2}^{L/2} y(x)y(x + \tau)dx \quad (2)$$

The finite sample approximation for equation (2) is

$$R_{xj} = \frac{1}{N-j} \sum_{i=1}^{N-j} y_i y_{i+j}; j = 0, 1, \dots, m \quad (3)$$

where $m = N/10$. The limit on m is required to avoid digital instabilities in a finite sample. The correlation length is defined as the lag, β , where $R_X(\beta) = R_X(0)/10$.

The variance is computed by evaluating

$$V = \frac{\sum_{i=1}^N (y_i - \bar{y})^2}{N} \quad (4)$$

and the root mean square height, S , is

$$S = \sqrt{V} \quad (5)$$

The skewness is computed by evaluating

$$Sk = \left[\sum_{i=1}^N (y_i - \bar{y})^3 \right] / N / S^3 \quad (6)$$

and kurtosis is computed by evaluating

$$Ku = \left[\sum_{i=1}^N (y_i - \bar{y})^4 \right] / N / S^4 - 3 \quad (7)$$

SECTION V

RESULTS OF THE TURBINE ENGINE BLADE MEASUREMENTS

Profiles were obtained for two sets of 30 1st stage turbine blades from each a TF-39 and F-100 engine. The TF-39 blades were all from the same turbine wheel, had shower head cooling, and had a service age of 3402 hrs. The F-100 blades were also all from the same wheel, had shower head cooling, and had a service age of 1600-1800 cycles.

Six profiles were taken on each blade for a total of 360 profiles. Profiles were taken in the region of the leading edge, the mid-chord, and the trailing edge on both the suction and pressure side. Figure 2 shows the approximate trace location and defines the numbering scheme used--1 for the leading edge suction, etc.

The three parameters which were obtained directly using the profilometer were the average roughness, R_a , the maximum peak to valley height, R_t , and the mean peak to valley height, R_{tm} . Figure 3 shows the mean value for each of these parameters for both engines. From the figure it is seen that the TF-39 blades were roughest on the pressure side near the mid-chord and the trailing edge. The F-100 blades are roughest on the suction side near the leading edge.

Figures 4, 5 and 6 show histograms of the distribution R_a , R_t , and R_{tm} at each trace location for the TF-39 engine. Inspection of the figures reveals that the data scatter for these roughness parameters is large. For example, the mean value of R_a for Trace 5 in Figure 4 is $6.85 \mu\text{m}$, the range is from $3.9 \mu\text{m}$ to $12.1 \mu\text{m}$, and the standard deviation is $2.04 \mu\text{m}$. The shape of the distributions shows a strong tendency toward positive skewness. Figure 7 shows scattergrams for

selected traces for the TF-39 engine. This figure shows that there is no obvious correlation between the traces. There is no reason to say that a blade with a larger than average roughness value for one trace location will have larger than average roughness values at other trace locations. That is, in this sample, there are not two sets of blades with one set rough and one set smooth.

Figures 8, 9 and 10 show the same histograms for the F-100 engine. Again it is seen that the scatter for these data is large. The shape of the distributions again shows a tendency for a positive skewness with the exception of Trace 6 which shows a zero to slightly negative skewness. Figure 11 shows scattergrams for selected traces for the F-100 engines. As before, no correlation is seen between the traces.

Statistical computations as discussed above were performed on each trace. Figure 12 shows an example of the results of the computation of the height distribution and the autocorrelation function. This autocorrelation is normalized by dividing the the height variance, V . The solid curve in the probability plot is the expected distribution for a gaussian surface, and the vertical bars are the actual values of the surface height occurrence. Similar plots were made for each trace; however, space limitations do not allow the inclusion of these plots. These computations can be summarized by means of the parameters S , the root mean square roughness height, S_k , the skewness, K_u , the kurtosis, and β , the correlation length.

Table 1 gives a summary of these calculations for the TF-39 engine. Figures 13, 14, 15, and 16 show these summaries in graphical form. The units on β and S are μm . From the figures several points are seen. For the TF-39 engine, the largest roughness magnitudes, S in

Figure 13, are at locations 1, 5 and 6--the leading edge suction side and the mid-chord and trailing edge regions on the pressure side. Figure 14 shows the skewness of the height distribution. This figure reveals a very interesting fact. Trace locations 1, 4, 5 and 6 have a fairly large positive skew, while locations 2 and 3 have a tendency for negative skewness. A positive skewness indicates a peak dominated surface, and a negative skewness indicates a valley dominated surface. This means that not only does the magnitude of the roughness vary greatly from trace location to trace location but also the nature of the roughness. Therefore, a blade cannot be said to have a roughness which is denoted by a single number.

Table 2 gives a summary of the statistical calculation for the F-100 engines. Figures 17, 18, 19, and 20 show these summaries in graphical form. The units on β and S are μm . Figure 17 shows that the roughness magnitude, S, is much greater at trace location 1 than at any of the other trace locations. Also, a very large range of scatter is observed in the data. Figure 18 shows the skewness of the height distribution function. Comparison with Figure 14 for the TF-39 engine shows that the F-100 blades have a more nearly zero skew. However, they show a wide scatter in skewness.

A comparison of Figure 19 and Figure 15 shows that while both the F-100 and TF-39 blades show positive kurtosis the F-100 blades show a very large value of kurtosis in many cases. A large positive kurtosis indicates a surface which is basically smooth but which has a few tall peaks and/or a few deep valleys.

SECTION VI

STATISTICAL SURFACE RECONSTITUTION

The statistical parameters presented in the preceding sections are useful for surface classification, but they are not directly useful for prediction of skin friction or heat transfer. Some appropriate flow theory must be used to relate these surface measurements to skin friction and heat transfer rates.

The discrete element method of Taylor, Coleman and Hodge (1984) [3] is one such theory. This method includes the effects of flow blockage, element drag and heat transfer directly in the boundary layer equations. Figure 21 shows the basic idea of the discrete element procedure. The physical presence of the elements blocks the flow passage. As the fluid flows over and around an element, form or pressure drag results; thus momentum is extracted from the flow. Also, the elements exchange heat locally with the fluid. The discrete element procedure was developed for uniform arrays of identical elements. It has been recently extended to pseudorandom nonuniform arrays of several element shapes and sizes, Scaggs, Taylor and Coleman (1988) [4]. This method is directly extendable to a random rough surface (Taylor, Coleman and Hodge, 1984) if some means exist to describe the geometry of the random surface.

One way to describe the geometry of a random surface would be to painstakingly map the surface details. However, as was shown with the profile measurements in the previous section, the variations of the

surface parameters from surface to surface within a sample can be very large. Therefore, predictions made using the map of a single surface from the sample could be misleading.

Patir (1978) [5] has presented a method which, given the height distribution function and the autocorrelation function, can generate a computer model of a statistically equivalent surface. This procedure can be used to generate a set of surfaces which are representative of the real surface sample. These computer generated surfaces can then be used to predict the distribution of skin friction and heat transfer rates for the random surface.

The procedure is to generate an $N \times M$ array of surface heights, z_{ij} , which has the same height distribution function and autocorrelation function as the real surface profile. These heights are obtained from the linear transformation

$$z_{ij} = \sum_{k=1}^n \sum_{l=1}^m \alpha_{kl} \eta_{i+k, j+l}; \quad \begin{matrix} i = 1, 2, \dots, N \\ j = 1, 2, \dots, M \end{matrix} \quad (8)$$

The array, η_{ij} , is an $(N+n) \times (M+m)$ matrix of random numbers. The distribution of these numbers sets the distribution of the surface heights. The coefficients α_{kl} are determined so that the computer generated surface has the same autocorrelation function as the real surface profile. If the random numbers, η_{ij} , have zero mean and unit variance, substitution of equation (8) into equation (3) yields

$$R_{pq} = S^2 \sum_{k=1}^{n-p} \sum_{l=1}^{m-q} \alpha_{kl} \alpha_{k+p, l+q}; \quad \begin{matrix} p = 0, 1, \dots, n-1 \\ q = 0, 1, \dots, m-1 \end{matrix} \quad (9)$$

Equation (9) results in a system of nm simultaneous nonlinear equations. Since the R_{pq} 's and S are known from the evaluation of equations (3) and (4), these equations can be solved for the coefficients a_{kl} .

Figure 22a shows a profilometer trace from a TF-39 blade. The statistics of this blade are shown in Figure 23 were used to reconstitute this surface. Figure 22b is a profile which was derived from the reconstituted surface. Comparison of the two profiles shows their kinship. Figure 24 shows a 3-dimensional projection of this surface.

REFERENCES

1. Rivir, R. B., (1986), Personal Communication.
2. Taylor, R. P., (1986), "Surface Roughness Effects on Heat Transfer and Skin Friction," Final Report 1986 Summer Faculty Research Program, Universal Energy Systems, Inc., Dayton, OH.
3. Taylor, R. P., Coleman, H. W. and Hodge, B. K., (1984), "A Discrete Element Prediction Approach for Turbulent Flow Over Rough Surfaces," Mechanical and Nuclear Engineering Department, Mississippi State University, TFD-84-1.
4. Scaggs, W. F., Taylor, R. P. and Coleman, H. W., (1988), "Measurement and Prediction of Rough-Wall Effects on Friction Factors in Turbulent Pipe Flow," Mechanical and Nuclear Engineering Department, Mississippi State University, Report TFD-88-1.
5. Patir, N., (1978), "A Numerical Procedure for Random Generation of rough Surfaces," Wear, Vol. 47, pp. 263-277.

NOMENCLATURE

Ku	Kurtosis, Eq. (7)
L	Profile length
N	Number of points in a profile record
N _{bin}	Number of bins in the height probability histogram
p	Probability
Ra	Average profile height = $1/L \int_0^L y dx$
R _{pq}	Autocorrelation function, Eq. (9)
Rt	Maximum peak to valley height
Rtm	Mean peak to valley height
R _x	Autocorrelation function, Eqs. (2) and (3)
S	Root mean square profile height, Eq. (5)
Sk	Skewness, Eq. (6)
V	Variance, Eq. (4)
x	Surface coordinate
y	Profile height coordinate
\bar{y}	Mean profile height = $1/L \int_0^L y dx$
z	Reconstituted surface heights, Eq. (8)
<u>Greek</u>	
α	Coefficient in Eq. (8)
β	Correlation length
η	Random number, Eq. (8)

Table 1

Summary of the Statistical Computations for the TF-39 Engine

TRACE	S	Sk	Ku	BETA
1	7.2	.807	1.65	488.1
1	4.5	1.238	2.20	167.0
1	3.4	1.599	4.97	96.4
1	3.1	.053	2.20	41.0
1	3.8	.289	.81	185.3
1	4.7	1.300	2.25	325.4
1	9.7	2.161	6.53	165.3
1	3.2	.467	.94	64.8
1	12.5	2.145	7.43	281.7
1	3.6	1.485	3.61	86.5
1	4.3	1.136	1.92	183.5
1	3.8	1.666	5.25	126.1
1	6.2	2.463	9.83	116.4
1	5.1	.474	.46	248.4
1	8.3	.782	.94	312.2
1	3.3	-.027	.96	91.4
1	4.2	.583	1.30	171.3
1	4.3	.829	1.39	149.3
1	4.1	1.243	1.87	103.5
1	8.1	2.445	8.79	90.9
1	6.1	1.303	2.20	190.8
1	6.1	.796	1.75	162.7
1	4.7	1.109	2.05	97.5
1	5.1	.835	1.25	358.0
1	5.4	1.539	2.58	126.3
1	4.9	.705	.37	78.9
1	8.0	1.947	4.66	88.6
2	1.3	-.119	-.13	269.6
2	1.5	-1.487	3.88	120.7
2	1.0	-.877	4.13	95.1
2	.9	-.665	.26	36.4
2	1.4	-.465	-.25	61.3
2	1.5	-.216	-.30	268.0
2	1.0	-.541	1.90	189.0
2	1.1	-.468	-.00	78.2
2	1.4	-1.368	3.67	109.8
2	1.5	-.114	.25	240.6
2	1.7	-.727	.79	352.5
2	1.5	-1.034	1.66	232.9
2	1.9	-1.613	10.25	248.4
2	1.3	-.301	.39	220.4
2	2.8	.276	-.15	383.9
2	.7	.067	-.14	253.9
2	1.5	-1.267	1.46	132.3
2	1.4	-1.100	3.03	116.9
2	1.5	-.838	.62	262.0

Table 1
(Continued)

TRACE	S	Sk	Ku	BETA
2	.9	-.080	.09	145.2
2	2.2	-.543	.55	328.9
2	1.6	.899	.57	77.0
2	1.1	-.574	.44	100.1
2	1.0	.484	4.00	89.0
2	1.1	-.460	-.07	118.0
2	.9	.273	1.94	30.4
2	1.4	-.283	-.17	56.6
3	1.6	-.988	2.85	48.4
3	1.9	.475	1.85	91.8
3	1.9	-1.030	7.54	61.6
3	2.1	.112	-.33	33.4
3	22.1	12.177	177.47	8.5
3	2.1	-1.245	3.87	65.6
3	2.4	.618	.57	205.6
3	2.0	.100	.11	293.1
3	1.8	-.507	2.04	126.6
3	2.3	.309	.72	95.1
3	1.6	.462	.68	103.3
3	2.0	-.466	1.40	97.9
3	2.2	-.486	1.31	67.8
3	1.8	.228	-.12	296.4
3	2.3	-.211	-.04	253.3
3	1.7	-.393	.30	223.5
3	3.3	-1.295	2.74	210.7
3	1.9	-.856	1.23	218.3
3	2.3	.186	.06	90.3
3	1.6	-.098	-.03	272.0
3	2.9	.213	-.38	347.4
3	1.7	-.421	.28	186.8
3	1.7	-.250	-.00	142.2
3	2.2	.790	3.29	90.8
3	1.6	-.203	-.27	40.0
4	6.2	-.064	-.02	693.9
4	3.9	.721	2.38	315.6
4	4.8	.706	.76	142.0
4	3.1	-.058	.35	124.5
4	2.4	.047	-.67	316.0
4	3.1	1.069	2.85	121.0
4	3.1	.160	-.15	102.1
4	2.7	.260	.14	104.4
4	2.3	.576	.72	47.6
4	3.1	.437	1.35	82.6
4	2.5	.516	.86	241.8
4	3.3	.826	1.42	118.9
4	3.4	.672	.38	233.7

Table 1

(Continued)

TRACE	S	Sk	Ku	BETA
4	3.3	.485	.01	79.9
4	2.6	.415	-.21	89.8
4	2.6	.764	.85	74.3
4	4.0	.264	-.33	303.9
4	3.2	.525	.96	254.6
4	2.9	.457	.53	127.4
4	3.1	.259	.71	122.8
4	3.1	.920	1.47	353.8
4	3.0	-.037	-.41	157.5
4	4.5	.080	-.30	250.5
4	3.3	.627	.45	116.9
4	3.4	.267	.57	87.4
4	3.6	.479	.14	204.4
5	15.9	.380	.08	695.7
5	10.1	.276	-.25	120.4
5	7.8	1.142	1.98	188.8
5	9.2	1.338	2.09	99.7
5	22.4	1.699	3.78	145.3
5	8.6	.819	.87	234.7
5	7.1	.188	-.55	154.1
5	12.8	1.257	2.32	127.8
5	8.4	.362	-.15	309.5
5	14.6	1.093	1.47	159.5
5	6.8	.192	-.53	126.1
5	11.7	.616	2.18	102.4
5	12.0	.126	-.57	195.9
5	7.3	.491	-.79	166.0
5	6.8	.063	-.65	123.5
5	9.5	-.106	-.01	360.4
5	12.3	.936	.83	221.6
5	7.5	.592	-.11	142.9
5	7.0	-.597	3.46	100.9
5	19.0	2.346	6.80	163.8
5	8.5	.106	-.75	137.1
5	7.6	.377	.25	101.2
5	15.8	.589	.11	254.0
5	6.2	.498	-.10	95.1
5	8.4	1.107	1.62	152.8
5	11.1	2.304	7.09	109.9
5	54.6	-3.162	28.80	72.4
6	13.4	.136	-.52	893.2
6	6.5	.907	.88	81.9
6	7.5	2.126	7.70	118.2
6	8.3	1.622	3.60	121.7
6	8.3	1.699	4.59	62.9
6	6.3	.602	.05	197.4

Table 1
(Concluded)

TRACE	S	Sk	Ku	BETA
6	5.8	.344	-.42	283.1
6	6.7	1.225	1.68	118.2
6	6.5	.866	1.31	81.2
6	9.0	1.924	5.45	120.7
6	6.8	.413	-.53	321.5
6	8.9	1.102	.78	111.1
6	15.0	1.670	3.14	136.6
6	8.9	1.957	4.93	94.5
6	14.1	2.135	4.99	117.7
6	8.4	1.090	.87	143.5
6	5.5	1.249	1.48	88.7
6	7.2	.791	.40	75.4
6	9.4	2.778	10.20	141.7
6	8.9	1.788	3.25	118.4
6	8.0	1.574	4.74	91.1
6	5.2	.973	.81	157.4
6	8.1	.299	1.56	87.8
6	8.1	1.685	4.60	201.6
6	7.7	1.429	3.74	295.9
6	5.0	.791	.44	256.4
6	6.3	.980	2.10	178.3

Table 2

Summary of the Statistical Computations for the F-100 Engine

TRACE	S	Sk	Ku	BETA
1	16.4	.842	1.21	302.0
1	21.8	.246	2.37	371.0
1	21.9	.723	.71	421.7
1	26.1	.436	.22	695.5
1	24.1	.780	.19	702.6
1	12.8	.674	.87	159.2
1	14.1	.555	1.16	339.5
1	33.9	.355	.07	436.1
1	16.3	.362	-.17	348.1
1	17.2	.770	1.27	229.8
1	23.7	.926	1.79	1051.4
1	21.5	.950	.90	425.5
1	24.0	.810	.47	816.2
1	21.5	1.176	2.95	223.7
1	22.0	.153	3.61	228.2
1	23.8	.594	.19	980.2
1	33.4	.758	.16	826.0
1	18.0	-.292	-.40	1043.8
1	22.3	.276	.52	672.7
1	14.4	1.073	1.31	197.3
1	24.5	.430	.56	1068.9
1	42.5	.934	.62	734.3
1	23.7	.206	-.70	720.0
1	27.1	.973	2.09	1064.9
1	23.0	1.094	2.45	422.8
1	22.8	.654	.49	848.4
1	22.9	-.017	.18	459.8
1	52.3	.822	-.11	1069.8
1	50.8	.976	1.16	1019.3
2	1.6	-.583	1.21	105.5
2	3.8	.559	.24	283.4
2	1.2	-.282	.62	119.2
2	1.8	-.255	.54	182.9
2	1.7	-.876	.44	217.9
2	1.3	.130	.01	94.4
2	3.4	-.162	2.09	294.7
2	2.1	.184	-.81	349.3
2	1.6	-1.520	10.31	91.9
2	1.7	-1.391	6.80	318.1
2	1.8	-.785	2.86	184.4
2	1.3	.382	-.02	182.5
2	2.2	-.181	.32	212.8
2	2.7	-.099	-.07	352.1
2	1.5	.874	2.38	156.6
2	1.8	2.460	20.14	208.6
2	1.0	.470	-.23	273.2

Table 2
(Continued)

TRACE	S	Sk	Ku	BETA
2	1.2	-1.552	13.83	243.7
2	1.6	.001	-.47	132.2
2	2.2	-4.401	36.87	142.1
2	1.7	1.405	8.03	191.3
2	2.2	.133	.11	197.2
2	2.2	.041	-.37	359.7
2	1.9	-.037	-.50	385.9
2	2.4	.218	-.47	377.3
2	2.3	-.488	1.82	263.5
2	1.4	2.081	18.28	84.3
2	2.4	-.386	-.42	285.0
2	2.1	.248	-.03	256.2
3	1.6	-1.014	13.51	98.2
3	1.3	-.491	1.42	75.5
3	1.6	.181	-.18	106.8
3	1.5	.241	.88	261.0
3	2.1	.275	1.51	208.1
3	3.2	.618	1.98	348.9
3	3.1	.815	.97	260.8
3	1.8	-1.474	12.08	105.9
3	2.3	-.197	.22	363.1
3	1.8	-1.575	11.12	224.4
3	3.1	.268	1.36	350.1
3	2.8	-.938	4.54	388.5
3	1.7	-.057	-.27	64.9
3	2.2	-1.325	1.37	139.3
3	1.8	-.182	-.50	361.5
3	2.9	.503	1.06	220.0
3	3.1	-.028	-.71	275.1
3	2.4	.078	-.36	323.7
3	1.9	.346	-.36	421.1
3	4.0	-1.360	2.74	70.8
3	2.1	.240	4.69	123.6
3	2.0	-.298	-.31	302.3
3	1.7	.662	4.18	142.3
3	3.0	.500	-.39	356.5
3	2.4	.009	-.39	377.4
3	1.3	.079	-.43	302.7
3	1.4	-.278	1.31	168.3
3	2.0	-.726	4.66	122.3
3	2.8	-1.304	6.32	251.0
3	2.6	.872	2.20	135.8
4	1.4	-1.092	10.01	137.0
4	1.1	.248	1.56	48.4
4	1.9	.463	1.25	152.2

Table 2

(Continued)

TRACE	S	Sk	Ku	BETA
4	18.3	-.641	1.79	217.1
4	1.9	.046	.00	209.9
4	2.3	.229	-.04	275.3
4	1.6	-.063	-.10	143.3
4	2.0	-.356	.16	357.1
4	1.8	.225	-.05	306.0
4	2.3	-.129	-.28	96.0
4	2.1	.241	-.16	183.3
4	3.0	-.368	.78	324.5
4	1.7	-.107	-.69	96.6
4	1.1	1.100	8.50	131.8
4	1.4	.909	7.91	76.5
4	1.8	-.171	2.43	43.5
4	2.3	.620	6.88	120.6
4	2.8	.863	3.33	338.8
4	2.0	.225	1.45	74.4
4	2.5	.528	2.91	179.8
4	2.3	2.016	15.80	60.0
4	2.1	2.194	17.46	170.7
4	1.8	.359	.49	172.4
4	2.4	.661	3.79	41.5
4	2.4	.009	-.39	377.4
4	2.5	.702	3.24	153.1
4	4.0	3.490	32.34	206.0
4	1.7	-.665	1.56	129.5
4	1.9	4.649	45.06	73.9
4	1.6	-.335	1.74	88.1
5	2.0	-.254	6.70	66.7
5	1.6	.841	2.55	209.1
5	3.1	.203	-.66	365.2
5	2.5	-1.204	6.62	312.8
5	2.1	.969	4.28	218.2
5	2.1	.262	.64	64.3
5	1.9	-.220	2.44	275.3
5	2.5	.108	.00	233.4
5	1.9	.124	2.57	38.6
5	2.4	-.388	2.39	275.0
5	2.3	.307	-.38	204.7
5	2.2	.271	.62	284.6
5	2.0	-.073	-.20	83.6
5	1.8	1.340	4.58	157.0
5	1.7	1.618	8.55	44.1
5	1.9	-.078	1.22	314.7
5	2.7	.209	.14	256.4
5	2.1	.828	.55	51.4
5	3.7	.282	-.72	357.3
5	1.6	.641	.88	184.8

Table 2
(Concluded)

TRACE	S	Sk	Ku	BETA
5	3.0	1.770	11.11	171.9
5	2.2	.803	2.69	332.0
5	2.3	1.354	11.29	210.2
5	2.4	.390	.50	257.2
5	1.8	1.471	9.36	181.5
5	2.8	1.433	4.87	234.1
5	2.1	1.392	12.17	59.8
5	1.4	.851	2.41	38.2
5	1.6	.597	1.77	39.3
5	2.4	.966	5.27	190.7
6	2.7	.234	-.16	70.0
6	2.9	.627	.43	38.8
6	2.4	-.727	6.16	118.7
6	2.6	.164	.59	259.6
6	31.0	-.024	-.21	150.8
6	3.4	.453	.04	63.4
6	3.4	-.663	3.86	232.3
6	3.7	.372	.03	246.6
6	3.2	-.368	3.18	290.4
6	2.6	-.251	1.36	252.9
6	3.5	-.393	.92	250.7
6	2.8	.271	.42	83.3
6	2.6	-.126	.33	137.6
6	2.3	-1.376	12.33	33.3
6	2.5	-1.000	9.15	193.8
6	2.1	-.134	1.85	37.5
6	3.4	.324	1.06	179.7
6	2.4	.596	.79	73.0
6	3.5	-.470	1.96	61.8
6	2.9	-.612	3.59	151.2
6	3.2	-.039	.88	323.7
6	3.7	-.460	.75	303.4
6	3.1	-.022	.64	169.4
6	2.7	-.014	2.09	46.7
6	3.4	.610	.07	297.7
6	4.8	-.470	4.56	297.6
6	4.0	.448	.82	166.7
6	2.7	-.351	1.45	94.1
6	5.2	.335	-.42	384.7
6	3.7	.392	.10	304.6

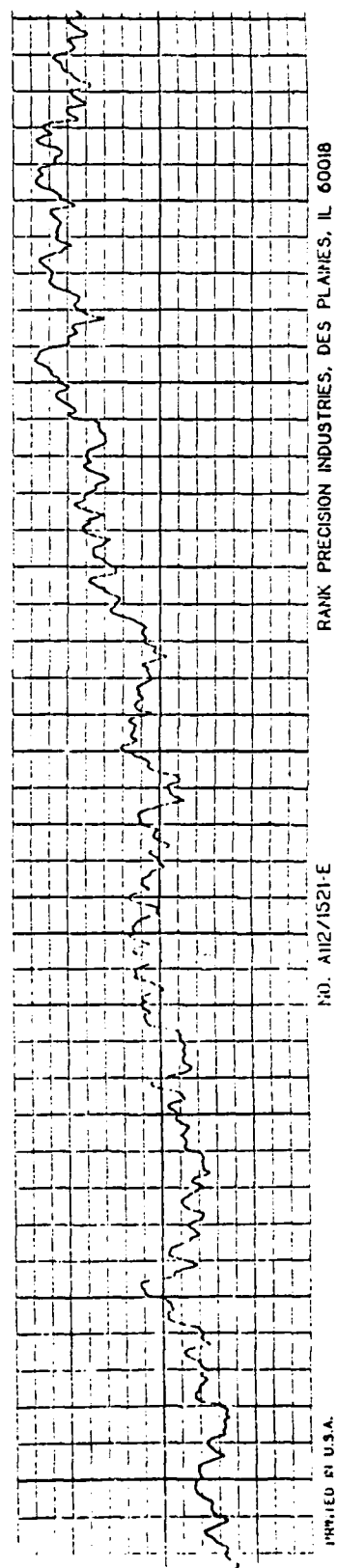


Figure 1. Sample Profilometer Trace.

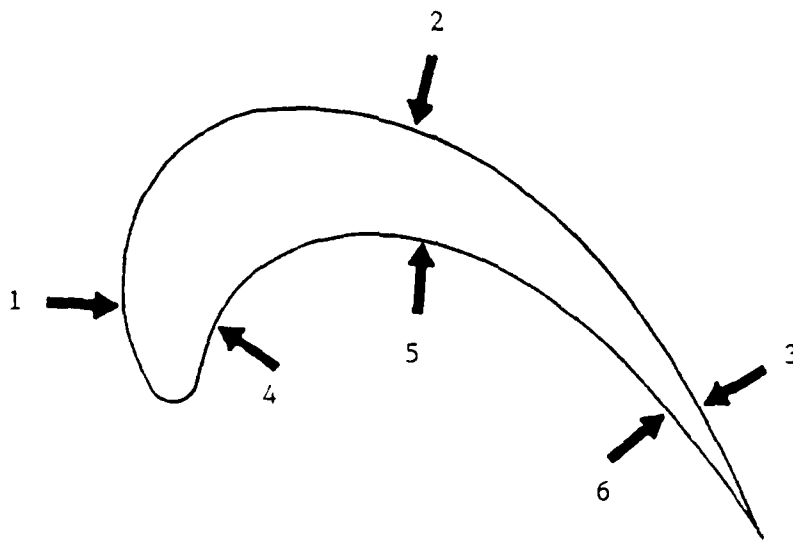
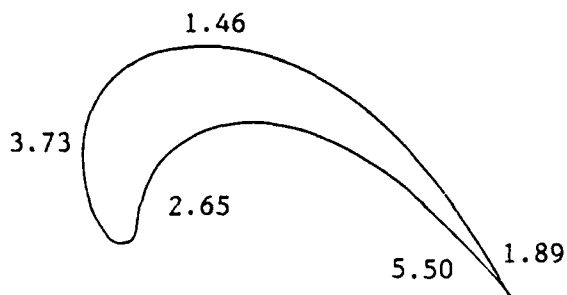
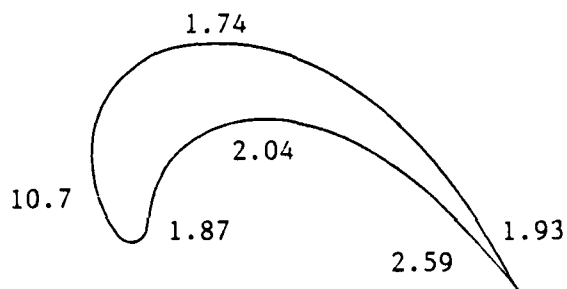


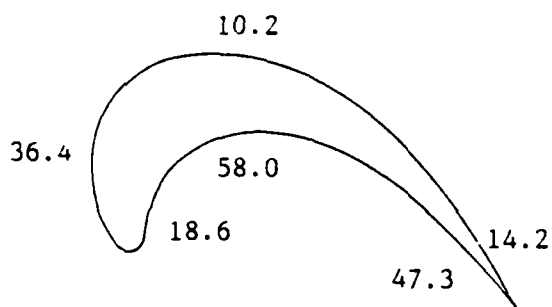
Figure 2. Approximate Trace Locations.



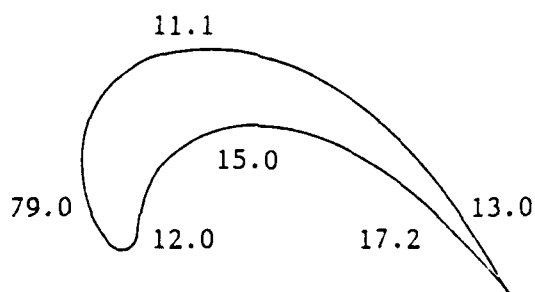
a) TF-39; mean value of Ra



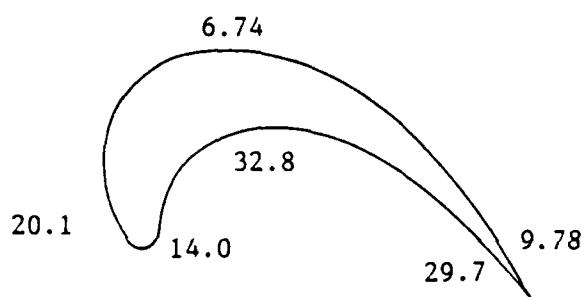
b) F-100; mean value of Ra



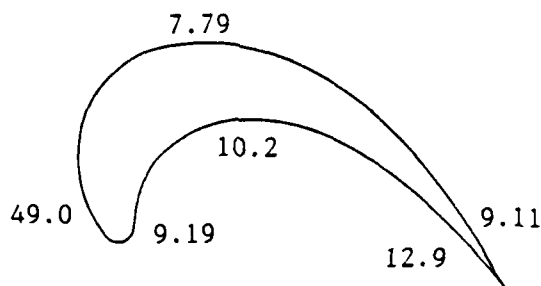
c) TF-39; mean value of Rt



d) F-100; mean value of Rt



e) TF-39; mean value of Rtm



f) F-100; mean value of Rtm

Figure 3. Summary of the Roughness Parameters Ra, Rt, Rtm;
All Values in μm .

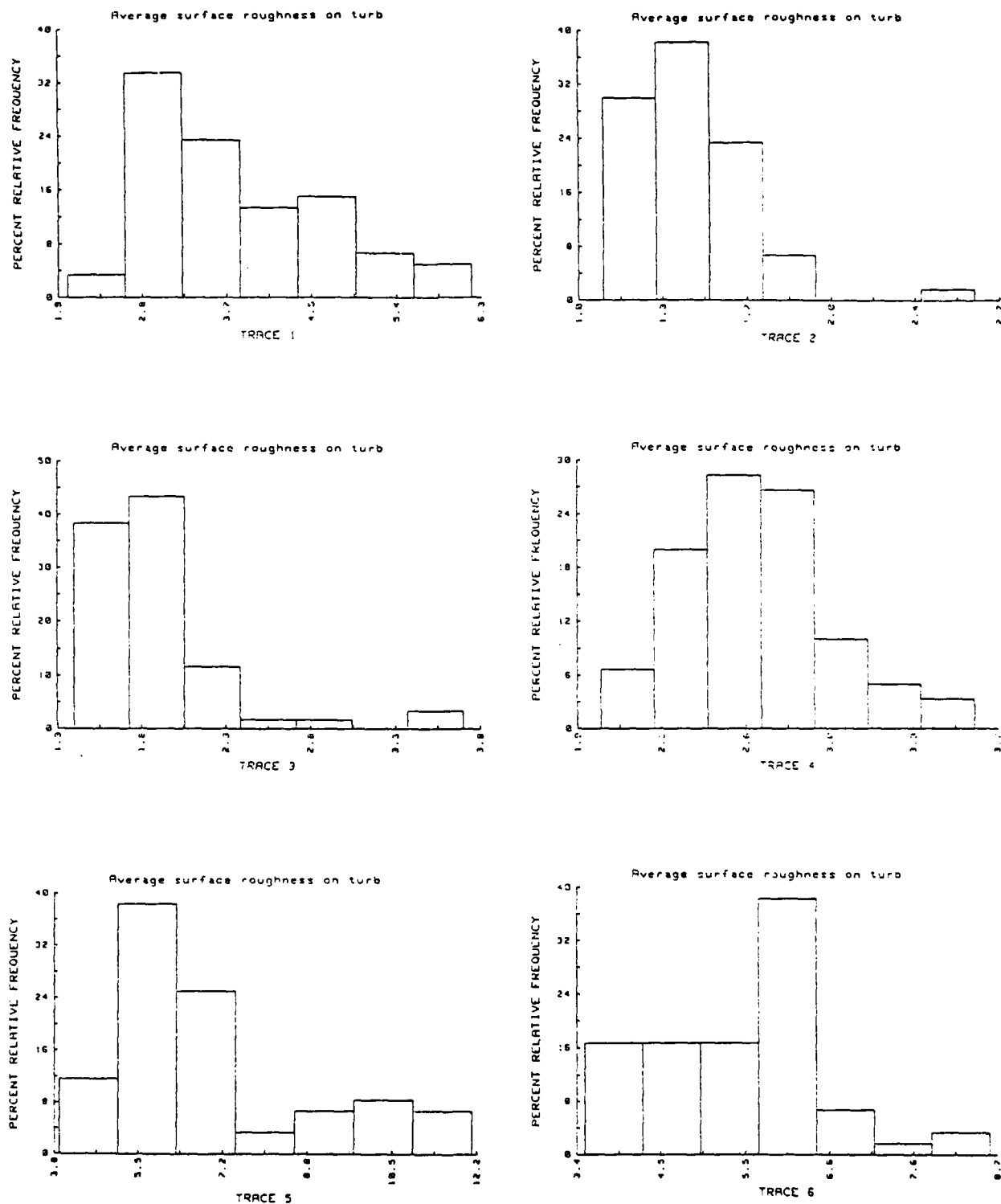


Figure 4. Histograms of the Distribution of Average Roughness Height, Ra, for the TF-39 Engine; All Heights in μm .

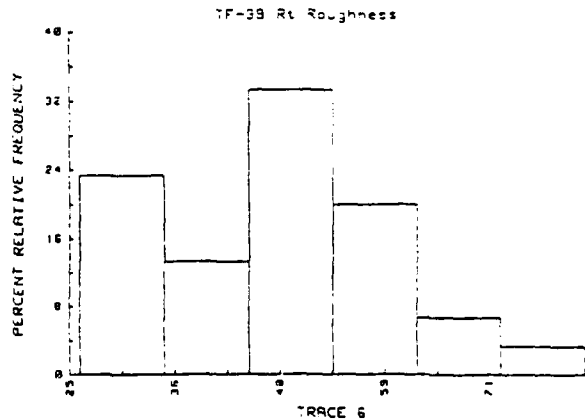
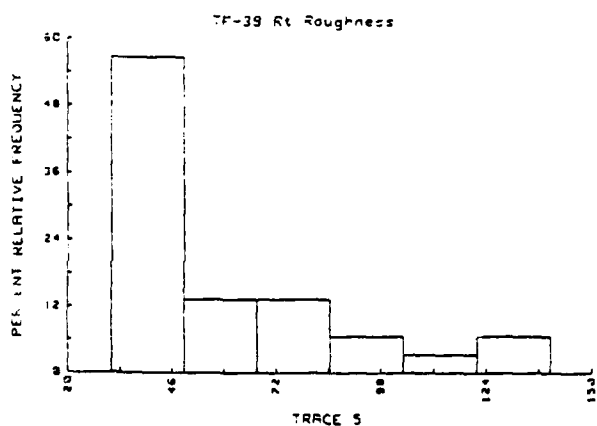
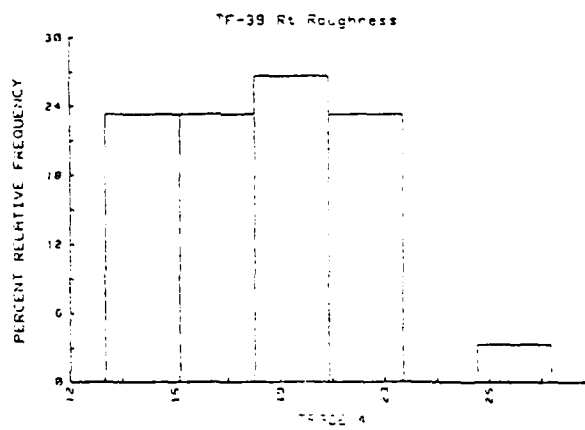
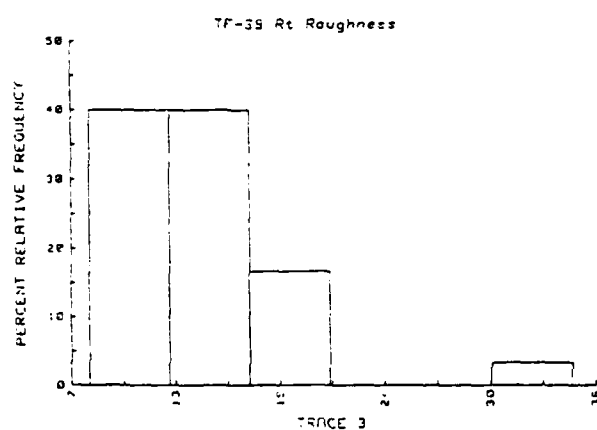
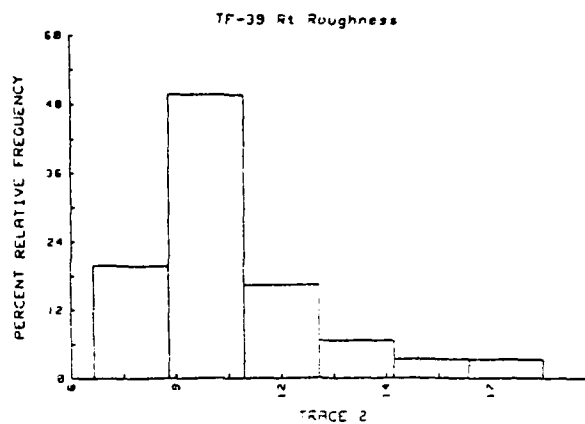
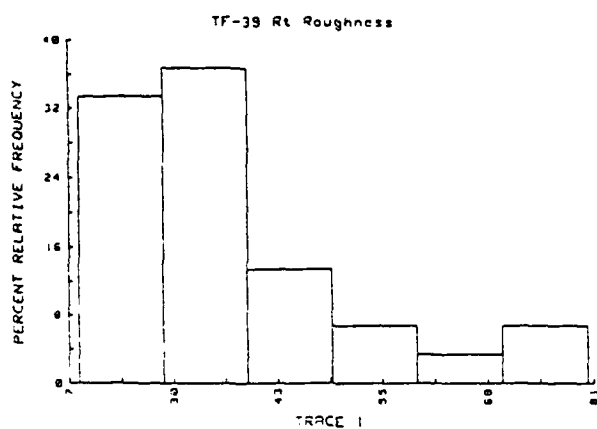


Figure 5. Histograms of the Distribution of Maximum Peak to Valley Height, Rt, for the TF-39 Engine; All Heights in μm .

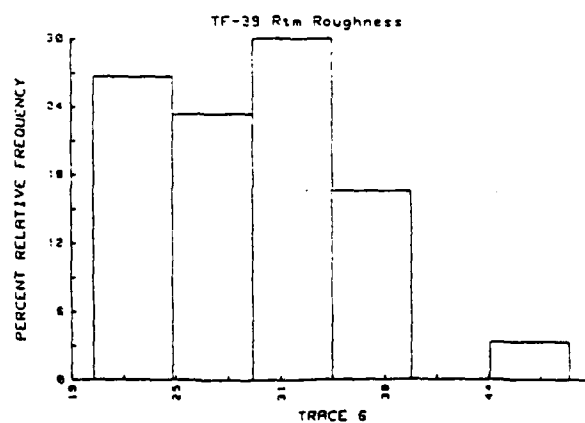
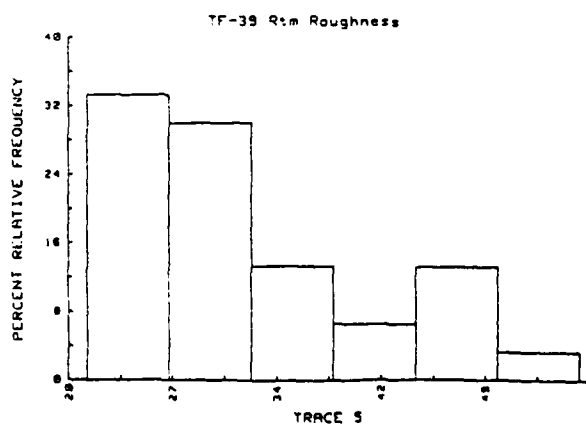
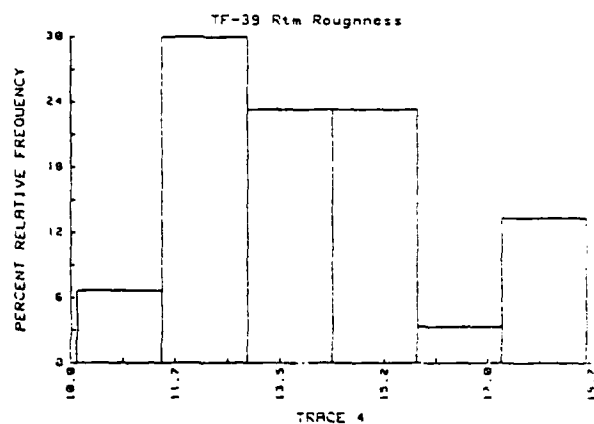
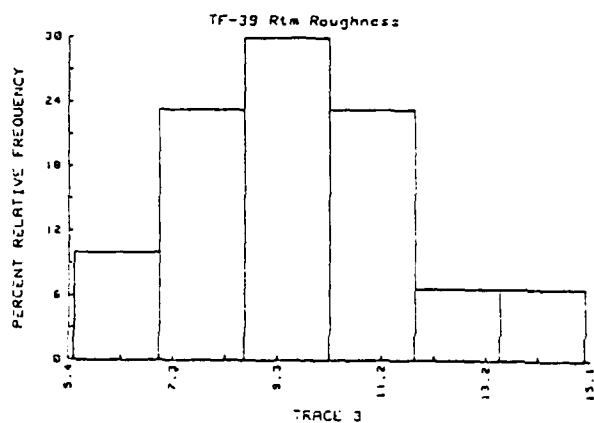
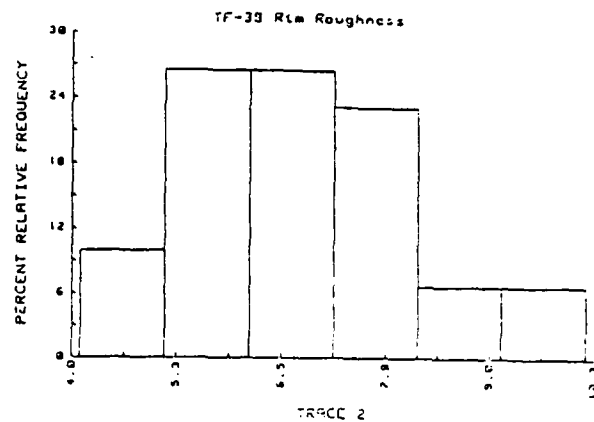
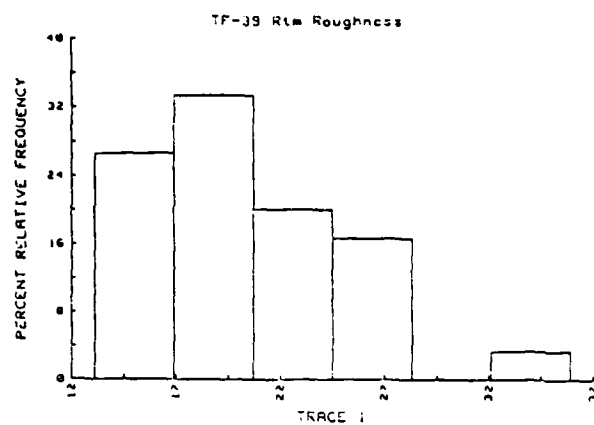


Figure 6. Histograms of the Distribution of Mean Peak to Valley Height, Rtm, for the TF-39 Engine; All Heights in μm .

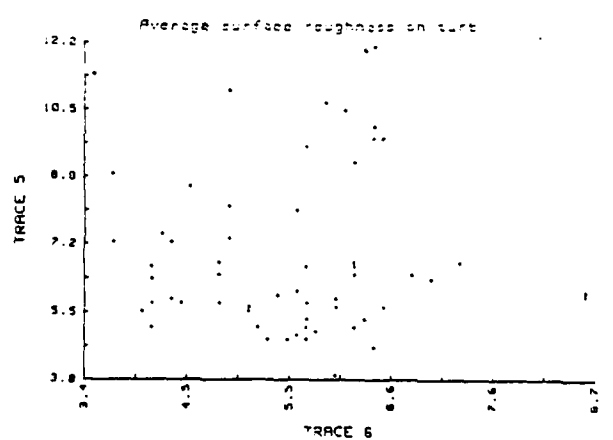
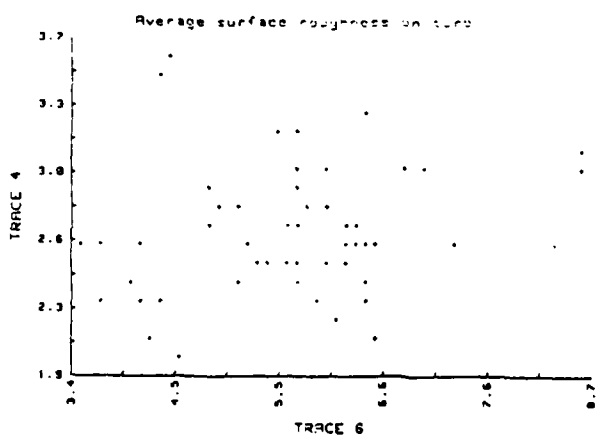
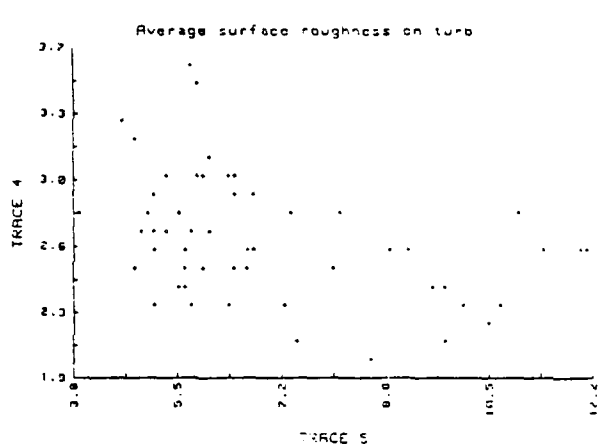
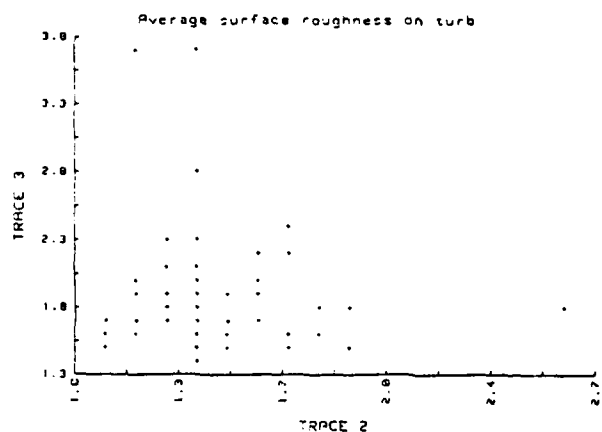
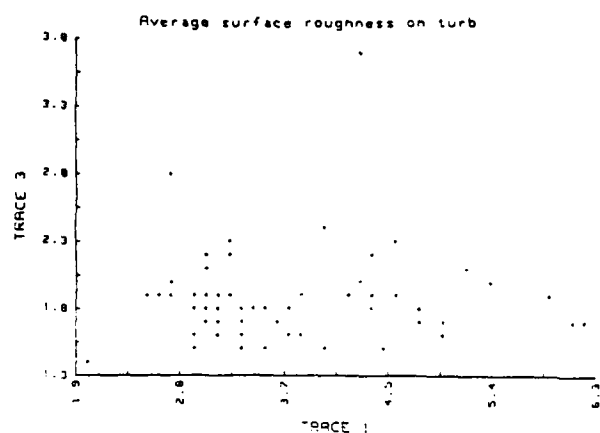
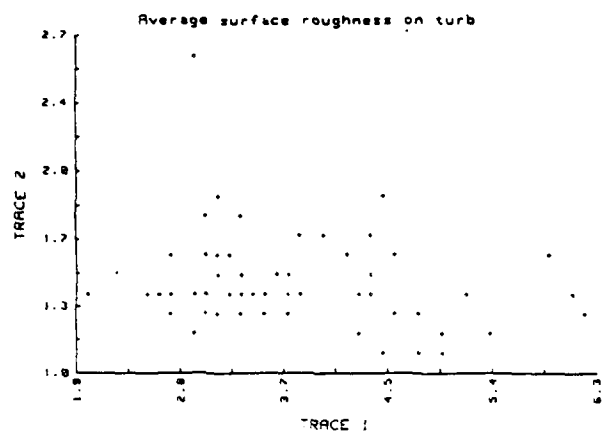


Figure 7. Scattergrams for the TF-39 Engine.

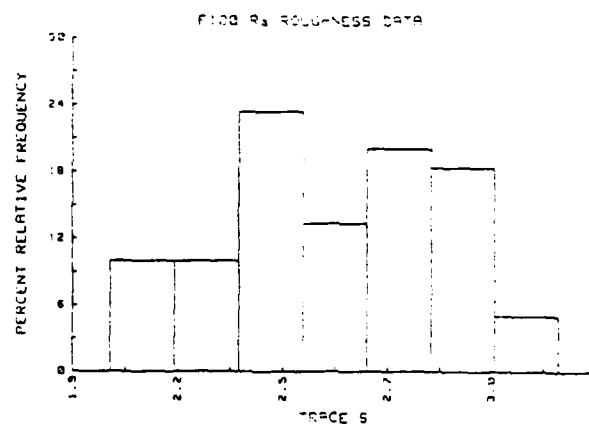
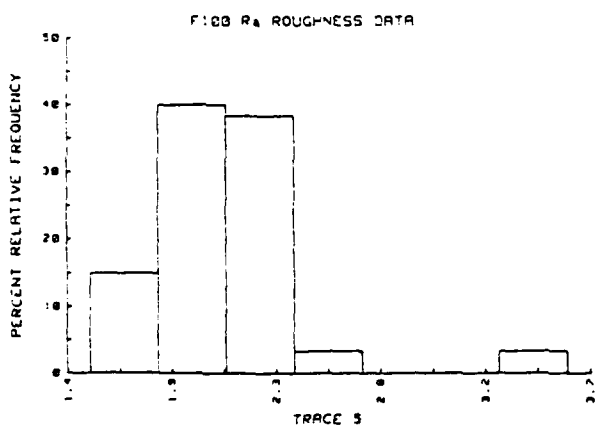
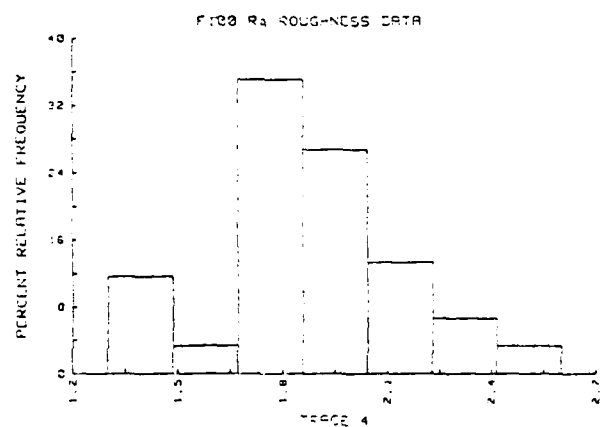
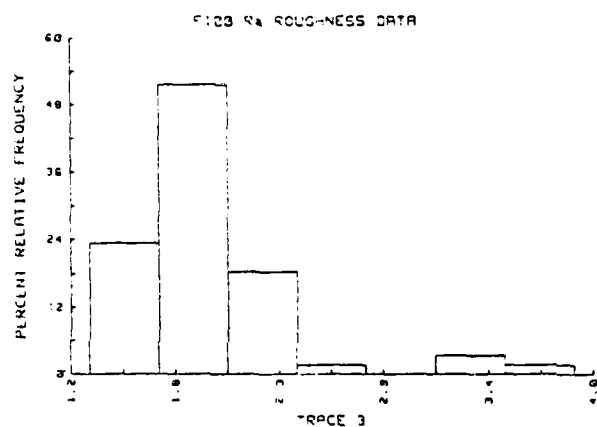
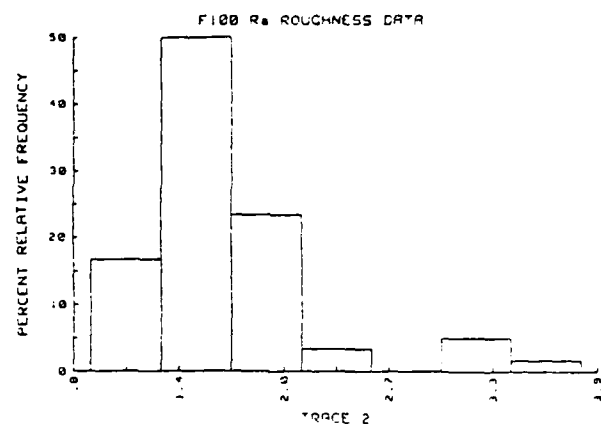
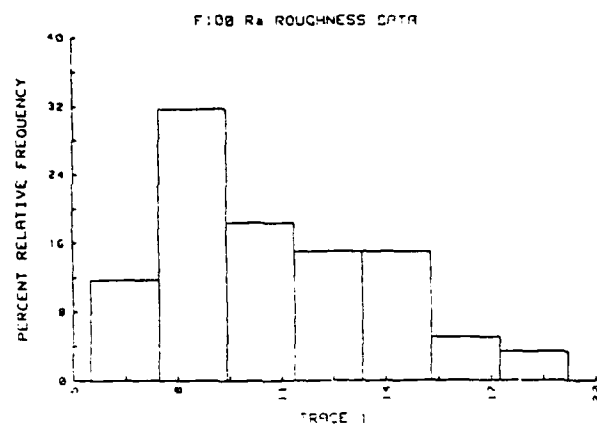


Figure 8. Histograms of the Distribution of Average Roughness Height, Ra, for the F-100 Engine; All Heights in μm .

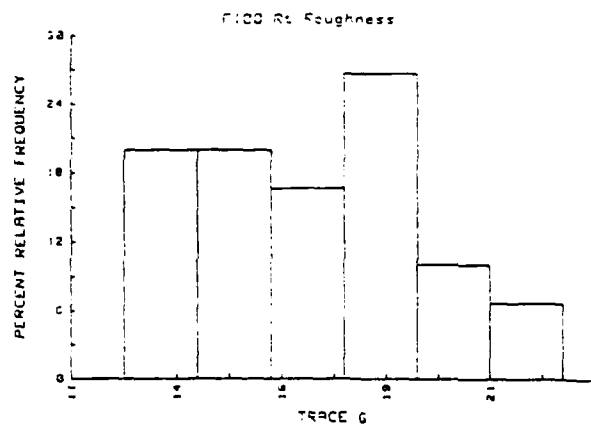
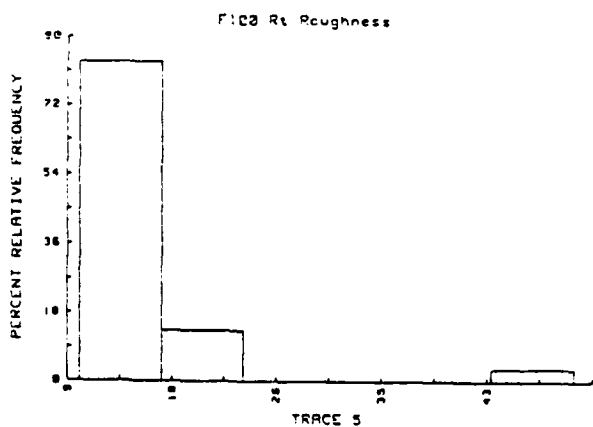
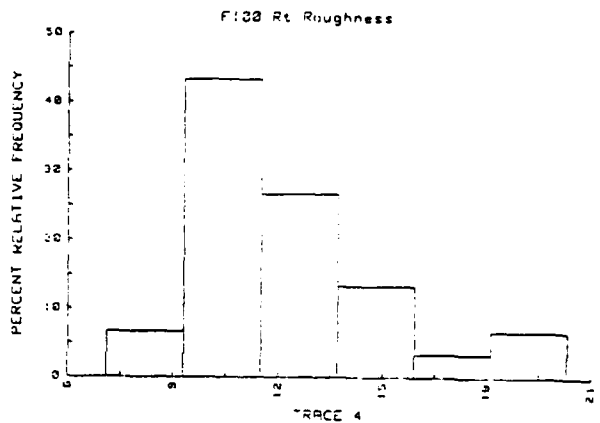
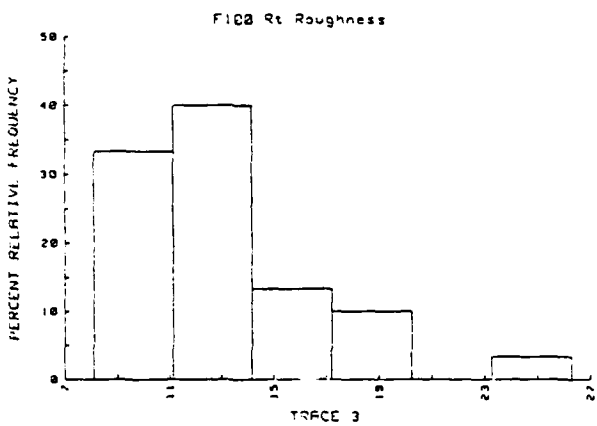
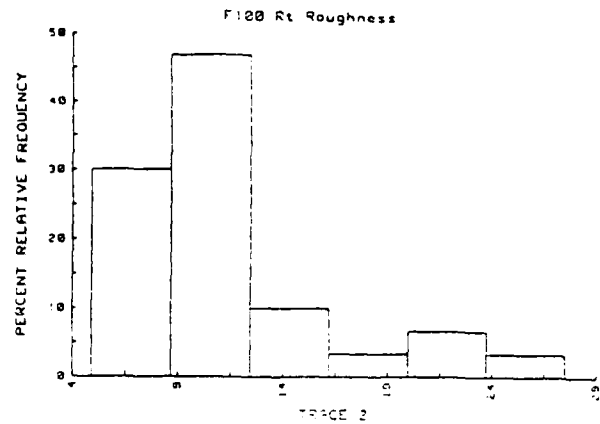
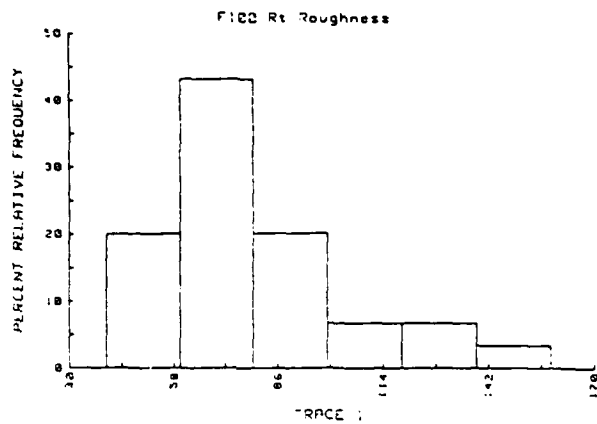


Figure 9. Histograms of the Distribution of Maximum Peak to Valley Height, Rt, for the F-100 Engine; All Heights in μm .

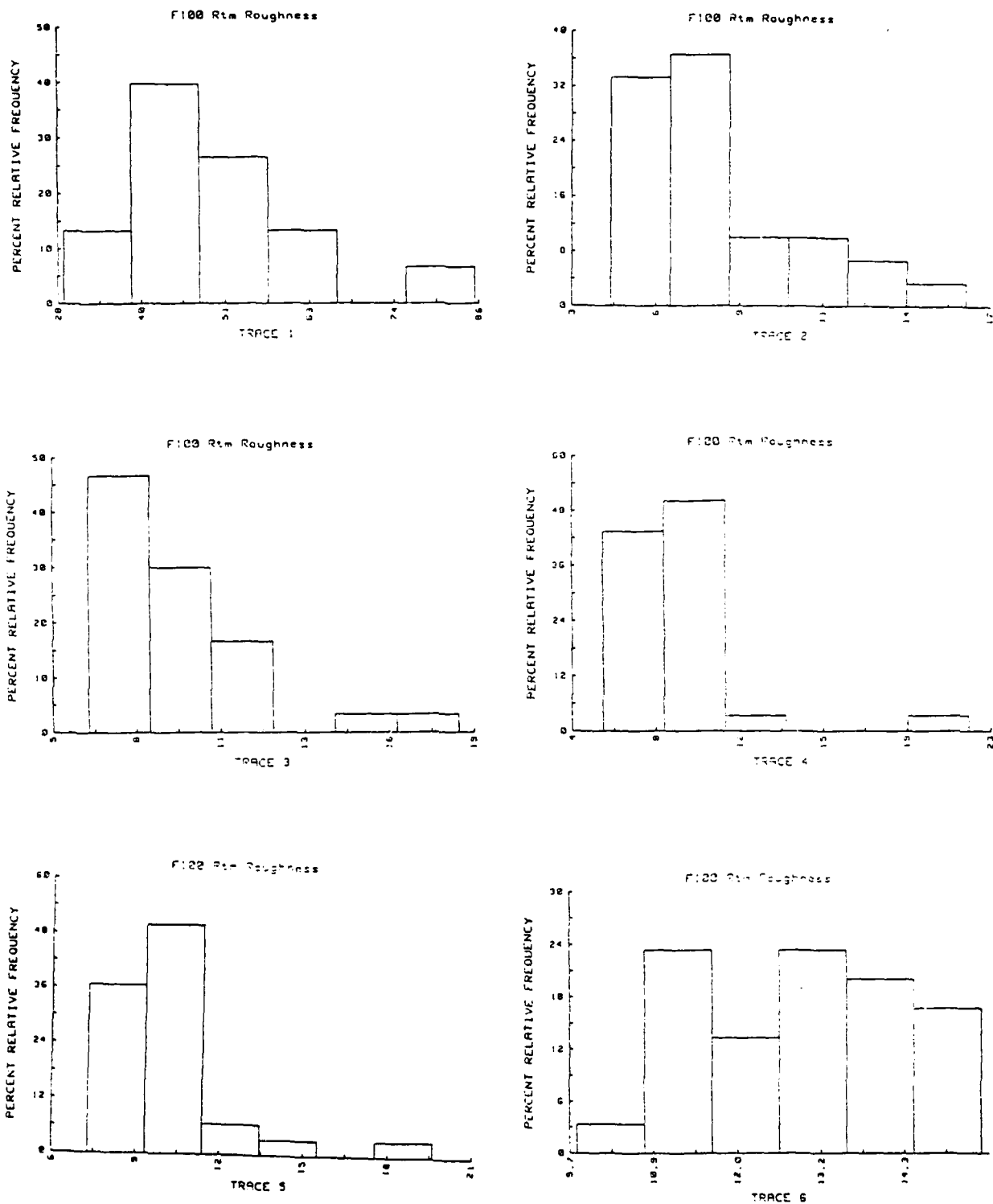


Figure 10. Histograms of the Distribution of Mean Peak to Valley Height, Rtm, for the F-100 Engine; All Heights in μm .

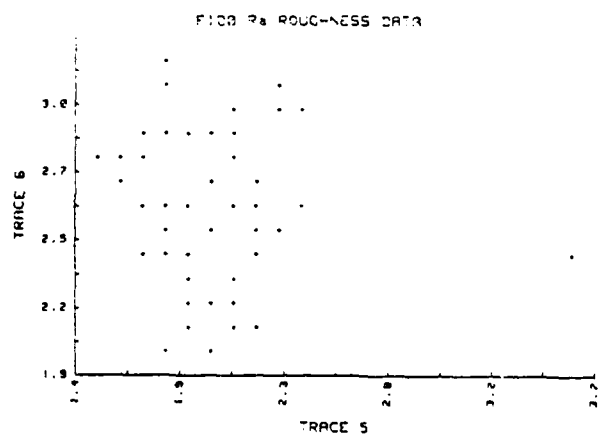
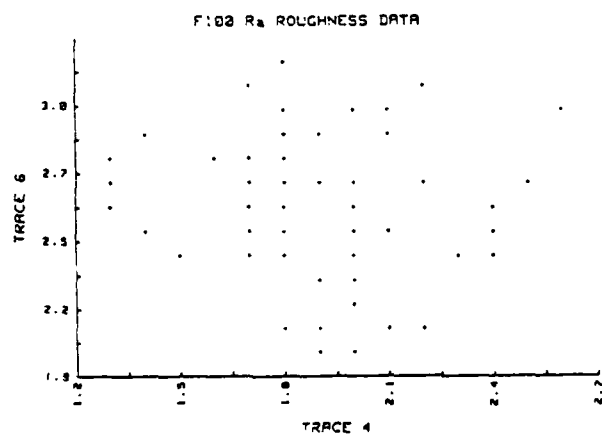
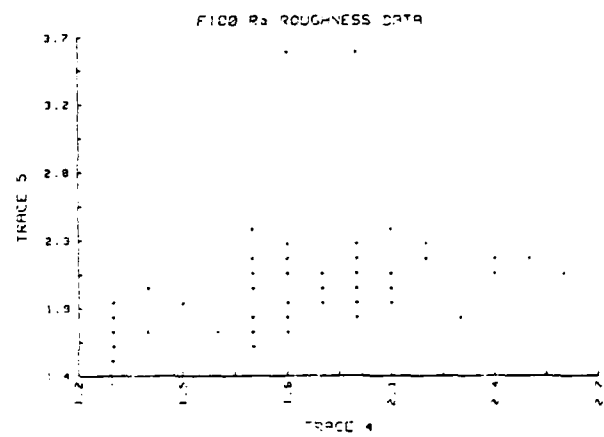
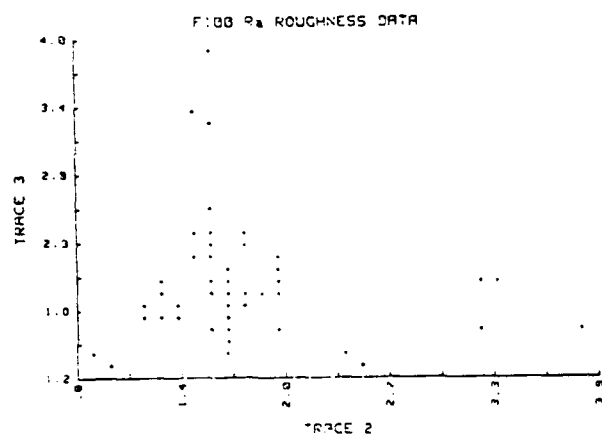
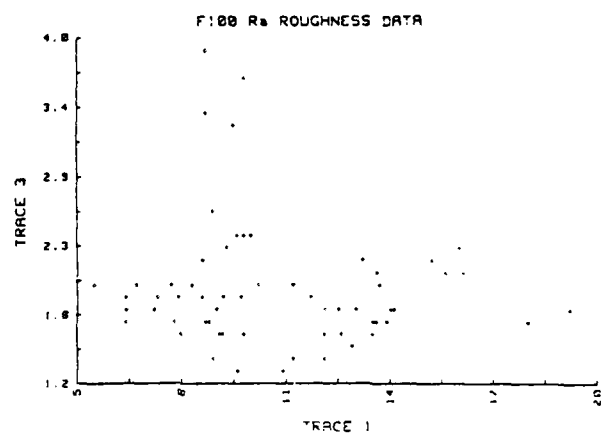
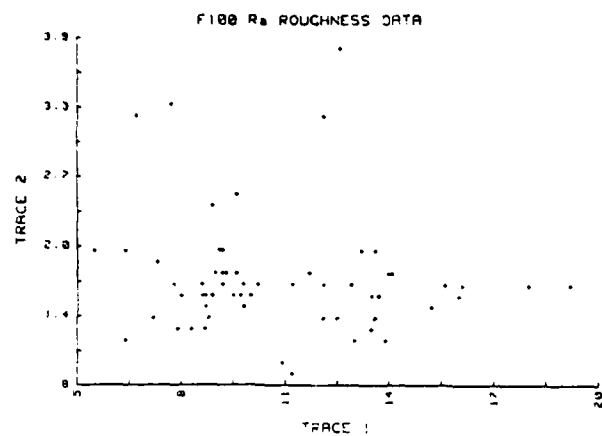


Figure 11. Scattergrams for the F-100 Engine.

TF-39 1ST STAGE SHOWER HEAD 3402 hrs.

LEADING EDGE PRESSURE SIDE -- TRACE TF193

S = .246 Mils

BETA = 27.319 Mils

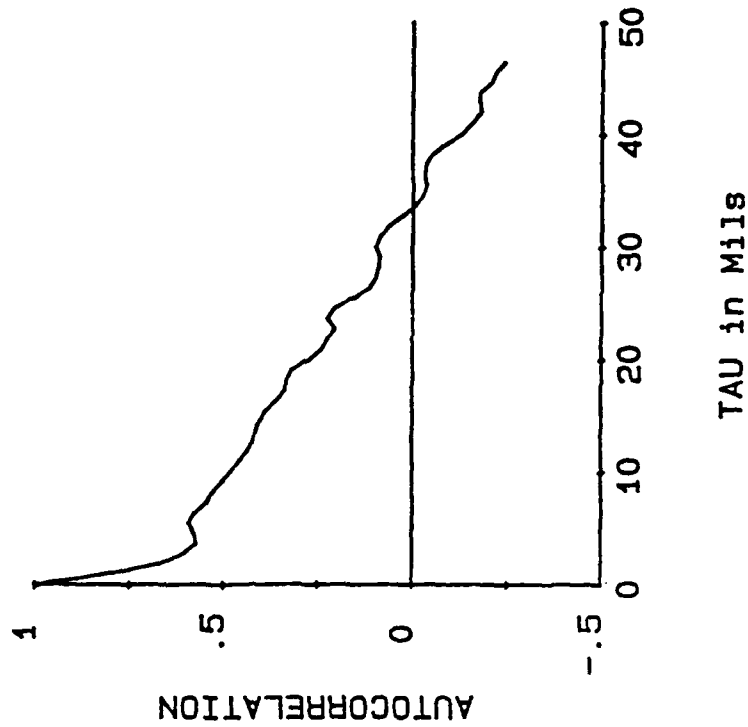
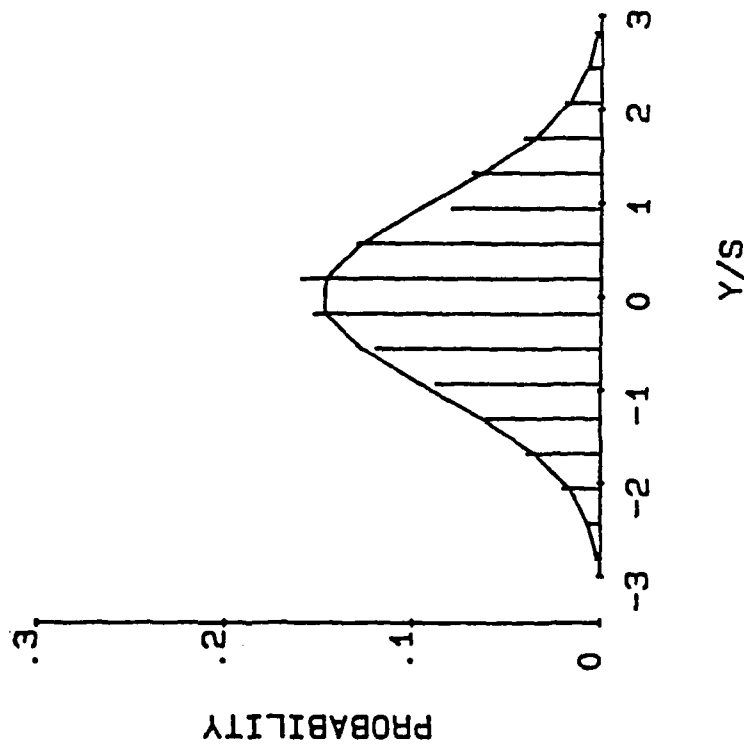


Figure 12. Example Results of Statistical Computations for the Height Distribution Function and the Autocorrelation Function.

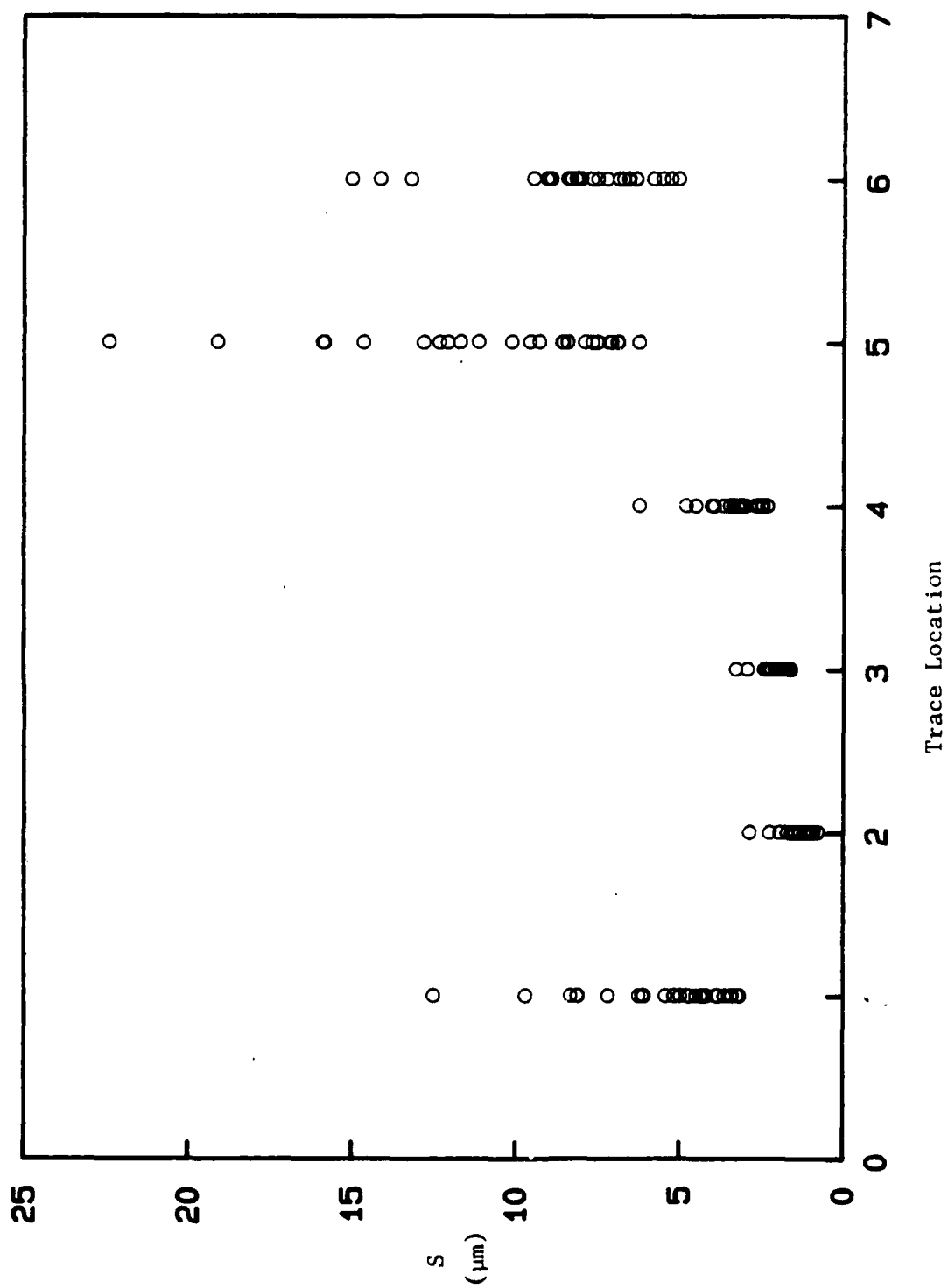


Figure 13. Summary of the Root Mean Square Roughness for the TF-39 Engine.

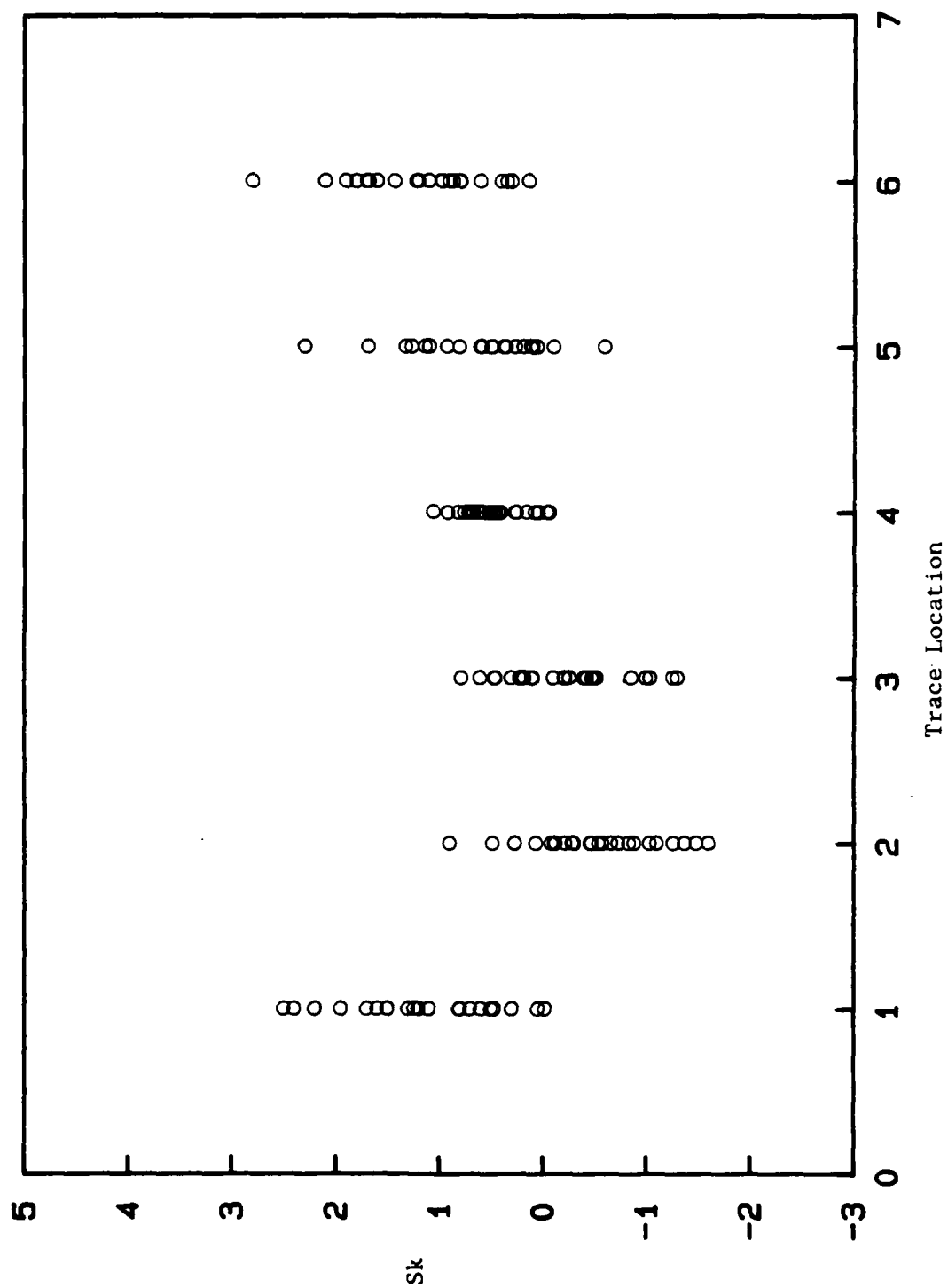


Figure 14. Summary of the Height Distribution Skewness for the TF-39 Engine.

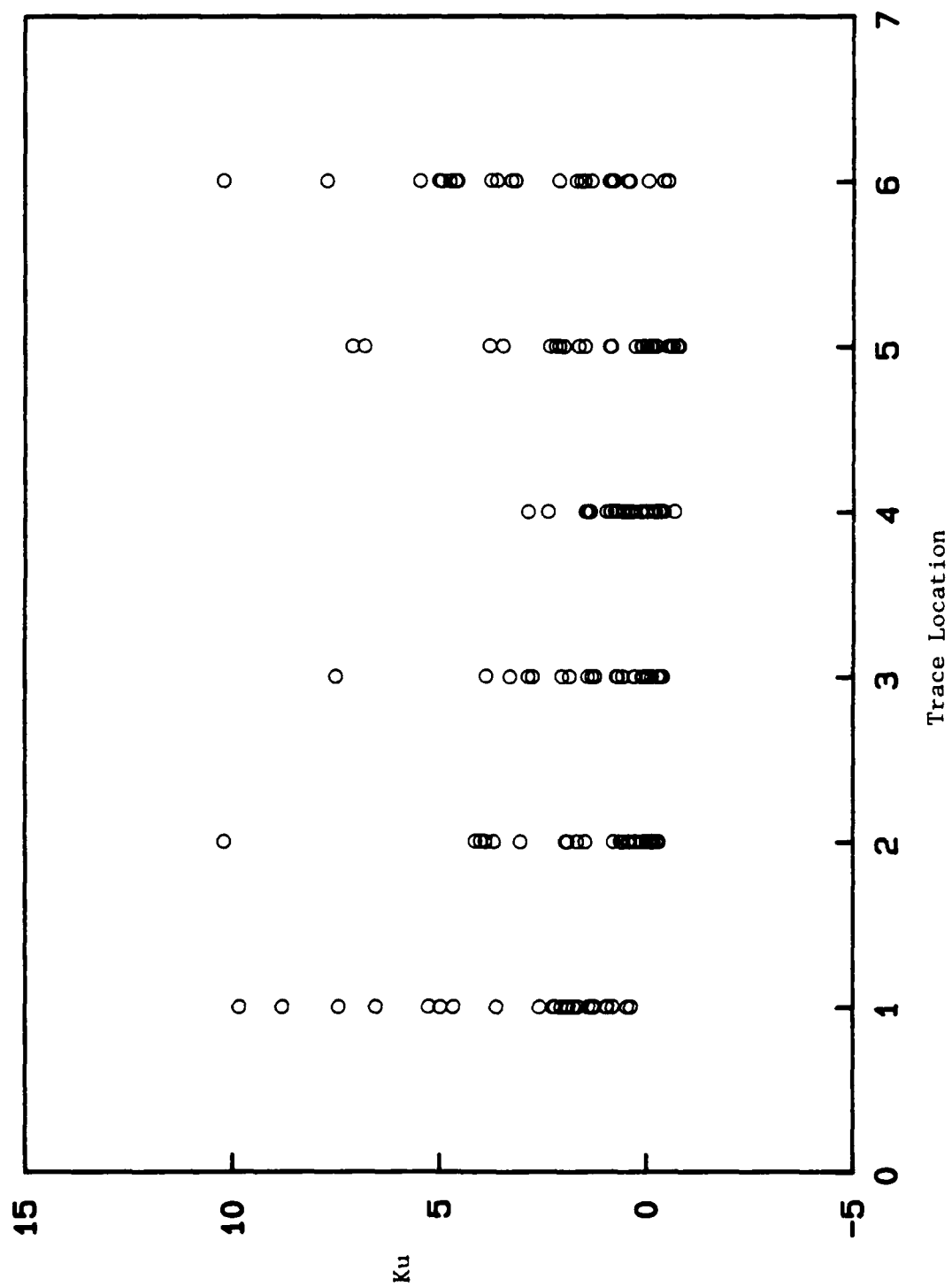


Figure 15. Summary of the Height Distribution Kurtosis for the TF-39 Engine.

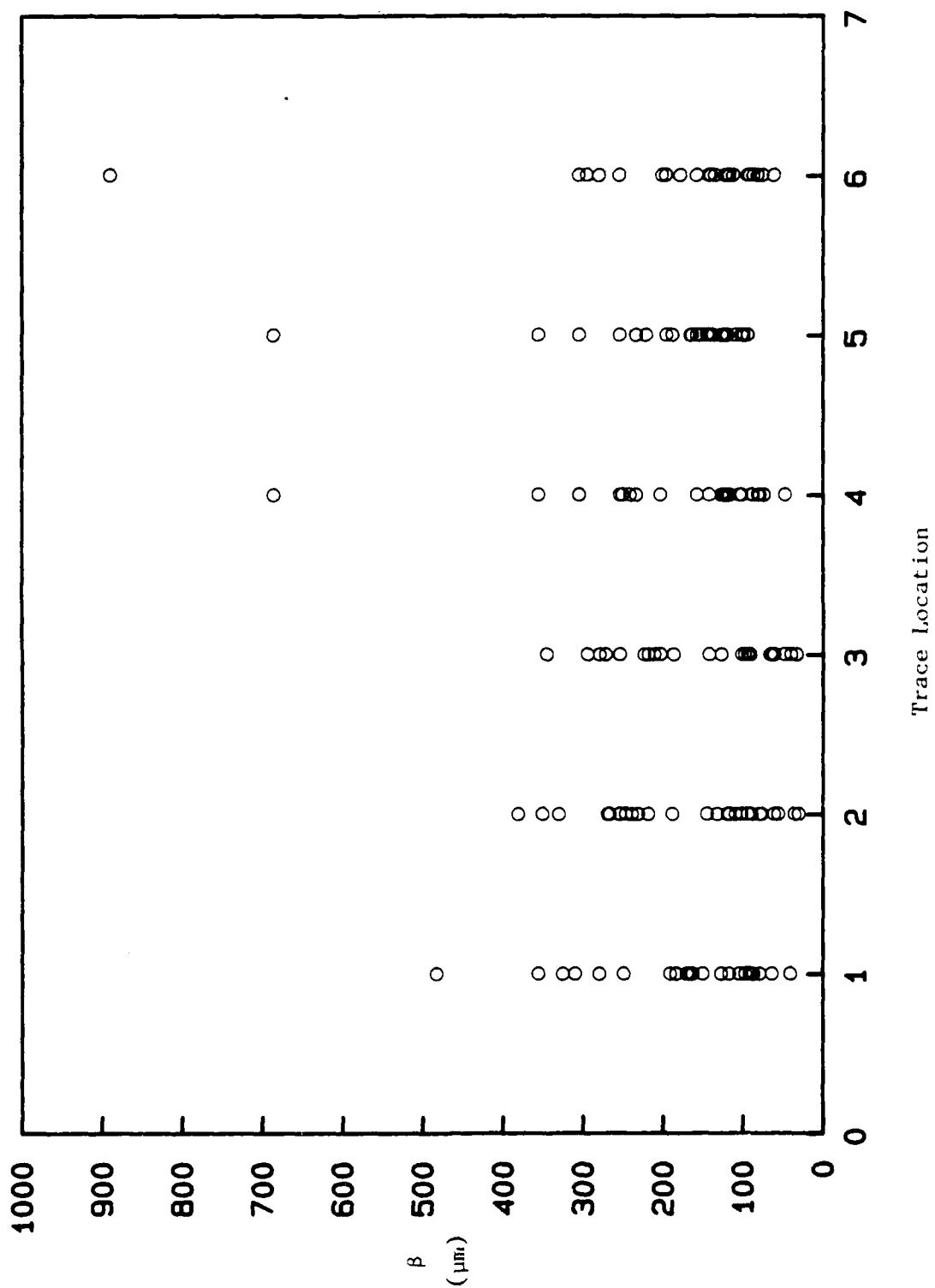


Figure 16. Summary of the Correlation Length for the TF-39 Engine.

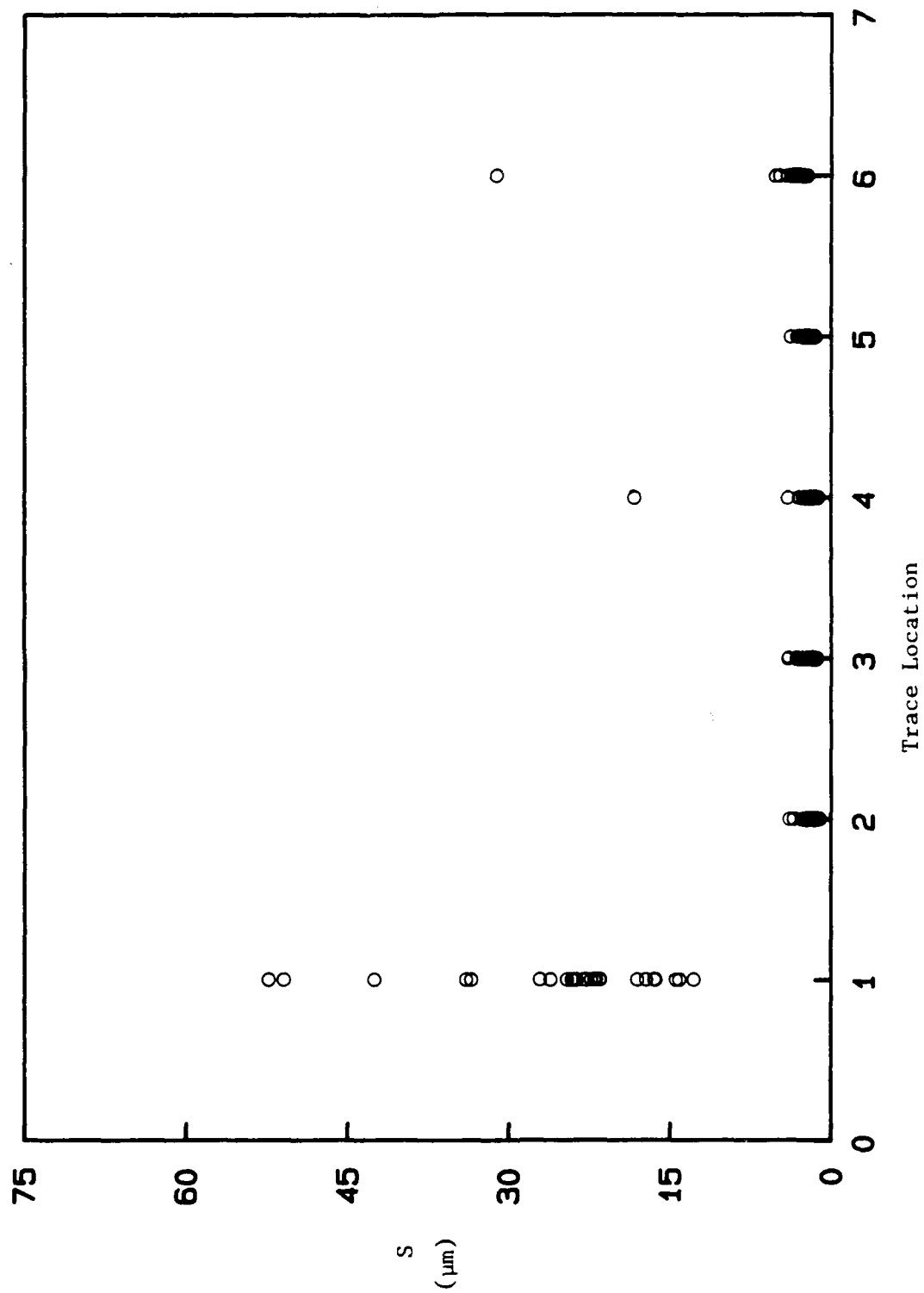


Figure 17. Summary of the Root Mean Square Roughness for the F-100 Engine.

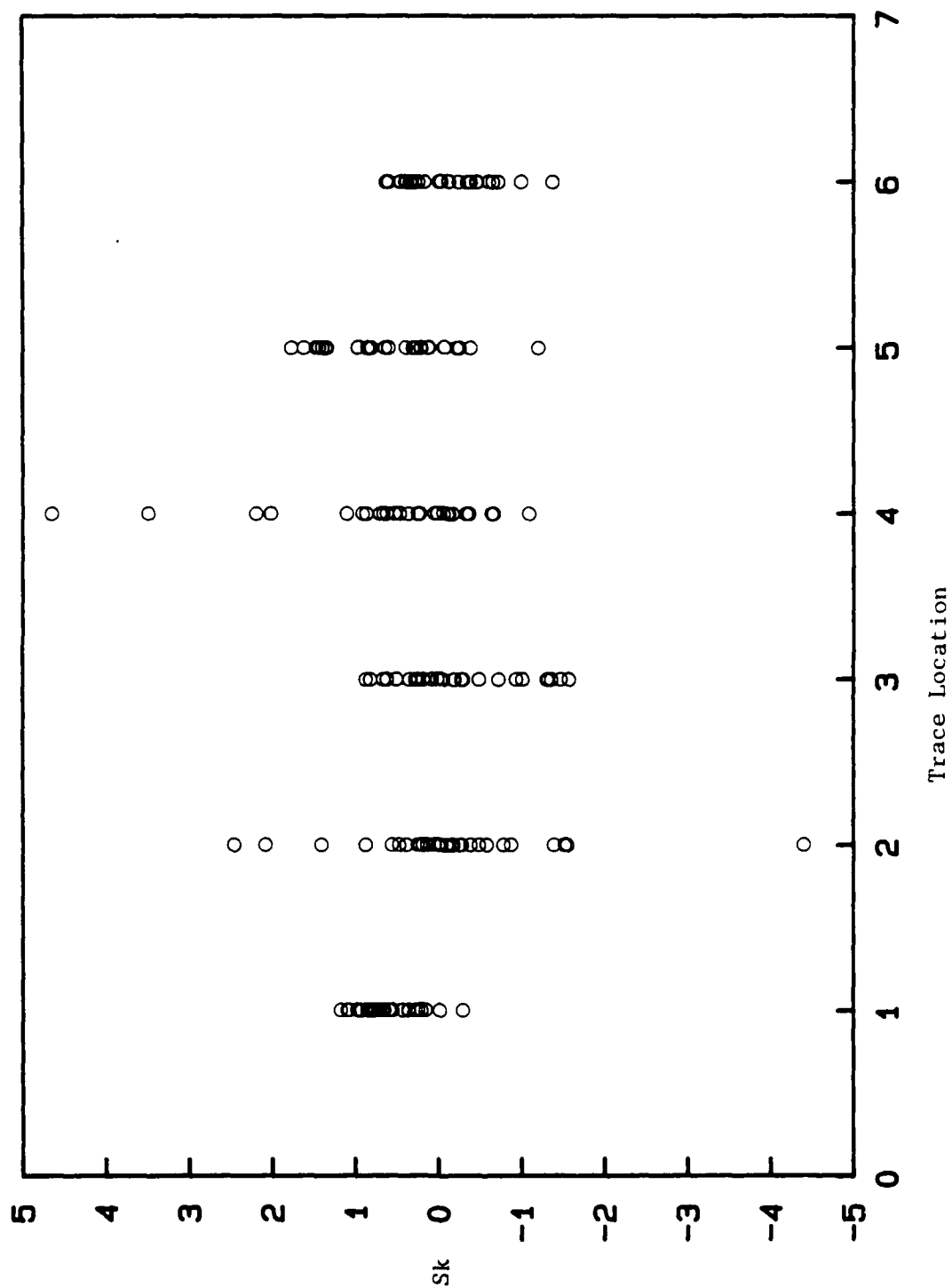
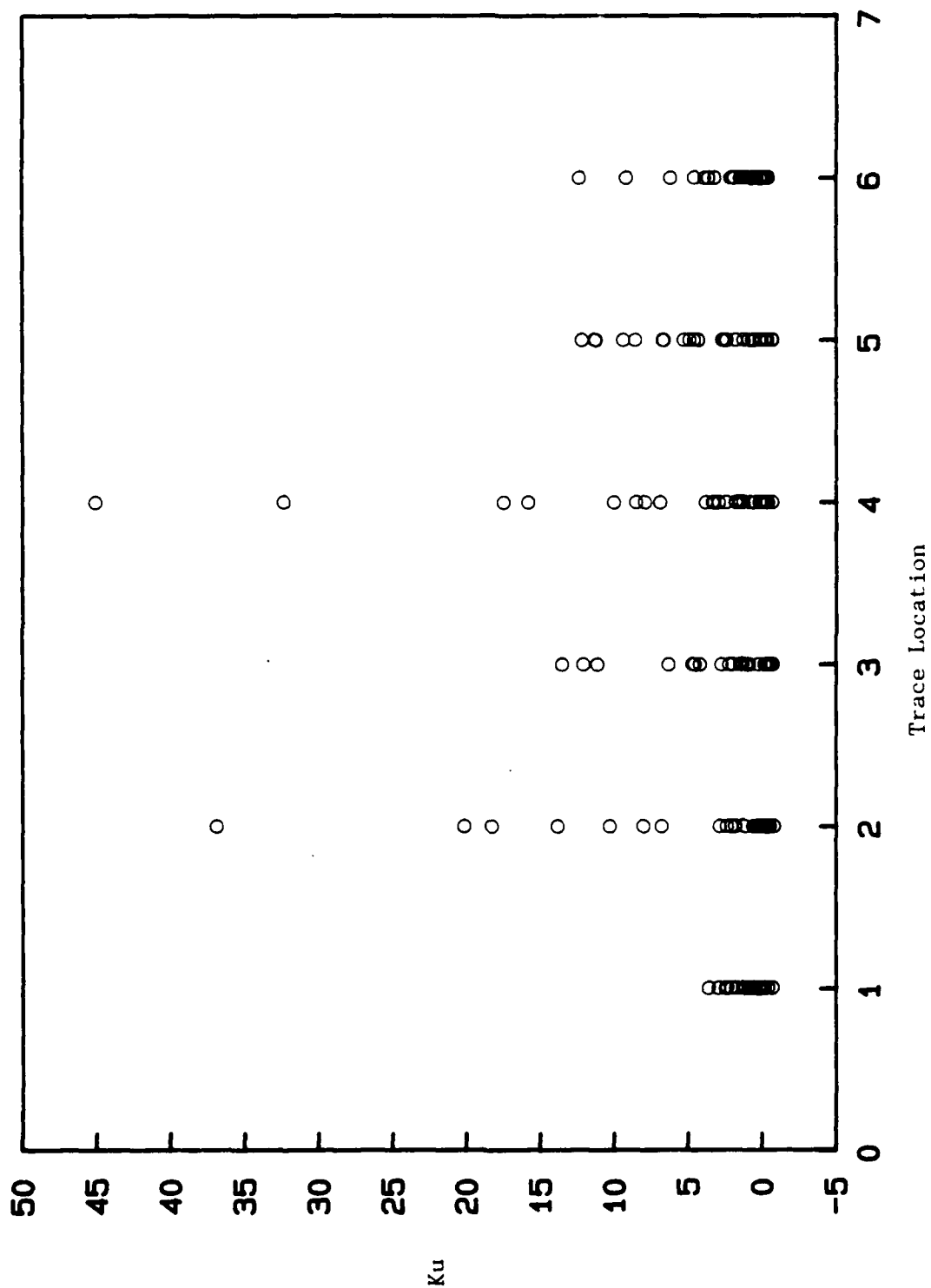


Figure 18. Summary of the Height Distribution Skewness for the F-100 Engine.



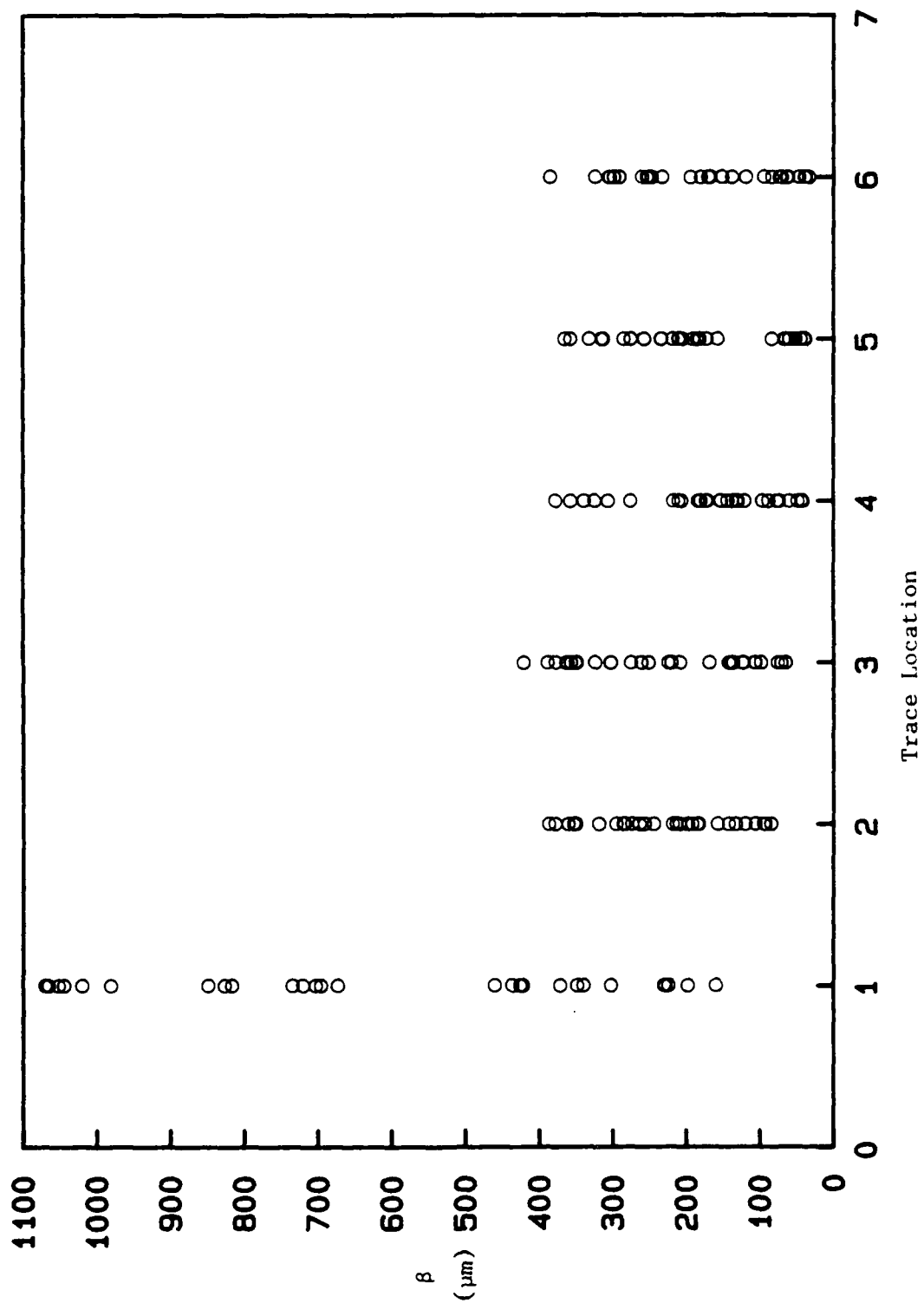


Figure 20. Summary of the Correlation Length for the F-100 Engine.

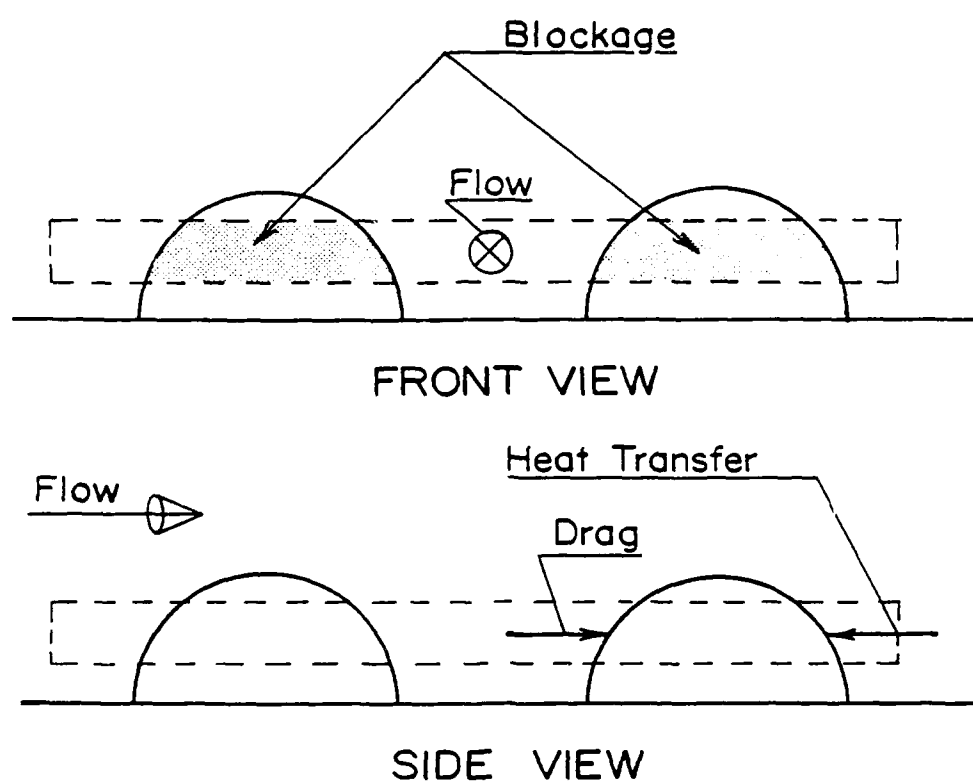
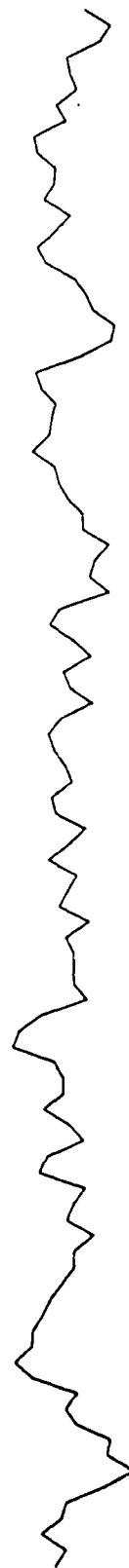


Figure 21. Schematic of a Rough Surface.

TF-39 1ST STAGE PRESSURE SIDE MIDCHORD
STRIP S059 AGE UNKNOWN



(a) Original profile



(b) Profile from reconstituted surface

Figure 22. Sample Profilometer Traces from a TF-39 Blade.

TF-39 1ST STAGE PRESSURE SIDE MIDCHORD

STRIP S059 AGE UNKNOWN

$S \approx .513$ Mils

$BETA \approx 6.55$ Mils

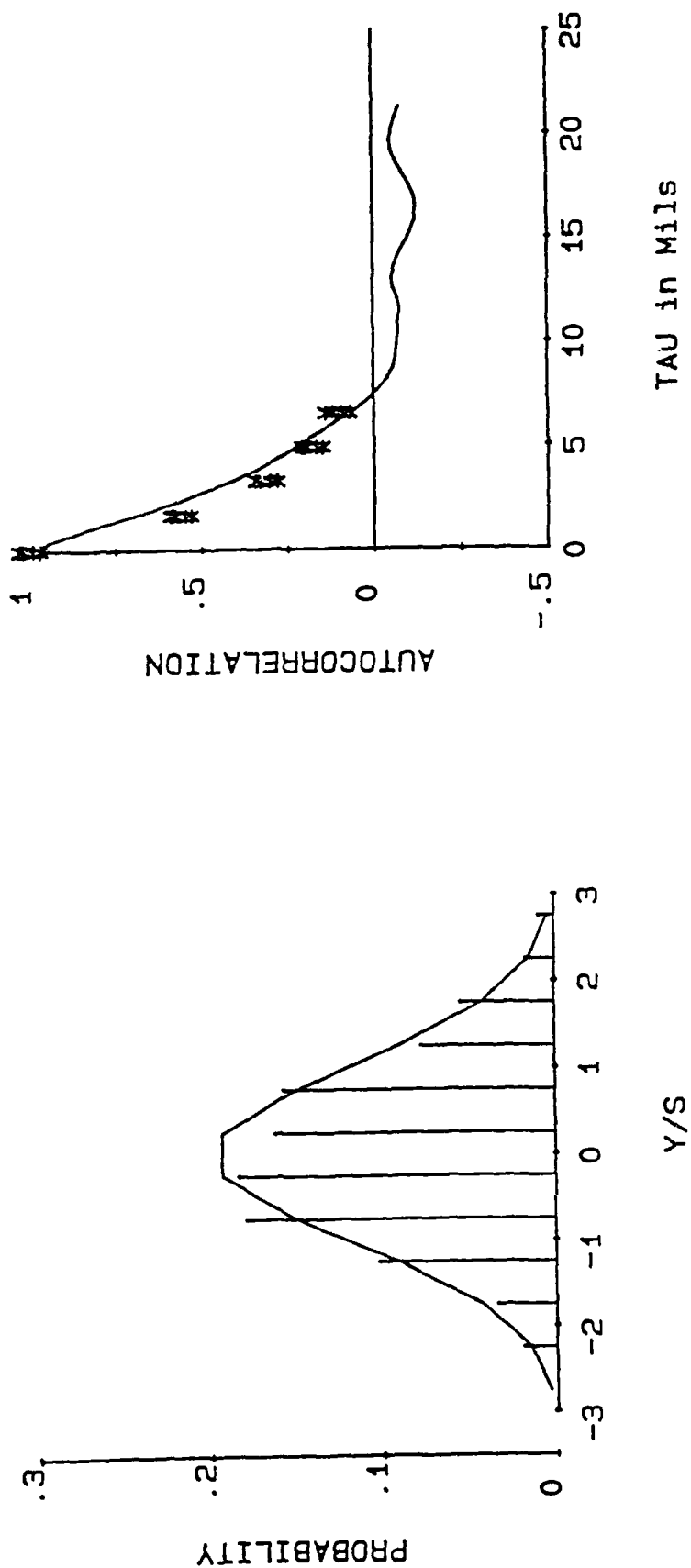


Figure 23. Sample Statistics for a TF-39 Blade.

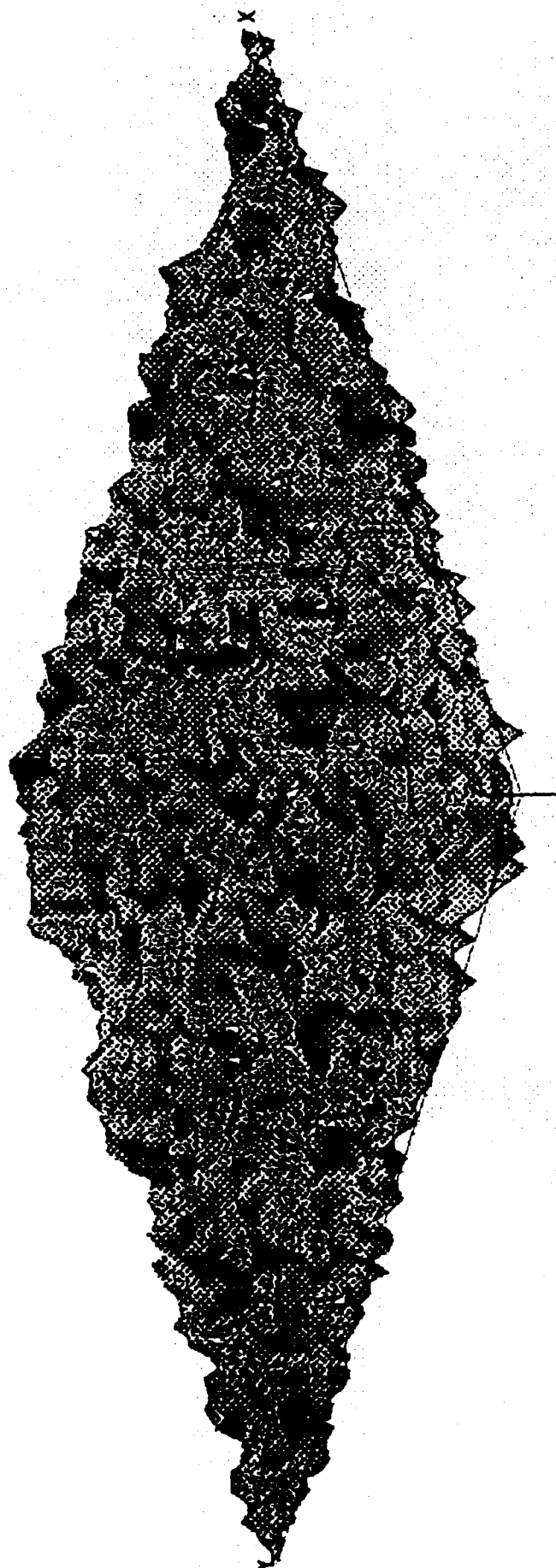


Figure 24. Three-Dimensional Projection of the Reconstituted Surface.

Final Report

EVALUATION OF ATMOSPHERIC EFFECTS
FOR OPERATIONAL TACTICAL DECISION AID

Submitted to
AIR FORCE OFFICE OF SCIENTIFIC RESEARCH

Research Program Conducted by
Universal Energy Systems

Contract Number
F49620-85-C-0013/SB5851-0360

Submitted by
Ken Tomiyama
Assistant Professor
Department of Electrical Engineering
Pennsylvania State University
University Park, Pennsylvania 16802
(814) 865-7667

August 28, 1986

ABSTRACT

The Tactical Decision Aid (TDA) is an integrated target/atmosphere/sensor model that is used to estimate target acquisition ranges for infrared sensors. It employs an extensive 8000-plus line computer code, LOWTRAN, to evaluate the atmospheric extinction of infrared signals for various climatological conditions. The Operational Tactical Decision Aid (OTDA) is a simplified version of the TDA housed on an HP-41CX, a hand-held computer, and is intended for field use. Since LOWTRAN is too voluminous to be employed for the OTDA, pre-computed extinction data tables are currently in use. Manual input of data from the tables to the OTDA is cumbersome and is prone to erroneous readings. Therefore, compact atmospheric extinction models were developed for various types of atmospheric extinction which are significant for the TDA application. The models were developed based on the LOWTRAN computation and were verified through extensive accuracy analysis. For automated generation of a data base for accuracy analysis, an interactive driver for LOWTRAN, called DGU, was developed. The program can create input decks for LOWTRAN from interactive sessions, run LOWTRAN, and post process the LOWTRAN generated data. Finally, the obtained models were integrated into a program, called CTRAN, and coded onto a VAX computer in FORTRAN and in Reverse Polish Notation for the HP-41CX.

1. Introduction

1.1 Background

The Tactical Decision Aid (TDA) is an integrated target/atmosphere/sensor model that is used to estimate target acquisition ranges for infrared sensors. It employs an extensive 8000-plus line computer code, LOWTRAN, (Kneizys et al. 1980, Kneizys et al. 1983) to evaluate the atmospheric extinction of infrared signals for various climatological conditions. The Operational Tactical Decision Aid (OTDA) is a simplified version of the TDA, and is intended for field use. It is housed on an HP-41CX, a hand-held computer. Because LOWTRAN is too voluminous to be employed in the OTDA, pre-computed extinction data tables are currently in use. However, it is inconvenient to carry the printed tables to the field, and the process of manual data input from the tables to the OTDA is prone to erroneous readings. It is preferred to have an extinction computation program as a part of the OTDA. Therefore, development of a compact atmospheric extinction computation code for the HP-41 was initiated (Tomiyaama 1986). The program will replace the transmittance tables, and automate the extinction evaluation process of the OTDA.

As an initial step towards this goal, compact atmospheric extinction models for various extinction mechanisms were developed based on the LOWTRAN models (Tomiyaama 1986). First, various components of the atmospheric extinction computation in LOWTRAN 6 were studied in detail, and the extinction mechanisms which are active over the wavelength interval of interest, 8 - 12

(um), were identified. Then, simple analytical expressions were selected to model these active extinction mechanisms. Optimal values for model parameters were obtained by minimizing the differences between the LOWTRAN computations and model predictions using parameter optimization techniques.

1.2 Project Objectives

The preliminary models in Tomiyama 1986 were shown to be in good agreement with LOWTRAN results. However, these models were not extensively tested for various combinations of climatological conditions which are typical of the TDA application. Furthermore, accuracies associated with some aerosol models may not be adequate in demanding applications. Critical testing of the developed models, including possible modifications, should be rendered before they can be coded to replace the extinction tables now in use.

To accommodate the general objective of developing an atmospheric extinction computation program for the OTDA, we have set the following specific objectives:

- (1) Develop a computer program to interactively generate extinction data for various extinction mechanisms using LOWTRAN, and to perform an error analysis of a given model. The program will be written as general as possible in order to facilitate its use for future error analysis.
- (2) Perform an exhaustive error analysis of the extinction models in Tomiyama 1986.

- (3) Modify the models to obtain better accuracy, if warranted.
- (4) Develop an extinction computation program for the HP-41CX based on the fully tested models.
- (5) Test the program developed in (4) against climatological conditions typical to the TDA application.

Before starting the summary of previous work, some underlying assumptions which are in effect will be stated.

1.3 Summary of Assumptions

Some basic assumptions were made to focus our modeling effort onto the OTDA applications. It was assumed that the quantity to be modeled is an average transmittance over 830 - 1250 (cm^{-1}), corresponding to 8 - 12 (μm), band which is the primary spectral region of sensitivity for infrared sensors considered in the OTDA. Optical paths between the sensors and targets are considered horizontal and are located below 2 km altitude. The altitude of 300 m (above sea level), which is the altitude of the sensor test cite at AFWAL/AARI, was designated as a standard height.

Finally, all simplified models should be consistent with LOWTRAN. Thus, the models will be derived from the LOWTRAN computation.

2. Atmospheric Extinction Models

Although the derivation of various extinction models from the LOWTRAN computation is reported in Tomiyama 1986, it is revised and repeated here for review and for completeness of this report. The results of extended error analysis and model upgrading will be given in the next chapter.

2.1 Introduction

Infrared radiation passing through the atmosphere loses its intensity as a result of interactions with atmospheric constituents. A quantity which characterizes this process is the atmospheric extinction in terms of the extinction coefficient k , or the atmospheric transmission in terms of the transmittance t . The transmittance t is defined as the ratio of the emitted and received infrared radiation intensities $I(\text{emitted})$ and $I(\text{received})$ as,

$$t = \frac{I(\text{received})}{I(\text{emitted})}, \quad (1)$$

and the extinction coefficient k is related to the transmittance t by

$$t = \exp(-k). \quad (2)$$

The extinction coefficient k includes contributions from two extinction mechanisms; absorption, and scattering. Each of these, in turn, consists of various individual contributions. The absorption includes molecular resonant absorptions, molecular continuum absorptions, aerosol (including fog) absorptions, and

rain absorption. The scattering includes molecular scattering and aerosol scattering.

LOWTRAN computes a LOW resolution TRANsmittance called the band transmittance. It is a degraded (or band) transmittance obtained by averaging the monochromatic transmittance over a small wavenumber interval using a triangular weighting function. LOWTRAN adopts the basic assumption of superposition, where the total extinction is the sum of individual contributions. Equivalently, the total transmittance is assumed to be the product of transmittances corresponding to individual sources. This assumption enables us to deal with various extinction mechanisms listed above separately.

As LOWTRAN suggests, some of the extinction mechanisms are inactive in the wavenumber region of interest, 830 - 1250 (cm^{-1}). As a result, we only need to consider the extinction due to the following: water vapor, uniformly-mixed gasses, ozone, water vapor continuum, aerosol, and rain.

As we discussed above, the requirement of the OTDA is the evaluation of the average transmittance over the 8 - 12 (μm) wavelength band. Therefore, the extinction models will be developed to represent the relationships between the average transmittance and various climatological conditions including the optical path length.

2.2 Molecular Resonant Absorptions

In LOWTRAN, various sources are considered for molecular resonant absorption including the three absorbers of concern; water vapor, uniformly-mixed gasses, and ozone. In the evalua-

tion of the absorption due to these three absorbers, two intermediate quantities, called an equivalent absorber amount U and a modified equivalent absorber amount x , are utilized in conjunction with two empirical transmittance models. Both the formulation of the modified equivalent absorber amount x and the computation formula for transmittance depend on the absorber, and are discussed later for each absorber.

Two empirical models, one for ozone and another for both water vapor and uniformly-mixed gasses, are stored as 67 pairs of numbers which represent transmittance t versus modified equivalent absorber amount x . The variation of the absorption with respect to the wavenumber are specified through sets of spectral parameters $C(v)$ which appear within x . The values of $C(v)$ are stored at 5 (cm^{-1}) interval over wavenumber regions of significant absorption, called the absorption bands, for each absorber. LOWTRAN computes the equivalent absorber amount U first and then the modified equivalent absorber amount x using the pressure, temperature, and wavenumber dependencies specific to each absorber. Finally, the transmittance is computed using the linear interpolation of empirical transmittance functions.

Transmittance profiles for those three absorbers over the 830 - 1250 (cm^{-1}) band were generated at 5 cm^{-1} intervals for various combinations of values for atmospheric variables using LOWTRAN 6. Then the resulting profiles are averaged and stored together with atmospheric variables into a data base. Analytical expressions based on the LOWTRAN computations are developed to model the relationship of the average transmittance versus other

variables. An optimal set of model parameters are found using linearization of model equations and the linear least square estimation technique.

2.2.1 Water Vapor Absorption

The transmittance expression used in LOWTRAN for a horizontal path with homogeneous meteorological conditions of pressure P (mb), temperature T (K), relative humidity RH (%), and path length R (km) at wavenumber ν (cm^{-1}) is as follows.

$$t = f(x), \quad (3-a)$$

$$x = C(\nu) P N^a T N^b U, \quad (3-b)$$

$$P N = P/P_0, \quad T N = T_0/T, \quad (3-c)$$

$$U = 0.1 WH R, \quad (3-d)$$

$$WH = 0.01 RH F(T_0/T), \quad (3-e)$$

where $f(\cdot)$, a , b , $P N$, $T N$, P_0 , T_0 , WH , and $F(\cdot)$ are the empirical transmittance function, absorber parameters ($a=0.9$, $b=0.45$), normalized pressure, normalized temperature, standard pressure (1013.25 mbar), standard temperature (273.15 K), water vapor density (g/m^3), and an empirical function for saturated water vapor density (g/m^3) at temperature T , respectively.

In earlier efforts on modeling of the molecular resonant absorption (Gruenzel 1978, Pierluissi et al. 1979), the following analytical expression, called the double exponential function, was found to have excellent agreement with the LOWTRAN empirical transmittance function.

$$t = \exp\{-10^{a_0 + a_1 x}\}, \quad (4-a)$$

$$x = \log C(v) + n \log(PN) + m \log(TN) + \log(U), \quad (4-b)$$

where a_0 , a_1 , n , and m are model parameters to be selected optimally.

This function was chosen as our model since it agrees excellently with the band transmittance which is a weighted average of transmittances and, therefore, is very similar to the average transmittance considered here. It is noted that the spectral parameter $C(v)$ in this equation may be eliminated in our model since only an averaged transmittance is to be modeled. As a result, the model can be simplified to

$$t = \exp\{-10^{a_0 + a_1 \log(PN) + a_2 \log(TN) + a_3 \log(U)}\}, \quad (5)$$

or

$$t = \exp\{-A_0 PN^{a_1} TN^{a_2} U^{a_3}\}, \quad (6)$$

where a_0 , a_1 , a_2 , a_3 , and $A_0 = 10^{a_0}$ are the adjustable model parameters.

For the optimal determination of the model parameters, we take the double logarithm of Eq. (5). This linearizes the model in terms of the unknown parameters.

$$\log\{-\ln(t)\} = a_0 + a_1 \log(PN) + a_2 \log(TN) + a_3 \log(U). \quad (7)$$

Linear regression techniques can then be utilized to obtain the optimal parameter values. Specifically, we take the difference

between the two sides of Eq. (7), square the difference, sum the squared differences, and minimize the sum with respect to the parameters. The minimization can be achieved by setting the partial derivatives of the sum of squared differences with respect to the unknown parameters to be zero. This process gives rise to a linear equation of the form $Ax=b$, commonly known as the normal equation, where A , x , and b are the symmetric coefficient matrix, unknown parameter vector, and the known vector, respectively. This type of equations can be solved by any linear equation solver.

2.2.2 Uniformly-Mixed Gasses

The absorber in question here is a mixture of various atmospheric gaseous molecules whose density profiles are relatively unperturbed, except for the pressure and temperature dependencies. Therefore, the corresponding absorber amount is a function of the pressure, temperature, and the path length only. Basically, the transmittance expression for this absorber is the same as that for the water vapor given in Eq. (3). The only difference is that the pressure and temperature dependencies within the absorber amount U can be integrated into these appearing in x . This leads to the following LOWTRAN model.

$$t = f(x), \quad (8-a)$$

$$x = C(v) P N^a T N^b U, \quad (8-b)$$

$$U = R, \quad (8-c)$$

where the absorber parameters a and b have values 1.75 and 1.375, respectively.

Thus, similar to the water vapor case, an appropriate model is given by, Eq. (5) or (6) with the expression for U being replaced by the path length R as in Eq. (8-c).

2.2.3 Ozone

The transmittance expression for ozone is the same as that for the water vapor, except the absorber parameter values, $a = 0.4$ and $b = 0.2$, and the expression for the absorber amount U which is given by

$$U = 46.667 W_0 R, \quad (9)$$

where W_0 is the ozone density in g/m^3 . Therefore, the appropriate model expression is again given by Eqs. (5) or (6) together with the absorber amount expression in Eq. (9).

2.3 Water Vapor Continuum Absorption

The LOWTRAN 6 expression for the water vapor continuum absorption consists of self and foreign components. The expression for a homogeneous path is given by,

$$t = \exp\{-v \tanh(hc/2kT) [R_s C_s + R_f C_f] W H R\}, \quad (10)$$

where $hc/k = 1.43879 \text{ (K/cm}^{-1}\text{)}$, R_s and R_f are self (water vapor versus total air at standard condition) and foreign (all other molecular species) number density ratios, and C_s and C_f ($1/(\text{cm}^{-1}\text{mol/cm}^2)$) are wavenumber dependent parameters for self and foreign components, respectively.

The temperature dependence of the self component C_s is taken into account through the linear interpolation from two values, C_{s1} at 296 K and C_{s2} at 260 K if the temperature is between these

two, or by setting at one of the two if the temperature is outside of the range. This can be expressed conveniently using a factor K_p defined by,

$$K_p = \begin{cases} 1, & T < 260, \\ (296 - T) / (296 - 260), & 260 < T < 296, \\ 0, & 296 < T, \end{cases} \quad (11)$$

as

$$C_s = (1 - K_p) C_{s1} + K_p C_{s2}. \quad (12)$$

The parameters C_{s1} , C_{s2} , and C_f are stored in LOWTRAN at 10 (cm^{-1}) wavenumber intervals over regions where the water vapor continuum absorption is non-trivial.

Now, various quantities in Eq. (10) are investigated. The number density ratio R_s is linearly dependent on the water vapor concentration W_H . The sum of the two densities, water vapor and all others, is linearly dependent on the product $PN*TN$ since it is the air density. Therefore, our model needs to carry two linear dependencies on $PN*TN$ and W_H in an additive fashion. The wavenumber dependent coefficient in Eq. (10), on the other hand, can be imbedded into C_s and C_f . Combining all of these observations to modify the expression in Eq. (10), we obtain,

$$t = e^{-[q(C_{s1}' + C_f') + K_p(C_{s2}' - C_{s1}')] W_H + r C_f' PN*TN] W_H R} \quad (13)$$

where q and r are wavenumber independent constants, and C_{s1}' , C_{s2}' , and C_f' are scaled wavenumber dependent parameters.

For our model, the averages of C_{s1}' , C_{s2}' , and C_f' over 830

- 1250 (cm^{-1}) region are computed from the LOWTRAN data, and these parameters in Eq. (13) are replaced with respective averages. Then the expression is simplified by combining the constants yielding,

$$t = \exp\{-C_0 [PN TN + (C_1 Kp + C_2) WH] WH R\}, \quad (14)$$

where C_0 , C_1 , and C_2 are the final model parameters.

2.4 Aerosol Extinction

Aerosols are active over 830 - 1250 (cm^{-1}) wavenumber region in both absorption and scattering. Since LOWTRAN has models for the extinction, we will consider the modeling of the extinction instead of the absorption and scattering individually.

The transmittance due to aerosols is given by an exponential law,

$$t = \exp\{-X H R\}, \quad (15)$$

where X is the aerosol extinction profile which is dependent on the type of aerosol, the relative humidity RH and the wavelength. H is the aerosol density profile which represents the visibility and the altitude dependencies.

We first consider the aerosol extinction profile X . There are ten aerosol types used in LOWTRAN, some are relative humidity dependent and some are not. Due to our assumption that the application of the OTDA is limited to horizontal paths below 2 km altitude, we only need to consider four humidity dependent aerosols; RURAL, URBAN, MARITIME, TROPOSPHERE, and two humidity independent ones; FOG1 and FOG2. LOWTRAN stores four extinction

profiles $X()$, corresponding to the relative humidities of 0, 70, 80, and 99 (%), for each humidity dependent aerosol and one each for FOG1 and FOG2. These profiles are first averaged to eliminate wavelength dependence. Then the humidity dependencies in four aerosols are modeled using the following empirical relationship which was suggested in Shettle 1979, based on the observation by Hanel (Hanel 1976),

$$X = c_1 (1 - RH/100)^{c_2}, \quad (16)$$

where c_1 and c_2 are model parameters. Noting that this relationship represents a straight line in log-log scale, optimal values for these parameters were obtained using the linear regression technique. This reduced the set of four profiles for each aerosol type to only two numbers. The same model is also used for the two humidity independent models, FOG1 and FOG2, by setting c_2 to 0 to eliminate humidity dependence.

Next, the visibility dependent aerosol density profiles H are studied. In the first 2 km height, it is represented by three empirical functions of the visibility at 0, and 1 (km) altitudes. First, these profiles are fitted by the inverse relationship,

$$H(VIS) = d_1 VIS^{-1} + d_2, \quad (17)$$

which is used in LOWTRAN for interpolation of the $H(.)$. Then, using the assumption that the typical altitude at which the OTDA is used is 300 (m) above sea level, the weighted average of the two profiles at 0 and 1 (km) heights is adopted as our model.

Finally, Eqs. (15), (16) and (17) are combined to form the

following aerosol model,

$$t = \exp\{-(\text{VIS}^{-1} + d_2') c_1' (1 - \text{RH}/100)^{c_2} R\}, \quad (18)$$

where d_1 is imbedded into c_1' by factoring it out to reduce the number of parameters. It is noted that d_2' is independent of the aerosol type.

2.5 Rain Model

Since the rain extinction model used in LOWTRAN is a simple analytic function of the rain rate RR (mm/hr) and the range R (km), we can adopt it with a slight modification. After combining some parameters to minimize the number of constants, the model becomes as follows,

$$t = \exp\{-0.3647 RR^{0.63} R\}. \quad (19)$$

2.6 Summary of Model Equations

The model equations derived in the previous subsections are summarized in Table 1 together with the obtained optimum parameter values. Table 2 lists the input variables together with the definitions and default values where applicable.

Table 1. Preliminary Extinction Models for the OTDA

(1) Molecular resonant absorption

$$t = \exp\{-A_0 (P/P_0)^{a_1} (T_0/T)^{a_2} U^{a_3}\}$$

Absorber	A ₀	a ₁	a ₂	a ₃
Water Vapor	0.0850	0.4981	0.2989	0.5582
	U = 0.1 WH R, WH = 0.01 RH F(T ₀ /T)			
Uniformly-mixed Gasses	0.0118	1.0792	0.8488	0.6178
	U = R			
Ozone	0.0076	0.3091	0.1541	0.7498
	U = 46.667 WO R			

$$F(s) = s \exp\{18.9766 - 14.9595 s - 2.43882 s^2\}$$

$$WO = 6.0E-05 \text{ (G/m}^3\text{)}.$$

(2) Water Vapor Continuum Absorption

$$t = \exp\{-C_0 [(P/P_0)(T_0/T) + (C_1 Kp + C_2) WH] WH U\}$$

$$C_0 = 1.655E-03 \quad C_1 = 0.5693 \quad C_2 = 0.5437$$

$$Kp = \begin{cases} 1 & T < 260 \\ (296 - T)/(296 - 260) & 260 < T < 296 \\ 0 & 296 < T \end{cases}$$

(3) Aerosol Extinction

$$t = \exp\{-(VIS^{-1} + d_2') c_1' (1 - RH/100)^{c_2} R\}$$

#	Model	c ₁ '	c ₂	Default VIS(km)
1	RURAL	0.3670	-0.02877	23
2	URBAN	0.3119	-0.08499	5
3	OCEAN	0.4013	-0.3417	23
4	TROPOSPHERIC	0.08054	-0.04621	50
5	FOG1	4.487	0	0.2
6	FOG2	1.309	0	0.5

$$d_2' = -0.005183 \text{ (independent of aerosol type)}$$

(4) Rain Extinction

$$t = \exp\{-0.3647 RR^{0.63} R\}$$

Table 2. Input Variables for Extinction Models

Variable	Notation (Units)	Default
Pressure	P (mbar)	None
Temperature	T (°C)	None
Relative Humidity	RH (%)	None
Visibility	VIS (km)	*
Aerosol Model	IHAZE (integer)	0 (No Aerosol)
Rain Rate	RR (mm/h)	0.0
Range	R (km)	None

* See Table 1 for model dependent default values.

3. Accuracy Evaluation

A preliminary accuracy evaluation was done at AFWAL/AARI-3 while the principal investigator was visiting the laboratory. The obtained results were reported in Tomiyama 1986. For more comprehensive accuracy study, a data base was generated using LOWTRAN according to the following scheme:

- a. For the molecular and water vapor continuum extinction, eight pressure values are used. Maximum and minimum pressure values of the 0 and 1 km layers of six atmosphere models in LOWTRAN are first chosen. Then, six more intermediate values, evenly distributed between the two extremes, are selected. They are: 1018.0, 999.4, 980.8, 962.2, 943.6, 925.0, 906.4, and 887.8 (mbar).
- b. Eight temperature values are chosen for temperature dependent models similarly to a. The values are: 35.0, 27.14, 19.29, 11.43, 3.57, -4.26, -12.14, -20.0 (C).
- c. Eight humidity levels; 99%, 95%, 90%, 85%, 75%, 50%, 30% and 10% are used for humidity dependent models.
- d. Eight visibility values are used for aerosols. The values are chosen at and about the default visibility values for each aerosol model. Therefore, the actual values are dependent on the aerosol model.
- e. Eight range values were used where the values were chosen so that the resulting transmittances are as well-distributed in [0, 1] interval. For aerosol models, this implies that the range value is comparable to the default visibility values.

Although the numbers of variations in each input parameter is small, combinations of the above set of variations can be very large. To automate the process of data generation, an interactive computer program, called DGU (Data Generation Utility), was developed. It was written mostly in the C programming language. It uses a FORTRAN routine for post processing of LOWTRAN generated data. (The listing of the DGU program is given in Appendix A.) Enough prompts are included in the program so that the user will need minimal effort in generating input data for LOWTRAN.

The program takes advantage of the UNIX operating system in creating input decks for LOWTRAN automatically from the interactive inputs. It also runs LOWTRAN for each set of input deck and post-processes the LOWTRAN generated data to compute the averaged transmittances. DGU repeatedly performs the combined task; generation of input deck, running LOWTRAN, and post-processing of LOWTRAN generated data file, rather than creating all the input deck and then running LOWTRAN. This is because the latter method creates impractically large data files. The adopted method reduces the entire output of one LOWTRAN run to a single line. Thus, the storage requirement is immensely reduced.

LOWTRAN was run over 6000 times to generate data for all possible input value combinations. Outputs produced from this extensive computation were utilized for accuracy evaluation and stored for later usage as well. Results of accuracy evaluations are summarized in Table 3, in which the column MODEL 1 represents RMS errors of the developed models.

Table 3. Accuracy Evaluation of Extinction Models

TYPE OF EXTINCTION	MODEL 1		MODEL 1A	
	R.M.S. Error	# of +/- Err.	R.M.S. Error	# of +/- Err.
Water Vapor	0.0123	1834/2262		
Uniformly-Mixed Gasses	0.0007	2008/2088		
Ozone	0.0015	592/3504		
Water Vapor Continuum	0.0064	416/3680		
Aerosol	0.0097	217/295	0.0084	234/278
RURAL	0.0170	219/293	0.0164	236/276
OCEAN	0.0108	199/313	0.0089	231/281
URBAN	0.0063	265/247	0.0040	295/217
TROPOSPHERIC	0.0013	13/26	0.0007	36/28
FOG1	0.0261	0/49	0.0071	16/33
FOG2				

4. Model Upgrading

Table 3 shows that the accuracy of most of the models are acceptably high, but some are not. Aerosol extinction models exhibit higher RMS errors. Especially, the RMS errors associated with RURAL, URBAN, and OCEAN models may be excessive for demanding applications. Note also that the numbers of positive (+) and negative (-) errors differ rather large in some models. This is not desirable since it indicates there exists a non-zero bias in the model. The accuracy of biased models can easily be improved by eliminating the biases. Based on these observations, it was decided to upgrade all the aerosol models.

Model improvements start from the identification of causes of the observed error. In developing the aerosol extinction models, each intermediate quantity was separately modelled from the LOWTRAN expressions and then combined. If better intermediate models are developed, then the total model accuracy should be improved. This approach leads us to, for example, quadratic models for the relative humidity dependent quantity X.

On the other hand, the component-wise modelling approach may be optimal for each individual component, but the combination of the individual components need not be optimal as a whole. This prompted the approach of obtaining optimal parameter values by directly minimizing the difference between model prediction and the LOWTRAN computation. Keeping the model formulation derived in Section 2.4, namely Eq.(18), unchanged, the difference was minimized in terms of three parameters $c1'$, $c2$, and $d2'$ simul-

taneously. Since the model equation, Eq.(18), is nonlinear in the unknown parameters, the method of choice here is nonlinear optimization.

The difference between the LOWTRAN and model transmittances are squared and summed to form a sum of squared errors which is to be minimized. A general approach for this minimization is to set the derivative of the sum of squared errors to be zero. However, if the model equation is nonlinear and complicated, derivation of derivative expressions is cumbersome and susceptible to error in analytical manipulation. Therefore, a subroutine called ZXSSQ of the IMSL library was adopted for this task because it directly minimizes the sum of squares without utilizing derivatives (IMSL 1984).

Table 4 summarizes the new optimal parameter values for aerosol models. Note that the parameter c_3 (formerly d_2') is no longer independent of the aerosol type. In Table 3, RMS errors corresponding to the new parameter set are listed in the MODEL 1A column. The new set of model parameters produces uniformly better modelling accuracies with the same number of parameters for each aerosol type. It was concluded that the obtained models have sufficient accuracy to be adopted in the OTDA.

Table 4. Upgraded Aerosol Extinction Model

$$t = \exp\{ -c_1 (1 - RH/100)^{c_2} (VIS^{-1} + c_3) R \}$$

#	Model	c_1	c_2	c_3
1	RURAL	0.3250795	-0.0698031	-0.0062501
2	OCEAN	0.407210	-0.346923	-0.0073294
3	URBAN	0.377737	-0.010870	-0.0055683
4	TROPOSPHERIC	0.084286	-0.018607	-0.0055992
5	FOG1	4.475481	0	0.0051780
6	FOG2	1.082089	0	0.2241563

5. Model Implementation

The models listed in Table 1 with the upgraded parameters given in Table 4 are now ready to be integrated into a transmittance computation code. First, a FORTRAN program, called CTRAN (Compact TRANsmittance code), was developed. Outputs from CTRAN were compiled for climatological conditions which were used for data generation. As a final check of the validity of the models, the CTRAN transmittance values were compared with the average LOWTRAN total transmittance computed within LOWTRAN. This is done using an error evaluation code called ILMAP (Interactive Lowtran Model Analysis Program). Tables 5-a through 5-g summarizes the obtained error statistics. The overall result was an RMS error of 0.00463 in the total transmittance for 6,272 cases. This shows an excellent accuracy of the adopted models, considering the simplicity of them.

The models are then implemented on the HP-41CX. The programming language of the HP-41CX, which is based on the Reverse Polish notation, has been carefully studied for its use and capabilities. We developed two versions; one utilizes interactive inputs, and the other uses stored input values. The developed program is thoroughly tested by computing the transmittance values for the input combinations used in accuracy test data generation, and then by comparing it with the results from the FORTRAN version. A user's manual for the HP-41CX version of CTRAN is prepared and is listed in Appendix B. The listing of CTRAN, both the FORTRAN and HP-41CX versions, is in Appendix C.

Table 5. Error Analysis of CTRAN

5-a. Molecular and Continuum Extinctions

MECHANISM	AVG % ERROR	RMS ERROR	POS/NEG
H2O	9.14734E-01	1.22954E-02	1834/2262
CO2	4.98500E-02	7.38009E-04	2008/2088
O3	9.97693E-02	1.45760E-03	592/3504
CONTINUUM	6.25526E+00	6.35660E-03	416/3680
TOTAL	5.85113E+00	4.58491E-03	558/3538

5-b. RURAL Aerosol Extinctions

MECHANISM	AVG % ERROR	RMS ERROR	POS/NEG
AEROSOL	3.42939E+00	8.38760E-03	234/278
H2O	3.34638E+00	2.75920E-02	176/336
CO2	4.86877E-02	6.78719E-04	256/256
O3	9.99364E-02	1.48416E-03	64/448
CONTINUUM	2.41252E+01	7.82923E-03	96/416
TOTAL	1.72796E+01	4.67787E-03	227/285

5-c. OCEAN Aerosol Extinction

MECHANISM	AVG % ERROR	RMS ERROR	POS/NEG
AEROSOL	7.27404E+00	1.64423E-02	236/276
H2O	3.34638E+00	2.75920E-02	176/336
CO2	4.86877E-02	6.78719E-04	256/256
O3	9.99364E-02	1.48416E-03	64/448
CONTINUUM	2.41252E+01	7.82923E-03	96/416
TOTAL	1.70245E+01	4.00414E-03	193/319

5-d. URBAN Aerosol Extinction

MECHANISM	AVG % ERROR	RMS ERROR	POS/NEG
AEROSOL	2.57359E+00	8.88108E-03	233/283
H2O	2.73274E+00	2.33742E-02	186/330
CO2	3.51118E-02	4.46355E-04	322/194
O3	6.79489E-02	9.30073E-04	130/386
CONTINUUM	2.46186E+01	7.99203E-03	80/436
TOTAL	1.83626E+01	3.76052E-03	222/294

Table 5. Error Analysis of CTRAN (contd.)

5-e. TROPOSPHERIC Aerosol Extinction

MECHANISM	AVG % ERROR	RMS ERROR	POS/NEG
AEROSOL	3.22787E-01	3.98972E-03	295/217
H2O	1.00691E+01	5.51320E-02	56/456
CO2	3.43206E-01	4.85434E-03	128/384
O3	6.63520E-01	9.08007E-03	64/448
CONTINUUM	2.81415E+01	6.68107E-03	240/272
TOTAL	2.56393E+01	5.71252E-03	266/246

5-f. FOG1 Aerosol Extinction

MECHANISM	AVG % ERROR	RMS ERROR	POS/NEG
AEROSOL	4.07248E+00	6.15750E-04	36/28
H2O	1.63183E-01	1.79755E-03	40/24
CO2	6.69137E-02	6.69395E-04	0/64
O3	8.31018E-02	8.56417E-04	0/64
CONTINUUM	5.64428E-01	4.60394E-03	0/64
TOTAL	3.08864E+00	4.86034E-04	48/16

5-g. FOG2 Aerosol Extinction

MECHANISM	AVG % ERROR	RMS ERROR	POS/NEG
AEROSOL	5.49332E+00	1.79535E-02	11/53
H2O	3.04797E-01	2.74605E-03	64/0
CO2	5.73236E-02	5.86308E-04	0/64
O3	1.06208E-01	1.06103E-03	0/64
CONTINUUM	2.79759E+00	1.13680E-02	0/64
TOTAL	7.33842E+00	8.88518E-03	7/57

6. Conclusions and Directions for Future Study

6.1 Conclusions

Simple models for atmospheric extinctions due to various atmospheric absorption mechanisms were developed for the Operational Tactical Decision Aid. These models were: for three molecular resonant absorptions due to the water vapor, uniformly-mixed gasses, and ozone, for water vapor continuum absorption, for aerosol extinction, and for rain extinction. All of those absorption mechanisms are active in the 8 - 12 (μ m) band which is the primary band of sensitivity for infrared sensors.

Set of preliminary models were developed from LOWTRAN by carefully simplifying the structures of the LOWTRAN models. The preliminary models were extensively compared with LOWTRAN computations for various combinations of input values. An interactive program, DGU, was written to automate the data generation for accuracy testing. It generates LOWTRAN input deck sets for all possible combinations of given input values, runs LOWTRAN, and post-processes the LOWTRAN generated data files.

Acceptable agreements were found in most models with the exceptions of the aerosol models. As a result, aerosol models were upgraded using the direct minimization of the discrepancies between the model predicted transmittances and the LOWTRAN results.

The final models with their optimal parameter values were integrated into a compact transmittance computation code, called CTRAN, in the FORTRAN language for mainframe computers. CTRAN

was then coded onto an HP-41CX using the HP-41CX programming language. The program was thoroughly tested against the data set used for accuracy testing. The HP-41CX version of CTRAN is now ready to be employed in the OTDA.

6.2 Directions for Future Study

The models obtained in this project are very simple. All of them are simple analytical functions with a small number of parameters. This was necessary because of the severe restriction of the computational capability of the HP-41CX hand-held computer. It is well understood that the portability is of utmost importance for the OTDA, and that this leads to the employment of HP-41CX computer. However, the availability of powerful but truly portable micro-computers is rapidly increasing. Newer machines are smaller, faster, of higher memory capacity, and longer operation time between rechargings. The choice of the HP-41CX for OTDA may need to be reconsidered. The capability of the HP-41CX can hardly be compared with that of a micro-computer. Since the portability of the two do not differ significantly, availability of high level languages alone may be a sufficient advantage of micro-computers. Also, because of the large memory capacity, a micro-computer can store the entire OTDA in a cluster of programs and data files. Therefore, it is highly recommended that a portable micro-computer instead of an HP-41CX be used for the OTDA.

The advantage of higher memory capacity of micro-computers can be exploited to employ more accurate but complicated atmospheric extinction models to the OTDA. It is even conceivable to

add another set of models for 3 - 5 (μ m) spectral band, which is also used by some infrared detectors. Furthermore, it should be possible to implement a program which generates simplified transmittance profiles for the two spectral regions. This point is currently under investigation.

REFERENCES

- Kneizys, F.X., E.P. Shettle, W.O. Gallery, J.H. Chetwynd, Jr., L.W. Abreu, J.E.A. Selby, R.W. Fenn, and R.A. McClatchey 1980. "Atmospheric Transmittance/Radiance: Computer Code LOWTRAN 5," Report AFGL-TR-80-0067, Air Force Geophysics Laboratory, Hanscom Air Force Base, Mass.
- Kneizys, F.X., E.P. Shettle, W.O. Gallery, J.H. Chetwynd, Jr., L.W. Abreu, J.E.A. Selby, S.A. Clough, and R.W. Fenn 1983. "Atmospheric Transmittance/Radiance: Computer Code LOWTRAN 5," Report AFGL-TR-83-0187, Air Force Geophysics Laboratory, Hanscom Air Force Base, Mass.
- Tomiyaama, K. 1986. "Atmospheric Modeling for Operational Tactical Decision Aid," Final Report, Contract Number F49620-85-C-0013, Air Force Office of Scientific Research.
- Gruenzel, R.R. 1978. "Mathematical Expressions for Molecular Absorption in LOWTRAN 3B," Applied Optics, 17, pp 2591-2593.
- Pierluissi, J.H., K. Tomiyama, and R.G. Gomez 1979. "Analysis of LOWTRAN Transmission Functions," Applied Optics, 18, pp 1607-1612.
- Shettle, E.P., and R.W. Fenn 1979. "Models for the Aerosols of the Lower Atmosphere and the Effects of Humidity Variations on Their Optical Properties," Report AFGL-TR-79-0214, Air Force Geophysics Laboratory, Hanscom Air Force Base, Mass.
- Hanel, G. 1976. "The Properties of Atmospheric Aerosol Particles as Functions of the Relative Humidity at Thermodynamic Equilibrium with the Surrounding Moist Air," Advances in Geophysics, Ed. by H.E. Landsberg and J. Van Mieghem, Academic Press, New York, 19, pp 73-188.
- IMSL 1984. IMSL User's Manual, V.4, Chapter Z, pp ZXSSQ1-ZXSSQ7.

ACKNOWLEDGEMENTS

I would like to thank Roger L. Cranos and Don L. Tomlinson, both of the Avionics Laboratory, the Air Force Wright Aeronautical Laboratory (AFWAL/AARI), for providing me with the opportunity to pursue this research. Valuable help in UNIX and the C programming language from Jeff D. Sweet, also at AFWAL/AARI is acknowledged. I would also like to thank Dennis W. Richardson for his help throughout this project.

Appendices can be obtained from
Universal Energy Systems, Inc.

Report Submitted to AFOSR Mini Grant Program

Title: An Investigation Concerning the Formation of a Dynamic Stall Vortex
on a Pitching Airfoil

by

T.R. Troutt

Associate Professor

and

Julie Albertson

Graduate Student

Department of Mechanical and Materials Engineering

Washington State University

Pullman, WA 99164-2920

Abstract

This experimental research program focuses on the events leading up to the development of the dynamic stall vortex on a pitching airfoil. These flow events are of extreme interest since large percentage increases in maximum lift coefficients for pitching airfoils appear to be connected to the flow development prior to the dynamic stall vortex production. The specific experimental situation involves a two-dimensional NACA 0015 airfoil undergoing constant pitch rate motion in a uniform airstream. The investigation concentrates on low nondimensional pitch rates since the largest rate of change of maximum lift coefficient with change in pitch rate is observed in this range. Direct comparisons between pitching and static airfoil situations are made to develop understanding concerning the influence of the unsteady airfoil motion on the attainment of high lift coefficients. The experimental investigations employ simultaneous flow visualization and multiple surface pressure measurements to relate the observed flow phenomena to the resulting pressure forces on the airfoil. The primary goal of this research program is to develop understanding concerning the enhancement of maximum lift coefficients by the unsteady motion of airfoils. This improved understanding can then be employed to develop new designs and techniques for improving the maneuverability and control of high performance aircraft. Results show that the greatest increases in lift due to the pitching motion occur prior to the nondimensional pitch rate of 0.1 for all three pivot locations. Lift to drag ratios tend to take on maximum values for nondimensional pitching rates between 0.02 and 0.1 indicating a region of enhanced performance possibilities.

Introduction

One of the most intriguing effects produced by unsteady flows on pitching airfoils concerns the large maximum lift enhancements obtainable from relatively low rotational pitching rates. Recent experimental results reported by both Walker, Helin and Chou (1) and by Jumper, Shreck, and Dimmick (2) indicate that increases in maximum lift coefficients over 100% can be produced by quite small nondimensional pitch rates.

Specifically, Walker, Helin and Chou (1) show that for nondimensional pitch rates, α^+ , ($\alpha^+ = \dot{\alpha}c/U_\infty$ where $\dot{\alpha}$ is the rotation rate, c is the chord length and U_∞ is the freestream velocity) as low as 0.05 that a maximum lift coefficient of approximately 1.98 can be obtained for a NACA 0015 airfoil. This value represents an increase of approximately 125% over the static airfoil situation. Jumper, Shreck and Dimmick (2) also find that large percentage increases in lift coefficient persist to even lower α^+ values. For example at their lowest α^+ value of 0.016 a 50% increase in maximum lift coefficient is observed.

A typical example from Albertson et al (3) and Troutt (4) demonstrating the large changes from static conditions that a relatively low pitch rate of $\alpha^+ = 0.2$ can produce on the lift coefficient curves as a function of α are shown in figure 1. Labels on the curves designate phenomenological events which occur associated with the development of the dynamic stall vortex on the airfoil surface. The association of identifiable dynamic vortex stall events with specific angles of attack has important implications concerning the interpretation of the dynamic stall process. A discussion of the important results from this study can be found in Albertson et al. (3), and Troutt (4).

One of the major differences between the static and the pitching airfoil results apparent

in figure 1 is the continuation of increase in the pitching airfoil curve to angles of attack far above the static stall angle with correspondingly high associated lift coefficients. The example illustrated in figure 1 shows that the leveling of the lift curve is delayed by approximately 20° in angle of attack over the static stall case, an increase of approximately 150% in stall angle. Flow visualization studies show that the extension of the lift curve for the dynamic situation occurs prior to the formation of the dynamic stall vortex itself. This finding indicates that the effects of the pitching motion should be visually apparent in the development of the thin separation region on the top surface of the airfoil at angles of attack below the onset of the dynamic stall vortex.

At these low values of α^+ the rotation of the airfoil can be viewed as no more than a perturbation to the static flow situation. Computations by Albertson et al. (3) have shown that the unsteady motion of the airfoil for an $\alpha^+ = 0.05$ should produce local vorticity flux levels typically less than 10% of a local vorticity flux levels produced by the pressure gradients associated with the flow over the airfoil. The surprisingly large influence of the pitching motion of the airfoil must thus result from a strong nonlinear amplification of the airfoil motion within the flow which is probably most appreciably expressed through changes in the flow very near the surface of the airfoil.

These strong nonlinear effects associated with applied perturbations to separated flows have been observed previously by Bhattacharjee, Scheelke and Troutt (5) for an acoustically perturbed downstream facing step flow and by Ahuja (6) for an acoustically perturbed separated flow on a static airfoil at moderate to high attack angles. Although the exact mechanisms by which the acoustic perturbation and the airfoil pitching motion interact with the flow may be somewhat different, all of these results show the considerable sensitivity

of separated flows to unsteady perturbations of the boundary conditions. This is in contrast to the well known relative insensitivity of separated flows to significant static changes in boundary conditions. For example substantial changes in airfoil surface curvature seem to have little effect on the overall character of the separation regions observed at poststall attack angles (7).

Based on the previous considerations there is substantial need for the development of improved understanding concerning the influence of airfoil pitching motions at angles of attack prior to and during the initiation of the dynamic stall vortex. The primary focus of this investigation will be to examine the differences in the near surface separation region caused by unsteady airfoil motion at these low to moderate attack angles. The investigation will employ the flow visualization and point surface pressure measurement techniques employed in the previous study (3) which concentrated on the analysis of the growth of the dynamic stall vortex after its inception. The investigation has considerable potential for the development of new important insights since it focusses on the extremely important enhanced lift region associated with the pre- and incipient dynamic stall conditions.

Subject of Investigation and Major Objective

For a static airfoil the development of the separated flow over the top surface apparently starts in the adverse pressure region near the airfoil trailing edge at quite low attack angles and spreads upstream with increasing pitch angle resulting in a large catastrophic stall at an angle of attack near 12° . The exact stall angle depends somewhat on the specific airfoil geometry. The initial separated flow region near the trailing edge is relatively thin and represents only a slight disturbance to the general airfoil flow pattern. The catastrophic

stall that inevitably occurs at the higher pitch angles in the static situation involves a region which covers the entire upper airfoil surface with a maximum thickness on the order of the airfoil chord length. This sequence of events seems to be followed similarly for a dynamically pitching airfoil with the major exceptions that the growth of the initial thin separation region is retarded as a function of attack angle and that one or more compact dynamic stall regions are generated prior to the large reduction in lift associated with the departure of the dynamic vortex from the airfoil surface. A considerable amount of previous research has concentrated on understanding the development and movement of this dynamic vortex region. This subject was in fact the primary focus of our 1986 summer faculty/graduate student research project (4) at the Frank J. Seiler Research Laboratory.

Although a considerable amount of information has now been obtained concerning the later development and departure of the dynamic vortex very little quantitative information regarding the early stages of the thin separation region growth near the airfoil and the initial development of the dynamic vortex region has been obtained. This early angle of attack development region appears to be a crucial area for the practical application of unsteady aerodynamics since it corresponds to the large delay in the leveling and eventual reduction in the lift curve as a function of angle of attack. Moreover, as previously discussed in the Introduction, these large delay effects are producible by relatively small rotation rates.

This research study involves simultaneous point pressure measurements and flow visualization techniques for conducting a detailed examination of the flow events leading up to and including the formation of the dynamic stall vortex on a NACA 0015 airfoil. This investigation covers a range of pitch rates from static conditions to $\alpha^+ = 0.2$ such that direct comparisons between the statically and the dynamically pitched airfoil flows can be

obtained. In addition three pivot positions on the airfoil chord of $0.25c$, $0.50c$, and $0.75c$ were selected to study the effects of pivot location on the flow character prior to and including the formation of the dynamic stall vortex. It was shown in our previous analysis discussed in references (3) and (4) that the location of the pivot position should have an influence on the vorticity generation distribution by the unsteady motion of the airfoil. This analysis follows a development by Morton (8) concerning the generation of vorticity by surface pressure gradients and unsteady surface motions. Morton's boundary condition on the vorticity generation can be given as

$$\frac{d\Gamma}{dt} = \frac{dU_s}{dt} + \frac{1}{\rho} \frac{dp}{ds}$$

where dU_s/dt is the tangential acceleration of the surface in the direction s , dp/ds is the surface pressure gradient in the s direction, and $d\Gamma/dt$ is the local flux of vorticity from the surface. The vorticity flux term, $d\Gamma/dt$, is associated with a vorticity component which is tangential to the surface and normal to the s direction. If the unsteady acceleration term is evaluated for a pitching airfoil the result is

$$\frac{dU_s}{dt} = r_o \left[\dot{\alpha}^2 \cos(\theta + \xi) + \ddot{\alpha} \sin(\theta + \xi) \right]$$

where r_o is the radial distance from the pivot point to specified surface position, $\dot{\alpha}$ is the rotation rate, θ is the angle between the chord axis and r_o , ξ is the angle between the local surface tangent and the chord axis and $\ddot{\alpha}$ is the rotational acceleration.

For constant pitch rates this relation reduces to

$$\frac{dU_s}{dt} = r_o \dot{\alpha}^2 \cos(\theta + \xi)$$

From this relation it is easy to show that for constant pitch rates competition between the surface acceleration term and the pressure gradient term can be expressed as a ratio of

$\dot{\alpha}^2 c^2$ to U_∞^2 if density is assumed constant. This nondimensional parameter $\dot{\alpha}^2 c^2 / U_\infty^2$ or $\dot{\alpha} c / U_\infty = \alpha^+$ has previously been noted by Helin and Walker (9) as a controlling parameter in their experiments on pitching airfoils. If this analysis is correct, then changes in the pivot location should also produce significant modifications in the prestall development events for fixed pitching rates.

The primary objective of the proposed experiments is thus to explicitly identify the changes in the flow and surface pressure fields on the airfoil surface that are involved in the extension of the lift curve for a dynamically pitched airfoil. Once these changes are identified explanations for their cause using our recently developed vorticity generation analysis may allow us to generalize these results to new designs or techniques for aerodynamic applications.

Experimental Methods

The experiments discussed here were conducted at the US Air Force Academy in the Frank J. Seiler Research Laboratory's 0.91 m x 0.91 m low speed wind tunnel. A NACA 0015 airfoil with a 15 cm chord and a 58 cm span was pitched at a constant rate from 0° to 60° around pivot locations of 25%, 50% and 75% the chord. The airfoil motion was accomplished using a stepper motor assembly controlled by a MassComp 5500 microcomputer system. Instantaneous surface pressure measurements were obtained from eighteen Endevco 8507-2 miniature pressure transducers mounted in close-coupled connection to surface pressure ports. Visualization of the flow was accomplished using a smoke wire located 30 cm upstream of the airfoil leading edge in conjunction with a LOCAM II 16 mm high speed movie camera operating at 200 frames per second. Illumination was provided by three Strobrite stroboscopic lights synchronized with the camera. Pressure measurements were

taken with a tunnel speed of 25 ft/sec, while flow visualization was done with a tunnel speed of 20 ft/sec to allow higher resolution. A range of nondimensional pitch rates, α^+ , from 0 to 0.2 was evaluated. It has been shown previously that α^+ can be treated as a similarity parameter in flows such as the one studied here (Cook (10)), and its importance in previous experiments has been noted (9).

Results

The relationship between the maximum lift coefficients and nondimensional pitch rate can be seen in figure 2. The behavior of the maximum lift coefficients with respect to the α^+ is similar for all three pivot locations. Maximum lift values increase rapidly between $\alpha^+ = 0$ and 0.05, and then level off at higher α^+ . This is similar to results reported by Francis and Keesee (11) concerning airfoils pitched about 0.32c and 0.38c at pivot locations. The maximum lift values for the 50% chord position are lower than the other two cases between $\alpha^+ = 0.075$ and 0.2, with the 75% chord position having the greatest maximum lift overall.

The maximum drag coefficients versus nondimensional pitch rate are shown in figure 3. These curves increase rapidly between $\alpha^+ = 0$ and 0.075 for all three pivot points. A sharp peak occurs at $\alpha^+ = 0.075$ for the 0.25c and 0.75c pivot locations. These two curves then decrease until $\alpha^+ = 0.1$ before increasing again between $\alpha^+ = 0.1$ and 0.2 for the 0.50c pivot point. The curve levels off between $\alpha^+ = 0.075$ and 0.15 and then begins to increase. The 75% chord position also has the greatest maximum drag coefficient overall.

The behavior of the attack angle, corresponding to maximum lift, with respect to nondimensional pitch rate is given in figure 4. The curves are similar for all three pivot locations, with the values at a pivot point of 0.25c leveling off slightly sooner than those at 0.50c and

0.75c. The maximum lift occurs at smaller attack angles for corresponding pitch rates for the 0.5c pivot point case.

The attack angle associated with the maximum drag coefficient is shown as a function of nondimensional pitch rate in figure 5. The curves for pivot points of 0.25c and 0.75c increase rapidly between $\alpha^+ = 0$ and 0.075, take on a negative slope between $\alpha^+ = 0.075$ and $\alpha^+ = 0.1$, and then begin to increase again. Values for the 0.75c pivot location are higher than those at a pivot point of 0.25c. For the 0.50c chord position the maximum drag angle increases between $\alpha^+ = 0$ and 0.075, then levels off for a short period before decreasing to $\alpha^+ = 0.15$. The maximum drag attack angles increase again between $\alpha^+ = 0.15$ and 0.2, but remain lower than the values for the other two pivot locations. The maximum drag angles are also lower for the 0.50c pivot point between $\alpha^+ = 0$ and 0.075.

An additional study was made to determine the effects of pitching motion and pivot location on the airfoil lift to drag ratios. Lift to drag ratios for all three pivot points are shown in figure 6 at nondimensional pitch rates of 0, 0.01, 0.02, and 0.1. Values for the quarter chord pivot location are given in figure 6a. Lift to drag ratios at $\alpha^+ = 0.01$ are greater than those for $\alpha^+ = 0$ between attack angles of 0° and 14° , where 14° corresponds to stall. The values at $\alpha^+ = 0.01$ are greater than those at $\alpha^+ = 0$ between 14° and 18° , after which the two curves become identical. Lift to drag ratios for $\alpha^+ = 0.02$, and 0.1 are virtually identical, with values at $\alpha^+ = 0.1$ being slightly lower between attack angles of 7° and 14° . Lift to drag ratios for the pitching cases after $\alpha = 18^\circ$ asymptote towards the static values.

Lift to drag ratios for the half chord pivot location are shown in figure 6b. Values are higher for $\alpha^+ = 0.01$ than for $\alpha^+ = 0$ until an attack angle of 12° , which is close to static

stall. Lift to drag ratios for $\alpha^+ = 0.01$ are less than those for $\alpha^+ = 0$ between attack angles of 12° and 16° , after which the two curves become identical. The values at $\alpha^+ = 0.02$ are greater than those at $\alpha^+ = 0.01$ between 0° and 15° . Above 15° the curves are virtually identical. Lift to drag ratios for $\alpha^+ = 0.1$ remain higher than at $\alpha^+ = 0.02$ until an attack angle of 30° .

Lift to drag ratios for the 75% chord position are given in figure 6c. Values for $\alpha^+ = 0.01$ are significantly lower than the static case between $\alpha = 0^\circ$ and 15° . Lift to drag values for $\alpha^+ = 0.01$ and $\alpha^+ = 0.02$ are similar for α above 5° . Lift to drag ratios for $\alpha^+ = 0.1$ are consistently lower than those at $\alpha^+ = 0.02$ and 0.01 until 20° . Values at $\alpha^+ = 0.1$ are only slightly higher than $\alpha^+ = 0.01$ and 0.02 for a period of 10° beyond that.

An evaluation was also made to determine the effect of pivot location on lift to drag ratios. Values at $\alpha^+ = 0, 0.01$, and 0.1 are shown in figure 7 for all three pivot points. Figure 7a shows that the lift to drag ratios for an $\alpha^+ = 0$ are virtually identical for all three pivot points. Values for $\alpha^+ = 0.01$ are given in figure 7b. Behavior of the 0.25c and 0.75c curves are similar throughout the pitching motion. The 0.50c pivot location values exhibit a different trend, with lift to drag ratios at 0.50c being higher than the other two cases between attack angles of 0° and 12° and lower between 12° and 18° .

Lift to drag ratios at $\alpha^+ = 0.1$ are shown for all three pivot locations in figure 7c. Values for the half chord position are consistently higher than the other two pivot points prior to an attack angle of 20° . Lift to drag ratios corresponding to the quarter chord pivot are significantly lower than those at the 0.50 pivot point during this period. The values for the 75% chord position are somewhat lower than those for the the 25% pivot location. All curves are equal at attack angles greater than 20° .

Smoke flow visualization was done in addition to pressure measurements to reveal relationships between the pressure field and dynamic stall vortex behavior. The dynamic stall vortex at the attack angle corresponding to maximum lift is shown for the nondimensional pitch rates of 0.01, 0.03, 0.05, 0.1 and 0.2 in figure 8. A dynamic stall vortex is present at the maximum lift attack angle even at the low nondimensional pitch rate of 0.01, shown in figure 8a. A dynamic stall vortex is also present at the maximum lift attack angle for the $\alpha^+ = 0.03$ case, as seen in figure 8b, although in this case it is larger than at $\alpha^+ = 0.01$. This trend continues to $\alpha^+ = 0.05$, shown in figure 7c, where the dynamic stall vortex is still more developed at the attack angle coinciding with maximum lift. The dynamic stall vortex is less developed at the maximum lift attack angle for a nondimensional pitch rate of 0.1 than it was at $\alpha^+ = 0.05$, as can be seen in figure 8d. For the $\alpha^+ = 0.2$ case, given in figure 8e, the dynamic stall vortex is just beginning to form.

The dynamic stall vortex at the attack angle corresponding to maximum drag is shown for various nondimensional pitch rates in figure 9. The vortex appears less defined at the maximum drag angle for $\alpha^+ = 0.01$, shown in figure 9a. In addition, the vortex is not clearly attached to the airfoil surface. The dynamic stall vortex has been disrupted at $\alpha^+ = 0.03$, as seen in figure 9b, and there is evidence of a counter-rotating vortex forming on the trailing edge. The dynamic stall vortex is larger at $\alpha^+ = 0.05$ than at $\alpha^+ = 0.03$. The vortex at the maximum drag angle for $\alpha^+ = 0.1$, is given in figure 9d. This vortex is noticeably smaller and more tightly defined. The dynamic stall vortex is even smaller at $\alpha^+ = 0.2$ than at $\alpha^+ = 0.1$ as shown in figure 9e.

Conclusions

The major conclusions of this study are outlined as follows:

1. The maximum lift coefficient increases rapidly with nondimensional pitch rate prior to $\alpha^+ = 0.1$ for all three pivot locations studied. The effects on lift of the airfoil motion approach a constant at nondimensional pitch rates above 0.1.
2. The evolution and detachment of more than one dynamic stall vortex on the upper airfoil surface over the $0^\circ - 60^\circ$ pitching range creates a local maximum in the drag at a nondimensional pitch rate of $\alpha^+ = 0.075$.
3. For low nondimensional pitch rates, lift to drag ratios for the pivot location of $0.50c$ are lower than those for the pivot locations of $0.25c$ and $0.75c$.
4. The lift to drag ratio curves are only weakly dependent on pitch rate between $\alpha^+ = 0.02 - 0.1$ for the $0.25c$ pivot location. This weak dependence is not apparent at the two other pivot locations studied.
5. Lift to drag ratios take on maximum values between $\alpha^+ = 0.02 - 0.1$ for the $0.25c$ pivot location.
6. Flow visualization shows that between nondimensional pitch rates of 0.02 and 0.1, the dynamic stall vortex at the maximum lift attack angle increases in size with increasing pitch rates for the quarter chord pivot location.

Acknowledgements

The authors gratefully acknowledge the support and guidance of Major J.M. Walker and Dr. M.C. Robinson. They also thank Mr. C.R. Kedzie and Captain E. Stephen for their help with the experimental preparations, and the support staff of the F.J. Seiler Research Laboratory for general assistance with the experimental facilities. The financial support of the Air Force Office of Scientific Research and Universal Energy Systems is also greatly appreciated.

References

1. Walker, J., Helin, H. and Chou, D., "Unsteady Surface Pressure Measurements on a Pitching Airfoil," AIAA Paper 85-0532, AIAA Shear Flow Control Conference, Boulder, CO, March 1985.
2. Jumper, E.J., Shreck, S.J. and Dimmick, R.L., "Lift-Curve Characteristics for an Airfoil Pitching at Constant Rate," AIAA Paper 86-0117, The Aerospace Sciences Conference, Reno, NV, January 1986.
3. Albertson, J.A., Troutt, T.R., Siuru, W.D., and Walker, J.M. "Dynamic Stall Vortex Development and the Surface Pressure Field of a Pitching Airfoil," AIAA Paper 87-1333, 1987.
4. Troutt, T.R., "An Investigation of Unsteady Vorticity Production by a Pitching Airfoil," USAF-UES Summer Faculty Research Program/Graduate Student Summer Support Program Report, 1986.
5. Bhattacharjee, S., Scheelke, B. and Troutt, T.R., "Modifications of Vortex Interactions in a Reattaching Separated Flow," *AIAA Journal*, Vol. 24, No. 4, 1986, pp. 623-692.
6. Ahuja, K.K., "Acoustic Control of Separation," *Bull. APS*, Vol. 28, 1983, p. 1388.
7. McCroskey, W.J., "Unsteady Airfoils," *Ann. Rev. Fluid Mech.*, 14, 1982, pp. 285-311.
8. Morton, B.R., "The Generation and Decay of Vorticity," *Geophys. Astrophys. Fluid Dynamics*, 28, 1984, 277-308.
9. Helin, H.E. and Walker, J.M., "Interrelated Effects of Pitch Rate and Pivot Point on Airfoil Dynamics Stall," AIAA Paper 85-0130, 1985.
10. Cook, R.J., "Similarity Conditions for Flows About Pitching Airfoils," FJSRL-TM-97-003, June 1987.
11. Francis, M.S. and Keesee, J.E., "Airfoil Dynamic Stall Performance with Large-Amplitude Motions," *AIAA J.*, Vol. 23, No. 11, November 1985, pp. 1653-1659.

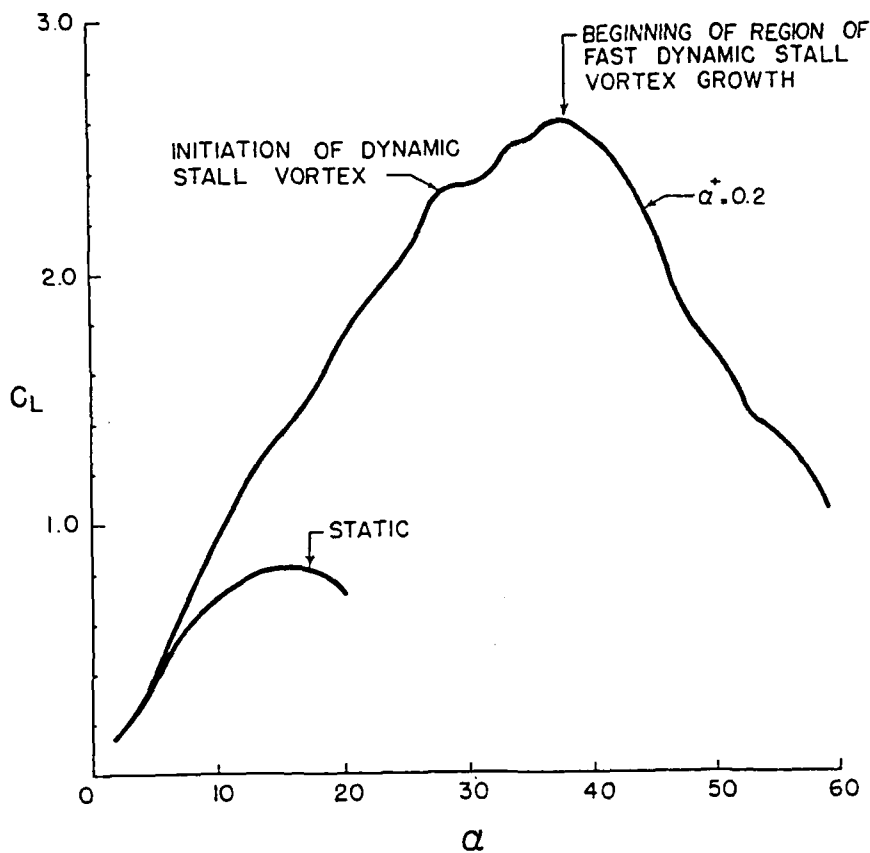


Figure 1. Lift coefficient as a function of angle of attack. Pivot location = $0.25c$.

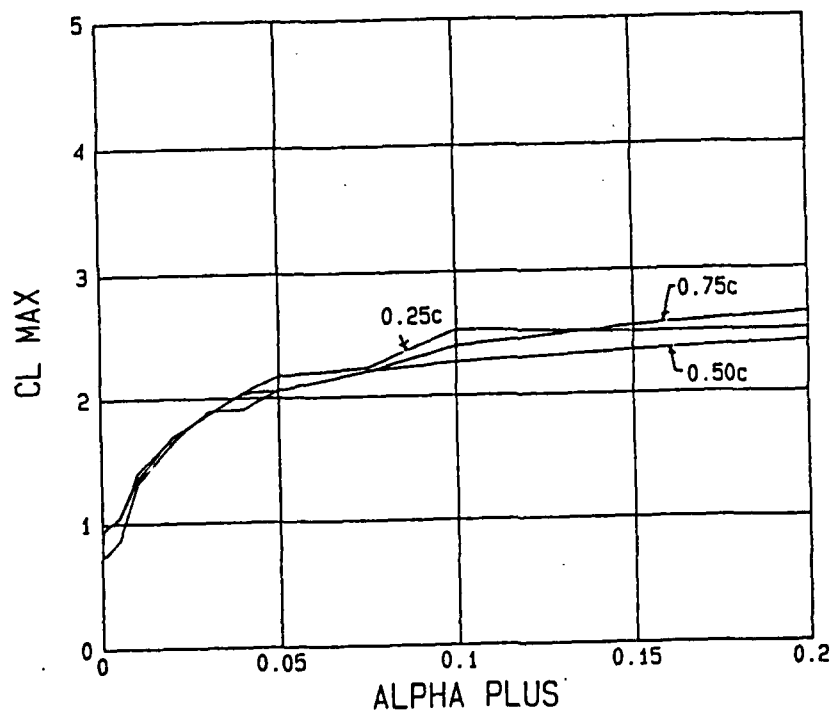


Figure 2. Maximum lift coefficient as a function of α^+ .

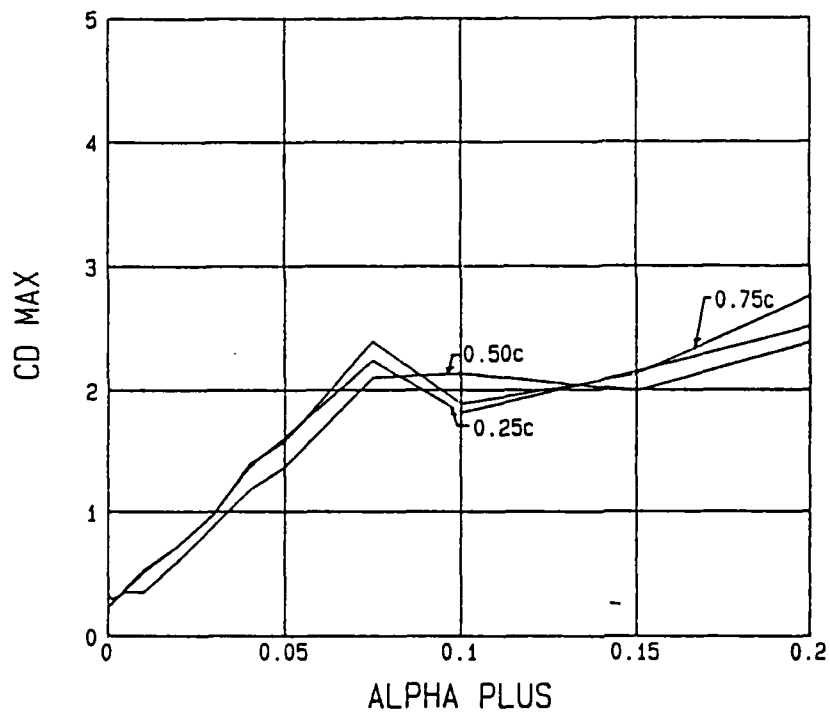


Figure 3. Maximum drag coefficients as a function of α^+ .

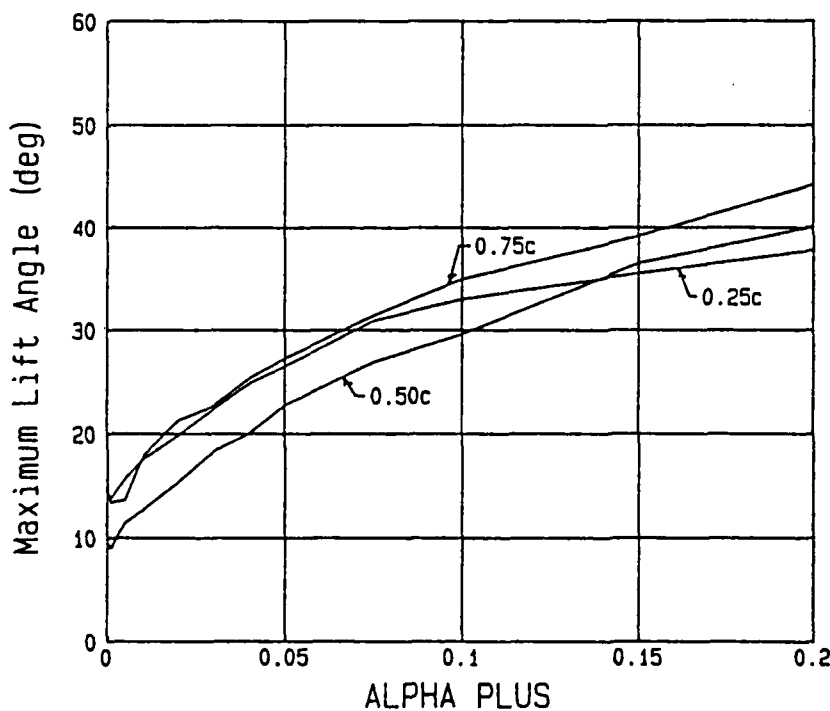


Figure 4. Attack angle at maximum lift coefficient as a function of α^+ .

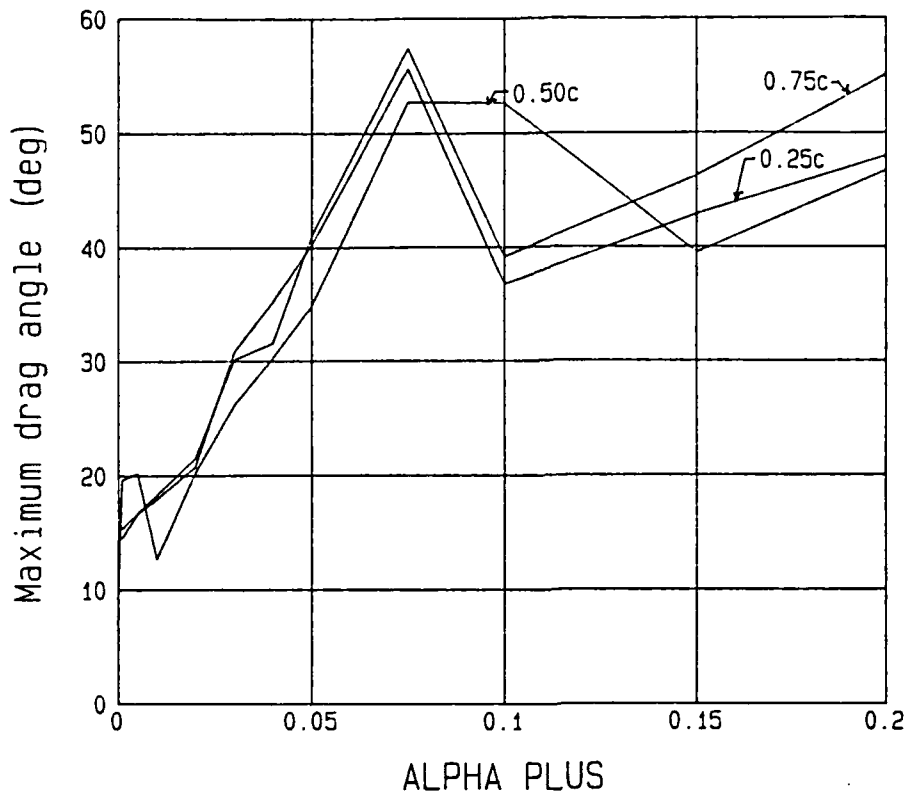


Figure 5. Attack angle at maximum drag coefficient as a function of α^+ .

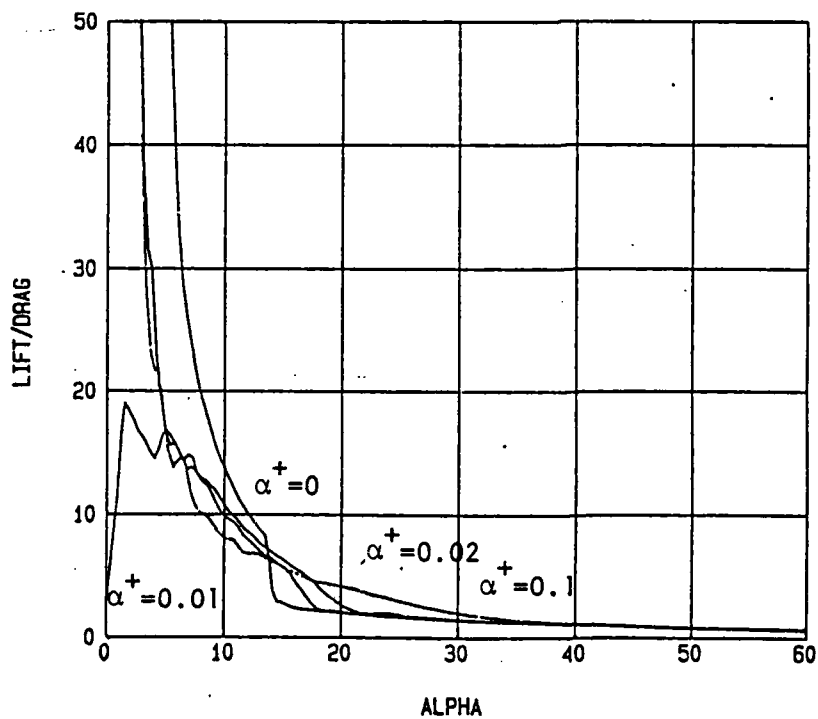


Figure 6a. Lift to drag ratios as a function of attack angle. Pivot location = $0.25c$.

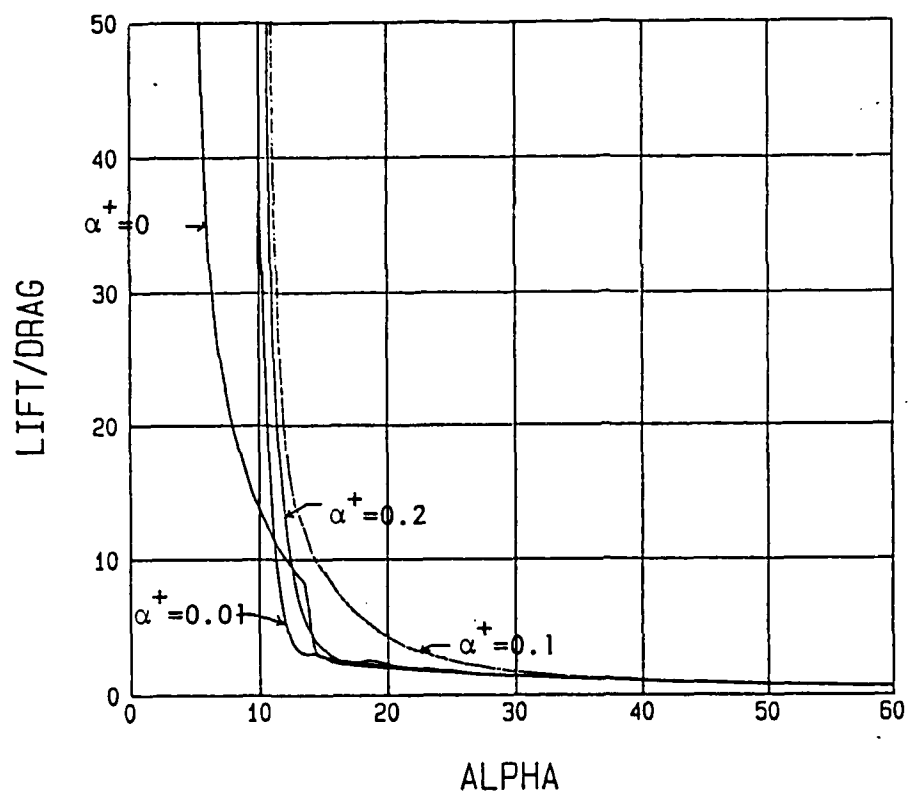


Figure 6b. Lift to drag ratios as a function of attack angle. Pivot location = 0.50c.

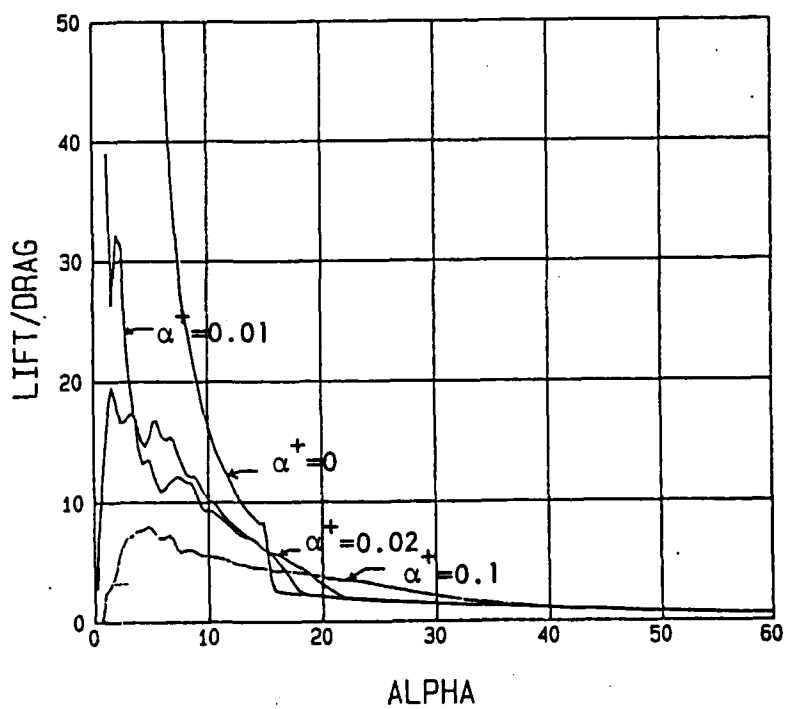


Figure 6c. Lift to drag ratios as a function of attack angle. Pivot location = 0.75c.

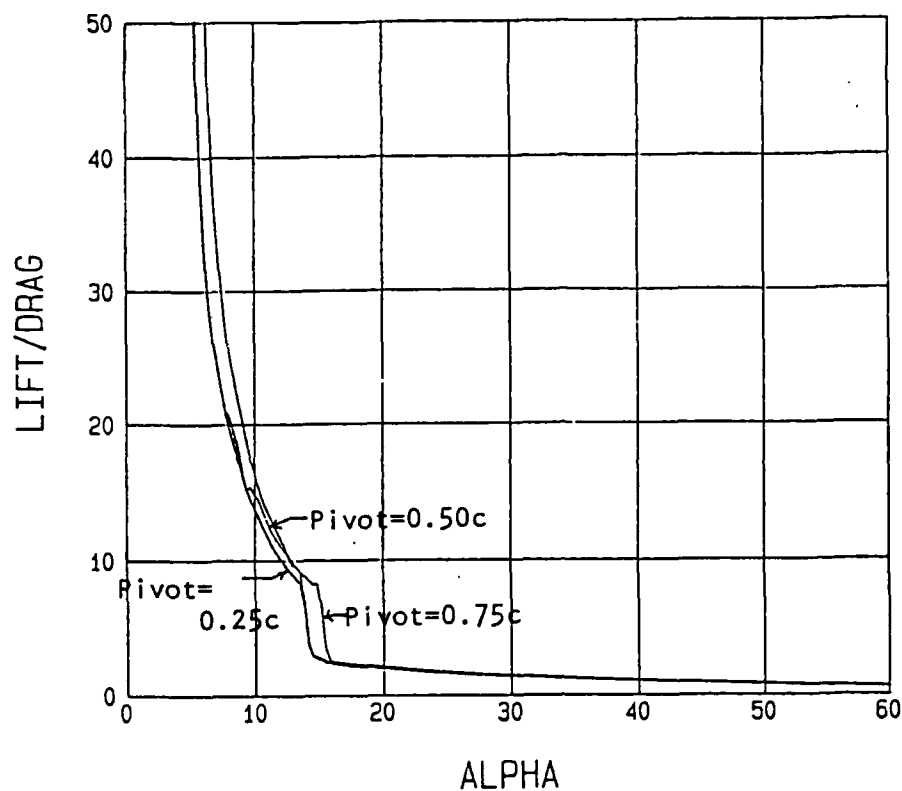


Figure 7a. Lift to drag ratios as a function of attack angle. $\alpha^+ = 0$.

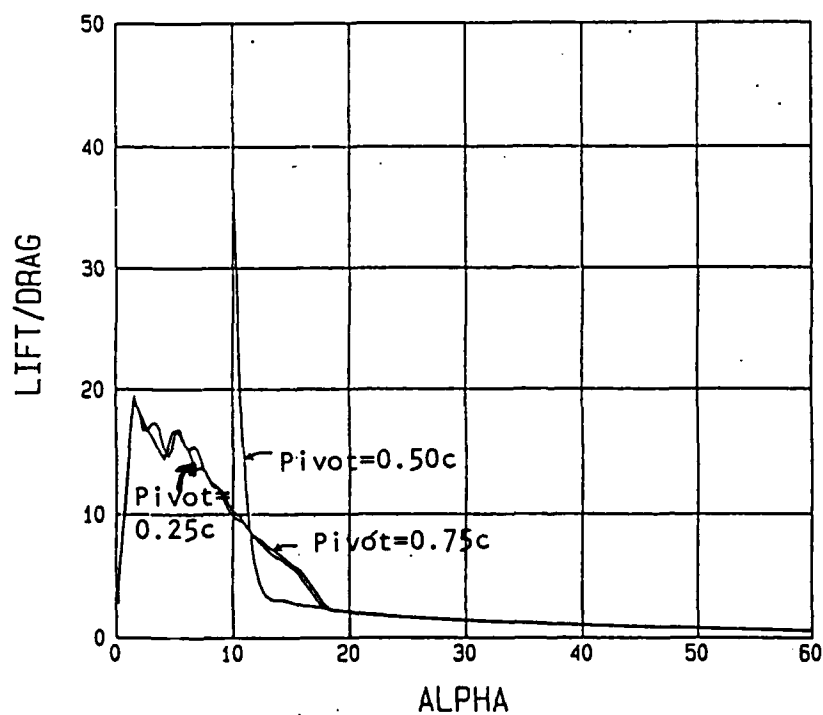


Figure 7b. Lift to drag ratios as a function of attack angle. $\alpha^+ = 0.01$

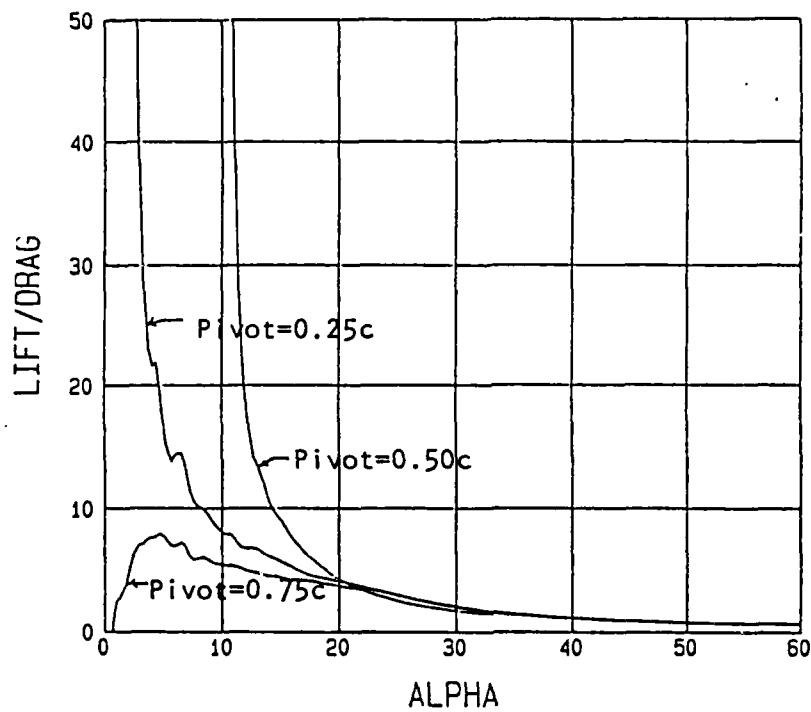
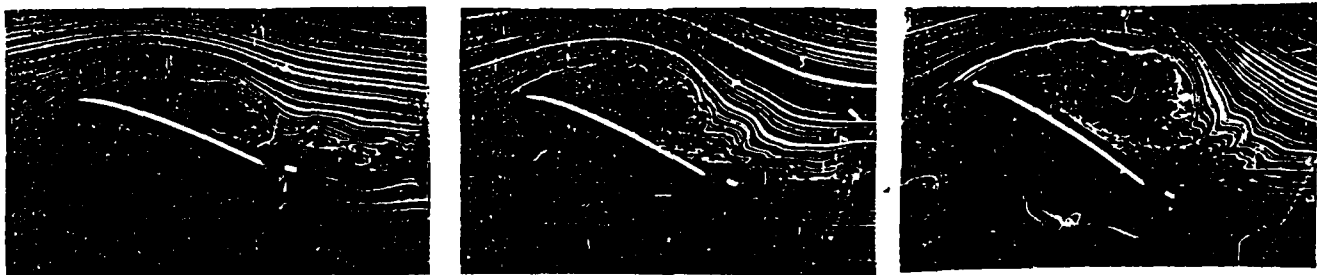


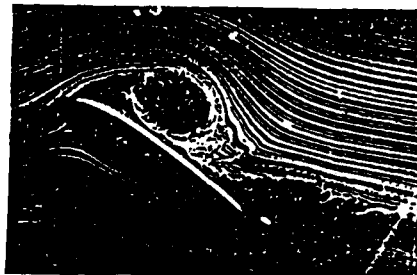
Figure 7c. Lift to drag ratios as a function of attack angle. $\alpha^+ = 0.1$



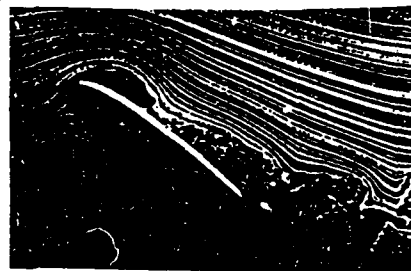
a. $\alpha^+ = 0.01$

b. $\alpha^+ = 0.03$

c. $\alpha^+ = 0.05$



d. $\alpha^+ = 0.1$



e. $\alpha^+ = 0.2$

Figure 8. Dynamic stall vortex at the attack angle corresponding to maximum lift. Pivot location = 0.25c.

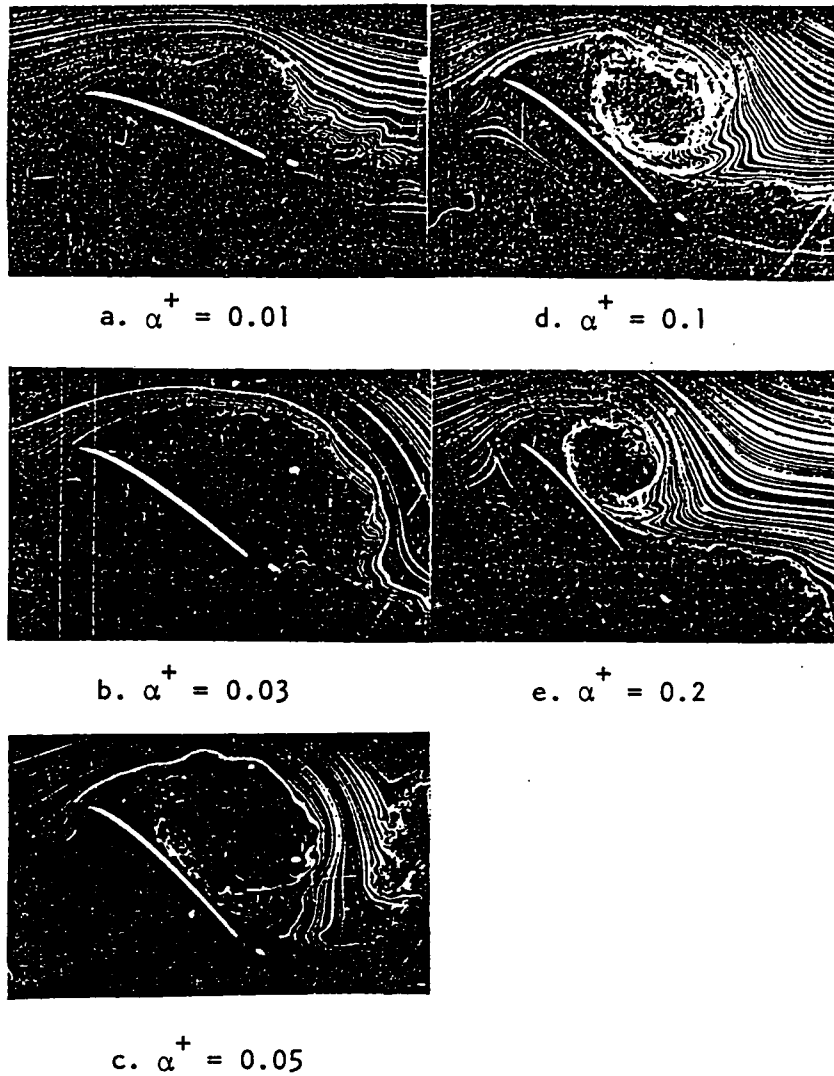


Figure 9. Dynamic stall vortex at the attack angle corresponding to maximum drag. Pivot location = $0.25c$.

BIODEGRADATION OF AQUEOUS FILM FORMING FOAM COMPONENTS
IN LABORATORY SCALE MICROCOSMS

A FINAL REPORT

SUBMITTED TO

AFOSR Mini Grant Program
Universal Energy Systems, Inc.
4401 Dayton Xenia Road
Dayton, Ohio 45432

Investigators:

Roy M. Ventullo, Ph.D.
Michael G. Stockelman
Department of Biology
University of Dayton
Dayton, Ohio 45469-0001

ABSTRACT

Biodegradation of Aqueous Film Forming Foam Component in Laboratory Scale Microcosms

Roy M. Ventullo
Michael G. Stockelman
Department of Biology
University of Dayton
Dayton, Ohio 45469

Beginning Date: December 30, 1986
Ending Date: December 30, 1987

- Objectives:** The primary objective of this project was to measure the biodegradation of the surfactant and non-surfactant organic components of the 3M Company aqueous film forming foam (AFFF) in laboratory microcosms. Specific goals were 1) to measure the disappearance of the components of AFFF by specific methods including MBAS, CTAS, and gas chromatography. 2) to improve available methods for isolating and quantifying the various components of AFFF.
- Methods:** Batch culture microcosms inoculated with activated sludge were used as a test system. Duplicate microcosms with variable amounts of nitrogen and phosphorus, and 1% (v/v) 3M AFFF were established and assayed regularly for MEAS and CTAS (1,16), general methods for the analysis of anionic and nonionic surfactants, respectively. A major volatile organic constituent of AFFF (diethylene glycol monobutyl ether) was measured by gas chromatography. Further, the application of solid phase extraction and liquid chromatography in separating and quantifying the surfactants was investigated.
- Significance:** Current usage of AFFF as a fire suppressant and/or extinguishing agent in Air Force firefighting operations has created a significant disposal problem. Onsite biological treatment of AFFF wastewaters may be a cost effective disposal option (10). However, there is a dearth of information on the biodegradation of AFFF components which is due to both lack of study and lack of analytical tools. In this project we determined the biodegradability of AFFF components using mixed microbial communities from activated sewage sludge, and tested specific methods of analysis for the individual AFFF components.

INTRODUCTION

Aqueous film forming foam (AFFF) is a special purpose material used in Air Force crash/rescue operations and fire fighting training. The products currently used by the Air Force were developed and improved by the 3M Company and Ansul Corporation. AFFF's are proprietary products containing as major components: 5% hydrocarbon surfactant (HCS), 5% flourosurfactant (FS), 15% diethylene glycol monobutyl ether (DEGMBE), and 75% water. The product is diluted to a final concentration of 6% (v/v) for use in the field. This AFFF/water mixture foams and spreads across the surface of a hydrocarbon fuel and provides an effective vapor sealing blanket. The present mixtures are far superior to the protein foams used in the past (3).

The Defense Department purchases over 1 million gallons of AFFF per year. Approximately one-half is used at fire fighting schools, fire/rescue stations, and hangar deluge systems at over 100 Air Force facilities. It has been estimated that the AFFF concentrate used by the Navy is diluted 125 fold during use (3). Using this figure, the final volume of liquid waste produced Air Force wide may be as high as 80 million gallons per year. The widespread use of this material at so many locations, usually at remote sites on Air Force bases, has produced a significant disposal problem.

AFFF laden wastewaters have been shown to be detrimental to biological treatment operations (6,7,13,14,15,21). At low concentrations (150 mg/L) both Ansul and FC-206 (3M) were amenable to biological treatment as measured by BOD/COD (7). The Air Force has examined the biodegradation of 5 AFFF's and found significant reductions in BOD and COD (13,14,15,21). Process failures were evident however, mainly due to increased organic load in the systems, foaming problems, and toxicity of the components to the active biomass. A comprehensive study of toxicity of AFFF was conducted in a long-term flowthrough bioassay system (23). It was concluded that AFFF was toxic to both invertebrate and algal populations, and appears to inhibit fish reproduction. It was recommended that the toxicant be used for training purposes only when proper containment and/or treatment was possible.

It should be noted that both 3M and Ansul have changed the formulation of their respective AFFF's to decrease the toxicity and BOD/COD since some of these tests were done (2,3). Recently published results indicate that the material is still toxic at relatively low concentrations (96 hour LC50 for minnow, 1,080 ppm; 96 hour LC50 for Daphnia, 1922 ppm; Microtox 30 min EC50 of 383 ppm)(2,3,6).

Previously, environmental considerations when using potentially toxic materials was subordinate to the importance the material had to day-to-day Air Force operations. However, with the passage of local, state, and federal legislation, materials and systems used in carrying out Air Force missions must be environmentally evaluated. Passage of the Clean Water Act requires that a permit be obtained to discharge pollutants directly into U.S. waters. The National Pollutant Discharge Elimination System (NPDES) permits that are required impose strict

standards on the effluents released. They may also require other compliance duties such as monitoring and frequent reports on operations.

Indirect discharges to off-base treatment plants are controlled by the local facilities themselves by issuance of permits. These permits strictly define the quality of waters received by the plant. The quality of the influent waters is in part controlled by the water quality restrictions placed on the local plant effluents.

For remote bases or those located at sites where the treatment plant cannot accept all the AFFF wastewaters, containment and off-site disposal are suggested. In these cases the materials must be containerized and subsequently hauled off, metered into a treatment plant, or treated on site. The Resource Conservation and Recovery Act requires evaluation of storage sites where significant quantities of potentially hazardous chemicals might seep into the ground. In order to avoid continuous monitoring of soils and groundwater, confirmation of reduction in toxicity and/or removal of the material is required. It is expected that future legislation and tightening of present standards will require (and already has (6,12)) onsite treatment of AFFF containing wastewaters.

Several physical-chemical treatments have been assessed for their ability to remove AFFF from fire training wastewaters (5,6,11,18,21). Oil/water separation systems have been found effective at removing unburned oil for reuse but not for AFFF removal (5). Chemical coagulation is also effective in clarifying the wastewater but again did not remove AFFF (18). Carbon adsorption of the wastewater organic constituents has been extensively studied (5,11,18). Engineering Sciences, Inc. (18) and the Air Force (11) concluded that carbon could

remove over 85% of AFFF from distilled water. However, AFFF in wastewater was poorly sorbed and significantly greater amounts of carbon was required for effective removal. An added complication was encountered while testing the feasibility of disposing of the spent carbon (18). The material appears to leach continuously from the carbon which requires expensive chemical fixation or disposal in a sealed container. Since a greater amount of carbon is required to substantially remove AFFF from wastewater, and the disposal of the carbon is difficult, this method of cleanup was deemed not to be cost effective.

In a more recent study (21) the use of ultrafiltration and reverse osmosis was shown to be a superior alternative to all other treatments (6). This expensive system requiring trained personnel and constant attention, will be a cost effective AFFF removal and recovery method at some of the larger training facilities but would not be so (at a cost of \$260,000) at the many smaller facilities which exist.

A simple, low maintenance system for treating fire training waste water would clearly be more desirable. Biological treatment in lagoons could be one such system. Most organic waste is treatable in standing bodies of water provided a microbial community is given time and stable conditions to adapt. This treatment can be improved by manipulations such as aeration, circulation within the pond, addition of nutrients, and the depth of the pond (16).

Potential biological treatment methods for AFFF wastewater have suggested and have been reviewed by Chan (6). Several of the studies indicated that biodegradation of AFFF is possible (11,13,14,15,21, 22,23). However, all of these studies used the indirect measurements of

BOD and COD to assess biodegradability. No attempt was made to determine which components were degraded. Since over 80% of the AFFF organic matter is the biodegradable glycol and urea one would expect a high BOD value, indicative of biodegradability. One could not be sure the surfactant components which may be responsible for the toxicity are being degraded. Only one attempt to separate and quantitate the components of AFFF has been made (3). It is not clear however that the peaks detected by UV absorption from HPLC separations and used to indicate biodegradation were, in fact, surfactant components.

Accurate determination of the success of biological treatment in degrading AFFF waste would require that each specific component be individually measured over time. In this study we measured the biodegradation of the specific components of AFFF using lab scale microcosms. Microbial communities from activated sewage sludge were used as inocula, since this is a ready source of bacteria acclimated to a wide range of organic materials including the surfactants and jet fuel hydrocarbons in AFFF wastewater. The microcosms contain varying amounts of nitrogen and phosphorus, and AFFF at levels normally expected in the containment ponds. Specific methods for the analysis of the components of AFFF were tested and used. Data obtained in this study will be useful for designing simple onsite biological treatment pits as well as determining the efficacy of other treatment methods since specific components of AFFF will be quantitated.

OBJECTIVES

The primary objective of this project has been to measure the biodegradation of the surfactant and non-surfactant organic components of the 3M Company aqueous film forming foam (AFFF) in laboratory microcosms. The data generated can be used by the USAF to estimate the effectiveness of using onsite biological treatment to clean up AFFF wastewaters.

The objective was accomplished by fulfilling the following tasks:

a. Construction of laboratory scale microcosm test systems containing microbial communities found in activated sewage sludge. The effect of nutrient manipulation (phosphorus and nitrogen) on biodegradation was studied.

b. Measurement of biodegradation (disappearance of parent compound) of the components of AFFF in the microcosms by gas chromatography and spectrophotometry (methylene blue active substances and cobalt thiocyanate active substances assays).

c. Investigation of the application of HPLC with UV and fluorescence detection, ^{19}F NMR, and solid phase extraction in detection and quantitation of the surfactant components of AFFF.

MATERIALS AND METHODS

Microcosms. Batch microcosms in 20-liter glass carboys were prepared to test the effect of varying concentrations of nitrogen and phosphorus on microbial metabolism of AFFF components. All flasks contained 8 liters deionized water, 0.9 liters activated sewage sludge, and 90 ml FC 206 AFFF concentrate (3M). The microcosms were incubated at room temperature in the dark, and were stirred weekly. The starting conditions of the microcosms are shown in Table 1.

Table 1

Flask #	Condition	K ₂ HPO ₄ (g/9L)	NH ₄ NO ₃ (g/9L)
1	sterile control ^a	----	----
2	unamended	----	----
3	unamended	----	----
4	low nutrient ^b	0.505	2.572
5	low nutrient	0.505	2.572
6	high nutrient ^b	5.05	25.72
7	high nutrient	5.05	25.72

^a Killed by autoclaving sludge inoculum and adding 0.1 g HgCl₂/L.

^b A nutrient stock of 28.06 g K₂HPO₄ and 142.89 g NH₄NO₃ in 500 ml H₂O was prepared. Low nutrient = 1 ml nutrient stock/L final vol. = 10 ppm P and 100 ppm N. High nutrient = 10 ml nutrient stock/L final vol. = 100 ppm P and 1000 ppm N.

Sampling. Samples (20 ml) for chemical analysis were collected weekly from the microcosms. The samples were centrifuged at 15,000 x g for 20 min to remove solids, preserved with 1% formalin, and stored at -20°C until processing.

Analysis of AFFF components. The diethylene glycol monobutyl ether (DEGMBE) solvent in the 3M AFFF was assayed by the method suggested by 3M (22). Gas chromatographic analyses were carried out on a Varian 3700 equipped with a FID. A 2 m Carbowax 20-M terphthalic column (Alltech) operated at 180 C was used for separation. A calibration curve of DEGMBE (Aldrich Chemical Co.) was used for quantitation (Fig. 1a).

The fluorosurfactants and the hydrocarbon anionic surfactant were assayed together by the methylene blue active substances assay (MBAS) (1,17). MBAS involves ion pairing between anionic surfactants and methylene blue dye to make a lipid-soluble complex that is extracted into chloroform and measured spectrophotometrically. The reagent volumes used in the MBAS assay were cut in half to increase sensitivity. A standard curve (Fig. 2a) was prepared using a standard LAS solution (Procter and Gamble, Cincinnati, OH). For the initial concentration of AFFF in the microcosms (1%), a one ml sample was sufficient to detect the surfactants.

The nonionic surfactant component of AFFF was assayed by the cobalt thiocyanate active substances method (CTAS)(1,19). In the CTAS method, nonionic surfactant forms a transition-metal complex with cobalt, extracted into methylene chloride, and measured

spectrophotometrically. Interference from anionic surfactants is minimal, due to their poor solubility in methylene chloride. The CTAS standard curve (Fig. 3a) was made using standard nonionic surfactant (US EPA Cincinnati, OH).

Method development. The potential use of sorbent extraction columns (solid phase extraction) in separating the components of AFFF was assessed. Strong anion exchange (SAX) 100 mg columns (Analytichem International, Harbor City, CA) were conditioned with 2 ml CH_3OH and then with 1 ml water. Varying amounts of standard anionic surfactant (LAS) or AFFF were applied to the columns, washed with water (1-5 ml), and eluted with 2-5 ml 1:1 0.1 N $\text{HCl}:\text{CH}_3\text{OH}$. The retention of surfactants was checked by MBAS or CTAS measurement of the individual sample, wash, and elution fractions.

High performance liquid chromatography (HPLC) was employed in detecting and quantifying anionic surfactants (e.g. LAS) and nonionic surfactants (e.g. NPE) using separation by alkyl chain lengths (homologs), or alkyl substitution position (isomers). A Hypersil SAS (C1) column, with 5 μm particles (Alltech/Applied Science) allowed resolution to homologs. The solvent system was 0.15 N NaClO_4 (Fisher Scientific) in water and tetrahydrofuran (Burdick & Jackson). A typical solvent ratio was 0.15 N NaClO_4 in 65:35 $\text{H}_2\text{O}:\text{tetrahydrofuran}$. Greater separation, by isomers was achieved on a $\mu\text{Bondpak C18}$ column (Waters Associates). The solvent system was 0.15 N NaClO_4 in water and acetonitrile (Burdick & Jackson). A typical solvent ratio was 0.15 N NaClO_4 in 65:35 $\text{H}_2\text{O}:\text{acetonitrile}$.

¹⁹F Nuclear magnetic resonance of AFFF fluorosurfactant component. Solid samples of FM-3820 (3M) and Ansulite fluorosurfactant A (Ansul Corp.) were examined by ¹⁹F NMR spectroscopy using a Varian Model EM 360L NMR spectrometer. The samples were dissolved in a mixture of methanol and ethylene glycol with CFC1₃ added as an internal reference. Standard NMR tubes of 5 mm O.D. were used. Instrument conditions are listed below.

Spectrum amplitude	8000
Filter	0.05 sec
RF Power	0.2 mG
Sweep time	10 min
Sweep width	100 ppm
End of sweep	+ 100 ppm

RESULTS

Degradation of AFFF components. The microcosms were incubated for seven weeks. By the end of this time the various components had shown different degrees of removal. As shown in Figure 1, diethylene glycol monobutyl ether (DEGMBE) was undetectable (<75 ug/ml) within a week in the high nutrient microcosms, and after two weeks was unmeasurable even in the unamended ones. In contrast, the DEGMBE level in the killed control was essentially unchanged after that time.

The MBAS results (Figure 2) show an initial decrease in anionic content, which quickly levelled off. Nutrient levels had no apparent effect on either the rate of decrease or the final amounts remaining.

Similarly, nonionic surfactant showed an initial dropoff and a levelling (Figure 3). Final concentrations appeared somewhat lower under high nutrient conditions.

Method development. Ideally, anion exchange of a mixture of anionic and nonionic surfactants as in AFFF on sorbent extraction columns would allow nonionic surfactants to pass through the column in either the sample or the wash that follows, while the charged anionic surfactants is retained by ionic interaction until removed by the elution solvent. We achieved good retention of anionic surfactant on SAX columns through sample application and washing, and were able to recover it during elution (Table 2). However, nonionic surfactant also was retained on the column, and was recovered as much or more during elution as in the unretained and wash fractions.

Table 2

vol. 1% AFFF (ml)	initial CTAS (mg)	CTAS recovery from SAX cartridge (mg(%))			
		unretained	wash ^a	elution ^b	total
5	0.64	0.29 (45)	0.07 (11)	0.20 (31)	0.56 (88)
10	1.28	0.60 (47)	0.06 (5)	0.38 (30)	1.04 (81)
15	1.92	0.69 (36)	0.22 (11)	0.69 (36)	1.60 (83)
20	2.56	0.55 (21)	0.56 (22)	1.07 (42)	2.18 (85)

1 ml 1% AFFF	MEAS recovery:	0%	3.5%	81.7%	85.2%

^a Wash was 15 ml distilled deionized H₂O.

^b Eluting solvent was 2.5 ml 1:1 CH₃OH: 0.1 N HCl.

The nature of surfactants, their property of concentrating at surfaces and interfaces, may account for this. The nonionic surfactants were retained not by the positive charge of the column but

simply by the large surface area of the packing material. Future work should be toward finding a more polar wash solvent that will remove nonionic surfactant without disturbing the ionic interactions retaining the anionic surfactant.

Liquid chromatography of linear alkylbenzenesulfonate (LAS, an anionic surfactant) allowed resolution to either homologs (alkyl chain length) or isomers (site of alkyl chain attachment to the aromatic ring) depending on the hydrophobicity of the solid phase. Separation of LAS to homologs on the Hypersil SAS (C1) column is shown in Figure 4. LAS could be separated to isomers (Figure 5) on the uBondpak C18 column.

Our chromatographic separation of nonylphenol polyethoxylate (NPE, a nonionic surfactant) on the C1 column gave poor resolution but it was clear that refinement of the solvent system should allow separation of isomers (Figure 6).

NMR spectra of the fluorosurfactant are shown in Figure 7. Integration individual resonances and their chemical shifts relative to CFCl_3 are listed below.

Chemical shift, ppm	Relative intensity
82	3
115	2
123,124	8
127	2

CF_3	----	CF_2	----	$(\text{CF}_2)_4$	----	CF_2	----	R
82ppm		127ppm		123,124ppm		115ppm		

The spectra are interpreted according to standard references (9a, 16a). The fluorinated portion of the molecule appears to be a 7 carbon aliphatic chain fully substituted with fluorine atoms. The chemical shifts and integrated intensities associated with the chain are consistent with perfluoroalkane spectra.

DISCUSSION

Diethylene glycol monobutyl ether is a low molecular weight (f.w. 162.2) substituted glycol. Its precursors, butanol and ethylene glycol, are both common labile organic compounds. There is little literature regarding its fate since it has never been a cause for concern. Zahn (24) found 79-97% loss of a similar compound, triethylene glycol monohexyl ether, in a batch culture over a 28-day period. In our own work we found complete disappearance (>99%) of DEGMBE within 15 days.

Considering DEGMBE constitutes about 80% of the organic carbon in AFFF (4), and that DEGMBE is so easily degraded, the assumption that a high BOD/COD ratio reflects successful treatment may be somewhat misleading in the case of AFFF wastewaters. 3M reports in its product environmental data sheet for FC206 a 20-day BOD that is 82.5% of the COD. Metabolism of DEGMBE can account for all of this while the more problematic surfactant components remain.

The initial decreases in MBAS (Figure 2) are most likely a result of adsorption of the surfactant to bacteria and other solids in the inoculum. However, as the adsorbable surfaces become saturated, further loss of material from solution will occur only through

metabolism or accumulation by cells (20). Thus the decrease in MBAS after the first week most likely represent actual degradation.

LAS has been found to be inhibitory above certain concentrations. Biodegradation of LAS will only occur when LAS is below this critical concentration, which varies from system to system. In general the inhibiting concentration is higher in homologs of shorter chain length (20). The initial concentrations of LAS in 1% AFFF are about 130 ug/ml based on MBAS, near the inhibitory concentration of C₁₀LAS and above that reported for longer homologs. More rapid degradation might occur with a more dilute initial concentration of 0.5-0.8% AFFF.

There is substantial evidence that complete mineralization of LAS can be achieved. Typically the sequence of events proceeds as chain oxidation, ring oxidation and sulfate production. Since such diverse metabolic capabilities are required, a mixed community, such as occurs in activated sludge, will be most successful utilizing LAS completely (20).

Decomposition of APEs depends greatly on acclimation of the microbial community following exposure. Degradation greater than 90% is common once this occurs. However this is not typically ultimate or complete degradation but only metabolism to the point that some change in the molecule is detectable (20). Giger et al. (8,9) report that APEs tend to be stripped of their ethoxylate groups in activated sludge, leaving toxic alkyl phenols. Most of the ethoxylate chain was cleaved under aerobic conditions leaving alkylphenol mono- and diethoxylates. These were further oxidized anaerobically to alkylphenols.

The ^{19}F NMR technique tested here could show whether any degradation of the fluorosurfactant occurs. Alteration of the non-fluorinated portion of the molecule would result in a change in the 115 ppm position, and lesser changes in the 123,124 ppm region. Degradation of the perfluoro chain, on the other hand, would result in gross changes in chemical shifts and relative intensities, indicative of changes in molecular structure of the surfactant.

The advantage of ^{19}F NMR over ^1H NMR for this project is that interference due to protonic solvents and other hydrogen-containing molecules contained in the surfactant mix is eliminated. If the perfluoro surfactant could be separated from the other components of the mixture, ^1H NMR could be employed by dissolving samples in perdeutero solvents commercially available. In this way chemical changes in the nonfluorinated group could be determined.

CONCLUSIONS

Under the laboratory conditions used in this investigation, essentially complete disappearance of DEGMBE, the greatest organic constituent of AFFF, was achieved. This can easily account for the BOD/COD ratios observed in AFFF. The anionic and nonionic components show limited disappearance in the seven weeks of the study.

The slower degradation of the surfactant components may be accounted for in several ways. Microbial acclimation to both LAS and APEs is well documented (20). During the resulting lag in growth by surfactant utilizers, DEGMBE utilizers would likely outcompete them for nutrients in the medium. Also, the metabolic pathways to break down

surfactant may be suppressed as long as a more suitable substrate (e.g. DEGMEE or its metabolites) is available. Considering these processes, a sequential degradation of AFFF wastewater, allowing DEGMEE degradation without fresh inflow and perhaps with reinoculation, may be the most successful approach.

Further work on the problem of AFFF wastewater disposal should include confirmation of these results based on more specific techniques including HPLC, and ^{19}F NMR of the fluorosurfactant to detect possible changes occurring in it. Solid-phase ion exchange can be used in this as well. The effect of such factors as temperature, reinoculation, pH, and aeration should also be characterized.

Following this, the usefulness of the biological treatment approach on a larger scale under conditions more closely resembling those of the real sites should be examined. Here such factors as sorption, nutrient availability, precipitation, temperature change, and wastewater influx and efflux can be considered.

ACKNOWLEDGEMENTS

We would like to thank Dr. H. Knachel for assistance with NMR work.

FIGURES

Figure 1. Diethylene glycol monobutyl ether concentrations in the microcosms. (A) Standard curve of GC peak heights. (B) DEGMEE concentration in replicate unamended flasks (●, ○), killed control (◆). (C) DEGMEE concentration in replicate low nutrient flasks (▲, △), killed control (◆). (D) DEGMEE concentration in replicate high nutrient flasks (■, □), killed control (◆).

Figure 2 Anionic surfactants in microcosms measured as MEAS. (A) Representative standard curve for standard LAS. (B) Anionic surfactant in unamended flasks (●, ○), killed control (◆). (C) Anionic surfactant in low nutrient flasks (▲, △), killed control (◆). (D) Anionic surfactant in high nutrient flasks (■, □), killed control (◆).

Figure 3. Nonionic surfactant in microcosms measured as CTAS. (A) Representative standard curve made from standard nonionic surfactant. (B) Nonionic surfactant in unamended flasks (●, ○), killed control (◆). (C) Nonionic surfactant in low nutrient flasks (▲, △), killed control (◆). (D) Nonionic surfactant in high nutrient flasks (■, □), killed control (◆).

Figure 4. Separation of homologs of LAS by reverse phase HPLC. 20 μ l LAS (2 μ g/ml) were separated on a Hypersil SAS (C1) column using 0.15 N NaClO_4 in (60:40 H_2O :tetrahydrofuran). Flow rate was 1 ml/min; chart speed was 1 cm/min. Fluorescence detection was used, with excitation at 225 nm and emission at 285 nm.

Figure 5. Separation of isomers of LAS by reverse phase HPLC. 20 μ l LAS (2 μ g/ml) were separated on a uBondpak C18 column using 0.15 N NaClO_4 in (65:35 H_2O :acetonitrile). Flow rate was 1 ml/min; chart speed was 1 cm/min. Fluorescence detection was used, with excitation at 225 nm and emission at 285 nm.

Figure 6. Separation of OPE (octylphenyl polyethoxylate) by alkyl and ethoxylate chain lengths. 20 μ l OPE (diluted 1:1000 in H_2O) were separated on a Hypersil SAS (C1) column using 0.15 N NaClO_4 in (65:35 H_2O :tetrahydrofuran). Flow rate was 0.8 ml/min; chart speed was 0.5 cm/min. Fluorescence detection was used. The excitation wavelength was 225 nm; the emission wavelength was 285 nm.

Figure 7. ^{19}F nuclear magnetic resonance spectra of (A) Ansulite fluorosurfactant A and (B) 3820 fluorosurfactant of FC-206.

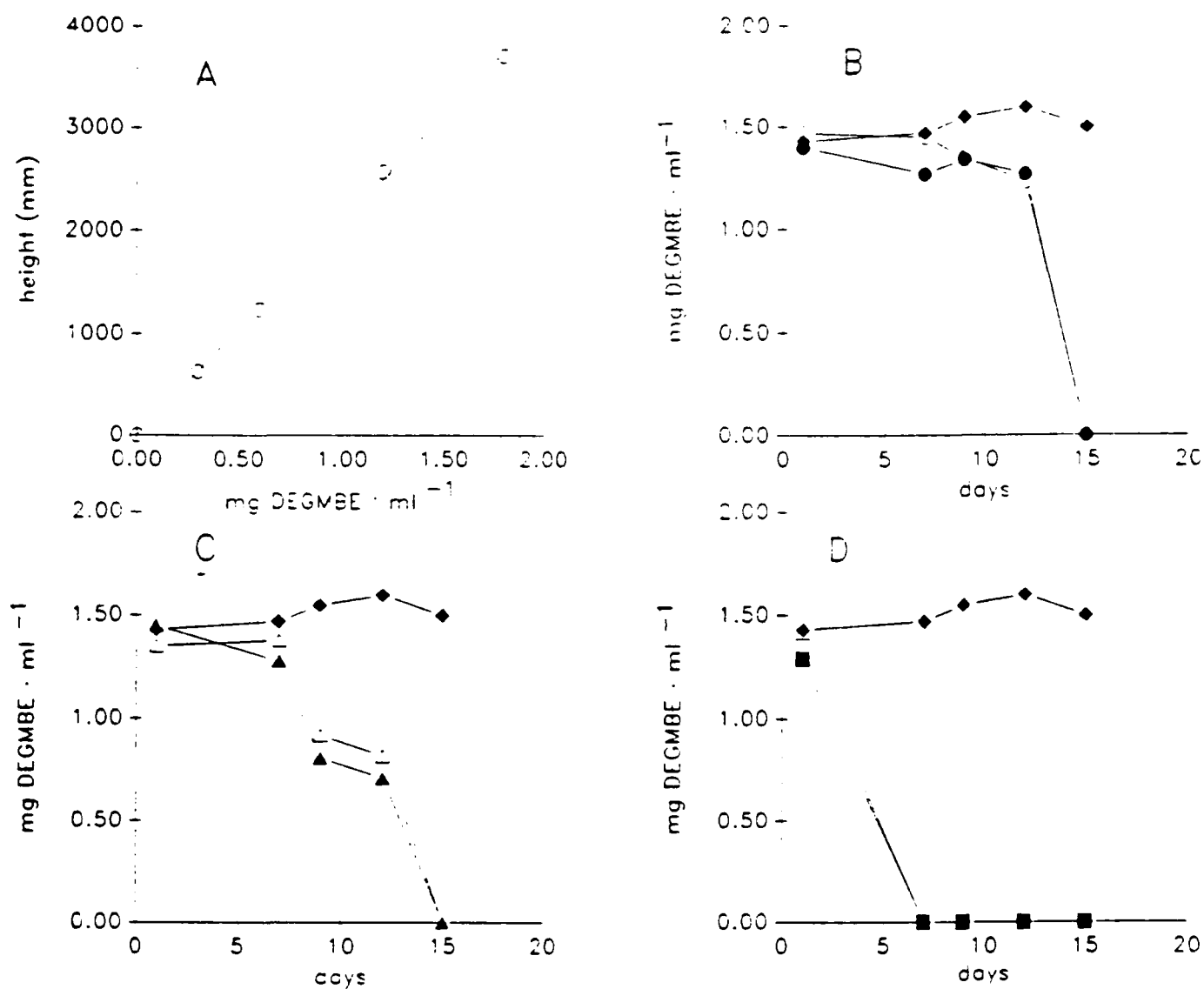


Figure 1

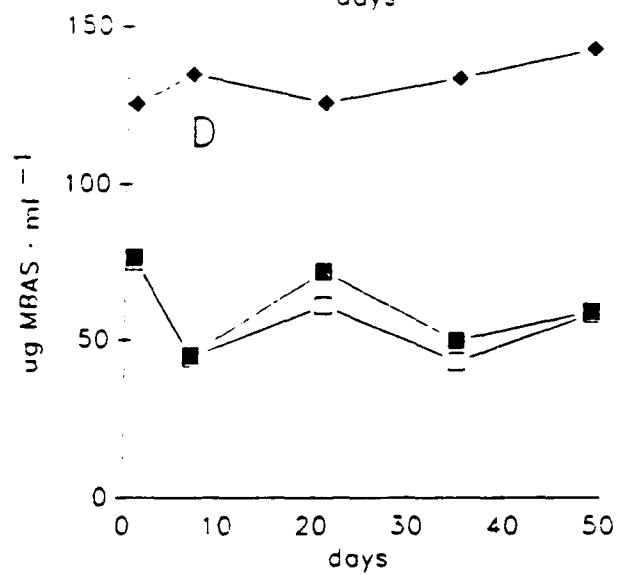
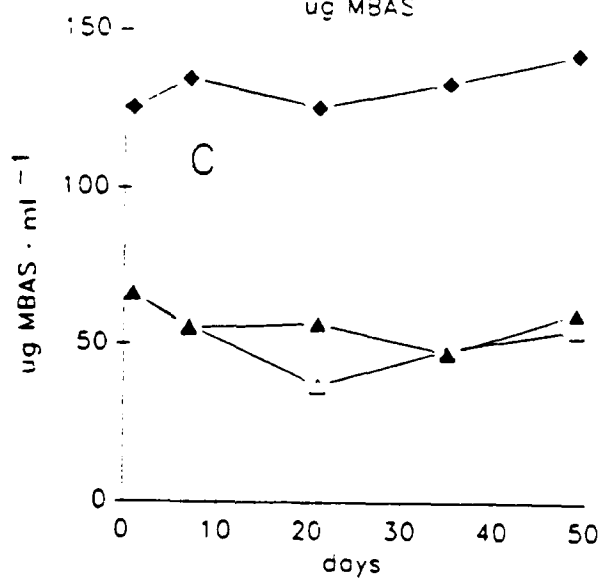
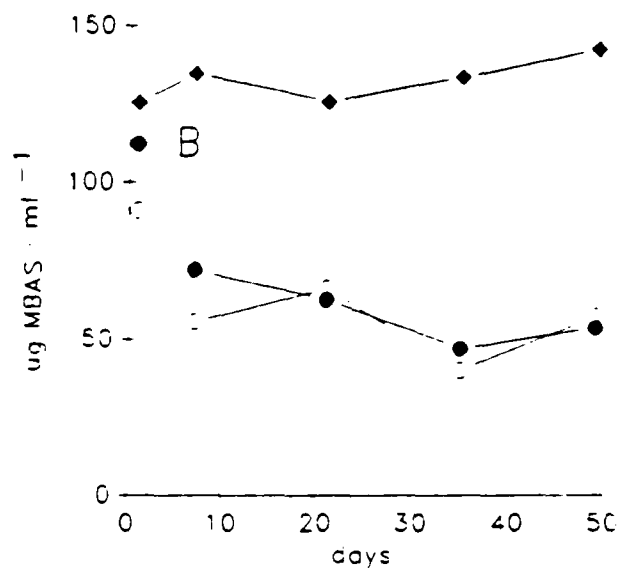
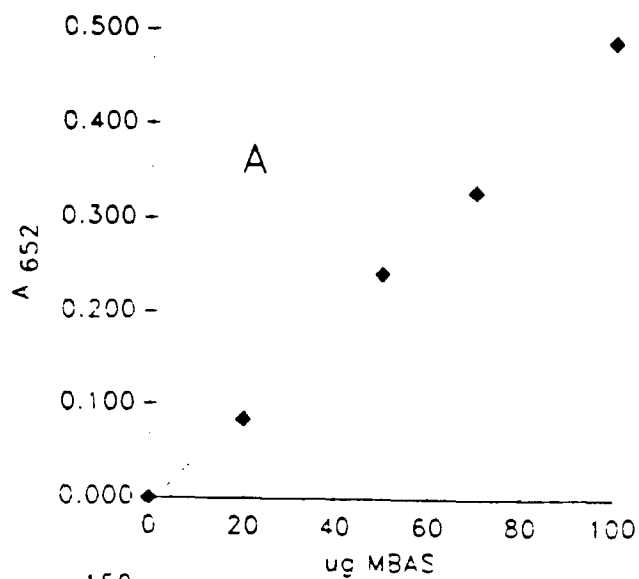


Figure 2

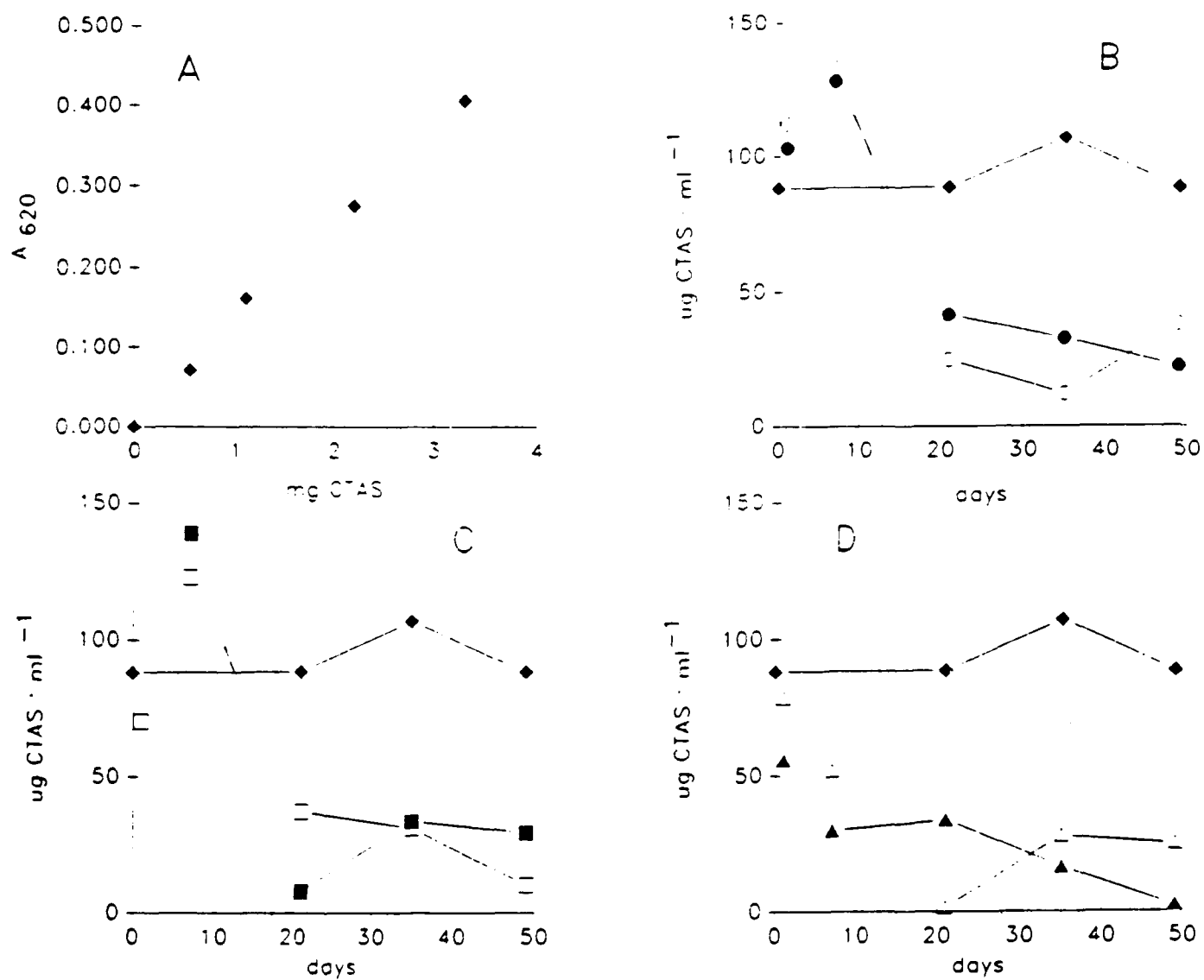


Figure 3

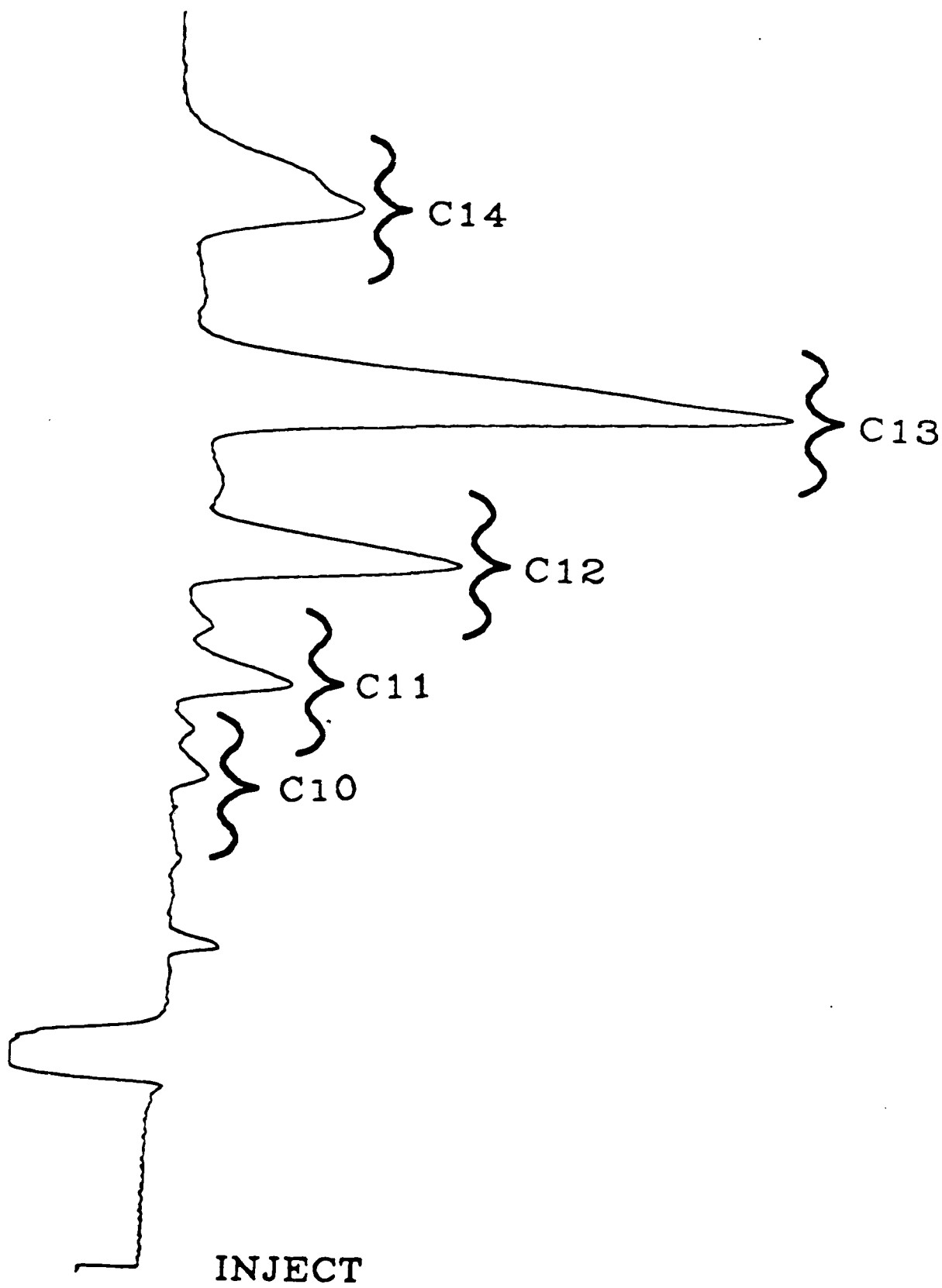
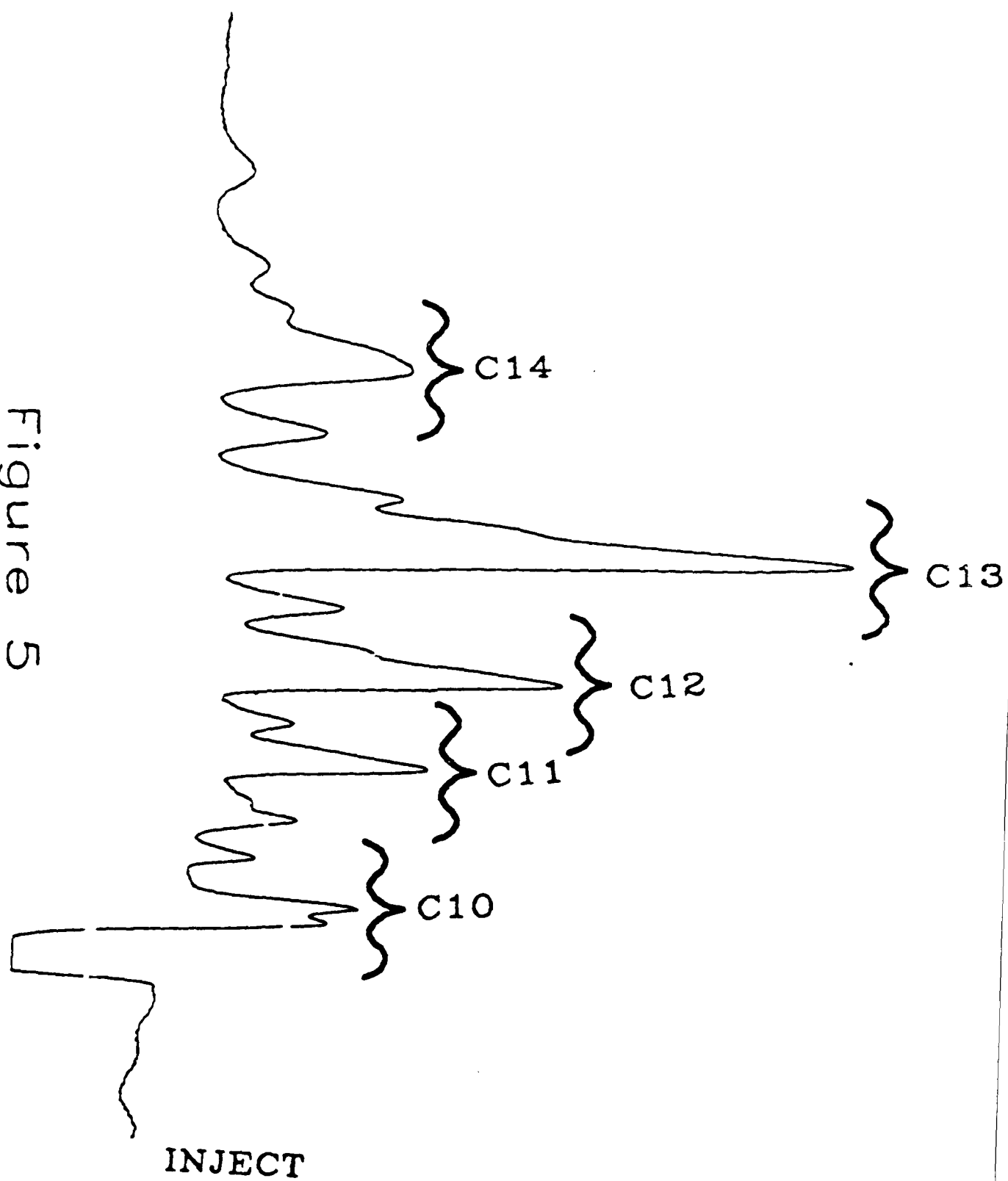


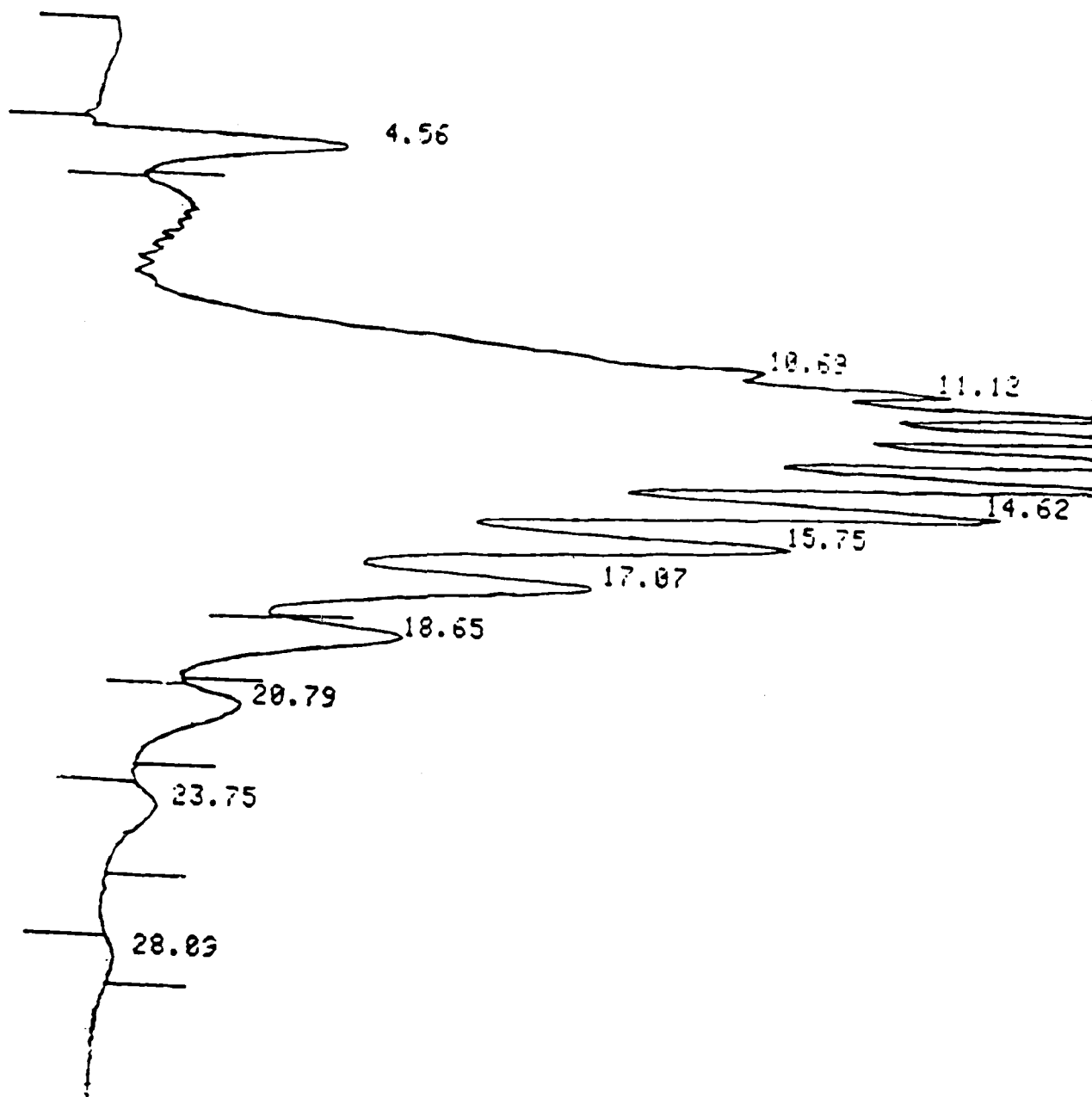
Figure 4

Figure 5



INJECT

Figure 6



^{19}F NMR SPECTRA

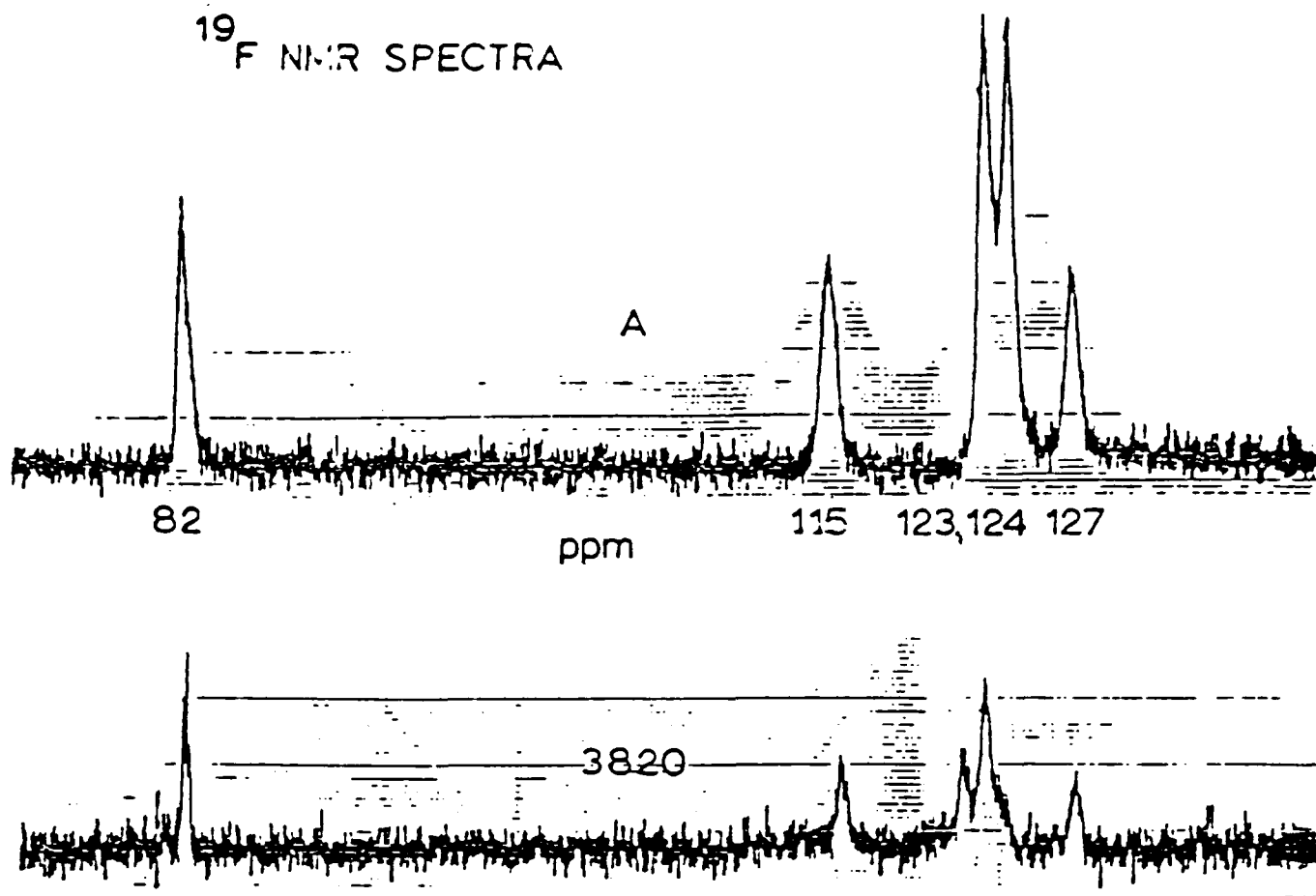


Figure 7

REFERENCES

1. American Public Health Association. Standard Methods for the Examination of Water and Wastewater, 15th ed., 1983.
2. ANSUL and 3M Product Data Sheets, 1986.
3. Bass, C.M., The fate and effects of aqueous film forming foam (AFFF) as it passes through sand, soil, or activated carbon biofilter with appendices on high performance liquid chromatography and the Beckman Microtox toxicity monitor applications to AFFF. Ph.D. Dissertation, University of Oklahoma, Norman, OK, 1982.
4. Chan, D.B., Civil Engineering Laboratory Technical Memorandum No. M-54-78-08, "Analytical method of aqueous film forming foam (AFFF)", The U.S. Navy Civil Engineering Laboratory, Port Hueneme, CA, 1978.
5. Chan, D.B. 1979. NCEL Technical Memorandum TM 54-79-19. "Disposal of wastewater containing AFFF by physiochemical processes." The U.S. Navy Civil Engineering Laboratory, Port Hueneme, CA, 1979.
6. Chan, D.B. 1983. Civil Engineering Laboratory Technical Memorandum No. M-54-83-14. "Initial feasibility report on AFFF-laden wastewater treatment/recovery." The U.S. Navy Civil Engineering Laboratory, Port Hueneme, CA, 1983.
7. Fink, P.T., Air Force Technical Report, CEEDO-TR78-45, "Aqueous film forming foam treatability", Civil and Environmental Engineering Development Office, Tyndall AFB, FL, 1978.
8. Giger, W., P.H. Brunner, and C. Schaffner. 1984. 4-Nonylphenol in sewage sludge: accumulation of toxic metabolites from nonionic surfactants. Science 225:623-625.
9. Giger, W., E. Stephanou, and C. Schaffner. 1984. Persistent organic chemicals in sewage effluents: I. Identification of nonylphenols and nonylphenolpolyethoxylates by glass capillary gas chromatography/mass spectroscopy. Chemosphere 10:1253-1263.
- 9a. Gordon, A.J. and R.A. Ford. 1972. The Chemist's Companion. Wiley-interscience
10. Kilroy, M.D. 1986. Observations of the oil/water separator conducted during firetraining exercise March 1, 1986. Memorandum Subtask 4.31. Dynamac Corporation, Panama City, FL..
11. Kroop, R.K. and J.E. Martin., Air Force Technical Report, AFWL-TR-279, "Treatability of aqueous film-forming forms used for fire fighting", Air Force Weapons Laboratory, Kirtland AFB, NM, 1974.

12. Lammi, P.E. 1985. Environmental considerations associated with storage and disposal of AFFF. Letters and recommendation concerning Beale AFB.
13. LeFebvre, E.E., and Inman, R.C., Report No. EHL(K) 74-26, "Biodegradability and toxicity of FC-206 aqueous film forming foam". USAF Environmental Health Laboratory, Kelly AFB, TX, 1974.
14. LeFebvre, E.E. and Inman, R.C., Report No. EHL(K) 75-3, "Biodegradability and toxicity of ANSUL K74-100 aqueous film forming foam, USAF Environmental Health Laboratory, Kelly AFB, TX, 1975.
15. LeFebvre, E.E., and Thomas, J.F., "Biodegradability and toxicity of AER-O-WATER 3 and AER-O-WATER 6 aqueous film forming foam" USAF Environmental Health Laboratory, Kelly AFB, TX, 1974.
16. Middlebrooks, E.J., N.B. Jones, J.H. Reynolds, M.F. Torpy, and R.P. Bishop. 1978. Lagoon information source book. Ann Arbor Science Publishers Inc. Ann Arbor, MI.
- 16a. Mooney, E.F. 1970. An Introduction to ¹⁹F NMR Spectroscopy. Heyden-Sadtler.
17. Osburn, Q.W. 1986. Analytical methodology for linear alkyl benzene sulfonate (LAS) in water and wastes. JAOCS 63: 257-263.
18. Physical-chemical treatment of wastewater from Navy firefighting schools. Contract No. N00035-74-0004, Engineering Science, Inc.
19. Schmitt, T.M., M.C. Allen, D.K. Brain, K.F. Guin, D.E. Lemmel, and Q.W. Osburn. 1987. HPLC determination of ethoxylated alcohol surfactants in wastewater. In Press JAOCS.
20. Swisher, R.D. 1987. Surfactant biodegradation, 2nd ed. Marcel Dekker, Inc. New York, NY.
21. Thomas, J.F., and LeFebvre, E.E., Report No. EHL(K) 74-3, "Biodegradability and toxicity of FC-200, aqueous film forming foam", USAF Environmental Health Laboratory, Kelly AFB, TX, 1974.
22. 3M Analytical Handbook. 1986. 3M Environmental Engineering and Pollution Control, St. Paul, Minn.
23. Wang, E.H., Air Force Technical Report, CEEDO-TR77-7, "Bioassay of Air Force FC-206 fire fighting foam", Civil and Environmental Engineering Development Office, Tyndall AFB, FL, 1977.
24. Zahn, R. and H. Wellens. 1980. Determining biodegradability in a static test: Further experiments and new possibilities. 2. Wass.-Abwass-Forsch. 13:1-7.

FINAL REPORT NUMBER 85
REQUESTED A NO-COST TIME EXTENSION
TO BE SUBMITTED IN 1987 MINI-GRANT FINAL REPORT
Dr. Doris Walker-Dalhouse
760-6MG-080

FINAL REPORT NUMBER 86
RECEIVED A NO-COST TIME EXTENSION
TO BE SUBMITTED IN 1987 MINI-GRANT FINAL REPORT
Dr. Donald Welch
760-6MG-091

EFFECTS OF TELECOMMUNICATION MEDIA UPON GROUP DECISION MAKING
PROCESSES WITHIN A MULTI-TEAM SITUATION ASSESSMENT TASK

A. Rodney Wellens
Department of Psychology
University of Miami
Coral Gables, Florida

Final Report for Contract Number F49620-85-C-0013/SB5851-0360
Purchase Order No. S-760-6MG-085

Submitted to the Air Force Office of Scientific Research
via
Universal Energy Systems
4401 Dayton-Xenia Road
Dayton, Ohio 45432

December 31, 1987

Abstract

A brief review of theoretical concepts related to decision making, group dynamics and communications processes is made. A generic "psychological distancing" model of electronic media is described. Issues related to the role of electronic media in networking decision makers within situation assessment settings are highlighted. A series of hypotheses dealing with the effects of media on group processes and task outcomes are advanced.

Details are given regarding a new computer-based situation assessment game developed specifically for the current project. The C.I.T.I.E.S. game is modeled after key aspects of a metropolitan crisis control center. Two remotely located teams interact over pre-selected communication channels to assess situations surrounding an increasing number of emergency events. Each team must respond to events for which they hold responsibility by allocating resources from a finite resource pool.

A multi-channeled telecommunication laboratory designed for the project is also described. The laboratory allows the systematic selection of computer, audio and video teleconferencing for connecting teams located in separate rooms. The laboratory provides for the videotaping of all interpersonal group activity as well as the recording of all events and responses to events within the experimental game.

An experiment is described that was conducted to test a set of hypotheses dealing with communication bandwidth, group dynamics and task performance. Eighty men and eighty women participated in the experiment in same-sexed groups. Forty groups composed of two two-person teams played the C.I.T.I.E.S. game using a scenario that increased task difficulty over time. Ten groups played the game without benefit of a team-to-team communication link. A like number of groups played the game using either a computer conferencing link, an audio conferencing link or a two-way television conferencing link. Measures were taken of individual team member talking times, the number and type of messages exchanged between groups, action latencies when responding to game events and effectiveness in team allocation of resources. Measures were taken post-experimentally of feelings of group cohesiveness and liking, role and communication satisfaction, perceived workload, leadership emergence and awareness of underlying event patterns.

The results of the experiment are discussed in terms of the hypotheses forwarded. Only partial support for the hypothesis that increased communication bandwidth would increase feelings of cohesiveness and satisfaction was found. No support for the hypothesis that increased bandwidth would lead to increased situational awareness and performance was found. Recommendations are given regarding the need to revise current predictive models to account for the complex patterns of results observed. A careful analysis of media liabilities as well as benefits is needed. Future studies need to examine effective media use in addition to available channel capacity.

I. Introduction

Organizational decision making has become increasingly dependent upon electronic media for information gathering, transmission and integration. Corporate as well as military decision makers would find it difficult to function effectively without the global telecommunication network used to coordinate the flow of information across space, time and individuals. Audio, video and computer based messaging and storage systems form the ears, eyes and dynamic memory of modern organizational information networks. While technological advances continue to transform the physical components of decision support systems, there is still much to be learned about the impact of such systems upon decision making processes.

The purpose of the present effort was to extend the available knowledge base regarding the effect of electronic media upon the processes involved in group decision making within the context of a distributed situation assessment task. This was accomplished by first reviewing a set of theoretical concepts related to group interaction, decision making and communication processes. Next a research framework for studying team decision making and media effects was developed. A new computer-based situation assessment game was created and a multi-media laboratory constructed. An experiment designed to test hypotheses derived from an analysis of the theoretical and empirical literature was conducted. Results of the experiment are discussed and recommendations regarding future studies are advanced.

1. Assumptions About Groups, Decision Making and Communication Processes

Groups. McGrath (1984) has recently reviewed the group psychology literature and provided a conceptual framework within which to study group processes. According to McGrath, a group may be defined as an aggregation of two or more people who are to some degree in dynamic interrelation with one another. The individual characteristics of group members, the structural relationships between them, the environment within which they exist and the tasks they are expected to perform all serve to shape group interaction. McGrath believes the "essence" of a group lies in the interaction of its members. "Groupness" is assumed to decrease as barriers to mutual awareness and interaction increase.

A special kind of group that has begun to receive increased attention is the team. According to Dyer (1984), a team consists of (a) at least two people who (b) are working toward a common goal, where (c) each person has been assigned specific roles or functions to perform, and where (d) completion of the mission requires some form of dependency among group members. It is assumed that medical, military, business or emergency teams have members who must each choose coordinated actions to accomplish agreed upon goals. Team members usually have complementary areas of expertise and monitor different aspects of the environment for information sources.

Decision Making. Several authors have outlined basic concepts associated with decision making processes. A decision can be defined as a risk-taking selection among alternative actions. These actions are assumed to be connected in a deterministic way to outcomes. If a decision maker knows which outcomes will occur with each act, the act resulting in the most valued outcome is expected to be chosen (Tribus, 1969). The number of pieces of information that need to be considered simultaneously to reach an optimal decision reflects the degree of complexity associated with the situation. The extent to which information is lacking to feed into a decision structure reflects the degree of situation uncertainty. The extent to which the decision rules themselves are vague or unknown reflects the degree of fuzziness associated with the situation (Dompere, 1982). Within dynamically alterable environments where information is constantly changing and combination rules may still be evolving, frequent situation assessment may be necessary to clarify the current state of knowledge.

Communication. A major function of communication within decision making systems is the reduction of situational uncertainty and fuzziness through information gathering and exchange. For individual decision makers, information may be sought in the form of special evidence or indicators that can be combined with prior knowledge to help assign probability values to various actions and outcomes. For group decision making additional communication between group members is necessary to form a cohesive decision making unit. Within functionally operating teams, communication is also necessary to carry out coordinated actions that result from the decision making process.

2. Issues Related to Communication Networking, Group Process and Decision Making

Connecting Decision Makers via Electronic Media. Much of what has been learned about group decision making was acquired by observing group behavior in face-to-face meetings. However, many alternatives to traditional face-to-face interaction now exist. Computer, audio and video teleconferencing systems allow decision makers to interact without the necessity of traveling to a common location. While the use of electronic media has tended to shrink time and space by instantly linking key decision makers, all media are not the same in their ability to transmit critical information.

Several authors have attempted to illustrate the selective filtering that occurs across communication modalities as a function of communication bandwidth (e.g., Kaplan, 1977; Korzenny, 1978; Connors, Harrison & Akin, 1985). Narrow bandwidth media, like electronic mail, constrict the immediate flow of information across limited capacity communication links; broadband media, like full motion video, allow a wider spectrum of information to pass across larger capacity channels.

Wellens (1986) recently reviewed the empirical and theoretical literature dealing with comparisons between telecommunication media and described a "generic distancing model" of electronic media. A representation of various media along a psychological distancing dimension is depicted in Figure 1. According to the model, as communication bandwidth decreases the physical representation of an interlocker is experienced less directly and appears more psychologically remote. In general, information "rich" media tend to promote the socio-economic aspects of group

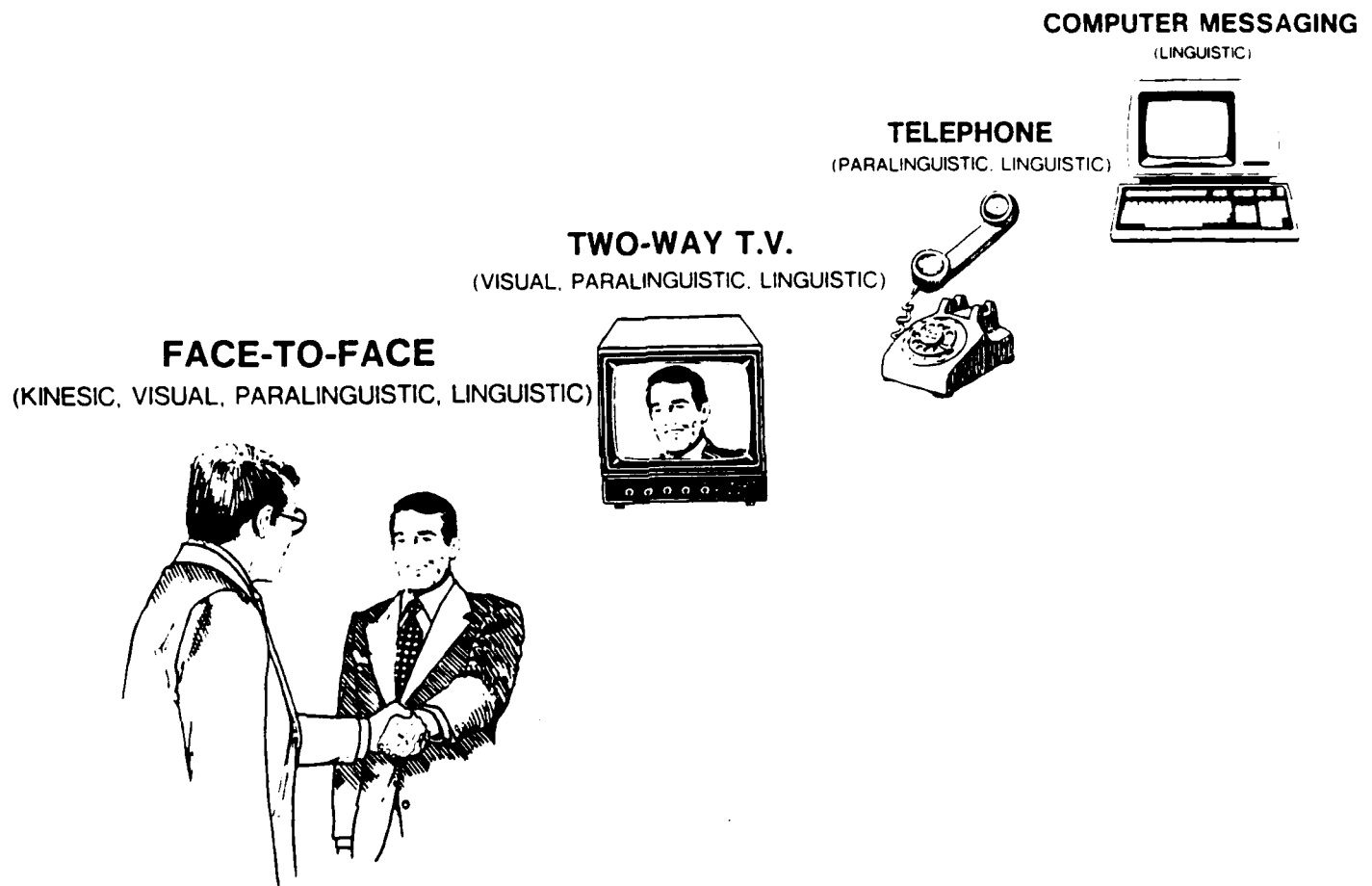


Figure 1. Diagram depicting a generic psychological distancing model of telecommunication media. Reduction in the number and kind of communication channels leads to decreased feelings of psychological closeness. (Reprinted from Wellens, 1986.)

interaction like the establishment of positive interpersonal bonds, cooperation, role differentiation and compliance. Information "lean" media tend to increase interpersonal formality and focus interactants on the exchange of task related factual information.

Early studies of communication networking within problem solving groups (Leavitt, 1951; Shaw, 1964) demonstrated the potential impact of manipulating communication structure upon team performance, leadership emergence and productivity. By varying the number of person-to-person communication links feeding into various group positions, investigators could predetermine group member satisfaction (the more links the greater satisfaction), leadership emergence (central positions, where communication links converged, exercised more information power than peripheral positions) and overall group performance (centralized structures worked best for easy tasks, decentralized structures worked best for difficult tasks).

While these early networking studies broke new ground by pointing out the power of communication structure on group problem solving, they manipulated only the presence or absence of communication links between participants and did not deal with the more complex issue of the particular communication channels employed. On the other hand, more recent studies of media bandwidth effects have focused primarily upon two-person interactions rather than on larger problem solving groups. There is a clear need to study the impact of media type upon performance and process variables within the context of larger decision making groups.

Impact of Group Dynamics on Group Performance. One major advantage of group decision making is the potential of pooling members' expertise and knowledge to reach a more informed decision than individuals working alone. The study of group dynamics, however, has led to the realization that both task and socio-emotional factors may lead to information processing biases that may interfere with rational decision making (see Brandstatter, 1982; Swap, 1984). For example, in judgmental tasks where there exists no commonly accepted system of logic that would lead to an unambiguously correct decision (see Laughlin, 1980), there appears to be a bias toward discussing information that is already shared in common among participants; presentation of uniquely held information is inhibited, especially when it conflicts with already held beliefs (Stasser & Titus, 1985). On the other hand, when decision rules are clear, but information indicators are uncertain, people may turn to others as sources of information (Festinger, 1954) and conform to the perceived group norm. A related phenomenon may also lead to groups making riskier decisions than individuals (Stoner, 1961). On the socio-emotional side, when concurrence seeking is high, as is the case when the establishment or maintenance of positive social bonds between group members is given high priority, compliance to the majority (Asch, 1951) and "Groupthink" (Janis, 1972; Callaway & Esser, 1984) may replace rational decision making. Similarly, where power hierarchies are present within a group, obedience to authority (Milgram, 1965) may supercede independent judgement.

Given the selective filtering capabilities of electronic media, it may be possible to reduce the negative impacts of group dynamics on performance while enhancing the positive effects of resource pooling. For example, Johansen, Vallee and Collins (1978) have suggested that computer-based teleconferencing is a "highly cognitive medium that, in addition to providing technological advantages, promotes rationality by

providing essential discipline and by filtering out affective components of communication." These authors go on to say that "computer-based teleconferencing acts as a filter, filtering out irrelevant and irrational interpersonal "noise" and enhances the communication of highly-informed "pure reason", a quest of philosophers since ancient times (Johansen, Vallee and Collins, 1978, p.3)." Of course, this statement should be balanced against other concerns of decision makers, such as the need for communication speed and the role of socio-emotional factors in motivating group members. Nevertheless, it underscores the potential benefits of exploring alternatives to face-to-face decision making environments and reinforces the need to examine media effects.

The Role of Situation Assessment in Group Decision Making. Group decision making encompasses a broad range of problem solving tasks. Brandstatter (1982, p. 629) recently described group decision making as "exchanging ideas about the structure of and the possible solutions to a problem of some importance, and collectively choosing an action from a number of alternatives, with risks involved." He goes on to note that most experiments have dealt with only single components or single stages of this complex process. "Usually they exclude defining the problem, or generating possible solutions to it. The risk of choosing a non-optimal alternative may be perceived as virtually zero.... The importance (values at stake) may be minimized, and there may be no more than a rudimentary implication of action.... Collectivity of choice may be reduced by imposing all the responsibility on the group leader, if he has to decide alone after having discussed the problem with the group." If one strives for a theoretical integration of a broad range of concepts and empirical findings related to group decision making, a new research paradigm that captures the complexity of "natural" situations is needed.

One important aspect of group decision making that has escaped the careful scrutiny of most investigators is the information assimilation and problem identification process. Ben-Bassat & Freedy (1982) identify situation assessment tasks as a general family of problem-solving tasks. The generic nature of this family is characterized as a "multiperspective, multimembership hierarchical pattern recognition problem (p. 479)." Situation assessment constitutes a fundamental stage in many kinds of decision making problems including medical diagnosis, battlefield reading, and corporation status assessment for merger or acquisition purposes. Wohl (1985) places the integration and assessment phase of decision making downstream from the initial collection of raw data from multiple information sources and upstream from the application of decision rules to allow selection of alternative action options.

In many ways, situation assessment lies at the heart of the group decision making process. It is at the crossroads of individual input and group output. It is the point at which situational fuzziness and information uncertainty reveal themselves. Ironically, it is the stage at which information pooling and rational thinking are most desired while it is also the point at which consensus seeking pressures heighten the negative effects of group interaction.

Situation assessment settings provide a rich testbed for studying the impact of communication media upon group structure, processes and performance. Because they require interpersonal cooperation and exchange of information for effective

functioning, these environments would be expected to be especially sensitive to communication media effects.

II. Research Plan

The goal of the proposed research was to explore the impact of electronic communication media upon group decision making processes within a situation assessment setting. Both social process and task outcome variables were measured within an experimental game that links semi-autonomous working groups together via different kinds of electronic media. The media examined varied in communication bandwidth, ranging from computer messaging and voice channels to full motion two-way television. A no communication control group was also studied for base line comparisons. The social process variables measured included individual perceptions of group cohesiveness, interpersonal liking, role satisfaction, workload assessment, frequency and duration of messages exchanged, message type, and leadership rankings. Task outcome variables included action response latencies, successful detection of patterned environmental events and resource allocation effectiveness.

1. Experimental Task

An important part of the proposed work effort was the development of an experimental task that enabled the experimenter to observe changes in group decision making processes by monitoring task related choice behavior and the interpersonal social interactions that preceded and followed them. The task was to be psychologically engaging and easily grasped to facilitate the movement of subjects into their assigned roles. The task was also to display the fundamental characteristics of a situation assessment problem with information impinging upon groups from multiple information sources. The task environment was to be dynamic and interactive such that events evolve and are transformed according to the actions taken by group members. Finally, the task was to allow the sharing of information across pre-determined communication channels that could be systematically varied in bandwidth.

Originally it was felt that a computer-based "city management" game that was under developed by Perceptronics for AAMRL/HEA met many of the above requirements. The research proposal was made with the understanding that the city management game would be made available to the investigator for his use in the proposed experiment. Unfortunately the game software was never delivered to the investigator or even seen by him.

The development of an appropriate situation assessment task became a major part of the work effort. After discussing the major features of the city management game with one of its co-developers, Maj. Robert G. Eggleston, it was decided that a similar game entitled "C.I.T.I.E.S" (C³ Interactive Task for Identifying Emerging Situations) would be written at the University of Miami using computer hardware already available to the investigator. The crisis control center theme of the city management game was adopted, however, the game parameters and user interfaces that contribute to the game's look and feel were developed independently. A detailed description of the C.I.T.I.E.S. game may be found at the end of this report in Appendix A. Only a brief description of the game will be presented here.

The computer-based CITIES game simulates many aspects of a metropolitan crisis control center. Teams view a dynamically alterable, computer generated "city map" that displays a grid system upon which symbols, representing emergency events, are shown. One team, comprised of a "police chief" and his or her "advisor" views a police-oriented map that displays events such as robberies, gang fights, and traffic jams. This team allocates police and tow resources (e.g., squad cars and tow trucks) to handle events as they emerge. This is accomplished by moving symbols, representing resources, to grid positions showing emergency events by touching a touch-sensitive screen placed over the city map. A second team, comprised of a "fire marshal" and his or her "advisor", views a similar map displaying events such as residential and business fires and accidents involving personal injury. This team is responsible for allocating resources such as fire trucks and ambulances.

Emergency events are announced by flashing red icons that appear on the city map. A team may learn more about the event by touching the flashing icon and then touching a "More Info" bar at the bottom of their display screen. When this is done a one or two sentence description of the event appears. In order to learn more about the intensity of the event, the More Info bar must be touched again, whereupon a summary table of the affected region appears showing the intensity levels of all active events at the selected grid position as well as the number of resources already assigned. The higher the intensity value of an event (values can range between 0 and 99) the more resources needed to bring it under control. Unattended events grow in intensity; the higher the beginning intensity the quicker the growth.

Game scenarios can be written to accommodate a wide variety of research interests. This is accomplished by changing the number and type of events the game computer is to display. For each event presented the experimenter must compose the accompanying message, select a desired intensity and specify the time the event is to occur. When all event information is loaded into the game computer, the computer will faithfully reproduce the scenario each time it is selected.

The scenario used in the present experiment was designed to require increased cooperation between fire and police officials as the timing and complexity of events progressed. The "Visiting Senator" scenario involves a series of events that follow the trail of a senator who moves about the grid system in a orderly manner. The Police team is given an itinerary that outlines where the senator will be at any given time during the team's workshift. The Fire team is not given this information. Serious Police and Fire events pop up in regions visited by the senator. Using the itinerary information can help teams predict where the next disaster will strike. This allows the anticipatory movement of resources to the appropriate grid location and thus prevent a rapid escalation of event intensities. Communicating itinerary information from Police to Fire teams was expected to increase team performance.

During the first ten minutes of the game no cooperation between teams is needed in order for each team to maintain control over emergency events under their jurisdiction. Fourteen Police and Tow events plus fifteen Fire and Rescue events occur with a total intensity value of 345 units. During the second ten minute period, approximately the same number of events occur (15 Police-Tow and 15 Fire-Rescue with a combined intensity value of 435 units). However, three of these events are "contingency" events that require the joint effort of both teams to control (e.g., a fire-rescue vehicle cannot

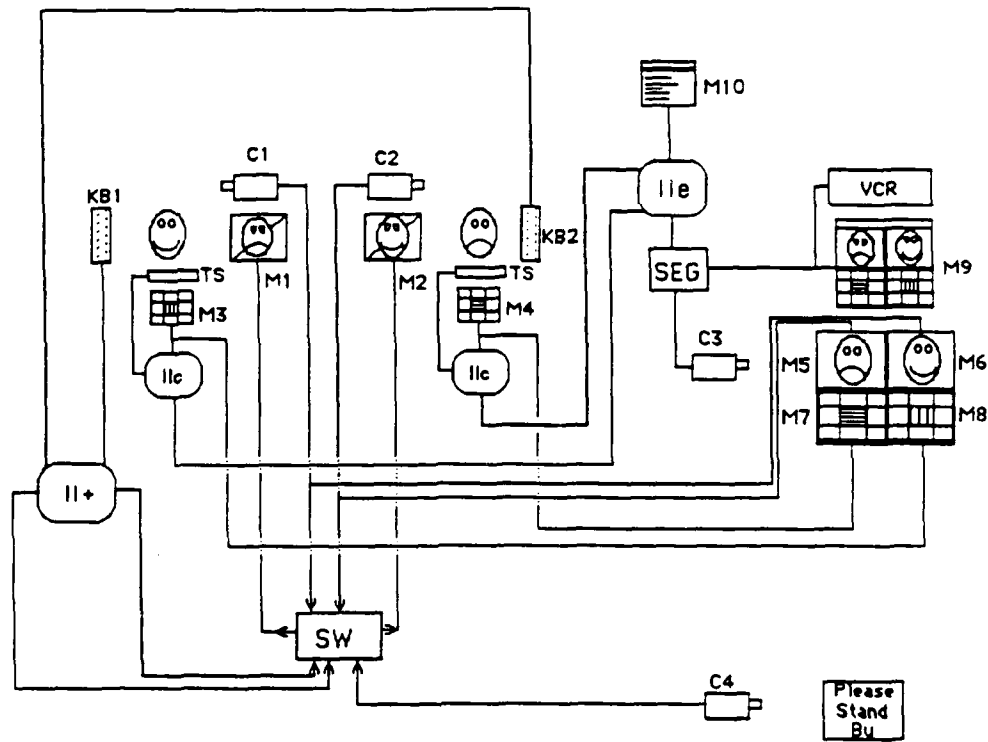
proceed to an emergency before the police clear a freeway). Communication and cooperation between teams during this period was expected to lead to better overall performance. During the last ten minutes of the game the same number of events occur (15 Police-Tow and 15 Fire-Rescue with a combined intensity value of 531 units including 1 contingency event. However, several high intensity events occur in conjunction with the senator's movements. Not focusing upon the senator's movements and accompanying events was expected to lead to several events going out of control. Thus, the complexity of handling events increased from the first, to second and last third of the game.

2. Communication Setting

The research was conducted within the Interactive Television Laboratory at the University of Miami Department of Psychology. The laboratory (described by Wellens, 1979) consists of a control facility that links a series of physically isolated rooms that can be connected by a two-way television systems (Wellens, 1978), open channel audio system or a recently completed synchronous computer messaging system (Ergener and Wellens, 1985). The facility allows the simultaneous videorecording of individuals located at each communication node.

Figure 2 shows the major computer and video components used in the present experiment. The main game computer was an Apple IIe equipped with two serial ports that allowed it to communicate with two Apple IIc computers. The Apple IIc computers were used to generate the electronic map and information screens for each team. Each IIc was also attached to a Personal Touch touch screen that allowed teams to interact with the game software. The Apple IIe polled the IIc's every five seconds to record each team's moves and update the displays. An Apple II+ computer equipped with a specially programmed Videx 80-column card was used to operate the keyboard messaging system. Two Tandy 100 lap-top computers equipped with internal terminal programs were connected to the II+ by way of two serial ports. The video output from the II+ was feed back to team monitors so that each team could see what was being typed on both keyboards. Hard copies of all messages could be output in the experimental control room.

The video outputs from each Apple IIc were fed to monitors in the control room as well as to monitors within the team Dispatch centers. Similarly the video outputs from cameras placed within each Dispatch center were fed to control room monitors as well as to a master switch that could route the video back to either Dispatch center to establish a two-way video link. A third camera was focused upon an extra cluster of control room monitors housed in a darkened area to generate a composite image of teams and their game displays. This image was sent to a JVC special effects generator. The main game computer, equipped with a Video Associates VB-3 Micro Keyer system that allowed it to be genlocked to the special effects generator, provided a line of continuously updated numerical game data. (The game computer was also used to collect and record heart rate information from team dispatchers. However, this aspect of the computer's function was not part of the present task and will not be discussed.) The resulting composite video picture with game data added was sent to a Panasonic VCR for recording.



VIDEO COMPONENTS

C1 - C4	JVC GX- S700U Color Video Camera
M1 - M2	NEC CT2510 25" Color TV Monitor
M3 - M4	Amdec 300 13" Color Monitor
M5 - M10	Panasonic 9" B/W Monitor
SEG	JVC KM1200SPG Special Effects Generator
VCR	Panasonic AG-6300 Video Cassette Recorder

COMPUTER COMPONENTS

IIe	Apple IIe Computer with VB-3 Micro Keyer
IIc	Apple IIc Computer
II+	Apple II+ Computer with 2 Super Serial Cards
KB1-2	Tandy 100 Portable Computers
TS	Personal Touch IIc Touch Screen

ROTARY SWITCH THAT CONTROLS FEED TO M1 AND M2

SW Position

- 1 Pickup from C4 feeds to M1 and M2
- 2 Pickup from II+ feeds to M1 and M2
- 3 Pickup from C1 and C2 feeds to M2 and M1

Figure 2. Diagram showing the major video and computer components used in the C.I.T.I.E.S. task.

A fourth camera was focused upon a cue card rack that contained messages like, "Please Stand By" and "Game in Progress, Audio On." Output from this camera was routed to team wall monitors via a master rotary switch. Outputs from each of the dispatch center cameras as well as from the Apple II+ electronic mail computer were also connected to this switch. By manipulating the switch the experimenter could select the media condition for groups. Figure 3 shows a photograph of the experimental control room that contained the video recording and switching equipment.

Figure 4 shows a photograph of one of two 8 by 7 foot meeting rooms that were constructed as Police-Tow and Fire-Rescue dispatch centers. Each room was designed to accommodate an in-wall two-way television system, a table holding a touch sensitive television monitor and keyboard, and two chairs for each team's Dispatcher and Advisor. The two-way television system consisted of a 25 inch color television monitor and color television camera placed behind an 18 inch square opening cut in one wall of the room. A piece of lightly silver glass (i.e., one-way mirror) was placed in a downward sloping position between the monitor and opening in the wall so that each team could view their monitor while their reflected images were unobstrusively picked up by a television camera placed below the monitor. All components located behind the wall opening were encased in a black felt-lined shadow box that concealed their presence.

Each two-person team was seated side-by-side at the long side of a 3 by 4 foot table placed immediately in front of the two way television opening. The two-way television monitor was located at eye level with respect to the seated subjects. The table supported a smaller 13 inch color monitor, equipped with a touch screen and placed below the 25 inch monitor opening. The smaller monitor was used to display the "city map" used in the city management game. A momentary contact switch was mounted to a small box that was affixed to the center front edge of the table. Pressing the switch lever to the left or right allowed teams in either the audio or two-way television conditions to both talk and listen to the other dispatch center team members. (Figure 4 also shows a small finger-mounted photoplethysmographic probe that was attached to the third digit of the Dispatcher's left hand. This data was collected as a secondary pilot study and will not be discussed here.)

Within the two-way television condition, the 25 inch television monitor displayed a "Please Stand By" message until mutual contact had been established by teams. When contact was made a head and shoulders image of the remote team members appeared. A full face orientation appeared when team members looked at their wall monitors. The specially designed mirror system within the wall allowed remotely located team members to establish direct eye-contact across the TV system by simply looking directly at their wall monitor (see Wellens, 1978).

In the audio only condition, a "Game in Progress, Audio On" message appeared on the wall monitor during game sessions. Within the computer messaging condition, the wall monitor displayed a pair of alphanumeric windows containing messages being typed by the two teams via the keyboards placed in front of the smaller table-supported monitor. Each display window scrolled independently and showed messages as they were being typed. The messaging system (Ergener and Wellens, 1985) was modeled

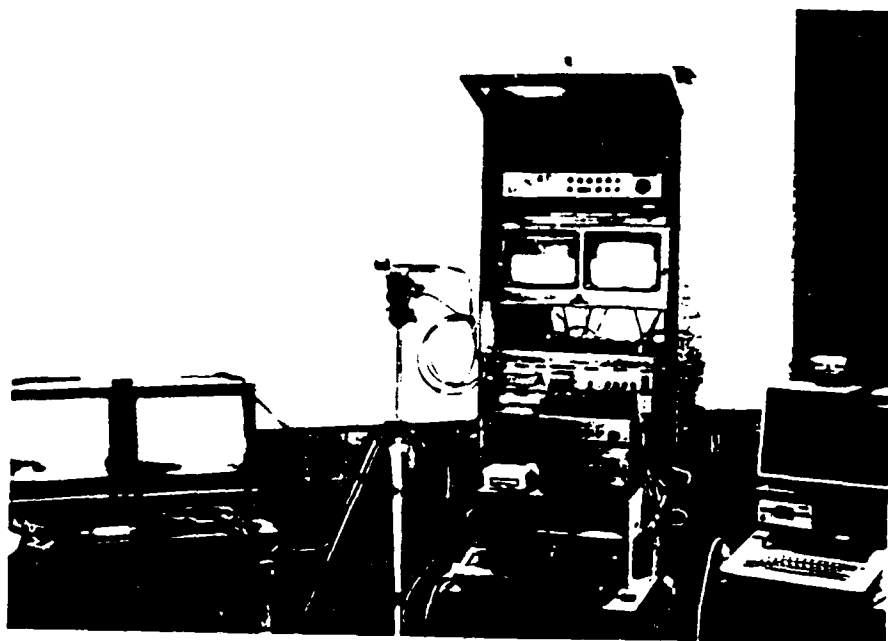


Figure 3. Laboratory control room showing major video recording and switching equipment together with main game computer and computer messaging system.



Figure 4. One of two rooms used to house the Police and Fire "dispatch centers".

after one described by Murrell (1984) and Kiesler, et al., (1985). All messages typed were later printed out on a dot matrix printer with game times printed adjacent to each message for further analysis.

Within the no communication condition the wall monitors simply displayed a "Game in Progress" message. Within all conditions, the television cameras hidden behind the two-way television wall unobtrusively recorded all team members' activities. Within all conditions, subjects wore earphones with head-mounted microphones for audio communication with their same-room partner. These headsets also served to connect remote team members in the audio only and two-way television conditions. In all conditions, the headsets helped reduce the possibility of subjects being interrupted by extraneous laboratory noises and allowed all voice communications to be recorded.

Each team's voice communications were recorded on separate audio channels within the videorecordings made of teams' activities. The composite video recordings allowed observers to later attend to the audio and video portions of each team's activities either together or separately. On playback, the experimenter could determine what each team member was saying and visually attending to at any point in the game.

3. Procedures

Subjects arrived individually for the experimental sessions at staggered five minute intervals. Four to six subjects were recruited per session from separate class sections with the hope of obtaining unacquainted individuals. Only members of the same sex were recruited for any game session. After signing a informed consent form subjects were immediately led to one of the two "Dispatch Centers" by one of three female experimenters.

Subjects were assigned the role of Fire or Police "Dispatcher" and "Advisor" on a random basis. Dispatchers were assigned the role of interacting with the touch screen to assign resources. Advisors were assigned the role of assisting the Dispatcher and communicating with the remote team when appropriate. Dispatchers and advisors on the same team met for the first time within their respective dispatch centers. Between team meetings took place only during practice and game sessions across the telecommunication medium provided.

After all subjects were seated in their respective dispatch centers an interactive computer training session was begun. Each team used their respective touch sensitive screens to proceed through approximately 65 short text pages that explained how to play the C.I.T.I.E.S. game. The training session contained numerous opportunities for each team to practice responding to events by gathering information from information screens and assigning and recalling resources from the central resource pool. The training session was self-paced and took approximately 20-25 minutes for most teams to complete.

Following the training session, a five minute practice session began. During the practice session an experimenter entered each dispatch center to make sure each team knew how to play the game. Following the practice session, the experimenter instructed teams assigned to one of the media conditions on how to operate the

communication equipment they would be using to contact the other team. Team advisors were asked to practice using the communication equipment by introducing themselves as well as their partners to the other team. Following this introduction the experimenters left the dispatch center and the game was started.

The game was designed to last approximately 30 minutes. During the first ten minute period events were presented that required no cooperation between teams for successful allocation of resources. This period was designed to allow subjects to become familiar with the game rules and try out the communication link. During the second ten minute period, events were presented that required a modest amount of cooperation between teams to contain. The third ten minute period required the greatest amount of information sharing and resource pooling to keep events from escalating out of control.

Following the game episodes, team members were separated and asked to complete a post experimental questionnaire. Using a format similar to that employed by Baker (1982), subjects were presented with a series of five-point Likert type items assessing each subject's liking for their partner and remote team members, their judgement regarding who was the group leader, their perception of "we" feelings within the group, subjective feelings of workload during each phase of the game, and overall satisfaction with their role in the experiment. Subjects were also asked to describe any pattern they perceived in the events presented and asked if their team moved any resources in anticipation of events occurring. Finally, subjects were debriefed concerning the purpose of the experiment and asked to sign a videotape release form.

Subjects. The majority of subjects were recruited from the University of Miami introductory psychology subject pool. This subject pool draws approximately 2000 subjects per year. Students receive research familiarization credits for their participation which is used to satisfy a course requirement. Additional subjects were recruited from introductory courses in business management, sociology and communications. A total of 160 subjects were used in the main study with 10 pairs of two-person teams assigned to each of the three communication and control conditions. An equal number of male and female subjects were used. Assignment to conditions was random with the exception that all teams were comprised of same-sexed subjects with five all female and five all male groups participating in each condition. Sex of subjects was a counterbalanced variable within the present experiment rather than a separately considered independent variable due to time and resource limitations.

Research Design. The research design was representative of a 4 x 3 factorial design with repeated measures on the second factor. The first, between subjects factor, represented the four communication conditions (no link, computer link, audio link, television link). The second, within subjects factor, represented the three consecutive 10 minute phases of the game situation that gradually increased situation complexity.

Data Reduction and Statistical Analyses. There were two levels of data analyses performed. The first level used groups (composed of four individuals divided into two teams) as the unit of analysis. This level of analysis was used to examine the effect of

communication media condition upon overall group cohesiveness, positive social feelings, group leadership emergence, subjective estimates of workload and overall group member satisfaction. Individual scores on the Likert-type items assessing these social dimensions of the post experimental questionnaire were computed and aggregated into group scores. There were 10 group scores per communication condition for each of these dependent variables, except for occasional missing data due to subjects skipping one or two items. These group scores were submitted to a series of one-way analyses of variance that treated communication media as a between group factor. Retrospective estimates of workload were measured for each of the three phases of the experimental game and were submitted to a two-way analysis of variance that assessed the impact of both communication media and event complexity.

Outcome variables were also assessed at the group level. An index of team resource allocation effectiveness was computed by summing the total intensity values of events showing on each team's city map for each 5 second update during each of the three phases of the game situation. A measure of average response latency was also taken as an indirect measure of processing time needed to reach a decision within each game phase. This was computed by counting the number of 5 second update periods event icons were left flashing red without a team response. The effectiveness and latency group scores were calculated from data stored by the computer game software on floppy disks for each game session. Average group scores were submitted to separate two-way analyses of variance that assessed the independent and interactive effects of media conditions and situation complexity. An additional group pattern recognition score, derived from post-experimental reports of strategies used in evaluating events and assigning resources was also submitted to a one-way ANOVA.

The second level of analyses used individual team members as the unit of analysis. The frequency and duration of each team member's vocal activity was computed from ratings of videotapes of each experimental session. The proportion of time each person spoke was correlated with individual responses to the post experimental questionnaire items to determine the relationship of this variables to leadership ratings. The amount of time each team spent communicating with a remote team was estimated from examination of computer logs that indicated the presence or absence of a closed communication switch during each five second update during the game. Examination of computer printouts of typed messages provided the same information within the keyboard messaging group. The content of individual inter-team messages was also sampled from videotapes and computer printouts of team-to-team communications. All messages were sorted into task related versus socio-emotional related communications. Group averages of total time, frequency, as well as content category scores, were submitted to two way analyses of variance to determine the main and interactive effects of communication media and situation complexity upon these variables. The distribution of talking frequencies within each group was also examined within one way analyses of variance to determine the effects of communication media upon homogeneity of group communication.

All statistical analyses were performed using a standard statistical package (MacSS from StatSoft, Tulsa, Oklahoma) that ran on a Macintosh+ computer.

III. Hypotheses and Results

Based upon a review of the theoretical and empirical literatures presented at the beginning of this report, a representative series of hypotheses were made together with the statistical methods proposed for their test. Hypotheses and obtained results are grouped according to their relationship to group processes and anticipated task outcomes. Group processes were emphasized over outcomes because of their generalizability to many other settings and their role in mediating outcomes.

1. Expected and Obtained Group Process Effects

A. Duration and frequency of messages exchanged between teams was expected to increase as communication bandwidth increased and as event complexity increased.

Communication opportunity was expected to drive actual communication; uncertainty created by increased event complexity was expected to increase demand for sharing information between teams. A two-way analysis of variance performed upon group message frequency and duration scores was expected to yield significant main effects for both communication media and time block (event complexity). A significant interaction effect between these two variables was also expected, however, the precise form of this interaction effect was a matter of speculation. One expectation was that information overload factors would curtail increased communication at the highest communication bandwidths when event complexity was also high.

Two measures of inter-team communication were analyzed. The first measure was derived from game computer logs that included counts of the number of five second intervals each team's hand operated audio switch was engaged. This switch had to be engaged by one or the other teams in order to verbally communicate in either the audio or two-way TV conditions. A parallel measure of the number of five second intervals each team spent typing messages was derived from time stamped computer logs of all messages within the keyboard messaging condition. The second measure considered the number of messages sent between teams and will be described later in this section.

A two-way analysis of variance (ANOVA) that included the four communication media conditions and three time blocks as independent factors, was performed upon time estimates of inter-team communication. Results of the ANOVA yielded a significant main effect for media condition ($F=7.52$, $df=3,36$, $p<.001$), a significant main effect for time block ($F=15.67$, $df=2,72$, $p<.001$) and a significant interaction effect between media and time block ($F=2.34$, $df=6,72$, $p<.05$).

While the pattern of significant effects found in the ANOVA was consistent with predictions, an examination of means associated with these effects yielded a pattern different from that expected. Thus, the main effect associated with media showed the highest amount of inter-team communication time being spent in the keyboard condition (46.50 time units) followed by the audio (23.33), TV (20.93) and control (0) conditions. The main effect associated with time blocks (complexity) showed an increase in communication time from the first third of the game (14.25 time units) to the second third of the game (32.53) and then a decrease in

communication time during the last third of the game (21.30). This inverted "V" pattern was most pronounced in the audio condition, followed by the keyboard and TV conditions. Of course, the no communication control condition maintained a flat zero communication time contributing to the significant interaction between media and time block.

The second measure of inter-team communication was derived from verbatim transcripts of team-to-team messages obtained from videotapes of the audio and TV communication conditions and from printouts of messages exchanged in the keyboard condition. Due to technical difficulties, two of the audio and one of the TV videotapes were not usable. Therefore only 37 groups were included in this analysis. Individual messages (sentences and phrases bounded by periods of silence) were counted and submitted to a two-way ANOVA identical in design to that used in the communication time analysis.

Results of the ANOVA again showed a significant main effect for media ($F=5.82$, $df=3.33$, $p=.003$) and time block ($F=36.01$, $df=2.66$, $p<.001$) as well as a significant interaction effect between media and time block ($F=8.14$, $df=6.66$, $p<.001$).

Examination of individual means associated with the media main effect showed the largest number of messages being sent in the audio condition (Mean=20.17), followed by the TV (12.96), keyboard (11.30) and control (0) conditions. Means associated with the time block effect showed more messages being transmitted during the second third of the game (Mean=19.04) than the first (5.28) or final (9.00) third of the game. The interaction of media and time block showed the peaking during the middle third of the game to be most pronounced for the audio condition, followed by the TV and keyboard conditions. Of course, the control condition maintained a flat zero message count.

Expectations regarding the duration and frequency of messages exchanged between groups were only partially confirmed. Communication opportunity and event complexity did not drive actual messaging in a simple linear fashion. Groups given a communication link used it to produce more messages than the control group. However, the amount of time it took to send these messages varied inversely with bandwidth (keyboarding took the most time while TV took the least). The audio condition was the wordiest and was the most sensitive to changes in event complexity (it peaked the most during the second time block). The drop off of messages during the final third of the game may have been due to complexity overload or other factors that will be discussed in subsequent sections.

B. The ratio of socio-emotional versus task related messages exchanged between teams was expected to increase as communication bandwidth increased and decrease as event complexity increased. Opportunities for "socializing" with distant group members was expected to increase with the increased physical representation of remote teams. As task demands increased, more attention was expected to be focused on task related information exchange. A two-way analysis of variance performed upon an aggregated group index of socio-emotional/task message frequencies derived from a content analysis of team members' verbal and computer messaging activities was expected to lead to significant main effects for media type and event complexity. As in Hypothesis A, a significant interaction effect between these two variables was also expected, but the precise form of the interaction was not predicted.

The communication transcripts used to test hypotheses regarding the total number of messages exchanged between groups were examined further to determine the task-relevant nature of the messages. Sentences and phrases whose content related directly to the task at hand (e.g., "Send a police unit to Ghettoville" or "We need fire assistance at Oak Woods") were classified as task messages. Those messages referring to the social aspects of the group (e.g., "Let's send out for pizza" or "How are you guys doing?") were classified as socio-emotional messages. Two-way ANOVAs identical in design to those used to test earlier hypotheses were performed upon each of these more refined message measures.

The results of the ANOVA performed upon the number of task related messages counted were almost identical to those found for total messages transmitted. A significant main effect for media ($F=6.23$, $df=3,33$, $p=.002$) showed more task messages transmitted in the audio (Mean=17.00) than TV (10.74) or keyboard (7.70) condition. Of course, no messages were transmitted in the no communication control condition. A significant main effect for time block ($F=35.05$, $df=2,66$, $p<.001$) showed more task related messages transmitted during the second time block (Mean=16.14) than during the first (2.87) or last (7.57) third of the game. Examination of means associated with a significant media by time block interaction effect ($F=7.74$, $df=6,66$, $p<.001$) showed the inverted "V" trend was most pronounced in the audio condition, followed by the TV and the keyboard condition. Of course, the no communication control condition maintained a flat zero message level across all time blocks.

The results of a two-way ANOVA performed upon counts of the number of socio-emotional messages exchanged between groups showed a different trend than that observed for task related messages. A significant main effect for media ($F=4.19$, $df=3,33$, $p=.01$) showed a decrease in the transmission of socio-emotional messages from the keyboard (Mean=3.60) to audio (3.17) to TV (2.22) conditions. A significant main effect for time block ($F=3.58$, $df=2,66$, $p=.03$) showed an increase from the first third of the game (Mean=2.41) to the middle third of the game (2.90) with a decrease occurring during the final third (1.43) of the game. The same trend across time blocks held in each of the media conditions with no significant interaction between media and time blocks observed.

Expectations regarding the use of socio-emotional and task related messages exchanged between teams were not confirmed. Rather than increasing the use of socio emotional messages as media bandwidth increased, there was a tendency to decrease social emotional messages. Both task and socio-emotional messages tended to follow the same inverted "V" pattern of increasing and then decreasing as event complexity increased across time blocks.

C. Subjective estimates of workload were expected to increase as communication bandwidth increased and as event complexity increased. As situation attentional demands increased, subjects' reported estimates of workload were expected to increase. A two-way analysis of variance performed upon subjects' self-reported workload estimates was expected to yield significant main effects for both communication media type and event complexity.

Following the experimental game session, subjects were asked to retrospectively assess their own personal workload during the first, middle and last third of the game on a post-experimental questionnaire. Subjects responded by marking a series of five-point Likert-type items whose response categories were bounded by the phrases "Very Light" and "Very Heavy." A combined team score was computed for each of these three segments of the game by summing across the four individual team member responses to each item.

Team workload scores were submitted to a two-way ANOVA assessing the effects of time blocks and media. Results of the ANOVA showed a significant ($F=216.92$, $df=2,72$, $p<.001$) main effect for time block but no significant or interaction effect associated with media condition. Perceived workload increased steadily from the first third of the game (Mean=3.75) to the middle (8.82) and last (12.88) third of the game, in all media conditions.

Expectations regarding the effect of game manipulations (i.e., increased complexity across time) upon perceived workload were confirmed. However, the expectation that perceived workload would also increase as media bandwidth increased was not confirmed.

D. The proportion of messages initiated by individual group members was expected to be distributed less evenly as communication bandwidth increased. Individual differences in communication style were expected to become more apparent as socio-emotional cues became more available and competition for "floor-time" increased. A one-way analysis of variance conducted upon an index of group communication heterogeneity (variance estimates of distributions) was expected to yield a significant main effect for communication media.

The amount of time each team member spent talking during each game session was derived from videotapes made during each game session. This was accomplished by having two trained observers depress hand held momentary contact switches each time a team member they were observing talked. Each observer was responsible for rating either the two members of the Police-Tow team or the two members of the Fire-Rescue team. The momentary contact switches were connected to an Apple IIe computer that was programmed to calculate the number of five second time intervals each button was depressed during each segment of the game.

The observers rated 34 game sessions. Due to recording difficulties, three videotapes were unavailable from the audio and TV conditions as well as three tapes from the keyboard and control conditions. Two game sessions within each of the four media conditions were re-rated with observers exchanging roles to obtain an estimate of

inter-rater reliability. The Pearson product moment correlation obtained between these two sets of ratings was $r=.96$ ($p<.001$), indicating a high level of inter-rater reliability.

Variance scores were calculated for the distribution of individual talking times observed within each team. These team variance scores were submitted to a one-way ANOVA to determine the effect of media condition. No significant media effect was found.

In order to further explore the effect of communication media upon team talking behavior, individual team member talking times were submitted to a two-way ANOVA that examined the independent effects of individual role position (i.e., Police Dispatcher, Police Advisor, Fire Dispatcher, Fire Advisor) and communication media. The results of the analysis revealed a significant main effect for role position ($F=3.23$, $df=3,90$, $p=.03$) with Police and Fire Advisors (Means=210.59 and 236.96 time units) talking more than Police and Fire Dispatchers (187.80 and 191.96 time units). There was also a tendency for team members who had access to an audio communication channel (i.e., audio and TV media conditions) to talk more than those without an audio channel (i.e., control and keyboard conditions). However, this tendency did not reach statistical significance ($F=1.31$, $df=3,30$, $p=.29$).

Expectations regarding the effect of media upon the distribution of individual talking behavior within groups was not confirmed. Individual talking times were dictated more by role position than by media availability.

E. Leadership rankings were expected to be positively associated with individual message frequencies. Leadership has traditionally been associated with dominance and social influence; this was expected to be reflected in communication behaviors. A Pearson correlation coefficient computed between average leadership rankings and the proportion of messages contributed by individuals within each group was expected to be significantly greater than zero.

Following each game session individual team members were asked to rank themselves and their teammates with regard to the degree of influence each exhibited throughout the game. These rank orderings were summed across team members to yield average leadership scores for each participant within each team. The number of five second intervals each team member was observed talking (calculated in tests of Hypothesis D) was divided by the total amount of talking observed within his or her four person group. This yielded a proportion of talking time score for each team member.

A Pearson product moment correlation was calculated between average leadership scores and the proportion of talking time scores for all groups for which talking data was available (34 groups). The overall correlation was weakly negative ($r= -.16$, $p=.08$) indicating only a modest tendency for persons who talked more to be ranked higher as a leader.

In an attempt to discover what effect role position may have had upon leadership rankings, average leadership scores were submitted to a two-way ANOVA that examined the independent effects of individual role position (i.e., Police Dispatcher,

Police Advisor, Fire Dispatcher, Fire Advisor) and communication media. The results of the analysis revealed a tendency for Police and Fire Dispatchers to be ranked higher than Police and Fire Advisors (Means = 9.05 and 9.03 versus 9.79 and 10.03). However, this tendency did not reach statistical significance ($F=.79$, $df=3,23$, $p=.51$).

The expectation regarding the relationship between leadership ratings and talking time behavior received only weak support. Leadership rankings may have been affected by assigned roles.

F. Feelings of group cohesiveness and liking were expected to increase as communication bandwidth increased. Subjects' reports of "we" feelings were expected to increase as the salience of remote team members increased. One-way analyses of variance performed upon post-experimental reports of cohesiveness and liking were expected to yield significant main effect for communication media.

Following each game session team members were asked to estimate the extent to which the two dispatch centers operated as one large team. Responses were made on a five point Likert-type scale that ranged from "No Team Feeling" to "Strong Team Feeling." Individual responses were summed across team members to yield a group cohesiveness score for each team.

A one-way ANOVA performed upon group cohesiveness scores yielded a significant main effect for media ($F=7.54$, $df=3,32$, $p<.001$). The control condition yielded the lowest cohesiveness score (8.43) followed by the audio (13.00) and TV (13.10) conditions. The greatest degree of "group feeling" was experienced by those exposed to the keyboard condition (15.67).

Individual ratings of the degree of liking for other team members were also assessed post-experimentally. Each team member was asked to indicate how much he or she liked their partner as well as the other team Dispatcher and Advisor using three five point Likert-type scales ranging from "Dislike Very Much" to "Like Very Much." Each team member's ratings of the opposite team's Dispatcher and Advisor was summed. These sums were then added across all four team members to yield a liking index for each team.

A one-way ANOVA performed upon team liking index scores yielded a significant main effect for media ($F=3.52$, $df=3,32$, $p=.02$). The no media control group showed the least amount of liking across teams (Mean=17.43) followed by the audio group (18.60) and the TV group (21.6). The greatest amount of liking for remote team members was in the keyboard condition (22.56).

Expectations regarding the effect of media upon group cohesion and liking were partially confirmed. Providing a communication link between teams increased feelings of cohesion and liking for remote team members. However, narrow bandwidth media (i.e., the keyboard condition) appeared to be more effective in bringing about this effect than broadband media (i.e., the TV condition).

G. Feelings of group member satisfaction were expected to increase with increased communication bandwidth. Opportunities for satisfying socio-emotional as well as task related needs were expected to be higher in the high bandwidth settings. A one-way ANOVA performed upon average group scores of post-experimental satisfaction ratings was expected to yield a significant main effect for communication media.

Two kinds of satisfaction ratings were collected after each game session. The first dealt with the communication link connecting remote teams. Each team member was asked how satisfied they were with the communication link provided. Responses were made using a five point Likert-type scale bounded by the phrases "Completely Dissatisfied" and "Completely Satisfied." The other post-experimental question asked each subject to assess how satisfied they were with their role in the game. Again, a five point scale ranging from "Completely Dissatisfied" to "Completely Satisfied" was used. For each question responses were summed across team members to yield a team index of satisfaction.

A one-way ANOVA performed upon communication satisfaction ratings yielded a significant main effect for media ($F=19.57$, $df=3,34$, $p<.001$). Teams with no communication link were the least satisfied (Mean=9.56). The most satisfied teams were those exposed to the TV communication condition (18.00) followed by the audio condition (15.80) and the keyboard (15.22) condition.

A one-way ANOVA performed upon team members' role satisfaction ratings yielded no significant effects for media ($F=.11$, $df=3,34$, $p=.95$). Team members in each media condition appeared to be equally satisfied with their role in the game (Mean=15.36).

Expectations regarding satisfaction ratings were confirmed regarding media satisfaction, but were not confirmed for role satisfaction. Satisfaction with media increased with the bandwidth of communication, however, role satisfaction remained uniformly high across media conditions.

2. Expected and Obtained Task Outcome Effects

G. Action response latencies were expected to increase as event complexity increased and as communication bandwidth increased. Information processing time was expected to increase, and thus delay action, as the number of information sources needing to be consulted increased. A two-way analysis of variance performed upon an index of average response times within groups was expected to yield significant main effects for communication media and event complexity.

An index of action response latencies was derived from computer logs of team action patterns. One component of the computer log was a count of the number of event icons that were flashing red during any five second update interval. Icons flashed red whenever a team response was needed and stopped flashing as soon as the team touched the icon to gather critical information. Approximately the same number of events were introduced during each third of the game (29 during the first third, 30 during the second and 30 during the last third of the game). The number of five second

time units each icon remained flashing red was computed for both the Police and Fire teams. These numbers were summed within the first, middle and last time blocks of the game for teams exposed to each media condition.

A two-way ANOVA was performed upon the latency index to examine the effects of media event complexity (time block). No significant main or interaction effect was found for media. However, a significant main effect was found for time block ($F=12.97$, $df=2,77$, $p<.001$). The number of time units icons remained flashing increased from the first third of the game (Mean=91.5) to the middle third of the game (115.18) and continued upward to the last third of the game (156.92).

Expectations regarding the effect of event complexity and media upon response latencies were partially confirmed. Increases in event complexity were associated with increased response times. However, increased communication bandwidth had no detectable impact on response latencies.

H. Detection of patterned environmental events were expected to increase with increases in communication bandwidth. Information pooling via communication media was expected to increase the probability of teams discovering the underlying patterns built into the more complex event scenarios. The percentage of teams becoming situationally aware of patterned events was expected to increase from the no communication control, to keyboard, audio and two-way television media conditions.

There was only one underlying pattern of events for teams to discover and that related to emergency events following the movements of the senator in the "Visiting Senator" game scenario. Team members were asked on their post-experimental questionnaires to list three of the most significant emergency events that occurred during their work shift. They were then asked if they perceived any causal connection between these events and if so, what. Teams were scored as "aware" if at least one member correctly reported the connection between the senator's movements and emergency events.

Results of these calculations showed two interesting trends. First, only the Police-Tow teams correctly identified causal events. In none of the media conditions did the Fire-Rescue teams report awareness of the senator connection. Second, the percentage of Police-Tow teams that correctly tied the senator's movements to emergency events increased from the no communication control condition (60%) to the keyboard (70%) and TV (80%) conditions, but decreased for the audio condition (30%).

Expectations regarding the detection of patterned events were not confirmed. Increasing communication bandwidth had no effect on making remote teams cognizant of patterns detected by primary teams. One media type (the audio only condition) appeared to deter primary teams from becoming situationally aware of patterns to which they already had access.

I. Team resource allocation effectiveness was expected to decrease as event complexity increased. This effect was expected to be less apparent as communication bandwidth increased. Simple, unidimensional tasks were expected to be easier to solve than complex, multidimensional tasks. Pooling information resources was expected to increase each team's ability to solve the more complex problem presented by increased event complexity. A two-way analysis of variance performed upon a measure of resource allocation effectiveness was expected to yield a significant main effect for event complexity and a significant two-way interaction effect between complexity and communication media. The exact form of the interaction effect was expected to depend upon a balance of incremental information pooling versus distraction induced by increased communication bandwidth (see Hypotheses A-C).

Teams monitored their own overall effectiveness by attending to a "feedback bar" that appeared at the top of their city maps. The amount of red showing in the feedback bar changed in proportion to the sum of intensity values of ongoing events for which the teams were responsible. As resources were applied to events overall intensity values decreased. A record of these values was available within the computer logs recorded for each game episode. The total intensity values showing for each team was summed for each five second update interval within the three time blocks of the game. These cumulative values were summed across Police-Tow and Fire-Rescue teams and used as an index of overall resource allocation effectiveness.

A two-way ANOVA performed upon team cumulative intensity scores showed a significant main effect for time block ($F=47.08$, $df=2,72$, $p<.001$), but no significant main or interaction effect associated with media. Intensity scores increased with event complexity from the first third of the game (Mean=5261.58) to the middle third (8770.05) to the last third (24505.45) of the game.

An alternative index of team effectiveness was the number of events each team allowed to "get out of control" (reach a maximum value of 99). This information was recoverable from the computer logs of each game session. A two-way ANOVA was performed upon the total number of events that reached a maximum intensity of 99 during each time block. Results of the ANOVA showed a significant main effect for time block ($F=21.19$, $df=2,72$, $p<.001$), but no significant main or interaction effects for communication media. More events went out of control as events became more complex. The average number of out of control events increased from the first third of the game (Mean=0.0) to the middle third (.02) to the last third (1.72) of the game.

Expectations regarding team resource allocation effectiveness were confirmed for the effect of event complexity, but not confirmed for the anticipated effect of media. The total intensity of events increased across time blocks as did the number of events that went out of control. This pattern remained the same across all media conditions.

IV. Discussion, Insights and Lessons Learned

The results of the first experiment using the C.I.T.I.E.S game has made salient the diversity of behavioral effects that can be related to telecommunication media. The results also suggest that current models used to predict media differences are not yet sophisticated enough to capture the complexity of these effects. Thus, despite the large number of differences observed between media conditions regarding various group process effects (e.g., time spent communicating, number and type of messages exchanged, liking and feelings of group cohesiveness), no significant differences were found between media conditions regarding task effectiveness.

These results appear to be understandable only by considering a number of situational factors in addition to the traditional theoretical concepts already reviewed. For example, it was found that more time was spent communicating with remote teams when narrow bandwidth communication links were used as compared to broad bandwidth links. However, it was also observed that fewer messages were actually sent in the narrow band media conditions compared to the broadband conditions. This paradox was probably due to the extra time needed by teams to type messages in the keyboard condition compared to simply speaking in the audio and TV conditions.

A more subtle effect seemed to underlie the additional finding that more messages were sent in the audio condition than in the TV or keyboard conditions. After reviewing a number of videotaped game sessions, it appeared that when events transpired that required a remote team's attention, there was a tendency within the audio group to simply blurt out a message. On the other hand, TV groups were more likely to look up at the remote team on their monitor *before* deciding to interrupt them. This may have curtailed the number of messages sent in the TV condition. Perhaps because of the energy required to type messages, the keyboard condition remained the most conservative in message generation and thus appeared to be more "sluggish" in response to increases in situational complexity.

Rather than communication volume being driven simply by channel availability as originally predicted, it would appear that each kind of media carries with it a unique set of constraints dictated by physical limitations of input (e.g., typing rather than talking) as well as rules of procedure (e.g., not interrupting when the other team appears busy). The implicit assumption that channel capacity will be fully utilized simply because it is made available also appears faulty. The finding that communication time and number of messages exchanged between teams decreased during the final, highest workload segment of the game suggests that teams were more concerned with immediately responding to events within their jurisdiction rather than gathering additional information from remote team members.

Perhaps the cost of communication has been underemphasized. While many benefits can be gained by exchanging information with remote team members, the act of communicating takes time. Under high workload conditions a communication intrusion by a remote team member may be viewed negatively. This may help explain why teams who were linked via a computer messaging system liked each other more than those linked via an audio or TV system. In reviewing the videotaped game segments it became apparent that several teams that had access to an audio link became agitated

when a remote team would insist they send unavailable resources to an area. The audio link was immediate and demanding. On the other hand, teams responding to written messages on a television monitor could choose to ignore any message without risking additional harassment.

The cost of communicating concept may also help explain why awareness of patterned events was lowest within the media condition exhibiting the greatest number of inter-team messages. Only about one third of the teams in the audio condition reported awareness of the connection between the senator's movements and emergency events. This was in contrast to the 70 to 80 percent awareness in the other media conditions and 60 percent awareness in the no communication control condition. Perhaps those teams in the audio condition spent too much time talking and not enough time reflecting upon the events in front of them.

Several other personal misconceptions became apparent after analyzing the results of the present experiment. First, the idea that "keyboarding" represents a stiff, formal medium of communication turned out to be in error. While it took longer to communicate and fewer total messages were transmitted between teams over the keyboard medium, a higher percentage of socio-emotional messages were exchanged using this medium. Kiesler, Siegel & McGuire have discussed the possible disinhibiting effects of communicating over electronic mail systems. Perhaps there is also a compensatory effect whereby more social-emotional messages are transmitted to make up for missing nonverbal channels. While broadband media was preferred over narrowband media in subjects' communication satisfaction ratings, this apparently had no effect on their overall role satisfaction ratings or workload estimates.

Second, the idea that increased talking would necessarily be associated with increased influence and emergent leadership was probably misdirected given a setting where role requirements isolated communication behavior from other task activities. Thus, Dispatchers were assigned the task of making the actual game moves within the C.I.T.I.E.S. task while Advisors were assigned the role of communicating with remote team members. Analyses of individual team member behaviors showed that Advisors tended to talk proportionately more than Dispatchers. Examination of means associated with leadership rankings showed Dispatchers to be ranked higher than Advisors. In making leadership rankings, team members probably reflected upon who had the role of actually moving resources (Dispatchers) as well as who talked the most. Thus, it is not surprising that only a weak correlation was found between talking behavior and leadership. The tendency for Advisors to follow the role requirement of talking more than Dispatchers probably also contributed to the finding of no significant differences in team talking distributions (variances) between media conditions.

The finding that media had no significant effect on team resource allocation effectiveness was unexpected. However, this finding may be understood in terms of the game parameters selected, the use of media by teams as well as the role behaviors adopted by team members. Thus, the "Visiting Senator" scenario used in the C.I.T.I.E.S. game assumed that teams would share uniquely held information. It was expected that the Police-Tow team would share information they had regarding the senator's itinerary with the Fire-Rescue team. Sharing this information would have

helped the Fire-Rescue team anticipate trouble before it happened. This sharing did not occur. Only in one or two instances did the Police-Tow team even mention the movement of the senator to the Fire-Rescue team. Instead, communication links were used primarily to ask for assistance when events became more difficult. Many teams did not begin to communicate with their remote partners until they became aware of events during the middle of the game that required both teams' attention to resolve.

In the end none of the Fire-Rescue teams reported awareness of the correlation between the senator's movements and emergency events. They were unaware because critical information regarding the senator's movements was not made available to them by their remote team partners. Without this information anticipatory movement of resources was not possible for the Fire-Rescue teams and any game advantage was lost.

In attempting to understand why sharing of critical information did not occur, videotapes of the game sequences were reviewed. For many of the teams it became obvious that the assigned role of Advisor took on additional meaning to subjects than originally intended. Rather than passively observing events being handled by the Dispatcher and communicating with the other team, many Advisors "micro-managed" the Dispatcher to whom they were assigned. The focus of attention within teams was upon the events that occurred within their own jurisdiction. With both Dispatcher and Advisor focusing in on the details of the moment, there was little time for the Advisor to "pull back" and observe the "big picture" that incorporated the other team.

Teams were not motivated to establish an information baseline with their remote partners. Instead, they were more inclined to view the other team as a resource upon which to call in times of emergency. The extent to which this egocentric tendency occurs in actual field operations is not known. However, future studies using the C.I.T.I.E.S. game will take note of this tendency and establish alternative procedures for the Advisor's role.

One change will be the introduction of several "briefings" to be conducted by team advisors at various points throughout the game. This will force a temporary refocusing of attention to summarize the team's status for the remote team and open up the possibility of a "big picture" being formed. A second change will be the introduction of a second workstation at each Dispatch center to allow the Advisor access to information without interrupting the team Dispatcher.

V. Conclusions and Recommendations

The present effort has been a productive enterprise. The development of the C.I.T.I.E.S. task represents a major contribution to the tools available to researchers interested in studying situation awareness and distributed decision making. Advances have also been made in developing technologies used to upgrade the Interactive Television Laboratory. The design and execution of the comparative media study provided new insights into media differences that can be used to reformulate existing media concepts.

In attempting to codify the major findings of the present effort, the following list of conclusions and recommendations is offered.

1. Unidimensional models of media differences that structure media on a dimension of psychological closeness are unable to account for the complex pattern of group process effects observed in the present study.
2. Knowledge of media mechanics (input and output characteristics) should be taken into account when predicting media usage patterns.
3. Increasing communication bandwidth does not guarantee increased sharing of information between remotely located groups.
4. Communication links with remotely located groups can detract as well as enhance team situation awareness.
5. Computer messaging can be as effective as audio or television communication in bringing about feelings of group cohesion and liking between remotely located groups.
6. Computer messaging can promote the use of socio-emotional messages exchanged between groups.
7. Audio communication tends to facilitate the generation of messages between groups.
8. Future models of communication networking should take into account a balanced view of the benefits and liabilities associated with communicating in predicting optimal media-task combinations.
9. Future experiments should include some consideration of enhancing effective media usage. Procedures and training may be as important as media channel capacity in optimizing information transfer and integration.

VI. References

- Asch, S. (1951). Effects of group pressure upon the modification and distortion of judgment. In H. Guetzkow (Ed.), Groups, leadership and men. Pittsburgh, PA: Carnegie Press.
- Baker, E. (1982). Some psychological variables in visually augmented teleconferencing. IEEE Global Telecommunication Conference Record, 3, 971-975.
- Bales, R. F. (1950). Interaction process analysis: A method for the study of small groups. Cambridge, MA: Addison-Wesley.
- Ben-Bassat, M., & Freedy, A. (1982). Knowledge requirements and management in expert decision support systems for (military) situation assessment. IEEE Transactions on Systems, Man and Cybernetics, 12, 479-490.
- Brandstatter, H. (1982). Recent research on group decision making. In H. Brandstatter, J. Davis & G. Stocker-Kreichgauer (Eds.), Group decision making. New York: Academic Press.
- Callaway, M., & Esser, J. (1984). Groupthink: Effects of cohesiveness and problem-solving procedures on group decision making. Social Behavior and Personality, 12, 157-164.
- Connors, M., Harrison, A., & Akins, F. (1985). Living aloft: Human requirements for extended spaceflight. Washington, DC: National Aeronautics and Space Administration.
- Dompere, K. (1982). The theory of fuzzy decisions. In M. Gupta & E. Sanchez (Eds.), Approximate reasoning in decision analysis. New York: North-Holland.
- Dyer, J. L. (1984). Team research and team training: A states-of-the-art review. In F. Muckler (Ed.), Human factors review: 1984. Santa Monica, CA: The Human Factors Society.
- Ergener, D., & Wellens, A. R. (1985). A split-screen electronic messaging system for Apple II computers. Behavior Research Methods, Instruments & Computers, 17, 556-564.
- Festinger, L. (1954). A theory of social comparison processes. Human Relations, 7, 117-140.
- Janis, I. (1972). Victims of groupthink. Boston: Houghton Mifflin.
- Johansen, R., Vallee, J., & Collins, K. (1978). Learning the limits of teleconferencing. In M. Elton, W. Lucas & D. Conrath (Eds.), Evaluating new telecommunication systems. New York: Plenum.

- Kaplan, K. (1977). Structure and process in interpersonal "distancing." Environmental Psychology and Nonverbal Behavior, 1, 17-29.
- Kiesler, S., Siegel, J., & McGuire, T. (1984). Social psychological aspects of computer-mediated communication. American Psychologist, 39, 1123-1134.
- Kiesler, S., Zubrow, D., Moses, A., & Geller, V. (1985). Affect in computer-mediated communication: An experiment in synchronous terminal-to-terminal discussion. Human-Computer Interaction, 1, 77-104.
- Korzenny, F. (1978). A theory of electronic propinquity: Mediated communication in organizations. Communication Research, 5, 3-23.
- Laughlin, P. R. (1980). Social combination processes of cooperative problem-solving groups on verbal intellectual tasks. In M. Fishbein (Ed.), Progress in social psychology, Vol. 1. Hillsdale, NJ: Erlbaum.
- Leavitt, H. J. (1951). Some effects of certain communication patterns on group performance. Journal of Abnormal and Social Psychology, 46, 38-50.
- McGrath, J. E. (1984). Groups: Interaction and performance. Englewood Cliffs, NJ: Prentice-Hall.
- Milgram, S. (1965). Some conditions of obedience and disobedience to authority. Human Relations, 18, 57-75.
- Murrell, S. (1984). Computer communication systems design affects group performance. Proceedings of the 7th International Conference on Computer Communication, 30 Oct. - 2 Nov., Sydney, Australia.
- Stasser, G., & Titus, W. (1985). Pooling of unshared information in group decision making: Biased information sampling during discussion. Journal of Personality and Social Psychology, 48, 1467-1478.
- Stoner, J. F. (1961). A comparison of individual and group decisions involving risk. Unpublished masters thesis, Massachusetts Institute of Technology. (Cited in Wallack, M., Kogan, W., & Bem, D. (1962). Group influence in individual risk. Journal of Abnormal and Social Psychology, 65, 75-86.)
- Shaw, M. E. (1964). Communication networks. In L. Berkowitz (Ed.), Advances in Experimental Social Psychology, Vol. 1, 111-147.
- Swap, W. (Ed.). (1984). Group decision making. Beverly Hills: Sage.
- Tribus, M. (1969). Rational descriptions, decisions, and design. New York: Pergamon Press.

- Wellens, A. R. (1978). A device that provides an eye-to-eye video perspective for interactive television. Behavior Research Methods and Instrumentation, 10, 25-26.
- Wellens, A. R. (1979). An interactive television laboratory for the study of social interaction. Journal of Nonverbal Behavior, 4, 119-122.
- Wellens, A. R. (1982). Applying computerized interactive video technology to nonverbal communication research. Journal of Nonverbal Behavior, 7, 121-123.
- Wellens, A. R. (1986). Use of a psychological distancing model to assess differences in telecommunication media. In L. Parker & C. Olgren (Eds.), Teleconferencing and electronic media, Vol. V. Madison, Wisconsin: Center for Interactive Programs, University of Wisconsin.
- Wellens, A. R., & Ergener, D. (in press). An improved videomultiplexer for behavioral research. Behavior Research Methods, Instruments and Computers.
- Wohl, J. G. (1985). Subtask 4 report "Build a top-level concept" for AW/AA proactive integration and assessment. (SP-491, Contract Number BOA-11-860015-39 Task 1.) Burlington, MA: Alphatech, Inc.

Appendices can be obtained from
Universal Energy Systems, Inc.

FINAL REPORT NUMBER 88
REPORT NOT RECEIVED IN TIME
WILL BE PROVIDED WHEN AVAILABLE
Dr. Stephen Welstead
760-6MG-063

1987 USAF-UES RESEARCH INITIATION PROGRAM

Sponsored by the

AIR FORCE OFFICE OF SCIENTIFIC RESEARCH

Conducted by the

UNIVERSAL ENERGY SYSTEMS, INC.

FINAL REPORT

CAN A SUPERVISORY CONTROL SIMULATION SYSTEM

ASSESS COGNITIVE ABILITIES?

Prepared by:	Shih-sung Wen
Academic Rank:	Professor of Psychology
Department & University:	Department of Psychology Jackson State University
USAF Researcher:	John C. Patterson SAM/NGN, Brooks AFB, TX
Date:	December, 1987
Contract Number:	F49620-85-C-0013

CAN A SUPERVISORY CONTROL SIMULATION SYSTEM
ASSESS COGNITIVE ABILITIES?

BY

SHIH-SUNG WEN

ABSTRACT

The present study intended to investigate the ability of the NASA-Ames Supervisory Control Simulation (SCS) to measure general intelligence (as measured by Wechsler Adult Intelligence Scale - Revised) and visuospatial ability (as measured by Halstead Category Test) of college Undergraduates. The results showed (a) under the staggered SCS condition, significant positive correlations between the number of task elements performed and the scaled score of Information, Vocabulary, and the Verbal IQ of WAIS-R and (b) under the massed SCS condition, significant negative correlations between the total score achieved and the Verbal IQ, the number of task elements performed and the scaled score of Comprehension, the number of performance hits and the scaled score of Arithmetic, the number of performance hit and the scaled score of Block Design, and a positive correlation between the number of tasks selected and the Verval IQ. The SCS, however, failed to covariate with Performance IQ, Full Scale IQ and the HCT measure.

ACKNOWLEDGEMENTS

This research was supported by the Air Force System command, Air Force Office of Scientific Research through the Research Initiation Program of Universal Energy Systems, Inc. Thanks are due to Dr. John C. Patterson of the Psychology Division at the School of Aerospace Medicine, Brooks AFB, for providing the software needed for the present study.

CAN A SUPERVISORY CONTROL SIMULATION SYSTEM ASSESS COGNITIVE ABILITIES?

I. Introduction

Recent advancement in avionic technology has altered a great deal of the traditional man-machine relationship in cockpit. The highly sophisticated computers and intelligent software systems in the aircraft⁶ are able to assume control and monitoring of a routine flight, handle repetitive tasks, and automatically diagnose and correct mechanical errors. The achievement in automation has drastically reduced psychomotor or physical task demands on piloting (Hart & Sheridan, 1984). Demands on cognitive skills, on the other hand, have greatly increased and become a major concern for a pilot.

Currently, few instruments are available to measure the type of cognitive processes required in the cockpit environment (Hart & Sheridan, 1984; Wen, 1985; Wierwille, Rahimi, & Casali, 1985). In their effort to introduce a new, comprehensive workload assessment instrument, Hart and her associates (1984) developed a Supervisory Control simulation System (SCS). The system combines workload-sensitive multiple tasks, includes time pressures on performance, varies task difficulty levels, requires decision making in forming or choosing task strategies, allows dynamic interactions to occur between the subject and tasks, and obtain subjective ratings of mental workload. The SCS has initially proven to be successful in

differentiating type A and Type B behaviors (Hart, et al, 1985). Other capabilities of the SCS to measure cognitive abilities, however, remain to be attested. In his recent review of the avionic workload assessment techniques, Wen (1985) suggested that some important cognitive abilities could be identified by the NASA-Ames SCS developed by Hart & her associates.

II. Purpose of the Research

The present research attempted to investigate some selected cognitive correlates of the SCS performance of college undergraduates. The criterion measures were general intellectual abilities (as measured by the Wechsler Adult Intelligence Scale - Revised) and a visuospatial skill (as measured by the Halstead Category Test).

III. Method

Subjects

Subjects were college undergraduates enrolled in the Honors section of General Psychology classes. Of 31 subjects selected 12 were male and 19 were female. The average age was 18.9.

Tests

Wechsler Adult Intelligence Scale - Revised (Wechsler, 1981). The revised WAIS is to measure an adult's general intellectual skills in terms of the purposefulness, rationality, and adaptability of behavior. Of eleven subtests, Information (INF), Digit Span (DSP), Vocabulary (VOC), Arithmetic (ARI), Comprehension (COM), and

Similarities(SIM) are classified as verbal, while Picture Completion (PCO), Picture Arrangement (PAR), Block Design (BDE), Object Assembly (OAS), and Digit Symbol (DSY) are classified as performance. The scale yields Verbal IQ, Performance IQ, and Full IQ. It has been the most frequently administered individual adult intelligence scale.

Halstead Category Test - A Computer Version (Hill & McLeod, 1984) is a computer administered adult category test. The test was originally developed by Halstead (1947) to measure an individual's capacity to deduce general principles from the presented graphic displays. The test also measure problem-solving, hypothesis generation and modification, and the ability to profit from experience. The computer version was shown compatible with the original test (DeFilipis & McCampbell, 1979).

Instrument

The SCS system is a real time, interactive, multifunction display system of tasks in which certain activities take place that need to be monitored and performed. The simulation system was programmed on an enhanced IBM PC-AT hardware with a 12- inch graphic color monitor. A visual mouse system is plugged into a RS232 port to manipulate the task functions on the computer screen.

Simulation Tasks

The SCS is performed through a game like graphic display consisting of five different boxes of task elements

(represented by the symbol of *, +, -, ‡, and =) and of thirteen function keys to manipulate boxes and task elements (See Figure 1 below).

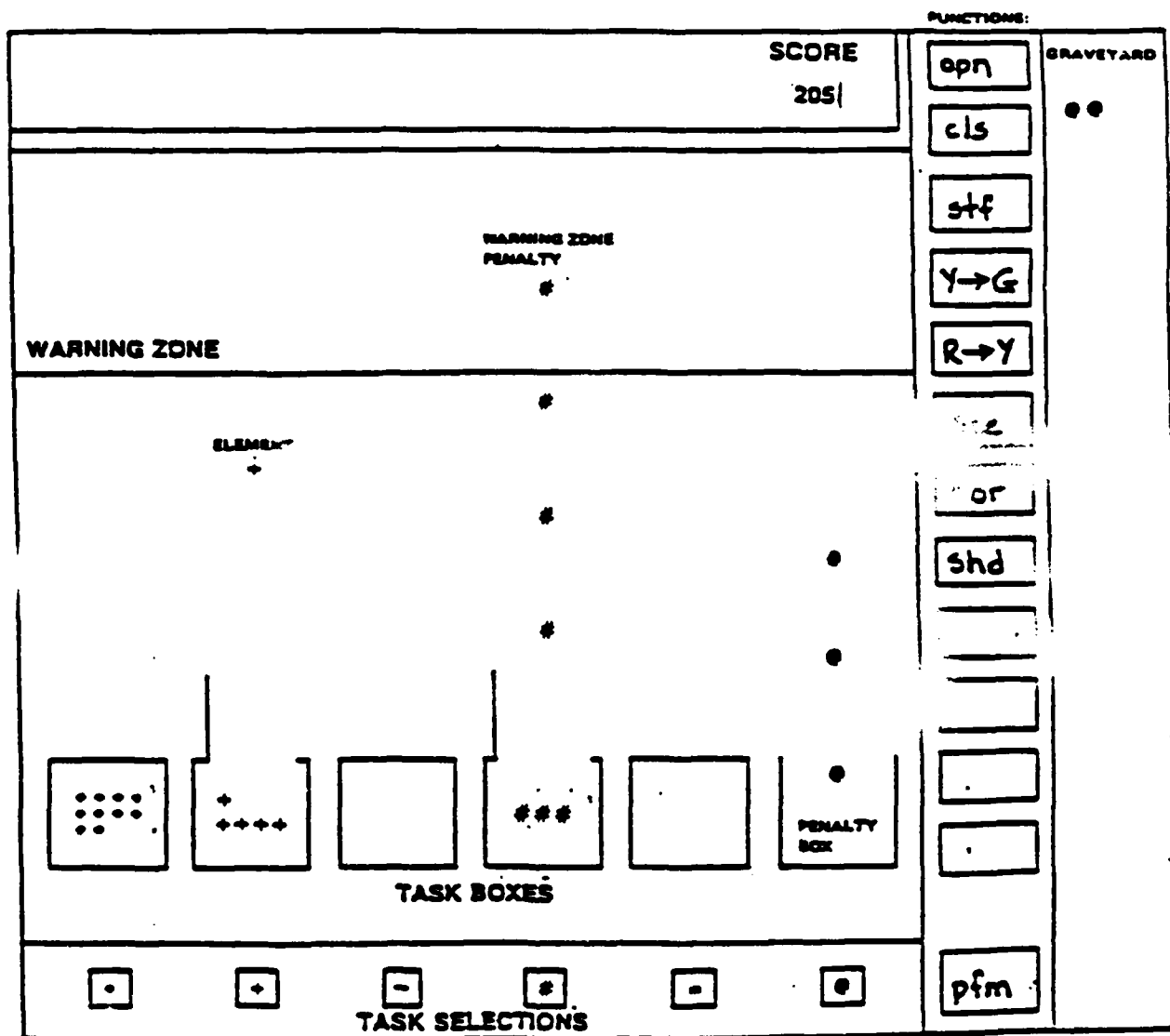


Figure 1. SCS Task, Elements, and Functions on the CRT

Each subject's task is to select, monitor, and perform the rule-guided semi-automatic tasks by achieving the maximum score with a minimum penalty. For example, when a task key and a function key (e.g. OPEN) are sequentially pointed by and clicked (hence called selection) by an arrow cursor with a mouse control device, the box will open for task elements to exit in successive order. The up-moving task elements soon need to be removed by selecting performance (PFM) key as a hit before they reach the warning zone. A performance hit of each task element is awarded by five (5) points. On the other hand, when a task element passes through the warning zone and then enters the graveyard, a penalty of five (5) points will be imposed for each element. Task elements remain in the box will mill around with increasing speed.

Two scenarios were designed for the present study. Scenario FLYA presents five tasks in sequence (staggered) while FLYB presents all five tasks simultaneously (massed). The initial rate and the acceleration rate of element milling and traveling in both scenarios are identical across tasks.

Procedure

Administrations of the WAIS-R, the HCT, and the SCS for subjects were counterbalanced to avoid any systematic sequential effect. Each subject was informed

about the purpose of the study and the activities required for the study. The WAIS-R was administered by this researcher in a quiet room. The HCT and the SCS were administered in a human research laboratory with the computer and the appropriate softwares. For the SCS simulation tasks, each subject was allowed 30 minutes to practice after a 15-minute session of task demonstrations, explanations, questionings, and clarifications. Each task scenarios was 400 seconds long. For the HCT, the instruction was given on the screen for the subject to follow. It was totally computerized. The results of both SCS and HCT were automatically recorded and saved on the hard disk in the computer.

The key measures of the SCS are total score achieved (SC), the number of tasks selected (TS), the number of task elements performed (EP), and the number of performance hits (PH). The HCT measure was represented by the total number of errors made across the seven subtests. The WAIS-R measure consisted of six verbal subscale scores, five performance subscale scores, a verbal IQ, a performance IQ, and a full scale IQ.

IV. Results

The means and standard deviations of all measures are presented in Table 1. The correlation coefficients between

- - - - -
Insert Tables 1 and 2 about here
- - - - -

some selected SCS measures and the mental ability measures are presented in Table 2. The result showed that, under the sequential task presentation (staggered SCS condition), there were significant positive correlations between the number of task elements performed and the scaled score of Information ($r = .45$, $p < .05$), Vocabulary ($r = .43$, $p < .05$), and the Verbal IQ ($r = .43$, $p < .05$) of the WAIS-R.

The data also indicated that, under the simultaneous task presentation (massed SCS condition), there were significant negative correlations between the total score achieved and the Verbal IQ ($r = -.42$, $p < .05$), the number of elements performed and the scaled score of Comprehension ($r = -.43$, $p < .05$), the number of performance hits and the scaled score of Arithmetic ($r = -.47$, $p < .01$), and the number of performance hits (PH) and the scaled score of Block Design ($r = -.43$, $p < .05$). Under the same condition, however, there was a significant positive correlation ($r = .45$, $p < .05$) between the number of tasks selected and the Verbal IQ (VIQ).

In summary, the data collected for the present study partially validated the NASA-Ames Supervisory Control Simulation. When SCS tasks were sequentially presented under the staggered condition) for subjects to perform, the task performance correlated with Verbal IQ. However, when SCS tasks were simultaneously presented (under the massed condition) for subjects to perform, the task performance was mostly negatively related to Verbal IQ.

V. Discussion

Recent research has attempted to associate general intelligence with information processing. In general, there is a negative correlation between the information processing speed (such as reaction time and inspection time) and general intelligence (Barrett, Eysenck, & Lucking, 1986; Brand & Deary, 1982; Jensen, 1980). However, the relationship between the two is rather complex (Cerella, Dicara, Williams, & Bowles, 1986; Mackenzie & Bingham, 1985).

The present study provided more information regarding the relationship between the two dimensions. The NASA-Ames Supervisory Control Simulation data confirmed that facility in monitoring multiple inputs covaries with abstract intelligence (Jensen, 1980). In addition, the two SCS conditions, staggered and massed, created relatively different Time X Task pressures. Consequently, the direction of correlations between the SCS and the WAIS-R differ significantly. Under the staggered condition, the task elements were presented in a stable and sequential manner so that subjects were able to perform the tasks in relatively predictable ways. As a result, with a mild time pressure, the correlations between the SCS and the WAIS-R were mostly positive with only a few exceptions. Under the massed condition, however, subjects had to face and perform the simultaneously presented multiple tasks.

Thus, a time pressure was created. An increase in mis-hits from 19.7 for FLYA to 27.4 for FLYB is an indication of time pressure on subjects. Correlations between the SCS and the WAIS-R under this condition clearly demonstrated the negative effect of time pressure on task performance as generally observed.

One advantage of using the SCS to measure some aspects of general intelligence is that, with variations of task scenarios, it could identify aspects of intelligence that are not functioning well under time pressure. In the present study, for example, the abilities measured by Arithmetic, Comprehension, and Block Design subscales were negatively associated with the time pressure imposed by the massed task monitoring condition.

REFERENCE

- Barrett, P., Eysenck., & Lucking, S. (1986). Reaction time and intelligence: A replicated study. Intelligence, 10, 9-40.
- Brand, C. R., & Deary, I. J. (1982). Intelligence and "inspection time." In H> J> Eysenck (Ed.), A model for intelligence (pp. 133-148). New York: Springer.
- Cerella, J., DiCara, R., Williams, D., & Bowles, N. (1986). Relation between information processing and intelligence in elderly adults. Intelligence, 10, 75-91.
- DeFilipis, N. A., & McCampbell, E. (1979). The booklet category test. Psychological Assessment Resources.
- Halstead, W. C. (1947). Brain and intelligence. Chicago: University of Chicago Press.
- Hart, S. G., & Sheridan, T. B. (1984). Pilot workload, performance, and aircraft control automation. In R. T. Hennesy (Ed.), Human factor considerations in high performance aircraft. AGARD-CP-371.
- Hart, S. G., Battiste, V., & Lester, P. T. (1984). POPCORN: A supervisory control simulation for workload and performance research. 20th Annual Conference on Manual Control. Sunnyvale, CA.

- Hart, S. G., Battiste, V., Chesney, M., Ward, M., & McElroy, M. (1985). Comparison of workload, performance, and physiological measures: Type A personalities vs Type B. Unpublished manuscript.
- Hill, M., & McLeod, N. (1984). Halstead category test: A computer version. Jacksonville, FL: Precision People.
- Jensen, A. R. (1980). Bias in mental testing. New York: Macmillan.
- Mackenzie, B., & Bingham, E. (1985). IQ, inspection time, and response strategies in a university population. Australian Journal of Psychology, 37, 257-268.
- Wechsler, D. (1981). Wechsler adult intelligence scale - Revised. New York: Psychological Corporation.
- Wen, S. S. (1985). POPCORN as a tool for future cognitive workload assessment: A conceptual analysis. 1985 USAF-UES Summer Faculty Research Program, Final Report. Universal Energy System, Inc., Dayton, OH.
- Wierwille, W. W., Rahimi, M., & Casali, J. G., (1985). Evaluation of 16 measures of mental workload using a simulated flight task emphasizing mediational activity. Human Factors, 27, 489-502.

TABLE 1. Means and SDs of SCS, HCT, and WAIS-R

Variables		Mean	SD
<u>SCS</u>	FLYA - Score (SC)	395.00	110.45
	Tasks selected (TS)	28.14	7.29
	Elements performed (EP)	138.57	16.22
	Performance hits (PH)	158.28	15.46
	FLYB - Score (SC)	305.00	107.55
	Tasks slected (TS)	30.57	10.71
	Elements performed (EP)	117.71	19.91
	Performance hits (PH)	145.14	17.89
<u>HCT</u>	Errors (ER)	47.86	11.24
<u>WAIS-R</u>	Information (INF)	11.71	1.98
	Digit Span (DSP)	11.64	1.80
	Vocabulary (VOC)	11.29	2.14
	Arithmetic (ARI)	11.00	2.31
	Comprehension (COM)	14.14	2.91
	Similarities (SIM)	12.71	2.75
	Picture Completion (PCO)	9.14	2.73
	Picture Arrangement (PAR)	10.43	1.99
	Block Design (BDE)	10.54	1.72
	Object Assembly (OAS)	10.38	2.51
	Digit Symbol (DSY)	11.05	2.11
	Verbal IQ (VIQ)	111.35	10.21
	Performance IQ (PIQ)	102.43	12.23
	Full Scale IQ (FIQ)	107.86	11.02

TABLE 2. Correlations between SCS and HCT, WAIS-R

Variables	FLYA				FLYB			
	SC	TS	EP	PH	SC	TS	EP	PH
HCT Errors	-06 ^a	-25	-32	-31	21	-36	31	32
WAIS-R INF	10	34	45*	40	-33	40	-37	-28
DSP	-07	38	31	29	-21	26	-15	13
VOC	07	11	43*	41	-34	21	-30	-24
ARI	29	08	15	04	-16	-22	-31	-47**
COM	06	22	29	24	-35	37	-43*	-30
SIM	10	32	34	30	-24	40	-36	-33
PCO	17	-15	-23	-27	12	-08	-02	-18
PAR	17	-07	-09	-20	-05	10	-07	-33
BDE	31	02	02	-03	07	07	-17	-43*
OAS	17	-09	02	12	24	-31	02	04
DSY	06	-18	-26	-18	35	-41	21	25
VIQ	02	28	43*	37	-42*	45*	-40	-30
PIQ	15	-23	-25	-21	25	-25	06	09
FIQ	14	06	20	18	-21	22	-35	-39

a: The decimal point is removed.

* $p < .05$, ** $p < .01$.

1986 USAF-UES MINI-GRANT FOLLOW-ON TO SUMMER
FACULTY RESEARCH PROGRAM

Sponsored by the
AIR FORCE OFFICE OF SCIENTIFIC RESEARCH
BOLLING AFB, DC

Conducted by the
Universal Energy Systems, Inc.

FINAL REPORT

Effects on the BICFET of the Fermi Distribution
Factor and the Al Mole Fraction

Prepared by:	Dennis Whitson
Academic Rank:	Full Professor
Department:	Physics
University:	Indiana University of Pennsylvania (IUP)
Research Location:	IUP
USAF Researcher:	Gary McCoy and Chern Huang
Date:	Oct. 1, 1987
Contract No.:	F49620-85-C-0013/SB581-0360

ACKNOWLEDGMENTS

The author would like to thank the Air Force Office of Scientific Research at Bolling AFB, DC for the sponsorship of this research. The people at Avionics Laboratory of Wright Patterson Air Force Base have been very supportive. I would especially like to thank Gary McCoy and Chern Huang for their help and guidance and Ben Carroll for his patience in helping me to use the VAX system.

The work reported here comes mainly, though not entirely, from a Master of Science Thesis completed by Abdellatif Bounaim at Indiana University of Pennsylvania (IUP). The author would like to thank Mr. Bounaim for all his efforts in this work.

Effects on the BICFET of the Fermi Distribution
Factor and the Al Mole Fraction

by

Dennis Whitson

ABSTRACT

An analytical computer model was written to investigate the effect of the "Fermi-Factor" and the Al mole fraction, x , on the functioning of the N-P-N Bipolar Inversion Channel Field- Effect Transistor (BICFET). Attempts were also made to elucidate some of the effects of the ohmic contact and the inclusion of the space charge contained in the depleted semi-insulator.

It was found that the main effect of including the Fermi distribution factor was the reduction of the amount of effective negative charge located in the depleted p^+ spike layer. This reduced the positive charge located at the semi-insulator/semiconductor interface and thus increased the current gain.

The Al mole fraction, x , has a dramatic impact on the current gain of the BICFET device. It increases from approximately 2 at $x = 0.1$ to $3E10$ at $x = 1.0$.

Consideration of the ohmic contact and the space charge in the semi-insulator led to a better understanding of the BICFET but produced little quantitative change.

I. INTRODUCTION

The Bipolar Inversion Channel Field-Effect Transistor (BICFET) was first introduced by Taylor and Simmons (1,2) in 1985. The device is bipolar in nature but replaces the traditional base with an inversion layer which is induced by field effects. The current flows perpendicular to the inversion layer and is modulated by the amount of inversion charge contained in that layer. Since this layer is very thin the punch-through problem that exists with traditional Bipolar and MOSFET devices at sub-micron geometries may well be obviated. The BICFET theoretically has other attributes that if realized would make it an extremely attractive device. It has promise of very high current gain ($>E5$), very high current operation ($E6$ Amp/cm²), very high transconductance ($4E7$ S/cm²), high frequency operation (400 Ghz), and low input capacitance.

It was shown by Whitson and Schmidt (3) that the Fermi distribution factor may have important implications in the operation of the BICFET. It was found that with the consideration of the Fermi factor and collector stretch the collector current increased as the collector to emitter voltage decreased. At the time it was felt that this may be an artifact due to the behavior of the equations in the iteration loop of the computer program that included collector stretch. Indeed, it is shown in this work that when the equations are solved with the Fermi factor and without the collector stretch that the shape of the I-V curves are essentially flat as expected. Leaving out the collector stretch is probably not a major issue since it only has an effect at current levels of MegaAmps/cm² which are probably unobtainable. The effect of the inclusion of the Fermi factor is to reduce the effective amount of negative charge contained in the depleted p⁺ spike layer which reduces the positive charge (for npn configuration) contained in the inversion layer which in turn increases the current gain. Also, the choice of the amount of degeneracy of the acceptor levels in the spike layer affected the impact of the Fermi factor.

Since the current gain depends exponentially on the valence band discontinuity which depends on the Al mole fraction, x , it was felt that it would be useful to consider the properties of the BICFET with respect to x . Changing x does not change the shape of the I-V curves but does change the gain very substantially, e.g. from about 4 at $x = 0.1$ to $7.4E10$ at $x = 1.0$. This large a gain in the latter case would, of course, be limited by other physical factors not yet considered in the model; however, this does give some working room. The way one chooses to calculate the valence band discontinuity has, of course, a large impact on the gain of this system. Using more recent experimental results (4,5) for this parameter actually gives a more optimistic estimate of the current gain than that obtained from earlier work (6). When considering the current gain of this device it should always be considered that the gain is exponential with respect to the difference in the potential barriers that the electrons and the holes experience. For the N-P-N device one wants to increase the barrier for the holes and decrease the barrier for the electrons.

An ohmic contact to the semi-insulator (AlGaAs) layer is usually formed by putting a layer of n+ GaAs material on before the metal layer. This extra layer has possible serious implications in the functioning of the BICFET. In the model proposed here there is an intermediate n+ AlGaAs layer that has two effects: (1) it increases the gain through increasing the conduction band's effective density of states and (2) it allows tunneling action between the n+ AlGaAs and the n+ GaAs similar to that of the usual ohmic contact. Also, analyzing the ohmic contact in this manner led to doubt as to whether the semi-insulator is fully depleted when the device is conducting. Another insight gained through this approximation was an understanding of the origin of the emitter charge, Q_e .

In the model proposed by Taylor and Simmons (1) the semi-insulator layer (AlGaAs in our case) is treated as an insulator which means that the positive space charge due to the ionized donors in the depleted semi-insulator are neglected. Inclusion of this space charge does not have much effect on the properties of the BICFET, but it does make one of the approximations in their original paper less trustworthy which could change one of the equations in the iteration loop. This latter aspect was not explored here, but will be taken up later.

Another approximation made by Taylor and Simmons was that the spike layer was fully depleted. In order to gain some insight into this aspect it was assumed that the spike layer had a neutral zone. The calculations indicate that a neutral zone may well exist under certain conditions in the spike layer.

In order to investigate the above considerations three computer algorithms were written. The three programs BICFET, GAASBIC, and OHMBIC are outlined in Chapter VI.

Since the basic theory has been covered in detail elsewhere(1,3) only the new facets will be considered here.

II. FERMI FACTOR

When acceptor impurities of concentration N_A are added to a semiconductor crystal, the expression for ionized acceptors is

$$N_A^- = \frac{N_A}{1 + g \exp[\beta(E_A - E_F)]} \quad 2-1$$

where E_A is the energy of the acceptor levels, $\beta = (kT)^{-1}$, E_F is the Fermi level and g is the ground state degeneracy of the acceptor impurity level. The value usually accepted for g is four (4) because in GaAs and Si each acceptor impurity level can accept one hole of either spin and the impurity level is doubly degenerate as a result of two degenerate valence bands at $k = 0$. It should be noted that all energies and voltages are assumed to be electron volts.

In equilibrium, at the semi-insulator/semiconductor interface (see Fig.1), the denominator in Eq. 2-1 can be rewritten as

$$\{1 + g \exp[\beta(\epsilon_p - \Delta E_i^*)]\}^{-1} \quad 2-2$$

where

$$\epsilon_p = E_A - E_V \quad 2-3$$

is the energy of the acceptor level above the valence band and

$$\Delta E_i^* = E_F - E_V - \Phi_s^* \quad 2-4$$

where E_V is the valence band energy deep in the neutral semiconductor and Φ_s^* is the equilibrium surface potential of the semiconductor. The superscript asterisk will be used to represent quantities that are in equilibrium. The term in Eq. 2-2 is what will be referred to as the "Fermi factor". Without the asterisk it will be the Fermi factor for the non-equilibrium case.

When the Fermi factor is not taken into consideration the charge in the spike layer is

$$Q_i = -q N_i' \quad 2-5$$

and when it is considered we have

$$Q_i = \frac{-g N_i'}{1 + g \exp[\beta(\epsilon_p - \Delta E_i)]} \quad 2-6$$

where q is the electronic charge and N_i' is the acceptor dopant density per unit area (cm^{-2}). Adding asterisks to Q_i' and $\Delta E_i'$ would give the expressions for the equilibrium case. The energy $\Delta E_i'$ can be calculated using Eq. 2-4, but ΔE_i (non-equilibrium case) must be calculated from

$$p_o = N_V \exp[-\beta \Delta E_i] \quad 2-7$$

where N_V is the effective density of states of the valence band and p_o is the inversion charge density at the semi-insulator/semiconductor interface.

The charge balance equation

$$Q_i + Q_e + Q_c = 0 \quad 2-8$$

where Q_e is the emitter charge and Q_c is the collector charge (i.e., the charge in the semiconductor) can be written as

$$-C_i V_i = \frac{g N_i}{1 + g \frac{p_o}{N_V} \exp[\beta \epsilon_p]} - \left(\frac{2 g \epsilon_s}{\beta} \right)^{\frac{1}{2}} [p_o + \beta \Phi_s N_d]^{\frac{1}{2}} \quad 2-9$$

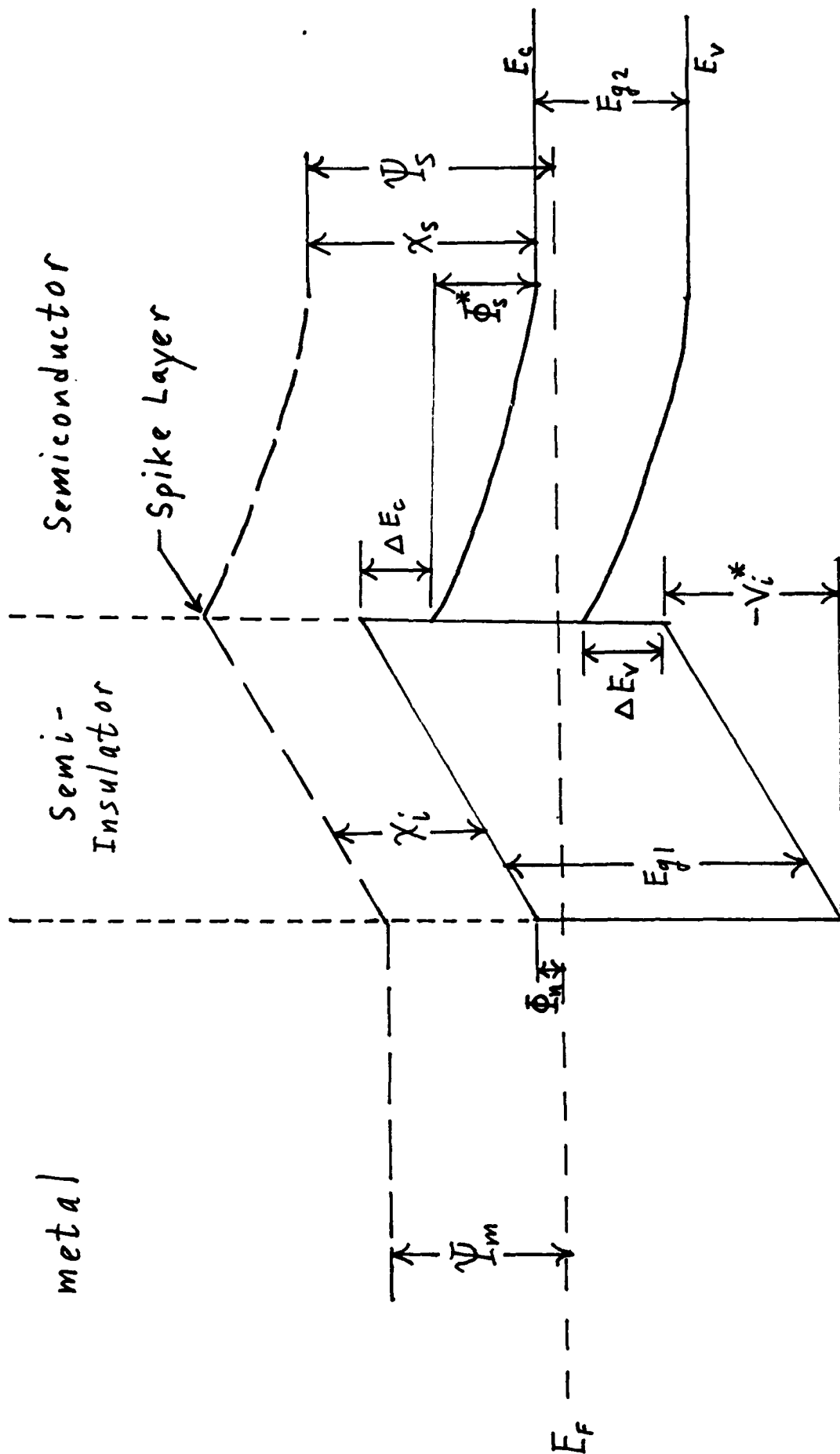


FIGURE 1. Energy band diagram of the NPN BICFET in equilibrium without the Ohmic Contact.

where $V_i = -Q_i/C_i$ is the voltage drop across the semi-insulator, ϵ_s the permittivity of the semiconductor, N_d the donor doping density per unit volume (cm^{-3}) in the semiconductor, and $C_i = \epsilon_i/d$ where ϵ_i is the permittivity of the semi-insulator and d the thickness of the semi-insulator. This equation can be rewritten as

$$A_3 x^3 + A_2 x^2 + A_1 x + A_0 = 0 \quad 2-10$$

where

$$x = p_0/N_V \quad 2-11$$

$$A_3 = (g \exp[\beta \epsilon_p])^2$$

$$A_2 = 2g \exp[\beta \epsilon_p] + (g \exp[\beta \epsilon_p])^2 \left\{ \frac{\beta \Phi_s N_d}{N_V} - C_i V_i^2 \left(\frac{\beta}{2g \epsilon_s N_V} \right) \right\} \quad 2-12$$

$$A_1 = 1 + 2g \exp[\beta \epsilon_p] \left\{ \frac{\beta \Phi_s N_d}{N_V} - C_i V_i \left(\frac{\beta}{2g \epsilon_s N_V} \right)^{1/2} \left[g N_i \left(\frac{\beta}{2g \epsilon_s N_V} \right)^{1/2} + C_i V_i \left(\frac{\beta}{2g \epsilon_s N_V} \right)^{1/2} \right] \right\}$$

$$A_0 = \frac{\beta \Phi_s N_d}{N_V} - \left\{ g N_i \left(\frac{\beta}{2g \epsilon_s N_V} \right)^{1/2} + C_i V_i \left(\frac{\beta}{2g \epsilon_s N_V} \right)^{1/2} \right\}^2$$

The other equations needed in the iteration loop are

$$V_{ce} = \Phi_s + V_i - \Psi_{ms} \quad 2-13$$

where V_{ce} is the applied collector to emitter voltage and Ψ_{ms} is the metal to semiconductor work function (which will be developed in detail later);

$$J_{pi} = q v_p p_0 \exp[\beta(V_i - \Delta E_V)] \quad 2-14$$

where J_{pi} is the hole current density in the semi-insulator, v_p is the thermal

velocity of the holes and ΔE_V is the valence band discontinuity at the heterojunction;

$$J_{pi} = J_s - J_{pc} \quad 2-15$$

where J_s is the source current density and J_{pc} is the hole current density from the source to the collector; and

$$J_{pc} = \frac{q D_p}{L_p} \{ p_0 \exp[-\beta \Phi_s] - p_{no} \} \quad 2-16$$

where D_p is the hole diffusion constant, L_p the hole diffusion length and p_{no} the bulk concentration of holes in the n-type semiconductor. Equations 2-14 and 2-15 can be rewritten as

$$V_i = kT \ln \left[\frac{J_s - J_{pc}}{q V_p \rho_o} \right] + \Delta E_v \quad 2-17$$

The iteration loop uses Equations 2-10, 2-13, 2-16 and 2-17. The values of J_s and V_{ce} are inputs and V_i , Φ_s , p_o and J_{pi} are unknowns. The loop starts by assuming a value of V_i and using Eq. 2-13 to solve for Φ_s and then using a Laguerre subroutine in order to solve the cubic equation for p_o in Eq. 2-10. After using Eq. 2-16 to solve for J_{pc} we can find a value for V_i from Eq. 2-17. This new value for V_i then goes to the top of the loop and the process is repeated until the final value of V_i agrees with the previous value to within some specified error.

Values of Q_e , Q_c , J_{ni} , J_c and G are calculated after the iteration loop using the following equations:

$$Q_e = -V_i C_i' \quad 2-18$$

$$Q = \left\{ \frac{2q\epsilon_s}{\beta} \right\}^{1/2} \{ p_o + \beta \Phi_s N_d \}^{1/2} \quad 2-19$$

$$J_{ni} = q v_n N_c \exp[\beta(V_i - \Phi_n)] \quad 2-20$$

$$J_c = J_{ni} - J_{pc} \quad 2-21$$

$$G = \frac{N_c}{\rho_o} \exp[\Delta E_v - \Phi_n] \quad 2-22$$

where J_{ni} is the electron current density in the semi-insulator, v_n the electron thermal velocity, N_c the effective density of states for the conduction band in the semi-insulator, Φ_n the barrier for the electrons at the metal/semi-insulator interface, J_c the collector current density and G the current gain of the BICFET where $v_n = v_p$ has been used.

Chapter III

EFFECTS DUE TO THE ALUMINUM MOLE FRACTION

There are many properties of the compound semiconductor $Al_xGa_{1-x}As$ that depend on the Aluminum mole fraction, x . The ones that are considered in this work are the conduction band discontinuity, ΔE_c , the valence band discontinuity, ΔE_v , the band gap, E_g , the effective density of states for the conduction band, N_{c1} , the effective density of states for the valence band, N_{v1} and the permittivity, ϵ_1 . The equations used to calculate the values of the latter four parameters are taken from Adachi's paper [6]. However, since recent work [4,5] has shown that the equations used by Adachi for the band discontinuities considerably underestimate the size of the valence band discontinuity

both sets of equations from the three sources are used to calculate these discontinuities.

From Adachi [6] (at 300K) we have:

$$E_{g1} = 1.424 + 1.247x \quad (0 \leq x \leq .45) \quad 3-1$$

$$E_{g1} = 1.900 + 0.125x + 0.143x^2 \quad (.45 < x \leq 1.0) \quad 3-2$$

$$N_{c1} = \left(\frac{0.067 + 0.083x}{0.067} \right)^{3/2} N_c \quad (0 \leq x \leq .45) \quad 3-3$$

$$N_{c1} = \left(\frac{0.85 - 0.14x}{0.067} \right)^{3/2} N_c \quad (.45 < x \leq 1.0) \quad 3-4$$

$$N_{v1} = \frac{N_v}{\left[(0.087)^{3/2} + (0.62)^{3/2} \right] \left[\frac{(0.087 + 0.063x)^{3/2}}{(0.62 + 0.14x)^{3/2}} + 1 \right]} \quad 3-5$$

$$\epsilon_1 = (13.18 - 3.12x) \epsilon_0 \quad 3-6$$

where ϵ_0 is the permittivity of free space, the subscript (1) refers to region (1) in Figure 2,

$$N_c = 4.7E17 \quad 3-7$$

$$N_v = 7.0E18 \quad 3-8$$

and

$$\Delta E_c = 1.1x \quad (0 \leq x \leq .45) \quad 3-9$$

$$\Delta E_c = 0.43 + 0.14x \quad (.45 < x \leq 1.0) \quad 3-10$$

$$\Delta E_v = E_{g1} - E_{g2} - \Delta E_c \quad 3-11$$

where E_{g2} is the band gap for GaAs (1.424 eV).

From Hill and Ladbroke [4] and Drummond and Fritz [5] we have

$$\Delta E_c = 0.779x \quad (0 \leq x \leq .45) \quad 3-12$$

$$\Delta E_c = 0.389 + 0.044x - 0.287x^2 \quad (.45 < x \leq 1.0) \quad 3-13$$

and ΔE_v is given by Eq. 3-11. These band discontinuities were calculated by assuming that the band alignment is determined at the gamma point in k space where

$$\Delta E_g^\Gamma = \Delta E_c^\Gamma + \Delta E_v \quad 3-14$$

where ΔE_g^Γ is the total band discontinuity at the gamma point and ΔE_c^Γ is the conduction band discontinuity at the gamma point and that

$$\Delta E_c^\Gamma = \alpha \Delta E_g^\Gamma \quad 3-15$$

$$\Delta E_v = (1 - \alpha) \Delta E_g^\Gamma \quad 3-16$$

where α is a constant independent of x . For $x > 0.45$ AlGaAs becomes an indirect transition material with the X-valley becoming lowest in energy, however the band alignment and ΔE_v (Eq. 3-16) are still determined at the gamma point. The direct-indirect conduction band discontinuity is found from

$$\Delta E_c(X - \Gamma) = \Delta E_g(X - \Gamma) - \Delta E_v \quad 3-17$$

where $\Delta E_g(X - \Gamma)$ is the well established indirect band gap. Hill and Ladbroke find α to lie in the range 0.59 to 0.67 and Drummond and Fritz give a range of 0.62 to 0.66. For this report it was assumed that

$$\alpha = 0.625 \quad 3-18$$

The total band gap discontinuity at the gamma point as a function of x is

$$\Delta E_g^\Gamma = 1.247x \quad (x \leq 0.45) \quad 3-19$$

$$\Delta E_g^\Gamma = 1.247x + 1.147(x - 0.45)^2 \quad (x > 0.45) \quad 3-20$$

which leads to

$$\Delta E_v = 0.468x \quad (x \leq 0.45) \quad 3-21$$

$$\Delta E_v = 0.468x + 0.430(x - 0.45)^2 \quad (x > 0.45) \quad 3-22$$

and thence to Eq.'s 3-12 and 3-13 after using Eq.'s 3-1, 3-2 and 3-17.

The effective densities of states were calculated using the effective masses as a function of x . For the valence band we have

$$M^*{}^{3/2} = M_l^{3/2} + M_h^{3/2} \quad 3-23$$

where M_l is the effective mass for light holes and M_h is the effective mass for heavy holes. The values for GaAs are

$$M_l = 0.087 m_0, \quad M_h = 0.62 m_0 \quad 3-24$$

where m_0 is the rest mass of the free electron, and for AlGaAs

$$M_l = (0.087 + 0.063x) m_0 \quad 3-25$$

$$M_h = (0.62 + 0.14x) m_0 \quad 3-26$$

In the case of the conduction band we have

$$M^* = 0.067 m_0 \quad 3-27$$

for GaAs and

$$M^* = (0.067 + 0.083x) m_0 \quad (0 < x \leq 0.45) \quad 3-28$$

$$M^* = (0.85 - 0.14x) m_0 \quad (0.45 < x \leq 1.0) \quad 3-29$$

for AlGaAs. The change in effective masses that occurs at $x = 0.45$ is due, of course, to the X-valley becoming lower in energy than the Γ -valley for values of the Al mole fraction greater than this. No attempt is made to treat the situation at exactly $x = 0.45$.

Chapter IV

SPACE CHARGE IN AND OHMIC CONTACT TO THE SEMI-INSULATOR

A. General Equations

It is assumed here (see Fig.'s 2,3 and 4) that there exists a space charge in the semi-insulator due to the ionized donor sites and that there is a n+AlGaAs layer on the semi-insulator in order to form the ohmic contact. The electric field in region (1) is

$$E = \frac{q}{\epsilon_1} N_{d1} x \quad 4-1$$

and the potential and the charge are

$$V_{b1} = - \frac{q}{2 \epsilon_1} N_{d1} x_1^2 \quad 4-2$$

$$Q_1 = q x_1 N_{d1} \quad 4-3$$

For region (2) we have

$$E = \frac{q}{\epsilon_1} N_{d2} x + E_{10} \quad 4-4$$

$$V_i = - \left(\frac{q}{2 \epsilon_1} N_{d2} d_1^2 + \frac{q}{\epsilon_1} N_{d1} d_1 x_1 \right) \quad 4-5$$

$$Q_2 = q d_1 N_{d2} \quad 4-6$$

With the identification

$$Q_e \equiv Q_1 \quad 4-7$$

we can write

$$V_{b1} = - \frac{Q_e^2}{2 q \epsilon_1 N_{d1}} \quad 4-8$$

$$V_i = - \frac{q}{2 \epsilon_1} N_{d2} d_1^2 - \frac{Q_e}{C_i} \quad 4-9$$

The first term in Eq. 4-9 is seen to be the contribution due to the space charge in the semi-insulator and the second term allows one to identify the

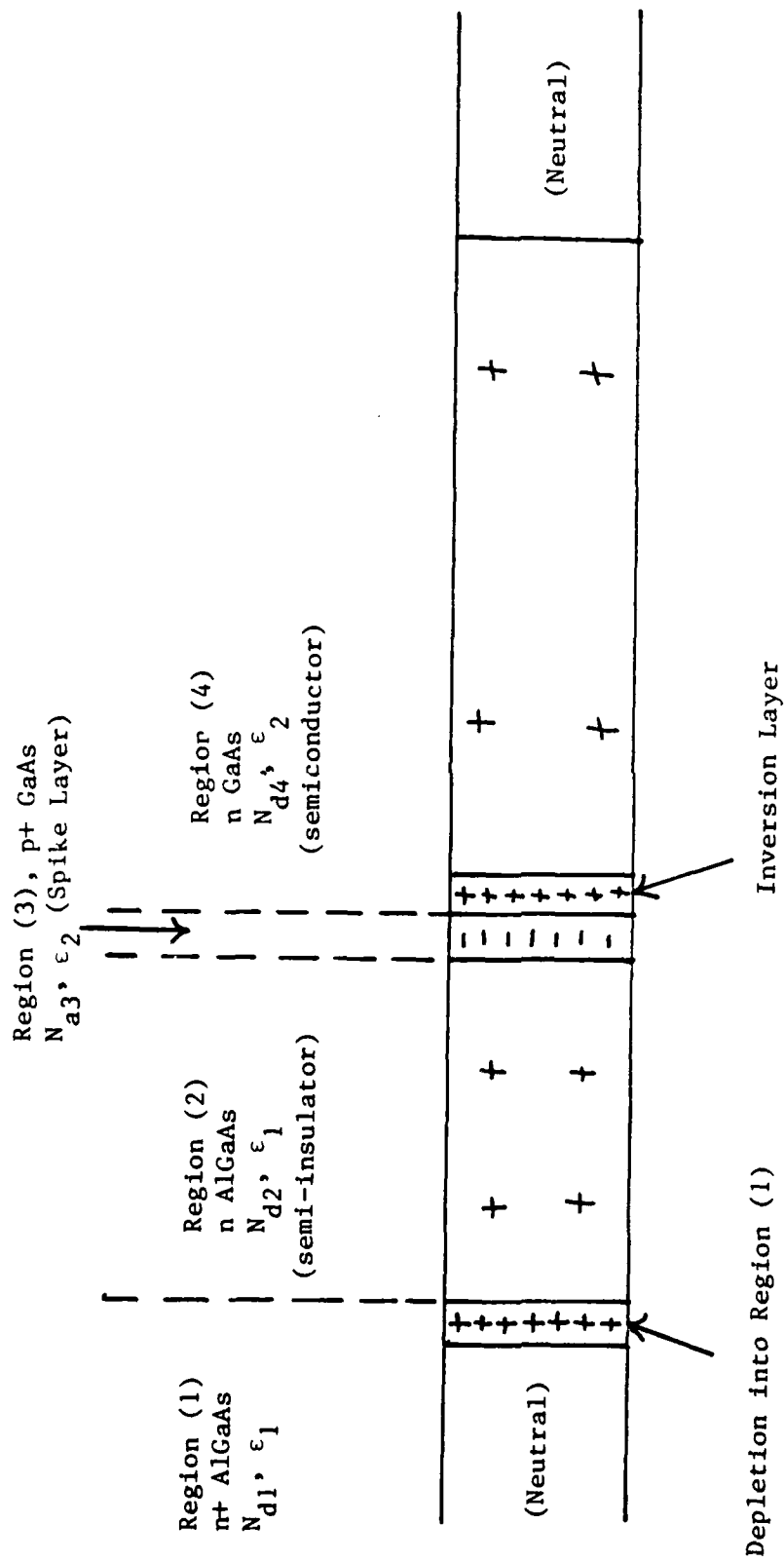


FIGURE 2. Space charge distribution in the NPN BICFET with the assumption of ohmic contact to and space charge in the semi-insulator. Not drawn to scale.

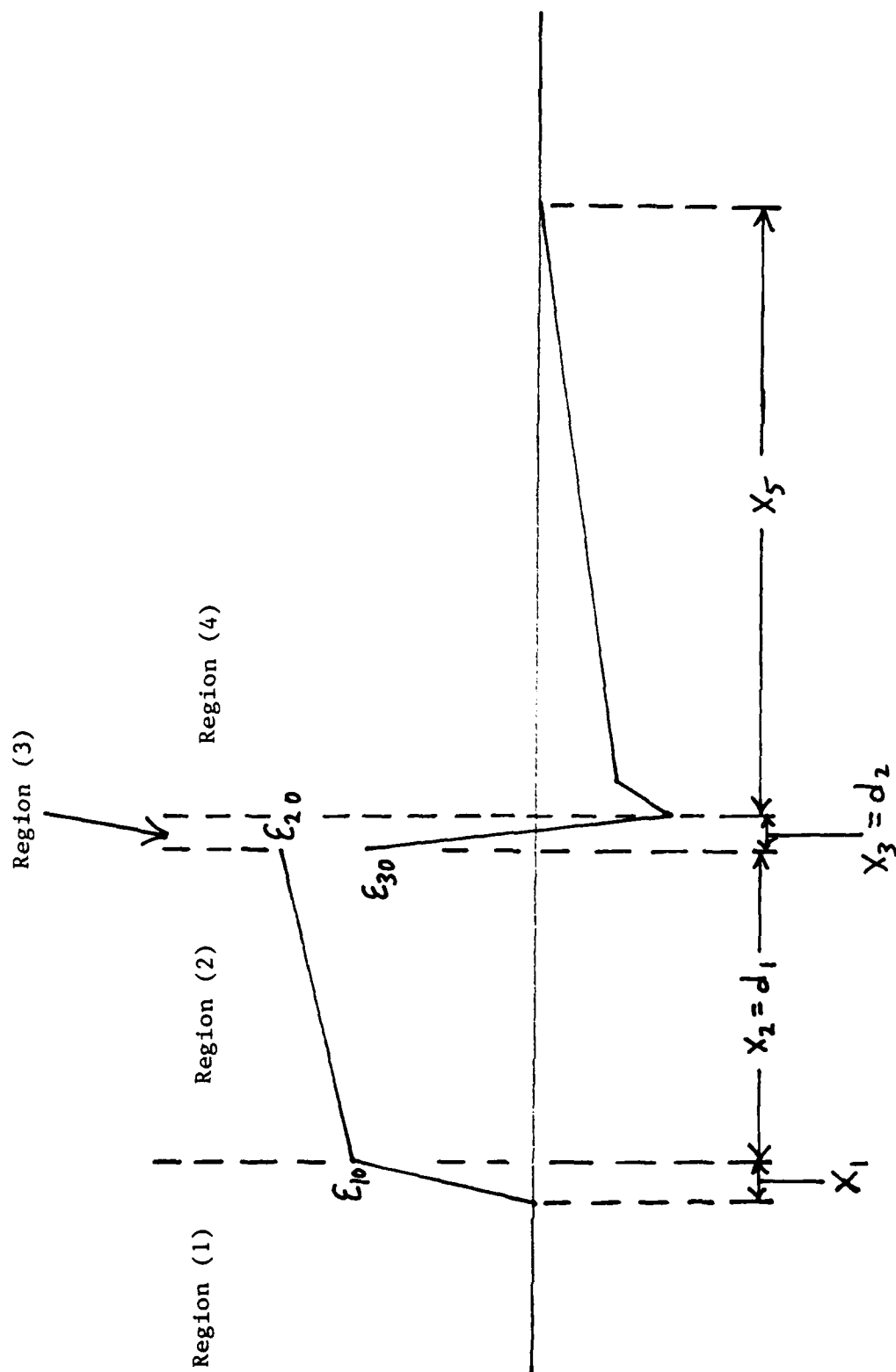


FIGURE 3. Electric fields in the NPN BICFET with the assumption of ohmic contact and space charge in the semi-insulator. The distance x_5 has been chosen to agree with the nomenclature in Figure 8. Not drawn to scale.

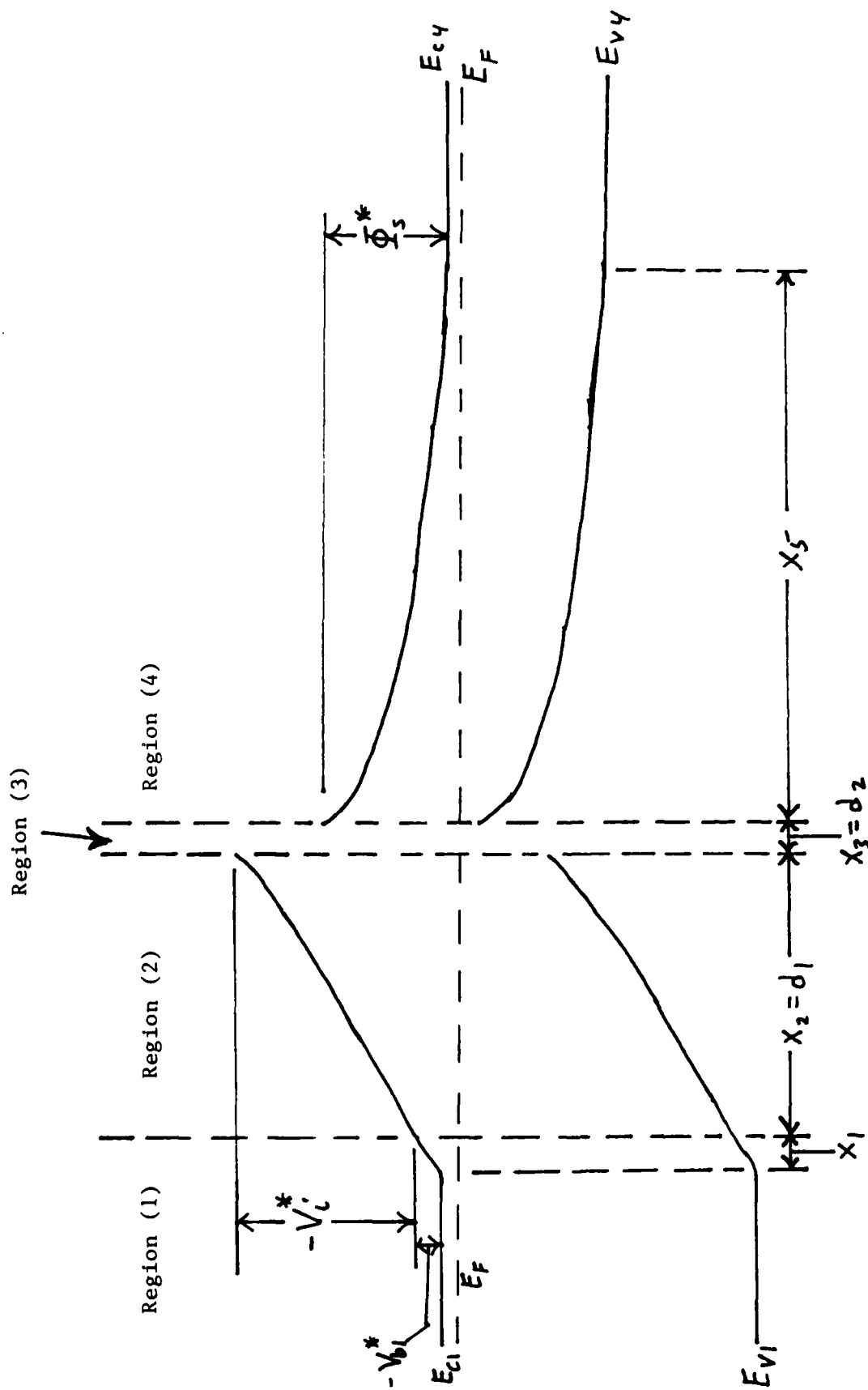


FIGURE 4. Energy band diagrams for the NPN BICFET with the assumption of ohmic contact and space charge in the semi-insulator. The distance x_5 has been chosen to agree with the nomenclature in Figure 8. The voltage drop in region (3) is assumed to be zero.

source of the emitter charge, Q_e , i.e. the depletion charge in the n+ ohmic contact region. Because of these approximations there are some changes in the equations used in the iteration loop. Equation 4-9 replaces 2-18, the charge Q_2 (Eq. 4-6) is added to the charge balance equation (Eq. 2-8) and V_{b1} (Eq. 4-8) is added to the right hand side of Equation 2-13. The hole current density is now

$$J_{pi} = q V_p p_0 e^{-\beta \Delta E_v} e^{\beta(V_{b1} + V_i)} \quad 4-10$$

where the additional barrier, V_{b1} , has been included. This barrier also has to be included in the electron current density, thus

$$J_{ni} = q V_n N_{c1} e^{\beta(V_i + V_{b1})} \quad 4-11$$

After the loop, values of V_{b1} , x_1 , and x_5 are calculated from Eq. 4-8,

4-2 and

$$x_5 = \left(\frac{2 \epsilon_2 \Phi_s}{q N_{d4}} \right)^{1/2} \quad 4-12$$

respectively, where the influence of the inversion charge density, p_0 , has been neglected and the distance x_5 has been used here and in Fig.'s 3 and 4 instead of x_4 so as to not cause confusion with the results in Chapter V. In addition there are changes in the current gain equation

$$G = \frac{N_{c1}}{p_0} e^{\beta \Delta E_v} \quad 4-13$$

where N_{c1} has replaced N_c and the barrier for electrons at the metal/semi-insulator interface, Φ_n , has been dropped from the equation. The first change occurs because the pool of electrons that are trying to make it over the barrier comes from the n+AlGaAs layer and the second because both the electrons and holes face the same barriers (see Fig. 4) except for ΔE_v , i.e. they both see V_{b1} whereas before only the electrons saw Φ_n . The potential Φ_n should probably have been included, because there is still a metal semiconductor barrier to account for. These changes are made in both the Fermi and no fermi cases.

B. Equilibrium Equations

With the inclusion of the space charge in the semi-insulator and the ohmic contact approximation the equations that have to be solved for the equilibrium case are

$$V_{b1}^* = - \frac{Q_e^{*2}}{2 q \epsilon_1 N_{d1}} \quad 4-14$$

$$V_i^* \equiv V_{b2}^* = - \frac{q N_{d2} d_1^2}{2 \epsilon_1} - \frac{Q_e^*}{C_i} \quad 4-15$$

$$\Phi_s^* = \Psi_{14} - V_{b1}^* - V_{b2}^* \quad 4-16$$

$$\Delta E_i^* = kT \ln \left(\frac{N_{d4}}{N_{c4}} \right) + E_{g2} - \Phi_s^* \quad 4-17$$

$$p_o^* = N_v \exp[-\beta \Delta E_i^*] \quad 4-18$$

$$Q_e^* = \frac{q N_a}{1 + q \exp[\beta(\epsilon_p - \Delta E_i^*)]} - q d_1 N_{d2} - \left(\frac{2q\epsilon_2}{\beta} \right)^{1/2} [p_o^* + \beta \Phi_s^* N_{d4}]^{1/2} \quad 4-19$$

$$\Psi_{14} = -\Delta E_c + kT \ln \left[\frac{N_{c1} N_{d4}}{N_{c4} N_{d1}} \right] \quad 4-20$$

where $N_a = N_{a2} d_2$ (where d_2 is the thickness of the spike layer) and $\Psi_{14} = \Phi_{m1} - \Phi_{m4}$ is the difference in work functions from the n-AlGaAs region to the semiconductor (see chapter V). For the no Fermi case the denominator of the first term on the right hand side in Eq. 4-19 is equal to one.

The iteration loop starts with assuming a value for Q_e^* and then the Eq.'s 4-14 thru 4-19 are solved in order with the value of Q_e^* from Eq. 4-19 then going to the top of the loop into Eq. 4-14 until the two values of Q_e^* agree to within some specified error.

C. Impact on Hole and Electron Current Densities

The inclusion of the space charge into the equations has an impact on the equations for the hole and electron current densities in the semi-insulator. Let us consider Eq. A16 from Taylor and Simmons [1]:

$$J_{ni} = \frac{-q v_n N_c \exp[-\beta(\Phi_n - V_i)]}{\left(\frac{d}{\beta V_i \ell_n} \right) [1 - \exp(\beta V_i)] + 1} \quad 4-21$$

For small values of V_i , the authors take

$$1 - \exp(\beta V_i) \cong -\beta V_i \quad 4-22$$

but $|V_i| > 0.09$ when the device is on and for $V = -0.09$ we have

$$\exp(\beta V_i) = \exp(-0.09/0.026) = 0.0314 \quad 4-23$$

A better approximation would seem to be

$$1 - \exp(\beta V_i) \cong 1 \quad 4-24$$

This means that J_{ni} would be larger by the factor

$$-\beta V_i = \frac{0.09}{0.026} = 3.5 \quad 4-25$$

and thus the actual current may be larger by a factor of 3 to 4 over that found by Taylor and Simmons. The incorporation of the space charge puts a lower limit on how small the absolute value of V_i' can become, e.g., for $N_{d2} = 1.0 \times 10^{17}$ the voltage due to the space charge is -0.068 V. Thus even if the second term in Eq. 4-9 were zero (i.e., $Q_0 = 0$) the approximation made by the authors would not seem to hold up. It should be pointed out that this approximation does not affect the gain since a similar factor would appear in the equation for the hole current density J_{pi}' which is derived in a fashion similar to J_{ni} . It might however affect the value of V_i' since the equation for J_{pi} does appear in the iteration loop (J_{ni} does not). The equation would then be

$$J_{pi} = q V_p (-\beta V_i) \exp(\Delta E_v - V_i') \quad 4-26$$

This equation was not considered in this work and the equations used were essentially the same as those of Taylor and Simmons' along with the modifications mentioned in previous sections.

D. Ohmic Contact Considerations

The usual ohmic contact is made with metal on n+GaAs which is deposited on the nAlGaAs as illustrated in Figure 5. This configuration could pose a problem as pointed out by L. Liou [7]. The n+/n junction would present an additional barrier to the flow of electrons and thus the gain equation would have $\Delta E_v - \Delta E_c$ in the exponent instead of just ΔE_v . One way around this problem would be to place a n+AlGaAs layer between the nAlGaAs layer and the n+GaAs layer (see Figure 6). This would obviate the problem at the n+/n junction and the n+/n+ junction would be similar to a metal/n+ ohmic contact. Perhaps the exponent in the gain equation would then become

$$\Delta E_v - \Phi_{n1} - \Phi_{n2} \quad 4-27$$

where Φ_{n1} is the effective barrier due to tunneling at the metal/n+GaAs interface and Φ_{n2} is the effective barrier due to tunneling at the n+GaAs/n+AlGaAs junction.

CHAPTER V

NEUTRAL ZONE IN THE SPIKE LAYER

One of the basic assumptions in the model for the BICFET is that the spike layer is completely depleted. By assuming a neutral zone in the spike layer (see Fig.'s 7, 8 and 9) one can gain some insight as to whether or not this assumption is valid. One of the results of this neutral zone would be that the mobile holes would be stored in the neutral zone in the spike layer instead of at the interface of the spike layer and the semiconductor. The description of the details of the functioning of the device would be different but the result should be qualitatively the same. As holes are pumped into the neutral zone it would expand which would drive down V_{b1} and V_i (see Fig. 9) which then would

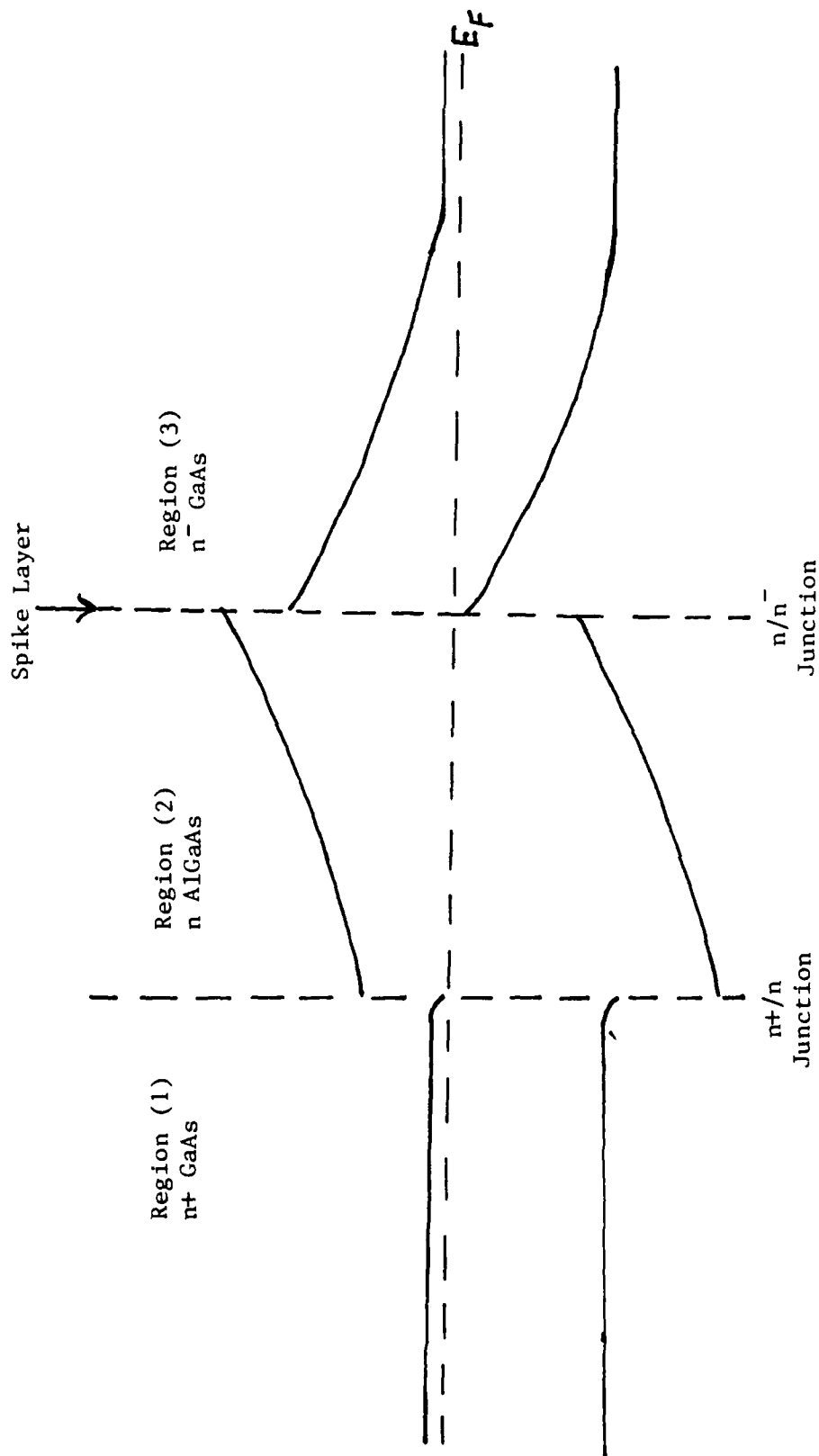


FIGURE 5. Ohmic contact made with n^+ GaAs on the semi-insulator. The spike layer is either n^+ GaAs or n^+ AlGaAs.

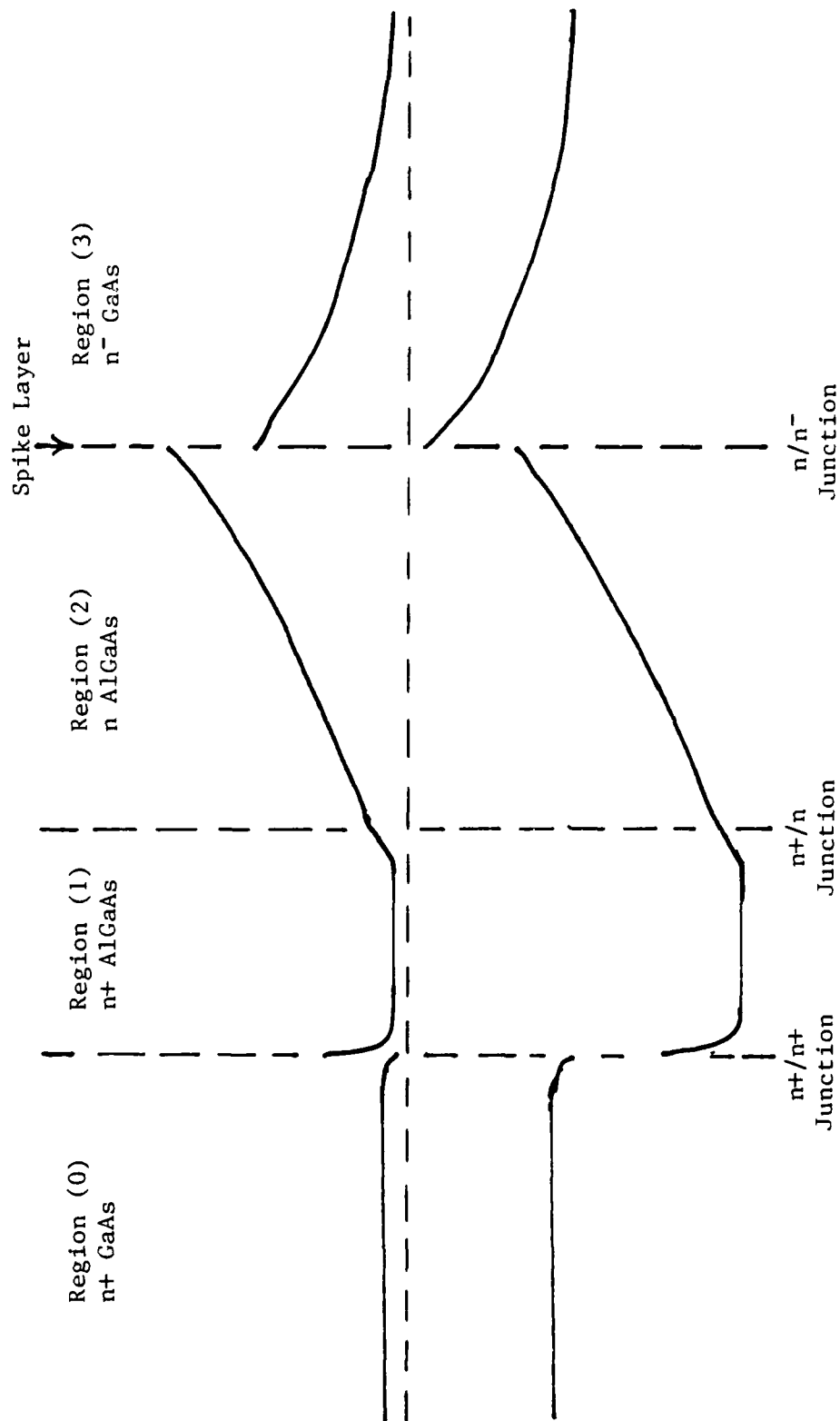


FIGURE 6. Ohmic contact made with n^+ GaAs/ n^+ AlGaAs on the semi-insulator. The spike layer is either n^+ GaAs or n^+ AlGaAs.

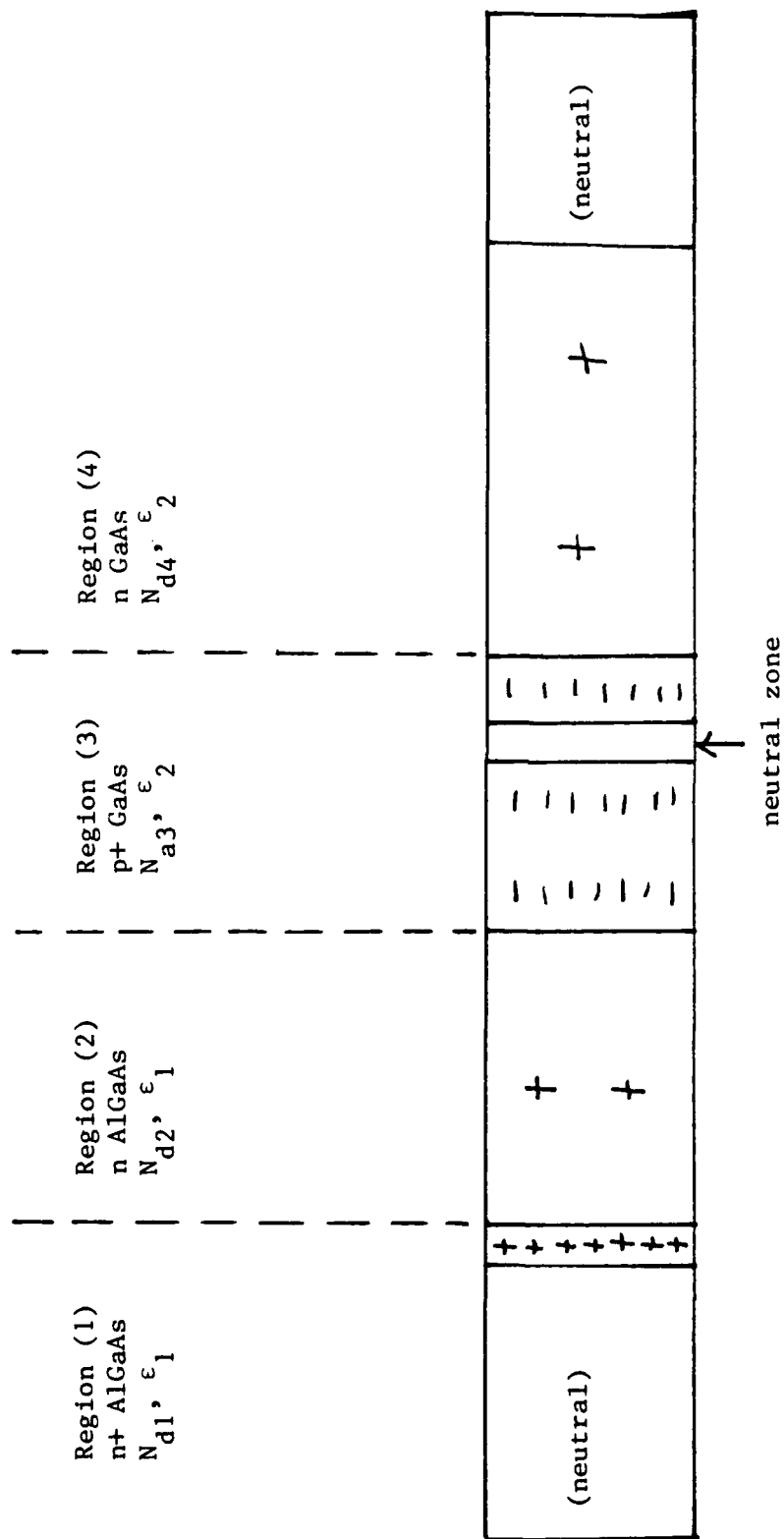


FIGURE 7. Space charge distribution for the NPN BICFET with the neutral zone in the spike layer, the ohmic contact and the space charge in the semi-insulator approximations. Not drawn to scale.

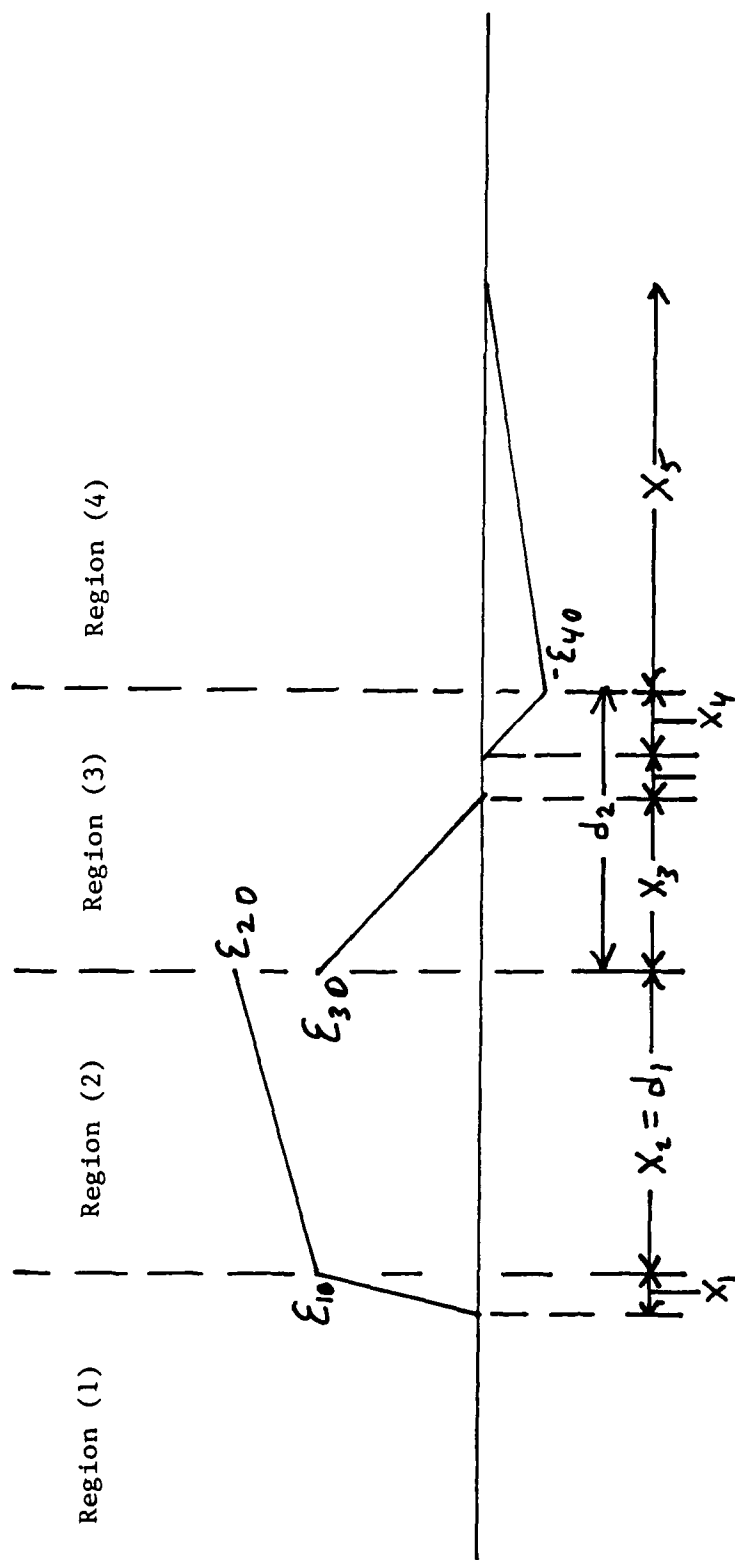


FIGURE 8. Electric fields for the NPN BICFET with the neutral zone in the spike layer, the ohmic contact and the space charge in the semi-insulator approximations. Not drawn to scale.

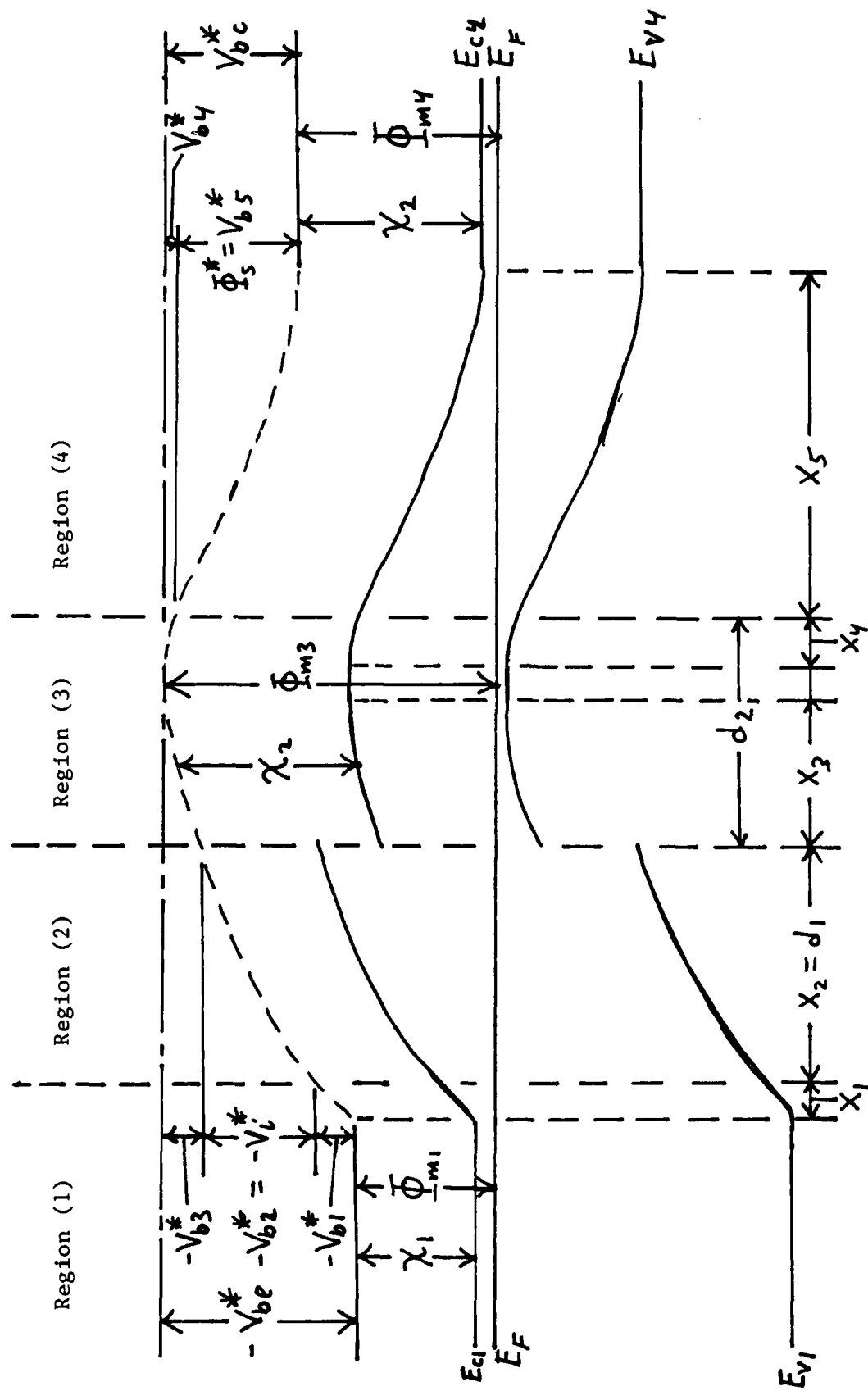


FIGURE 9. Energy band diagram for the NPN BICFET with the neutral zone in the spike layer, the ohmic contact and the space charge in the semi-insulator approximations. Not drawn to scale.

increase the electron flow. The real question becomes whether the current gain, G , is different than with the original description. Unfortunately the attempt to model this in detail for the non-equilibrium case met with some intractable equations. However, the results for the equilibrium case does shed some light on the issue.

From Fig. 9 it is seen that the relationships among the equilibrium Voltages V_{be}^* (the barrier voltage for the emitter) and V_{bc}^* (the barrier voltage for the collector) and the work functions are

$$V_{be}^* = \Phi_{m1} - \Phi_{m3} \quad 5-1$$

$$V_{bc}^* = \Phi_{m3} - \Phi_{m4} \quad 5-2$$

which implies that $V_{be}^* < 0$ and $V_{bc}^* > 0$. The work functions are defined only in the neutral zones of the different regions. The work functions

Φ_{m1} and Φ_{m4} are defined deep into the n+AlGaAs and the semiconductor regions respectively and Φ_{m3} is defined in the neutral zone of the spike layer. It is also seen that

$$\Phi_{m3} = \chi_2 + E_{g2} - (E_F - E_{v3}) \quad 5-3$$

$$\Phi_{m1} = \chi_1 + E_{c1} - E_F \quad 5-4$$

and

$$\Phi_{m4} = \chi_2 + (E_{c4} - E_F) \quad 5-5$$

where χ_1 and χ_2 are the electron affinities for AlGaAs and GaAs, respectively, E_{c1} and E_{c4} are the conduction band energies for the n+AlGaAs and the semiconductor deep in their respective neutral zones and E_{v3} is the valence band energy in the neutral zone of the spike layer. We have for the n-type material (regions 1 and 4)

$$E_{c1} - E_F = kT \ln (N_{c1}/N_{d1}) \quad 5-6$$

$$E_{c4} - E_F = kT \ln (N_{c4}/N_{d4}) \quad 5-7$$

while for the p-type material (region 3)

$$E_F - E_{v3} = kT \ln (N_{v3}/N_{a3}) \quad 5-8$$

The approximations in Eq.'s 5-6, 5-7 and 5-8 depend on the neutrality condition and the assumption of non-degeneracy. The neutrality condition is [8]

$$n + N_A^- = p + N_d^+ \quad 5-9$$

where N_A^- (N_d^+) is the number of acceptor (donor) sites ionized and

$$N_A^- = \frac{N_A}{1 + 4 \exp [\beta (E_A - E_F)]} \quad 5-10$$

$$N_d^+ = \frac{N_d}{1 + 2 \exp[\beta(E_F - E_D)]} \quad 5-11$$

where E_A (E_D) is the energy of the acceptor (donor) site. At room temperature and in the neutral zone we can take

$$N_A^- \cong N_A, \quad N_d^+ \cong N_d \quad 5-12$$

and for the n-type material ($p \ll n$, $N_A \ll N_D$)

$$n \cong N_d \quad 5-13$$

If it is assumed that the non-degenerate case holds then

$$n \cong N_c \exp[-\beta(E_c - E_F)] \quad 5-14$$

which leads directly to Eq.'s 5-6 and 5-7. In a p-type material under analogous conditions ($p \gg n$, $N_A \gg N_D$, $p \cong N_A$) we have

$$p \cong N_v \exp[-\beta(E_F - E_v)] \quad 5-15$$

and this leads directly to Eq. 5-8. In the degenerate case, however, we should use the Fermi-Dirac integral, $F_{1/2}$ where

$$n = N_c \frac{2}{\sqrt{\pi}} F_{1/2}[\beta(E_F - E_c)] \quad 5-16$$

$$p = N_v \frac{2}{\sqrt{\pi}} F_{1/2}[\beta(E_v - E_F)] \quad 5-17$$

The non-degenerate case is when

$$E_c - E_F \gg kT \quad \text{or} \quad N_d < N_c \quad 5-18$$

for n-type material and

$$E_F - E_v \gg kT \quad \text{or} \quad N_A < N_v \quad 5-19$$

for p-type material.

When conditions (5-18) and (5-19) hold we can use (5-14) and (5-15) to get (5-6), (5-7) and (5-8). When dealing with Si ($N_c = 2.8 \times 10^{19}$, $N_v = 1.04 \times 10^{19}$) we are almost always in the non-degenerate case; however, with GaAs ($N_c = 4.7 \times 10^{17}$, $N_v = 7.0 \times 10^{18}$) the degenerate case comes up fairly often. For the sake of convenience we will assume that the non-degenerate case holds, however it is not clear what effect this assumption has.

Also we will make the approximation

$$\chi_2 - \chi_1 = \Delta E_c \quad 5-20$$

which leads to

$$\Psi_{14} = \Phi_{m1} - \Phi_{m4} = -\Delta E_c + kT \ln \left[\frac{N_{c1} N_{d4}}{N_{c4} N_{d1}} \right] \quad 5-21$$

and

$$V_{be}^* = -\Delta E_c - E_{g2} + kT \ln \left[\frac{N_{v3} N_{c1}}{N_{a3} N_{d1}} \right] \quad 5-22$$

$$V_{bc}^* = E_{g2} - kT \ln \left[\frac{N_{v3} N_{c4}}{N_{a3} N_{d4}} \right] \quad 5-23$$

where N_{c4} and N_{v3} are the effective densities of states for GaAs and N_{c1} is that of AlGaAs and therefore depends on the Al mole fraction, x .

The electric field, the potential and the charge have already been solved for in regions 1 and 2 (see Chapter 4). For our purposes here all we have to do is to put asterisks in the proper places in Eq.'s 4-1 thru 4-6. For the area to the left of the neutral zone in region 3 we have

$$E^* = -\frac{q}{\epsilon_2} N_{a3} (X - X_3^*) \quad 5-24$$

$$V_{b3}^* = -\frac{q}{2\epsilon_2} N_{a3} X_3^{*2} \quad 5-25$$

$$Q_3^* = -q N_{a3} X_3^* \quad 5-26$$

and for the area to the right of the neutral zone in region 3 we have

$$E^* = -\frac{q}{\epsilon_2} N_{a3} X^* \quad 5-27$$

$$V_{b4}^* = \frac{q}{2\epsilon_2} N_{a3} X_4^{*2} \quad 5-28$$

$$Q_4^* = -q N_{a3} X_4^* \quad 5-29$$

Finally in region 4

$$E^* = \frac{q}{\epsilon_2} N_{d4} (X - X_4^*) \quad 5-30$$

$$V_{b5}^* = \Phi_5^* = \frac{q}{2\epsilon_2} N_{d4} X_5^{*2} \quad 5-31$$

$$Q_5^* = q N_{d4} X_5^* \quad 5-32$$

There must be charge balance in each of the two areas separated by the neutral zone, i.e.

$$Q_1^* + Q_2^* + Q_3^* = 0 \quad 5-33$$

$$Q_4^* + Q_5^* = 0 \quad 5-34$$

where we again make the identification that $Q_e^* = Q_1^*$.

The barrier voltages at the emitter and collector are, respectively

$$V_{be}^* = V_{b1}^* + V_{i1}^* + V_{b3}^* \quad 5-35$$

$$V_{bc}^* = V_{b4}^* + V_{b5}^* \quad 5-36$$

Using Eq.'s 4-3, 4-6, 5-26, and 5-33 we have

$$X_3^* = \frac{X_1^* N_{d1} + d_1 N_{d2}}{N_{a3}} \quad 5-37$$

and using Eq.'s 4-2, 4-5, 5-25, 5-35 and 5-37 we have a quadratic equation in x_1^* :

$$A X_1^{*2} + B X_1 + C = 0 \quad 5-38$$

where

$$\begin{aligned} A &= \frac{q N_{d1}}{2} \left(\frac{1}{\epsilon_1} + \frac{N_{d1}}{\epsilon_2 N_{a3}} \right) \\ B &= q d_1 N_{d1} \left(\frac{1}{\epsilon_1} + \frac{N_{d2}}{\epsilon_2 N_{a3}} \right) \\ C &= \frac{q}{2} d_1^2 N_{d2} \left(\frac{1}{\epsilon_1} + \frac{N_{d2}}{\epsilon_2 N_{a3}} \right) + V_{be}^* \end{aligned} \quad 5-39$$

Since V_{be}^* can be found from Eq. 5-22 the value of x_1^* can be calculated using Eq. 5-38 and then x_3^* , V_{b1}^* , V_{b3}^* , Q_e^* and Q_3^* can all be calculated from Eq.'s 5-37, 4-2, 5-25, 4-3 and 5-26, respectively. In order to solve for the other two equilibrium depletion distances Eq.'s 5-29, 5-32 and 5-34 are used to give

$$X_5^* = \frac{N_{a3}}{N_{d4}} X_4^* \quad 5-40$$

and Eq.'s 5-23, 5-28, 5-31, 5-36 and 5-40 are used for

$$X_4^* = \left[\frac{E_{g2} - K T \ln \left(\frac{N_{v3} N_{c4}}{N_{a3} N_{d4}} \right)}{\left(\frac{q N_{a3}}{2 \epsilon_2} \right) \left(1 + N_{a3}/N_{d4} \right)} \right]^{1/2} \quad 5-41$$

Note that p_0 has been neglected (with the assumption that it is much less than the density of holes in the neutral zone) and therefore does not show up in these equations.

In addition, after the iteration loop, the electric field at the semi-insulator/spike layer interface (see Fig. 8) is calculated using

$$E_{20}^* = \frac{q N_{d2} d_1}{\epsilon_1} + \frac{q N_{d1} X_1^*}{\epsilon_1} \quad 5-42$$

CHAPTER VI

COMPUTER PROGRAMS

Three computer programs BICFET, GAASBIC and OHMBIC were written in order to investigate the effects discussed in the previous chapters.

A. The BICFET Program

The BICFET program was written to investigate the Fermi factor and has both the Fermi and no Fermi option. In order to be able to compare the results to previous results [1,3] the parameters and the approximations used were those for the Si based device proposed by Taylor and Simmons [1]. The semi-insulator and the spike layer were both assumed to be completely depleted and the space charge in the semi-insulator was neglected. The ohmic contact was represented by a small barrier, Φ_n , for the electrons at the metal/semi-insulator interface. The following parameters were used for the Si device:

- 1) Band gap $E_{g2} = 1.12$ eV
- 2) Conduction band discontinuity $\Delta E_c = 0.1$ eV
- 3) Valence band discontinuity $\Delta E_v = 0.3$ eV
- 4) Effective density of states for the conduction band
 $N_c = 2.8E19$ cm⁻³
- 5) Effective density of states for the valence band
 $N_v = 1.0E19$ cm⁻³
- 6) Acceptor energy level above the valence band
 $\epsilon_p = 0.045$ eV
- 7) Metal to semiconductor work function $\Psi_{ms} = -0.32$ eV
- 8) Metal/semi-insulator interface electron barrier
 $\Phi_n = 0.02$ eV
- 9) Semiconductor hole and electron lifetimes
 $\tau_p = \tau_n = 1.0E-5$ sec
- 10) Semi-insulator dielectric constant $K_i = 8.0$
- 11) Semiconductor dielectric constant $K_s = 11.9$
- 12) Semi-insulator thickness $d_1 = 300$ Å
- 13) Spike layer thickness $d_2 = 30$ Å
- 14) Electron and hole thermal velocity $v_n = v_p = 1.0E7$ cm/sec
- 15) Semi-insulator and semiconductor hole diffusion constant
 $D_p = 12.5$ cm²/sec
- 16) Semi-insulator and semiconductor electron diffusion constant
 $D_n = 35.0$ cm²/sec
- 17) Semiconductor intrinsic carrier concentration $n_i = 1.5E10$ cm⁻³

B. The GAASBIC Program

The same approximations were made as in the BICFET program but the following parameters were calculated as a function of the Al mole fraction, x : N_{c1} , N_{v1} , ΔE_c , ΔE_v , E_{g1} and ϵ_1 . Also, the following parameters were used for the GaAs semiconductor, the nAlGaAs semi-insulator and the spike layer:

- 1) Band gap for semiconductor $E_{g2} = 1.424$ eV
- 2) Effective density of states for the semiconductor conduction band
 $N_c = 4.7E17$ cm⁻³
- 3) Effective density of states for the semiconductor valence band
 $N_v = 7.0E18$ cm⁻³
- 4) Acceptor energy level above the semiconductor valence band
 $\epsilon_p = 0.03$ eV
- 5) Metal to semiconductor work function $\Psi_{ms} = -0.32$ eV
- 6) Metal/semi-insulator interface electron barrier $\Phi_n = 0.02$ eV
- 7) Semiconductor hole and electron lifetimes
 $\tau_p = \tau_n = 1.0E-9$ sec
- 8) Semiconductor dielectric constant $\epsilon_2 = 13.18$

- 9) Semi-insulator thickness $d_1 = 300 \text{ \AA}$
- 10) Spike layer thickness $d_2 = 30 \text{ \AA}$
- 11) Electron and hole thermal velocity $v_n = v_p = 1.0E7 \text{ cm/sec}$
- 12) Semi-insulator and semiconductor hole diffusion constant
 $D_p = 10 \text{ cm}^2/\text{sec}$
- 13) Semi-insulator and semiconductor electron diffusion constant
 $D_n = 220 \text{ cm}^2/\text{sec}$
- 14) Semiconductor intrinsic carrier concentration $n_i = 1.79E6 \text{ cm}^{-3}$

C. The OHMBIC Program

This program includes the ohmic contact approximation and the space charge in the semi-insulator. In addition to calculating the equilibrium parameters with the above approximations it also calculates them assuming that in addition there is a neutral zone in the spike layer. All the parameters are the same as those listed above for the GAASBIC program.

CHAPTER VII

RESULTS

A. The BICFET Program

Using the BICFET program, I-V curves were generated with similar values for N_d , J_s , etc. as was done elsewhere [1,3]. The appearance of the graphs was exactly like these previous results, however there was a significant increase in the current gain, G . The Fermi factor causes a reduction in the amount of effective negative charge contained in the spike layer which reduces p_0 and raises the gain. This increase in gain is due entirely to the decrease in p_0 , e.g. with $N_i = 3.0E12 \text{ cm}^{-2}$, $N_d = 1.0E15 \text{ cm}^{-3}$, $V_{ce} = 3.0 \text{ V}$ and $J_s = 40 \text{ Amp/cm}^2$ it was found that with Fermi we had $p_0 = 1.8E18$ and $G = 7.4E5$; and without Fermi $p_0 = 2.5E19$ and $G = 5.4E4$. Note that the product $p_0 G$ is a constant. Also, if we reduce N_i to $6.0E11 \text{ cm}^{-2}$ (i.e. 20% of the original N_i) and run no Fermi we find the results agree with the Fermi results for $N_i = 3.0E12 \text{ cm}^{-2}$ (the Fermi factor is 0.2 in this case).

It was also found that the choice of the degeneracy factor, g , had an effect on the gain (see section C. below).

B. The GAASBIC Program

Changing the value of the mole fraction, x , also does not affect the slope on the I-V curves. It does, however, have a dramatic effect on the gain as can be seen from Tables 1 and 2. When the equations given by Adachi [6] are used to calculate the band discontinuities and thus the gain there is an increase

x	N_{c1} (10^{17} cm^{-3})	ΔE_v (eV)	ΔE_c (eV)	P_o (10^{17} cm^{-3})	Gain (Amp/Amp)
0.1	5.60	0.015	0.110	8.23	0.55
0.2	6.55	0.029	0.220	8.66	1.09
0.3	7.55	0.044	0.330	9.02	2.13
0.4	8.60	0.059	0.440	9.43	4.09
0.5	187	0.074	0.500	9.85	154
0.6	182	0.089	0.514	10.2	250
0.7	177	0.106	0.528	10.7	451
0.8	172	0.126	0.542	11.2	904
0.9	167	0.148	0.556	11.8	2020
1.0	162	0.174	0.570	12.5	5000

TABLE 1. Using the GAASBIC program with Adachi's equations [6] for

ΔE_v and ΔE_c , the Fermi factor, $N_i = 3 \times 10^{12} \text{ cm}^{-2}$, $N_d = 10^{15} \text{ cm}^{-3}$, $V_{ce} = 3V$, and $J_s = 40 \text{ amps/cm}^2$.

x	ΔE_v (eV)	ΔE_c (eV)	E_{gl} (eV)	Po (10^{17} cm^{-3})	Gain (Amp/Amp)
0.1	0.047	0.078	1.549	8.85	1.8
0.2	0.094	0.156	1.673	9.95	1.13×10
0.3	0.140	0.234	1.798	11.1	7.13×10
0.4	0.187	0.312	1.923	12.4	4.45×10^2
0.5	0.235	0.339	1.998	13.8	5.52×10^4
0.6	0.290	0.312	2.027	15.5	4.07×10^5
0.7	0.354	0.279	2.058	17.7	4.13×10^6
0.8	0.427	0.241	2.092	20.4	5.77×10^7
0.9	0.508	0.196	2.128	23.7	1.11×10^9
1.0	0.598	0.146	2.168	27.8	2.97×10^{10}

TABLE 2. Using the GAASBIC program with other equations [4,5]

for ΔE_v and ΔE_c , the Fermi factor, $N_i = 3 \times 10^{12} \text{ cm}^{-2}$,
 $N_d = 10^{15} \text{ cm}^{-3}$, $V_{ce} = 3V$ and $J_s = 40 \text{ amps/cm}^2$.

in gain from 0.55 at $x = 0.1$ to 5000 at $x = 1.0$ while the other set of equations [4,5] gives a gain of 1.8 at $x = 0.1$ and $3.0E10$ at $x = 1.0$. The latter numbers give a much more optimistic prognosis for the possibility of the BICFET device working in the manner hoped for. Of course, an actual device would not reach these large gains because of physical reasons not yet brought into the model, but it does give a lot of working room. Also, from table 2 it is seen that there is a value of x where $\Delta E_c = \Delta E_v$. (Setting Eq.'s 3-13 and 3-22 equal to each other one finds that this occurs at about $x = 0.62$; however, for a total match one would have to also consider the effect of the differences in effective densities of states N_c and N_v .) This would allow for the possibility of constructing complementary devices whereas for the values given in Table 1 the band discontinuities would never match. Note that in Table 2, ΔE_c decreases at larger values of x . This is due to finding the value of ΔE_v from the lineup of the bands at the Γ -valley and then calculating ΔE_c from what is left over of the difference in the band gaps.

There is a large increase in gain for $x > 0.45$ that is due to the shift from the Γ -valley being the lowest conduction band to the X-valley being the lowest conduction band. (This is also where the material changes from a direct transition semiconductor to an indirect transition semiconductor.) This is a result of the change in N_c due to the significant change in the effective masses that occurs when going from the narrow Γ -valley to the broader X-valley. Note that for $x < 0.45$, N_c increases with x as a result of the effective mass increasing (curvature at minimum of energy decreasing) as the Γ -valley ascends and that for $x > 0.45$ the values of N_c decrease with increasing x which is due to the effective mass decreasing for the X-valley as x increases.

The change in p_0 is essentially negligible compared to other changes.

C. The OHMBIC Program

The assumption of a neutral zone in the spike layer was made in order to gain some insight into the validity of the approximation that the spike layer is fully depleted. For the conditions in Table 3 it would seem that this approximation is all right for a spike layer thickness of 30 angstroms or less, i.e. the depletion distance x_3^* is more than that for all but $x = 1.0$. However, when one considers the results shown in Tables 6 and 7 where the device is under bias there begins to be some doubt as to whether or not the spike layer is fully depleted. For example, in Table 7 the depletion distance, x_1 is only 0.453 angstroms for $x = 0.4$ while it was 34.3 angstroms in the equilibrium case. If there was a corresponding decrease in x_3 then the spike layer would not be fully depleted. One can make the argument that the depletion distance x_v is large enough to deplete the spike layer from the semiconductor side (see Fig. 9), however $x_v^* = 1.36 \text{ \AA}$ for $N_{D3} = 1.0E19$ and $N_{D4} = 1.0E15$. The value of x_v^* (as well as x_5^* , V_{b5}^* and V_{b5}) do not depend on x because the spike layer is in the semiconductor and this part of the device is a simple homojunction. The depletion in the spike layer coming from the semiconductor depletion is not strong enough for full depletion. The other possibility is that the positive charge from the inversion layer is enough to deplete the spike layer, however it can be seen from Table 5 that p_0 is on the order of $1.0E18$ for the Fermi case. Also this inversion charge falls off

x	$x_1^{\circ}(\text{\AA})$	$x_3^{\circ}(\text{\AA})$	$V_{b1}^*(\text{eV})$	$V_{b3}^*(\text{eV})$	ϵ_1 (10^{-12}F/cm)
0.1	32.4	35.4	-0.0735	-0.0857	1.14×10^{-12}
0.2	33.1	36.1	-0.0786	-0.0890	1.11
0.3	33.7	36.7	-0.0837	-0.0922	1.08
0.4	34.3	37.3	-0.0888	-0.0951	1.06
0.5	32.5	35.5	-0.0823	-0.0865	1.03
0.6	31.3	34.3	-0.0781	-0.0805	1.00
0.7	29.9	32.9	-0.0736	-0.0744	0.974
0.8	28.5	31.5	-0.0686	-0.0681	0.946
0.9	27.0	30.0	-0.0636	-0.0618	0.918
1.0	25.5	28.5	-0.0582	-0.0555	0.891

TABLE 3. Equilibrium depletion distances and voltages assuming a neutral zone

in the spike layer and using the OMNIG program with $N_{a3} = 10^{19}\text{cm}^{-3}$
 $(N_a = 3 \times 10^{12}\text{cm}^{-2})$, $N_{d1} = 10^{19}\text{cm}^{-3}$, $N_{d2} = 10^{17}\text{cm}^{-3}$, $N_{d4} = 10^{15}\text{cm}^{-3}$,
 $V_{ce} = 3.0\text{V}$, $J_s = 40\text{Amp/cm}^2$ and ΔE_v the same as in Table 2.

rapidly and therefore may not be enough to do the job. If one could make an estimate of the total amount of inversion charge then a reasonable assessment of the situation could be made.

It is seen in Table 3 that the variables have a slight dependence on x , which comes from ϵ_1 and N_{c1} (which depend on x) in Eq.'s 4-14, 4-15, 5-25, 5-26, 5-37 and 5-39.

In Table 4 the equilibrium parameters are calculated with assuming an inversion layer at the spike layer/semiconductor interface, i.e. no neutral zone in the spike layer. The results for Fermi and no Fermi are essentially the same since the Fermi factor is approximately one for all calculated values. The value for x_5^* is overestimated since it is calculated from Eq. 4-12 which does not take into account the inversion charge, p_0 . While most of the parameters show a weak dependence on x , p_0^* varies by six orders of magnitude. This strong dependence comes from the variation of ϵ_1 (Table 3) and Ψ_{14} (Table 4) and the exponential behavior of Eq. 4-18. It is seen in Eq.'s 4-14 and 4-15 that V_{b1}^* and V_{b2}^* become more negative as ϵ_1 decreases with x and Q_e^* remains almost constant (note that this also includes the second term in Eq. 4-15 since C_i is proportional to ϵ_1). There is also the dependence of Ψ_{14} on ΔE_c in Eq. 4-20 so that as ΔE_c increases Ψ_{14} becomes more negative. These two factors combine in Eq.'s 4-16, 4-17 and 4-18 to give a strong dependence of p_0^* on x . For $x < 0.45$, ΔE_c increases and drives down the value of p_0^* , while for $x > 0.45$, ΔE_c decreases and thus both factors (ϵ_1 and Ψ_{14}) cause a rapid increase in the value of p_0^* as a function of x . This result illustrates that because of the exponential behavior of this device one cannot easily assume that certain dependencies (e.g. ϵ_1 on x) are essentially negligible. The reason that $x = 1.0$ was not calculated in Table 4 is that when

$$p_0^* > \beta \Phi_s^* N_{d4} \cong 3 \times 10^{16} \quad 7-1$$

the iteration loop (see section IV-B) becomes unstable. This happens because until the inequality in Eq. 7-1 is reached p_0^* is not a factor in Eq. 4-19.

The non-equilibrium values found using the OHMBIC program are shown in Tables 5, 6 and 7. The gains for the Fermi and no Fermi that are presented in Table 5 are seen to have the same qualitative behavior as those found for the BICFET program, i.e. the product $p_0 G$ is a constant for a given value of x and the gain is higher for the Fermi case. Comparing these results (Table 5 with Fermi) with the ones for the GAASBIC program (Table 2) it is seen that there is a slight insignificant difference in p_0 and a slight difference in the gain. The reason the gain for the OHMBIC case is larger than the GAASBIC case is that the OHMBIC gain does not include the electron barrier potential, Φ_n , as was done in the GAASBIC program. When this factor is included (as it probably should be) the two products $p_0 G$ are identical for the two cases. The above results mean that the inclusion of the space charge in the semi-insulator region had very little impact on the functioning of the device. However, this space charge could have more effect at lower values of V_{ce} . This could not be checked out since the program did not run at values of V_{ce} lower than 0.5 V. The voltage across the semi-insulator due to the space charge in the semi-insulator was found to be -0.068 V for $N_{d2} = 1.0E17$ and $d_1 = 300 \text{ \AA}$. This is more than half of V_i for many values of x .

x	$Po(cm^{-3})^*$	$V_{bi}(eV)^*$	$V_i(eV)^*$	$\phi_s(eV)^*$	$x_1^*(\text{\AA})$	$x_5^*(\mu m)$	$\psi_{14}(eV)$
0.1	3.30×10^{12}	-0.0469	-1.15	0.888	25.9	1.14	-0.312
0.2	6.32×10^{11}	-0.0483	-1.18	0.845	25.9	1.11	-0.385
0.3	1.27×10^{11}	-0.0496	-1.21	0.803	25.9	1.08	-0.460
0.4	2.68×10^{10}	-0.0510	-1.25	0.763	25.9	1.06	-0.534
0.5	6.89×10^{11}	-0.0521	-1.28	0.848	25.9	1.11	-0.482
0.6	7.32×10^{12}	-0.0534	-1.31	0.909	25.9	1.15	-0.456
0.7	1.03×10^{14}	-0.0547	-1.35	0.977	25.8	1.19	-0.424
0.8	1.88×10^{15}	-0.0560	-1.38	1.05	25.7	1.24	-0.386
0.9	2.55×10^{16}	-0.0562	-1.41	1.12	25.4	1.28	-0.342

TABLE 4. Equilibrium voltages and depletion distances using OHMBIC with assuming no

neutral zone in the spike layer, and using the same conditions as in Table

3. The results are the same for Fermi or no Fermi. The value of Q_e^* is

almost a constant for all values of x and is about $4.13 \times 10^{-7} \text{ Col/cm}^2$.

x	$N_{v1} (10^{18} \text{ cm}^{-3})$	NO FERMI		FERMI	
		$Po (10^{19} \text{ cm}^{-3})$	Gain (Amp/Amp)	$Po (10^{17} \text{ cm}^{-3})$	Gain (Amp/Amp)
0.1	7.27	1.23	0.28	7.70	4.44
0.2	7.53	1.37	1.79	8.65	2.83×10
0.3	7.81	1.51	1.14×10	9.68	1.78×10^2
0.4	8.08	1.65	7.27×10	10.8	1.11×10^3
0.5	8.36	1.79	9.22×10^3	12.0	1.38×10^5
0.6	8.65	1.96	7.00×10^4	13.4	1.02×10^6
0.7	8.93	2.15	7.37×10^5	15.3	1.03×10^7
0.8	9.22	2.36	1.08×10^7	17.6	1.44×10^8
0.9	9.52	2.60	2.20×10^8	20.5	2.78×10^9
1.0	9.82	2.87	6.23×10^9	24.2	7.41×10^{10}

TABLE 5. Non-equilibrium values using OHMBIC with the two options Fermi

and No Fermi. The conditions are the same as in Table 4.

x	$V_{b1}(10^{-3} \text{ eV})$	$V_i(\text{eV})$	$\phi_s(\text{eV})$	$Q_e(10^{-8} \text{ Col/cm}^2)$	$x_1(\text{\AA})$	$x_5(\mu\text{m})$
0.1	-2.04	-0.290	2.98	8.61	5.38	2.08
0.2	-1.28	-0.247	2.86	6.74	4.21	2.04
0.3	-0.703	-0.203	2.74	4.94	3.09	2.00
0.4	-0.303	-0.159	2.65	3.20	2.00	1.96
0.5	-0.0679	-0.114	2.63	1.50	0.934	1.96
0.6	-0.00451	-0.0605	2.60	-0.380	0.238	1.95
0.7	-0.191	0.00126	2.58	-2.44	1.53	1.94
0.8	-0.720	0.0719	2.54	-4.67	2.92	1.93
0.9	-1.69	0.152	2.51	-7.04	4.40	1.91
1.0	-3.19	0.240	2.47	-9.54	5.96	1.90

TABLE 6. No Fermi option using OHMBIC with the same conditions as

Table 4.

x	$V_{bi} (10^{-4} \text{ eV})$	$V_i (\text{eV})$	$\phi_s (\text{eV})$	$Q_e (10^{-8} \text{ Col/cm}^2)$	$x_1 (\text{\AA})$	$x_5 (\mu\text{m})$
0.1	-9.67	-0.220	2.91	5.94	3.71	2.06
0.2	-4.79	-0.176	2.79	4.13	2.58	2.02
0.3	-1.65	-0.133	2.67	2.39	1.50	1.47
0.4	-0.155	-0.0875	2.55	0.726	0.453	1.93
0.5	-0.248	-0.0437	2.56	-0.903	0.564	1.93
0.6	-2.27	-0.00894	2.54	-2.70	1.68	1.92
0.7	-7.01	-0.0701	2.51	-4.67	2.92	1.91
0.8	-15.3	0.140	2.48	-6.81	4.26	1.90
0.9	-28.1	0.218	2.44	-9.08	5.68	1.89
1.0	-46.2	0.306	2.41	-11.5	7.17	1.87

TABLE 7. Fermi option using OHMBIC with the same conditions as in Table 4.

The charge Q_e comes from the depletion charge in region 1, i.e. the n+AlGaAs area, and therefore cannot be negative. However, in Table 6 we see that it is negative for $x > 0.5$. Mathematically this is not a problem, but physically this cannot happen. What must be happening physically is that the neutral zone must be moving into the semi-insulator for $x > 0.5$. When Q_e goes negative the program should shift to a new set of equations that assumes that the neutral zone is moving into the semi-insulator. The depletion distance x_1 , is calculable (but somewhat meaningless) for $x > 0.5$ because the charge is squared (see Eq. 4-8) when the voltages are calculated. However, this distance x_1 can be used to estimate how much of the semi-insulator is not depleted. When Q_e goes negative it is compensating for the positive charge in the semi-insulator, therefore one can estimate the neutral zone incursion into the semi-insulator by multiplying x_1 by the ratio N_{d1}/N_{d2} (=100 in this case). For $x = 0.7$ this would give 292 Å. These results indicate that the assumption that the semi-insulator is depleted at all times may not always be correct, therefore if we wish to take advantage of the large jump in gain for $x > 0.5$ we need to find the conditions under which the semi-insulator is fully depleted.

Since the numerical value assigned to the degeneracy factor, g , for a dopant in a semiconductor is somewhat uncertain [9] it was varied in order to see the effect. From Table 8 we see that the larger g is, the more it reduces p_0 and increases the gain.

CHAPTER VIII

CONCLUSIONS AND RECOMMENDATIONS

Both the Fermi factor and the value of x have a significant impact on the gain. The Fermi factor reduces the effective amount of charge in the spike layer thereby decreasing p_0 and increasing the gain. Larger values of x mainly increase the gain thru the increase in ΔE_v , but also cause an increase in N_c , which also increases the gain significantly (especially for $x > 0.45$). It would be extremely interesting to process some devices with varying values of x to see if the gain actually depends on x in such a dramatic fashion.

Consideration of the ohmic contact resulted in a better understanding of where the emitter charge, Q_e , comes from (depletion zone in the n+AlGaAs layer) and the realization that the placing of a n+AlGaAs layer between the semi-insulator and the n+GaAs ohmic contact layer results in two distinct benefits: (1) an increase in gain thru an increase in N_c , and (2) a reduction in the effective barrier that the electrons see. This n+AlGaAs layer does not have to be very thick (10 angstroms or less, see Table 6) for it to be effective. Processing some wafers with this additional layer could lead to a better understanding of these effects and possibly to a better functioning device.

It appears that both the spike layer and the semi-insulator may not be fully depleted under some conditions. Since this is one of the basic assumptions in the model of the BICFET there should be more theoretical investigations as to what are the conditions under which they are not depleted and

^g (Degeneracy Factor)	Fermi Factor	Po (10^{19} cm^{-3})	Gain (10^7 Amp/Amp)
0	1.0	2.36×10^{19}	1.08
1	0.371	0.372	6.85
2	0.299	0.257	9.91
3	0.262	0.206	12.3
4	0.237	0.176	14.4

TABLE 8. The effect on the Fermi factor, the gain and po as to the choice of the degeneracy factor, g. Taking $g = 0$ is equivalent to the no Fermi case.

The conditions are the same as in Table 4.

what impact this has on the functioning of the device. Experimentally, one can vary the doping in the spike layer and observe the result. Reducing this doping level should raise the gain and also make it more likely that the spike layer is fully depleted.

Including the space charge in the semi-insulator did not affect the gain, but it did bring into question one of the approximations of the model (see Eq. 4-26). The equations should be solved again with this change to see the effects of the approximation. This change should increase the current levels.

There are two other parameters that depend on x where this dependence was not taken into consideration. The ionization energy ($\epsilon_p = E_A - E_V$) of the acceptor levels increases with x . This would have the same effect as raising g , the degeneracy factor, i.e. the gain would increase because it would lower the amount of negative charge in the spike layer and thus lower p_0 and raise the gain. The thermal velocity of the electrons is also a function of x . It appears that this could increase the gain by about a factor of 3 for $x < 0.45$ and by about 1.5 for $x > 0.45$.

The BICFET as now understood holds much promise, but the theoretical understanding and the experimental development of this device are still in the early stages and much needs to be explored.

REFERENCES

1. Taylor, G.W. and J.G. Simmons, "The Bipolar Inversion Channel Field-Effect Transistor (BICFET)-A new Field-Effect Solid-State Device: Theory and Structures", IEEE Transactions on Electron Devices, ED-32, 2345-67, Nov. 1985.
2. Taylor, G.W. and J.G. Simmons, "Small-Signal Model and High-Frequency Performance of the BICFET", IEEE Transactions on Electron Devices, ED-32, 2368-77, Nov. 1985.
3. Whitson, D.W. and W.D. Schmidt, "Analytical Computer Modeling of the NPN BICFET Device, "Final report, 1986 USAF-UES Summer Faculty Research Program, Air Force Office of Scientific Research, Contract No. F 49620-85-C-0013.
4. Hill, A.J. and P.H. Ladbroke, "Dependence of Conduction-Band Discontinuity on Aluminium Mole Fraction in GaAs/AlGaAs Heterojunctions", Electronics Letters, 22, 218-20, Feb. 1986.
5. Drummond, T.J. and I.J. Fritz, "Modulation-doped (Al,Ga)As/AlAs superlattice:Electron transfer into AlAs", Appl. Phys. Lett. 47(3), 284-6, Aug. 1985.
6. Adachi, S., "GaAs, AlAs, and $\text{Al}_x\text{Ga}_{1-x}\text{As}$: Material parameters for use in research and device applications", J. Appl. Phys., 58(3), R1-R29, Aug. 1985.
7. Liou, L., Private communication, AFWAL-AADR, Wright-Patterson AFB, Ohio.
8. Sze, S.M., "Physics of Semiconductor Devices", Wiley-Interscience, 2nd Edition, 1981.
9. Milnes, A.G., "Deep Impurities In Semiconductors", Wiley-Interscience, 1973.

REPORT
FACILITY RESEARCH PROGRAM

Sponsored by the
AIR FORCE OFFICE OF SCIENTIFIC RESEARCH
Conducted by the
UNIVERSAL ENERGY SYSTEMS, INC.

FINAL REPORT
THE JARREHOWSE LAYOUT PROBLEM

Principal Investigator:	Jesse Williams
Researcher's Rank:	Associate Professor
Institution and University:	Mathematics/Computer Science Cheyney University
Research Location:	Cheyne, University Cheyney, PA 19319
AFOSR Researcher:	Capt. Robert Furlison SMSgt William Eldridge Air Force Logistics Management Center AFLMCD/LOGS Bunker AFB, AL 36114-6670
Date:	31 January 1986
Contract No.:	F49620-83-C-0010/84-0001-0000
Contract No.:	8-761-2000-000

THE WAREHOUSE LAYOUT PROBLEM

IV

Jesse Williams

ABSTRACT

This paper is concerned with developing a microcomputer model that will rearrange items within an Air Force warehouse from their initial locations to desired locations. Such a rearrangement is necessary since the present arrangement of items within these Air Force warehouses was not designed by scientific principles. A efficient design would minimize the total travel distance, which is the number of times an item is picked up to the total distance from the warehouse storage location to the pickup and delivery area. As demands for items change it is not efficient to have low demand items near pickup and delivery area. A heuristic technique is developed for a microcomputer model which is to be used by base level personnel in the warehouse. The technique relocates items with higher demand for pickup and delivery closer to the pickup and delivery area. The development process takes place in two phases.

II. INTRODUCTION The United States Air Force (USAF) has determined that the location of items within its warehouses should be done with the objective that the warehouse is efficient in the use of manpower. The Air Force Logistics Management Center (AFLMC) was given this task and the first phase of this project was to develop a microcomputer model that could be used by base level warehouse personnel. The first phase of the project was completed during the summer of the 1985. The second phase of the project was completed through a mini-grant, December, 1986. The mini-grant proposal included weight and size considerations for isolated items in the warehouse. However, after consulting with AFLMC personnel it was determined that this type of data was not available nor did anyone have an interest in such data at the present time.

III. OBJECTIVES OF THE RESEARCH EFFORT At the present time the USAF does not utilize any scientific principles with respect to the location of items within the warehouse. When items are sent to the warehouse the personnel at the facility will locate an item in the first open bin available if the prescribed location is available. There is no systematic technique utilized to determine the location that would be most efficient for the item. Some common sense and intuition are used to place the items and not utilized when determining where an item should be located.

The AFLMC was given the task of developing a microcomputer model which would assist the warehouse personnel at the base level with

determining the most efficient location for an item. Here efficiency is measured as the product of the demand for an item and the distance the item is located from the pickup and delivery area. Reducing the total travel distance of an item, consequently, increases the efficiency of the warehouse.

In consultation with USAF Research Colleague it was determined that a user friendly microcomputer model should be developed which would be used by base level warehouse personnel and which would rearrange items in the warehouse. This rearrangement would reduce the total travel distance of the present (initial) layout. This model was to have the capability of rearranging consecutive rows or selective rows. The model should also be able to handle approximately 10,000 items. In addition to developing the microcomputer model a User's guide was to be developed that would enable the user of the model to do so with ease. The model would be tested on actual data from the Supply Data Bank.

During the second phase of the research the AFLHC personnel made the inclusion of a common customer identification into the item records of warehouse items and this identification would take precedence over the demand for an item. Common customer items were to be located in adjacent bins or each row.

III. HEURISTIC TECHNIQUE: The problem of warehouse layout can be described as follows. The total travel distance of an item is defined to be the product of times (demand) made to pickup the item and the distance traveled to pickup the item. The total

travel distance of the warehouse is the sum of the costs of the individual items in the warehouse. Our objective is to reduce this total travel distance (C) as much as possible. Formally, the problem is to

$$\text{minimize } C = \sum_{i=1}^N \sum_{j=1}^N T_{ij} D_{ij} \quad (1)$$

where T_{ij} = trips between location i and location j ,
 D_{ij} = distance from location i to location j ,
 and N = number of locations.

In the literature, e.g. [1], a solution technique to this problem starts with an arbitrary initial layout and then obtains a new layout by interchanging locations pairwise. Compute the travel distance of this new layout to the initial layout and continue developing new layouts until the total travel distance of a layout can no longer be reduced.

The proposed solution technique considered in this paper attempts to obtain an optimal or near optimal solution layout on the first rearrangement. The Williams' heuristic technique claims that the first rearrangement it produces is optimal or near optimal with respect to reducing the total travel distance of the layout. This technique uses a sorting technique to solve the problem. The items in order of trips to a pickup or item is sorted into descending order. The sum of distances between pair locations and item to be delivery is sorted in a descending order. The items are then placed in the line and put the item with shortest distance placed in the line with the longest distance. Then the

er, with the next highest value is placed in the bin with the fewest elements. This process is repeated until all items are distributed in bins and a complete layout has been obtained. This layout is claimed to have the minimum or near minimum total travel distance of all possible layouts.

The method described involving the Williams' technique can be found in the Appendix.

When no customer identifications are taken into consideration the total travel distance is not reduced as much as without common customer consideration. Common customer location does not take into the demand of an item when the common customer item location is present, but only considers the common customer location only. This means that some common customer items will have higher demands than non-common customer items and these items will be closer to the pick up and delivery area than some non-common customer items. However, a common customer item location is more important in the AFMC personnel with regard to locating the item than the demand for the item.

EXAMPLES OF THE METHOD: The following are written in AFMPC 77 format and are in IN-27 format later with a 40 percent of 60 percent 100 percent demand drive. The standard model was written in FORTRAN 77 and on a Digital I-240 with 1.7 megabytes of RAM and 40 megabyte hard drive, and a data controller. The standard program was extended into a 100 percent demand drive and a 100 percent demand drive. Both files are included as

bins of the rackside in order to make the use of the rackside as easy as possible. The advanced model sorts the demand of the items into descending order and places these items into bins according to distances of the bins from the pickup and delivery area. The output of the model selects the rows and bins to be rearranged within a specified area in the warehouse. The program generates distances in a matrix with respect to rows and bins selected by the user. The user must input distance of the picker to bin selected to the pickup and delivery area. The program generates distances in an ordinal manner for each row. The user inputs the level desired for rehousing. In the first version of the program the user selected the number of levels desired to be reworked. In the second version of the program the user selects the level to be reworked. When asked the distance of the picker with respect to locating items which will be first selected by the JPLRD personnel. Flexibility is offered to the user because the rows selected do not have to be consecutive in sequence.

The enhanced model considers common customer identification when locating items in the bins. Common customer items are placed on the same row or at least adjacent to each other on the same row. In the implementation of common customer identification, the program will not consider the demand of the item. All common customer items are located nearest the pickup and delivery area first. After the remaining items are located nearest to each other, they are located according to the demand for the item as

described above.

Output of the program includes a reformatted list of recommendations of the total travel distance of the initial level versus total travel distance of the recommended level. This information was not part of the model. Location of each demand zone was supplied by the user in an FDP file utilizing the AFMIO format.

Data provided for the program consists of approximately 100000 zones. In order to manipulate this size of file, the Shell-Hunter sort routine was utilized. Sorting was not necessary for saving large amounts of data.

Calculations were made for the total travel distance of the initial level and the total travel distance of the recommended level.

6. RECOMMENDATIONS:

a. Since the program is user friendly, utilization by base level personnel would increase efficiency within AFMIO operations. The resultant use of an efficient base level would allow the AFMIO personnel to work more effectively and provide a more efficient service.

b. The evaluation of the FDP program and its results was not a complete first for AFMIO personnel. AFMIO personnel are not familiar with the use of the

designed for large embedded systems. When FORTRAN 77 compilers will provide the facilities for embedded systems become available, the embedded control program should be recoded in the current version of FORTRAN. In order to take advantage of many new facilities of the language that are not available in FORTRAN 77.

APPENDIX

The method underlying the Williams' technique is as follows. Suppose we have two sets of nonnegative numbers defined as

$$(i, i+a, i+b) \text{ and } (j, j+c, j+d),$$

where $a \geq b$ and $c \geq d$. If we multiply the three numbers in each set pairwise and sum the products we have

$$[i^2 + (i+a)i + (i+b)i] + [j^2 + (j+c)j + (j+d)j].$$

This is one of $3! (= 6)$ possible sums of products. Of all these possible sums which is the minimum? The above sum is the maximum. The minimum can be obtained if we change the ordering of the two given sets such that the orderings are in cases which are opposite to each other. By this we mean that one set is in ascending order and the other set is in descending order. E.g.,

$$(i, i+a, i+b) \text{ and } (j+d, j+c, j)$$

are now multiplied pairwise and summed. The result is

$$[i^2 + (i+a)i + (i+b)j] + [j^2 + (j+c)j + (j+d)i].$$

All 12 of the summations will have the same set of variable terms and will differ only in the constant terms. In all summations have the same variable terms, then we are interested in the constant terms to determine the minimum summation. The constants for the 12 summations are

$$ad + bd, ad + cd, bd, ad, bd, ad, ad, ad, ad, ad, ad, ad.$$

It can be seen that ad is the minimum of this set. It was noticed above that $ad + bd$ is the maximum of this set. This can be seen by considering the other $ad + cd$ and $ad + bd$. This is shown in the following steps.

$$ad + bd \text{ and } ad + cd.$$

$$a \geq b$$

$$\begin{aligned}
 & \text{where} \\
 & \text{and} \\
 & (c-b) \text{ is the} \\
 & \text{unacknowledged} \\
 & \text{acknowledged} \quad \text{...} \\
 & \text{or} \\
 & \text{and} \\
 & (c-b) \text{ is the} \\
 & \text{acknowledged} \\
 & \text{acknowledged} \quad \text{...}
 \end{aligned}$$

Therefore, the summation obtained from pairwise multiplication with both sets sorted in ascending order (or both sets sorted in descending order) gives a maximum result. A similar result is obtained if the sets are sorted in reverse before multiplying the two sets.

ACKNOWLEDGEMENT

This research effort was made possible through the generous support of the Air Force Systems Command, Air Force Office of Scientific Research, and the Air Force Logistics Management Center. In particular, the contributions of Major Douglas A. Pinner and Captain Robert E. Pinner during phase one of the project, and the contributions of Captain Robert E. Pinner and Captain William H. Pinner during phase two of the project have played an important role in the research effort.

REFERENCES

1. Evans, Everett L., Jr. and Ronald G. Evans, *Facilities and Equipment Management*: Principles, Methods, and Applications, 2nd Edition. Englewood Cliffs, NJ: Prentice-Hall, Inc., 1975.
2. Brown, Frank, *Self-Service Engineering with Applications to Retail*. New York: The Benjamin Cummings Publishing Co., 1961.
3. Buffa, E. W. and B. J. Gass, *Facilities Management: Principles and Applications*, 2nd Edition. New York, John Wiley & Sons, Inc., 1978.
4. Christopoulos, Nicos and J. Corlett, "The Rearrangement of Items in a Warehouse." *Ergonomics Research Journal*, v. 2, No. 1, Mar. Apr. 1978, pp. 377-389.
5. Prince, L.R., "Techniques for Facilities Layout: Declining Number of Activities Should Be Adjacent." *Management Science*, Vol. 27, No. 10, December 1981, pp. 1414-1416.
6. Jackson, Gary K., "Facility Layout Optimization Using a Genetic Algorithm." *Industrial Engineering*, Vol. 16, No. 3, 1974, pp. 11-23.
7. Johnson, Richard A., William T. Jewell, and Roger L. Vander, *Operations Management: A System Approach*, 2nd Edition, Macmillan, 1972.
8. Menckner, S. and Dick Chudach, "Computer Aided Facility Layout: A Case Study Generates Alternatives To Increase Efficiency From a Retail Store." *Industrial Engineering*, Vol. 16, No. 3, 1974, pp. 24-30.
9. Gilbreth, Lillian and Loran Gilbreth, *Engineering of Man and Machine*. New York: Dover University Press, 1917.
10. Gilbreth, Lillian B., *Scientific Management*. Boston: Heath and the Company, a Division of Houghton Mifflin Co., 1911.

FINAL REPORT NUMBER 92
RECEIVED A NO-COST TIME EXTENSION
TO BE SUBMITTED IN 1987 MINI-GRANT FINAL REPORT
Dr. Shirley Williams
760-6MG-078

FINAL REPORT NUMBER 93
REPORT NOT RECEIVED IN TIME
WILL BE PROVIDED WHEN AVAILABLE
Dr. Billy Wooten
760-6MG-051

FINAL REPORT NUMBER 94
REPORT NOT RECEIVED IN TIME
WILL BE PROVIDED WHEN AVAILABLE
Dr. Tsun-wai Yip
760-6MG-109

1986 - 1987 USAF - UES FACULTY MINI-GRANT
Sponsored By The
AIR FORCE OFFICE OF SCIENTIFIC RESEARCH
Conducted By The
UNIVERSAL ENERGY SYSTEMS, Inc.

FINAL REPORT

CHANGES IN PERCEIVED WORKLOAD AND PHYSIOLOGICAL
RESPONSES ASSOCIATED WITH
MONOCULAR VERSUS BINOCULAR VIEWING CONDITIONS

Prepared By
Robert L. Yolton, O.D., Ph. D.
Pacific University
College of Optometry
Forest Grove, Oregon 97116

Submitted
December 31, 1987

Contract Number: F49620-85-C-0013/SB5851-0360
Purchase Order Number: S-760-6MG-037

ACKNOWLEDGEMENTS

This project would not have been possible without the assistance of Glenn Wilson and Gray Reid, Armstrong Aerospace Medical Research Laboratory (AAMRL), Wright-Patterson AFB, Iris Davis, Systems Research Laboratories, Inc., Dayton, OH, and my research associates at Pacific University: Kyle Kelly, Jim Simoens, Bill Woodman and Mike Young.

I am pleased to also acknowledge the support of Pacific University College of Optometry, the Air Force Office of Scientific Research, the AAMRL at Wright-Patterson AFB, OH and Universal Energy Systems, Inc.

ABSTRACT

This project investigated how disruption of normal binocular vision produced by monocular occlusion or dioptric blur affected selected workload/performance indicators. Indicators of workload/performance included subjective workload assessment technique (SWAT) ratings and button press reaction times (RT), as well as amplitudes and latencies of the P-300 and P-180 electroencephalographic (EEG) potentials (recorded from scalp locations Pz and Cz, respectively). Using an odd-ball paradigm in which subjects read and categorized stimuli presented on a video monitor, 21 subjects participated in four Experiment Sets: 1) monocular full field and stimulus field occlusion, 2) differential blurring of images from the eyes, 3) full field monocular occlusion without a button press requirement, and 4) full field occlusion with a task unfamiliar to the subjects. RTs and P-180 amplitudes showed no significant effects caused by binocular disruption in any of the Sets. For about half of the viewing conditions, SWAT, P-300 amplitude and latency and P-180 latency were significantly affected by binocular disruption. There was, however, not a consistent pattern of these effects across Experiment Sets. Within Experiment Sets, suggestively strong correlations were found between several of the workload/performance indicators but these correlations did not hold up when data from multiple Experiment Sets were combined. In summary, changes in EEG signals and SWAT ratings were produced in certain of the Experiment Sets by disruption of binocular vision but the changes did not translate into significant RT increases. If RT is considered to be the most important requirement for choosing a monocular or binocular display, these experiments show no significant advantage for either type of display.

INTRODUCTION

It is obvious that having two laterally placed eyes makes stereoscopic depth perception possible for humans. It is less obvious, however, that having two eyes viewing a flat, centrally located target provides significantly more information to the brain than would be provided by using one eye alone. The question of a "binocular advantage" is an important one with both military and civilian implications. From a military perspective, head-up displays (HUD) are available in both monocular and binocular form and it is certainly important to know if there are differences in the rate or quantity of information that can be transferred to an observer using one eye alone versus both eyes simultaneously. In the civilian sector, many presbyopic patients requiring different lens powers for distance and near vision are fit with contact lenses using the Mono-vision technique. In this technique, one eye is fit with a lens which allows clear vision at near only, and the other eye is fit with a lens (of a different power) which allows only clear distance vision. While many patients find Mono-vision a very satisfactory compromise, it is important to know if there are detrimental effects on mental information processing created by this technique. If shifting from binocular to monocular viewing has negative effects, both monocular HUDs and Mono-vision contact lens fitting may have significant disadvantages which need to be explored.

There are several studies in which monocular and binocular vision have been compared. In an early paper (with only three subjects), Poffenberger (1912) found a significant increase in

simple reaction time (RT) when a stimulus light was viewed monocularly. In 1954, Teichner noted that very little work had been done on monocular versus binocular RTs since Poffenberger's study, and suggested that this was probably because it seemed obvious to most researchers that there would be a binocular advantage due to summation of information coming from both eyes. Teichner and Krebs (1972) reviewed the literature and developed basic principles for simple visual RTs. Although some contradictory data were discussed, they concluded that the weight of evidence suggested that monocular RTs were longer than corresponding binocular RTs. In 1981, Jones and Lee conducted a series of ten experiments and also found a binocular advantage for several tasks which did not require stereopsis. The most recent publication in this area comes from Sheedy, Bailey, Buri and Bass (1986). Using behavioral techniques similar to those of Jones and Lee, Sheedy, et. al, found significant binocular advantages on tasks such as placing pointers in straws and needle threading which required stereopsis, and found non-significant (but suggestive) binocular advantages when performing non-stereoscopic tasks such as reading and letter counting.

Taken as a group, these studies suggest that there may be a small but significant advantage in RTs and performance abilities detectable when tasks not requiring stereoscopic depth perception are performed binocularly rather than monocularly. If such an information processing advantage does exist, it may not be of importance for tasks such as reading a single letter from a display

screen, but it may be very important in other situations. For example, small RT differences can be critical in life or death situations which require immediate decisions to be made based on monocularly or binocularly HUD presented information. Small differences may also be important if the overall task consists of a sequence of separate tasks and a small binocular advantage on each individual task cumulates to make a major difference in total task performance. Finally, it is possible that even though there is no monocular versus binocular performance difference on a given task, the workload associated with formulating a correct response may be very different when information is presented to one eye versus two. Subjects may have to do less work to produce a correct response if information is presented binocularly, but compensatory mechanisms could make RTs and other performance indicators the same for both monocular and binocular viewing.

WORKLOAD

The mental workload that a subject experiences when performing a task is a function of many factors. These include the effort required to obtain the sensory input needed to perform the task, the mental processing required to analyze the input data and determine a correct response and the complexity of the required response. Interacting with these factors are subject-specific conditions such as fatigue (Krueger, Armstrong and Cisco, 1985), attentional resources available for allocation to the task (Wickens, 1981), perceived task importance, etc. Changes in workload can be produced by altering any or all of the above factors.

To assess workload, several approaches have been used, the simplest of which involves measuring the time required to complete a task and noting the accuracy of the subject's responses (Sternberg, 1969). As workload increases, RT typically increases and accuracy decreases. A more sophisticated, and perhaps more valid way of assessing workload, involves obtaining a subjective rating immediately following the performance of a task. The subjective workload assessment technique (SWAT) system developed at AAMRL, Wright-Patterson AFB (Eggemeier, 1985; Reid, 1985; Reid, Shingledecker and Eggemeier, 1981; Reid, Shingledecker, Nygren and Eggemeier, 1981) uses subjective estimates of time, effort and stress to provide assessments of workload which are directly comparable across subjects. In this project, SWAT ratings will be considered to be "true" measures of workload and other indicators will be compared against them.

Physiologically, the effects of workload can be detected as alterations in EEG potentials (Brookhuis, Mulder, Mulder and Gloerich, 1983; Poon, Thompson and Marsh, 1976; Hillyard and Kutas, 1983). EEG changes related to workload/task performance have been reported to involve long latency event related potentials, such as the P-300 (Donchin, 1979; Donchin, 1981; Pritchard, 1981). In odd-ball tasks, latency of the P-300 is related to simple reaction times (Ritter, 1978) and is a good indicator of the difficulty subjects have in differentiating common from novel stimuli (Duncan-Johnson, 1981; McCarthy and Donchin, 1981; Kutas, McCarthy and Donchin, 1977). For visual tasks, this difficulty and the related

workload can be increased by blurring the stimuli, by decreasing their size (Fagan, Westgate and Yolton, 1986) or by forcing subjects to view them through optical prisms (Dirks 1987).

P-300 amplitudes may also be good indicators of task complexity/workload. Johnson (1986) has cited several studies in which P-300 amplitudes increased as tasks were made more complex or difficult. It is possible that this increase in amplitude might be mediated via an increase in attention required by the more complex stimuli, but the increase still provides a good indicator of workload change.

Thus, changes in workload/performance can be assessed in many ways. Subjectively, a sophisticated device such as the SWAT can be used to ask how hard a task was, and parallel data can be obtained objectively by assessing RTs and selected EEG signals. These measurement procedures will be used extensively in the experiments described below.

PROJECT GOAL

This project was designed to determine if disrupting normal binocular vision through occlusion of all or a relevant portion of the visual field of either eye, or through differentially blurring the vision of the eyes, would cause changes in the subjective and objective workload indicators discussed above.

Four sets of experiments were conducted in pursuit of this goal. In Experiment Set 1, the effects of total monocular occlusion and monocular occlusion of only the stimulus portion of one visual field were studied. In Set 2, binocular vision was disrupted by using plus lenses to blur the vision of one eye and to differentially

blur the vision of both eyes. Experiment Set 3 was designed to assess the effects on EEG signals of the activity required to press a response button each time a stimulus was displayed, and Set 4 involved a determination of the effects of monocular occlusion on an unfamiliar task.

Because the subject pool, stimulus display system, and data recording and analysis procedures were essentially the same for all Experiment Sets, they will be described below. Variations will then be noted in the presentations of the individual Sets.

SUBJECTS AND METHODS COMMON TO ALL EXPERIMENT SETS

SUBJECTS

The subject population consisted of 30 college students and spouses: 21 males and 9 females. Mean age was 27.0 (SD = 3.9; range = 20 to 35). All subjects had near equivalent Snellen visual acuities of at least 6/6 (20/20) and minimum stereo acuities of 40 arc sec as measured with the Titmus Stereo-fly test. Ocular dominance of each subject was determined by use of an aperture sighting task with a distant target (Beach, 1977). Most subjects required spectacle corrections to achieve 20/20 visual acuity and these corrections were worn at all times during the Experiment Sets. No subject had significant ocular or physiological anomalies which could have affected the results of the experiments.

METHODS

Stimulus Display

In the Experiment Sets, an odd-ball paradigm was used in which subjects viewed a series of names on a video monitor and

categorized them with respect to gender. If a boy's name was presented, the subject pressed one response button mounted on a mini-box; if the name was a girl's, the subject pressed a second button. In addition to pressing the appropriate button, subjects were instructed to keep a mental count of the number of girl's names they detected.

To view the stimuli, subjects were seated 50 cm from a Zenith ZVM-135 high resolution RGB video monitor controlled through a Taxan 410-64 interface board by an Apple IIe computer. The initial display consisted of an open horizontal 10.5 cm by 3.25 cm rectangle outlined with white asterisks. In the center of the rectangle was a horizontal row of 15 asterisks over which a strip of polarizing material was attached.

Luminance of the asterisks was measured with a Tektronix J-16 Photometer/Radiometer using a 1.0 degree J-6523 luminance probe which was set so that a single asterisk exactly filled the 1.0 degree field. Luminance of the asterisk was measured through the polarizer attached to the display screen and a second polarizer which the subjects wore during the experiments. With both polarizers aligned to transmit the maximum amount of light, the luminance of the asterisk was 9.0 candelas per meter squared. With the polarizers set for maximum extinction, the luminance was 1.3 candelas per meter squared (which was due predominantly to room light reflected from the front surface of the polarizer attached to the display screen).

To begin each trial, the computer used a pseudo-random sequence to determine if a boy's name or a girl's name was to be presented.

To obtain an odd-ball effect, the probability for a boy's name was 80% on each trial; in addition it was required that no more than 5 nor less than 2 boy's names be presented between each girl's name. After the gender of the name to be presented had been determined, the computer selected a specific name at random (Sparks, 1983; Hare, Russ and Faulkner, 1983) from a list of either 172 boy's names or 43 girl's names. Names on these lists were carefully selected to insure that they were not gender ambiguous and would be easily recognized by the subjects. To insure ease of recognition, printed lists of the names were given to subjects in advance of the experiments so they could become familiar with them. The mean character length of the boy's names was 6.0 (SD = .91; range = 5 to 8) and the mean length of the girl's names was also 6.0 (SD = .91; range = 5 to 8).

In addition to the set of "plain" names, a second set of boy's and girl's names was constructed with a nonsense consonant added to the beginning of each name. This condition is referred to as, "embedded", because the names were originally to be embedded between several nonsense consonants (see DISCUSSION section of Experiment Set 1).

To begin a trial, the IIE computer generated a synchronizing pulse corresponding to whether a boy's name (common stimulus) or girl's name (novel stimulus) was to be displayed. After 217 msec, a stimulus name replaced as many of the asterisks in the center horizontal row within the rectangle as there were letters in the name (Figures 1 and 2). The stimulus was visible for either 150

```

*****
*                                     *
*****
*                                     *
*****

```

```

*****
*                                     *
***** DAVID *****
*                                     *
*****

```

OR

```

*****
*                                     *
***** SUSAN *****
*                                     *
*****

```

```

*****
*                                     *
*****
*                                     *
*****

```

FIGURE 1: Schematic representations of plain name displays presented in Experiment Set 1. The top rectangle illustrates the initial display, the middle two show the common and novel options and the lower rectangle indicates the appearance of the display between trials.

*

*

*
*** WDAVID ***
*

OR

*
*** KSUSAN ***
*

*

*

FIGURE 2: Schematic representations of embedded name displays presented in Experiment Set 1. Details are the same as for Figure 1.

or 300 msec, depending on the experiment, and at the end of the exposure duration the asterisks returned. Inter-trial intervals were 2004 msec, as measured from synchronizing pulse to synchronizing pulse.

In each of the Experiment Sets, trials were continued until 40 novel stimuli had been presented. This usually required that approximately 160 common stimuli were also presented; the entire block of trials for one condition thus took approximately five minutes. At the end of a block of trials, subjects were given a five to seven minute rest period and then another experimental condition was presented.

Stimulus Viewing Conditions

During all of the Experiment Sets, subjects wore polarizing lenses over both eyes. (If a subject wore spectacles, the polarizing lenses were placed over them.) Different combinations of polarizing lenses were available, and these, in combination with the use of black felt occluders, allowed the following viewing conditions to be presented: 1) the entire display monitor, the rectangle of asterisks and the horizontal row of asterisks/stimuli could be seen with both eyes, 2) the monitor and the outer asterisk rectangle could be seen with both eyes, but the horizontal row of asterisks/stimuli could be seen with only one eye 3) the entire field of view of one eye at a time could be occluded by placing a felt patch over the polarizing lens for that eye, and 4) the vision of either or both eyes could be blurred by placing plus dioptric lenses in clips attached to the fronts of the polarizing

lenses. Thus, a wide variety of viewing conditions were available, each of which allowed the disruption of binocular vision in a slightly different manner. For the total occlusion conditions, significant pattern rivalry between the two eyes was unlikely, but for the stimulus line only occlusion, and for the differential blur conditions, rivalry was distinctly probable.

Subject Training

Following completion of a briefing session in which the nature of the study was explained and informed consent forms were signed, subjects were scheduled for two 1.5 h training sessions. During each of these sessions, five different viewing conditions were presented: binocular viewing, total occlusion of each eye, and stimulus line occlusion of each eye. Half of the subjects saw plain names during their first training session and the other half were presented with embedded names first. For each session, the order of viewing conditions was counter-balanced.

During the training sessions, subjects were required to press response buttons to indicate the gender of the names presented on the screen and to keep a mental count of girl's names. They were also asked to avoid blinking or making gross body movements during the trials. At the end of the training sessions, all subjects' button push RTs had stabilized and they were over 85% accurate in detecting girl's names.

SUBJECTIVE ASSESSMENT OF WORKLOAD

During the initial briefing session, SWAT procedures were explained and each subject completed a card sort. SWAT instructions

were given in accordance with information contained in the SWAT Users Guide (Dr. Gary Reid, AAMRL, Wright-Patterson AFB, Ohio 45433) and each subject was given a printed list of the time (T), effort (E) and stress (S) criteria for use during the card sort (and for later use during the Experiment Sets). Card sort sequences were analyzed and a group scale constructed for all subjects. Relative importances of 28% for factor T, 31% for factor E and 42% for factor S were found. These values were used in the Experiment Sets to translate the subjects' T, E and S ratings into SWAT ratings.

PHYSIOLOGICAL INDICATORS OF WORKLOAD

Reaction Time

When the Apple IIe displayed a stimulus, a clock was started which ran until the subject pressed a response button or until 1300 msec had elapsed. If the subject pressed a button, the time from display onset to button press was recorded along with the accuracy of the subject's response. If 1300 msec elapsed and no button press occurred, the computer recorded the subject's response as a "none" and initiated the next trial.

At the completion of each block of trials, a print-out provided latency and response accuracy information for each trial as well as summary statistics indicating the number of correct and incorrect responses for both the common and novel stimuli. Means and standard deviations of the RTs for correct and incorrect responses and the number of "none" responses were also printed:

EEG Recording

To record EEG signals, silver/silver-chloride electrodes were

placed at scalp locations Pz, Cz, and Oz, and on the mastoids (one mastoid served as ground, the other served as reference). An electrode was also placed 1 cm above the left eyebrow to record blinks. Inter-electrode impedences were checked with a Grass Impedence Meter and were 5.0 Kohms or less. These impedences were achieved by cleaning the skin with alcohol and then treating the electrode sites with Omniprep and electrode paste.

Signals from the electrodes were amplified using Gould Universal Isolation Amplifiers with frequency cutoffs set at 0.1 and 30.0 Hz. Fixed amplifier gains of 50,000 were used for the EEG channels and a variable gain was used for each subject to generate 3.0 volt signals from normal eye blinks.

EEG and blink signals were interfaced through a Lab-Master A/D converter to an IBM-AT computer running ASYST software (Wirth and Ford, 1986). Using ASYST, input signals were sampled every 2.0 ms and stored as separate files for each trial. File designators specified whether the stimulus presentation was common or novel as well as other essential information (such as electrode channel).

After all trials in a block had been presented, the IBM computer examined the eye blink data to determine if a blink or vertical eye movement creating a signal equal to or exceeding 40% of the amplitude of a normal blink had been produced during the trial. If this was the case, data from the trial was discarded. Information was then presented to the IBM indicating which trials had resulted in incorrect button presses or in no responses. These

trials were also deleted along with the trials immediately following them. The deletion of trials immediately following error trials was done so as to allow the "disruption" associated with missing a stimulus to pass. Therefore, for a trial to be retained, it could not be contaminated by an eye blink or a significant vertical eye movement, it had to have been preceded by a correct button press and the subject must have made a correct response on the trial itself. From the trials meeting these criteria, 30 common and 30 novel stimulus trials were selected at random. Data from these trials were separately ensemble averaged, filtered using the ASYST program to remove frequencies above 50 Hz and stored for subsequent analyses.

Two components of the EEG waveforms were deemed to be of particular importance for the experiments described below. These were the P-180, occurring about 180 msec after stimulus presentation (best seen in the Cz recording), and the P-300 response (best seen in the Pz recording). For each of these responses, the peak amplitude, measured in microvolts from the baseline established during the 217 msec between synchronizing pulse generation and presentation of the stimulus word, and the latency, measured in milliseconds from the presentation of the stimulus to the peak of the response, were recorded for each viewing condition/subject combination.

It was initially planned to use eye blink frequency and duration as indicators of workload in the various Experiment Sets (Stern, Walrath and Goldstein, 1984), but during the pilot phase of this project it was found that many subjects blinked on every trial.

For this reason, blink suppression instructions had to be given and this invalidated the use of blink data to assess workload.

EXPERIMENT SET 1 - MONOCULAR OCCLUSION

GOALS AND HYPOTHESES

Although Experiment Set 1 had multiple goals, the primary goal was to assess the effects of total monocular occlusion on subjective and objective indicators of workload/performance using the odd-ball task described above. It was hypothesized that if there was a significant effect caused by losing the information from one eye, it would be demonstrated in this condition.

If the monocular/binocular effect was somewhat more subtle, it was hypothesized that occluding only the stimulus portion of one eye's visual field would reveal it. With stimulus occlusion, the brain would receive in-register images from both eyes except for the stimulus. In this region, the brain would receive a dark image from one eye and the stimulus word from the other. Thus, most of both eyes' fields would be fused, but the stimulus region might elicit retinal rivalry and/or have to be actively suppressed by the brain. If it was more difficult for subjects to suppress only a portion of the visual field as opposed to the total field (i.e., total occlusion of one eye), the workload/performance indicators should show this.

The third hypothesis investigated in this Experiment Set involved which of the workload/performance measures co-varied with each other (i.e., assessed the same mental processes), and which were independent. Two procedures were used to investigate possible

correlations. First, the mean scores from all subjects for each of the workload/performance indicators were correlated across stimulus viewing conditions (e.g., binocular viewing, dominant eye totally occluded, dominant eye stimulus line only occluded, etc.), and, second, the entire set of viewing conditions were presented again to the subjects with a more difficult discrimination task - a nonsense consonant was added to the front of each stimulus name (the embedded viewing condition). It was presumed that this more difficult condition would significantly affect SWAT ratings which were "true" indicators of workload, and any of the other workload/performance variables which co-varied with changes in SWAT ratings would thus be valid workload indicators too.

The embedded stimulus conditions were also presented to insure that any monocular/binocular information processing differences which became manifest only with difficult tasks would not be missed.

In summary, Experiment Set one was designed to assess the effects of total and partial occlusion on various workload/performance measures, to determine if workload increases with monocular as compared to binocular viewing, and to determine which of the indicators co-varied significantly with SWAT ratings (i.e., were also "true" indicators of workload).

SUBJECTS

All 30 subjects from the pool participated in this experiment, but, as discussed in the Results section below, data from only 21 of them were used. Of these 21 subjects, 8 were female and 13 were male. Their mean age was 27.0 (SD = 4). Fourteen were right

eye dominant and 7 were left eye dominant; 19 were right handed, 2 were left handed and 5 had mixed eye/hand dominance.

STIMULI AND VIEWING CONDITIONS

Each subject participated in two 1.5 h testing sessions during each of which five viewing conditions were presented: binocular viewing, dominant and non-dominant eye total occlusion, and dominant and non-dominant eye stimulus line occlusion. For half of the subjects, the plain names were presented during the first testing session and the embedded names were presented first for the other half. Within each testing session, the sequence of viewing conditions was counter-balanced to compensate for presentation order effects.

Each viewing condition required about 5 min for the presentation of 40 girl's names and approximately 160 boy's names. Between conditions, an examiner obtained "T", "E", and "S" values from which SWAT ratings could be determined and chatted with the subject for about 7 minutes while data processing took place. After three viewing conditions, subjects were disconnected from the recording equipment (electrodes were left in place) and allowed to move about, use the restroom, etc. This break typically lasted 15 minutes.

The stimuli used in Experiment Set 1 were boy's and girl's names presented on the video monitor as described above. It was required that subjects produce at least 30 valid boy's and girl's names trials for each of the viewing conditions. Approximately 2% of the time, this criterion was not met, usually because of excessive blinking, and the viewing condition had to be repeated later in

the testing session. Because of this possibility, care was taken not to inform subjects regarding how many viewing conditions were left to be presented in a given testing session.

DATA ANALYSIS

Data derived from each subject/viewing condition combination included a SWAT rating, the mean and standard deviation of RTs for the girl's names trials on which the correct response button had been pressed, EEG signals from Cz, Pz and Oz electrodes, and blink data which was used during processing of the EEG signals. After data had been gathered from all 30 subjects, EEG signals for the plain name stimuli were ensemble averaged for the valid girl's trials. These data were then filtered as described previously and the averaged waveforms from electrode site Pz were viewed subject by subject. The quality of the P-300 signal in each waveform was assessed by two examiners using a four point scale based on ease of amplitude and latency determination. Twenty-one subjects were rated as "easy to read" or "reasonably easy to read" and 9 subjects were rated as "difficult to read" or "impossible to read". The classification process was then used on the embedded name data; there was almost total overlap with the classifications for the plain name data. Based on these classifications, the 9 subjects who gave difficult or impossible to interpret P-300 recordings were dropped from the study and the data presented below represent the remaining 21 subjects.

RESULTS

Grand average EEG waveforms from the 21 subjects are shown in

Figures 3a and 3b, and 4a and 4b (plain names and embedded names, respectively). These waveforms illustrate the large positive P-180 peak (generator site unknown) most predominant at electrode site Cz, the P-300 recorded from Pz and the visual evoked potentials occurring from about 80 to 300 msec after stimulus onset (electrode site Oz).

Numerical results from the various viewing conditions are summarized on Table 1. For each viewing condition, the grand means of the SWAT ratings, RTs, and EEG signals are shown. Values in parenthesis indicate standard deviations of the individual subject's mean values. For SWAT ratings, the "T", "E" and "S" values are integer means of the values that subjects gave. All other calculations were carried out to three decimal places and rounded.

To determine if there were significant effects produced by total or stimulus line occlusion, repeated measures analyses of variance (ANOVA) (significance level of 0.5) with Scheffe follow-up tests (significance level of 0.10, Ferguson, 1981) were used.

Data were initially analyzed separately for plain and embedded stimulus conditions. For plain stimuli, no significant viewing condition differences were found for RTs, SWAT ratings or P-180 amplitudes. For P-300s, a significant viewing condition effect was found (ANOVA, $p = 0.01$) and the Scheffe tests showed that the amplitude of the P-300 for binocular viewing was significantly greater than the amplitudes for either of the line occlusion conditions. The latency for binocular viewing was also found to be significantly faster (ANOVA, $p = 0.01$) than the latency for the

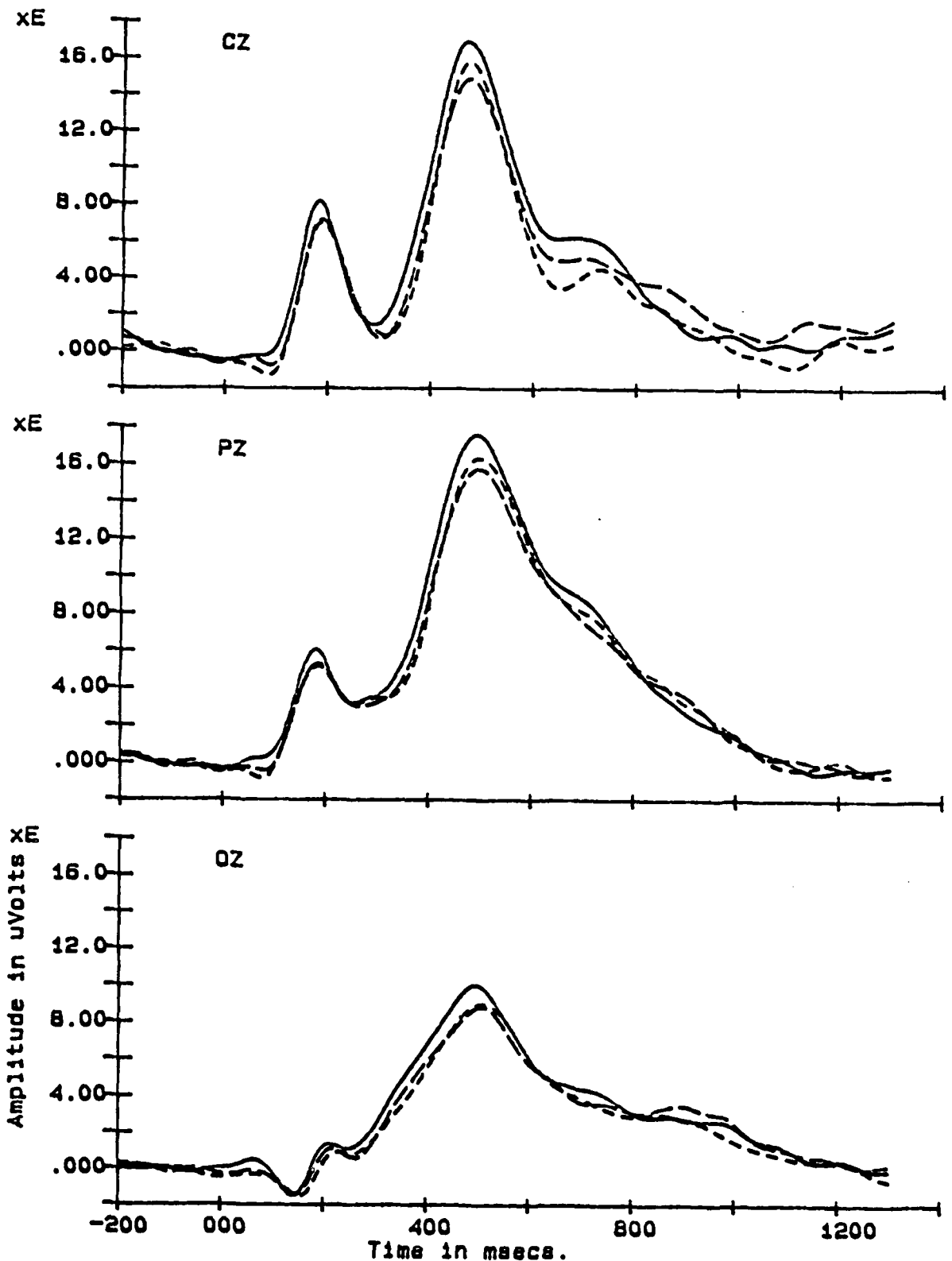


FIGURE 3a: These waveforms represent grand averages of the 30 novel stimulus plain name trials for each of the 21 subjects. Top panel curves are from electrode site Cz, middle panel curves are from Pz and lower panel curves are from Oz. Within each panel, the solid line represents binocular viewing, the short dash line represents total occlusion of the dominant eye and the long dash line represents total occlusion of the non-dominant eye.

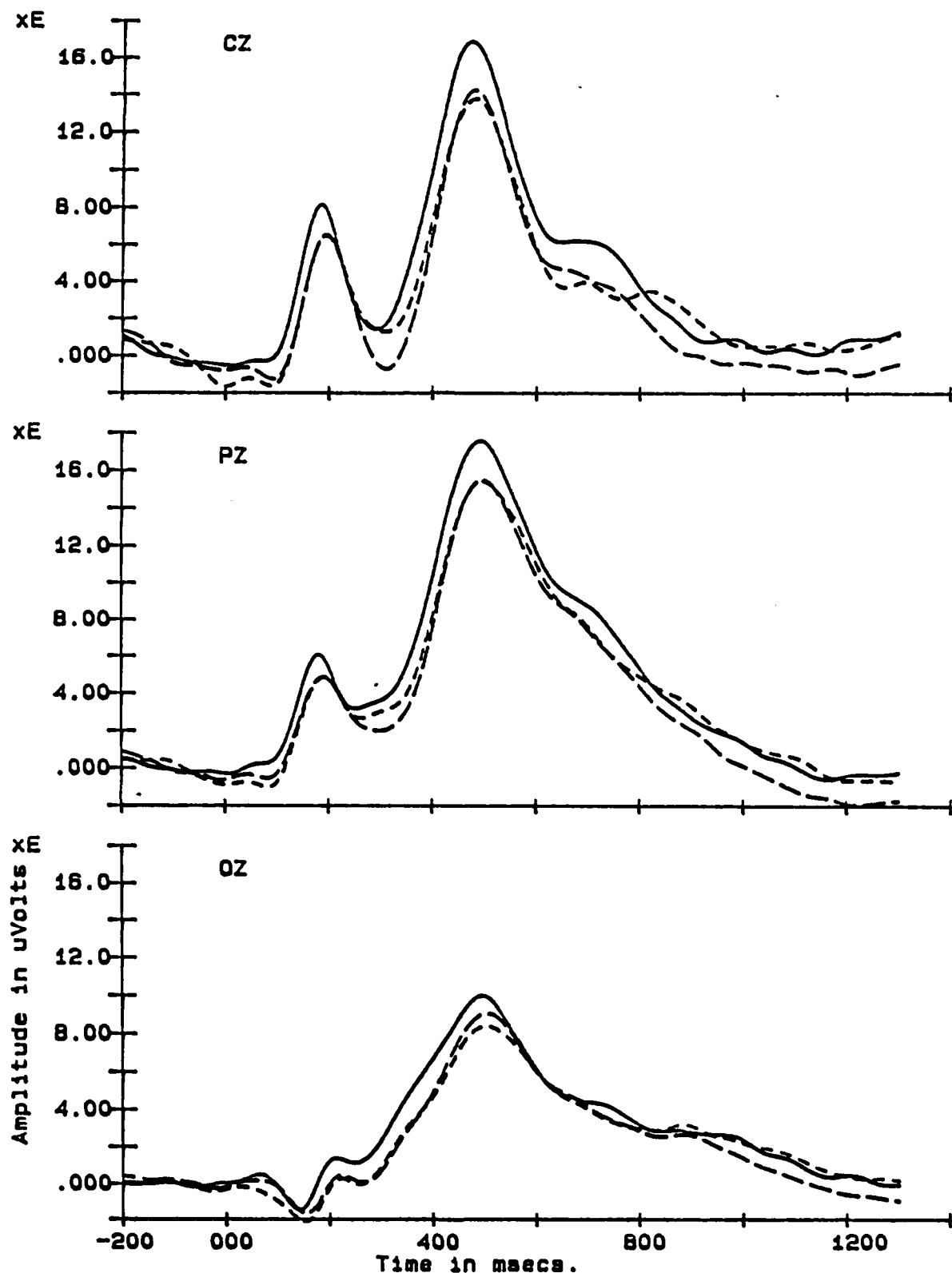


FIGURE 3b: These waveforms represent grand averages of the 30 novel stimulus plain name trials for each of the 21 subjects. Top panel curves are from electrode site Cz, middle panel curves are from Pz and lower panel curves are from Oz. Within each panel, the solid line represents binocular viewing, the short dash line represents line occlusion of the dominant eye and the long dash line represents line occlusion of the non-dominant eye.

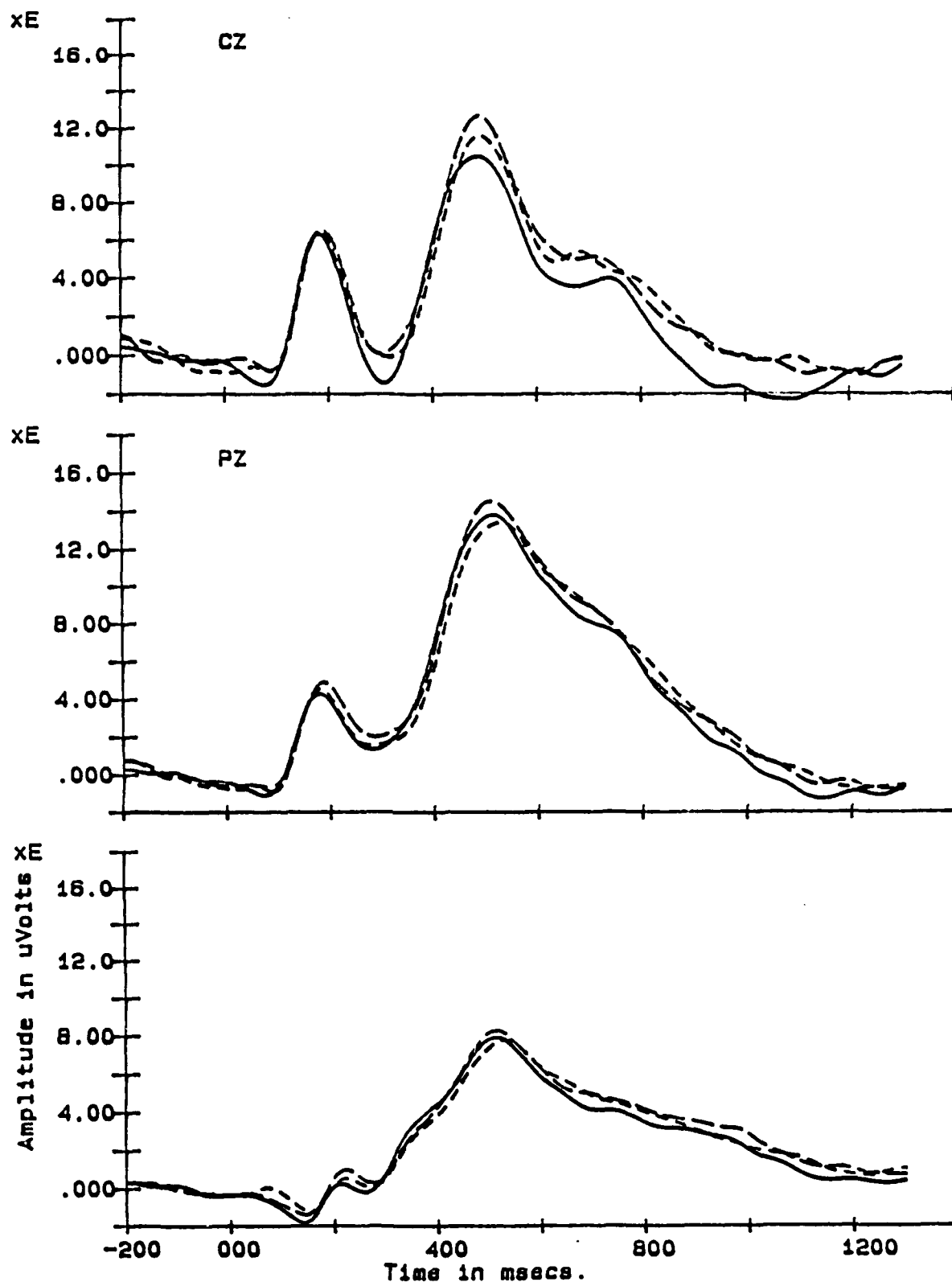


FIGURE 4a: These waveforms represent grand averages of the 30 novel stimulus embedded name trials for each of the 21 subjects. Top panel curves are from electrode site Cz, middle panel curves are from Pz and lower panel curves are from Oz. Within each panel, the solid line represents binocular viewing, the short dash line represents total occlusion of the dominant eye and the long dash line represents total occlusion of the non-dominant eye.

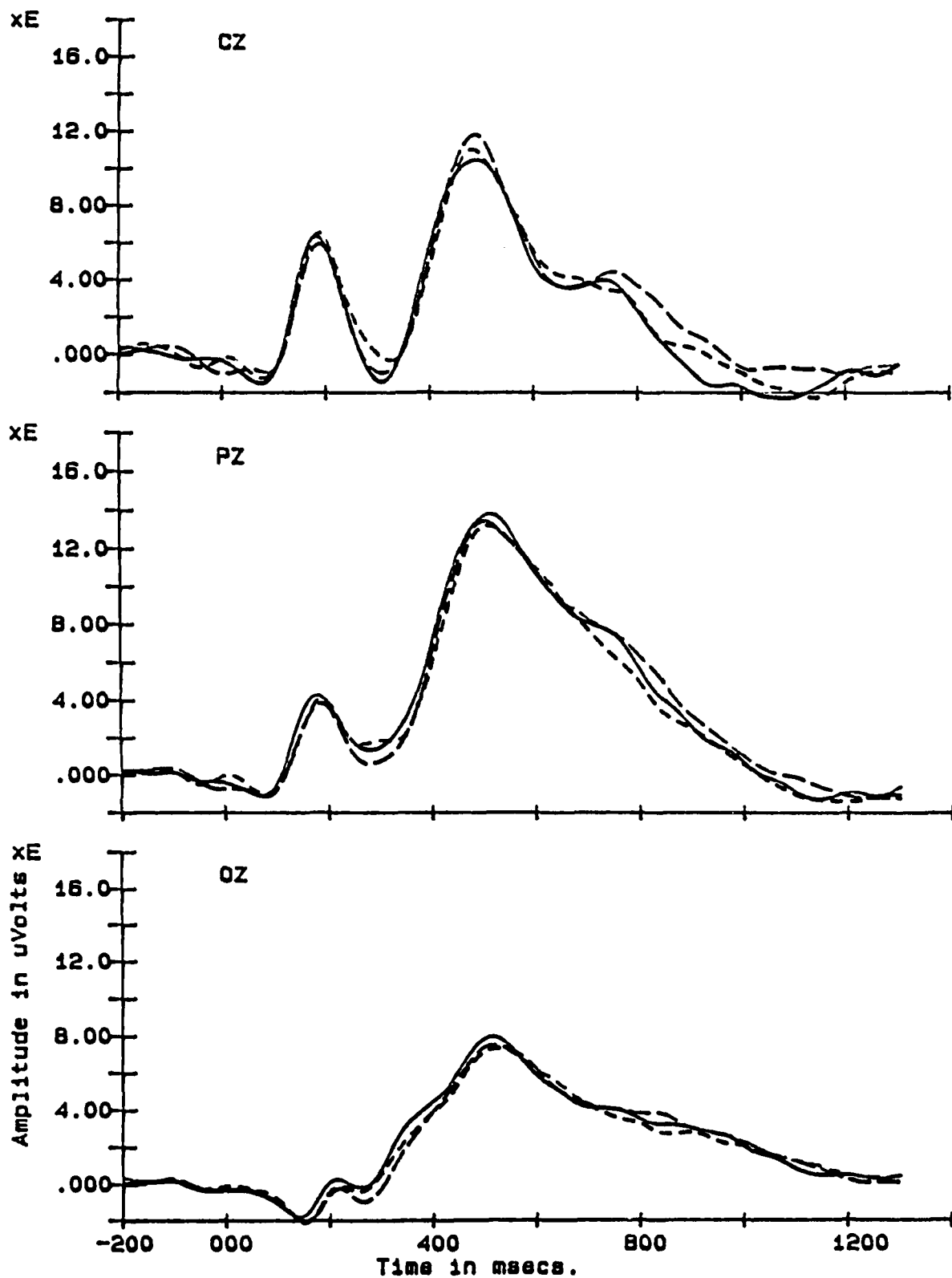


FIGURE 4b: These waveforms represent grand averages of the 30 novel-stimulus embedded name trials for each of the 21 subjects. Top panel curves are from electrode site Cz, middle panel curves are from Pz and lower panel curves are from Oz. Within each panel, the solid line represents binocular viewing, the short dash line represents line occlusion of the dominant eye and the long dash line represents line occlusion of the non-dominant eye.

**TABLE 1: SUMMARY DATA FOR EXPERIMENT SET 1
MONOCULAR OCCLUSION**

PLAIN NAMES WITH MONOCULAR OCCLUSION

	<u>DOM EYE:</u> <u>NON-DOM EYE:</u>	<u>OPEN</u> <u>OPEN</u>	<u>TOTAL OCCLUSION</u> <u>OPEN</u>	<u>OPEN</u> <u>TOTAL OCCLUSION</u>	<u>LINE OCCLUSION</u> <u>OPEN</u>	<u>OPEN</u> <u>LINE OCCLUSION</u>
REACT. TIME		595 (79)	604 (73)	613 (90)	609 (85)	599 (72)
SWAT						
T		1	1	1	2	2
E		2	2	2	2	2
S		2	2	2	2	2
SWAT#		27 (23)	34 (21)	30 (20)	34 (22)	30 (21)
P-300						
AMP		18.7 (5.9)	17.4 (6.1)	16.9 (4.8)	16.5 (5.0)	16.4 (4.7)
LAT		488 (35)	499 (38)	497 (39)	506 (34)	497 (30)
P-180						
AMP		8.9 (4.2)	7.5 (3.7)	7.8 (3.9)	7.3 (3.2)	7.6 (4.3)
LAT		181 (15)	187 (20)	189 (19)	192 (18)	190 (22)

EMBEDDED NAMES WITH MONOCULAR OCCLUSION

	<u>DOM EYE:</u> <u>NON-DOM EYE:</u>	<u>OPEN</u> <u>OPEN</u>	<u>TOTAL OCCLUSION</u> <u>OPEN</u>	<u>OPEN</u> <u>TOTAL OCCLUSION</u>	<u>LINE OCCLUSION</u> <u>OPEN</u>	<u>OPEN</u> <u>LINE OCCLUSION</u>
REACT. TIME		611 (77)	617 (60)	610 (65)	622 (78)	623 (74)
SWAT						
T		2	2	2	2	2
E		2	2	2	2	2
S		2	2	2	2	2
SWAT#		39 (20)	40 (21)	40 (23)	44 (21)	38 (20)
P-300						
AMP		14.9 (5.0)	14.8 (3.8)	15.7 (5.2)	14.6 (4.8)	14.4 (5.5)
LAT		509 (36)	523 (36)	517 (39)	516 (41)	518 (35)
P-180						
AMP		7.0 (4.3)	7.5 (4.8)	7.5 (5.3)	7.2 (5.6)	6.8 (5.5)
LAT		183 (17)	186 (20)	187 (20)	187 (17)	187 (19)

dominant eye total occlusion condition. For P-180s (ANOVA, $p = 0.003$), the latency of the binocular condition was found to be shorter than the latencies for the non-dominant eye total occlusion condition and for both of the line occlusion viewing conditions.

For embedded stimuli, the ANOVAs indicate that none of the workload/performance measures differed significantly across viewing conditions.

To assess the effects of adding a letter to the front of each name, two factor repeated measures analyses of variance were used. These analyses indicated no significant effects on RT, SWAT, P-300s or P-180s produced by adding a letter; embedding the name did not significantly change the workload associated with the discrimination task.

To determine if any of the workload/performance measures co-varied with each other, correlation matrices were constructed using the mean values from the viewing conditions shown on Table 1. The correlation matrices for plain names, embedded names and plain and embedded names combined are shown on Table 2. While interesting, these correlation matrices should be interpreted with some caution. Since only five viewing conditions contributed data for each correlation on the upper two matrices, and 10 contributed to the lower matrix correlations, the r value in each cell must reach approximately 0.88 for statistical significance (at the 0.05 level) in the upper two matrices and 0.63 in the lower one. Also, since 15 correlations were calculated for each matrix, use of a correction, such as the one advocated by Tukey (1977) in which the significance

TABLE 2: CORRELATION MATRICES FOR EXPERIMENT SET 1

PLAIN NAMES WITH MONOCULAR OCCLUSION

	MEAN RT	SWAT ^a	P300 LAT	P300 A...	P180 LAT	P180 A...
MEAN RT	1					
SWAT ^a	.538	1				
P300 LAT	.675	.904	1			
P300 AMP	-.576	-.57	-.783	1		
P180 LAT	.678	.678	.883	-.98	1	
P180 AMP	-.621	-.873	-.92	.891	-.928	1

EMBEDDED NAMES WITH MONOCULAR OCCLUSION

	MEAN RT	SWAT ^a	P300 LAT	P300 A...	P180 LAT	P180 A...
MEAN RT	1					
SWAT ^a	.262	1				
P300 LAT	.416	.045	1			
P300 AMP	-.847	-.04	-.104	1		
P180 LAT	.468	.393	.732	.065	1	
P180 AMP	-.444	.356	.462	.669	.367	1

PLAIN AND EMBEDDED NAMES WITH MONOCULAR OCCLUSION

	MEAN RT	SWAT ^a	P300 LAT	P300 A...	P180 LAT	P180 A...
MEAN RT	1					
SWAT ^a	.758	1				
P300 LAT	.886	.797	1			
P300 AMP	-.769	-.468	-.755	1		
P180 LAT	.978	.658	.911	-.815	1	
P180 AMP	-.779	-.524	-.817	.991	-.831	1

level is divided by the number of statistical tests conducted, is appropriate. When the Tukey procedure is used, the critical level becomes $p = 0.003$ and the r values required to reach this level become 0.99 for the top two matrices and 0.97 for the lower one. Only the correlation between RT and P-180 latency in the bottom matrix reaches significance under these conditions. It may also be the case that there is a significant restriction of range on some of the workload/performance indicators. In fact, most of the indicators vary by only 10% of their values across viewing conditions. For these reasons, the patterns of relationships revealed in the matrices should only be regarded as suggestive and additional data will be needed for more complete evaluation of them.

DISCUSSION

Experiment Set 1 was designed to demonstrate effects on workload/performance indicators produced by shifting from binocular to monocular viewing conditions and to show which of the performance indicators co-varied with SWAT ratings as workload was increased.

Contrary to expectation, shifting to either total monocular viewing or to a rivalry situation in which only the stimulus portion of one eye's field was blocked did not affect workload ratings or RTs significantly. While there were some significant changes in EEG signals, these changes are scattered and are very difficult to interpret without additional data (such as will become available in subsequent Experiment Sets).

Also contrary to expectation, adding a character to the beginning of each name did not affect the workload associated with

the information processing task. The embedded condition was to have been used in a validation of workload indicators other than SWAT but the two way analyses of variance demonstrated that none of the workload/performance indicators were sensitive to the addition of a character on the front of the names. While it is possible that adding a character really did change the workload and the tests used in this experiment were insensitive to the change, it is more probable that subjects simply learned to filter out the leading consonant without increasing their effort significantly. This possibility was considered in the design of the embedded name condition, and, in pilot projects not using subjects from the pool described in this experiment, the embedded condition involved adding three random consonants to the beginning and to the end of each name. Subjects found this task to be impossible, so the number of added consonants was gradually reduced to the level at which subjects could perform the task. For pilot subjects to perform with an accuracy of 90% or better, only one consonant could be tolerated for each name. Unfortunately, this did not produce a significant increase in workload for the subjects in the actual study.

EXPERIMENT SET 2 - MONOCULAR AND BINOCULAR BLUR

GOALS AND HYPOTHESES

In Experiment Set 2, it was hypothesized that producing viewing conditions in which the brain could not easily put the images from the eyes in precise register would cause confusion and/or an allocation of resources to suppress the image from the eye that

was producing a sub-optimal image. It was also considered possible that the brain would have to process (i.e., enhance) the sub-optimal image to a point at which it could be combined with the image from the clearer eye to produce simultaneous vision. Any of these mechanisms could draw mental resources, slow categorization of the names and increase mental workload.

To disrupt binocularity and reduce the quality of the image from one or both eyes, plus lens induced blur was used. In the first set of viewing conditions, acuity in one eye was reduced by the use of plus dioptric lenses to the point at which stimulus names could just barely be read. In the second series of viewing conditions, differential impairment was created, with the vision in one eye blurred to the point at which the names could just barely be read and the vision in the other eye blurred to the point at which the words could just barely not be read. These viewing conditions should have provided ample opportunity for retinal rivalry to manifest itself and were designed to make the discrimination task very difficult (i.e., increase the workload) for the subjects.

SUBJECTS

All 21 of the subjects who participated in Experiment Set 1 also participated in this Experiment Set.

STIMULI

The stimulus generation system described in Experiment Set 1 was used in this Experiment Set. All names were presented using the embedded format.

METHODS

Determination of Blurring Lens Powers

To assess the lens powers which would just allow viewing of the stimulus names, clips were placed on the polarizing glasses the subjects wore and one eye was totally occluded. The stimulus generation program was stopped with a name visible on the screen and plus lenses were added over the non-occluded eye until the subject could not read the name. The plus lens power was decreased until the name could easily be read and a bracketing procedure was used to find the strongest plus lens which would just allow reading of the name. This process was then repeated for the other eye. The resultant plus lenses reduced the subjects' near visual acuities to approximately 20/60 to 20/80 near Snellen equivalent for each eye.

A similar bracketing procedure was used to obtain plus lens powers which reduced acuity to a point at which the stimulus word could just not be read (approximately 20/120 near Snellen equivalent).

VIEWING CONDITIONS

Using the blurring lenses, six different viewing conditions were presented to the subjects: normal binocular viewing, monocular blur to 20/60-20/80 with the other eye unblurred, binocular blur to 20/60-20/80, and two differential blur conditions in which one eye was blurred to 20/120 and the other eye was blurred to 20/60-20/80. The monocular blur conditions set up a rivalry situation in which the brain had to either suppress or enhance the vision

from the blurred eye, and the differential blur conditions set up an even more difficult situation in which neither eye gave sharp vision but the brain had to determine which eye gave the most usable vision and then rely on it for information.

RESULTS

Grand average EEG waveforms for the viewing conditions presented in this Experiment Set are shown in Figures 5 and 6. The waveforms are quite similar to those obtained in Experiment Set 1.

Numerical summary data for the various viewing conditions are presented in Table 3. Details for this Table are the same as for Table 1. Repeated measures ANOVAs using all viewing conditions indicate that there are significant differences across conditions for SWAT data ($p = 0.0001$), P-300 amplitudes ($p = 0.0008$), P-300 latencies ($p = 0.008$), and P-180 latencies ($p = 0.002$). The monocular or differential blurring conditions did not affect any of the other performance/workload indicators.

Using Scheffe follow-up testing, the SWAT value for the binocular unblurred condition was found to be significantly lower than the SWATs for all of the other viewing conditions, the P-300 amplitude for the binocular unblurred condition was significantly greater than the P-300 amplitudes for the binocular blur and differential blur viewing conditions, the P-300 latency for the unblurred binocular condition was significantly shorter than the latency for the equal binocular blur condition, and P-180 latency for the clear binocular condition was significantly shorter than the latencies for any other viewing conditions except the dominant eye clear,

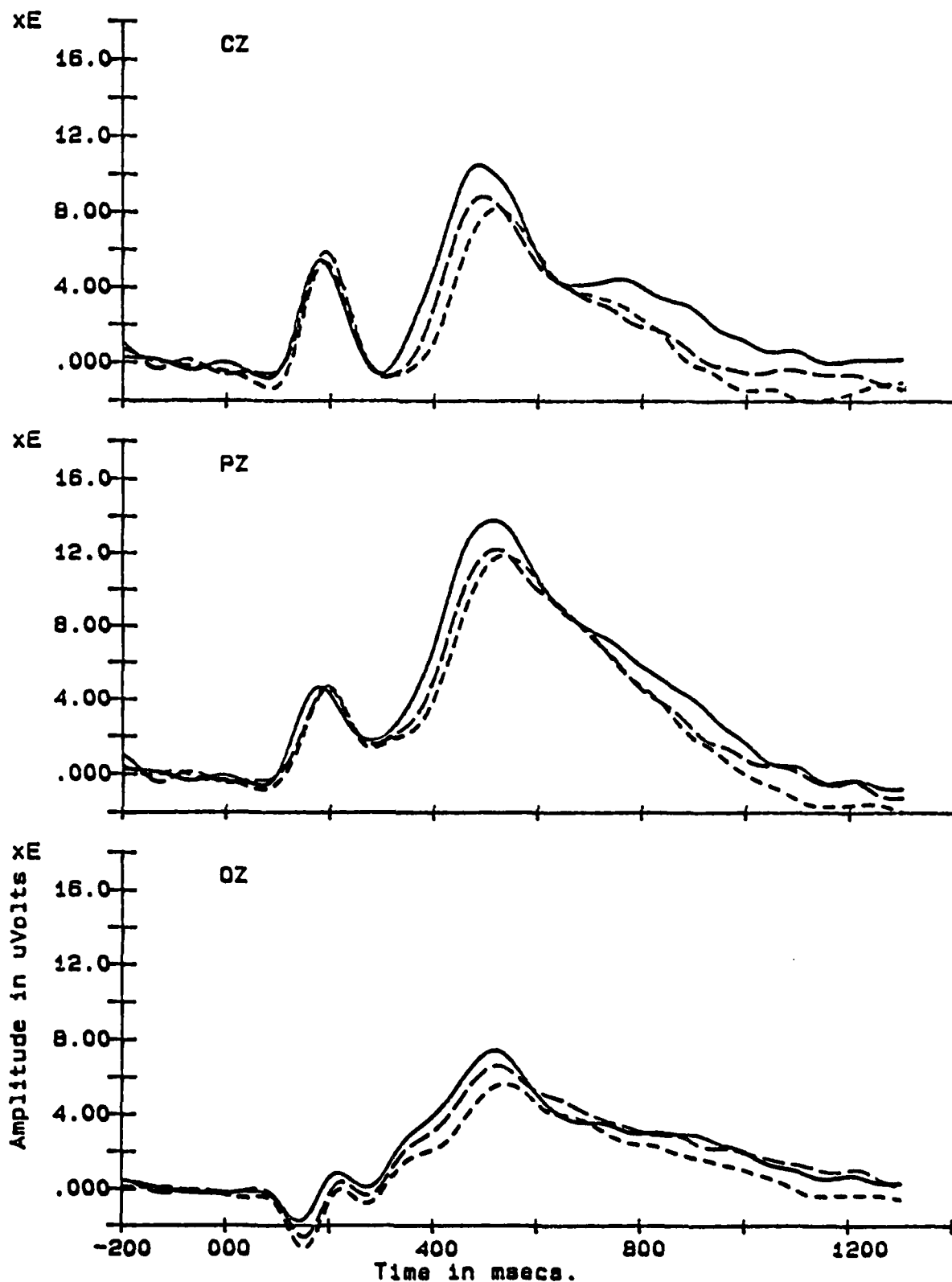


FIGURE 5: These waveforms represent grand averages of the 30 novel stimulus embedded name trials for each of the 21 subjects. Top panel curves are from electrode site Cz, middle panel curves are from Pz and lower panel curves are from Oz. Within each panel, the solid line represents clear binocular viewing, the short dash line represents blur to 20/60-80 of the dominant eye and the long dash line represents blur to 20/60-80 of the non-dominant eye.

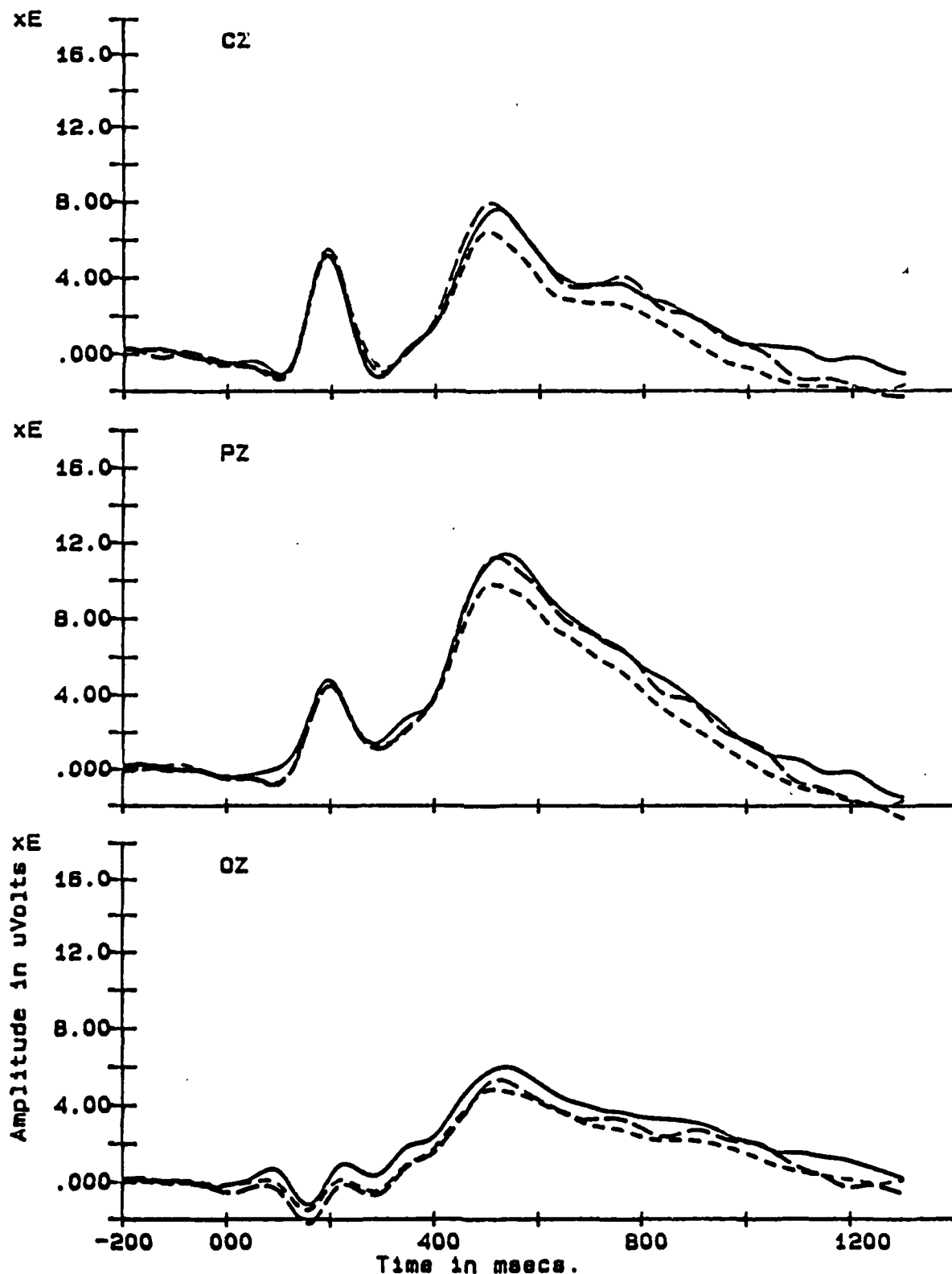


FIGURE 6: These waveforms represent grand averages of the 30 novel stimulus embedded name trials for each of the 21 subjects. Top panel curves are from electrode site Cz, middle panel curves are from Pz and lower panel curves are from Oz. Within each panel, the solid line represents equal binocular blur to 20/60-80, the short dash line represents blur to 20/120 of the dominant eye and the long dash line represents blur to 20/120 of the non-dominant eye. (In the latter two viewing conditions, the other eye was blurred to 20/60-80.)

TABLE 3: SUMMARY DATA FOR EXPERIMENT SET 2 - BLUR

VIEWING CONDITIONS			
DOM EYE: <u>NON-DOM EYE:</u>	<u>CLEAR</u>	20/60 - 80 BLUR <u>CLEAR</u>	<u>CLEAR</u> 20/60 - 80 BLUR
REACT. TIME	632 (71)	639 (84)	651 (78)
SWAT			
T	1	2	2
E	2	2	2
S	1	2	2
SWAT#	25 (16)	48 (22)	47 (17)
P-300			
AMP	15.2 (6.2)	13.1 (5.7)	13.3 (5.2)
LAT	513 (37)	534 (40)	525 (46)
P-180			
AMP	6.2 (3.4)	6.2 (3.3)	6.6 (3.0)
LAT	180 (23)	192 (22)	190 (19)

VIEWING CONDITIONS			
DOM EYE: <u>NON-DOM EYE:</u>	20/60 - 80 BLUR <u>20/60 - 80 BLUR</u>	20/60 - 80 BLUR <u>20/120</u>	20/120 <u>20/60 - 80 BLUR</u>
REACT. TIME	651 (70)	659 (71)	657 (79)
SWAT			
T	2	2	2
E	2	2	2
S	2	2	2
SWAT#	43 (19)	58 (19)	56 (24)
P-300			
AMP	12.5 (5.9)	11.2 (4.9)	12.2 (5.9)
LAT	539 (38)	523 (35)	536 (40)
P-180			
AMP	5.8 (2.9)	6.1 (2.5)	6.1 (2.6)
LAT	192 (16)	193 (15)	194 (16)

non-dominant eye 20/60-20/80 blur condition.

As in Experiment Set 1, the pattern of significant differences is not a simple one.

To assess relationships between the workload/performance indicators measured in this Experiment Set, a correlation matrix was constructed using the mean values shown on Table 3 for the six different viewing conditions combined and separately for the monocular blur and binocular blur viewing conditions. These correlation matrices are shown on Table 4. In the interpretation of these correlation matrices, the same cautions must be observed as were discussed for the matrices in Experiment Set 1. For a single correlation coefficient in either of the top two matrices to be significant with the Tukey correction, it needs to reach a level of 0.99. For the lower matrix, an adjusted level of 0.97 is required. Only the SWAT versus P-300 amplitude in the upper matrix reaches significance when these corrected values are used.

Even lacking statistical significance, it is still possible to compare the patterns in the correlation matrices for all data in Experiment Set 1 (Table 2) to the corresponding matrix for Experiment Set 2 (Table 4). The patterns are quite similar with respect to positive and negative coefficients which suggests that the coefficients may not be totally random. Especially notable are the magnitudes of the positive correlations seen between mean RT and SWAT values in both Experiment Sets, and the negative coefficients found in comparisons between P-300 amplitudes and mean reaction times, SWAT values and P-300 latencies. Also interesting

TABLE 4: CORRELATION MATRICES FOR EXPERIMENT SET 2

BINOCULAR CLEAR AND MONOCULAR BLUR 20/60-80

	MEAN RT	SWAT ^o	P300 LAT	P300 A...	P180 LAT	P180 A...
MEAN RT	1					
SWAT ^o	.757	1				
P300 LAT	.429	.915	1			
P300 AMP	-.724	-.999	-.934	1		
P180 LAT	.662	.991	.961	-.996	1	
P180 AMP	.931	.466	.071	-.423	.344	1

BINOCULAR 20/60-80 AND MONOCULAR BLUR 20/120

	MEAN RT	SWAT ^o	P300 LAT	P300 A...	P180 LAT	P180 A...
MEAN RT	1					
SWAT ^o	.993	1				
P300 LAT	-.824	-.75	1			
P300 AMP	-.835	-.764	1	1		
P180 LAT	.789	.857	-.302	-.321	1	
P180 AMP	.971	.992	-.663	-.679	.913	1

BINOCULAR CLEAR AND ALL BLUR CONDITIONS

	MEAN RT	SWAT ^o	P300 LAT	P300 A...	P180 LAT	P180 A...
MEAN RT	1					
SWAT ^o	.856	1				
P300 LAT	.436	.541	1			
P300 AMP	-.897	-.928	-.554	1		
P180 LAT	.814	.938	.79	-.921	1	
P180 AMP	-.144	-.037	-.463	.325	-.253	1

is the strong positive correlation between mean P-180 latency, mean RT and mean SWAT rating seen in both Experiment Sets.

DISCUSSION

This Experiment Set was designed to assess the effects on workload/performance produced by disruption of binocular vision resulting from reduction of one or both eyes' image quality. Surprisingly, even reducing the image quality in one eye to essentially an unusable level and making the other eye just barely able to detect the stimuli did not change reaction times (although suggestive but not significant increases in reaction times can be found in Table 3).

SWAT ratings tell another story, however. Subjects indicated their dislike of the blurring lenses to the examiners in conversations between viewing sessions and SWAT ratings show significant increases in workload even when only monocular blur was introduced. There are several possibilities to explain this subjective reaction. It may require more mental resources to suppress a blurred image, or to enhance it to the point at which it can be combined with the image from the other eye to allow simultaneous perception, and/or it is possible that, especially in the binocular blur conditions, plus lenses force a relaxation of accommodation and a corresponding decrease in accommodative convergence. Subjects may, therefore, have had a difficult time holding their eyes in alignment and pointed toward the stimuli; this may have contributed to the increase in workload/discomfort the subjects experienced.

As in Experiment Set 1, a few of the EEG parameters emerged as significant when the ANOVA testing was done, but it is difficult to find a solid pattern of changes from which a general theory can be constructed. This is especially a problem since no significant reaction time changes took place; any information interpretation problems created by blurring the stimuli are either compensated for at other points in the response generation process, or the inherent variability associated with producing the motor activity required to press a button overwhelms what may be the relatively small effects of blurring the image from one or both eyes.

The correlation matrices derived from the data in this Experiment Set are interesting, just as were the matrices from Experiment Set 1, but the number of viewing conditions and the limited spread of data for several of the variables make precise interpretation difficult. It appears, however, that the patterns in the correlation matrices for Experiment Sets 1 and 2 are sufficiently similar to warrant further testing with additional viewing conditions selected to produce a wider spread of data.

EXPERIMENT SET 3 - NO BUTTON PRESS

GOALS AND HYPOTHESES

The goal of this Experiment Set was to determine if the physical and mental activities associated with pushing a response button contributed to the EEG signals recorded in Experiment Sets 1 and 2. It was hypothesized that if such a contribution were found, it could be used to "correct" the waveforms recorded in the previous Experiment Sets and this might reveal which of the EEG

signal components were associated only with the information processing phase of the categorization task.

A secondary goal of this Experiment Set was to assess the degree of workload reduction associated with removal of the button press requirement. It was hypothesized that there would be some decrease in workload, but the reduction would be minimal since all of the mental processing required in Experiment Sets 1 and 2 would still be required in this Set; subjects would be required to keep a mental count of girl's names, and thus could not simply "space out" during the experiment. The only difference between the mental processing in Experiment Sets 1 and 2 and the processing required in this Set involved the actual mental and physical organization of the button press activity.

SUBJECTS

All 21 of the subjects who participated in Experiment Sets 1 and 2 also participated in this Experiment Set.

STIMULI

The stimulus generation system used in Experiment Sets 1 and 2 was used in this Set. Only embedded names were used. Three viewing conditions were presented in a counter-balanced order: binocular viewing, dominant eye total occlusion and non-dominant eye total occlusion. As in all Experiment Sets, polarizers were worn over both eyes.

METHODS

The recording and data analysis procedures were the same as

those used in Experiment Sets 1 and 2. Subjects were instructed to view names on the display and to keep a mental count of the girl's names.

RESULTS

Grand average EEG waveforms for the Experiment Set are shown on Figure 7. Note that the waveforms are very similar to those seen for Experiment Sets 1 and 2 except that as a group the P-300 amplitudes appear smaller than those from Set 1. A two factor repeated measures ANOVA comparing the viewing conditions presented in this Set to comparable conditions from Set 1 was significant ($p = 0.0003$) indicating that the P-300s were decreased in amplitude. No other EEG indicators showed significant differences between the Experiment Sets.

Since one of the goals of this Experiment Set was to determine what part of the waveforms recorded in Experiment Sets 1 and 2 were generated by the activity necessary to press a response button, the waveforms from Experiment Set 3 were subtracted from the corresponding binocular and monocular occlusion waveforms from Experiment Set 1. The results are shown as Figure 8. For electrode site Oz, the visual evoked potential components with latencies up to about 250 msec are common to both Experiment Sets and are thus removed by the subtraction process. For electrode site Cz, the P-180 component is also common to data from both Experiment Sets, thus it too is removed. The most obvious differences between the waveforms occur between 300 and 800 msec, and are best seen in the data from electrode site Pz. Because the P-300 amplitudes were

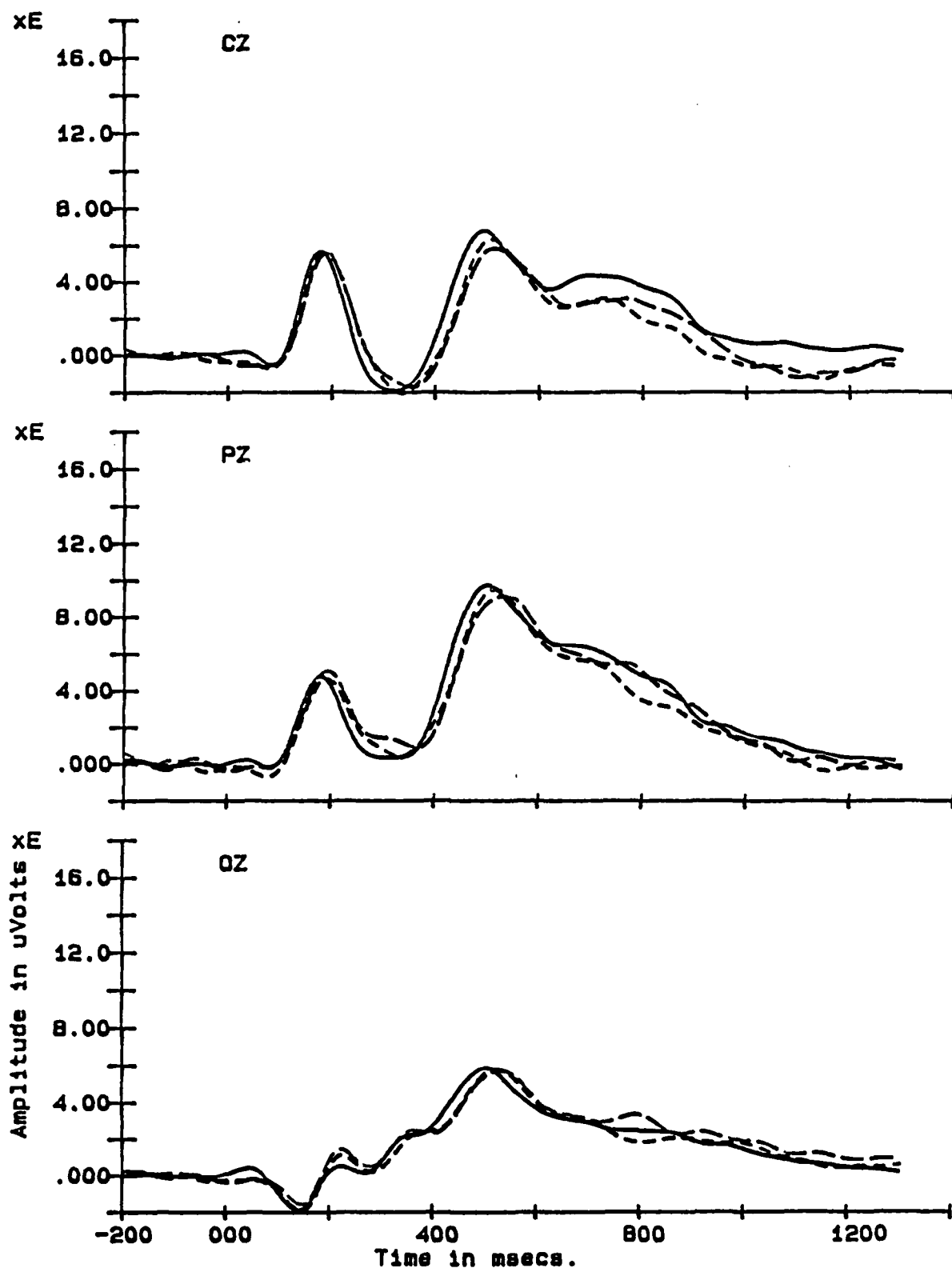


FIGURE 7: These waveforms represent grand averages of the 30 novel stimulus embedded name trials with "no button press" for each of the 21 subjects. Top panel curves are from electrode site Cz, middle panel curves are from Pz and lower panel curves are from Oz. Within each panel, the solid line represents binocular viewing, the short dash line represents total occlusion of the dominant eye and the long dash line represents total occlusion of the non-dominant eye.

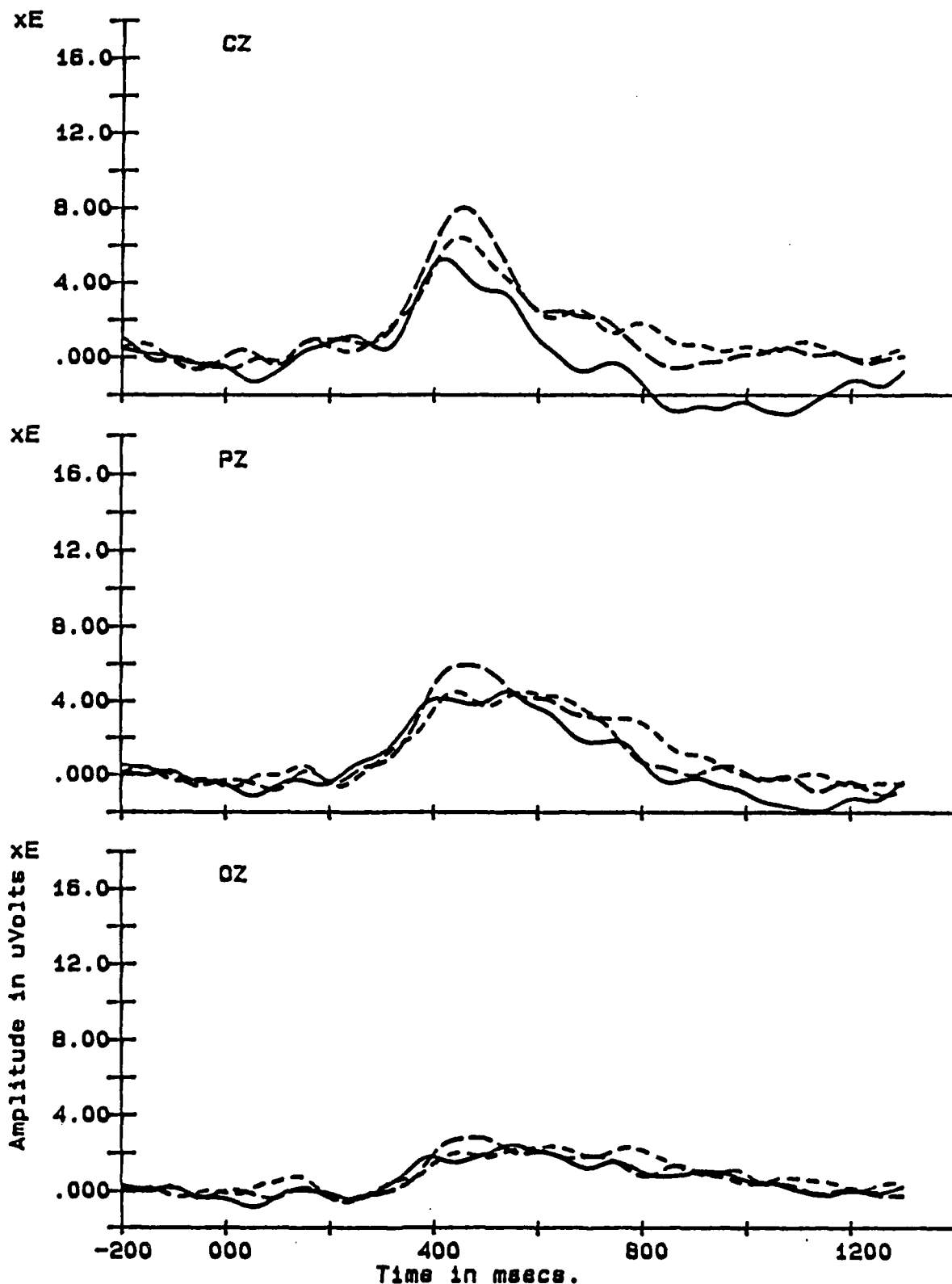


FIGURE 8: These waveforms represent the residual after subtraction of "no button press" waveforms from "button press" waveforms (subtraction of the waveforms in Figure 7 from the waveforms in Figure 4a). Top panel curves are from electrode site Cz, middle panel curves are from Pz and lower panel curves are from Oz. Within each panel, the solid line represents binocular viewing, the short dash line represents total occlusion of the dominant eye and the long dash line represents total occlusion of the non-dominant eye.

different for the Experiment Sets, there is a large residual P-300 component remaining after subtraction. There may also be a very subtle long latency difference occurring beyond 800 msec after stimulus presentation for the Pz electrode, binocular viewing condition, but the difference is not seen in the other viewing conditions and is therefore hard to evaluate. No evidence of the large amplitude, long latency signals previously reported (Yolton, 1986) are seen in these data.

Numerical summary data are presented in Table 5. Also shown in this Table are corresponding data from Experiment Set 1. Considering only data from Experiment Set 3, repeated measures analyses of variance and follow-up Scheffe tests indicate that both P-300 latencies (ANOVA, $p = 0.004$) and P-180 latencies (ANOVA, $p = 0.0002$) are significantly longer for the two occlusion conditions as compared to the binocular viewing condition. Especially the increase in P-300 latency suggests that it takes subjects longer to process information with one eye occluded as compared to having both eyes open.

Two factor analyses of variance were used to compare the workload/performance indicators between Experiment Sets 1 and 3. These analyses indicate that SWAT ratings were significantly lower for the no button push viewing conditions ($p = 0.0009$), as were P-300 amplitudes ($p = 0.0003$); subjects found that the task required less mental work and processing was done more quickly when no button press was required.

Because of the small number of viewing conditions in this Experiment Set, no correlation matrix was constructed.

**TABLE 5: SUMMARY DATA FOR EXPERIMENT SET 1
VERSUS EXPERIMENT SET 3
(BUTTON PRESS VS. NO BUTTON PRESS)**

VIEWING CONDITIONS - WITH BUTTON PRESS

DOM EYE: <u>NON-DOM EYE:</u>	<u>OPEN</u> <u>OPEN</u>	<u>TOTAL OCCLUSION</u> <u>OPEN</u>	<u>OPEN</u> <u>TOTAL OCCLUSION</u>
SWAT			
T	2	2	2
E	2	2	2
S	2	2	2
SWAT#	39 (20)	40 (21)	40 (23)
P-300			
AMP	14.9 (5.0)	14.8 (3.8)	15.7 (5.2)
LAT	509 (36)	523 (36)	517 (39)
P-180			
AMP	7.0 (4.3)	7.5 (4.8)	7.5 (5.3)
LAT	183 (17)	186 (20)	187 (20)

VIEWING CONDITIONS - NO BUTTON PRESS

DOM EYE: <u>NON-DOM EYE:</u>	<u>OPEN</u> <u>OPEN</u>	<u>TOTAL OCCLUSION</u> <u>OPEN</u>	<u>OPEN</u> <u>TOTAL OCCLUSION</u>
SWAT			
T	1	1	1
E	1	1	1
S	1	1	1
SWAT#	13 (14)	16 (13)	14 (13)
P-300			
AMP	10.8 (3.9)	10.5 (4.4)	9.8 (3.6)
LAT	510 (38)	526 (36)	536 (34)
P-180			
AMP	6.2 (2.3)	6.5 (2.9)	6.3 (2.1)
LAT	179 (16)	188 (19)	190 (20)

Discussion

The SWAT values indicate that subjects found the gender discrimination task much easier when they didn't have to signal their answers with a button press. In discussing this difference with them after the Experiment Set had been completed, a common theme emerged. Subjects felt that they could relax more during this Set because they were not competing against a clock, and they were aware that the researchers would not know if they made classification errors. With respect to the subjects' speed of processing, P-300 latencies did not show significant slowing as compared to the latencies for Experiment Set 1. Thus, the subjects were processing information and categorizing names with the same speed that they used when they needed to press a button.

The subjects perceived lack of a need to maintain accuracy in their discriminations is very interesting and may help to explain why P-300 amplitudes are lower in Experiment Set 3 as compared to Set 1. One possibility is that subjects may not have been detecting all of the girl's names in Set 3. Along with a loss of interest in the task because of a perceived reduction in the need to perform correctly, this could reduce P-300 amplitudes and SWAT ratings. These factors are worthy of consideration, but, since the subjects were still required to keep a mental count of the number of girl's names and these counts were never off by more than 3 or 4 names, they cannot fully explain why the P-300 amplitudes are reduced. Although the subjects felt they could relax more, their accuracy remained high.

Finally, the subtraction of waveforms indicates that there are no major long latency waveform components that can be directly ascribed to the button push activity itself. This means that the waveform components which Yolton (1986) believed to be associated with button pressing were probably artifacts, possibly produced by eye blinks. (These blink artifacts were not seen in the data presented in these experiments because of the blink rejection procedures described previously.)

EXPERIMENT SET 4 - NEW TASK

GOALS AND HYPOTHESES

The first three Experiment Sets did not reveal a robust pattern of performance differences based on monocular versus binocular viewing conditions. Since previous studies had found differences, it was considered possible that the effects of changing viewing conditions might be transient and therefore abolished by the intensive training given prior to Experiment Set 1. To investigate this possibility, Experiment Set 4 was designed in which a new discrimination task was presented to subjects having a minimum amount of training on it.

The task chosen for this Experiment Set was modeled loosely on the math processing sub-task of the Criterion Test Set battery (Shingledecker, 1984; Yolton, 1986). In this task, subjects were asked to discriminate equations with correct answers from those with incorrect answers and to indicate their choices by keeping a mental count of equations with correct answers and by pushing response buttons just as was done in Experiment Sets 1 and 2. It

was predicted that if the monocular occlusion effect was real, but was subject to rapid extinction, it should be detected with the new task.

SUBJECTS

All 21 subjects participated in this Experiment Set but only 11 were able to master it sufficiently to provide usable data. (It is probable that all 21 would have mastered the task had they been given more training, but the design of the Experiment Set precluded this.)

STIMULI

The basic design of the discrimination task was similar to the tasks used in the previous Experiment Sets except that arithmetic equations were presented instead of names. Each equation had two single digit numbers separated by a plus or minus operator, an equal sign and an answer. The answers were all positive single digits ranging between 1 and 9. Equations with correct answers took the place of girl's names as novel stimuli and equations with incorrect answers were the common stimuli (Figure 9).

Because subjects had difficulty determining if the equation was correct or incorrect (as compared to the ease of detecting the gender of a name), the stimulus exposure period was increased to 300 msec for this Experiment Set (it was 150 msec for the previous Experiment Sets).

TRAINING

Following a verbal explanation of the new task, subjects were

```

*****
*                                     *
*****
*                                     *
*****

```

```

*****
*                                     *
*** 4 + 3 = 6 ***
*                                     *
*****

```

OR

```

*****
*                                     *
*** 7 - 5 = 2 ***
*                                     *
*****

```

```

*****
*                                     *
*****
*                                     *
*****

```

FIGURE 9: Schematic representations of displays presented in Experiment Set 4. The top rectangle illustrates the initial display, the middle two show the common and novel options and the lower rectangle indicates the appearance of the display between trials.

given one binocular training block with 40 novel stimuli randomly mixed with common stimuli in a 20:80 ratio. The subjects' task was to press one response button for a correct equation and another button if the answer was wrong. They were also asked to keep a mental count of the novel stimuli. During this training session, 11 subjects were able to correctly respond to 32 or more of the novel stimuli and were retained in the study; the remaining 10 subjects were excused from participation.

VIEWING CONDITIONS

Binocular and total monocular occlusion viewing conditions were presented in a counter-balanced sequence. As in previous Experiment Sets, subjects wore polarizing lenses during all viewing conditions.

RESULTS

Grand mean EEG waveforms (Figure 10) show the expected P-180 response from Cz, the visual evoked potentials at Oz and a rather flattened P-300 from Pz. The flattened appearance is probably related (at least in part) to the variability of the reaction times produced by subjects on individual trials.

Summary data for this Experiment Set and comparable data from Experiment Set 1 are shown in Table 6. Repeated measures ANOVAs on the Experiment Set 4 data indicate that only the P-300 latencies differ significantly across viewing conditions ($p = 0.04$). Follow-up Scheffe testing indicates that the latencies for both monocular viewing conditions are significantly longer than the

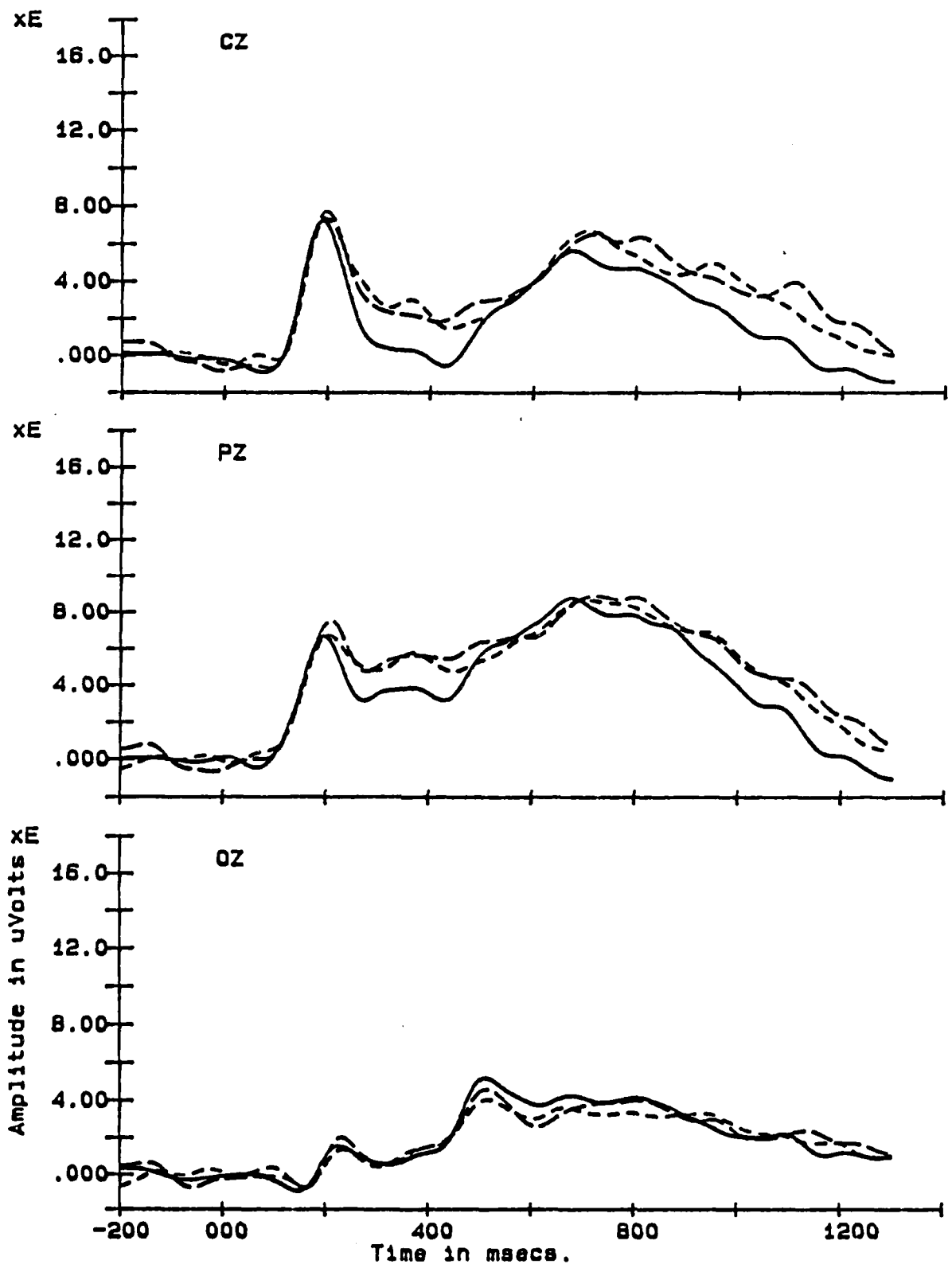


FIGURE 10: These waveforms represent grand averages of the 30 novel stimulus equation trials for each of the 11 subjects. Top panel curves are from electrode site Cz, middle panel curves are from Pz and lower panel curves are from Oz. Within each panel, the solid line represents binocular viewing, the short dash line represents total occlusion of the dominant eye and the long dash line represents total occlusion of the non-dominant eye.

**TABLE 6: SUMMARY DATA FOR EXPERIMENT SET 1
VERSUS EXPERMENT SET 4**

**VIEWING CONDITIONS FOR EXPERIMENT SET 1
(PLAIN NAMES)**

<u>DOM EYE:</u> <u>NON-DOM EYE:</u>	<u>OPEN</u> <u>OPEN</u>	<u>TOTAL OCCLUSION</u> <u>OPEN</u>	<u>OPEN</u> <u>TOTAL OCCLUSION</u>
REACT. TIME	622 (97)	627 (83)	633 (83)
SWAT			
T	1	1	1
E	2	2	2
S	2	2	2
SWAT#	22 (22)	30 (18)	28 (17)
P-300			
AMP	20.2 (6.1)	19.6 (6.3)	17.6 (4.4)
LAT	487 (31)	498 (29)	499 (32)
P-180			
AMP	9.6 (4.1)	9.5 (3.5)	7.9 (3.5)
LAT	183 (16)	194 (22)	195 (22)

**VIEWING CONDITIONS FOR EXPERIMENT SET 4
(EQUATIONS)**

<u>DOM EYE:</u> <u>NON-DOM EYE:</u>	<u>OPEN</u> <u>OPEN</u>	<u>TOTAL OCCLUSION</u> <u>OPEN</u>	<u>OPEN</u> <u>TOTAL OCCLUSION</u>
REACT. TIME	865 (102)	861 (83)	884 (80)
SWAT			
T	2	2	2
E	2	2	2
S	2	2	2
SWAT#	44 (30)	43 (32)	47 (29)
P-300			
AMP	9.2 (3.3)	10.6 (4.0)	10.0 (3.7)
LAT	677 (34)	720 (57)	717 (52)
P-180			
AMP	8.1 (2.4)	8.3 (2.6)	8.7 (2.8)
LAT	194 (19)	201 (19)	204 (20)

latency for the binocular viewing condition, but the latencies for the monocular conditions do not differ significantly from each other.

Comparing the data from this Experiment Set to the corresponding data from Experiment Set 1 (plain names, total occlusion) by use of two factor repeated measures analyses of variance indicates that RTs ($p = 0.0001$), P-300 amplitudes ($p = 0.0001$) and latencies ($p = 0.0001$) all differ significantly between the two Experiment Sets. SWAT values come close to reaching significance with a P value of 0.10, while P-180 amplitude and latency values do not approach significance. (The repeated measures analyses of variance compared the eleven subjects who completed Experiment Set 4 with the data from the same eleven subjects who participated in Experiment Set 1.)

As in Experiment Set 3, the small number of viewing conditions precludes the generation of a meaningful correlation matrix.

DISCUSSION

This Experiment Set again indicates a difference in information processing speed between monocular and binocular viewing conditions, but, again, there is no significant change in RT. As has been stated previously, either the variability in reaction time generation is so large as to overwhelm the difference in processing speed, or there are compensatory mechanisms which make up for this difference. The increase in processing latency is small (a little over 6%) but it does suggest a binocular advantage for complex, unfamiliar tasks. The difference would be more impressive if it

had also been seen in RT data, and perhaps a replication of this Experiment Set with a larger number of subjects would make the small differences in RT seen in Table 6 statistically significant.

The general conclusion that can be drawn from Experiment Set 4 is that a new task did not significantly change many of the information processing characteristics demonstrated by subjects in Experiment Sets 1 through 3. The trends in the data appear fairly uniform across Experiment Sets and suggest that there is a processing time decrement associated with monocular occlusion, but the effect is not large and does not manifest itself in RT data.

COMPARISON OF DATA FROM EXPERIMENT SETS

Because similar data were gathered under different viewing conditions in the four Experiment Sets, common trends in the Sets can be identified. The statistically significant relationships found in each of the Sets are presented in Table 7. For each of the Sets, the "control condition" (e.g., binocular viewing with no occlusion) was compared to each of the binocular disruption conditions; for an X to appear in the Table, the overall repeated measures ANOVA must have been significant at the 0.05 level and the follow-up Scheffe test for the comparison indicated must have been significant at the 0.10 level.

WORKLOAD/PERFORMANCE INDICATOR COMPARISONS

Reaction Times

The RT data shown in Table 7 indicate that none of the procedures used to disrupt binocular vision had a significant effect on

TABLE 7: SUMMARY OF STATISTICALLY SIGNIFICANT SCHEFFE F-TESTS*

<u>Binocular Viewing Plain Names vs.</u>	<u>RT</u>	<u>SWAT#</u>	<u>P300 Amp</u>	<u>P300 Lat</u>	<u>P180 Amp</u>	<u>P180 Lat</u>
Dom Eye Total Occulsion						X
Non-Dom Eye Total Occlusion						X
Dom Eye Line Occlusion			X	X		X
Non-Dom Line Occulsion			X			
<u>Binocular Viewing Embedded Names vs.</u>	<u>RT</u>	<u>SWAT#</u>	<u>P300 Amp</u>	<u>P300 Lat</u>	<u>P180 Amp</u>	<u>P180 Lat</u>
Dom Eye Total Occulsion						
Non-Dom Eye Total Occlusion						
Dom Eye Line Occlusion						
Non-Dom Line Occulsion						
<u>Binocular Viewing No Blur vs.</u>	<u>RT</u>	<u>SWAT#</u>	<u>P300 Amp</u>	<u>P300 Lat</u>	<u>P180 Amp</u>	<u>P180 Lat</u>
Dom Eye blur 20/60-80		X				X
Non-Dom blur 20/60-80		X				
Binoc. Viewing Blur 20/60-80		X	X	X		X
Dom Eye 20/120; Non-Dom 20/60-80		X	X			X
Non-Dom Eye 20/120; Dom 20/60-80		X	X			X
<u>Binocular Viewing No Button Press vs.</u>	<u>RT</u>	<u>SWAT#</u>	<u>P300 Amp</u>	<u>P300 Lat</u>	<u>P180 Amp</u>	<u>P180 Lat</u>
Dom Eye Total Occulsion				X		X
Non-Dom Eye Total Occlusion				X		X
<u>Binocular Viewing Math Equations vs.</u>	<u>RT</u>	<u>SWAT#</u>	<u>P300 Amp</u>	<u>P300 Lat</u>	<u>P180 Amp</u>	<u>P180 Lat</u>
Dom Eye Total Occulsion				X		
Non-Dom Eye Total Occlusion				X		

*Significant at $p < 0.10$ (Ferguson, 1981)

RT. Possibly, binocular disruption is irrelevant in the determination of RT or there may be enough variability in RTs to obscure small but real effects of disrupting binocular vision. It is also possible that humans can learn to very quickly compensate for loss of input from one eye, and, as a consequence, any change in RT produced by disruption of binocular vision was too transient to detect.

SWAT Ratings

Disrupting binocular vision by monocular full field or stimulus field occlusion did not have a significant effect on SWAT ratings. The only significant effects occurred in the differential blur conditions; subjects indicated that each of the blur conditions produced a higher workload than did clear binocular viewing. Occluding one eye did not make the subjects work harder, but blurring one or both eyes did; there are probably multiple causes for this. The blur certainly made it more difficult for the subjects to see the stimulus letters clearly, but an equally important factor might have been disruption of the accommodative convergence mechanism resulting from the use of plus lenses.

P-300 Amplitude

P-300 amplitudes were significantly affected in five of the comparisons shown on Table 7. In Experiment Set 1, the amplitudes were significantly lower for plain names when the stimulus line was occluded for either eye. In Experiment Set 2, comparisons to the clear binocular viewing condition showed that amplitudes were

significantly reduced for all three conditions in which both eyes were blurred.

P-300 Latency

Prior to conducting this study, P-300 latency increases were hypothesized to occur when binocular vision was significantly disrupted. Latency increases were found in each of the Experiment Sets, but the latency did not increase each time binocularity was disrupted. In Experiment Set 1, latency increased only for the plain name condition when the dominant eye stimulus field was occluded, and, in Experiment Set 2, latency increased only for the clear binocular viewing versus equal binocular blur comparison.

In Sets 3 and 4, the hypothesized result was found; latencies for each of the monocular occlusion conditions were significantly longer than the latency for binocular viewing. It is difficult to find common features in Experiment Sets 3 and 4 since subjects found the task in Set 3 to be considerably easier than the tasks in Experiment Sets 1 and 2, but the task in Set 4 was harder; task difficulty, therefore, seems to be irrelevant in determining whether P-300 latency will increase with monocular occlusion.

P-180 Amplitude

P-180 amplitudes were not significantly affected by disrupting binocular vision in any of the Experiment Sets.

P-180 Latency

In Experiment Set 1, using plain names the latencies for both full field and dominant eye line occlusions were significantly

longer than the latency for binocular viewing. In Experiment Set 2, the clear binocular viewing condition latency was shorter than the latencies for any of the blur conditions except non-dominant eye monocular blur, and, in Set 3, the latencies for both of the occlusion conditions were longer than the latency for binocular viewing.

CORRELATIONS BETWEEN WORKLOAD/PERFORMANCE INDICATORS

Combining data across Experiment Sets increases the number of viewing conditions that can be used to construct correlation matrices. Table 8 shows matrices for Experiment Sets 1 and 2 (top), 1, 2 and 4 (middle), and 1, 2, 3 and 4 (bottom). (Since RTs were not measured in Set 3, it was necessary to construct matrices with and without Set 3 data to show correlations with RTs.) There are 16 different viewing conditions represented in the top matrix which gives a critical r value ($p = 0.05$) for a single correlation calculation of 0.623 and a Tukey (1977) corrected r of 0.711. There are 19 conditions represented in the middle matrix and 21 in the lower matrix: critical single correlation calculation r values are 0.456 and 0.433; Tukey corrected r values are 0.669 and 0.612, respectively. (For all three matrices corrected p values are 0.003.) Correlation coefficients meeting corrected significance levels are indicated by asterisks in the cells on Table 8. To assist in evaluating these relationships, Figures 11, 12 and 13 show individual scatter plots for each of the correlations in the matrices.

TABLE 8: CORRELATION MATRICES FOR COMBINED EXPERIMENT SETS

COMBINED DATA FROM EXPERIMENT SETS 1 AND 2

	MEAN RT	SWAT ^o	P300 LAT	P300 A...	P180 LAT	P180 A...
MEAN RT	1					
SWAT ^o	.784*	1				
P300 LAT	.845*	.773*	1			
P300 AMP	-.93*	-.868*	-.898*	1		
P180 LAT	.566	.694	.545	-.597	1	
P180 AMP	-.876*	-.625	-.839*	.887*	-.493	1

COMBINED DATA FROM EXPERIMENT SETS 1, 2 AND 4

	MEAN RT	SWAT ^o	P300 LAT	P300 A...	P180 LAT	P180 A...
MEAN RT	1					
SWAT ^o	.367	1				
P300 LAT	.988*	.351	1			
P300 AMP	-.819*	-.749*	-.794*	1		
P180 LAT	.787*	.591	.799*	-.753*	1	
P180 AMP	.405	-.373	.425	.129	.179	1

COMBINED DATA FROM EXPERIMENT SETS 1, 2, 3 AND 4

	SWAT ^o	P300 LAT	P300 A...	P180 LAT	P180 A...
SWAT ^o	1				
P300 LAT	.318	1			
P300 AMP	-.103	-.646*	1		
P180 LAT	.559	.779*	-.515	1	
P180 AMP	.019	.434	.269	.249	1

Among the specific correlations most relevant to this study are those showing strong relationships with SWAT ratings (which are considered to be "true" indicators of workload). In the top two matrices of Table 8, SWAT ratings show significant negative correlations with P-300 amplitudes. The strength of the relationship decreases, however, when data from Experiment Set 3 are included (bottom matrix). The scatter plots show why; even though there is a large decrease in SWAT ratings in Set 3, the P-300 parameters do not change much (as compared to the corresponding values in the other Experiment Sets). This may suggest that limitation of P-300 amplitude range has attenuated the r value, or that P-300 amplitudes are not good indicators of workload.

Another group of correlation coefficients worth noting are those involving RTs. Very high positive r values are shown in the top two matrices for RTs versus P-300 latencies and a high negative correlation is shown for P-300 amplitudes. The RT versus SWAT correlation is high for Experiment Sets 1 and 2, but drops when data from Experiment Set 4 are added. Again the scatter plots show the reason for this. Clearly, many of the data from Experiment Set 4 are outliers (usually seen as three isolated points in the scatter plots) when compared to data from Sets 1 and 2. As a result, their inclusion in the analyses reduces the correlation coefficients. The reason that many of the correlations seen in Experiment Sets 1 and 2 do not hold up well as experimental conditions are changed is probably because the workload/performance indicators upon which they are based are not robust across different experimental conditions.

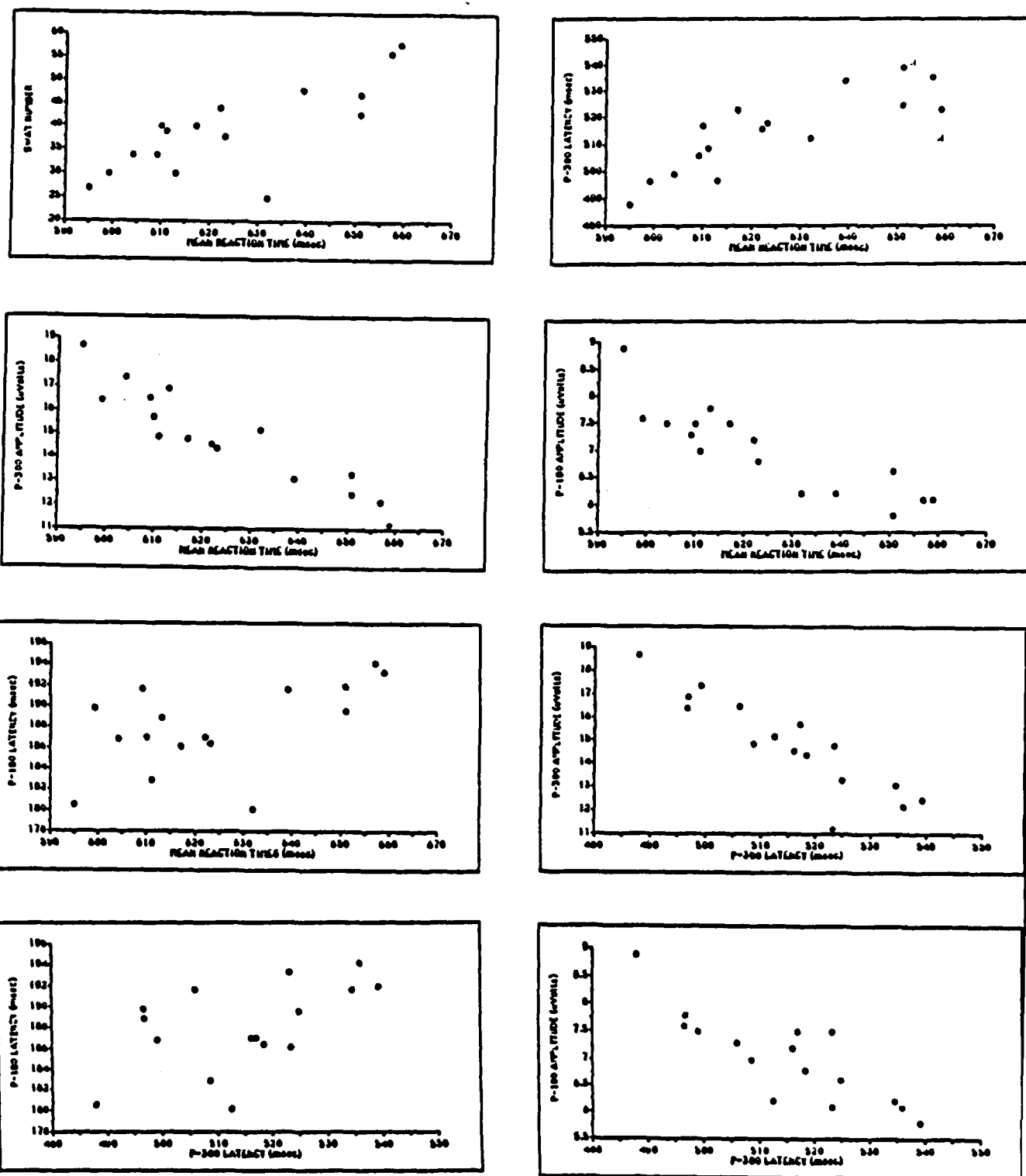


FIGURE 11: Scatter plots for data from Experiment Sets 1 and 2.

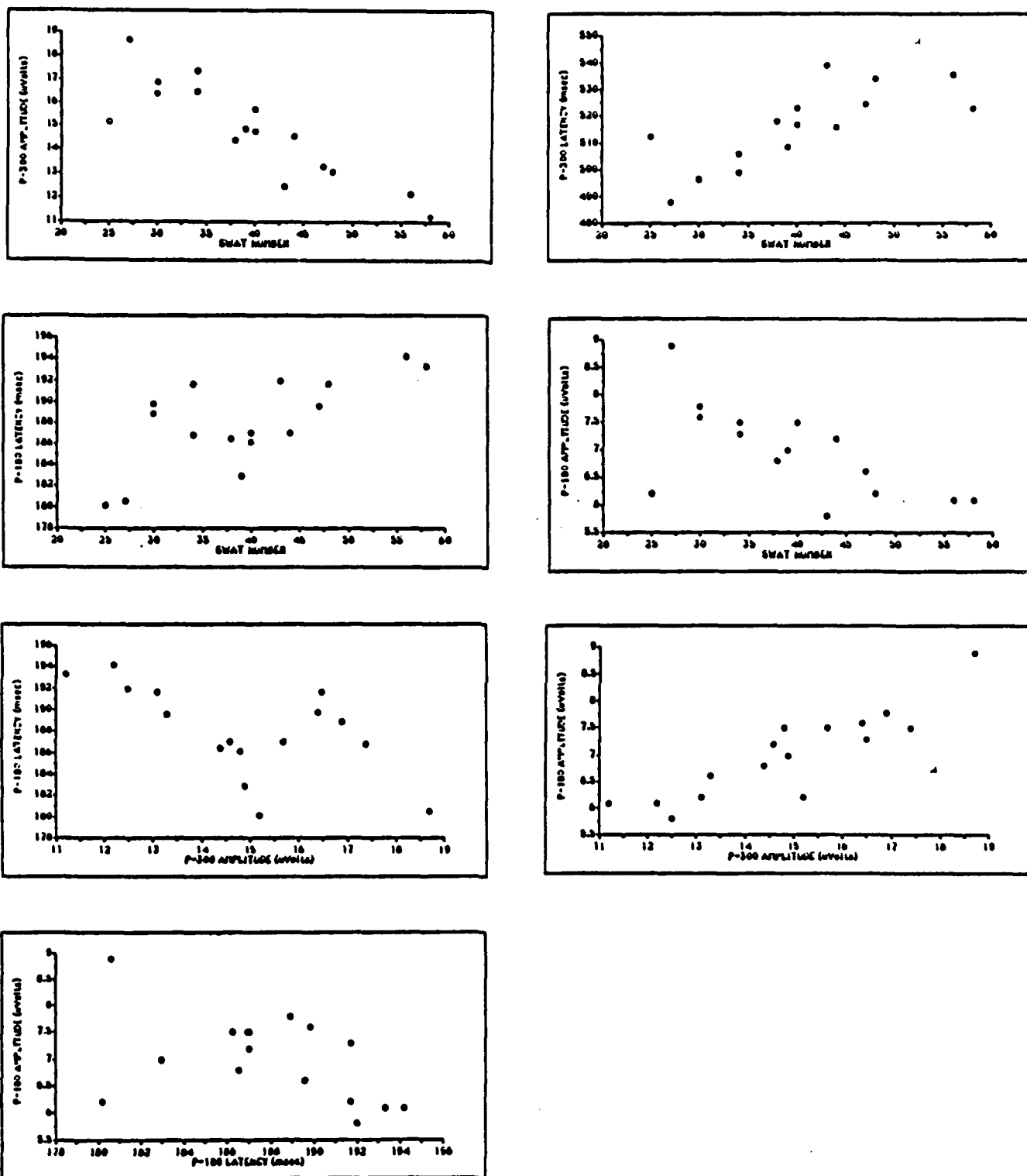


FIGURE 11: Scatter plots for data from Experiment Sets 1 and 2 continued.

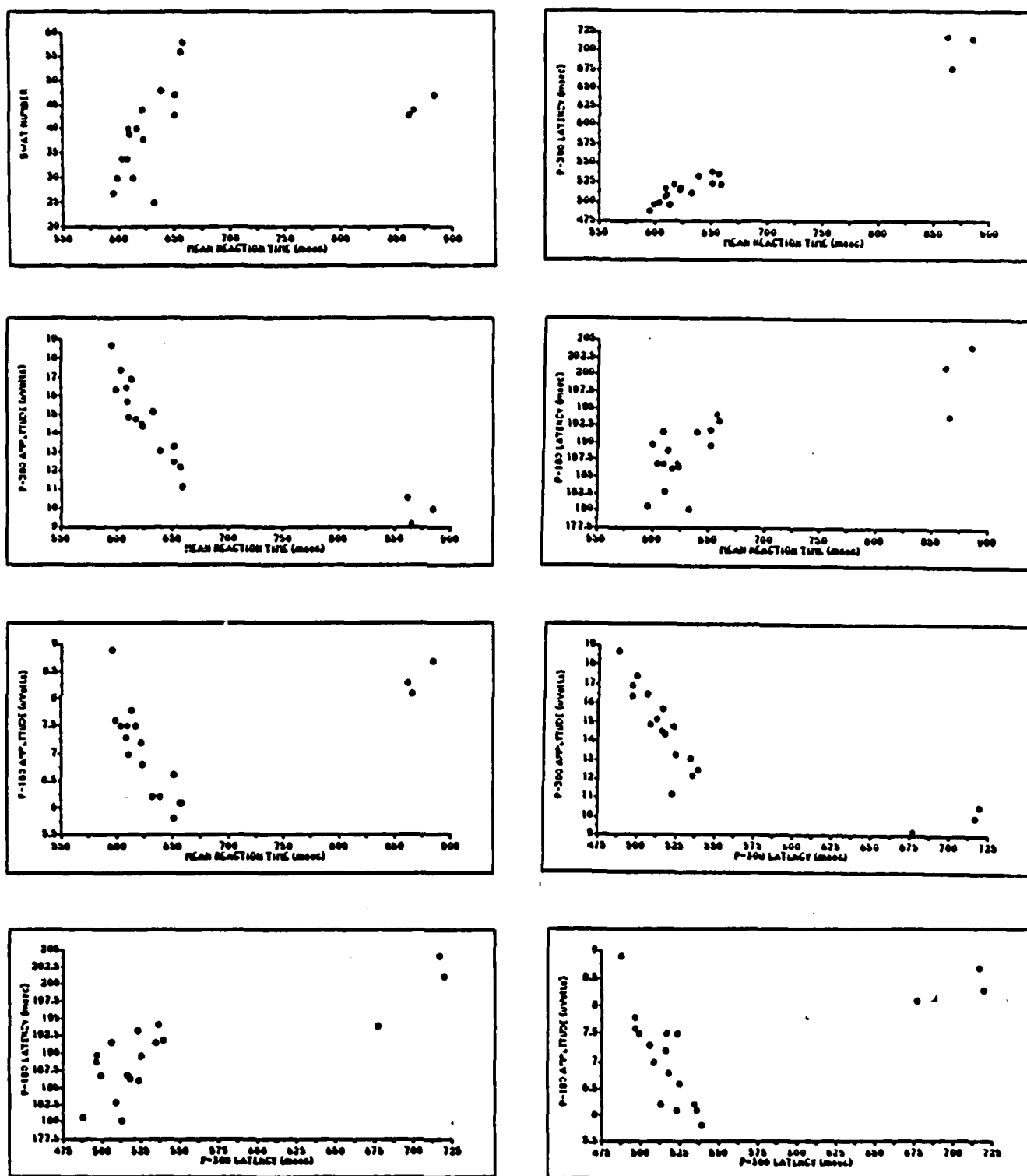


FIGURE 12: Scatter plots for data from Experiment Sets 1, 2 and 4.

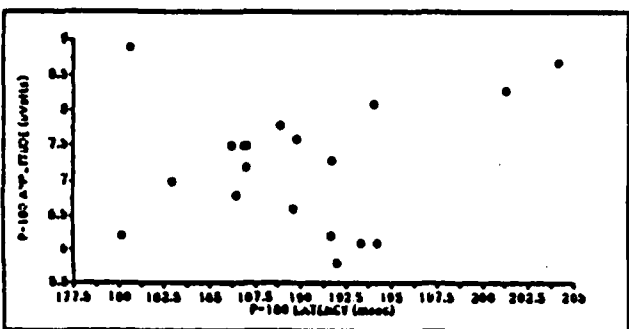
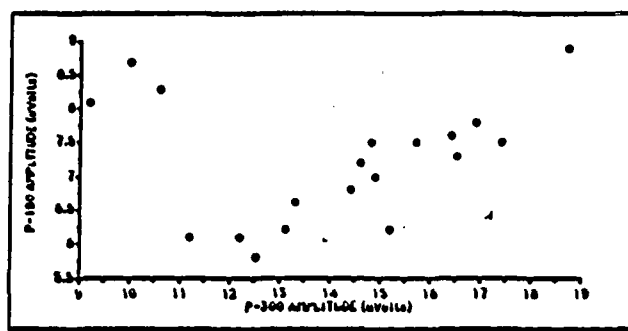
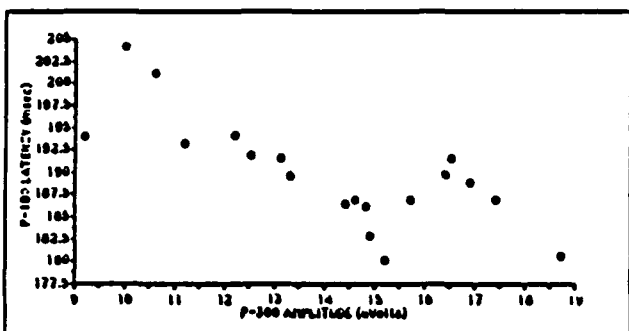
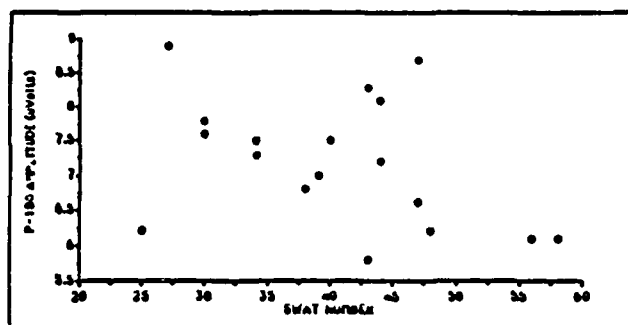
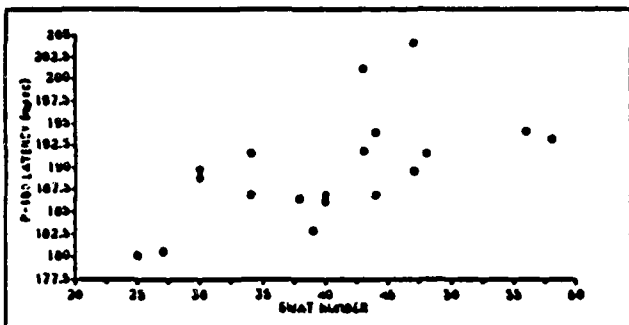
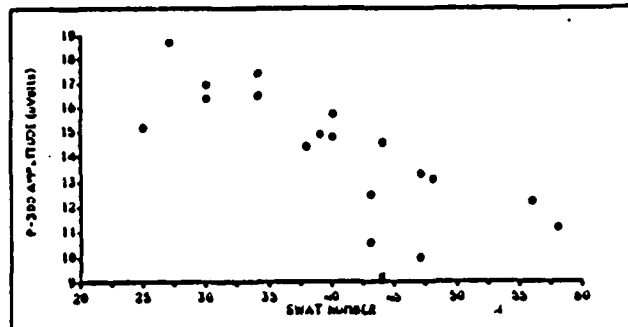
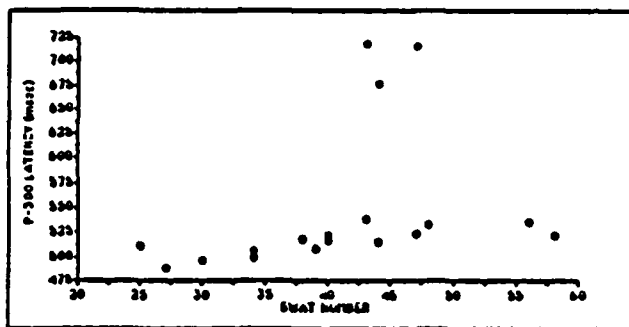


FIGURE 12: Scatter plots for data from Experiment Sets 1, 2 and 4 continued.

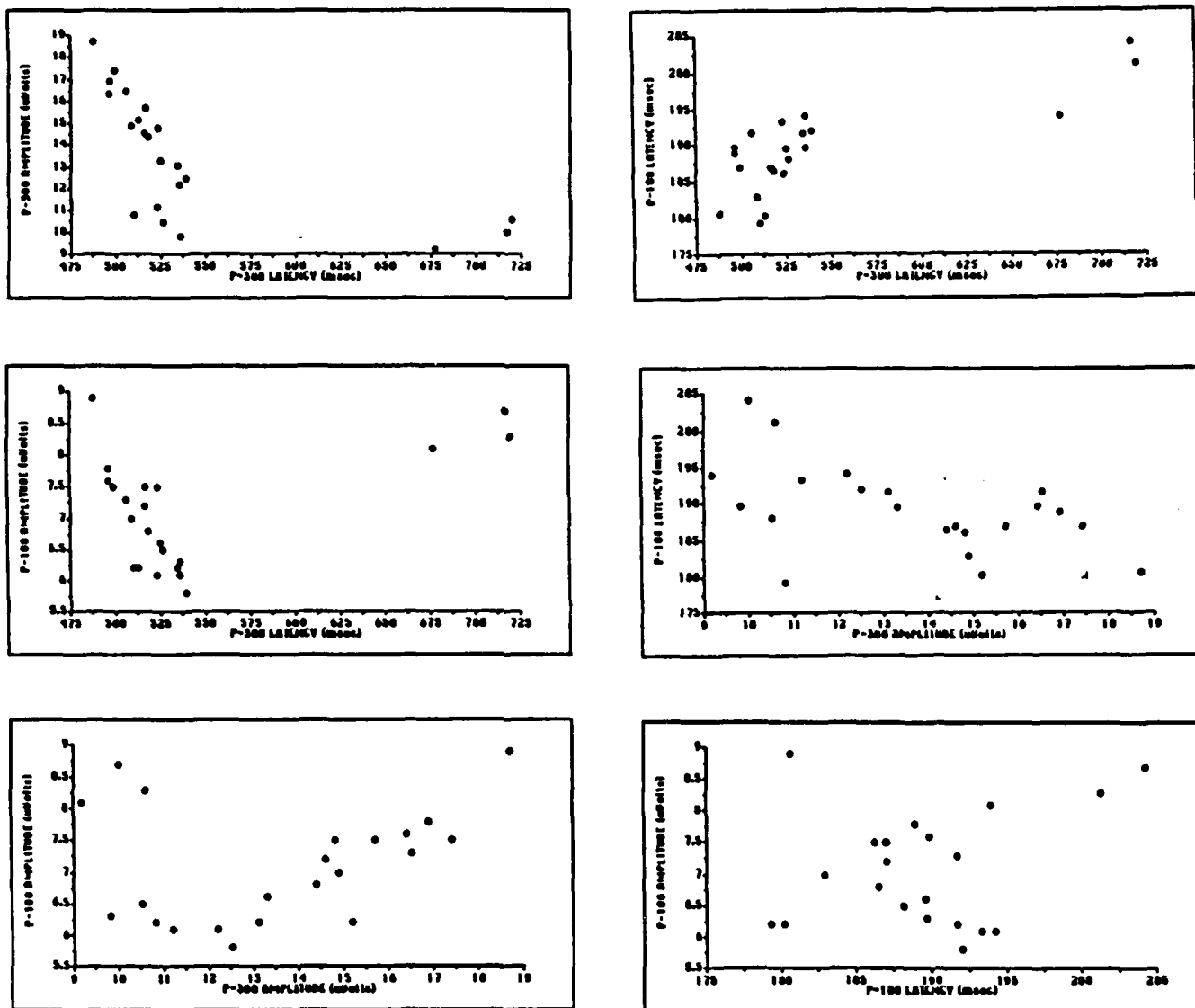


FIGURE 13: Scatter plots for data from Experiment Sets 1, 2, 3 and 4.

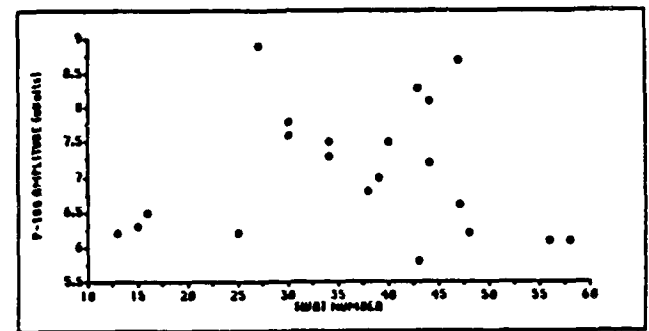
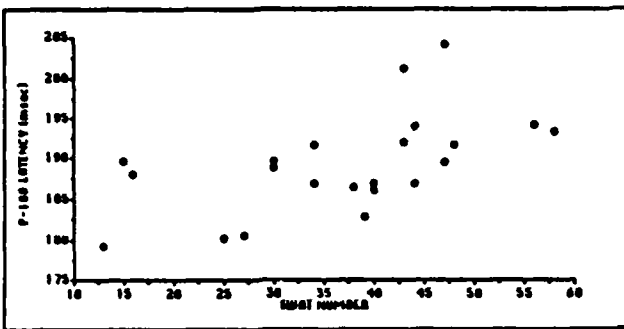
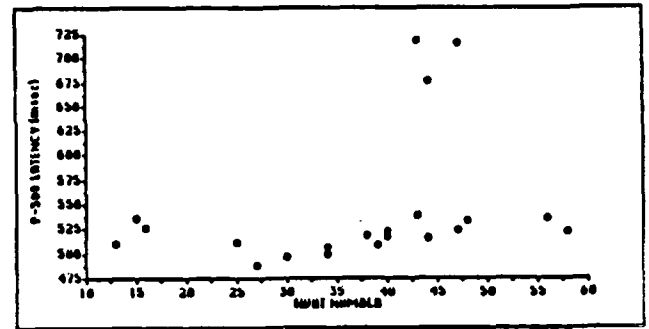
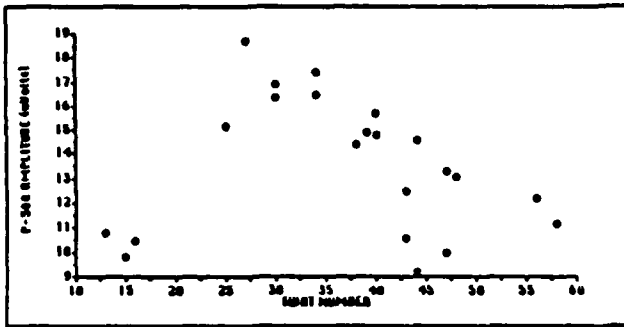


FIGURE 13: Scatter plots for data from Experiment Sets 1, 2, 3 and 4 continued.

There are several other interesting and suggestive relationships in the correlation matrices, but interpretation is risky without the addition of more viewing condition data obtained under similar experimental conditions. The correlation coefficients, especially those for P-300, SWAT and RT do, however, suggest that further work in this area would be fruitful.

SUMMARY

The goals of this project involved assessing the effects of binocular vision disruption on selected workload/performance indicators and the determination of which indicators correlated across experimental conditions. The four Experimental Sets demonstrated that none of the procedures used to disrupt binocular vision affected the subjects' RTs (nor P-180 latencies); the initial hypothesis regarding increased latencies produced by monocular occlusion was not confirmed.

Less conclusively demonstrated were effects on P-300s and SWAT ratings produced by binocular disruption. Under some conditions, significant changes were found but the effects were not universally present; the most likely conclusion is that there are real effects produced by disrupting binocular vision but the effects are small and easily lost below the level of variability in the workload/performance indicators.

The correlation matrices were also somewhat inconsistent. Within the parameters of Experiment Sets 1 and 2, strong correlations were found, especially between SWAT, RT and P-300 data, but these

relationships weakened when data obtained under other experimental conditions were introduced.

In summary, this project mapped out numerous areas in which there are open questions and in which further research will yield valuable information on how subjective and objective indicators of workload/performance can assess the ways that the human brain processes visual information.

References

1. Beach, GJ. The Relationship Between Apparent Fronto-Parallel Plane and Ocular Dominance Under Conditions of Unequal Retinal Illuminance. Doctor of Optometry Thesis, Pacific University, 1977.
2. Brookhuis, KA, Mulder, G, Mulder, LJM and Gloerich, ABM. The P3 Complex as an Index of Information Processing: The Effects of Response Probability. *Biological Psychology*, 1983; 277-296.
3. Dirks, B. The Effects of Prism-Induced Binocular Stress on P-300 Event Related Potentials. Masters Thesis. Pacific University, College of Optometry, Forest Grove, OR. 1987.
4. Donchin, E. Event-related Brain Potentials: A Tool For The Study of Human Information Processing. In: Begleiter H, ed. Evoked Brain Potentials and Behavior. New York: Plenum, 1979; 13-75.
5. Donchin, E. Surprise! ... Surprise? *Psychophysiology*, 1981(18); 493-513.
6. Duncan-Johnson, CC. P300 latency: A New Metric of Information Processing. *Psychophysiology*, 1981(18); 207-15.
7. Eggemeier, FT. Considerations in the Application of Subjective Measures of Workload; In Brown, ID, Goldsmith, R, Coombes, K, and Sinclair, MA, (eds). Ergonomics International 85, London, Taylor and Francis. 1985; 115-117.
8. Fagan, JE, Westgate, TM and Yolton, RL. Effects of Video Display Character Size, Clarity, and Color on P-300 Latency. *Am J Optom Physiol Optics*. 1986(63); 41-51.
9. Ferguson, GA. Statistical Analysis in Psychology and Education, 5th Ed. McGraw-Hill, New York. 1981; 307-9.
10. Hare, T, Russ, J, Faulkner, G. A New Pseudo-Random Number Generator. *Call-A.P.P.L.E.* Jan 1983; 33-4.
11. Hillyard, SA and Kutas, M. Electrophysiology of Cognitive Processing. *Annual Review of Psychology*. 1983; 33-61.
12. Johnson, R. A Triarchic Model of P-300 Amplitude. *Psychophysiology*. 1986(23); 367-84.
13. Jones, RK, Lee, DN. Why Two Eyes Are Better Than One: Two Views of Binocular Vision. *J Exp Psyc: Human Percept Perform*. 1981(7); 30-40.
14. Krueger, GP, Armstrong, RN and Cisco, RR. Aviator Performance in Week-long Extended Flight Operations in a Helicopter Stimulator. *Behav Res Meth, Instrum and Computers*. 1985(1); 68-74.

15. Kutas, M and McCarthy, G. Augmenting Mental Chronometry: The P300 as a Measure of Stimulus Evaluation Time. Science. 1977(197); 792-5.
16. Poffenberger, AT. Reaction Time to Retinal Stimulation with Special Reference to the Time Lost in Conduction Through the Nerve Center. Arch Psyc NY. 1912; 23.
17. Poon, LW, Thompson, LW and Marsh, GR. Average Evoked Potential Changes as a Function of Task Complexity. Psychophysiology. 1976; 43-49.
18. Pritchard, WS. Psychophysiology of P300. Psychol Bull. 1981(89); 506-40.
19. Reid, GB. The Systematic Development of a Subjective Measure of Workload: In Brown, ID, Goldsmith, R, Coombes, K, and Sinclair, MA, (eds). Ergonomics International 85, London, Taylor and Francis. 1985; 109-111.
20. Reid, GB, Shingledecker, CA and Eggemeier, FT. Application of Conjoint Measurement to Workload Scale Development. Proc Human Factors Society. 1981; 522-526.
21. Reid, GB, Shingledecker, CA, Nygren, TE and Eggemeier, FT. The Development of Multidimensional Subjective Measures of Workload. Proc 1981 International Conference on Cybernetics and Society. 1981; 403-406.
22. Ritter, W. Latency of the Event-Related Potentials and Reaction Time. In, Otto, DA, (ed), Multidisciplinary Perspectives in Event-Related Brain Potential Research. EPA-600-9-77-043. U.S. Environmental Protection Agency, Washington. 1978; 173-4.
23. Sheedy, JE, Bailey, IL, Buri, M and Bass, E. Binocular versus Monocular Task Performance. Am J Optom Physiol Optics. 1986(63); 839-46.
24. Shingledecker, CA. A Task Battery For Applied Human Performance Assessment Research. AFAMRL-TR-84-071 Air Force Aerospace Medical Research Laboratory, Wright-Patterson AFB, OH. 1984.
25. Sparks, D. RND is Fatally Flawed. Call-A.P.P.L.E. Jan 1983; 29-32.
26. Stern, JA, Walrath, LC and Goldstein, R. The Endogenous Eye Blink - An Indicant of Cognitive Activity and State. Psychophysiology. 1984(21); 22-3.
27. Sternberg, S. Memory Scanning: Mental Processes Revealed by Reaction time Experiments. American Scientist. 1969; 421-457.
28. Teichner, WH and Krebs, MJ. Laws of the Simple Visual Reaction Time. Psych Rev. 1972(79); 344-58.

29. Teichner, WH. Recent Studies of Simple Reaction Time. Psyc Bull. 1954(51); 128-49.
30. Tukey, JW. Some Thoughts on Clinical Trials, Especially Problems of Multiplicity. Science. 1977(198); 679-84.
31. Wickens, CD. Processing Resources and Attention, Dual Task Performance and Workload Assessment. Technical Memorandum EPL-81-3/ONR-81-3, Office of Naval Research, Arlington, VA. 1981.
32. Wirth, P and Ford, LE. Five Laboratory Interfacing Packages. Byte. 1986; 303-12.
33. Yolton, RL. Physiological Correlates of Behavioral Performance on the Mathematical Processing Subtest of the CTS Battery. Final Report, UES/AFOSR Summer Faculty Research Program. AAMRL/HEG, Wright-Patterson, AFB, OH. 1986.

1986 AFOSR MINIGRANT PROGRAM

Sponsored by the
AIR FORCE OFFICE OF SCIENTIFIC RESEARCH

Conducted by the
Universal Energy Systems, Inc.

FINAL REPORT

Finite Element Analysis of Thermomechanically Coupled
Stress and Temperature Fields

Prepared by: Richard W. Young

Academic Rank: Associate Professor & Assistant Department Head

Department and University: Aerospace Engineering and Engineering Mechanics
University of Cincinnati
Cincinnati, OH 45221-0070

ATTN: Dr. Vipperla B. Venkayya
Design and Analysis Methods Group (FIBRA)
Analysis and Optimization Branch
Structures and Dynamics Division
AFWAL/Flight Dynamics Laboratory
Wright-Patterson AFB, Ohio

Date: 25 November 1987

Contract No. F49620-85-C-0013/SB5851-0360

ACKNOWLEDGEMENTS

The author wishes to thank Mr. Diaa Hosny, PhD candidate in Aerospace Engineering and Engineering Mechanics at the University of Cincinnati, for his careful and patient work in this research, Dr. V.B. Venkayya of the Design and Analysis Methods Group, AFWAL/Flight Dynamics Laboratory, WPAFB, and Mr. Durwood Thrasher of the Air Force Rocket Propulsion Laboratory, Edwards AFB, for their support of earlier phases of this work and the Air Force Office of Scientific Services, Bolling AFB, D.C., for its sponsorship of this work.

ABSTRACT

When internal or external thermal sources (such as viscoelastic damping or laser attack) give rise to temperature changes or material modification sufficient to affect material properties, the equations of dynamic and thermal equilibrium can become nonlinearly coupled. The coupling is introduced through the material's constitutive functions. Solution of the equations generally requires an iterative numerical algorithm.

Analysis of one such problem, the thermomechanically coupled vibration of a cylindrical grain of solid rocket propellant, has been undertaken. Preliminary numerical results are presented for the low-amplitude, high-frequency forced vibration of the propellant. The data show reasonable profiles of temperature and displacement but contain some degree of scatter which suggests that the algorithm is not yet working up to its full potential.

Results are presented over a wide range of a scalar parameter used for relative weighting of error measures and are seen to be independent of the parameter over a portion of that range.

Continued development of the algorithm is recommended and two supplementary variations in methodology are proposed.

INTRODUCTION

Significant progress was made during this mini-grant toward the long-term goal of having an algorithm capable of predicting steady-state thermal and displacement fields for the two-dimensional vibration of a thermoviscoelastic solid rocket propellant. The reviews of the constitutive theory and the derivation of the equations of thermal and dynamic equilibrium, largely undertaken during the principal investigator's tenure as a USAF Summer Fellow at the Design and Analysis Methods Group, AFWAL/Flight Dynamics Laboratory, Wright-Patterson AFB, were extended.

The primary accomplishment of this aspect of the project was the derivation of functional forms of the residual, or relaxed, moduli which are more consistent with the forms of the storage and loss moduli. The functional forms are left in sufficiently general form to allow for the thermal dependence of the viscoelastic analog of Poisson's ratio. The analytical details of the derivation of the relaxed moduli are presented in Appendix I of this report.

A good portion of the work under the mini-grant involved the review and debugging of the FORTRAN-based finite element code used for numerical implementation of the algorithm. The work done in 1986 [1] led to major revision of the original constitutive model as well as the notation used in the derivation of the field equations of equilibrium. There was not time fully to integrate those changes into the existing software in 1986, but that has now been accomplished.

As a result of the extensive review and revision of the software it has been possible to generate reasonable-looking solutions to an example problem. There is reason to believe that the solutions presented are not yet very accurate and that coding errors remain. These concerns will be discussed after a sample problem is presented.

SAMPLE PROBLEM

Consider the forced steady-state vibration of an annular body shown in Figure 1. The outer circumference is subjected to a low-amplitude, high-frequency vibration while the inner and outer surfaces are held at ambient temperature. Because of the large number of variables required in the analysis of thermomechanically coupled vibration (steady, in-phase and out-of-phase components of displacement in both the radial and circumferential directions, temperature, and two spatial derivatives of all of the above), a small finite element mesh gives rise to a surprisingly large computer storage requirement. For this reason the sample problem chosen for initial debugging of the algorithm was simple and intended to be modeled by a very small finite element mesh.

Given the axisymmetry of the problem only a sector of the body needs to be analysed. A 15-node, 4-element model of a twenty degree sector is shown in Figure 2. The following boundary conditions were applied to the model:

1. the driving displacement
 - a. radial, in-phase displacement (U1) set to 0.00046" at $r=4"$
 - b. radial, out-of-phase displacement (U2) set to zero at $r=4"$
2. thermal boundary conditions

temperature increase (τ) set to zero at $r = 2"$ and $4"$
3. axisymmetric response
 - a. Circumferential components of displacement (V1,V2,V3) set to zero at the sides of the sector. Not enforced at the center nodes of the model to test the predictive capabilities of the algorithm.
 - b. Theta derivatives of all variables set to zero at the sides of the sector.
4. elimination of rigid body motion

Analytically prohibited by conditions 3a. Redundantly enforced by setting the steady component of radial displacement (U3) to zero at one point as a guard against possible ill-conditioning of the equilibrium equations due to the "weak" prohibition against radial drift.

Other physical and material parameters used in the problem are:

ambient temperature: 65 degrees F.

mass density: 0.00107 slug/(cubic inch)

thermal conductivity: 0.02 lb/(sec degree F.)

driving frequency: 6000. rad/sec

driving displacement: 0.00046 inches

dynamic moduli at ambient temperature:

storage modulus: 4.086 ksi

loss modulus: 2.510 ksi

bulk modulus: 9.244 ksi

relaxed moduli at ambient temperature:

storage modulus: 1.074 ksi

bulk modulus: 13.95 ksi

DISCUSSION OF THE ALGORITHM AND EXPECTED RESULTS

The discretization of the field variables by the finite element method introduces errors into the homogeneous forms of the field equations. These errors can be minimized by least-squared error methods, but that in turn imposes severe continuity requirements on the problem and its modeling [2]. Rather than try to use higher-order continuity finite elements, it is simpler to reduce the problem to first order by introducing as "independent" variables the two first derivatives of each of the seven field variables. This artifice introduces a new source of error, the discrepancy between the spatial derivatives of the quadratic finite element interpolations of the field variables and the linear finite element interpolations of the variables representing the spatial derivatives.

The volume integrals of the squares of these errors are weighted by a scalar parameter and added to like measures of the original errors. The scalar parameter, A , is chosen so as to insure that one error measure does not numerically dominate the other.

It is to be expected that the solution of the problem should be independent of the weighting parameter over a reasonable range of values. A second a priori test of the quality of the numerical solution is the extent to which values of the calculated variables are independent of the polar coordinate θ .

DISCUSSION OF THE NUMERICAL RESULTS

Numerical results are presented for four values of the scalar weighting parameter, A , namely $\log A = 3, 5, 7$ and 9 .

Independence of θ is not always achieved. The degree of independence seems to depend strongly upon the weighting factor, A .

<u>log A</u>	<u>variation of U1, U2, U3 and tau with theta</u>
9	none (to four significant figures)
7	none (to four significant figures) for displacements, two digit variance in 4th place for one of three thermal checks
5	one to six digit variance in fourth place
3	third significant figure usually not reliable

The θ components of displacement at the center nodes of the sector are calculated to be zero within the limits of "near double" precision. Their values are about ten orders of magnitude less than the driving displacement's. It is of note that their magnitudes depend inversely on the magnitude of A .

Table 1 shows some typical numerical values. Values in the second through fourth columns are taken after "convergence" of tau to within 0.1 degree F. at all points in the mesh.

TABLE 1 SOLUTIONS AS A FUNCTION OF THE WEIGHTING FACTOR, A
(Evaluations at $r = 3$ ")

log A	tau, deg. F	$U1, 10^{-4}$ in.	$V1, \text{ in.}$	ITERATIONS	tau at iter. 1
9	13.68	-1.298	6.97D-15	8	21.74
7	13.69	-1.298	6.97D-13	8	21.75
5	14.14 <u>+0.02</u>	-1.286	6.96D-11	8	22.70 <u>+0.03</u>
3	18.28 <u>+0.43</u>	-1.175 <u>+0.004</u>	6.76D-09	9	31.52 <u>+0.71</u>

Profiles of the in-phase component of radial displacement ($U1$) and the temperature increase (τ) are presented in Figures 3 and 4 for various values of A. The profiles for $\log A = 3$ are based on averaged values. It is seen that the profiles are essentially identical for $\log A$ equal to 7 and 9, differ only slightly for $\log A = 5$ and start to vary significantly for $\log A = 3$. It is also seen that the temperature profile is far more sensitive to A than is the displacement profile.

CONCLUSIONS FROM THE NUMERICAL DATA

It is clear from the profiles in Figures 3 and 4 that the finite element mesh is too coarse to enable good predictions. First radial derivatives of the field variables are based on linear interpolations between nodal values at $r = 2, 3$ and 4 inches. The field variables themselves are quadratically interpolated between nodal values at $r = 2, 2.5$ and 3 inches and at $r = 3, 3.5$ and 4 inches. The spatial variations of $U1$ and τ are large enough in this problem that good correlation between these two modelings of derivatives is not possible. Calculations at a lower driving frequency might avoid this problem, but at the possible cost of losing significant thermomechanical coupling.

It is also disturbing that the lack of axisymmetry in the solution is as pronounced as it is. It does seem to be reduced by the weighting factor, A, as do the values of $V1$. This suggests that some coding or logic error is still present. Because the errors seem to diminish with increased A and A gives more relative weight to the "derivative errors" it seems likely that the problem lies in the field equations of thermal or perhaps dynamic equilibrium or in the manipulation of the matrices representing those errors. The effect of the error seems to be small, but it would be unwise so to assume.

RECOMMENDATIONS

The numerical results just presented show that the algorithm is capable of calculating reasonable results for thermomechanically coupled temperature and displacement fields. The first objective of the mini-grant research has thus nearly been accomplished, but more debugging remains to be done. Once the source of the lack of axisymmetry has been uncovered and corrected, the effects of the weighting factor should be investigated further. Establishing an upper limit on the range of A for which the solution is essentially independent of A and examining the form of the solutions beyond those limits should shed some light on the mathematical properties of the solution algorithm.

One alternative formulation of the finite element modeling of the problem seems to warrant investigation. Rather than to model the first derivatives of the field variables solely by the "derivative variables", it seems reasonable to model them in part by spatial derivatives of the field variables as one would were the "derivative variables" not introduced. In general one could write, for U_1 for instance,

$$U_{1,r} = (1-s) (\underline{n}_{2,r})^T \underline{U}_1 + s (\underline{n}_1)^T \underline{U}_{1r} \quad (1)$$

where \underline{U}_1 and \underline{U}_{1r} are vectors of nodal values of U_1 and its r -derivative respectively, \underline{n}_1 and \underline{n}_2 are quadratic and linear finite element interpolation function vectors respectively and s is the splitting factor, $0 < s \leq 1$. The mathematical effect of letting s be less than unity is to introduce the errors associated with the discrepancy in derivatives into the field equations themselves in a perhaps more logical manner. Setting s equal to unity recaptures the original formulation of the problem.

A second, quite different approach to the question of dealing with the two disparate error sources is to use the "derivative error" measure alone as a means of optimizing the "derivative variables" with respect to the original field variables. This approach has been thought of only recently and there has not been time to investigate the numerical tractability of the procedure. If indeed it proves to be a viable approach it will present three quite important advantages:

1. It will eliminate the arbitrary weighting and splitting factors as parameters in the solution algorithm.
2. It will reduce the dimension of the largest matrix by 50%, cutting the total memory requirements of the program by somewhat less than 75%. This is helpful because it will be necessary to run larger finite element models of the test case presented and other tests as well. It will thus be necessary to work on a mainframe or a more powerful minicomputer or else find a way to make the algorithm less memory intensive.

3. It will provide an alternative algorithm which can be used as a second source of solutions to test problems, a valuable feature to have available in the analysis of such nonlinear phenomena as thermomechanical coupling.

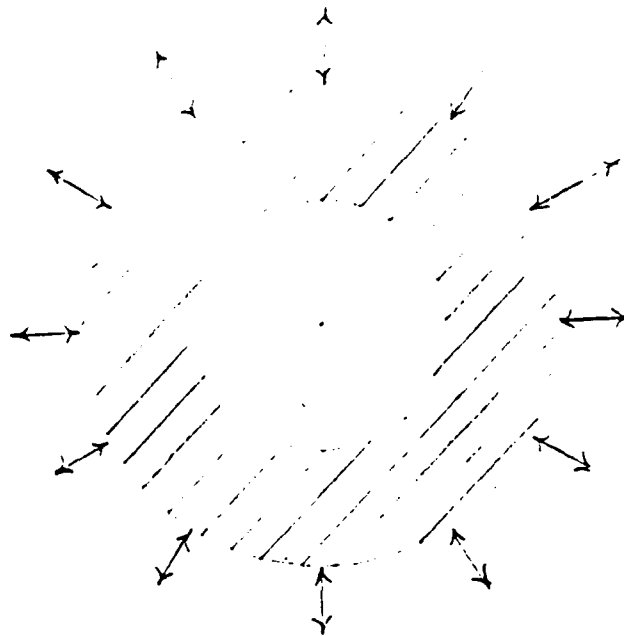


Figure 1 Annular Grain Subjected to Radial Vibration

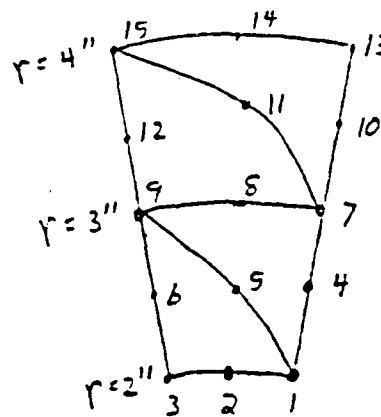


Figure 2 15-Node, 4-Element Model of 20° Sector

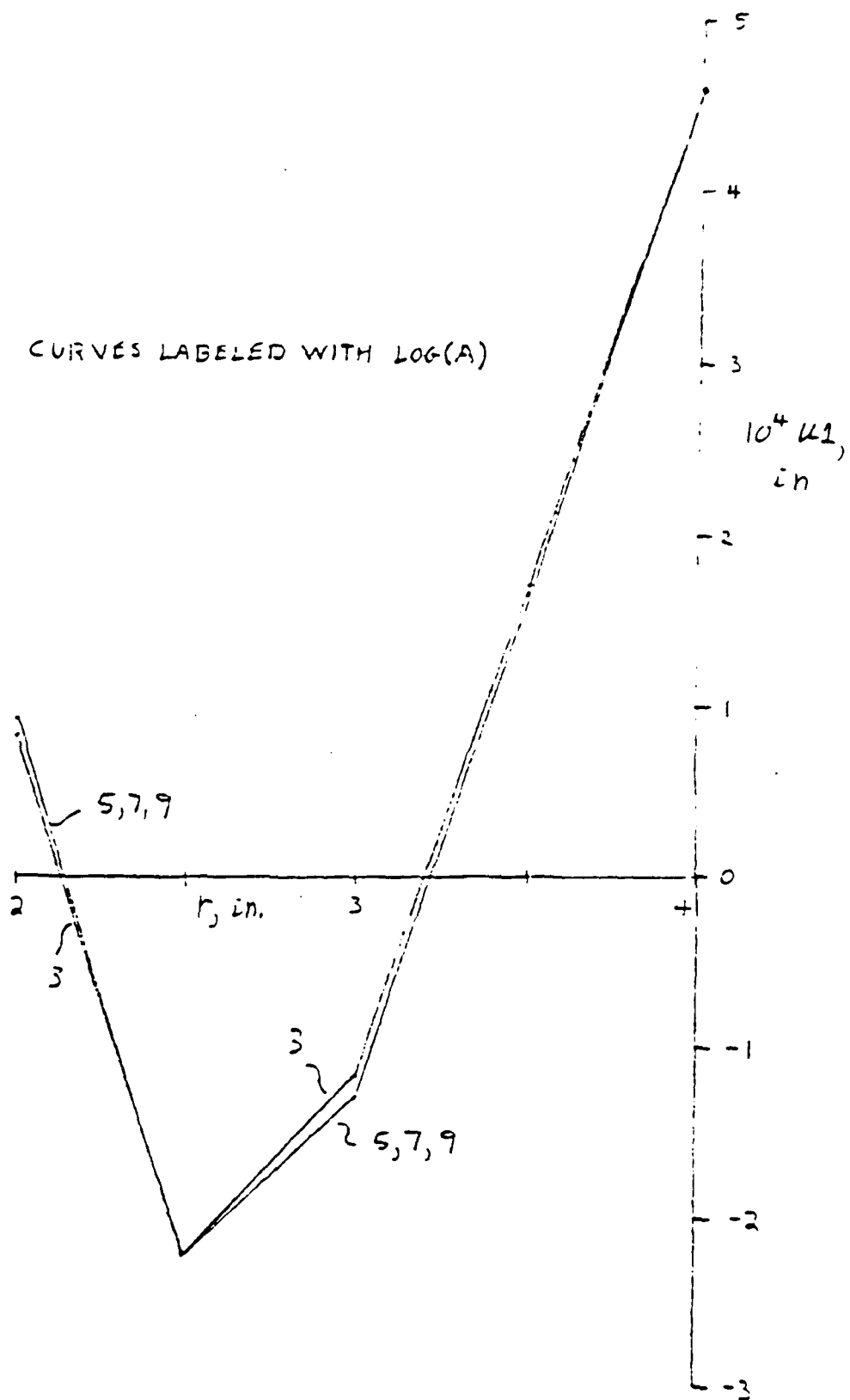


Figure 3 Radial, In-Phase Displacement Component Profile

20 - CURVES LABELED WITH $\log(A)$

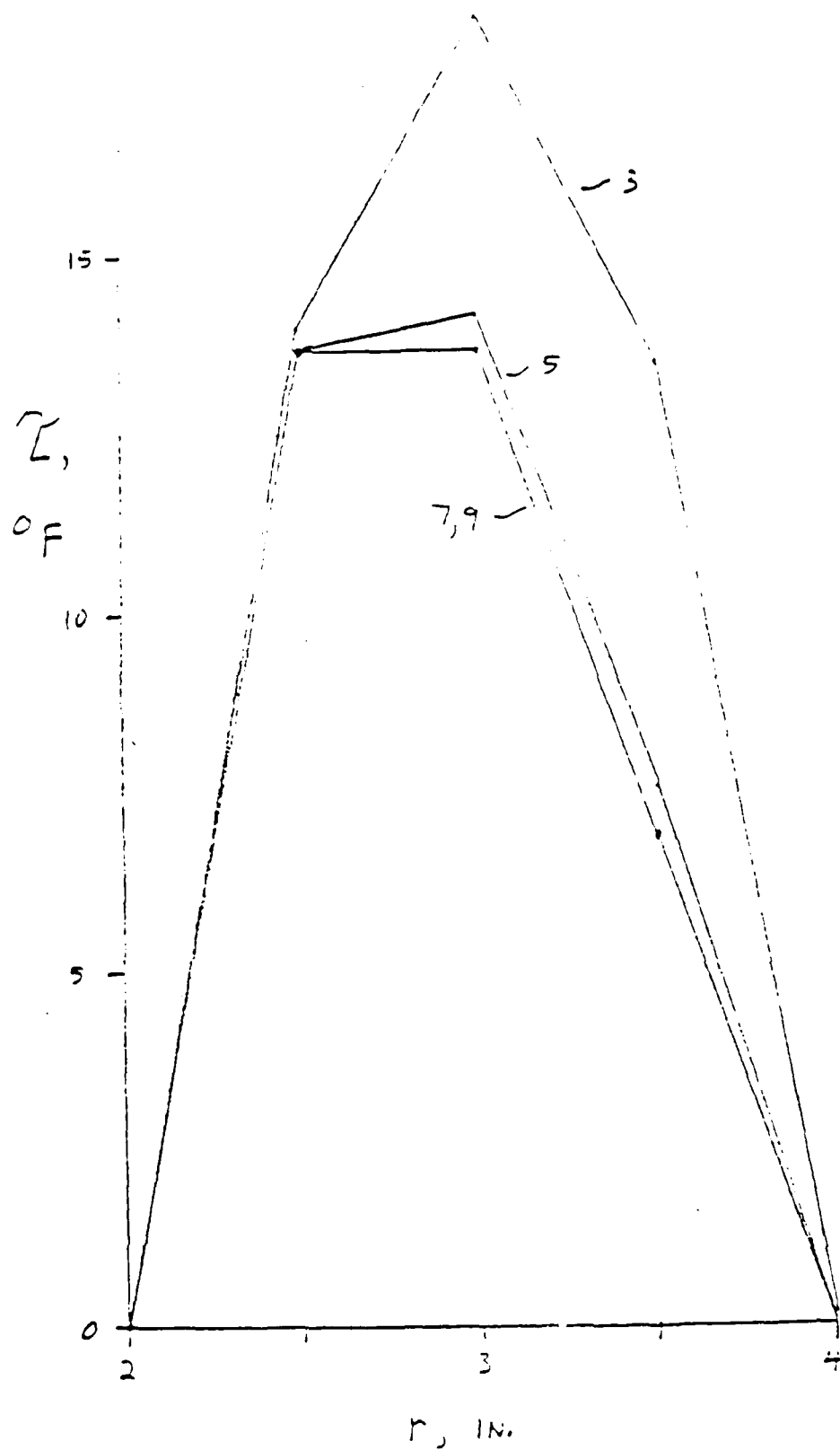


Figure 4 Temperature Elevation Profile

APPENDIX I. Relaxed Moduli as Functions of Frequency and Temperature

We start with two equations from Christianson [3] put in our notation,

$$G_1(\omega, T) = G_0(\omega, T) + \omega \int_0^{\infty} \hat{G}(\omega, T, \eta) \sin(\omega \eta) d\eta \quad A.1$$

and

$$G_2(\omega, T) = \omega \int_0^{\infty} \hat{G}(\omega, T, \eta) \cos(\omega \eta) d\eta \quad A.2$$

where G_1 , G_2 and G_0 are the storage, loss and relaxed moduli respectively. We will now assume that the storage and loss moduli can be written using separation of variables, consistent with

$$\hat{G}(\omega, T, \eta) = a(\omega) b(T) e^{-\omega_0 \eta} \quad A.3$$

and recall the Laplace transforms

$$\int_0^{\infty} e^{-st} \begin{Bmatrix} \sin(ct) \\ \cos(ct) \end{Bmatrix} dt = \begin{Bmatrix} c \\ s \end{Bmatrix} (s^2 + c^2)^{-1} \quad A.4$$

Thus

$$G_2(\omega, T) = \omega a(\omega) b(T) \omega_0 / (\omega_0^2 + \omega^2) \quad A.5$$

and

$$a(\omega) b(T) = (\omega_0^2 + \omega^2) G_2(\omega, T) / (\omega_0 \omega) \quad A.6$$

Then from Equation A.1 we have

$$G_0(\omega, T) = G_1(\omega, T) - \omega a(\omega) b(T) \int_0^{\infty} e^{-\omega_0 \eta} \sin(\omega \eta) d\eta \quad A.7$$

which integrates to

$$G_0(\omega, T) = G_1(\omega, T) - (\omega/\omega_0) G_2(\omega, T) \quad A.8$$

Because Equations A.1 and A.2 hold for volumetric moduli as well, Equation A.8 can be written with the following substitutions:

$$G_0 \rightarrow E_{K0}$$

$$G_2 \text{ ----> } E_K \sin \phi$$

which gives us

$$E_{K0}(\omega, T) = E_K(\omega, T) \{ \cos[\phi(\omega, T)] - (\omega/\omega_0) \sin[\phi(\omega, T)] \}. \quad A.9$$

The relaxed moduli G_0 and E_{K0} are now given as functionals of $G_1(\omega, T)$, $G_2(\omega, T)$, $E_{K0}(\omega, T)$ and $\phi(\omega, T)$.

Bibliography

1. Young, R.W. "Final Report: Application of Finite Element Analysis to Two Disparate Structural Problems: Thermomechanical Coupling and Optimal Sizing of Truss Members," AFOSR 1986 USAF-UES Summer Faculty Research Program, August 1986. Parts I-V
2. Lynn, P.P. & S.K. Arya, "Finite Elements Formulated by the Weighted Discrete Least Squares Method," IJNME 8, 1974, P. 71.
3. Christensen, R. M., Theory of Viscoelasticity, An Introduction, Academic Press, New York, 1971.

AFOSR-UES MINI GRANT PROGRAM

Sponsored by the
AIR FORCE OFFICE OF SCIENTIFIC RESEARCH
Conducted by the
Universal Energy Systems, Inc.

FINAL REPORT

SIMPLIFICATION OF H^∞ -COMPENSATORS

Prepared by:	Ajmal Yousuff
Academic Rank:	Assistant Professor
Department and	Department of Mechanical Engineering and Mechanics
University:	Drexel University
Date:	January 26, 1987
Contract No.:	F 49620-85-C-0013/SB5851-0360

SIMPLIFICATION OF H^∞ -COMPENSATORS

by

Ajmal Yousuff

Department of Mechanical Engineering and Mechanics

Drexel University

Philadelphia, PA 19104

phone: (215) 895-1868

Abstract

One of the recent methods developed for control synthesis is the H^∞ -optimization method. Though powerful conceptually, this method yields large order compensators. Consequently, simplification of these compensators is required to meet on-line hardware requirements. This requirement becomes crucial in the case of vehicles that undergo rapid dynamic changes, such as hypervelocity and supermaneuverable aircrafts.

The research effort reported herein attempts to develop such a simplification scheme. The method employed is the (M,N)-approximation scheme developed by the author at WPAFB during the summer of 1986. The approach is to view the compensator as a subsystem of the overall closed loop system, and to use (1,2)-approximation to reduce the compensator. The results reported herein include the application of this scheme to q-COVER extraction, the pole locations of the H^∞ -compensators, and the non-minimality of observer-based controllers.

1. Introduction

The recent innovation of hypervelocity and supermaneuverable aircrafts poses a challenge to flight control engineers. These vehicles undergo rapid dynamic changes resulting in considerable variation in the parameters of the assumed mathematical models, thus requiring compensators that are robust to such parameter variations. The high velocities and the rapid dynamic changes demand the compensators to be fairly simple (without involving intricate and time-consuming in-flight computations), and yet be optimal with respect to mission specifications.

The H^∞ -optimization method [1], a recently developed method that unifies both classical and modern control theories, is one compensator synthesis method that is capable of efficiently incorporating the issues of robustness and optimality. The resulting compensators, however, are often quite complex. Hence, in order to employ the theoretically appealing H^∞ -compensators in real life, one needs a means of simplifying these compensators without adversely sacrificing their guaranteed robustness and optimality. The results of an effort to develop such a simplification scheme are presented in this report.

2. (M,N)-Approximation

Now, the closed loop system including the compensator can be viewed as a system consisting of two interconnected subsystems - the plant (i.e. the aircraft/vehicle) and the compensator. Hence, the compensator reduction problem is to simplify one subsystem (namely, the compensator) of these two subsystems. This problem has been investigated during the 1986 Summer as a (1,2)-approximation problem which is a special case of the more general (M,N)-approximation which is defined as follows.

In order to present the approach to (M,N)-approximation, we begin with (1,1)-approximation, the standard model reduction. Consider the linear system $S(n)$ given below, where the argument n denotes the order of the system.

$$\begin{aligned}\dot{x} &= A x + B w ; \quad x \in \mathbb{R}^n \\ y &= C x + D w ; \quad y \in \mathbb{R}^k ; \quad w \in \mathbb{R}^m\end{aligned}\tag{2.1}$$

Now, depending upon the nature of inputs w (such as Gaussian, energy bounded, etc.), one could use an appropriate reduction method (such as q-COVER [2], internal balancing [3], Hankel-norm approximation [4], etc.) to obtain an approximation $\underline{S}(r < n)$ that preserves certain properties of $S(n)$ (such as root-mean-square values, covariance sequences, grammians, Hankel norm, etc.). Let such an $\underline{S}(r)$ be

$$\begin{aligned}\dot{\underline{x}}_r &= \underline{A}_r \underline{x}_r + \underline{B}_r w ; \quad \underline{x}_r \in \mathbb{R}^r \\ \underline{y}_r &= \underline{C}_r \underline{x}_r + \underline{D}_r w ; \quad \underline{y}_r \in \mathbb{R}^k\end{aligned}\quad (2.2)$$

Many of the approximation schemes that use state space representations proceed as follows. Transform $S(n)$ to a suitable set of coordinates/basis as demanded by the properties to be preserved in $\underline{S}(r)$. Let $x = \underline{T}\underline{x}$ be the transformation. Such a \underline{T} is obtained, for example, via internal balancing [3], cost-decoupling [5]. Let

$$\begin{aligned}\underline{T} &= [\underline{T}_r \underline{T}_t] ; & \underline{T}_r &\in \mathbb{R}^{(n,r)} \\ \underline{L} &= \begin{bmatrix} \underline{L}_r \\ \underline{L}_t \end{bmatrix} = \underline{T}^{-1} ; & \underline{x} &= \begin{bmatrix} \underline{x}_r \\ \underline{x}_t \end{bmatrix}\end{aligned}\quad (2.3)$$

Then $\underline{S}(r)$ is produced from the representation of $S(n)$ in the basis \underline{x} . It is essential to point out that the basic need for computing \underline{T} is to identify the states \underline{x}_r and \underline{x}_t as $\underline{x}_r \in \text{Im}(\underline{T}_r)$ and $\underline{x}_t \in \text{Ker}(\underline{L}_r)$. Then $\underline{S}(r)$ is obtained either (a) by deleting \underline{x}_t , as, for example, in balancing, q-COVER; or (b) by absorbing some information about \underline{x}_t in \underline{x}_r and then deleting \underline{x}_t , as in singular perturbation [6], Hankel norm approximation [4], etc.. In this paper we will focus only on case(a), in which case the parameters $\{\underline{A}_r, \underline{B}_r, \underline{C}_r, \underline{D}_r\}$ are obtained as $\underline{A}_r = \underline{L}_r \underline{A} \underline{T}_r$, $\underline{B}_r = \underline{L}_r \underline{B}$, $\underline{C}_r = \underline{C} \underline{T}_r$, and $\underline{D}_r = \underline{D}$. With some abuse of language, they also can be viewed as $\underline{A}_r = \underline{P} \underline{A} \underline{P}$, $\underline{B}_r = \underline{P} \underline{B}$, $\underline{C}_r = \underline{C} \underline{P}$, where $\underline{P} = \underline{T}_r \underline{L}_r$ is an oblique projection (since $\underline{L}_r \underline{T}_r = \underline{I}_r$) on $\text{Im}(\underline{T}_r)$ along $\text{Ker}(\underline{L}_r)$. (Strictly speaking, the above equations are not defined, since for example, the maps \underline{B}_r and $\underline{P} \underline{B}$ are defined on different but isomorphic spaces). Clearly, $\text{Im}(\underline{P}) = \text{Im}(\underline{T}_r)$ and $\text{Ker}(\underline{P}) = \text{Ker}(\underline{L}_r)$. From this point of view many of the existing approximation schemes basically identify the subspaces $\text{Im}(\underline{P})$ and $\text{Ker}(\underline{P})$, since a projection is uniquely defined by its image and kernel.

We will now formulate the (M,N)-approximation problem in this context. Suppose that $S(n)$ consists of N interacting subsystems $S_i(n_i)$, each described by its associated states x_i , $i=1,2,\dots,N$, and that there are N_w input vectors w_i , and N_y output vectors y_i , such that

$$\begin{aligned}
x^T &= [x_1^T, x_2^T, \dots, x_N^T]^T ; w^T = [w_1^T, w_2^T, \dots, w_{N_w}^T] ; y^T = [y_1^T, y_2^T, \dots, y_{N_y}^T] \\
x_i &\in \mathbb{R}^{n_i} ; w_i \in \mathbb{R}^{m_i} ; y_i \in \mathbb{R}^{k_i} \\
n &= \sum_{i=1}^N n_i ; m = \sum_{i=1}^{N_w} m_i ; k = \sum_{i=1}^{N_y} k_i
\end{aligned} \tag{2.4}$$

The system $S(n)$ of Eqn.(2.1) is then written in its subsystem form as

$$\begin{aligned}
\dot{x}_i &= \sum_{j=1}^N A_{ij} x_j + \sum_{j=1}^{N_w} B_{ij} w_j , \quad i = 1, 2, \dots, N \\
y_i &= \sum_{j=1}^N C_{ij} x_j + \sum_{j=1}^{N_w} D_{ij} w_j , \quad i = 1, 2, \dots, N_y
\end{aligned} \tag{2.5}$$

In order to obtain an approximation $S(r)$ which preserves the identities of all subsystems $S_i(\cdot)$, $i=1,2,\dots,N$, we seek $S(r)$ in the form

$$\begin{aligned}
\dot{x}_{ir} &= \sum_{j=1}^N A_{ijr} x_{jr} + \sum_{j=1}^{N_w} B_{ijr} w_j ; x_{ir} \in \mathbb{R}^{r_i} , \quad 0 \leq r_i \leq n_i , \quad i = 1, 2, \dots, N \\
y_{ir} &= \sum_{j=1}^N C_{ijr} x_{jr} + \sum_{j=1}^{N_w} D_{ijr} w_j ; y_{ir} \in \mathbb{R}^{k_i} , \quad i = 1, 2, \dots, N_y
\end{aligned} \tag{2.6}$$

so that each state vector x_{ir} is associated with $S_i(r_i)$ which is an approximation of $S_i(n_i)$ and $r = r_1 + r_2 + \dots + r_N$. Note that (a) $r_i = 0$ implies that $S_i(n_i)$ is approximated by a static system, and if in addition $D_{ij} = 0$ for all j , then $S_i(n_i)$ is completely ignored in the overall approximation $S(r)$; and (b) $r_i = n_i$ implies that $S_i(n_i)$ is retained as it is (without any reduction) in $S(r)$. In an (M, N) -approximation $(N-M)$ r_i s should satisfy $r_i = n_i$, indicating that $(N-M)$ subsystems are not reduced.

A convenient, but perhaps imprudent, approach is to consider each subsystem $S_i(n_i)$ independently, i.e., to ignore the interaction terms A_{ij} , $j \neq i$, and then approximate each subsystem independent of other. Such an approach may also be enforced by the limited capacity of the computers, especially when n , the order of the overall system $S(n)$, is very large. Ignoring the interaction terms in the process of approximating each subsystem would not take into consideration the effect of this approximation on other subsystems. Hence, this approach should be avoided whenever possible.

The (1,1)-approximation satisfies the above requirement, since it is developed based on the overall system $S(n)$. Note that in the development of the oblique projection \underline{P} (through the transformation \underline{T}), even though the interactions among all subsystems are taken into account, the requirement that the approximation $\underline{S}(r)$ should be of the form (2.6) is not enforced. As a consequence, $\underline{S}(r)$ does not preserve the identities of the subsystems. One way of enforcing this requirement is to constrain the oblique projection to be of the form

$$P = \text{block diag}\{P_1, P_2, \dots, P_N\} \quad (2.7)$$

where $(N-M)$ P_i s are identity maps, and the remaining M arbitrary projections P_i s satisfy $P_i = T_{ir}L_{ir}$ for some T_{ir} and L_{ir} satisfying $L_{ir}T_{ir} = I_{ri}$. This would yield $A_{ijr} = L_{ir}A_{ij}T_{jr}$, $B_{ijr} = L_{ir}B_{ij}$, $C_{ijr} = C_{ij}T_{jr}$, thus clearly indicating the approximation of $S_i(n_i)$ by $S_i(r_i)$ - this is what we mean by "preserving the identities of subsystems"; for example, if $S_i(n_i)$ represents a solar panel, then $S_i(r_i)$ is an approximate model of the same solar panel.

Thus far two oblique projections have been presented: (1) the (1,1)-approximation projection \underline{P} which focuses on the properties to be preserved in $S(r)$, but does not satisfy the sufficient condition (2.7) required of an (M,N) -approximation; (2) the (M,N) -approximation projection P that satisfies (2.7) but does not consider the properties. Now, since the parameters of $\underline{S}(r)$ and $S(r)$ can be written in terms of the corresponding projections as $\{\underline{P}A\underline{P}, \underline{P}B, C\underline{P}, \underline{D}_r\}$ and $\{PAP, PB, CP, D_r\}$, respectively, the difference between the transfer functions $\underline{G}(s)$ of $\underline{S}(r)$ and $G(s)$ of $S(r)$ is given by

$$\underline{G}(s) - G(s) = C[\underline{P}(sI - \underline{P}A\underline{P})^{-1}\underline{P} - P(sI - PAP)^{-1}P]B.$$

Using the idempotent properties of the projections (i.e. $\underline{P}\underline{P} = \underline{P}$, $PP = P$), and the identity

$$(sI - A)^{-1} = Is^{-1} + As^{-2} + A^2s^{-3} + \dots$$

the above equation can be reduced to

$$\underline{G}(s) - G(s) = C[\underline{P}(sI - A)^{-1}\underline{P} - P(sI - A)^{-1}P]B,$$

which can alternately be written as

$$\underline{G}(s) - G(s) = C[\underline{P}(sI - A)^{-1}(\underline{P} - P) + (\underline{P} - P)(sI - A)^{-1}\underline{P} - (\underline{P} - P)(sI - A)^{-1}(\underline{P} - P)]B.$$

Therefore, since there are M arbitrary P_i s in (2.7), we choose these P_i s in P such that P approximates \underline{P} in a suitable norm sense. In order to obtain such a P we propose the following two steps:

Step 1. Determine $X = \text{block diag}\{X_1, X_2, \dots, X_N\}$; ($X_i : (n_i, n_i)$ matrix) to minimize

$$\delta = \|\underline{P} - X\|_2 \quad (2.8)$$

Step 2. Determine $P_i = T_{ir} L_{ir}$ such that $L_{ir} T_{ir} = I_{r_i}$, and $\text{Im}(P_i) = \text{Im}(X_i)$ and $\text{Ker}(P_i) = \text{Ker}(X_i)$.

The solution X to minimize (2.8) is not unique [7]: there exists a central solution, which is $X_i = \underline{P}_{ii}$, $i = 1, 2, \dots, N$, where \underline{P}_{ii} is the (i, i) block entry of \underline{P} ; and several non-central solutions. The central solution is also a 1-norm and ∞ -norm minimizing solution. Obtaining the non-central solution for (1,2)-approximation becomes a constant matrix dilation problem, for which solutions are known. However, the non-central solution to general (M, N) -approximation seems to be an open problem. For any solution (central or non-central) $X = \text{block diag}\{X_i\}$ in step1. above, the explicit construction of P_i , $i = 1, 2, \dots, N$ in step2. can be obtained as given below.

Theorem 1.

Given X_i , the projection P_i with $\text{Im}(P_i) = \text{Im}(X_i)$ and $\text{Ker}(P_i) = \text{Ker}(X_i)$ is constructed as

$$P_i = T_{ir} L_{ir} ; \quad L_{ir} = V_{li}^T ; \quad T_{ir} = U_{li} Y_i^{-1} \quad (2.9a)$$

where U_{li} , V_{li} , and Y_i are obtained from the singular value decomposition of X_i :

$$X_i = \begin{bmatrix} U_{li} & U_{2i} \end{bmatrix} \begin{bmatrix} \Sigma_i & 0 \\ 0 & 0 \end{bmatrix} \begin{bmatrix} V_{li}^T \\ V_{2i}^T \end{bmatrix} ; \quad Y_i \triangleq V_{li}^T U_{li} \quad (2.9b)$$

Corollary 1.

If X_i is idempotent for some i , then the P_i obtained by Theorem1 satisfies $P_i = X_i$.

Corollary 2.

If X_i is isometric (i.e., full rank) for some i , then the P_i obtained by Theorem1 is $P_i = I_{n_i}$.

We summarize our approach to solving the (M, N) -approximation problem in the following procedure:

(M,N)-approximation Procedure:

Step1: Construct the parameters $\{A,B,C,D\}$.

Step2: Determine \underline{P} . (This step is problem dependent; namely, it depends on the properties to be preserved in $S(r)$; see next section for example.).

Step3: Determine the structure of P . (This depends on the internal structure of the system).

Step4: Obtain P_i to minimize $\|\underline{P} - P\|$; $i = 1, 2, \dots, M$. The remaining P_i are unity maps.

(a1) For central solution, set $X_i = \underline{P}_i$.

(a2) For (1,2)-approximation only: for non-central solution, compute X_i by using the expressions given in [7].

(b) Compute L_{ir} and T_{ir} according to Theorem1.

Step5: Obtain the parameters $\{A_{ijr}, B_{ijr}, C_{ijr}\}$ of $S_i(r_i)$ as $A_{ijr} = L_{ir} A_{ij} T_{jr}$, $B_{ijr} = L_{ir} B_{ij}$, $C_{ijr} = C_{ij} T_{jr}$.

3. Application to LQG-controller reduction by q-COVER theory

As an illustration, we apply the above (M,N)-Approximation procedure to the reduction of LQG controllers. Let $S_1(n_1)$ be a model of a plant:

$$\begin{aligned} \dot{x}_1 &= A_{11} x_1 + B_1 w_1 + E y_2 \\ y_1 &= C_{11} x_1 \\ z &= M x_1 + w_2 \end{aligned} \quad \begin{matrix} w_i \in \mathbb{R}^{m_i} \\ y_i \in \mathbb{R}^{k_i} \end{matrix}, \quad i = 1, 2 \quad (3.1)$$

where w_1 is a zero-mean white Gaussian disturbance with intensity $W_1 > 0$, y_2 are the control variables, y_1 are the controlled variables, and z are the measurements corrupted by the zero-mean Gaussian noise w_2 with intensity $W_2 > 0$. Also let the LQG-controller $S_2(n_2)$, with $n_2 = n_1$.

$$\begin{aligned} \dot{x}_2 &= A_{22} x_2 + F z \quad ; \quad x_2 \in \mathbb{R}^{n_2} \\ y_2 &= G x_2 \end{aligned} \quad (3.2)$$

be obtained from minimizing

$$\lim_{t \rightarrow \infty} E \int_0^t \{y_1^T(s) Q_1 y_1(s) + y_2^T(s) Q_2 y_2(s)\} ds \quad (3.3)$$

We wish to obtain a reduced controller $S_2(r_2)$ from $S_2(n_2)$ so that the reduced closed loop system consisting of $S_1(n_1)$ and $S_2(r_2)$ preserves the RMS (root-mean-square) values of every component of some output vector y (y may or may not include y_1 and/or y_2 ; in other words let y be an arbitrary linear combination of x_1 and x_2). This can be achieved via q-COVERs of [2]. This controller reduction process is an (1,2)-approximation. We now illustrate *Steps 1,2 and 3* of the (M,N)-approximation procedure.

Step1: In order to include the interactions between $S_1(n_1)$ and $S_2(n_2)$ in the reduction process, we first need to 'close the loop' as below. In closed loop form the overall system $S(n)$ has dimension $n = n_1 + n_2 = 2n_1$ with two subsystems. The parameters in the subsystem representation of $S(n)$ are now given by $A_{11}=A_{11}$, $A_{12}=EG$, $B_{11}=B_1$, $B_{12}=0$, $A_{21}=FM$, $A_{22}=A_{22}$, $B_{21}=0$, $B_{22}=F$. And let the definition of y lead to arbitrary C_{11} and C_{12} , and $D_{11} = 0$, $D_{12} = 0$.

Step2: Since we wish to use the q-COVER algorithm [2], we elaborate this step as shown below. Now, in order to obtain the projection \underline{P} , we adopt the q-COVER algorithm of [2], with a modification to account for the arbitrary y . We summarize the resulting algorithm below, without proof (the proof follows from a minor modification of that in [2]).

q-COVER algorithm:

a. Define:

$$C_a \triangleq C_{11} + C_{12}$$

b. Construct:

$$O_q^T = \left[C_a^T, A_{22}^T C_a^T, \dots, (A_{22}^T)^{q-1} C_a^T \right]$$

c. Let X_{22} be the steady state covariance of x_2 . Then find the following SVD

$$O_q X_{22} O_q^T = \begin{bmatrix} U_1 & U_2 \end{bmatrix} \begin{bmatrix} \Sigma_2 & 0 \\ 0 & 0 \end{bmatrix} \begin{bmatrix} U_1^T \\ U_2^T \end{bmatrix} ; \quad r_2 = \text{rank}(\Sigma_2).$$

d. Compute:

$$\underline{L}_{2r} = U_1^T O_q ; \quad \underline{T}_{2r} = X_{22} \underline{L}_{2r}^T \Sigma_2^{-1} ; \quad \underline{P}_2 = \underline{T}_{2r} \underline{L}_{2r}.$$

e. Then the desired projection yields

$$\underline{P} = \begin{bmatrix} I_{n_1} & -\underline{P}_2^\perp \\ 0 & \underline{P}_2 \end{bmatrix} ; \quad \text{where} \quad \underline{P}_2^\perp \triangleq I_{n_2} - \underline{P}_2$$

Step3: Since we do not wish to reduce the model of the plant, we set $P_1 = I_{n_1}$. Hence, the required structure for P is block-diag $\{I_{n_1}, P_2\}$.

Proceeding with the (M,N)-approximation procedure, we get $X_1 = I_{n_1}$, and $X_2 = \underline{P}_2$. Since both I_{n_1} and \underline{P}_2 are idempotent, we get the projection $P = \text{block-diag}\{P_1, P_2\} = \text{block-diag}\{I_{n_1}, \underline{P}_2\}$. Notice from $P_1 = I_{n_1}$ that the plant is not being reduced, while the controller is being reduced according to $P_2 = \underline{P}_2$. Thus, from (d) above, we obtain the reduced controller as

$$\begin{aligned} \dot{x}_{2r} &= L_{2r} A_{22} T_{2r} x_{2r} + L_{2r} F z ; \quad x_{2r} \in \mathbb{R}^{r_2} \\ y_{2r} &= G T_{2r} x_{2r} . \end{aligned} \quad (3.4)$$

Remarks:

- (1) When the output vector y , whose values were to be preserved, represents just the control inputs y_2 , the C_a in the q-COVER algorithm becomes G , and the algorithm becomes identical to that in Ref.[8]. The algorithm presented herein is hence a minor generalization of that in [8].
- (2) In the special case when $C_a = G$, both the current method and that in [9] yield the same reduced controller - a fact proven in [8].
- (3) Observe that the minimum value of δ is given by

$$\delta_{\min} = \|\underline{P}_2^\perp\| = \|I_{n_2} - \underline{P}_2\| .$$

4. Properties of Observer based Compensators

The H^∞ -compensators is a derivative of the Youla's parametrization [10] of all stabilizing controllers in terms of a stable parameter matrix. The design aspect of the H^∞ -compensators is based upon observer-based compensators, as proposed by Doyle, et al. [11]. Hence, in order to realize lower order H^∞ -compensators, we will investigate the pole locations, and non-minimality properties of the observer-based compensators. The important results of this investigation are:

- (1) The poles of the closed-loop system with the observer-based controller parametrization are the regulator poles, the observer poles, together with the poles of the added stable parameter matrix.
- (2) If the controller is realized by a minimal realization, then the closed-loop poles will include all the poles of the added stable parameter matrix and a subset of the regulator and the observer poles.

These details are provided in Appendix, which is a copy of a paper submitted to IEEE Transactions in Automatic Control, for possible publications.

References

- [1]. B. A. Francis, J. W. Helton, G. Zames, " H_∞ Optimal Feedback Controllers for Linear Multivariable Systems," *IEEE Trans. Auto. Control*, Vol.AC-29, pp.888-900, 1984.
- [2]. A. Yousuff, D. A. Wagie, R. E. Skelton, "Linear System Approximation via Covariance Equivalent Realizations," *J. Math. Anal. Appl.*, Vol.106, pp.91-115, 1984.
- [3]. B. C. Moore, "Principal Component Analysis in Linear Systems: Controllability, Observability, and Model Reduction," *IEEE Trans. Auto. Control*, Vol.AC-26, pp.17-32, Feb. 1981.
- [4]. K. Glover, "All Optimal Hankel-norm Approximations of Linear Multivariable Systems and their L_∞ -error bounds," *Int. J. Control*, Vol.39, pp.1115-1193, 1984.
- [5]. R. E. Skelton, A. Yousuff, "Component Cost Analysis of Large Scale Systems," *Int. J. Control*, Vol.37, pp.285-304, 1983.

- [6]. P. V. Kokotovic, R. E. O'Molloy, P. Sannuti, "Singular Perturbation and Order Reduction in Control Theory - An Overview," *Automatica*, Vol.12, pp.123-132, 1976.
- [7]. C. Davis, W. M. Kahan, H. F. Weinberger, "Norm-preserving Dilations and their Applications to Optimal Error Bounds," *SIAM J. Numer. Anal.*, Vol.19, pp.445-469, 1982.
- [8]. A. Yousuff, R. E. Skelton, "An Optimal Controller Reduction by Covariance Equivalent Realizations," *IEEE Trans. Auto. Control*, Vol.AC-31, pp.56-60, 1986.
- [9]. A. Yousuff, R. E. Skelton, "Controller Reduction by Component COst Analysis," *IEEE Trans. Auto. Control*, Vol.AC-29, No.6, pp.520-530, June 1984.
- [10]. D. C. Youla, J. J. Bongiorno, H. A. Jabr, "Modern Wiener-Hopf Design of Optimal Controllers, Part II: The Multivariable Case," *IEEE Trans. Auto. Control*, Vol.AC-21, pp.319-338, 1976.
- [11]. J. Doyle, Lecture Notes, *ONR/Honeywell Workshop on Advances in Multivariable Control*, Minneapolis, MN, Oct. 1984.

Appendices can be obtained from
Universal Energy Systems, Inc.

FINAL REPORT NUMBER 98
LATE APPOINTMENT
FINAL REPORT WILL BE PROVIDED WHEN AVAILABLE
Dr. George Zobrist
760-6MG-055

**END
FILMED**

DATE:

8-90

DTIC